Department of Civil and Environmental Engineering

Imperial College London

Effective Seismic Retrofitting of Substandard Multi-Storey Buildings using Shear Walls

Moemen Hajjar

A thesis submitted in fulfilment of the requirements for the degree of Doctor of Philosophy of Imperial College London and the Diploma of Imperial College London

April 2022

'Your living is determined not so much by what life brings to you as by the attitude you bring to life; not so much by what happens to you as by the way your mind looks at what happens.'

Khalil Gibran (1883-1931)
Lebanese-American writer, poet and visual artist

'One day, in retrospect, the years of struggle will strike you as the most beautiful.'

Sigmund Freud (1856-1939)
Austrian Neurologist and the Founder of Psychoanalysis

'Success is not final; failure is not fatal: It is the courage to continue that counts.'

Sir Winston Churchill (1874-1965)
UK prime minister and Nobel Prize-winning writer

'If you really look closely, most overnight successes took a long time.'

Steve Jobs (1955-2011)
CEO and Co-founder of Apple Inc.

Statement of Originality

I hereby certify that the thesis presented in this document is the outcome of my independent and original work. I confirm that ideas and information extracted from work that is produced by others are appropriately acknowledged and referenced throughout the report.

Copyright Declaration

The copyright of this thesis rests with the author. Unless otherwise indicated, its contents are licensed under a Creative Commons Attribution-Non Commercial 4.0 International Licence (CC BY-NC).

Under this licence, you may copy and redistribute the material in any medium or format. You may also create and distribute modified versions of the work. This is on the condition that: you credit the author and do not use it, or any derivative works, for a commercial purpose.

When reusing or sharing this work, ensure you make the licence terms clear to others by naming the licence and linking to the licence text. Where a work has been adapted, you should indicate that the work has been changed and describe those changes.

Please seek permission from the copyright holder for uses of this work that are not included in this licence or permitted under UK Copyright Law.

Abstract

This thesis presents a novel simplified approach for the practical assessment and retrofitting of multi-storey reinforced concrete (RC) buildings located in seismic hazard regions using shear walls, with emphasis on the buildings of Lebanon. In view of this, the retrofitting of existing buildings is currently a process that relies heavily on engineering judgment and layout constraints, which can be an onerous task. Even when retrofitted, such structures would likely respond inelastically under a major earthquake, where the response is most realistically represented by computationally expensive nonlinear time history analysis (NLTHA). Towards reducing such computational demands, a simplified modelling approach is developed based on the capacity spectrum method (CSM), which utilises nonlinear static pushover analysis in conjunction with the dynamic characteristics of a structure to establish whether the seismic capacity of the structure meets the demands of seismic ground motion. The reliability of the CSM requires satisfying the main assumption that the maximum lateral storey drifts are governed by deformations of the fundamental mode of the originally elastic system. This research presents an approach that reduces the torsional effects in the fundamental mode which consequently enforces the predominance of the latter in the seismic response, and this is accomplished by reducing the average Euclidean eccentricity at all storeys. Furthermore, it encompasses a simplified numerical approach that determines the dynamic characteristics of buildings in a simplified manner that avoids the need for assembling the mass and stiffness matrices that is required by conventional eigenvalue analysis. The work is also complemented with a simplified procedure that estimates the pushover response of RC frame buildings reinforced with shear walls through direct application of static analysis. Last, the aforementioned findings are assembled in the context of the CSM in order to build a solid retrofitting strategy that facilitates and guides the strengthening of existing substandard RC frame buildings. Finally, the proposed work is demonstrated using a few case studies of existing RC buildings, and the results are verified against a complete NLTHA performed on ETABS. Therefore, the proposed work offers a new context on structural assessment and promises to bring immediate impact in an attempt to enhance the safety of multi-storey RC buildings under seismic action.

Acknowledgments

First, I want to express my deepest gratitude to my family and in particular to my parents for their love and support throughout my entire life, I would have never been able to achieve anything without them standing by my side, and for that I will be indebted forever.

I also send deepest recognition and appreciation to my PhD supervisors Prof. Bassam Izzuddin and Dr. Lorenzo Macorini. I acknowledge their continual support and patience, particularly during the difficult period dashed by the pandemic, and I will always be grateful for them to help me overcome the challenges encountered during my PhD journey. Indeed, their constructive feedback and constant guidance were key for me to develop new skills and to grow as a person besides achieving the biggest accomplishment of my career to date.

Special thanks are also extended to my co-supervisor in Lebanon Prof. Mounir Mabsout for his encouragement and support, and for his assistance during the data gathering stage conducted in Lebanon. The collaboration with Prof. Mabsout was exciting, and I am always grateful for his mentorship and kindness.

Last, I want to thank all of my current and former colleagues in the Computational Structural Mechanics group for the unforgettable memories we shared in room 317A. To this end, many thanks to Dr. Corrado Chisari, Dr. Adeleke Soyemi, Dr. Bartolomeo Panto, and Dr. Stanyslav Grosman for sharing their knowledge and resources, and for the fruitful discussions that enhanced my knowledge. I also deeply thank Dr. Luis Santos, Dr. Stanyslav Grosman, Dr. Alexandros Nordas, and Dr. Adrien Boyez for their warm welcome and for helping me to integrate when I joined the group, and I hold special regards towards each of Dr. Luca Modenese, Dr. Qili Fang, (Dr.) Haochen Xie, (Dr.) Burak Sahin, (Dr.) Deema Abu Salma, (Dr.) Maria Liapopoulou, (Dr.) Ayse Mujdeci, (Dr.) Xi Chen, (Dr.) Matthew Chuo, (Dr.) Joao Sio, and (Dr.) Mohamed El Ashri for their genuine love and for all the beautiful moments that will always live in my heart.

Table of Contents

Statement of Originality ..... **iv**

Copyright Declaration ..... **v**

Abstract ..... **vi**

Acknowledgments ..... **vii**

Table of Contents ..... **viii**

List of Figures ..... **xii**

List of Tables ..... **xxv**

List of Abbreviations ..... **xxix**

Chapter 1 Introduction **1**

1.1 Introduction 1

1.2 Research Aims and Objectives 5

1.3 Thesis Outline 7

Chapter 2 Literature Review **10**

2.1 General Overview of Earthquakes 10

2.2 Seismic Hazard Assessment of Lebanon 11

2.3 Seismic Hazard and Performance-Based Assessment 13

2.3.1 Level of Seismic Hazard 13

2.3.2 Performance-based Assessment in the Context of Eurocode 8 14

2.4 Seismic Analysis Methods 17

2.5 The Capacity Spectrum Method 19

2.6 The N2 Method 30

2.7 Limitations of Nonlinear Static Procedures and of the CSM 35

2.8 Conventional Seismic Retrofitting Methods of RC Buildings 39

2.9 Shear Capacity of RC Members in Eurocode 41
2.10 Design of Shear Walls According to Eurocode 8 45
2.10.1 General Overview 45
2.10.2 Special Provisions for the Design of Ductile Walls According to Eurocode 8 46
2.10.3 Specialised Detailing for Ductile walls 48
2.11 Concluding Remarks 52

Chapter 3 Seismic Assessment of RC Buildings in the Context of the CSM 54

3.1 Introduction: 54
3.2 Checking against Ductile Failure 56
3.3 Checking against Brittle Shear Failure 60
3.4 Checking the Global Stability of the Building 62
3.5 Seismic Assessment of Existing Buildings in the Context of the CSM 64
3.6 Illustrating Example: Case Study 66
3.6.1 Structural characteristics of the building 66
3.6.2 Modelling of the building and pushover analysis performed on ETABS 69
3.6.3 Pushover analysis in the horizontal X-direction 74
3.6.4 Pushover analysis in the horizontal Y-direction 86
3.6.5 Validation against a complete nonlinear time history analysis 94
3.6.6 The N2 Method 102

Chapter 4 Strategy for Minimising Torsional Effects in the Fundamental Mode 108

4.1 Introduction 108
4.2 Individual and Cumulative Centre of Mass 109
4.3 Centre of Rigidity 110
4.4 Verification of Evaluation of Centre of Rigidity 112
4.5 Optimising Mass Participation 115
4.5.1 Regular building 116
4.5.1.1 Variation of centre of mass in X-direction 117

4.5.1.2 Variation of centre of mass in Y-direction 119
4.5.1.3 Variation of centre of mass in the X- and Y-directions simultaneously . 121
4.5.2 Irregular Building 125
4.6 Summary and Conclusions 129
Chapter 5 Static Analysis and Simplified Frequency Analysis 131
5.1 Introduction 131
5.2 Static Approach 132
5.3 Novel Integrated Static/Frequency Analysis Approach 136
5.3.1 Isolated Shear Wall 136
5.3.2 Integrated Static/Frequency Analysis of a Multi-storey Building 139
5.3.2.1 Assumptions 140
5.3.2.2 Main Challenges 141
5.3.2.3 Establishing Equilibrium Conditions 142
5.3.2.4 Compatibility Requirements 145
5.3.2.5 Influence of flexible base on the force correction at the current level 148
5.3.2.6 Influence of force correction at current floor on lower floors 150
5.3.2.7 Integrated frequency analysis approach 152
5.3.2.8 Finding the vibration characteristics of higher modes 155
5.4 Inclusion of Original Frame 158
Chapter 6 Pushover Response and Contribution of the Original Structure 164
6.1 Introduction 164
6.2 Plastic Limit Analysis 165
6.3 Pushover Response Using Incremental Static Analysis 169
6.3.1 Configurations of walls 170
6.3.2 Simplified approach 171
6.4 Influence of the Original Frame on the Pushover Response 173
Chapter 7 Application and Case Studies 182

7.1 Introduction: 182
7.2 Illustrating the Procedure 183
7.3 Regular Building Scenario 198
7.4 L-shaped Scenario 217
7.5 Building Having Irregularity in Elevation 237
7.6 Effect of the Original Frame and of the Wall Reinforcement 254

Chapter 8 Conclusion and Recommendations 259

8.1 Summary and Conclusion 259
8.1.1 Assessment of Substandard Buildings Located in Seismic Hazard Regions 259
8.1.2 Basis for Ensuring the Applicability of the CSM 259
8.1.3 Static Analysis and Simplified Frequency Analysis 260
8.1.4 Simplified Pushover Response 262
8.1.5 Simplified Strategy for Retrofitting Substandard RC Frame Buildings 263
8.2 Recommendations for Future Work 265
8.2.1 Applicability of the CSM 265
8.2.2 Contribution of the Original Frame into the Overall Response 266
8.2.3 Simplified Retrofitting Strategy 266
8.2.4 General 267

Bibliography 269

Appendices 279

Appendix 2 279
Appendix 3 280
Appendix 4 284
Appendix 7 291

List of Figures

Figure 1.1: Total collapse of construction in Onagawa, Japan after 2011 earthquake (Lekkas et al., 2012) 2

Figure 1.2: Christchurch earthquake (Grant, 2018) 2

Figure 1.3: Illustration of the Capacity Spectrum Method (Peter & Badoux, 2000) 4

Figure 1.4: Capacity Spectrum Method – graphical solution (Zameeruddin & Sangle, 2016) 4

Figure 2.1: Active Faults within Lebanon (Elias et al., 2007) 12

Figure 2.2: Typical hazard curve for a hypothetical site for time intervals of 1 year and 50 years (Solomos et al., 2008) 14

Figure 2.3: Overall process of the CSM (Najam, 2017) 20

Figure 2.4: Graphical solution of the CSM (Zameeruddin & Sangle, 2016) 20

Figure 2.5: Correspondence of a MDOF system into an equivalent SDOF system (ATC, 1996) . 22

Figure 2.6: Evaluation of equivalent viscous damping via the bilinear representation of the capacity spectrum (ATC, 2005) 24

Figure 2.7: Variation of damping modification factor against the displacement ductility ratio (ATC, 1996) 26

Figure 2.8: Variation of the equivalent (effective) damping with the displacement ductility ratio (ATC, 1996) 27

Figure 2.9: Locating the trial performance point through the equal displacement approximation (ATC, 2005) 28

Figure 2.10: Evaluation of the damping coefficient in terms of the effective damping ratio (ATC, 2005) 30

Figure 2.11: Approximating the pushover curve into an equivalent elastic-perfectly plastic bilinear curve (CEN, 2004a) 31

Figure 2.12: Inelastic response spectra for constant ductility values in the N2 method (Fajfar, 2021) 33

Figure 2.13: Evaluation of the seismic displacement demand in the N2 method (Aşıkoğlu et al., 2021) 34

Figure 2.14: Definition of the area of the tensile reinforcement considered in the shear capacity (CEN, 2004b) 43

Figure 2.15: Truss model used in designing the shear reinforcement of members (CEN, 2004b) .. 44

Figure 2.16: Capacity design requirement for flexural design of shear walls (Booth, 2018) 47

Figure 2.17: Capacity design shear requirement for walls under seismic action (Booth, 2018) 48

Figure 2.18: Confined boundary element at the end of the wall's cross-section along with the strains at ultimate curvature (CEN, 2004a) 49

Figure 2.19: Minimum dimensions of boundary elements (CEN, 2004a) 52

Figure 3.1: Illustration of the chord rotation (Murad, 2015) 57

Figure 3.2: Confined and unconfined parts of a member's: (a) circular cross-section with circular hoops; (b) square section and multiple ties (Fardis, 2009) 59

Figure 3.3: Graphical solution of the CSM (Zameeruddin & Sangle, 2016) 65

Figure 3.4: Ground floor plan of the typical building (all dimensions in cm) 68

Figure 3.5: Elastic response spectrum conforming to a PGA of 0.3g – UBC-97 (ICBO, 1997) ... 70

Figure 3.6: Generalised force-deformation relationship of structural members according to ASCE 41-17 (ASCE, 2017) 72

Figure 3.7: Typical modelling of a flexural hinge in ETABS: Immediate Occupancy (DL), Life Safety (SD), Collapse Prevention (NC) 73

Figure 3.8: Modelling of a typical shear hinge in ETABS 74

Figure 3.9: Capacity curve of pushover analysis in the X-direction 75

Figure 3.10: Capacity spectrum of pushover analysis in the X-direction 75

Figure 3.11: Determining the performance point of the CSM in line with the Push-X analysis 76

Figure 3.12: Formation of flexural plastic hinges at the performance point in the Push-X analysis 78

Figure 3.13: Shear hinges obtained in beams and columns at the performance point – Push-X analysis 79

Figure 3.14: Typical sketch of the forces acting on a loaded beam element 80

Figure 3.15: Shear Demand-to-Capacity (D/C) ratio in the beams – Push-X 82

Figure 3.16: Typical sketch of the forces acting on a column 83

Figure 3.17: Shear Demand-to-Capacity (D/C) ratio in the Columns – Push-X 84

Figure 3.18: Interstorey drift ratios – Push-X 85

Figure 3.19: Capacity Curve of pushover analysis in the Y-direction 87

Figure 3.20: Capacity spectrum of pushover analysis in the Y-direction 87

Figure 3.21: Determining the performance point of the CSM in line with the Push-Y analysis 88

Figure 3.22: Flexural plastic hinges obtained at the performance point – Push-Y analysis 89

Figure 3.23: Shear hinges obtained at the performance point – Push-Y analysis 90

Figure 3.24: Demand-to-Capacity shear ratio in the beams – Push-Y 91

Figure 3.25: Demand to Capacity shear ratio in the Columns – Push-Y 92

Figure 3.26: Interstorey drift ratios – Push-Y 93

Figure 3.27: The three components of the CNRS ground motion time history: (a) EW direction, (b) NS direction, (c) Z-direction 96

Figure 3.28: Spectral matching of the EW component of the ground motion “CNRS” with the response spectrum corresponding to the SD limit state 97

Figure 3.29: Flexural plastic hinges obtained at the end of the NLTHA 98

Figure 3.30: Shear D/C ratios in the beams under NLTHA 99

Figure 3.31: Shear D/C ratio in the columns in the X-direction under NLTHA 100

Figure 3.32: Shear D/C ratio in the columns in the Y-direction under NLTHA 101

Figure 3.33: Interstorey drift ratios– NLTHA 102

Figure 3.34: Idealisation of the capacity spectrum in the Y-direction (mode 1) into a bilinear curve 103

Figure 3.35: Idealisation of the capacity spectrum in the X-direction (mode 2) into a bilinear curve 104

Figure 3.36: Evaluation of the target displacement in the Y-direction (mode 1) according to the N2 method 105

Figure 3.37: Evaluation of the target displacement in the X-direction (mode 2) according to the N2 method 105

Figure 3.38: Definition of spectral load case in the elastic dynamic analysis performed on ETABS 107

Figure 4.1: First layout of the six-storey building used to verify the calculation of the CR..... 112

Figure 4.2: Second layout of the 6-storey building used to verify the accuracy of the developed procedure 114

Figure 4.3: Typical floor plan of regular six-storey building 116

Figure 4.4: Six-storey regular building with the centre of mass varying in the X-direction 117

Figure 4.5: Plot of the mass participation in the Y-direction versus the cumulative eccentricity as the centre of mass varies in the X-direction 118

Figure 4.6: Plot of the mass participation in the Y-direction versus the average Euclidean eccentricity as the centre of mass varies in the X-direction 119

Figure 4.7: Six-storey regular building with the centre of mass varying in the Y-direction 119

Figure 4.8: Plot of the mass participation in the X-direction versus the cumulative eccentricity as the centre of mass varies in the Y-direction 120

Figure 4.9: Plot of the mass participation in the X-direction versus the average Euclidean eccentricity as the centre of mass varies in the Y-direction 121

Figure 4.10: Six-storey regular building with the centre of mass varying in the X- and Y-directions 122

Figure 4.11: Plot of the mass participation in the X-direction versus the cumulative eccentricity as the centre of mass varies in the X and Y directions simultaneously 123

Figure 4.12: Plot of the mass participation in the Y-direction versus the cumulative eccentricity as the centre of mass varies in the X and Y directions simultaneously 123

Figure 4.13: Plot of the mass participation in the X-direction versus the average Euclidean eccentricity as the centre of mass varies in the X and Y directions simultaneously . 124

Figure 4.14: Plot of the mass participation in the X-direction versus the average Euclidean eccentricity as the centre of mass varies in the X and Y directions simultaneously . 124

Figure 4.15: Nine-storey irregular building with the centre of mass varying in the X and Y directions: (a) Storeys 7 to 9, (b) Storeys 1 to 6..... 126

Figure 4.16: Plot of the mass participation in the Y-direction versus the cumulative eccentricity in the X-direction in the irregular building..... 126

Figure 4.17: Plot of the mass participation in the Y-direction versus the average Euclidean eccentricity in the irregular building 127

Figure 4.18: Plot of the mass participation in the X-direction versus the cumulative eccentricity in the Y-direction in the irregular building..... 128

Figure 4.19: Plot of the mass participation in the X-direction versus the average Euclidean eccentricity in the irregular building 129

Figure 5.1: Assembly of stiffness matrix of each vertical element in the building 133

Figure 5.2: Typical representation of the walls displacements and the floor resultant displacements 134

Figure 5.3: Typical wall elevation 137

Figure 5.4: Wall segment at typical floor 138

Figure 5.5: Sketching the main DOFs and the flow of events in the static analysis of the building 142

Figure 5.6: Typical floor plan – interaction between the walls and the mode shape 143

Figure 5.7: Ideal and realistic behaviours in response to a force correction at the top of the wall segment 149

Figure 5.8: Carry-over of moment at top of wall segment to the base 150

Figure 5.9: Expression of rotation at the top of the wall segment 151

Figure 5.10: Flowchart of the static analysis procedure 154

Figure 5.11: Flowchart of the frequency analysis procedure 154

Figure 5.12: Flowchart of the integrated approach combining the iterations of the static and frequency analyses 155

Figure 5.13: Illustrating the process of finding the stiffness contribution of the original frame ... 160

Figure 5.14: Typical floor plan of original frame building along with the reinforcing walls 161

Figure 6.1: Typical 3-D representation of applied loads 167

Figure 6.2: Typical floorplan and applied loading 168

Figure 6.3: Configurations of walls 170

Figure 6.4: Typical pushover response obtained using the simplified approach 172

Figure 6.5: Equivalent pushover response including the frame effect: left vertical axis (Base Shear P), right vertical axis (Collapse Load Factor λ), horizontal axis (Displacement d) .. 174

Figure 6.6: Typical floor plan of original frame building along with the reinforcing walls 177

Figure 6.7: Location of the plastic hinges in the walls 178

Figure 6.8: Pushover response in proportion to the fundamental mode 178

Figure 6.9: Complete pushover response in proportion to the fundamental mode 181

Figure 7.1: Total loads applied on the wall 187

Figure 7.2: Variation of moment and curvature in the shear span of a typical cantilever (Fardis, 2009) 191

Figure 7.3: Confined and unconfined parts of a member's: (a) circular cross-section with circular hoops; or (b) square section and multiple ties (Fardis, 2009) 196

Figure 7.4: Ground floor plan and typical layout of the regular-shaped building (dimensions in cm) 199

Figure 7.5: Location of reinforcing walls in the rectangular building (dimensions in cm) 200

Figure 7.6: Typical detailing of walls above the critical region 201

Figure 7.7: Detailing of Walls in the critical region (dimensions in mm) 202

Figure 7.8: Procedure of finding the performance point of the Push-X analysis (Mode 2) at the NC limit state in the rectangular building (Step 1) 204

Figure 7.9: Procedure of finding the performance point of the Push-X analysis (Mode 2) at the NC limit state in the rectangular building (Step 2) 205

Figure 7.10: Procedure of finding the performance point of the Push-X analysis (Mode 2) at the NC limit state in the rectangular building (Step 3) 206

Figure 7.11: Checking the flexural requirements of walls in the rectangular building..... 208

Figure 7.12: Checking the shear requirements of walls in the rectangular building 208

Figure 7.13: Flexural hinges at the NC limit state in the rectangular building..... 210

Figure 7.14: Flexural hinges at the SD limit state in the rectangular building 210

Figure 7.15: Labels of beams and columns in the rectangular building 211

Figure 7.16: NSPA results of the shear D/C ratio measured along the major bending axis of columns in the rectangular building..... 212

Figure 7.17: NSPA results of the shear D/C ratio measured along the weak axis of columns in the rectangular building..... 212

Figure 7.18: NSPA results of the shear D/C ratio measured along the strong bending axis of beams in the rectangular building..... 213

Figure 7.19: Flexural hinges obtained at the end of the NLTHA performed in the rectangular building (ecc. ±5% in X) 214

Figure 7.20: Flexural hinges obtained at the end of the NLTHA performed in the rectangular building (ecc. ±5% in Y) 215

Figure 7.21: NLTHA results of the shear D/C ratio measured along the major bending axis of columns in the rectangular building 216

Figure 7.22: NLTHA results of the shear D/C ratio measured along the weak axis of columns in the rectangular building 216

Figure 7.23: NLTHA results of the shear D/C ratio measured along the strong bending axis of beams in the rectangular building 217

Figure 7.24: Optimising the mass participation ratio of the fundamental modes in the L-shaped building 218

Figure 7.25: Ground floor plan and reinforcing walls in the L-shaped building (dimensions in cm) 218

Figure 7.26: Alternative retrofitting scenario of the L-shaped building (dimensions in cm) 219

Figure 7.27: Checking the flexural requirements of walls in the L-shaped building 224

Figure 7.28: Checking the shear requirements of walls in the L-shaped building 225

Figure 7.29: Flexural hinges at the NC limit state in the L-shaped building 226

Figure 7.30: Flexural hinges at the SD limit state in the L-shaped building 227

Figure 7.31: Labels of beams and columns in the L-shaped building 228

Figure 7.32: NSPA results of the shear D/C ratio measured along the major bending axis of columns in the L-shaped building 229

Figure 7.33: NSPA results of the shear D/C ratio measured along the weak axis of columns in the L-shaped building 229

Figure 7.34: NSPA results of the shear D/C ratio measured along the strong bending axis of beams in the L-shaped building 230

Figure 7.35: Flexural hinges obtained at the end of the NLTHA performed in the L-shaped building (ecc. +5% in X) 231

Figure 7.36: Flexural hinges obtained at the end of the NLTHA performed in the L-shaped building (ecc. -5% in X) 232

Figure 7.37: Flexural hinges obtained at the end of the NLTHA performed in the L-shaped building (ecc. +5% in Y) 233

Figure 7.38: Flexural hinges obtained at the end of the NLTHA performed in the L-shaped building (ecc. -5% in Y) 234

Figure 7.39: NLTHA results of the shear D/C ratio measured along the major bending axis of columns in the L-shaped building 235

Figure 7.40: NLTHA results of the shear D/C ratio measured along the weak axis of columns in the L-shaped building 236

Figure 7.41: NLTHA results of the shear D/C ratio measured along the strong bending axis of beams in the L-shaped building 236

Figure 7.42: Optimising the mass participation of the fundamental modes in the vertically irregular building 238

Figure 7.43: Ground floor plan of the vertically irregular building and characteristic layout up to the 7^{th} floor (dimensions in cm) 238

Figure 7.44: Eighth floor plan and characteristic layout of the 8^{th}, 9^{th}, and 10^{th} floors of the vertically irregular building (dimensions in cm) 239

Figure 7.45: Detailing of Wall 6 in the critical region in the vertically irregular building (dimensions in mm) 240

Figure 7.46: Checking the flexural requirements of walls in the vertically irregular building 243

Figure 7.47: Checking the shear requirements of walls in the vertically irregular building 244

Figure 7.48: Flexural hinges at the NC limit state in the vertically irregular building 246

Figure 7.49: Flexural hinges at the SD limit state in the vertically irregular building 247

Figure 7.50: Labels of beams and columns in the in the vertically irregular building 248

Figure 7.51: NSPA results of the shear D/C ratio measured along the major bending axis of columns in the vertically irregular building 248

Figure 7.52: NSPA results of the shear D/C ratio measured along the weak axis of columns in the vertically irregular building 249

Figure 7.53: NSPA results of the shear D/C ratio measured along the strong bending axis of beams in the vertically irregular building 249

Figure 7.54: Flexural hinges obtained at the end of the NLTHA performed in the vertically irregular building (ecc. +5% in X) 250

Figure 7.55: Flexural hinges obtained at the end of the NLTHA performed in the vertically irregular building (ecc. -5% in X) 251

Figure 7.56: Flexural hinges obtained at the end of the NLTHA performed in the vertically irregular building (ecc. ±5% in Y) 252

Figure 7.57: NLTHA results of the shear D/C ratio measured along the major bending axis of columns in the vertically irregular building 253

Figure 7.58: NLTHA results of the shear D/C ratio measured along the weak axis of columns in the vertically irregular building 253

Figure 7.59: NLTHA results of the shear D/C ratio measured along the strong bending axis of beams in the vertically irregular building 254

Figure 7.60: General layout of building and location of shear walls 255

Figure 7.61: Variation of the pushover response in the Y-direction against the plastic capacity of the walls 256

Figure 7.62: Variation of the pushover response in the X-direction against the plastic capacity of the walls 256

Figure 7.63: Roof displacement measured at the performance point at the NC limit state 257

Figure A3.1: Detailing of longitudinal and transversal reinforcement in the columns cross-sections 280

Figure A3.2: Detailing of longitudinal and transversal reinforcement in the beams cross-sections 281

Figure A3.3: Modelling parameters and acceptance criteria for RC beams (ASCE, 2017) 282

Figure A3.4: Modelling parameters and acceptance criteria for RC rectangular columns (ASCE, 2017) 283

Figure A4.1: Criteria for regularity of buildings in elevation in the presence of setbacks (CEN, 2004a) 290

Figure A7.1: General layout of rectangular building (Dimensions in cm) 291

Figure A7.2: Performance point of the Push-Y analysis (Mode 1) at the NC limit state in the rectangular building scenario 292

Figure A7.3: Performance point of the Push-X analysis (Mode 2) at the NC limit state in the rectangular building scenario 292

Figure A7.4: Performance point of the Push-Y analysis (Mode 1) at the SD limit state in the rectangular building scenario 292

Figure A7.5: Performance point of the Push-X analysis (Mode 2) at the SD limit state in the rectangular building scenario 293

Figure A7.6: General layout of L-shaped building (Dimensions in cm) 293

Figure A7.7: Performance point of the Push-Y analysis (Mode 1) at the NC limit state in the L-shaped building (+5% eccentricity in X) 294

Figure A7.8: Performance point of the Push-Y analysis (Mode 1) at the NC limit state in the L-shaped building (-5% eccentricity in X) 294

Figure A7.9: Performance point of the Push-Y analysis (Mode 1) at the SD limit state in the L-shaped building (+5% eccentricity in X) 295

Figure A7.10: Performance point of the Push-Y analysis (Mode 1) at the SD limit state in the L-shaped building (-5% eccentricity in X) 295

Figure A7.11: Performance point of the Push-X analysis (Mode 2) at the NC limit state in the L-shaped building (+5% eccentricity in Y) 295

Figure A7.12: Performance point of the Push-X analysis (Mode 2) at the NC limit state in the L-shaped building (-5% eccentricity in Y) 296

Figure A7.13: Performance point of the Push-X analysis (Mode 2) at the SD limit state in the L-shaped building (+5% eccentricity in Y) 296

Figure A7.14: Performance point of the Push-X analysis (Mode 2) at the SD limit state in the L-shaped building (-5% eccentricity in Y) 296

Figure A7.15: General layout of vertically irregular building from the Ground till the 7th floor (dimensions in cm) 297

Figure A7.16: General layout of vertically irregular building from the 8th till the 10th floor (dimensions in cm) 297

Figure A7.17: Performance point of the Push-Y analysis (Mode 1) at the NC limit state in the vertically irregular building (+5% eccentricity in X) 298

Figure A7.18: Performance point of the Push-Y analysis (Mode 1) at the NC limit state in the vertically irregular building (-5% eccentricity in X) 298

Figure A7.19: Performance point of the Push-Y analysis (Mode 1) at the SD limit state in the vertically irregular building (+5% eccentricity in X) 299

Figure A7.20: Performance point of the Push-Y analysis (Mode 1) at the SD limit state in the vertically irregular building (-5% eccentricity in X) 299

Figure A7.21: Performance point of the Push-X analysis (Mode 2) at the NC limit state in the vertically irregular building (±5% eccentricity in Y) 299

Figure A7.22: Performance point of the Push-X analysis (Mode 2) at the SD limit state in the vertically irregular building (±5% eccentricity in Y) 300

Figure A7.23: The three components of the artificially generated ground motion “ATL1” 300

Figure A7.24: The three components of the artificially generated ground motion “CERD” 300

Figure A7.25: The three components of the artificially generated ground motion “CHYA” 301

Figure A7.26: The three components of the artificially generated ground motion “CLWE” 301

Figure A7.27: The three components of the artificially generated ground motion “CNRS” 301

Figure A7.28: The three components of the artificially generated ground motion “ECPT” 302

Figure A7.29: The three components of the artificially generated ground motion “MTSA” 302

Figure A7.30: Analysis cases considering all possible scenarios of accidental eccentricity (Avramidis et al., 2016)..... 303

List of Tables

Table 3-1: Allowable deformation in existing buildings in compliance with EC8-3 (CEN, 2005a) 57

Table 3-2: Maximum allowable limit of interstorey drift ratio as recommended by ATC-40 (ATC, 1996) 64

Table 3-3: Dimensions and reinforcement of beams at all storey levels 68

Table 3-4: Dimensions and steel reinforcement of columns 69

Table 3-5: Vibration characteristics of the fundamental mode in the main horizontal directions 71

Table 3-6: Iterative process of finding the performance point in the Push-X analysis 76

Table 3-7: Results of the Push-X analysis at the performance point 77

Table 3-8: Calculation of the shear D/C ratio in the beams – Push-X 81

Table 3-9: Interstorey drift results – Push-X 85

Table 3-10: Checking the second-order effect (P-Δ) in the Push-X analysis 86

Table 3-11: Iterative process of finding the performance point in the Push-Y analysis 88

Table 3-12: Results of the Push-Y analysis at the performance point 88

Table 3-13: Interstorey drift results – Push-Y 93

Table 3-14: Checking the second-order effects (P-Δ) in the Push-Y analysis 94

Table 3-15: Load combinations of EN 1992-1-1 (CEN, 2004b): DL (total dead load), LL (live load), EQ (ground motion earthquake load) 96

Table 3-16: Direction of shear for all categories of columns 100

Table 3-17: Interstorey drift results obtained from the NLTHA 102

Table 3-18: Calculating the ductility ratio by equivalent linearisation of the capacity curve 104

Table 3-19: Calculating the seismic displacements using the N2 method 106

Table 3-20: Comparing the CSM and the N2 method against the integrated NLTHA 107

Table 4-1: Calculation of the centre of rigidity of the first building scenario 113

Table 4-2: Calculation of the centre of rigidity of the second building scenario 114

Table 5-1: Fundamental mode shape and frequency based on the walls 162

Table 5-2: Calculating the stiffness of the frame and the effective frequency of vibration of the building 162

Table 5-3: Illustrating the iterative process towards convergence of the integrated frequency analysis approach 163

Table 6-1: Initial pushover loads proportional to the fundamental mode 177

Table 6-2: Setting up the solution for plastic limit analysis 179

Table 6-3: Bending moments in the walls obtained from plastic limit analysis 179

Table 7-1: Load combinations of EN 1990 (CEN, 2002): DL (dead load), LL (live load), EQ (earthquake load) 198

Table 7-2: Verification of the axial load-resisting capacity per unit length of wall in the rectangular building 200

Table 7-3: Preliminary estimate of the base moment and shear demand in the rectangular building 201

Table 7-4: Dimensioning of boundary elements and the major checks performed in the rectangular building 201

Table 7-5: Fundamental vibration characteristics of the rectangular building 202

Table 7-6: Summary of all the CSM analyses performed in the rectangular building 203

Table 7-7: Provisioned flexural and shear reinforcement of walls in the rectangular building 207

Table 7-8: Checking the flexural requirements of walls in the rectangular building 207

Table 7-9: Checking the shear requirements of walls in the rectangular building 208

Table 7-10: Verification of the local ductility requirements in the shear walls of the rectangular building 209

Table 7-11: Groups of columns considered in the rectangular building 211

Table 7-12: Preliminary dimensions of walls in the L-shaped building 220

Table 7-13: Modal mass participation of the retrofitting scenarios considered in the L-shaped building 220

Table 7-14: Verification of the axial load-resisting capacity per unit length of wall in the L-shaped building 220

Table 7-15: Preliminary estimate of the base moment and shear demand in the L-shaped building 221

Table 7-16: Fundamental vibration characteristics of the L-shaped building 221

Table 7-17: Summary of all the CSM analyses performed in the L-shaped building 222

Table 7-18: Provisioned flexural reinforcement of walls in the L-shaped building 222

Table 7-19: Provisioned shear reinforcement of walls in the L-shaped building 223

Table 7-20: Checking the flexural requirements of walls in the L-shaped building 223

Table 7-21: Checking the shear requirements of walls in the L-shaped building 224

Table 7-22: Verification of the local ductility requirements in the shear walls of the L-shaped building 225

Table 7-23: Verification of the axial load-resisting capacity in the vertically irregular building. 239

Table 7-24: Preliminary estimate of the base moment and shear demand in the vertically irregular building 240

Table 7-25: Boundary elements and the associated checks performed in the vertically irregular building 240

Table 7-26: Fundamental vibration characteristics of the vertically irregular building 241

Table 7-27: Summary of all the CSM analyses performed in the rectangular building 241

Table 7-28: Provisioned flexural reinforcement of walls in the vertically irregular building 242

Table 7-29: Provisioned shear reinforcement of walls in the vertically irregular building 242

Table 7-30: Checking the flexural requirements of walls in the vertically irregular building..... 243

Table 7-31: Checking the shear requirements of walls in the vertically irregular building..... 244

Table 7-32: Verification of the local ductility requirements in the walls of the vertically irregular building 245

Table 7-33: Characteristic properties of the three wall scenarios considered..... 255

Table A7.1: Typical dimensions of beams in the rectangular building (dimensions in mm)..... 291

Table A7.2: Typical dimensions of columns in the rectangular building (dimensions in mm) 291

Table A7.3: Typical dimensions of beams in the L-shaped building (dimensions in mm)..... 294

Table A7.4: Typical dimensions of columns in the L-shaped building (dimensions in mm) 294

Table A7.5: Typical dimensions of beams in the vertically irregular building (dimensions in mm) 298

Table A7.6: Typical dimensions of columns in the vertically irregular building (dimensions in mm) 298

List of Abbreviations

ADRS	Acceleration-Displacement Response Spectrum
ASCE	American Society of Civil Engineers
ATC	Applied Technology Council
CCM	Cumulative Centre of Mass
CQC	Complete Quadratic Combination
CR	Centre of Rigidity
CSM	Capacity Spectrum Method
D/C	Demand-to-Capacity Ratio
DCM	Medium Ductility
DCH	High Ductility
DL	Damage Limitation
DOF	Degree of Freedom
DSA	Design Seismic Action
EC8-1	Part 1 of Eurocode 8 (EN 1998-1:2004)
EC8-3	Part 3 of Eurocode 8 (EN 1998-3:2005)
FEMA	Federal emergency Management Agency
IBC	International Building Code
MMP	Multi-Mode Pushover
MDOF	Multiple Degree of Freedom
MRF	Moment Resisting Frame
NC	Near Collapse
NLTHA	Nonlinear Time History Analysis
NSP	Nonlinear Static Procedure
NSPA	Nonlinear Static Pushover Analysis
P-Δ	P-Delta (Second-Order Effects)
PGA	Peak Ground Acceleration
Push-X	Pushover Analysis in the X-Direction

Push-Y	Pushover Analysis in the Y-Direction
RC	Reinforced Concrete
SD	Significant Damage
SDOF	Single Degree of Freedom
SRSS	Square Root of Sum of Squares
UBC	Uniform Building Code
US	United States

Chapter 1 Introduction

1.1 Introduction

Historical seismic records have always shed light on the devastating consequences of earthquakes in terms of fatalities and extent of damage (Figure 1.1). It is estimated that the planet has suffered more than 1200 destructive earthquakes during the twentieth century which caused an annual loss of $10 billion (Coburn & Spence, 2002), while other studies by Bolt (1999, 2004) estimated an average loss of 10,000 people per year during that period due to earthquakes. According to Dowrick (1988), the extent of damage and loss of lives during earthquakes mostly depends on the type and quality of construction rather than the strength of the seismic event (Figure 1.2). Fardis (2009) also pointed out that provisions for seismic design and detailing of buildings have only been introduced in the mid-70's in the US standards and in the mid-80's in the European standards. Prior to these dates, the lateral resistance of buildings around the world was mostly limited to the resistance to wind loading. In this respect, a great proportion of existing buildings located in seismic regions are considered to be seismically deficient as they were not designed to resist any form of earthquake loading (Fardis, 2009). In this respect, seismic retrofitting of existing vulnerable buildings is as important as properly designing new buildings, especially in countries that were recently re-evaluated to be located in seismic hazard regions. Seismic records also reported that many fine old buildings have been replaced upon exposure to earthquakes, despite the cost of repair and strengthening being much cheaper (Dowrick, 1988). Hence, the assessment and strengthening of existing substandard buildings is essential in order to avoid potential loss of human lives and is also crucial from an economic and social perspective as well. This research is mainly concerned with the assessment and retrofitting of multi-storey buildings located in seismic hazard regions, with emphasis on reinforced concrete (RC) buildings and on the use of shear walls as a retrofitting solution. Hence, the research will target selecting typical multi-storey building configurations for detailed assessment of their seismic capacity and adequacy against earthquakes, and the development of practical seismic retrofitting methods.

In light of the above, most of the internationally recognised design codes require buildings located in seismic hazard regions to be designed and detailed to resist seismic loading. To this end, linear versus nonlinear and static versus dynamic offer a framework for the classification of the various methods available for the analysis of existing buildings and design of new ones. While static analysis consists of approximating the earthquake through a load that is statically applied to the structure, dynamic analysis is considered to be the most accurate approach to model the structural response to earthquakes (Elnashai & Di Sarno, 2015), despite being more technically and computationally demanding compared to static analysis. Furthermore, studies by Campbell & Bozorgnia (2004) have shown that most types of

structures respond inelastically to major earthquakes. To this end, strong ground motions result in large deformations and are accordingly associated with high levels of stress that most structures could not

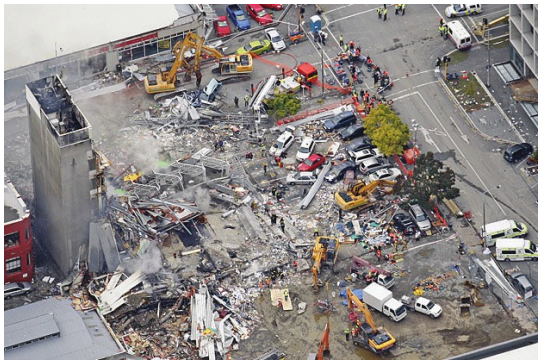


Figure 1.1: Total collapse of construction in Onagawa, Japan after 2011 earthquake (Lekkas et al., 2012)

CANTERBURY TELEVISION BUILDING (1980S DESIGN)



CTV Building before the 2011 Christchurch earthquake. Following 2010 event, engineer's report recommended repair of superficial damage but declared building safe. (http://thenamelessblog-john.blogspot.com/)



Aerial view of collapsed CTV Building (NZ Herald / Sarah Ivey)



185 people killed in CTV building collapse(NZ Herald / Dean Purcell)

Figure 1.2: Christchurch earthquake (Grant, 2018)

sustain in the elastic range (Biot, 1941). Hence, most structures are expected to surpass the elastic limit and behave inelastically under severe earthquakes, and their survival mainly depends on their proper inelastic behaviour and hysteretic energy dissipation (Campbell & Bozorgnia, 2004).

In this context, most of the modern seismic design codes encompass provisions for the application of nonlinear time history analysis (NLTHA), which is a form of dynamic analysis that is considered to provide the most realistic representation of the response of structures to seismic loading (Chopra, 2005). The earthquake load is represented by a ground motion record that is directly applied to the structure, which permits the evaluation of the response of the structure to the applied seismic loading. Unlike linear time history analysis which assumes constant structural properties (stiffness parameters) over the entire duration of loading, NLTHA is based on adjusting the stiffness properties at the beginning of each time step to account for the accumulating inelasticity. Hence, NLTHA is considered to provide the most accurate representation of the response of buildings to earthquake loading and is widely adopted in the seismic design of new buildings and the assessment of existing ones.

Notwithstanding the above benefits, NLTHA is criticised for being too complex and time consuming especially when used for the analysis of large-scale structures. Not to mention that most of the commonly applied seismic codes, including the provisions of Eurocode 8 known as EN 1998-3:2005 (CEN, 2005a) as well as provisions of the American Society of Civil Engineers ASCE 7-16 (ASCE, 2016) and the International Building Code IBC 2016 (ICC, 2015), require a minimum set of 7 ground motion time histories to represent the earthquake loading, with the ultimate response being evaluated as the average of the individual responses to the ground motions considered. To this end, the computational requirements can be substantially reduced if a nonlinear static analysis is used instead in combination with a simplified procedure to determine the maximum dynamic deformations of the structure. In light of this, the capacity spectrum method (CSM) utilises nonlinear static pushover analysis in conjunction with the initial dynamic characteristics of the structure to establish whether the seismic capacity meets the demands of seismic ground motion (ATC, 1982, 1996; Freeman, 1998). The CSM is an approximative nonlinear static analysis method that was originally developed as a tool to assess the seismic vulnerability of buildings at the Puget Naval Shipyard (Freeman et al., 1975). Few years later, the procedure was used as a graphical solution to compare the seismic capacity of a structure against the earthquake ground motion demand (ATC, 1982). In the context of the CSM, the pushover response is referred to as the capacity curve and represents a plot of the base shear versus the lateral roof displacement. Using the dynamic vibration characteristics of the structure, the capacity curve is converted into the capacity spectrum, a plot of the spectral acceleration versus the spectral displacement (Figure 1.3). This allows for a direct comparison with the earthquake demand which is also plotted in the form of spectral acceleration versus spectral displacement, which is better known as the acceleration-displacement response spectrum (ADRS). Hence, the final output of the CSM is a graphical representation of the capacity of a structure versus the demands of earthquake loading,

permitting a visual evaluation of the response of the structure when subjected to the specified ground motion (Figure 1.4). The CSM was shown to be an efficient and reliable tool for the seismic analysis of frame buildings (Freeman, 1998; Sasaki et al., 1998).

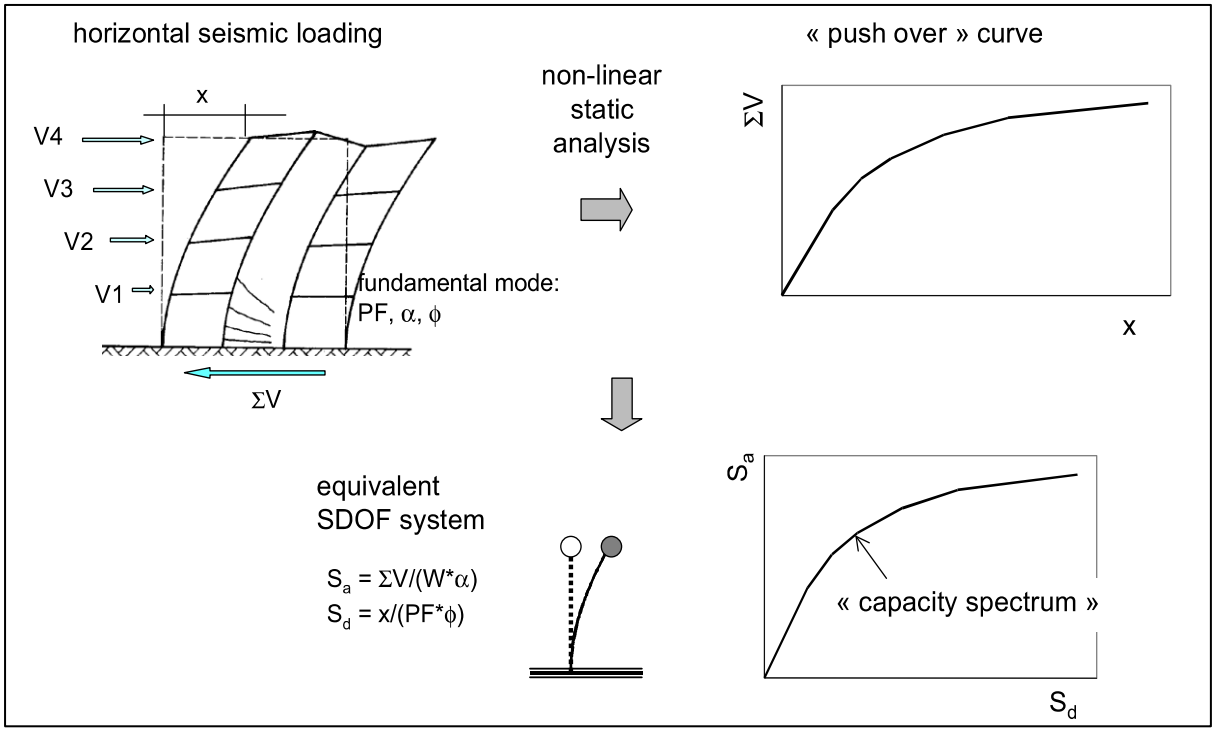


Figure 1.3: Illustration of the Capacity Spectrum Method (Peter & Badoux, 2000)

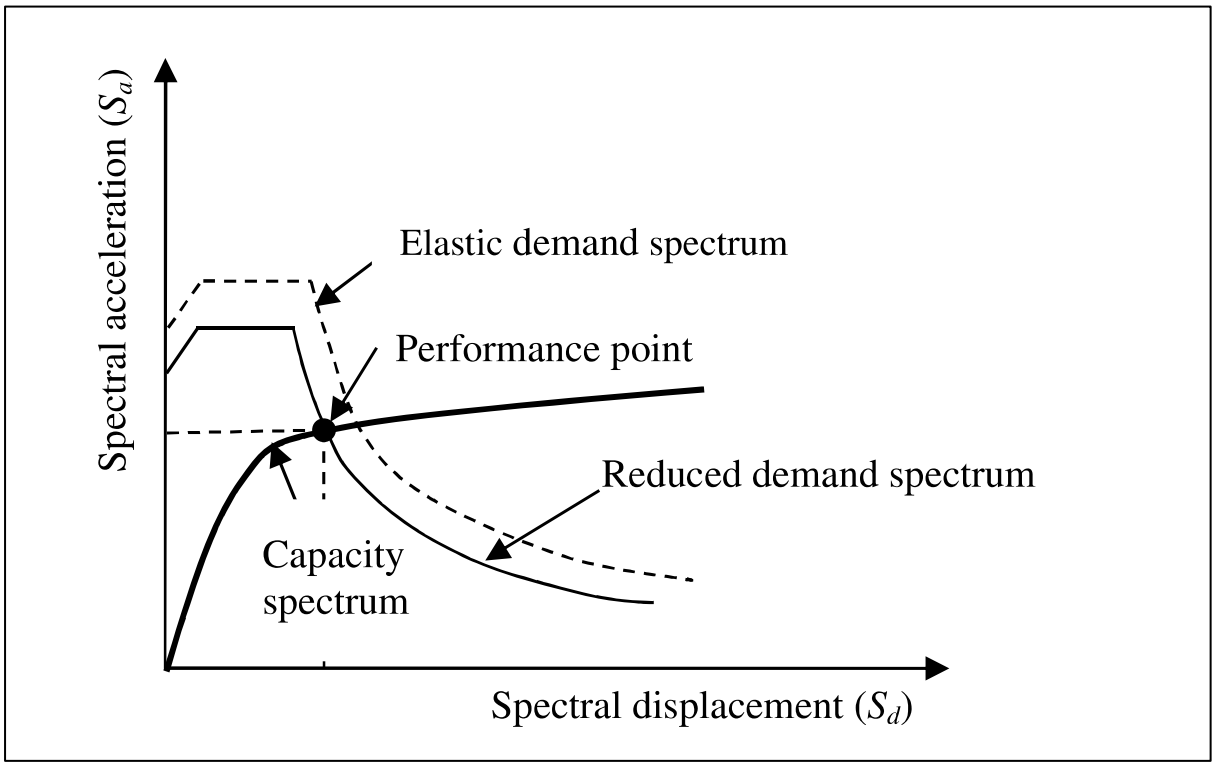


Figure 1.4: Capacity Spectrum Method – graphical solution (Zameeruddin & Sangle, 2016)

Referring to Figure 1.4, the intersection of the capacity and demand curves marks the response of the structure (performance point) when subjected to the applied seismic loading. The maximum lateral roof displacement and other performance criteria are subsequently determined and compared against the limits permitted by design codes to check the adequacy of the structure against the applied seismic loading.

This research aims at enhancing the seismic performance of substandard multi-storey RC buildings located in seismic hazard regions. It presents a novel simplified approach for the practical assessment and retrofitting of substandard multi-storey RC buildings located in seismic hazard regions, with emphasis on the buildings of Lebanon, a country located in a seismically active region while most of its buildings were not designed to resist earthquakes. In this context, the retrofitting of an existing substandard building is currently a process that relies heavily on engineering judgment and layout constraints, which can be an onerous task, and this is exacerbated with the use of computationally demanding NLTHA. In view of this, this research focuses on developing simplified and practical methods for determining the dynamic characteristics and the nonlinear pushover response of RC buildings. The simplified methods are then applied in conjunction with the CSM in order to develop a design method that facilitates the sizing and proportioning of retrofitting systems for substandard RC buildings using shear walls. Hence the work could be idealised as a simplified method to design the seismic retrofitting practice of multi-storey RC buildings subjected to earthquakes. Results are finally checked against the full nonlinear dynamic analysis (NLTHA) with the aim of validating the effectiveness of the proposed approach in determining the seismic response.

Therefore, the proposed work offers a practical set of methods in support of the structural assessment of RC building structures retrofitted with shear walls, promising to bring immediate impact towards enhancing the safety of multi-storey RC buildings under seismic action.

1.2 Research Aims and Objectives

This research aims at presenting a novel simplified approach for the practical assessment and the use of shear walls to retrofit substandard multi-storey RC buildings located in seismic hazard regions. Hence, the ultimate objective is to establish a practical approach to ease and optimise the design of retrofitting systems for seismically deficient RC buildings.

To begin with, this research is pivoted around the CSM which is an already established nonlinear static pushover analysis that makes use of the dynamic characteristics of a structure to establish whether the seismic capacity of the structure meets the demands of seismic ground motion. The CSM is based on the simplified assumption that the maximum lateral storey drifts are governed by deformations of the fundamental mode of the originally elastic system (Freeman, 1998). Therefore, the method is considered to be inappropriate for the analysis of buildings where the maximum storey drifts are not governed by

the fundamental mode, such as tall buildings (more than about 15 stories) or buildings under shock-like impacts (Peter & Badoux, 2000). Furthermore, multi-storey buildings having structural plan or vertical irregularities generally vibrate in a coupled lateral-torsional motion when subjected to ground seismic motions (Doudoumis & Doudoumis, 2017). Hence, the presence of plan or vertical irregularities is expected to reduce the mass participation of the translational component of the fundamental mode and to reduce the reliability of the CSM, especially if an elastic first mode force distribution is adopted. It is therefore essential to develop an approach that enforces the predominance of the fundamental mode of vibration on the structural response such that the CSM can be applied with confidence, and the implemented retrofitting procedure could be standardised to be applied to various configurations including regular and irregular buildings. This is one of the main objectives of the current research, and it involves a novel approach proposed for maximising the translational component of the fundamental mode and ensuring the applicability of the CSM, which is the focal point of the retrofitting strategy that is developed in this research.

As already noted, the CSM makes use of the dynamic characteristics of a structure to establish whether the seismic capacity of the structure meets the seismic demands. Therefore, the procedure requires finding the fundamental vibration mode, which is ordinarily obtained using conventional direct modal analysis that requires assembling the mass and stiffness matrices to solve the eigenvalue problem (Chopra, 2014). This typically imposes a significant computational bottleneck for practical application in the optimal design of retrofitting, where numerous retrofitting strategies would typically need to be considered. In this respect, another main objective of this research focuses on the development of a simplified modelling approach that determines the translational modes of vibration and the associated periods for a retrofitted building structure in both horizontal directions. The simplified approach avoids the need for assembling the mass and stiffness matrices and is verified for realistic building structures against direct eigenvalue analysis.

Beyond the determination of the fundamental vibration characteristics, modal pushover analysis based on the CSM will follow in order to determine the capacity of the structure and test it against the earthquake demand. In this respect, the first contribution is complemented with the development of a simplified method that predicts the pushover response of the structure after retrofitting knowing the pushover response prior to strengthening. Hence, the work aims at estimating the pushover response of RC frame buildings reinforced with shear walls in a simplified form that is based on the application of basic static analysis. This reduces the computational time and effort typically required with structural analysis software to model the building and to determine the pushover response, and it will also allow for a faster and smoother application of the CSM. The accuracy of the proposed approach is verified for realistic structures via comparisons against detailed nonlinear pushover analysis performed on computerised software ETABS (2017).

With the previous objectives attained, the findings are assembled in the context of the CSM with the aim to achieve the ultimate objective of the work, in the form of a simplified retrofitting strategy that facilitates the strengthening of existing buildings subjected to seismic action with the effective use of shear walls. In practice, the addition of a seismic retrofitting system to an existing structure mostly depends on engineering judgment and the architectural constraints in the structure. The structure is checked afterwards to determine the effectiveness of the applied strengthening. Therefore, the process is technically and computationally demanding for a multi-storey building, starting with an arrangement of retrofitting system and modifying it persistently until the structure becomes safe to resist the applied loads. To this end, the anticipated approaches would facilitate the design of a retrofitting system by allowing a faster and smoother application of the CSM. In conclusion, the major contributions are directly applied within the CSM framework to provide a practical tool for the design of seismic retrofitting of substandard RC buildings. Finally, the proposed approach is demonstrated using a case study of substandard RC buildings that are typical of the multi-storey building stock in Lebanon.

In summary, the main novel contributions of the present work are as follows:

- An efficient technique that maximises the translational component of the fundamental mode of vibration, which consolidates the applicability of the CSM.
- A simplified procedure that determines the vibration characteristics of RC buildings in a practical way that avoids the cumbersome assembly of the stiffness and mass matrices.
- A simplified approach that determines the pushover response of RC buildings reinforced with shear walls through direct application of basic static analysis.
- A retrofitting strategy that guides and facilitates the strengthening of existing buildings using shear walls.

1.3 Thesis Outline

This thesis consists of 8 chapters, the first of which is an introductory part that serves to illustrate the research background and the main objectives. This is followed in Chapter 2 by an extensive review of the literature in order to discuss the major topics addressed in the research. To this end, the chapter includes an extensive illustration of nonlinear static procedures (NSPs), with a particular focus on the CSM which forms the focal point of this research. The literature review also consists of an extensive review of the current Eurocode provisions involved in the design of frame and wall buildings.

Chapter 3 presents the procedure implemented for the assessment of existing multi-storey RC buildings in compliance with the provisions of Eurocode 8 (Part 3) which is denoted as EC8-3 (CEN, 2005a). According to the code provisions, an existing building is deemed adequate to resist the seismic hazards in its vicinity under the condition that every structural component should meet the required verification criteria that conform with the performance level (limit state) under consideration. In this respect, the

structural members of a frame building are generally susceptible to potential ductile and/or brittle failure. The check against ductile failure basically consists of verifying that the deformation in all the ductile elements subjected to flexural loading does not exceed the maximum value defined by the code. Conversely, potential brittle failure is checked by verifying that the shear forces do not the exceed the shear capacity of the brittle elements. In view of this, this chapter provides a detailed description of the performance checks conducted in the context of the CSM, in order to assess the adequacy of existing buildings and to decide on the need for retrofitting. The chapter concludes with an applied example that illustrates the seismic assessment procedure applied in the CSM framework and verified against the results of a complete NLTHA.

Chapter 4 proposes a strategy that maximises the mass participation of the translational component of the fundamental mode of vibration, in order to support the case for using the CSM to establish the maximum seismic response. The CSM is based on the simplified assumption that the maximum lateral storey drifts are governed by deformations of the fundamental mode of the originally elastic system (Freeman, 1998). It is therefore suggested that the method is only reliable when the translational first mode governs the dynamic response of the structure (Peter & Badoux, 2000; ATC, 1996, 2005). Accordingly, a new approach is proposed for maximising the mass participation of the translational component and minimising the rotational torsional counterpart based on reducing the average Euclidean eccentricity at all storeys. This strategy is shown to offer a viable framework for applying the CSM in the retrofitting of RC buildings, including those with an irregular configuration.

Chapter 5 illustrates a novel simplified approach developed for determining the vibration characteristics of RC frame buildings in a practical way that avoids assembling the mass and stiffness matrices as required in conventional eigenvalue analysis. The proposed frequency analysis approach is initially developed to establish the vibration characteristics of the retrofitted building considering the walls to be the main source of stiffness, and the contribution of the original frame is subsequently incorporated to obtain the overall vibration characteristics. The approach is also verified for realistic structures, and the results revealed an excellent correlation with those obtained from direct eigenvalue analysis.

Chapter 6 presents a simplified approach based on static analysis to estimate the pushover response of RC frame buildings reinforced with shear walls. The procedure establishes the pushover response by monitoring the successive formation of plastic hinges at the base of vertical elements. In parallel to the frequency analysis approach proposed in the previous chapter, the static pushover approach is developed on the basis of determining the response with respect to the walls in the first instance and subsequent incorporation of the effect of the original frame in a simplified manner. The proposed simplified approach reduces the computational demands and modelling effort required with standard structural analysis software, and the results obtained have shown a good correlation with the pushover response obtained directly from the industry-standard software ETABS (2017).

In chapter 7, the major findings of the previous parts are assembled to form a simplified retrofitting strategy for existing substandard RC frame buildings using shear walls. In this regard, the addition of shear walls to strengthen existing buildings subjected to seismic loading is currently performed on a trial and error basis and in accord to the computationally demanding NLTHA. Hence, the major developments of this research, including the simplified approaches developed in regard to the frequency and the pushover analyses, as well as the findings regarding the optimisation of the modal mass participation are assembled in the context of the CSM to build a simplified strategy that guides the retrofitting of existing substandard RC frame buildings subjected to seismic loading. The procedure is verified for a range of buildings that represent the typical building stock of Beirut (Lebanon), and the results are tested against those obtained from the direct NLTHA performed on ETABS (2017).

The thesis is concluded in Chapter 8 which summarises the major contributions of the research and highlights the practical advantages offered by the simplified retrofitting strategy and the potential impact of the work in the retrofitting of substandard RC buildings. Furthermore, the chapter outlines the shortcomings of the current work and points at potential improvements in future research.

Chapter 2 Literature Review

This chapter presents an extensive review of the literature introducing the major topics discussed in this thesis. It starts with a brief illustration of the earthquake mechanism and the seismic hazard as well as the concepts surrounding the retrofitting of buildings located in seismic regions. The chapter then proceeds with a detailed presentation of nonlinear static procedures with a particular focus on the capacity spectrum method which forms the basis of the research, and which is also compared against the Eurocode-based N2 method. Noting that retrofitting of buildings in this research is performed with the use of shear walls, the literature review also includes a detailed presentation of the design and detailing of shear walls according to Eurocode 8.

2.1 General Overview of Earthquakes

The earth's crust, namely the lithosphere, is composed of tectonic plates that are in continuous movement with respect to each other (Kanai, 1983; Dowrick, 1988; Bertero & Bozorgnia, 2004). An earthquake is the vibration of earth which is mostly caused by the sudden release of energy due to movements of tectonic plates (Newmark & Rosenblueth, 1971; Scholz, 1990, 2002). The earthquake mechanism is explained by the "Elastic rebound theory", which was first introduced by Reid in 1910 and which states that elastic strain energy is accumulated along the fault as plates try to move relative to one another until the level of built-up stress reaches or exceeds the strength of the crust. At this level, rupture and slip occur along the boundary between the plates, causing a sudden release of accumulated energy in the form of seismic waves which propagate through the earth's crust to the surface (Kanai, 1983).

The earthquake magnitude, source-to-site distance, local site conditions, and direction of fault propagation are believed to be the main factors that determine the strength of the earthquake (Reiter, 1990; Broderick et al., 1994; Kramer, 1996). Records have indicated that the world has suffered more than 1200 destructive earthquakes during the twentieth century, with the incurred damages exceeding $1 trillion (Coburn and Spence, 2002). These earthquakes were responsible for killing an average of 10000 people per year during the past century (Bolt, 1999, 2004). To this end, structures located in a seismically active zone are likely to sustain damage when exposed to a severe earthquake unless they are properly designed to resist the associated shaking. Existing structures that were not properly designed to resist earthquakes must also be assessed and retrofitted in case proven to be inadequate, in order to avoid potential failure and loss of human lives. In view of this, many existing buildings located in regions of high seismicity are originally designed and detailed to resist a low to moderate seismic hazard (Goltz, 1994; Broderick et al., 1994; Elnashai, 1998, 1999). Furthermore, Fardis (2009) has pointed out that provisions for seismic design and detailing of buildings have only been introduced in the mid-70's in the US standards and in the mid-80's in the European standards. Prior to these dates,

the lateral resistance of buildings around the world was mostly limited to the resistance of wind loading. In this respect, existing buildings located in seismic regions are widely regarded to be seismically deficient as they were not designed to resist any form of earthquake loading (Fardis, 2009). In consequence, a detailed seismic assessment is required to determine the adequacy of existing buildings that were not originally designed to resist earthquakes despite being located in a seismic hazard region.

2.2 Seismic Hazard Assessment of Lebanon

Despite being one of the small countries of the Middle East, Lebanon has historically witnessed many documented strong earthquakes which have caused massive destruction and high death tolls. Some of these earthquakes are highly noticeable and stand out from the records because of the massive devastation left behind, such as the event of July 9, AD 551, the day on which Lebanon was struck by an earthquake of an estimated moment magnitude (M_W) of 7.5, followed by a tsunami (Elias et al., 2007). Another major event is the earthquake of May 20, AD 1202, which caused severe damage and destruction throughout the region between the Lebanese coast and western Syria, with an estimated moment magnitude (M_W) around 7.5 (Daëron et al., 2005; Elias et al., 2007). On October 30 and November 25 of the year AD 1759, Lebanon also suffered two strong earthquakes with an estimated moment magnitude (M_W) of 6.7 and 7.4, respectively (Daëron et al., 2005). Strong earthquakes were also recorded in the recent history of the country, the most recognizable are the earthquake of September 29, 1918 with an estimated moment magnitude (M_W) around 6.8 (Plassard & Kogoj, 1981; Harajli et al., 1994), the double-shock earthquake of March 16, 1956 with an estimated moment magnitude (M_W) of 6.3 and 6.1 (Khair et al., 2000), and two earthquakes occurring during same day on March 21, 1997, with an estimated moment magnitude (M_W) of 5.6 and 5 (Khair et al., 2000). The latest significant earthquakes were recorded back in 2008, when a series of shaking hit South Lebanon, with a highest moment magnitude (M_W) of 5.1 recorded on February 15 (European-Mediterranean Seismological and Euro-Med, 2010).

Lebanon is crossed by the 1000-km-long left-lateral Levant fault system (LFS), which is responsible for most of the earthquakes historically occurring in the eastern Mediterranean (Huijer et al., 2016). The LFS extends from the seafloor spreading in the Red Sea to the Taurus Mountains in South Turkey, and splits into three main branches as it enters Lebanon, consisting of the Rachaya-Serghaya Fault, the Yammouneh Fault, and the recently discovered Mount Lebanon Thrust (MLT) system (Huijer et al., 2016; Salameh et al., 2016). Figure 2.1 shows the map of Lebanon, the red lines represent the boundaries of the country while the thick dark lines represent the faults. Note that apart from the three aforementioned major fault systems, there are a few smaller secondary faults which add to the overall seismic hazard in the country. In view of this, it was established that the AD 551 earthquake (M_W approx. at 7.5 and followed by a tsunami) that destroyed most of the coastal cities of Lebanon including Beirut, Tripoli, Saida and Tyre, has occurred along the MLT system and has a return period between 1500 and

1750 years (Elias et al., 2007). Studies have also shown that the return period is around 1100 years for strong earthquakes along the Yammouneh Fault (Daëron et al., 2007) and around 1300 years for earthquakes along the Serghaya Fault (Gomez et al., 2003).



Figure 2.1: Active Faults within Lebanon (Elias et al., 2007)

Although the previous discussion proves Lebanon to be located in a high-seismic-hazard region, official building code or regulations taking into consideration seismic risks were only recently introduced in the country. Seismic regulations were first introduced back in 2005 when decree No. 14293 was issued to regulate safety procedures in buildings for the protection against fire and earthquakes. It was further updated in 2012 by decree No. 7964, which characterised seismic hazard all over Lebanon by a minimum horizontal peak ground acceleration (PGA) on rock equal to 0.25 g (Brax et al., 2016). In parallel, the Lebanese Standards Institution (LIBNOR) concurrently issued the Lebanese norms relative to the protection from earthquakes NL 135 (2012), which recommended the same seismic coefficient (0.25g) specified in decree No. 7964 as a reference to the seismic level in the whole country (Brax et al., 2016).

However, recent studies by Huijer et al. (2016) proposed to increase the seismic zone parameter for the coastal cities between Saida and Beirut to 0.3 g, while maintaining the PGA of 0.25 g for other parts of the country. These studies were based on the fact that the MLT fault was only recently discovered (Briais et al., 2004; Carton et al., 2009). Hence, its presence would significantly alter the seismic hazard

map of Lebanon, especially along the coastal cities which accommodate more than 70% of the population and capital investments and which are more likely to be affected by a seismic event occurring along this fault (Huijer et al., 2016).

Construction history in Lebanon is mostly characterised by recent (less than one century old) reinforced concrete building stock. Due to the scarcity of land in major cities and particularly in Beirut, construction growth shifted towards vertical expansion with numerous underground and aboveground floors (Salameh et al., 2016). Regarding the quality and control of construction, it is already noted that seismic regulations came into light in 2005 (decree No. 14293). It is also worth noting that the country witnessed a civil war between 1975 and 1991 which is characterised by a minimum or no control that was associated with a drop in the quality of construction during that period. The level of control is yet to be strictly enforced to this date because local authorities (especially at the municipal level) are not qualified enough to control the application of building codes and regulations. Adding this to the vertical expansion taking over in Beirut, it is safe to conclude that Lebanon is one of the most seismically vulnerable Mediterranean countries (Salameh et al., 2016).

2.3 Seismic Hazard and Performance-Based Assessment

2.3.1 Level of Seismic Hazard

Ground motion excitations are commonly described by the exceedance probability or the mean return period. These two notions are interchangeably used to describe the level of seismic action at a particular site. The former one refers to the probability of exceeding a specific Peak ground Acceleration (PGA) in a fixed time interval (the next number of years), and it is based on the annual rate of exceedance which is defined as the number of exceedances of the PGA in a year. The return period provides another means to interpret the same information as it is the inverse of the annual rate of exceedance. In this context, the probability of exceedance in years of a seismic level (associated with a given PGA) can be related to the mean return period by means of a Poisson model that leads to the following established relationship (Solomos et al., 2008):

$$T_R = -\frac{T_L}{\ln(1-P_R)} \tag{2.1}$$

where:

P_R is the probability of exceedance of the seismic excitation in T_L years, and

T_R is the mean return period of the seismic motion.

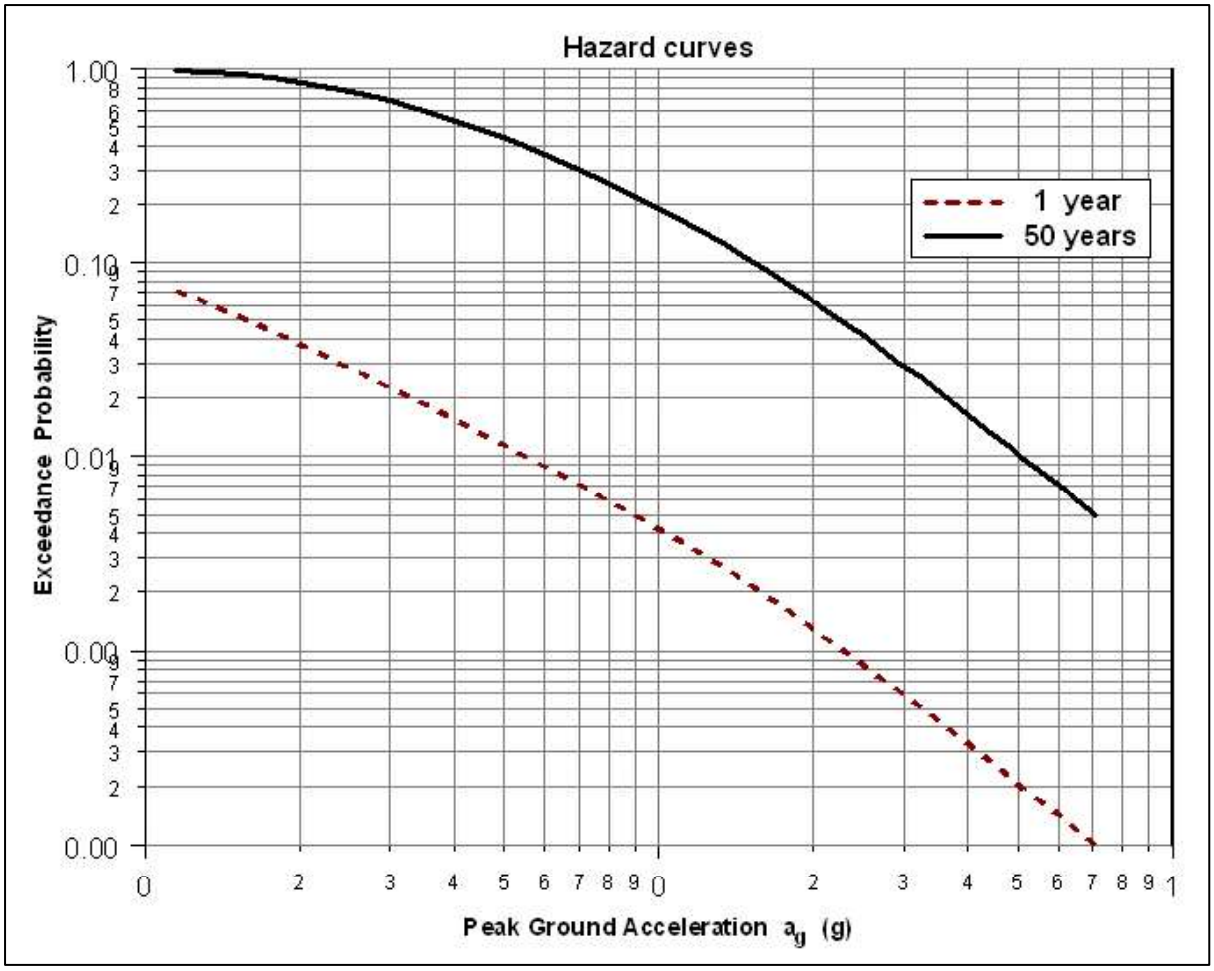


Figure 2.2: Typical hazard curve for a hypothetical site for time intervals of 1 year and 50 years (Solomos et al., 2008)

The seismic hazard at a site is most appropriately represented by a probabilistic approach referred to as Probabilistic Seismic Hazard Analysis (PSHA) by virtue of the uncertainties surrounding the location and occurrence of future earthquakes (Solomos et al., 2008). The probabilistic approaches most commonly used to model the seismic hazard are based either on the Poisson model or on extreme value (Gumbel) distributions (Milne, 1969; Solomos, 1979). Counting on the history of earthquakes and the site properties, the Poisson model is widely employed to quantify the probability of exceedance of certain ground motion levels (specified PGA) at the site (Cornell, 1968). It consists of deriving a mathematical formulation to represent the probability of exceedance of a particular PGA in a specified time interval at the site. This permits to construct the hazard curve of the site by calculating the probability of exceedance of different seismic excitations (different PGA levels) in a fixed time span. A typical hazard curve of a hypothetical site is shown in Figure 2.2.

2.3.2 Performance-based Assessment in the Context of Eurocode 8

Part 1 of Eurocode 8, referred to as EC8-1 (CEN, 2004a), discusses the general rules applied in the design of structures to resist earthquakes and requires that human lives are protected and that structures

remain operational in the aftermath of an earthquake. Towards meeting this objective, buildings are designed to meet the requirements of two performance limit states, the first of which is the No-collapse limit state which entails that the building should be able to sustain the design seismic action without local or global collapse. The second limit state to be satisfied is the Damage Limitation which requires that the building must not experience excessive damage in response to seismic events having a higher probability of occurrence than the design seismic action. In this context, the design seismic action (No-collapse limit state) is defined as the seismic motion having a probability of exceedance of 10% in 50 years, while the Damage Limitation is defined by a seismic action having a probability of exceedance of 10% in 10 years. It is worth noting that the seismic motion is mostly represented by the Reference Peak Ground Acceleration (PGA) measured on Type A ground that corresponds to rock or rock-like formation. To this end, the elastic response spectrum defined in EC8-1 (CEN, 2004a) corresponds to seismic motions pertaining to the No-collapse limit state (design seismic action). It is also worth noting that EC8-1 (CEN, 2004a) recommends the same elastic response spectrum for both the Damage Limitation and the No-collapse limit states.

In light of this discussion, Part 3 of Eurocode 8, entitled as "Assessment and retrofitting of buildings" and referred to as EC8-3 (CEN, 2005a) specifies three performance limit states for assessing existing structures. The Damage Limitation (DL) is associated with minor damage such that the structure does not require repairing afterwards, and it has an estimated mean return period of 225 years which corresponds to a probability of exceedance of 20% in 50 years. The Significant Damage (SD) is associated with significant damage such that the structure can still survive moderate-intensity earthquakes, it has an estimated mean return period of 475 years corresponding to a probability of exceedance of 10% in 50 years. Last, the Near Collapse (NC) limit is characterised by substantial damage such that the structure cannot even withstand a moderate earthquake, and it is associated with a return period of 2475 years which corresponds to a probability of exceedance of 2% in 50 years. According to the standards of EC8-3 (CEN, 2005a), the NC limit state involves maximum exploitation of the deformation capacities of structural elements and therefore provides a more realistic simulation of the real collapse of the building than the No-collapse state defined by EC8-1 (CEN, 2004a) which is comparable to the SD limit state defined in EC8-3 (both have a probability of exceedance of 10% in 50 years). To conclude, when assessing the performance of an existing building, it is recommended to check the performance at both the ultimate NC limit state which characterises rare seismic events having a high intensity (high PGA), as well as the SD limit state which simulates more frequent seismic motions of lower intensity.

In view of this, the provisions of EC8-3 (CEN, 2005a) declare that the design ground motion defined by EC8-1 (CEN, 2004a) should be scaled to match the limit states of EC8-3 (CEN, 2005a). However, the code provisions do not provide any specific recommendation regarding the design ground acceleration needed to verify the three limit states of EC8-3. As discussed earlier, the SD limit state of

EC8-3 is equivalent to the No-collapse limit state of EC8-1 and is accordingly represented by the elastic design spectrum defined in EC8-1. In regard to the design ground acceleration of the two other limit states and particularly the NC limit state, it should be defined in reference to the hazard curve of the site under consideration. In this respect, Fardis (2009) suggests a simplified relationship that relates the PGAs of two seismic events at the site assuming a linear hazard curve (constant slope) plotted in a log-log format:

$$\frac{a_{g1}}{a_{g2}} = \left[\frac{T_R(a_{g1})}{T_R(a_{g2})}\right]^{1/k} \tag{2.2}$$

where:

a_{g1} is the PGA corresponding to a mean return period $T_R(a_{g1})$, and

a_{g2} is the PGA corresponding to a mean return period $T_R(a_{g2})$.

The exponent *k* in the equation reflects on the seismicity of the site. Regions where rare seismic events having a high PGA are almost as frequent as moderate earthquakes having lower PGA values are typically characterised by a relatively high *k* value (k>4). In this case, it is enough to check for the seismic hazard associated with the lower PGA as it is more likely to be governing. However, regions where the PGA of rare seismic excitations is much larger than that that of more frequent ones are characterised by lower *k* values (around 2). In this case, seismic assessment at multiple limit states (both the SD and NC limits) is recommended as either limit state could be governing.

On the same hand, Penelis and Penelis (2014) recommend that the seismic action corresponding to the NC limit state is equivalent to 150% of the design seismic action (DSA) specified in Eurocode, and the seismic intensity associated with the DL limit state is equivalent to 70% of the DSA, noting that the SD limit state corresponds directly to the DSA defined in the code.

Drawing on the previous discussion, assessment of the buildings in this research is performed at both the SD and NC limit states, noting that the seismic action associated with the SD limit state is represented by the elastic response spectrum defined in the code and which is associated with a PGA of 0.3g according to the Lebanese norms as discussed earlier in the chapter. Whereas for the NC limit state, the level of seismic action is assumed to be equal to 150% of the DSA (Penelis & Penelis, 2014), hence amounting to a PGA of 0.45g. In view of the absence of hazard curves in Lebanon and noting that rare seismic hazards having high PGA values were historically encountered in the country, a value of 2 could be a reasonable estimate for the coefficient *k* that reflects on the seismicity of the country as recommended in the aforementioned equation by Fardis (2009). For a *k* value of 2, the PGA of the NC limit state (return period of 2475 years) is 170% that of the SD limit state (return period of 475 years) by using the aforementioned equation. This latest simulation proves that the value of 150% recommended by Penelis and Penelis (2014) for the PGA of the NC limit state is reasonable as it is

relatively close to the one calculated using the equation when assuming a reasonable value for the k coefficient.

To conclude, the buildings investigated in this research represent extracts of the building stock of Lebanon and are accordingly checked against the requirements of the SD limit state (PGA of 0.3g) as well as those of the NC limit state characterised by a PGA of 0.45g.

2.4 Seismic Analysis Methods

Elnashai and Di Sarno (2015) have indicated that dynamic analysis is the most accurate approach to represent the response of structures to seismic loading. Most structures were also shown to respond inelastically under a major earthquake (Campbell & Bozorgnia, 2004). Furthermore, recent studies by Fajfar (2021) reported that the response of most structures to strong earthquakes is dynamic and nonlinear. In view of this, strong ground motions are associated with large deformations and demand high levels of stresses that most structures could not attain while maintaining an elastic behaviour (Biot, 1941). Therefore, the survival of structures under severe earthquakes depends on their proper inelastic behaviour and hysteretic energy dissipation (Campbell & Bozorgnia, 2004). It is also worth adding that structural members become more vulnerable upon exposure to longer duration and repeated cycles of loadings (Bertero et al., 1977; Jeong & Iwan, 1988; Di Sarno, 2013). In conclusion, it is obvious that the seismic response is most realistically represented by the nonlinear dynamic analysis. Nevertheless, most of modern seismic design codes encompass linear and nonlinear as well as static and dynamic procedures for the analysis of structures subjected to seismic loading (Chopra, 2005).

Linear elastic analysis is the most simplified type of analysis and is usually restricted for regular and low- to medium-rise buildings located in regions of low seismicity. The structure is designed to resist lateral static forces which generally depend on the structural properties (mainly the fundamental period of vibration) and on the seismicity in the region (Chopra, 2005).

Linear dynamic analysis is mostly represented by the response spectrum analysis, although it can also be represented by the linear time history analysis which is discussed shortly. The dynamic ground motion is represented by a response spectrum, a plot of the response property (acceleration, velocity, displacement) versus the natural period of vibration of the structure (Housner, 1959; Campbell & Bozorgnia, 2004). Most types of spectra, such as the elastic/inelastic response and design spectra, represent the elastic or inelastic response of single-degree-of-freedom (SDOF) systems when excited by free-field ground motion. In a response spectrum analysis, the maximum response of the structure is calculated for each mode of vibration, and the overall response is approximated by a probabilistic superposition of the individual modal responses. The modal responses are generally combined by the square root of sum of squares (SRSS) or by the complete quadratic combination (CQC) method. In the SRSS method, the combined response (acceleration, velocity, displacement) of all modes is estimated

as the square root of the sum of the squares of individual modal responses. However, the CQC method includes factors that account for correlation between different vibration modes, such that the response of two modes having close vibration frequencies is correlated, which eventually contributes to a more accurate representation of the global response. It is worth noting that most spectral analysis procedures include a response modification coefficient or behaviour factor specified to reduce the seismic forces associated with the elastic spectra (Newmark & Hall, 1982; Krawinkler & Nassar, 1992; Miranda & Bertero, 1994; Vidic et al., 1994).

Since the response of buildings to earthquakes is associated with large inelastic demand, adopting a linear elastic analysis is expected to be associated with a high level of uncertainty and conservatism in estimating the demand (Fajfar, 2021). Accordingly, accounting for material and geometric nonlinearity provides more accurate and realistic results. To this end, nonlinear static procedures (NSPs) are widely used in the seismic assessment and design of buildings, and they employ an approximative approach that estimates the global inelastic response of a MDOF system from an equivalent SDOF system having the same force-deformation properties of the original system (Freeman, 1975; ATC, 1996, 2005; FEMA, 1997, 2000; Fajfar, 2021). NSPs are generally applicable under specific conditions where they produce a reasonable approximation of the nonlinear response of structures subjected to seismic loading. Nonlinear static pushover analysis (NSPA) forms the focus of this research and is further discussed in subsequent sections.

As previously noted, the response of most structures to strong earthquakes is dynamic and nonlinear (Campbell & Bozorgnia, 2004; Elnashai & Di Sarno, 2015; Fajfar, 2021). Therefore, nonlinear dynamic analysis provides the most realistic representation of the actual response of structures subjected to seismic loading. In view of this, time history analysis is a procedure in which the response is evaluated at consecutive increments of time as the structure is being excited by a ground motion time history. Unlike the response spectrum analysis which strictly provides maximum values, time history analysis returns the response of the structure at each time step. Although the procedure can be performed linearly where constant structural properties (stiffness parameters) are assumed over the entire duration of loading, nonlinear time history analysis (NLTHA) provides more accurate results since it requires adjusting the stiffness properties at the beginning of each time step in order to account for the nonlinearity developing in the structure. NLTHA is therefore one of the most powerful methods in seismic engineering because it permits to evaluate the nonlinear response of the building at every increment of time when subjected to a ground motion time history. Nevertheless, the method has always being criticised for being technically and computationally demanding, with many designers and researchers potentially leaning towards simplified NSPs as a reliable alternative to the more sophisticated NLTHA. This topic is addressed in detail in the upcoming sections which discuss the limitations and the accuracy of using NSPs in estimating the seismic response.

2.5 The Capacity Spectrum Method

The capacity spectrum method (CSM) is a commonly used form of NSPA which generally estimates the response of a MDOF system from an equivalent SDOF system having the same force-deformation properties of the original system. The CSM was originally developed as a tool to assess the seismic vulnerability of buildings at the Puget Naval Shipyard (Freeman et al., 1975). Few years later, the method was used as a graphical solution to compare the seismic capacity of a structure against the earthquake ground motion demand (ATC, 1982). In the context of the CSM, the pushover response is referred to as the capacity curve and represents a plot of the base shear versus the lateral roof displacement. Using the dynamic vibration characteristics of the structure, the capacity curve is converted into the capacity spectrum, which represents the spectral acceleration versus the spectral displacement. This allows for a direct comparison with the earthquake demand which in turn is described in the acceleration-displacement response spectrum (ADRS) format, which is a plot of the ground motion in the form of spectral acceleration versus spectral displacement (Figure 2.3). Hence, the method utilises nonlinear static pushover analysis in conjunction with the dynamic characteristics of a structure to graphically establish whether the seismic capacity of the structure meets the demands of seismic ground motion (ATC, 1982; Freeman, 1998). The CSM was shown to be an efficient and reliable tool for the seismic analysis of frame buildings (Freeman, 1998; Sasaki et al., 1998). The method is mainly described by the following steps which are further illustrated in the subsequent discussion:

(i) **Capacity curve**: is the initial outcome of the pushover analysis and is graphically represented in the form of a plot of the base shear versus the roof displacement.

(ii) **Capacity spectrum**: is a plot of the spectral acceleration versus the spectral displacement of the structure that is obtained upon converting the initially obtained capacity curve using the dynamic characteristics of the structure.

(iii) **Response spectrum**: represents the earthquake ground motion in the form of a response spectrum plotted in the ADRS format.

(iv) **Performance point**: is the graphical solution which is obtained at the intersection of the demand and capacity curves, and which represents the response of the structure to the applied seismic loading (Figure 2.4).

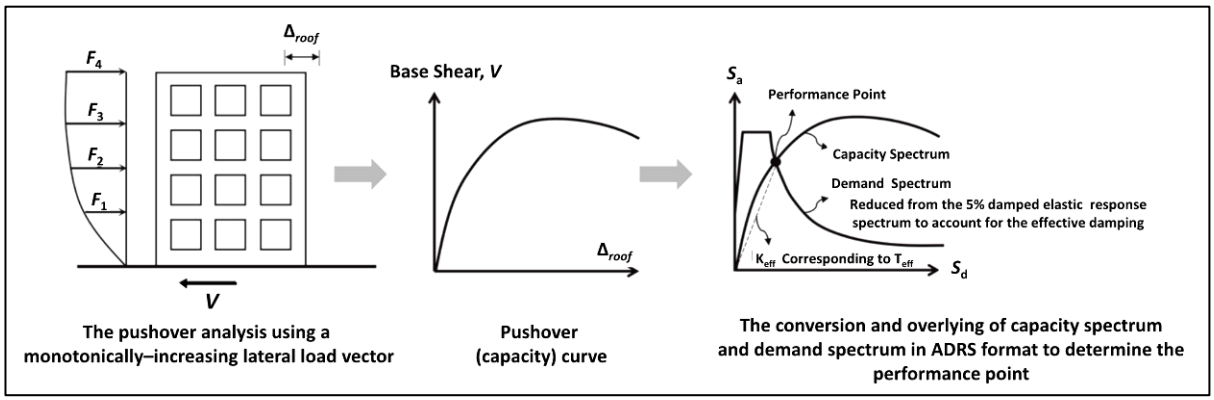


Figure 2.3: Overall process of the CSM (Najam, 2017)

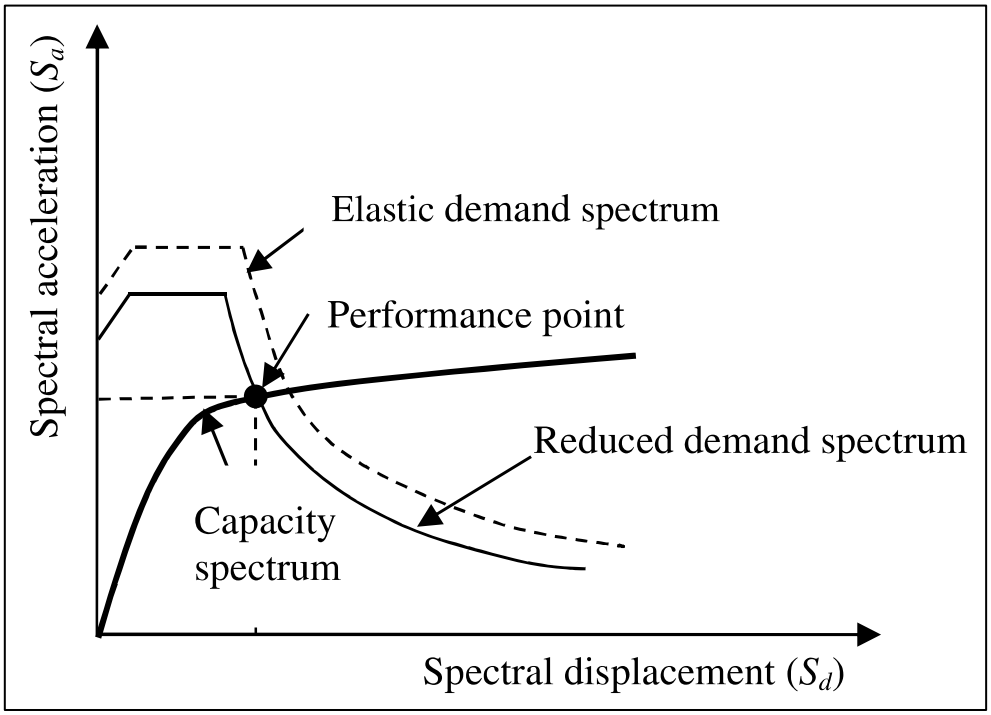


Figure 2.4: Graphical solution of the CSM (Zameeruddin & Sangle, 2016)

Capacity curve

Capacity is a measure of the strength and deformation capability of the major structural elements responsible of resisting the applied loading. It is graphically represented by the nonlinear force-deformation curve (pushover response) which is referred to as the capacity curve and which represents the sequential yielding of structural elements as the structure is being displaced beyond the elastic limit. The capacity curve is mostly plotted in the form of base shear versus roof displacement and is considered to provide a good approximation of the real behaviour when the elastic limit is exceeded (ATC, 1996, 2005).

Capacity spectrum

Nonlinear static procedures generally estimate the response of a MDOF system from an equivalent SDOF having the force-displacement properties of the MDOF system. In view of this, the CSM is based

on equivalent linearisation which estimates the response of a nonlinear SDOF oscillator from the elastic response of an equivalent linear SDOF oscillator having a larger period and damping ratio than the original one. In this context, each mode of vibration of the MDOF system can be represented by a SDOF having an effective mass and stiffness (Figure 2.5). As the MDOF system experiences a top floor displacement in response to an applied earthquake, the equivalent SDOF is displaced by an amount equal to the spectral displacement. The equivalency between the displacement of these two systems is represented by the participation factor. Similarly, the effective mass coefficient relates the total mass of the MDOF system to that of the SDOF system. Accordingly, the CSM makes use of the elastic dynamic characteristics of the structure to convert the capacity curve into the capacity spectrum using the following transformations (ATC, 1996, 2005):

$$S_a = \frac{V}{\alpha W} \tag{2.3}$$

$$S_d = \frac{\Delta_{Roof}}{PF\,\phi_{Roof}} \tag{2.4}$$

$$\alpha = \frac{\left[\sum_{i=1}^{N} m_i \phi_i\right]^2}{\left[\sum_{i=1}^{N} m_i\right]\left[\sum_{i=1}^{N} m_i \phi_i^2\right]} \tag{2.5}$$

$$PF = \frac{\left[\sum_{i=1}^{N} m_i \phi_i\right]}{\left[\sum_{i=1}^{N} m_i \phi_i^2\right]} \tag{2.6}$$

where:

S_a is the spectral acceleration,

S_d is the spectral displacement,

α is the effective mass coefficient of the fundamental mode,

PF is the modal participation factor of the fundamental mode,

V is the base shear,

W is the seismic weight of the structure,

Δ_{Roof} is the roof displacement,

ϕ_{Roof} is the amplitude of the fundamental mode at the roof,

m_i is the lumped storey mass at level *i*, and

ϕ_i is the amplitude of the fundamental mode at level *i*.

It is worth noting that the CSM is based on the simplified assumption that the maximum lateral storey drifts are governed by deformations of the fundamental mode of the originally elastic system (Freeman, 1998). According to ATC-40 (ATC, 1996), this assumption is valid for low- to medium-rise buildings having a period that does not exceed one second. Other studies by Peter and Badoux (2000) have accordingly considered the method to be inappropriate for buildings where the maximum storey drifts are not governed by the fundamental mode and to be reliable only when the elastic translational first mode governs the dynamic response of the structure (Peter & Badoux, 2000). It is worth noting that the method allows for inclusion of higher modes through multi-mode pushover (MMP) analyses which are described in other sections, and the applicability of the CSM is further discussed later in this chapter.

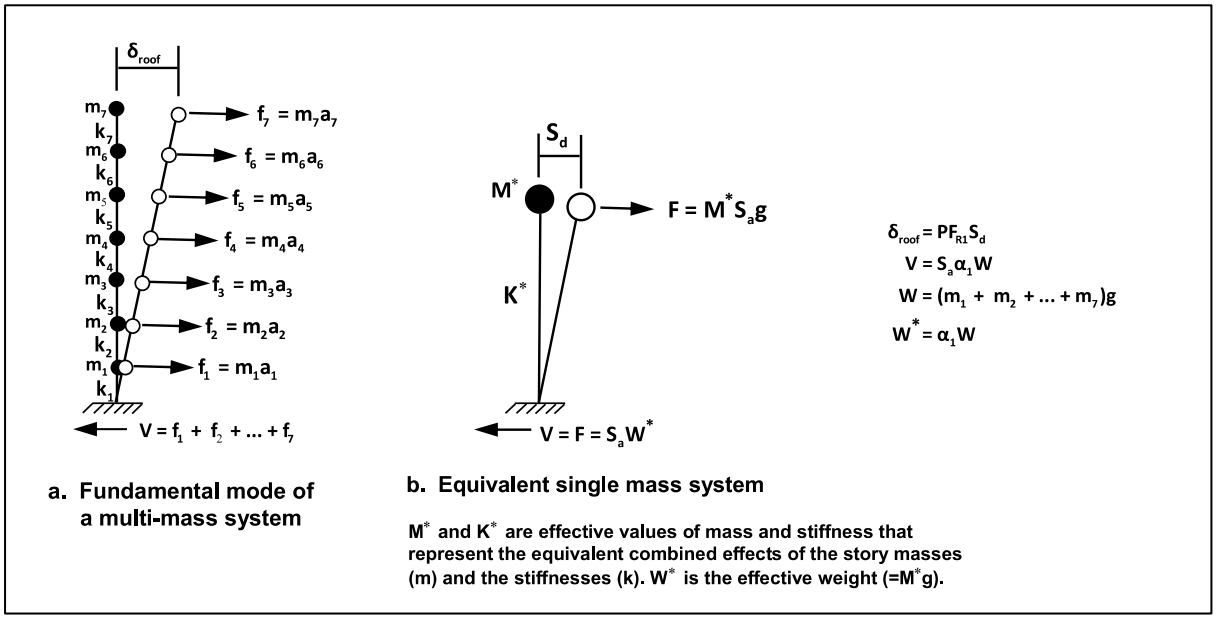


Figure 2.5: Correspondence of a MDOF system into an equivalent SDOF system (ATC, 1996)

Response spectrum

The level of seismic ground motion is represented by the elastic response spectrum defined according to any internationally approved seismic design code. In the provisions of ATC-40 (ATC, 1996), the elastic spectrum follows the requirements of the California Building Code (CBSC, 1995) which is very similar to the spectrum defined by the Uniform Building Code (UBC, 1997). The level of seismicity is described by the seismic zone which reflects on the proximity of the site to nearby faults and by the soil profile characteristics. This permits to construct the elastic response spectrum characterised by a 5% damping ratio, noting that RC structures are widely assumed to possess an inherent viscous damping

ratio of 5% (ATC, 1996, 2005). The conventional response spectrum, a plot of the spectral acceleration versus the period of vibration, is converted into the acceleration-displacement response spectrum (ADRS) format. The latter is a plot of spectral acceleration versus spectral displacement, with the period represented by lines radiating from the origin, and is obtained through the following transformation:

$$S_d = \frac{1}{4\pi^2} S_a T^2 \tag{2.7}$$

where T is the period of vibration.

Performance point

Last, the capacity spectrum and the elastic response spectrum are both plotted on the same graph and in the same format, allowing for a direct comparison between the capacity and the seismic demand. The displacement demand is measured at the performance point or the intersection of the capacity and demand curves, and it represents the maximum lateral displacement experienced in response to the applied ground motion. The maximum lateral roof displacement is subsequently evaluated from the spectral displacement of the performance point and is compared against the allowable limits set by design codes.

Owing to the equivalent linearisation which assumes that the response of a nonlinear SDOF oscillator is estimated from the elastic response of an equivalent SDOF having a larger period and damping ratio than the original one, the effective damping is calculated and is used to obtain the inelastic response spectrum that is used to find the performance point. In view of this, the elastic response spectrum defined in the seismic design codes characterises a 5% damping ratio which amounts to the inherent viscous damping present in RC buildings (ATC, 2005). The total or effective damping consists of the hysteretic damping as well as the inherent viscous damping. Hysteretic damping can be proportioned to equivalent viscous damping and is proportional to the area enclosed by the loops of the force-deformation curve as shown in Figure 2.6 (ATC, 1996, 2005), and is accordingly estimated using the following formulation (Chopra, 1995):

$$\beta_0 = \frac{1}{4\pi} \frac{E_D}{E_{so}} \tag{2.8}$$

where:

β_0 is the hysteretic damping (represented as equivalent viscous damping),

E_D is the energy dissipated by damping in a single cycle of motion, and

E_{so} is the maximum strain energy.

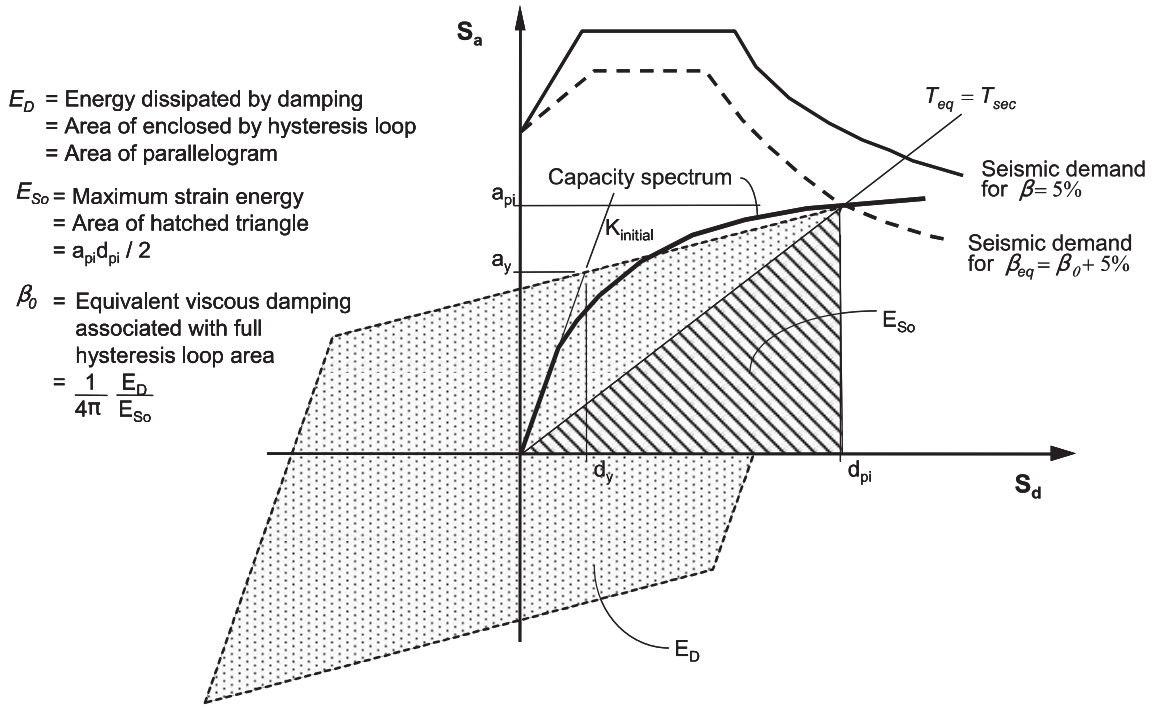


Figure 2.6: Evaluation of equivalent viscous damping via the bilinear representation of the capacity spectrum (ATC, 2005)

In light of this, the capacity spectrum is approximated into an equivalent bilinear curve to derive a simplified expression for hysteretic damping (Figure 2.6). The bilinearisation is based on the equal energy assumption which requires that the total area under the capacity spectrum and its bilinear representation are equal, while the initial stiffness of the capacity spectrum is adopted as the slope of the elastic part of the bilinear curve. It is also worth noting that Figure 2.6 depicts a perfect hysteretic response with no pinching or degradation, which is ideally observed under short duration ground motions and in buildings possessing an adequately detailed seismic resisting system that ensures a ductile behaviour. However, strength degradation is expected at longer duration events, and a corresponding reduction factor is specified to account for imperfections in the actual hysteretic response. Taking into consideration the bilinearisation of the capacity spectrum and the imperfections, the hysteretic damping is mathematically reduced which consequently allows to derive formulations for the total or effective damping and for the effective period (secant period) measured at the intersection of the capacity spectrum and the reduced demand spectrum (ATC, 1996, 2005):

$$\beta_0 = \frac{2}{\pi}\frac{(\mu-1)(1-\alpha)}{\mu(1+\alpha\mu-\alpha)} \tag{2.9}$$

$$\beta_{eff} = \kappa\beta_0 + 0.05 = \kappa\frac{2}{\pi}\frac{(\mu-1)(1-\alpha)}{\mu(1+\alpha\mu-\alpha)} + 0.05 \tag{2.10}$$

$$T_{eff} = T_0 \sqrt{\frac{\mu}{1+\alpha\mu-\alpha}} \tag{2.11}$$

$$\alpha = \frac{\left(\frac{a_{pi}-a_y}{d_{pi}-d_y}\right)}{\left(\frac{a_y}{d_y}\right)} \tag{2.12}$$

$$\mu = \frac{d_{pi}}{d_y} \tag{2.13}$$

where:

β_0 is the hysteretic damping,

β_{eff} is the total or effective damping (accounting for imperfections in the hysteretic response),

T_0 is the initial period of vibration of the nonlinear system (obtained at the initial tangent to the nonlinear force-deformation curve),

T_{eff} is the effective period of vibration,

μ is the displacement ductility ratio,

α is the post-yield stiffness ratio of the inelastic system,

κ is the damping modification factor which accounts for imperfect hysteretic response in RC structures. The provisions of ATC-40 (ATC, 1996) categorise 3 types of buildings in that regard. Type A buildings have a perfect hysteretic behaviour, while Type B represents a moderate hysteretic response with moderate reduction of the area under the hysteretic loops, and Type C characterises buildings having a severely degraded hysteretic response. The complete variation of the damping modification factor with the ductility ratio is presented in Figure 2.7 for all hysteretic types (ATC, 1996),

a_y & d_y are the coordinates of the yield point in the bilinear curve, and

a_{pi} & d_{pi} are the coordinates of the initial performance point in the bilinear curve.

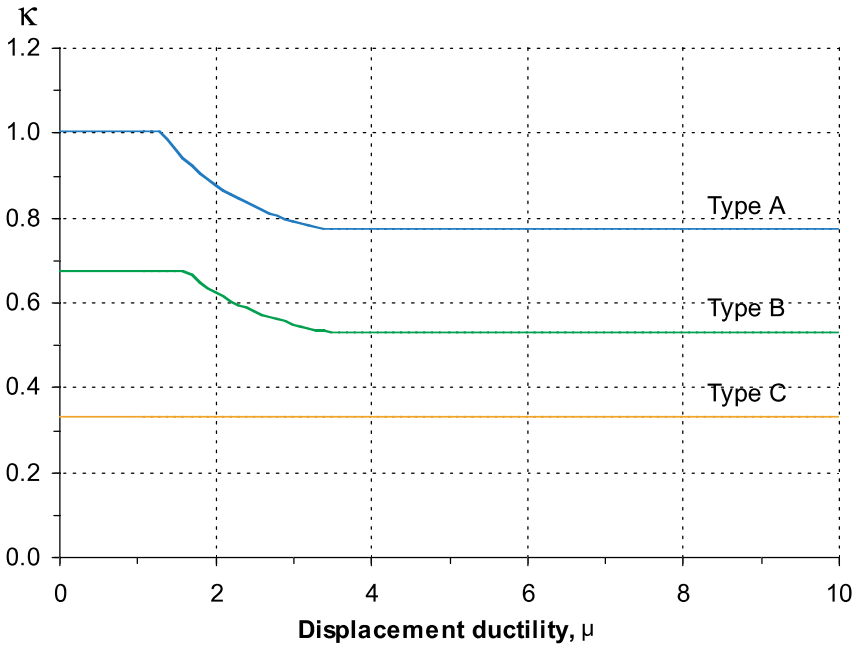


Figure 2.7: Variation of damping modification factor against the displacement ductility ratio (ATC, 1996)

The standards of ATC-40 (ATC, 1996) impose a limit on the equivalent damping ratio which maintains a constant value for any displacement ductility ratio exceeding the limit of 3.4 for all the hysteretic modes (Figure 2.8). Once the effective damping is evaluated, the provisions of ATC-40 (ATC, 1996) recommend the spectral reduction factors of Newmark & Hall (1982) to reduce the elastic 5% damped spectrum:

$$SR_A = \frac{3.21 - 0.68 \ln(100\beta_{eff})}{2.12} \tag{2.14}$$

$$SR_V = \frac{2.31 - 0.41 \ln(100\beta_{eff})}{1.65} \tag{2.15}$$

where:

SR_A is the spectral reduction factor in the constant-acceleration part of the spectrum, and

SR_V is the spectral reduction factor in the constant-velocity part of the spectrum.

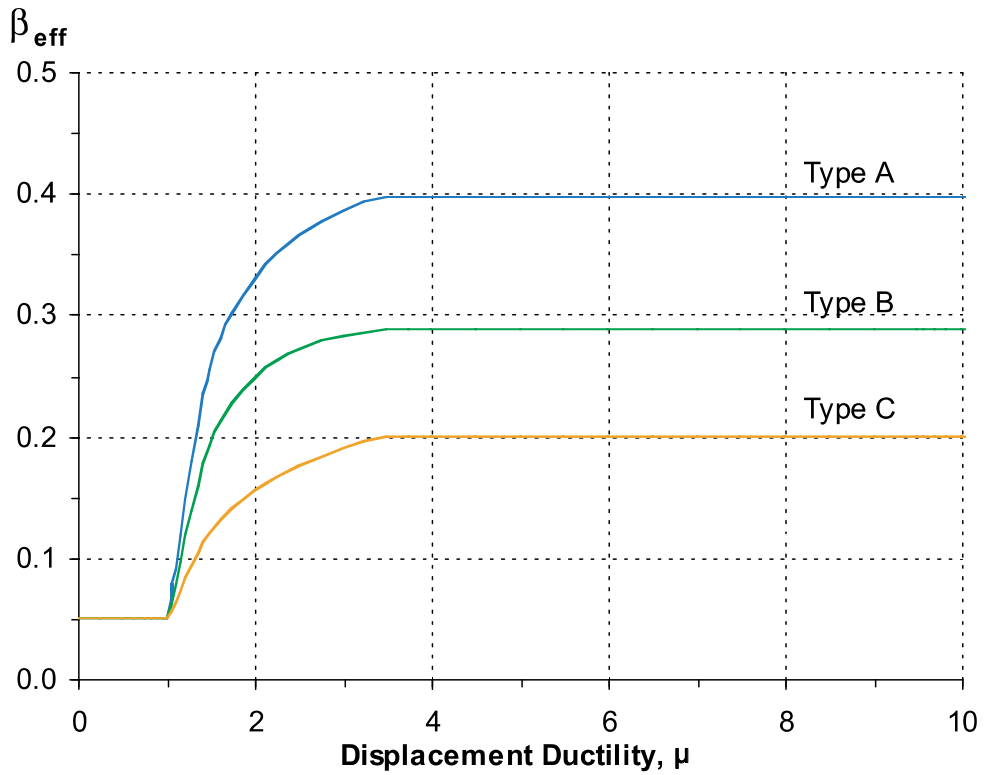


Figure 2.8: Variation of the equivalent (effective) damping with the displacement ductility ratio (ATC, 1996)

With reference to the aforementioned discussion, it should be noted that calculating the effective period and damping and the spectral reduction factors requires a prior knowledge of the displacement ductility ratio. Hence, knowing the performance point is a prerequisite for calculating the effective damping and getting the reduced inelastic spectrum. The procedure is therefore iterative, and it begins with a trial performance point that is mostly estimated using the equal displacement approximation (Velestos and Newmark, 1960), which states that the displacement of an inelastic SDOF is approximately equal to that of the equivalent linear system having the same period and accordingly calculates the inelastic displacement from an equivalent purely elastic response (Figure 2.9). A preliminary estimate of the effective damping is obtained, which allows to construct the reduced inelastic spectrum. The new estimate or the resultant performance point is obtained at the intersection of the last-obtained inelastic demand spectrum with the capacity spectrum. Accordingly, if the newly calculated displacement of the resultant performance point lies within 5% of the trial performance point, then the latter is the real performance point. Otherwise, another iteration is performed with the last-obtained performance point being used as the trial value, and the whole procedure is repeated until convergence which is marked by the 5% difference between the trial and the output performance point.

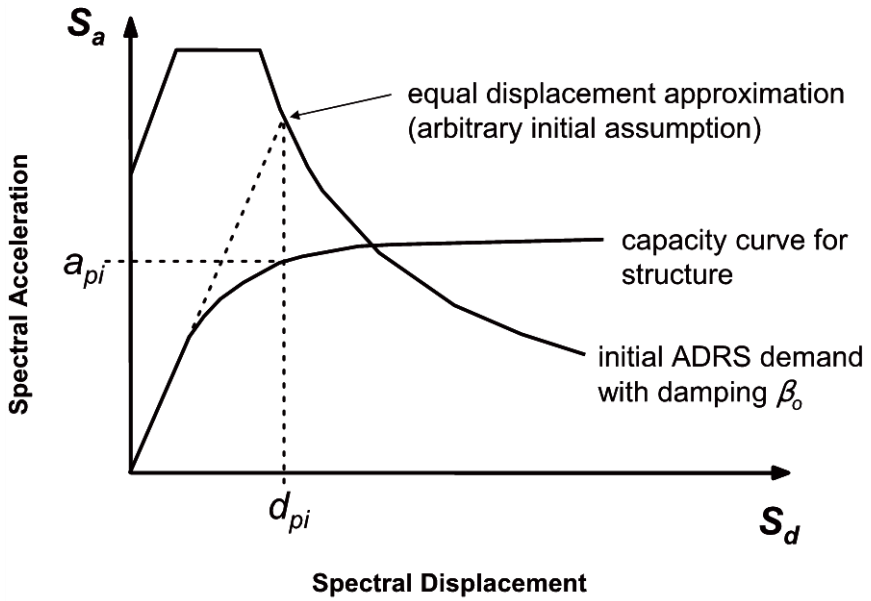


Figure 2.9: Locating the trial performance point through the equal displacement approximation (ATC, 2005)

The aforementioned procedure illustrated to find the performance point is withdrawn from the regulations of ATC-40 (ATC, 1996). In view of this, the ATC-55 report (ATC, 2005) supersedes the ATC-40 report (ATC, 1996) and addresses the shortcomings of the older one. The new regulations have indicated that the ATC-40 approach was shown to overestimate the global displacement for short-period systems having a period of vibration less than 0.5 second. Furthermore, it was reported that the old provisions lead to an underestimation of the global displacement for Type A buildings having a period in excess of 0.6 second and for Type B buildings having a period in excess of 0.8 second, while the displacement is overestimated for all Type C buildings irrespective of the period. Furthermore, studies by Chopra and Goel (1999a,b, 2000) and Miranda and Akkar (2002) have reported a convergence issue of the procedure when actual response spectra were rather used instead of the code-based design (smooth) response spectra. To this end, the provisions of ATC-55 (ATC, 2005) recommend new expressions to estimate the effective period and effective damping. The new expressions are statistically derived such that the difference between the actual displacement of the equivalent linear SDOF and that of the inelastic SDOF is minimised. Furthermore, the analysis considered three different forms of hysteretic response, including the bilinear hysteretic, the stiffness-degrading, and the strength-degrading model, and empirical formulas were derived to estimate the effective damping and effective period for each hysteretic type. However, it is difficult to find a system that fully exhibits one of the three aforementioned hysteretic types, since different components usually exhibit disparate hysteretic behaviour, and the overall response would likely involve a combination of the aforementioned hysteretic types. Therefore, the procedure was amended to improvise optimised expressions that estimate the effective damping and the effective period for all hysteretic model types:

$$For\ 1.0 < \mu < 4.0:\ \ \beta_{eff} = 4.9(\mu - 1)^2 - 1.1(\mu - 1)^3 + \beta_i \tag{2.16}$$

$$For\ 4.0 < \mu < 6.5:\ \ \beta_{eff} = 14.0 + 0.32(\mu - 1) + \beta_i \tag{2.17}$$

$$For\ \mu > 6.5:\ \ \beta_{eff} = 19\left[\frac{0.64(\mu - 1) - 1}{\left[0.64(\mu - 1)\right]^2}\right]\left(\frac{T_{eff}}{T_0}\right)^2 + \beta_i \tag{2.18}$$

where β_i is the inherent viscous damping (usually taken as 5% in RC structures as described earlier).

$$For\ 1.0 < \mu < 4.0:\ \ T_{eff} = \left[0.2(\mu - 1)^2 - 0.038(\mu - 1)^3 + 1\right] T_0 \tag{2.19}$$

$$For\ 4.0 < \mu < 6.5:\ \ T_{eff} = \left[0.28 + 0.13(\mu - 1) + 1\right] T_0 \tag{2.20}$$

$$For\ \mu > 6.5:\ \ T_{eff} = \left[0.89\left(\sqrt{\frac{(\mu - 1)}{1 + 0.05(\mu - 2)}} - 1\right) + 1\right] T_0 \tag{2.21}$$

The modified expressions are generally expected to yield more accurate estimates of the global displacement, particularly for systems having a short period which is less than 0.5 second. To note also that ATC-55 pointed out that the new equations might not be reliable for cases having an extremely high ductility ratio (between 10 and 12). Concerning the reduction of the elastic spectrum, ATC-55 (ATC, 2005) recommends damping coefficients which are the inverse of the spectral reduction factors defined earlier. Accordingly, the inelastic spectrum is obtained by dividing the spectral acceleration of the elastic spectrum by the damping coefficient. There are several resources in the literature that define the damping coefficient (Figure 2.10), and ATC-55 recommends the following expression as well:

$$B = \frac{4}{5.6 - \ln(100\beta_{eff})} \tag{2.22}$$

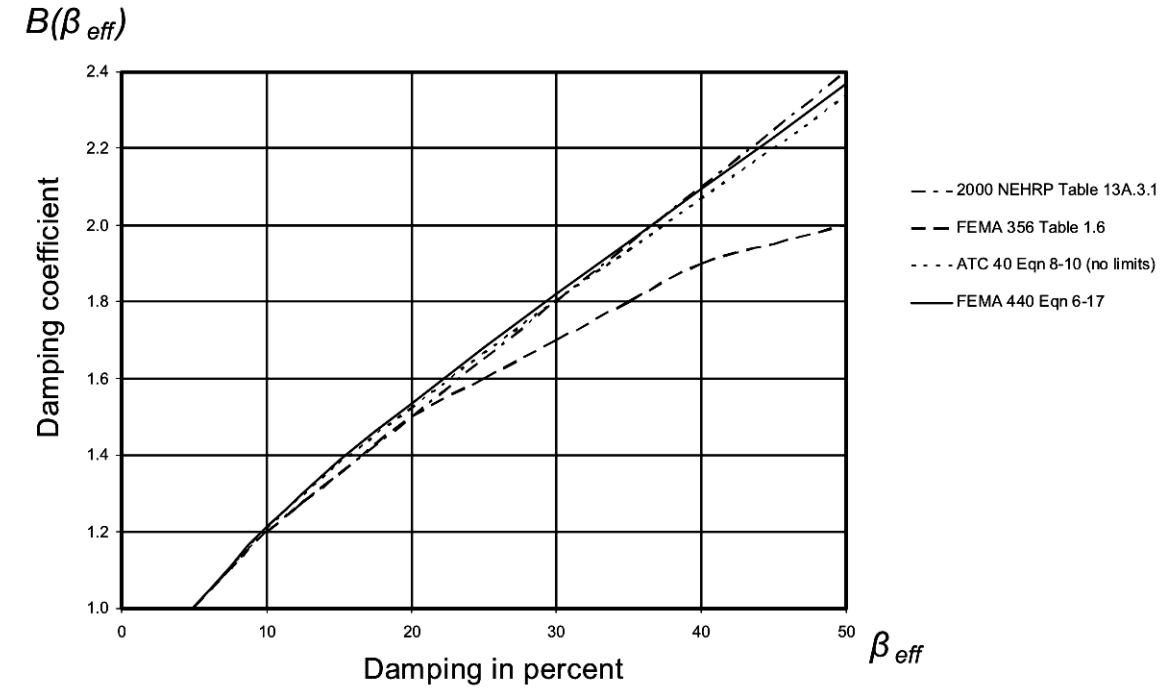


Figure 2.10: Evaluation of the damping coefficient in terms of the effective damping ratio (ATC, 2005)

2.6 The N2 Method

This section briefly presents the N2 method (Fajfar & Fischinger, 1988), another commonly used form of NSPA, which was implemented in Part 1 of Eurocode 8 or EC8-1 (CEN, 2004a). Like the CSM and other pushover analyses, the N2 method relies on estimating the response of a MDOF system from an equivalent SDOF system and is therefore criticised for being a single-mode method that is reliable only when the response is mainly dictated by a single mode of vibration. To this end, the original method has been expanded to accommodate plan-asymmetric structures which are expected to feature a significant contribution of higher modes into the overall response. The new version of the method, known as the Extended N2 method (Fajfar, 2005), estimates the inelastic response through a combination of nonlinear static pushover analysis and an elastic dynamic analysis. Accordingly, the Extended N2 method assumes that the amplified displacements due to torsional effects can be estimated by the linear dynamic analysis and assumes also that the torsional amplification of displacements in the inelastic range is approximated from the one in the elastic range, despite the latter being a conservative approximation (Fajfar, 2005). The extended N2 method is explained in the following steps:

(i) Pushover analysis

As in the CSM, the force-deformation response is obtained by applying a set of incremental loads at the centre of mass of each floor and plotting the response in the form of base shear versus roof displacement. While the N2 method can be generally performed with any reasonable load pattern, EC8-1 (CEN, 2004a) recommends applying at least two distributions of lateral forces and enveloping the results to obtain the pushover response. The following load distributions are recommended by EC8-1:

Uniform pattern: consists of a uniform load distribution that is proportional to the storey mass at each level

Modal pattern: consists of a vertical load distribution proportional to the fundamental mode of vibration (similar to the CSM).

(ii) Equivalent SDOF system

In parallel to what is performed in the CSM, the MDOF system is converted into an equivalent SDOF system having an equivalent mass and stiffness. While there are several ways to model the structure as a SDOF, the N2 method adopts the same transformations which are used in the CSM to convert the conventional pushover response (capacity curve) into the ADRS format. Accordingly, the spectral acceleration and spectral displacement are obtained using the effective mass coefficient and participation factor previously defined in the CSM. The resultant curve is approximated into an equivalent elastic-perfectly plastic bilinear curve (Figure 2.11). The bilinearisation is generally based on engineering judgment, with EC8-1 (CEN, 2004a) adopting the equal energy principle which requires that the area under the original curve and its bilinear approximation should be equal. A prior knowledge of the displacement demand (target displacement) is therefore needed to perform the bilinearisation. Hence, the procedure is iterative, assuming an initial displacement demand and finding the corresponding bilinear approximation and resultant displacement demand, with the latter being used as the new trial displacement in the next iteration and so on, until the procedure converges into the actual displacement demand. In view of this, it is worth noting that EC8-1 (CEN, 2004a) proposes using the displacement associated with the formation of a plastic mechanism (as the target displacement) and states that the iterative process is accordingly optional though not mandatory.

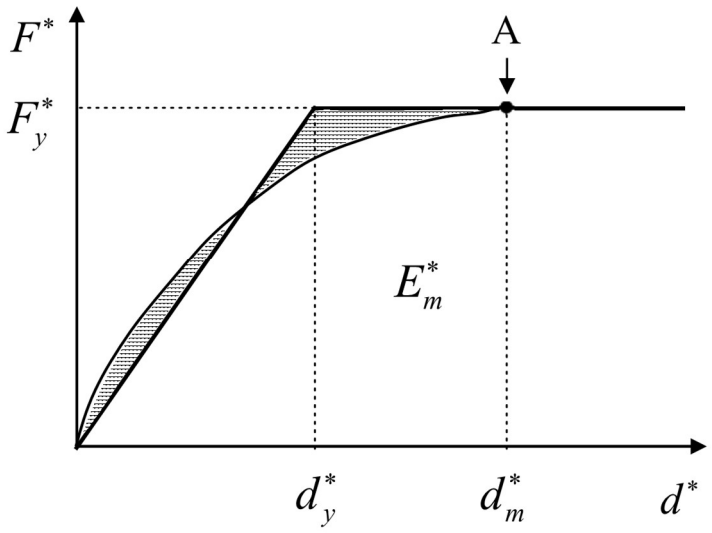


Figure 2.11: Approximating the pushover curve into an equivalent elastic-perfectly plastic bilinear curve (CEN, 2004a)

(iii) Response spectrum

Seismic ground motion is represented by the elastic response spectrum, which is converted into the acceleration-displacement response spectrum (ADRS) format in a similar fashion to what is performed in the CSM (Equation 2.7). While the CSM relies on equivalent damping, the N2 method adopts ductility reduction factors to calculate inelastic response spectra for constant ductility values (Figure 2.12):

$$S_a = \frac{S_{ae}}{R_\mu} \tag{2.23}$$

$$S_d = \frac{\mu}{R_\mu} S_{de} \tag{2.24}$$

$$R_\mu = (\mu - 1)\frac{T}{T_C} + 1 \qquad for\ T < T_C \tag{2.25}$$

$$R_\mu = \mu \qquad for\ T \geq T_C \tag{2.26}$$

where:

S_{ae} & S_{de} are the spectral acceleration and spectral displacement in the elastic spectrum respectively,

S_a & S_d are the spectral acceleration and spectral displacement in the inelastic spectrum respectively,

T is the period of vibration,

T_C is the characteristic period, which is defined at the intersection of the constant acceleration and the constant velocity regions of the spectrum,

μ is the ductility factor or the ratio of maximum displacement to yield displacement, and

R_μ is the ductility reduction factor which accounts for hysteretic energy dissipation.

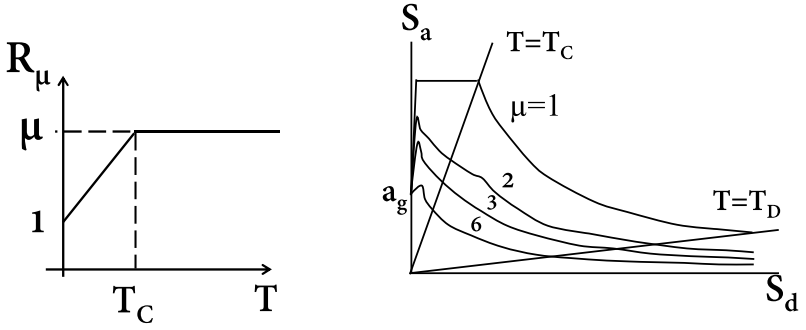


Figure 2.12: Inelastic response spectra for constant ductility values in the N2 method (Fajfar, 2021)

(iv) Seismic displacement demand

The last step involves plotting the bilinear capacity and the demand curve on the same plot in the ADRS format. For medium- and long-period structures, the seismic demand is obtained using the equal displacement approximation (Velestos and Newmark, 1960), which assumes that the inelastic displacement is equal to the equivalent elastic displacement that is measured at the intersection of the elastic period (radial line) with the elastic response spectrum. The ductility reduction factor is accordingly calculated as the ratio between the inelastic and elastic acceleration and is equal to the displacement ductility ratio by virtue of similar triangles (Figure 2.13).

$$For\ T \geq T_C: \qquad R_\mu = \frac{S_{ae}}{S_{ay}} \tag{2.27}$$

$$\mu = R_\mu \tag{2.28}$$

$$S_d = S_{de} \tag{2.29}$$

For short periods that are smaller than the characteristic period of vibration T_C, the ductility reduction factor is calculated as the ratio between the inelastic and elastic acceleration as in the previous case. However, the ductility ratio is obtained by rearranging the expression in Equation 2.25. Last, the displacement demand is calculated using the yield displacement and the ductility ratio (Figure 2.13):

$$For\ T < T_C: \qquad R_\mu = \frac{S_{ae}}{S_{ay}} \tag{2.30}$$

$$\mu = 1 + \left(R_\mu - 1\right)\frac{T_C}{T} \tag{2.31}$$

$$S_d = \mu S_{dy} = \frac{S_{de}}{R_\mu}\left(1 + \left(R_\mu - 1\right)\frac{T_C}{T}\right) \tag{2.32}$$

where:

S_{dy} is the yield displacement obtained from the bilinear approximation.

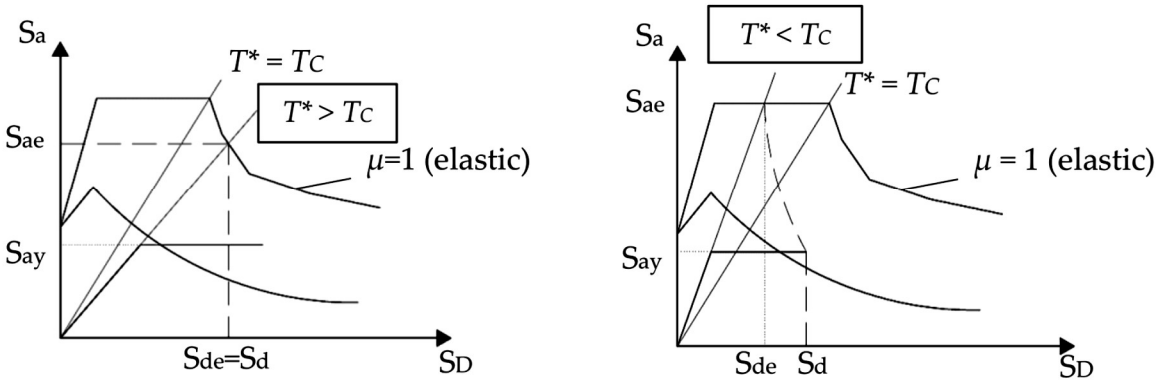


Figure 2.13: Evaluation of the seismic displacement demand in the N2 method (Aşıkoğlu et al., 2021)

In light of this discussion, it is worth noting that the final (actual) displacement demand corresponds to the intersection of the bilinear capacity curve and the inelastic response spectrum reduced for the ductility factor. Hence, convergence is achieved when the ductility factor obtained from the capacity diagram is equal to the ductility factor corresponding to an inelastic spectrum that intersects the capacity curve at the displacement demand.

The final step involves converting the spectral displacement of the SDOF system into the corresponding maximum roof displacement of the MDOF system and comparing the latter to the limit permitted by the code.

(v) <u>Torsional effects</u>

A linear dynamic analysis (response spectrum analysis) is separately performed in each horizontal direction, using the SRSS or CQC rule for combining the results of different modes. The results obtained from both horizontal directions are combined by the SRSS rule to determine the torsional effect that is assumed to be overlooked by the ordinary pushover analysis, since the latter involves applying loads at the centre of mass of each storey (Fajfar et al., 2005). To this end, pushover results such as the deformations of ductile elements or the forces in brittle elements are modified by correction factors which represent the ratio of the normalised roof displacement obtained from linear dynamic analysis to that obtained from pushover analysis. The normalised displacement at a particular location is equal to the roof displacement at that location divided by the roof displacement at the centre of mass. It is worth noting that the N2 method does not allow for de-amplification at the stiff side due to torsional effects. Hence, the correction factor is taken as 1.0 should the normalised roof displacement obtained from the pushover analysis exceed that obtained from the elastic dynamic analysis. It is worth noting that comparison against NLTHA has proven the Extended N2 method to be conservative (Fajfar et al., 2005). Indeed, the bilinearisation of the capacity curve by Eurocode 8 is assumed to be conservative and to yield a low effective stiffness (high period).

2.7 Limitations of Nonlinear Static Procedures and of the CSM

It is reported that the response of most structures to strong earthquakes is dynamic and nonlinear, while the majority of problems in structural engineering are based on or are approximated by a linear static analysis (Fajfar, 2021). Nonlinear time history analysis (NLTHA), also called nonlinear response history analysis (NLRHA), is a nonlinear dynamic analysis that reasonably depicts the actual inelastic response of structures subjected to severe earthquakes. Although the method has always been crucial for the design and assessment of the most important structures, it has been rarely used in the design or check of common structures by virtue of its complexity and computational requirements. To this end, pushover-based seismic analysis was initially introduced by Freeman et al. (1975) in the form of the capacity spectrum method (CSM) and have since then served as a simplified yet reliable alternative that approximates the nonlinear response of structures subjected to earthquake loading. In general, nonlinear static pushover (NSP) methods convert MDOF systems into an equivalent SDOF system and represent earthquakes in the form of response spectra, unlike the NLTHA which uses multiple ground motion records. The method is based on estimating the global displacement of the structure from an equivalent SDOF system having the same force-deformation properties of the original system, while storey drifts and component actions are consequently determined from the global demand parameters through the pushover curve.

In light of this discussion, there are two widely used forms of nonlinear static pushover analysis (NSPA), namely equivalent linearisation techniques and the displacement coefficient method, which differ in the procedure adopted to determine the global inelastic displacement. Equivalent linearisation techniques, such as the CSM (Freeman, 1975, 1998) are based on the assumption that the total displacement of a nonlinear SDOF oscillator is estimated from the elastic response of an equivalent SDOF having a larger period and damping ratio than the original one. The displacement coefficient method is originally presented in the FEMA-273 document (FEMA, 1997) and in the modified version or the FEMA-356 document (FEMA, 2000). As the name implies, the total displacement of the structure is obtained by multiplying the elastic displacement of the equivalent SDOF system by a series of coefficients termed C_0 through C_3. The coefficients are empirically determined and basically represent the equivalence between the spectral displacement and the roof displacement and the relationship between a linear and a bilinear oscillator, and they also account for imperfections (pinching) in the hysteretic behaviour as well as for increased deformation due to P-Delta effects. It is worth noting that both methods are equally recommended in NSPA, and both are subjected to the same criticism as explained in the next discussion.

Besides determining the ultimate capacity, NSPs provide information about the ductility of the structure and also permit to visualise the sequential progressive failure of structural components in the inelastic range which eventually lead to the formation of a mechanism, all of which cannot be obtained using

linear elastic analysis (Leslie, 2013). In view of this, the pushover analysis involves defining hinges within the structural model, which represent the critical locations where potential yielding and cracking is expected. Flexural, shear, and axial hinges are usually defined, and each hinge represents the localised force-displacement relationship of an element displaced into the inelastic range. Hence, a prior knowledge of the dimensions and reinforcement of the member is anticipated to obtain a realistic definition of the hinge properties. Pushover analysis is therefore considered a second stage analysis and is preferably used for the seismic assessment of existing structures which were not previously evaluated to be located in seismic regions. Indeed, the detailing of existing structures helps defining the input data (hinge properties) required to perform the pushover analysis, which could assist in determining the location and the amount of retrofitting needed (Leslie, 2013).

Although NSPA has been widely regarded as a simplified alternative that requires a fraction of the computation time needed by NLTHA, the method is surrounded with a high degree of uncertainty which mainly stems from the correspondence between the original structure and an equivalent SDOF oscillator. Therefore, an in-depth understanding of the limitations of NSPs is required to obtain a solid basis for the applicability and reliability of pushover-based methods.

In view of this, the Applied Technology Council (ATC) issued the ATC-40 report, entitled "seismic evaluation and retrofit of concrete buildings" which particularly focuses on the application of the CSM in the seismic assessment of buildings. According to ATC-40 (ATC, 1996), the prevalence of the first mode in the seismic response is a valid assumption for structures having a fundamental period less than one second. However, the effect of higher modes becomes more pronounced in taller and flexible buildings having longer fundamental periods. Peter & Badoux (2000) also consider the CSM to be inappropriate for the analysis of buildings where the maximum storey drifts are not governed by the fundamental mode, such as tall buildings (more than about 15 stories) or buildings under shock-like impacts (near source effects).

Several researchers have similarly reported that the seismic demand values obtained by NSPs are reliable for symmetric low- and mid-rise structures whose seismic response is governed by deformations of the fundamental mode and which are characterised by a uniform distribution of inelastic action throughout the height (Lawson et al., 1994; Kim & D'Amore, 1999; Zamfirescu & Fajfar, 2001; Albanesi et al., 2002; Bento et al., 2004). Further recent studies by Deierlein et al. (2010) have similarly concluded that NSPs produce reliable results for regular and symmetric low-rise structures up to five stories. Furthermore, Fajfar (2021) claimed that the correspondence between the original structure and an equivalent SDOF in NSPs is valid under the condition that the deformation of the structure is governed by a single mode of vibration, which can readily be approximated by the SDOF oscillator.

In this context, attempts to mitigate the limitations of NSPs mainly focus on incorporating higher modes into the seismic response through the multi-mode pushover (MMP) procedures (Sasaki et al., 1998;

Gupta & Kunnath, 2000; Chopra & Goel, 2002). MMP involves conducting a series of independent pushover analyses using force distributions representing the predominant translational modes of vibration. The overall seismic response is then evaluated by combining the response quantities (floor displacement, interstorey drift, plastic hinge rotation, etc.) obtained from all the single-mode pushover analyses using the SRSS or CQC method. To this end, the ATC-55 report (ATC, 2005) suggests that the accuracy of the MMP procedures depend on the parameter of interest and that further studies should be performed in order to accurately assess their effectiveness in light of the additional computational time incurred by these procedures. Furthermore, ATC-55 recommends using the first-mode distribution over other types of invariable single load patterns, since the former was shown to provide reasonable estimate of the displacement compared to NLTHA except for tall flexible structures.

Further studies by Oguz (2005) performed on two- and five-storey RC frame buildings have shown that the selection of load pattern in NSPs is not critical for low- to mid-rise frames characterised by a fundamental period that is smaller than one second. However, the same study revealed that the "Code" lateral load pattern (mass proportional) provided the most accurate distribution of storey and interstorey drift values for eight- and twelve-storey buildings, and the results coincided with the average of those obtained by the "Multi-Modal (SRSS)" and "Elastic First Mode". This might be due to the fact that the storey drifts at upper floors are influenced by higher modes in tall buildings. It is also reported that both the "FEMA-273" load distribution and the "Multi-Modal (SRSS)" on its own did not offer any advantage over other techniques, although both methods are supposedly tailored to represent higher mode effects.

Kusuma & Anwar (2010) have tested the effectiveness of three MMP techniques at determining the seismic response of a 20-storey RC frame building. The three methods include the Modal Pushover Analysis (MPA) which is originally introduced by Goel and Chopra (2001) and basically consists of a straightforward application of the MMP discussed earlier. The second procedure is referred to as the consecutive modal pushover (CMP) and consists of a first-stage application of MPA, which is followed by a second stage that starts with the state of deformations and stresses obtained at the end of the first stage (Poursha et al., 2009). The third method investigated is referred to as upper-bound pushover analysis (UBPA), it is originally developed by Jan et al. (2004) and consists of combining the first and second modes in determining the lateral load vector. Comparison against NLTHA have proven all three MMP techniques to produce conservative yet acceptable values of displacements and interstorey drifts. However, the CMP and UBPA did not offer any advantage over the traditional MMP procedure (the MPA), since the MPA provided relatively better estimates of the base shear and storey shear forces as well as for the plastic hinge rotation of beams and columns which were severely underestimated by the UBPA. It is therefore concluded that the CMP and UBPA offer no advantage compared to the ordinary MMP technique despite being technically and computationally more demanding.

Recent studies by Najam (2017) suggested that incorporating higher modes is computationally expensive and offers limited advantage compared to simplified pushover techniques, and accordingly cannot be justified as a reliable alternative to NLTHA. To this end, the author pointed out that the modal interactions are continuously changing and causing variations in the actual dynamic response, while this effect is not accounted for by MMP techniques which are based on the invariant elastic modes of vibration. The report also stresses the importance of simulating the actual hysteretic behaviour, including strength and stiffness degradation, pinching effects, and energy dissipation while most of the existing NSPs are limited in that regard and rely on generalised approximations of the hysteretic response. In conjunction with previous research, it is suggested that NSPs are not appropriate for the analysis of high-rise buildings characterised by a fundamental period exceeding one second as well as for structures featuring torsional responses and bi-directional effects. It is also mentioned that attempts to include torsional effects in the seismic response are still subject to further research and discussion.

Similar studies performed by Bhandari et al. (2018) tested the accuracy of the CSM in predicting the response of 5-storey and 10-storey RC frame buildings. The results were tested against a complete NLTHA using a series of ground motion time histories with PGA values ranging from 0.1g to 0.5g. The ground motions were scaled to match the response spectrum recommended by ATC-40 (ATC, 1996) to allow for a direct comparison with the CSM. It was reported that the CSM provided a good estimation of the top storey displacement and the maximum interstorey drift (error within 10%) for PGA values up to 0.3g. However, the discrepancy between the CSM and NLTHA is larger for higher PGA values, as the CSM overestimated the maximum displacement (by 50%) and the maximum interstorey drift (by 70%) for a PGA of 0.5g. This is attributed to the inelastic behaviour of the frame at higher PGA values. It was therefore concluded that the CSM can be applied with reasonable accuracy for ground motion intensities in the range 0.2g to 0.3g.

Another improvement of NSPs involves incorporating the effect of the soft storey mechanism into the structural response through adaptive pushover analysis that allows for redistribution of lateral inertia forces (Bracci et al., 1997; Requena & Ayala, 2000; Elnashai, 2001). Adaptive pushover analysis is a single-mode pushover analysis in which the modal properties and the associated load pattern are constantly updated upon the successive formation of plastic hinges. Studies by Najam (2017) have also reported that adaptive pushover analysis outperforms other NSPs in predicting the displacement demand of the structure.

To conclude, the previous discussion served to shed the light on the applicability of NSPs in general and the CSM in particular. It is accordingly safe to claim that MMP techniques offer little advantage in light of the computational burden associated with them. Indeed, most of the research did report that MMP procedures did not return an accurate estimate of the response of tall flexible buildings characterised by the contribution of higher modes or governed by a torsional mode. Furthermore, adaptive pushover analysis was shown to depict the soft storey mechanism and to return better estimate

of displacements than the ordinary pushover analysis; yet the method is technically and computationally exhaustive as it requires constant update of the input parameters. Drawing on these conclusions and recalling that the objective is to develop a simplified retrofitting strategy that entails reducing the computational requirements, a single-mode pushover analysis is adopted in this research. However, it is necessary to add that the anticipated retrofitting strategy aims at reducing the torsional effects and at increasing the mass participation of the fundamental mode in the translational direction, which consequently eliminates the uncertainties associated with the method and enforces the essential conditions required for an accurate and reliable application of the CSM (or any other NSP).

2.8 Conventional Seismic Retrofitting Methods of RC Buildings

In reinforced concrete (RC) buildings that are not originally designed to resist earthquakes, columns generally exhibit brittle shear failure upon exposure to seismic loading, especially when the amount of shear reinforcement supplied is not sufficient (Kobatake, 1998; Moehle et al., 2008). In view of this, jacketing of columns is a viable solution adopted in seismic retrofitting, with reinforced concrete, steel, carbon-fibre-reinforced polymer being commonly used as a jacketing material. Jacketing is a type of seismic retrofitting that is performed at the element level, that is strengthening targets specific weak elements in the structure. Conversely, other methods are referred to as global structural seismic retrofitting techniques, that is strengthening is achieved by adding new elements or components that modify the global behaviour of the existing structure (Bai, 2003). This section discusses the retrofitting techniques that are widely used to retrofit common buildings especially in developing countries, noting that the discussion does not target the sophisticated retrofitting solutions that require advanced knowledge and specialised expertise.

- ***Column Concrete Jacketing***: Column jacketing is mostly performed by adding concrete, longitudinal and transversal reinforcement around existing reinforced concrete columns (Rodriguez & Park, 1991). In general, this technique is used for the overall strengthening of columns against vertical and lateral loadings. Jacketing enlarges the cross-section of the column (more longitudinal reinforcement is accordingly added), and therefore increases its axial, shear, and flexural strengths (Bai, 2003). Concrete jacketing also strengthens the beam-column connection, and significantly contributes to increasing the strength and stiffness of the structure but does not remarkably enhance the ductility of the system.
- ***Steel Jacketing***: Embracing concrete columns by a steel jacket is another effective method of seismic retrofitting. Steel jacketing provides a strong confinement which strengthens the column against compression and spalling of the shell concrete. In fact, the loss of shell concrete exposes the longitudinal steel reinforcement to buckling which is barely resisted by conventional hoops. In view of this, a steel jacket provides a strong additional confinement without adding much to the volume of the column (Sakino & Sun, 2000). It is usually performed

by wrapping welded steel bars all around the column, although experimental results proved that tying the steel jacket to the column by bolts is more efficient than welded connections. Several research have pointed out that rectangular steel jacketing does not provide effective lateral confinement due to the bulging out of the steel jacket (Sun et al., 1993; Harries et al., 1998; Tsai & Lin, 2001). Results have also shown that octagonal steel jackets provide a better confinement compared to the rectangular ones, since the compressive forces acting on the column trigger tension (enhanced behaviour or more resistance) in steel plates in the octagonal configuration (Tsai & Lin, 2002).

- ***Seismic Retrofitting Using Carbon-Fibre-Reinforced Polymer (CFRP)***: Carbon fibres (CF) have a higher tensile strength than steel and present a better retrofitting solution in regard to cost and time efficiency (Kobatake, 1998). Hence, a relatively viable solution for seismic retrofitting involves winding a coil of CF spirally around the column's circumference or wrapping CF sheets all around the column. The supply of CF strands or sheets adds to the shear reinforcement and the associated shear strength of columns and helps increasing the flexural strength as well. However, CFRP sheets could fracture suddenly under high strain conditions because of their brittle nature, which makes them inefficient at improving the axial ductility of columns compared to steel jacketing (Tsai & Lin, 2002).

- ***Addition of Reinforced Concrete Walls (Shear Walls)***: One of the most common seismic retrofitting practices, this method involves infilling structural walls (shear walls) in the bays in order to increase the lateral stability of the structure and to reduce the lateral displacement (Di Sarno & Elnashai, 2002; Bai, 2003). The infilling walls are generally reinforced concrete walls, but steel walls or precast panels can also be used. The advantage of this technique is the ease of adding the shear walls which need no special expertise to be performed, although it poses some difficulties in the excavation and execution of the foundations of the newly added walls. Although this technique has proven to be the most reliable retrofitting practice against earthquakes, execution of shear walls takes more time compared to other techniques such as adding steel braces, and it causes an undesirable significant increase in the weight of structure as well (Kobatake, 1998).

- ***Addition of Masonry Infill Walls***: Another effective technique involves adding brick masonry walls between frames in the aim of increasing the lateral strength and stiffness of the building (Klingner & Bertero, 1976; Bertero & Brokken, 1983; Mander et al., 1993; Angel et al., 1994). Unreinforced or reinforced masonry infill walls can be added, where reinforced ones have been shown to provide more resistance as they tend to crack at higher lateral drifts. However, masonry bricks could potentially crack under high deformations, and thus could become ineffective as the loads in such case will be mainly resisted by the frames. Therefore, masonry walls need to be carefully applied and are not generally recommended in regions of high

seismicity and in case large deformations are possibly encountered (Di Sarno & Elnashai, 2002).

- ***Steel Bracing***: This method involves adding steel braces between existing frame members to enhance the lateral stiffness of moment-resisting frames, and it is widely considered amongst the most effective methods for global strengthening of frame buildings against earthquakes. Steel braces have proven to be efficient at increasing the lateral stiffness and at reducing the lateral displacement of RC frame buildings (El-Amoury & Ghobarah, 2005). Steel braces can either be concentric where both ends of the diagonal braces are connected to the framing columns, or they can be eccentric such that one or both ends of the diagonal braces do not connect with framing columns (Rodriguez & Park, 1991). The ease of execution is one of the main advantages of this technique compared to columns jacketing or addition of shear walls, since the braces are diagonally added between framing members above ground level and do not intervene with the ground or foundation (Vijayakumar & Babu, 2011). However, there is one concern whenever concentric steel bracing is used, as buckling can be initiated in compression braces due to applied horizontal compressive forces or because of tensile forces (in tension braces) which increase after yielding and strain-hardening (Di Sarno & Elnashai, 2002). Additionally, compression braces were experimentally shown to lose a significant amount of their initial compressive strength after buckling. Buckling effects can therefore lead to an unbalanced force concentration in the beam-brace connection which potentially causes failure in the beams at mid-span. To this end, checking the beam capacity at mid-span is always emphasized for a proper selection of a steel bracing scheme in order to prevent buckling (Di Sarno & Elnashai, 2002).

2.9 Shear Capacity of RC Members in Eurocode

Eurocode 2 or EN 1992-1-1 (CEN, 2004b) specifies different approaches for calculating the shear resistance of RC members which depend on whether the member does or does not require shear reinforcement. In this regard, the axial load contribution is only considered when evaluating the shear capacity of members that do not require shear reinforcement. Accordingly, the shear capacity of the case not involving shear reinforcement might be governing in columns and walls by virtue of the significant axial load in these members despite the contribution of shear reinforcement in the other formulation. In sum, the shear capacity of a shear-reinforced member is taken as the highest value calculated from both formulations corresponding to the cases requiring and not requiring shear reinforcement.

(i) Members not requiring shear reinforcement

Starting with members that do not require shear reinforcement, the design shear capacity is estimated as the largest of these two expressions:

$$V_{Rd,c} = \left[C_{Rd,c}\, k\, (100\, \rho_1\, f_{ck})^{1/3} + k_1\, \sigma_{cp} \right] b_w\, d \tag{2.33}$$

$$V_{Rd,c\min} = \left[\nu_{\min} + k_1\, \sigma_{cp} \right] b_w\, d \tag{2.34}$$

$$k = 1 + \sqrt{\frac{200}{d}} \le 2.0 \;\; with\, d\, in\, mm \tag{2.35}$$

$$\rho_1 = \frac{A_{sl}}{b_w d} \le 0.02 \tag{2.36}$$

where:

σ_{cp} is the compressive stress in concrete due to axial load or prestress and is given by the following:

$$\sigma_{cp} = \left(N_{ED} / A_c \right) < 0.2 f_{cd} \;\; [MPa]$$

N_{ED} is the axial force with compression being positive (N),

A_c is the area of concrete cross-section (mm^2),

A_{sl} is the area of tensile reinforcement that extends more than (l_{bd} + d) beyond the critical section (Figure 2.14),

b_w is the width (thickness) of the web,

d is the depth of the cross-section, and

$C_{Rd,c}, \nu_{\min}, k_1$ can be found in the National Annex of a given country with the following values being recommended:

$$C_{Rd,c} = 0.18 / \gamma_c$$

$$\nu_{\min} = 0.035\; k^{3/2}\; f_{ck}^{\,1/2}$$

$$k_1 = 0.15$$

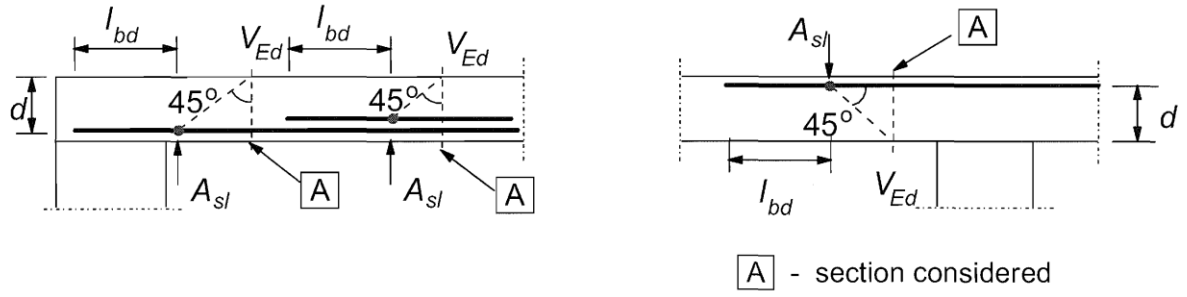


Figure 2.14: Definition of the area of the tensile reinforcement considered in the shear capacity (CEN, 2004b)

(ii) Members requiring shear reinforcement

For members that require shear reinforcement, EN 1992-1-1 (CEN, 2004b) recommends designing the shear reinforcement using a truss model (Figure 2.15), and the shear resistance is accordingly evaluated as the smaller value obtained from the following expressions:

$$V_{Rd,s} = \frac{A_{sw}}{s} z f_{ywd} \cot\theta \tag{2.37}$$

$$V_{Rd,\max} = \frac{\alpha_{cw} b_w z \nu_1 f_{cd}}{\cot\theta + \tan\theta} \tag{2.38}$$

where:

A_{sw} is the cross-sectional area of shear reinforcement,

s is the spacing of stirrups,

z is the inner lever arm (Figure 2.15), with an approximate value equal to 0.9d being suggested for the shear analysis of reinforced concrete without axial force,

f_{ywd} is the design yield strength of shear reinforcement,

θ is the angle between the concrete compression strut and the axis perpendicular to the shear force. Its value can be found in the National Annex of each country and is generally bound by the following limits:
$1 \le \cot\theta \le 2.5$

b_w is the minimum width between the tension and the compression chords,

ν_1 is a strength reduction factor for concrete cracked in shear. EN 1992-1-1 (CEN, 2004b) recommends evaluating it using the following expression:

$$\nu_1 = 0.6\left[1 - \frac{f_{ck}}{250}\right] \left(f_{ck} \ in \ MPa\right)$$

α_{cw} is a coefficient that accounts for the state of stress in the compression chord and is evaluated as per the following:

1.0	for non-prestressed structures
$\left(1 + \sigma_{cp} / f_{cd}\right)$	for $0 < \sigma_{cp} \le 0.25\, f_{cd}$
1.25	for $0.25\, f_{cd} < \sigma_{cp} \le 0.5\, f_{cd}$
$2.5\left(1 - \sigma_{cp} / f_{cd}\right)$	for $0.5\, f_{cd} < \sigma_{cp} < 1.0\, f_{cd}$

α is the angle between the shear reinforcement and the axis perpendicular to the shear force,

F_{td} is the design value of the tensile force in the longitudinal reinforcement, and

F_{cd} is the design value of the concrete compression force in the direction of the longitudinal member axis.

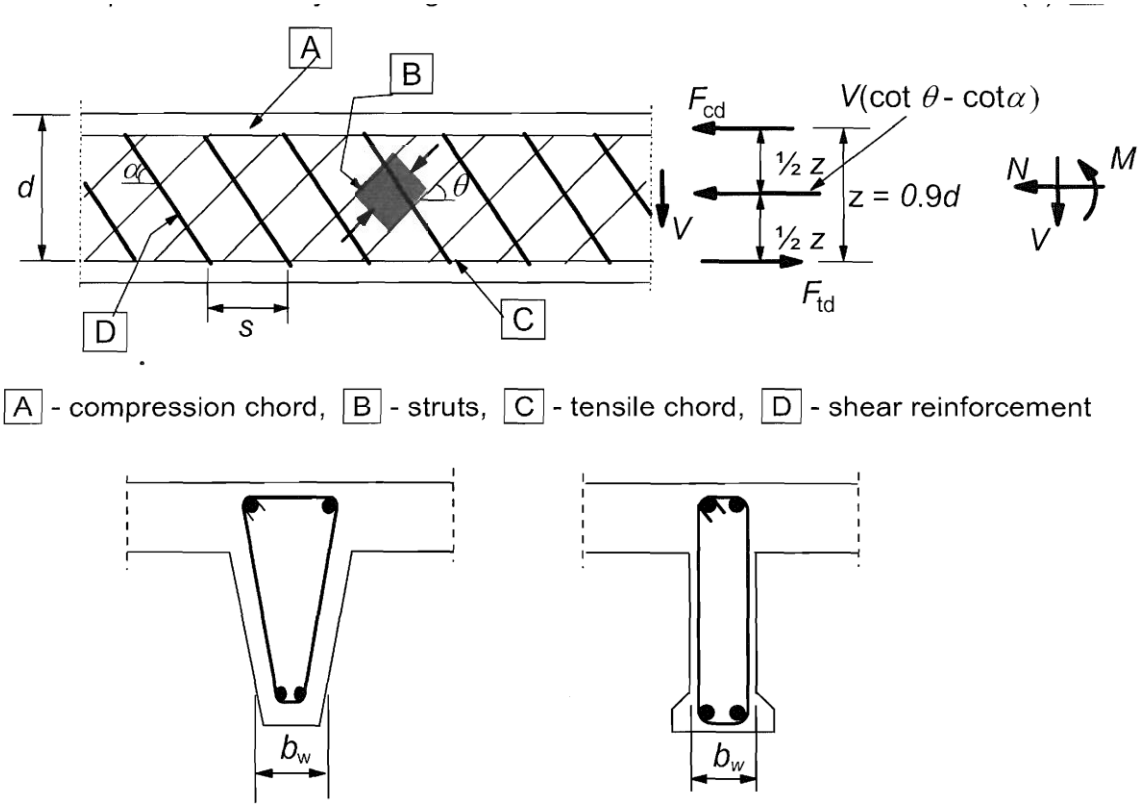


Figure 2.15: Truss model used in designing the shear reinforcement of members (CEN, 2004b)

In light of this, it is worth noting that EC8-1 (CEN, 2004a) recommends the same formulas adopted in EN 1992-1-1 (CEN, 2004b) for calculating the design shear resistance of RC members.

2.10 Design of Shear Walls According to Eurocode 8

2.10.1 General Overview

According to Part 1 of Eurocode 8, entitled as "General rules for the design of structures for earthquake resistance" and mostly referred to as EC8-1 (CEN, 2004a) throughout this thesis, a structural wall is defined as an element supporting other elements and possessing an elongated cross-section with a length-to-thickness ratio greater than 4. In fact, Eurocode distinguishes two major types of walls, the first of which is ductile walls which are designed to resist earthquakes by dissipating energy upon the formation of flexural plastic hinges at their fixed base. The second type is characterised by a large cross-section and are referred to as large lightly reinforced walls with a length exceeding two-thirds of the height. These latter cannot develop plastic hinges by virtue of lack of fixity at the base and are expected to experience limited cracking and inelastic behaviour when subjected to seismic loading. Energy dissipation mostly happens at the soil-structure interface through rigid body rocking. This latter type is not commonly encountered in buildings, and accordingly the walls involved in this research are strictly ductile walls that can dissipate energy through the formation of flexural hinges at their base.

Shear walls are generally introduced into the structural system in the aim to prevent the formation of storey-mechanism along the main direction of the wall. However, installation of walls is not usually accompanied with a verification check that plastic hinges are forming in beams rather than in columns. In this regard, walls must act as vertical cantilevers that can only develop plastic hinges at their fixed base in order to enforce the beam sway mechanism (Fardis, 2009). Towards satisfying this condition, the wall must primarily possess a relatively higher stiffness and strength compared to the beams at which it is connected at all storeys. Furthermore, Fardis (2009) adds that besides possessing a large cross-section (length-to-thickness ratio), walls must have a considerably large absolute length (irrespective of the thickness) in order to behave as a cantilever. To this end, the corresponding length of walls is estimated to be at least 1.5 meters for low-rise buildings and 2.0 meters for medium and high-rise ones, considering the commonly used beam sizes in buildings. To note that walls might have a sufficiently elongated cross-section but might not act as cantilevers and would rather behave as frame columns if they are connected to stiff and strong beams.

As the building is subjected to seismic loading, the resultant overturning moment is balanced by bending moments at the base of the walls. Hence, each wall is represented as a cantilever with lateral forces applied at the storey levels by virtue of having a sufficiently elongated cross-section that exacts the formation of a plastic hinge at the base only. In this respect, the wall is expected to develop large bending moment and consequently long shear span (moment to shear ratio, $L_s = M/V$) at the base. Under these conditions, the shear span is approximated as a fixed fraction of the total height of the wall which is estimated around one-half of the total height for commonly used beam sizes. In light of this discussion, Fardis (2009) also proved that the optimum shear span ratio (ratio of shear span to the depth

of the wall's cross-section, L_s/h) is in the range 2.5 – 3.0, since the wall response might be impacted by shear effects if the shear span ratio is further reduced. This can actually be used to obtain a preliminary estimate of the wall length that is needed to ensure appropriate structural wall behaviour. Assuming a target shear span ratio (L_s/h) of 3.0 and a typical shear span equal to half of the total height ($L_s = 0.5H_t$), a reasonable preliminary estimate of the length of the wall can be obtained ($h = H_t/6$), where H_t is the total height of the wall.

It is worth noting that the previous discussion serves to shed some light on the anticipated length of the wall and the shear span ratio that is required to ensure the wall acts as a cantilever. Nevertheless, in the context of retrofitting of buildings in this research, the dimensioning of walls is addressed from a practical perspective while taking into consideration the Eurocode requirements. This practically means that the length of walls is mostly bound by the span length between the columns, and more walls are added in a given direction to ensure the target of seismic retrofitting is achieved.

2.10.2 Special Provisions for the Design of Ductile Walls According to Eurocode 8

In line with ensuring a ductile behaviour, the capacity design requirements of Eurocode 8 recommend special detailing that exact flexural yielding at the base of the wall before shear failure occurs. This is promoted by providing excessive bending strength at the upper parts of the wall in order to prevent unanticipated flexural failure at these locations. In this respect, the provisions of EC8-1 (CEN, 2004a) require modifying the bending moment diagram obtained from the analysis through a tension shift that is associated with shear lag effects (Figure 2.16). The resultant design bending moment diagram increases from zero at the top to a maximum at the base, where it is displaced upwards by the tension shift as required by the code (Figure 2.16). The tension shift is approximated in Eurocode 2 as the product of half of the internal lever arm at the base of wall ($z = 0.5 * 0.8\, l_w$) and the strut angle assumed in the shear strength calculation (CEN, 2004b). Accordingly, the seismic bending moment at a distance x from the base is expressed by the following (Figure 2.16):

$$M_x = M_{base} \frac{H_{tot} - x}{H_{tot} - z\cot\theta} \tag{2.39}$$

where:

$$1 \le \cot\theta \le 2.5$$

To note that if $cot\theta$ is conservatively taken as 2.5, the tension shift would approximately become equal to the length of the wall.

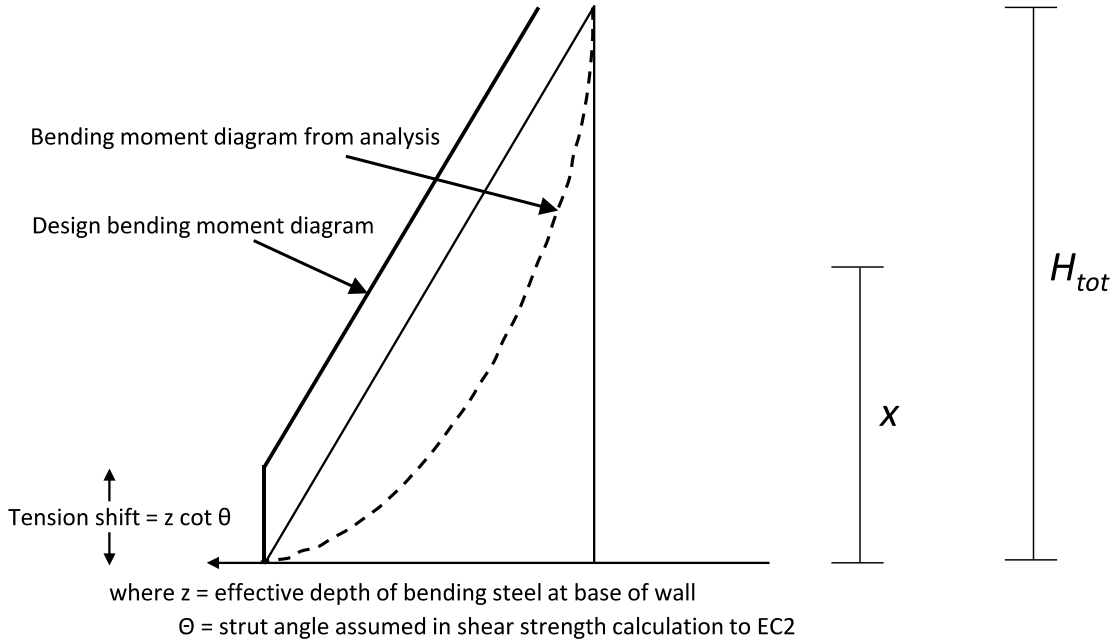


Figure 2.16: Capacity design requirement for flexural design of shear walls (Booth, 2018)

At this stage, it is worth recalling that EC8-1 (CEN, 2004a) does not entail any specific requirements in regard to the flexural capacity and accordingly approves the formulations of Eurocode 2 EN 1992-1-1 (CEN, 2004b) along with considering the axial load associated with the seismic design situation. To note also that the code requires including the vertical web reinforcement as well as the effect of perpendicular walls connected at the ends of the wall when calculating the flexural strength.

EC8-1 (CEN, 2004a) also requires modifying the shear diagram obtained from the analysis, such that the design shear diagram increases from zero at the top to a maximum at the base which is obtained by multiplying the base shear obtained from the analysis by a magnification factor (Figure 2.17). Again, EC8-1 (CEN, 2004a) recommends the same formulas adopted in EN 1992-1-1 (CEN, 2004b) for calculating the design shear resistance of ductile walls.

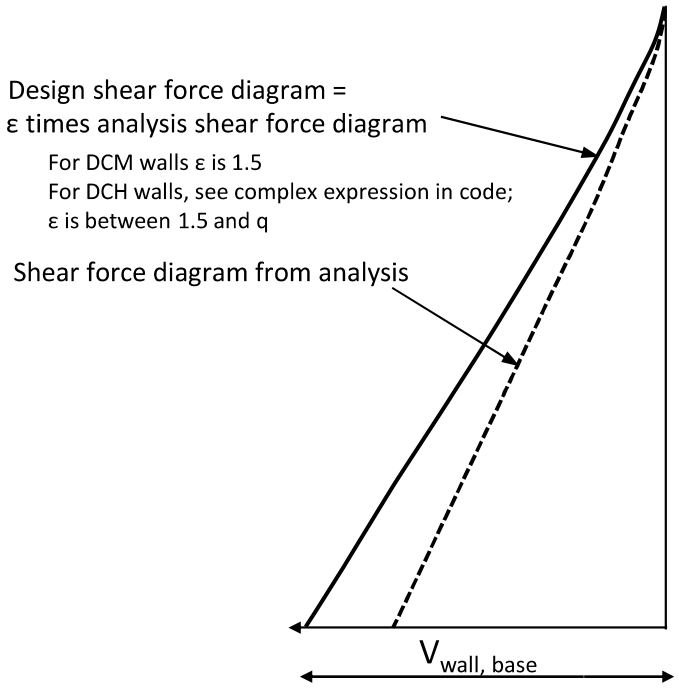


Figure 2.17: Capacity design shear requirement for walls under seismic action (Booth, 2018)

Furthermore, EC8-1 (CEN, 2004a) requires that the normalised axial load must not exceed the limit of 0.4 for DCM and 0.35 for DCH walls in the aim to limit buckling effect and to ensure that sufficient rotational ductility is provided.

2.10.3 Specialised Detailing for Ductile walls

EC8-1 (CEN, 2004a) specifies a minimum wall thickness (b_{w0}) evaluated according to the following expression:

$$b_{w0} \geq \max\left[0.15,\ h_s / 20\right] \tag{2.40}$$

where:

h_s is the clear storey height in meters.

Furthermore, EC8-1 (CEN, 2004a) entails the presence of specifically confined and reinforced regions at the ends of wall, referred to as boundary elements or boundary columns. The purpose of these confined areas is to resist the large compressive strains associated with the high flexural stresses at the ends of the wall (Figure 2.18). The confined areas must extend from the base and span through the critical height (h_{cr}) which is determined by the following:

$$h_{cr} = \max\left[l_w, h_w / 6\right] \tag{2.41}$$

$$h_{cr} \le \begin{cases} 2\,l_w & \\ h_s & for\ n \le 6\ storeys \\ 2\,h_s & for\ n \ge 7\ storeys \end{cases} \tag{2.42}$$

where:

l_w is the length of wall,

h_w is the total height of the wall, and

h_s is the storey height.

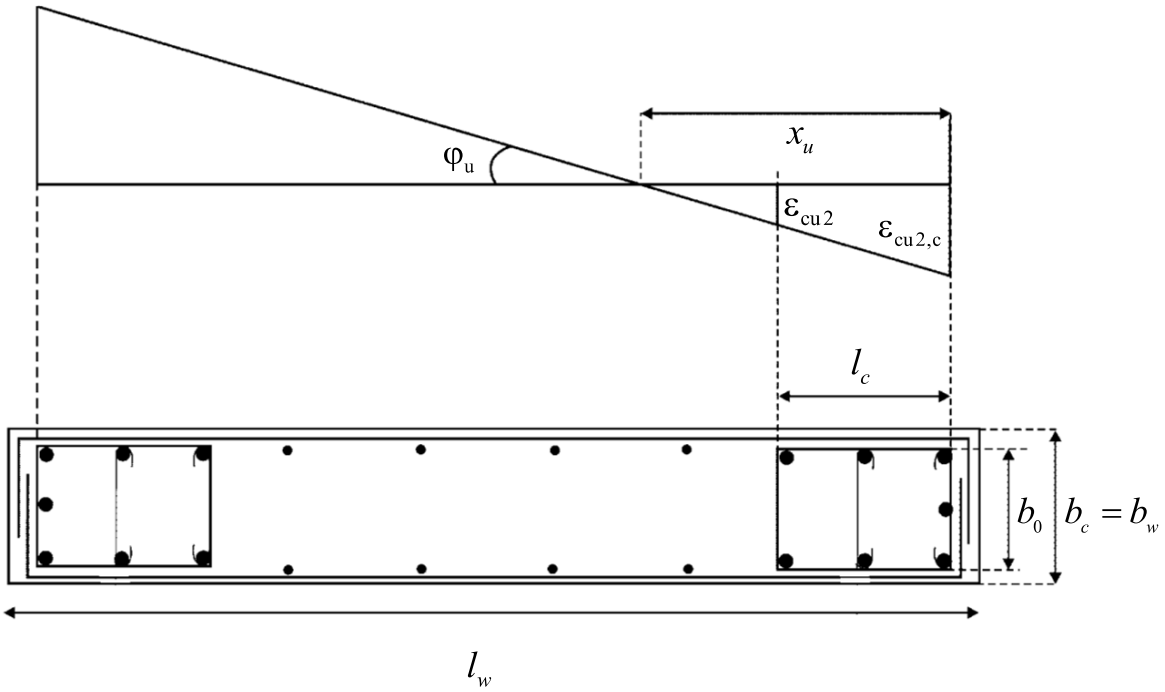


Figure 2.18: Confined boundary element at the end of the wall's cross-section along with the strains at ultimate curvature (CEN, 2004a)

In light of this discussion, the confinement at the ends of the wall should be extended horizontally to cover the region of high compressive strains that can cause spalling of concrete. EC8-1 (CEN, 2004a) specifies a limit strain of 0.0035 above which spalling of concrete is expected. This permits to evaluate the horizontal length of the boundary element using the similar triangles (Figure 2.18), while the ultimate compressive strain at the end of wall is estimated according to Eurocode 2 or EN 1992-1-1 (CEN, 2004b) as per the following:

$$l_c = x_u \left(1 - \frac{\varepsilon_{cu2}}{\varepsilon_{cu2,c}}\right) \tag{2.43}$$

$$l_{c,\min} = \max(0.15 l_w, 1.5 b_w) \tag{2.44}$$

$$\varepsilon_{cu2,c} = 0.0035 + 0.1 \alpha \omega_{wd} \tag{2.45}$$

where:

l_c is the calculated length of the confined boundary element,

$l_{c,\min}$ is the minimum length of confined boundary element,

x_u is the depth of the compressive zone,

ε_{cu2} is the compressive strain at which spalling of concrete is expected (taken as 0.0035), and

$\varepsilon_{cu2,c}$ is the ultimate strain at the extreme compression fibre.

EC8-1 (CEN, 2004a) specifies a minimum ratio of 0.005 for the longitudinal (vertical) reinforcement in the boundary element, and the mechanical volumetric ratio of confining reinforcement in rectangular walls is determined according to the following expression:

$$\alpha \omega_{wd} \geq 30 \mu_\varphi (\nu_d + \omega_v) \varepsilon_{sy,d} \frac{b_c}{b_0} - 0.035 \tag{2.46}$$

where:

ω_{wd} is the mechanic volumetric ratio of the confining reinforcement, defined by the following:

$$\omega_{wd} = \left[\frac{volume\ of\ confining\ hoops}{volume\ of\ confining\ core} \cdot \frac{f_{yd}}{f_{cd}}\right]$$

f_{yd} is the design yield strength of steel (confining hoops),

f_{cd} is the design compressive strength of concrete,

α is the confinement effectiveness factor which is determined as per the following expression for rectangular sections:

$$\alpha = \alpha_n \alpha_s$$

$$\alpha_n = 1 - \sum_n b_i^2 / 6 b_0 h_0$$

$$\alpha_s = \left(1 - s/2b_0\right)\left(1 - s/2h_0\right)$$

n is the total number of longitudinal bars laterally engaged by hoops,

b_i is the distance between bars that are consecutively engaged by hoops,

b_0 is the width of confined core, measured to the centreline of the hoops (Figure 2.18),

h_0 is the depth of confined core, measured to the centreline of the hoops,

s is the spacing of stirrups,

μ_φ is the curvature ductility factor which is briefly explained in Appendix A2.1,

ν_d is the normalised axial load and is expressed by the following and which should not exceed the limit of 0.4:

$$\nu_d = \frac{N_{Ed}}{h_c\, b_c\, f_{cd}} \leq 0.4$$

N_{Ed} is the applied axial load,

b_c is the gross cross-sectional width of the boundary element (Figure 2.18),

h_c is the gross cross-sectional depth of the boundary element,

ω_v is the mechanical ratio of vertical web reinforcement (in the confined region) which is given by the following:

$$\omega_v = \frac{A_{sv}}{h_c\, b_c}\,\frac{f_{yd,v}}{f_{cd}}$$

A_{sv} is the total area of vertical reinforcement in the boundary column,

$f_{yd,v}$ is the design yield strength of vertical web reinforcement, and

$\varepsilon_{sy,d}$ is the design value of tension steel strain at yield.

The minimum thickness of the boundary element must be greater than 200 mm and is further bound by the length of the boundary element as reflected in Figure 2.19 along with the following notations:

h_s is the clear storey height, and

l_w is the length of the wall.

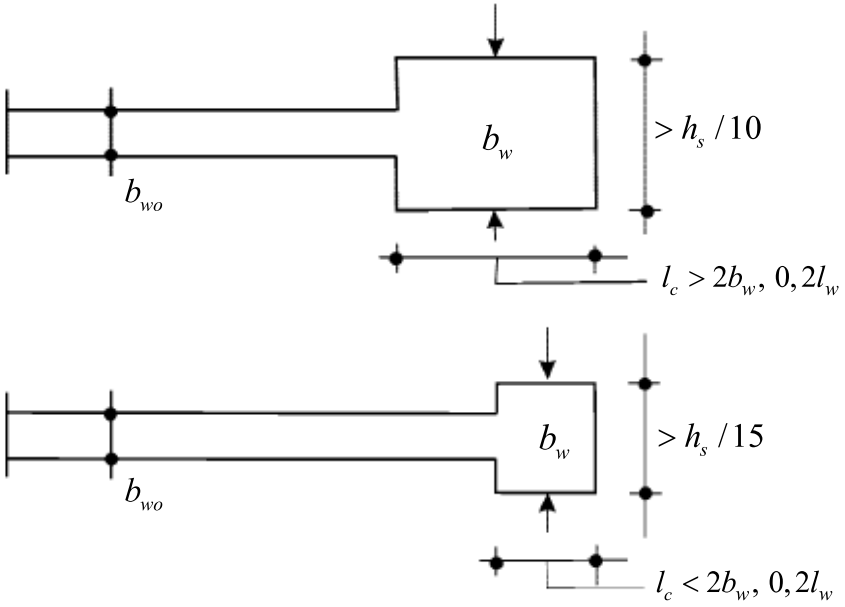


Figure 2.19: Minimum dimensions of boundary elements (CEN, 2004a)

To note also that the maximum spacing of confining hoops (in millimetres) in the boundary element is similar to that in normal columns and is given by the following (CEN, 2004a):

$$s = \min\left\{b_0 / 2;\ 175;\ 8d_{bL}\right\} \tag{2.47}$$

where:

b_0 is the minimum dimension of the concrete core, measured to the centreline of the hoops, and

d_{bL} is the minimum diameter of the longitudinal bars.

2.11 Concluding Remarks

This chapter presented an up-to-date and comprehensive review of the literature concerned with the seismic retrofitting of RC buildings. As noted in the first section, NLTHA has always been regarded as the most accurate method that represents the nonlinear response of structures subjected to earthquake loading. Because of the significant computational demands associated with the method, NSPA has always been viewed as a simplified yet reliable alternative. This research relies on the CSM, a special form of NSPA applicable under specific conditions, in order to design a retrofitting strategy for substandard RC buildings located in seismic hazard regions. First of all, it is pointed out in the literature that the accuracy of single-mode NSPA is subject to the predominance of the fundamental mode of vibration; otherwise MMP techniques are to be used, which is computationally disadvantageous and which only provides a slight improvement compared to the single-mode pushover analysis. Accordingly, Chapter 4 presents a technique that ensures the predominance of the fundamental mode of vibration on the response, which subsequently enforces the applicability and reliability of the CSM.

Furthermore, Chapter 5 presents an iterative approach that determines the vibration characteristics of multi-storey RC buildings by way of direct application of static analysis, which saves the computational effort and time needed to assemble the mass and stiffness matrices as required by conventional eigenvalue analysis. On the same hand, Chapter 6 presents a simplified approach devised to find the pushover response of buildings in a simplified manner which does not require modelling of the building. Accordingly, the findings of Chapters 5 and 6 allow for a faster application of the CSM, which is employed in this research to develop a simplified strategy that facilitates and guides the retrofitting of substandard RC buildings subjected to seismic loading using shear walls.

Chapter 3 Seismic Assessment of RC Buildings in the Context of the CSM

3.1 Introduction:

The design of new buildings located in seismic hazard regions and the retrofitting of existing ones have been subject to controversy among researchers over the past few decades. Fardis (2009) has pointed out that provisions for seismic design and detailing of buildings have only been introduced in the mid-70's in the US standards and in the mid-80's in the European standards. Prior to these dates, the lateral resistance of buildings around the world was mostly limited to the resistance of wind loading. Existing buildings located in seismic regions are mostly considered to be seismically deficient since they were not designed to resist any form of earthquake loading (Fardis, 2009). A detailed seismic assessment is therefore required in order to decide on the adequacy and the potential need to retrofit existing buildings located in seismic hazard regions.

In light of this discussion, several international codes and standards have specified a list of relevant performance checks that guide the seismic assessment and upgrading of existing buildings. Part 3 of Eurocode 8 (CEN, 2005a) which is also known as EN 1998-3:2005 and which is referred to as EC8-3 in this thesis, stands out as one of the elite international standards that address the seismic assessment and retrofitting of existing buildings. EC8-3 (CEN, 2005a) defines three limit states of damage in the structure described by the following:

- Damage Limitation (DL) is the seismic level that incurs minor damages on the structure, such that structural components retain their lateral strength and stiffness with minimum yielding behaviour, and the structure does not require any repairing after being subjected to the DL seismic event (estimated return period of 225 years).
- Significant Damage (SD) is the seismic level that produces significant damages in the structure and a drop in the lateral strength and stiffness, such that the structure can still survive moderate-intensity earthquakes (return period of 475 years).
- Near Collapse (NC) characterises the seismic level that produces substantial damages that lead to a significant decrease in the lateral strength and stiffness of the structure such that it cannot even sustain a moderate earthquake (return period of 2475 years).

It is up to the national authorities in each country to decide on the limit state to be checked at (CEN, 2005a). In this research, the seismic behaviour of buildings is checked at both the SD and the NC limit states, with particular focus on the NC state since it provides a better simulation of the real collapse of buildings.

According to the provisions of EC8-3 (CEN, 2005a), for any existing building (prior to retrofitting) and for any retrofitted building to be deemed adequate to resist the seismic hazards in its vicinity, every structural member (primary or secondary) should meet the required verification criteria that conform with the performance level (limit state) under consideration. In this respect, the components of the structural system may generally suffer a ductile and/or a brittle failure. The ductile mechanism is usually addressed in the form of deformations in the ductile components while the brittle mechanism is controlled by the shear forces in the brittle components. Checking against the ductile mechanism of failure basically consists of verifying that the deformation in all ductile elements including beams, columns, and walls which are subjected to flexural loading with or without an axial force does not exceed the maximum value entailed by the code at the limit state under consideration. Similarly, the check against potential brittle failure is verified by checking that the shear forces developing in the brittle elements (beams, columns, walls, and joints) are not exceeding the ultimate shear capacity at the limit state being considered. In this context, provisions of EC8-3 (CEN, 2005) specify the following criteria for the three limit states:

- At the DL state, the deformations in all the ductile components should not exceed the yield limit while the forces in the brittle elements should not exceed the yield capacity.
- At the SD limit state, the deformation of ductile elements should not exceed the specified "damage-related deformations" while the forces in the brittle elements should not exceed the "conservatively estimated strengths".
- At the limit state of NC, the deformation of ductile elements should not exceed the ultimate deformation limit specified in the code while the forces should not exceed the ultimate strength or capacity of the brittle elements.

The provisions of EC8-3 (CEN, 2005a) also specify three types of knowledge level (KL) based on the state of knowledge of the geometric and material properties of the building. The KLs are represented by a confidence factor and are described in the following:

- Limited Knowledge (KL1)
- Normal Knowledge (KL2)
- Full Knowledge (KL3)

Confidence factors (CF) of 1.35, 1.2, and 1.0 are assigned to knowledge levels KL1, KL2, and KL3, respectively. A Normal Knowledge (KL2) with a corresponding CF of 1.2 is considered for the assessment of buildings in this research. Accordingly, the material properties are divided by the CF when evaluating the capacity of brittle and ductile elements in a nonlinear analysis while the action or effect exerted by the ductile components on the brittle components is conversely multiplied by the CF (CEN, 2005a).

This chapter presents the procedure implemented for the assessment of existing multi-storey RC buildings in compliance with the provisions of EC8-3 (CEN, 2005a). The procedure involves evaluating the following response parameters which are discussed in depth in the following sections and checking them against the code-permitted value pertaining to the limit state under consideration:

- Chord rotation (ductile mechanism of failure)
- Shear demand (brittle mechanism of failure)
- Interstorey drift (global stability of the building)

The chapter concludes with an application of the seismic assessment procedure to check the resistance of an existing 10-storey RC building located in Beirut (Lebanon) against potential earthquake loading.

3.2 Checking against Ductile Failure

The potential ductile failure of structural components is checked by confirming that the deformation of these elements does not exceed the limit specified by the code at the performance limit state under consideration.

In this regard, the chord rotation is a measure of the deformation capacity of the ductile components including beams, columns, and walls which are subjected to flexural loading with or without an axial force. The chord rotation at one end is the angle between the tangent to the deformed shape (the normal to the cross-section) at that end and the chord spanning through the point of contraflexure and connecting both ends of the member in the deformed configuration (Figure 3.1). The chord rotation at the ends of a member is deemed as the most appropriate measure of the deformation of concrete elements (Fardis, 2009) since they are equal to the flexural nodal rotations after subtracting the rigid-body displacements. The distance between the yielding end and the point of contraflexure is called the shear span and is equal to the moment-to-shear ratio at the end of beam/column. As shown in the rightmost part of the figure, the chord rotation is also equal to the drift ratio, which is the relative displacement at the point of contraflexure with respect to the tangent at the member's end divided by the shear span.

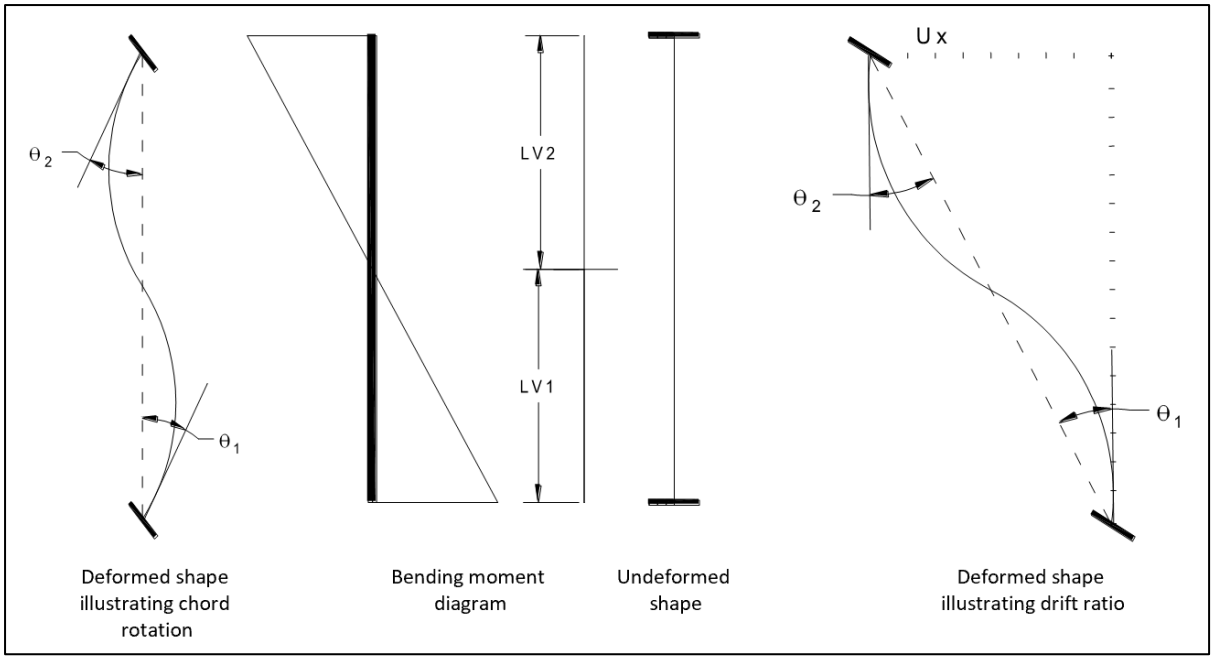


Figure 3.1: Illustration of the chord rotation (Murad, 2015)

In the context of seismic assessment, the demand chord rotation is evaluated for every structural member and is checked against the code-allowable limit associated with the performance limit state under consideration. In this regard, EC8-3 (CEN, 2005a) recommends the limits in Table 3-1 for the DL, SD, and NC limit states, where θ_y and θ_{um} respectively represent the yield and ultimate chord rotations and M_y represents the yielding moment.

Table 3-1: Allowable deformation in existing buildings in compliance with EC8-3 (CEN, 2005a)

Damage Limitation (DL)	Significant Damage (SD)	Near Collapse (NC)
$\theta \le \theta_y \;\; or \;\; M \le M_y$	$\theta \le 0.75\,\theta_{um}$	$\theta \le \theta_{um}$

The following expression defines the ultimate chord rotation allowed in beams and columns (CEN, 2005a), noting that a reduction factor of 0.58 is applied to the expression when evaluating the ultimate chord rotation of walls:

$$\theta_{um} = \left(\frac{1}{\gamma_{el}}\right) 0.016 \left(0.3^{\nu}\right) \left[\frac{\max(0.01;\omega')}{\max(0.01;\omega)} f_c\right]^{0.225} \left[\min\left(9;\frac{L_v}{h}\right)\right]^{0.35} 25^{\left(\alpha\rho_{sx}\frac{f_{yw}}{f_c}\right)} \left(1.25^{100\rho_d}\right) \quad (3.1)$$

where:

θ_{um} is the ultimate chord rotation in beams and columns. It is multiplied by 0.58 to obtain the ultimate chord rotation of wall elements,

γ_{el} is equal to the 1.5 for primary seismic elements and to 1.0 for secondary ones,

h is the depth of the cross-section,

L_v is the shear span length and is equal to the moment to shear ratio ($L_v = M / V$). It is denoted by LV1 and LV2 in Figure 3.1,

ν where b is the width of the compression zone and N is the axial force with a positive value for compression,

$$\nu = \left(N / bhf_c \right)$$

ω is the mechanical reinforcement ratio of longitudinal tension reinforcement (including the web reinforcement),

$$\omega = (\rho_1 + \rho_v) f_{yl} / f_c$$

ω' is the mechanical reinforcement ratio of longitudinal compression reinforcement,

$$\omega' = (\rho_2) f_{yl} / f_c$$

ρ_1 & ρ_2 respectively represent the ratio of longitudinal tension and compression reinforcement, which are obtained by dividing the respective area of steel reinforcement by the area of the cross-section,

ρ_v is the ratio of longitudinal tension reinforcement in the web (obtained by dividing the area of steel reinforcement by the area of the cross-section),

f_{yl} is the yield strength of longitudinal reinforcement (MPa) divided by the confidence factor,

f_c is the mean concrete compressive strength (MPa) divided by the confidence factor,

f_{yw} is the mean stirrup yield strength (MPa) divided by the confidence factor,

ρ_{sx} is the ratio of transverse steel in the direction x of loading where A_{sx} is the area of reinforcement and s_h is the stirrup spacing,

$$\rho_{sx} = \left(A_{sx} / b_w s_h \right)$$

ρ_d is the ratio of diagonal reinforcement in each diagonal direction (obtained by dividing the area of diagonal steel reinforcement by the area of the cross-section),

α is the confinement effectiveness factor. It is given by the equation below and should always be positive. If the expression below yields a negative value, the confinement effectiveness factor should be taken as 1.0,

$$\alpha = \left(1 - \frac{s_h}{2b_0} \right) \left(1 - \frac{s_h}{2h_0} \right) \left(1 - \frac{\sum b_i^2}{6h_0 b_0} \right)$$

b_0, h_0 are the dimensions of the confined core (Figure 3.2), and

b_i is the centre-to-centre spacing of longitudinal steel bars (indexed by *i*) which are braced by a stirrup corner or a crosstie along the perimeter of the cross-section (Figure 3.2).

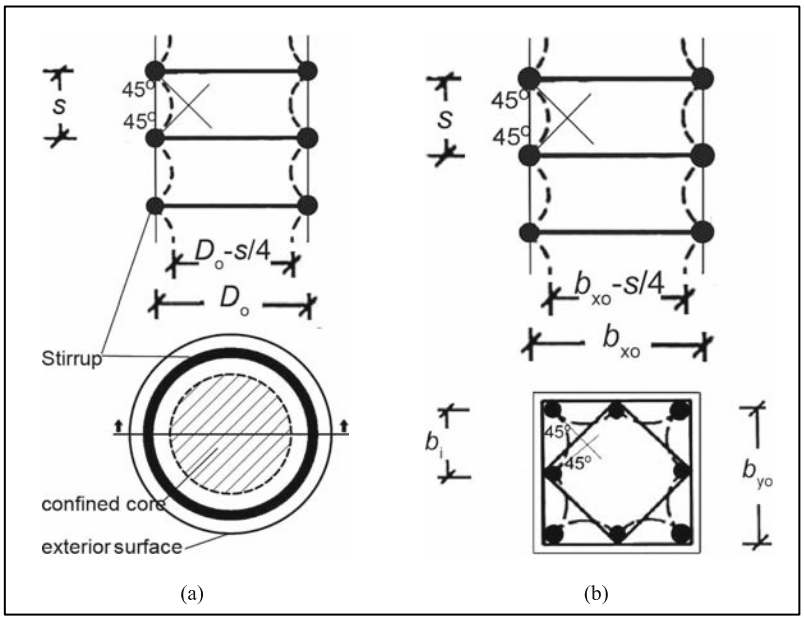


Figure 3.2: Confined and unconfined parts of a member's: (a) circular cross-section with circular hoops; (b) square section and multiple ties (Fardis, 2009)

Similarly, the yield value of the chord rotation is given by the following equations (CEN, 2005a):

For beams and columns: $$\theta_y = \phi_y \frac{L_v + a_v z}{3} + 0.0014\left(1 + 1.5\frac{h}{L_v}\right) + \frac{\varepsilon_y}{d - d'}\frac{d_{bL} f_y}{6\sqrt{f_c}} \quad (3.2)$$

For walls of rectangular, T-, and barbelled section: $$\theta_y = \phi_y \frac{L_v + a_v z}{3} + 0.0013 + \frac{\varepsilon_y}{d - d'}\frac{d_{bL} f_y}{6\sqrt{f_c}} \quad (3.3)$$

where:

ϕ_y is the yield curvature of the end section,

z is the lever arm which is taken as (d – d') for beams, columns, and walls having a barbelled or a T-section, while z is equal to 0.8h for walls having a rectangular cross-section,

$a_v = 1$ if shear cracking at the end section occurs before flexural yielding at the end section ($M_y > L_v V_{R,C}$) with M_y being the yield moment and $V_{R,C}$ being the member's shear resistance without shear reinforcement,

$a_v = 0$ if $M_y < L_v V_{R,C}$,

ε_y is the yield strain and is equal to (f_y / E_s),

d, d' are the depths to the tension and compression reinforcement respectively, and

d_{bL} is the mean diameter of the tension reinforcement.

It is noted in Eurocode that the ultimate and plastic components of the chord rotation capacity are divided by 1.2 in members that not detailed for earthquake resistance (CEN, 2005a).

3.3 Checking against Brittle Shear Failure

Potential brittle shear failure occurs when the shear force in the brittle elements (beams, columns, walls, and joints) exceeds the member's ultimate shear capacity.

In this respect, the provisions of EC8-3 (CEN, 2005a) state that the ultimate shear capacity cannot exceed the value calculated using the provisions of Eurocode 2-Part 1 or EN 1992-1-1 (CEN, 2004b). Accordingly, the shear resistance is evaluated according to the provisions of both EC8-3 and EN1992-1-1, and the smallest value represents the ultimate shear capacity of the member when the structure is subjected to seismic loading. The shear capacity defined by EN 1992-1-1 is already covered in Section 2.9 in Chapter 2, and the current section presents the shear provisions of EC8-3.

Shear Provisions of Eurocode 8-Part 3 (EN 1998-3:2005)

According to the provisions of EC8-3 (CEN, 2005a), the ultimate shear capacity of structural elements (beams, columns, and walls) at the NC limit state decreases with the plastic component of the ductility factor, which is the ratio of the plastic component of the chord rotation (or displacement) that is normalised with respect to the yielding value. The expression below is adopted to evaluate the shear capacity of beams, columns, and walls at the NC limit state. It is worth noting that EC8-3 does not suggest any specific requirement for the DL and SD limit states and recommends using the same expression adopted for the NC state when evaluating the ultimate shear capacity.

$$V_R = \frac{1}{\gamma_{el}}\left[\frac{h-x}{2L_v}\min(N;0.55A_c f_c) + \left(1-0.05\min\left(5;\mu_\Delta^{pl}\right)\right)\left[0.16\max\left(0.5;100\rho_{tot}\right)\left(1-0.16\min\left(5;\frac{L_v}{h}\right)\right)\sqrt{f_c}A_c + V_W\right]\right] \quad (3.4)$$

where:

V_R is the ultimate shear capacity of beams, columns, and walls,

μ_Δ^{pl} is the plastic ductility factor,

$$\mu_\Delta^{pl} = \frac{\theta^{pl}}{\theta_y} = \frac{\theta - \theta_y}{\theta_y}$$

θ^{pl} is the plastic component of the chord rotation,

γ_{el} is equal to the 1.15 for primary seismic elements and to 1.0 for secondary ones,

h is the depth of cross-section and is equal to the diameter in circular cross-sections,

x is the depth of the compression zone,

N is the compressive axial force (always positive and taken as zero for tension),

L_v is the shear span length and is equal to the moment to shear ratio at the end section,

A_c is the cross-sectional area and is equal to $b_w d$ for rectangular cross-sections having a width b_w and depth d, while A_c is equal to ($\pi D_c^2 / 4$) for circular cross-sections with D_c being the diameter of the concrete core to the inside of the hoops,

f_c is the mean concrete compressive strength (MPa) and is divided by the partial factor of concrete in primary seismic elements (is also divided by the CF for all the elements),

ρ_{tot} is the total longitudinal reinforcement ratio,

V_W is the contribution of transverse reinforcement to the shear resistance,

For rectangular cross-sections: $V_W = \rho_W \, b_W \, z \, f_{yw}$

ρ_W is the ratio of transverse reinforcement,

z is the length of the internal lever arm,

f_{yw} is the yield stress of the transverse reinforcement and is divided by the partial factor for steel for seismic elements (besides being divided by the confidence factor for all elements), and

b_W is the width (thickness) of the web.

The code provisions also require that the shear capacity of walls cannot exceed the limit corresponding to failure by web crushing which is determined by the following equation:

$$V_{R,\max,Wall} = \frac{0.85\left(1-0.06\min\left(5;\mu_\Delta^{pl}\right)\right)}{\gamma_{el}}\left(1+1.8\min\left(0.15;\frac{N}{A_c f_c}\right)\right)\left(1+0.25\max\left(1.75;100\rho_{tot}\right)\right)\left(1-0.2\min\left(2;\frac{L_v}{h}\right)\right)\sqrt{f_c}\,b_W z \quad (3.5)$$

According to further code requirements, if the shear span ratio (L_v/h) at the end having the higher moment in a concrete column is less than or equal to 2, then the shear strength of the column should not exceed the limit value corresponding to failure by web crushing along the diagonal of the columns after flexural yielding, which is evaluated using the following expression (units in MN and meter):

$$V_{R,\max,Col} = \frac{4/7\left(1-0.02\min\left(5;\mu_{\Delta}^{pl}\right)\right)}{\gamma_{el}}\left(1+1.35\frac{N}{A_c f_c}\right)\left(1+0.45\left(100\rho_{tot}\right)\right)\sqrt{\min(40;f_c)}\,b_w\,z\,\sin 2\delta \quad (3.6)$$

where:

$V_{R,\max,Col}$ is the maximum shear strength of the column that corresponds to failure by web crushing after flexural yielding, and

δ is the angle between the diagonal and the axis of the column ($\tan\delta = h/2L_v$).

3.4 Checking the Global Stability of the Building

According to Fardis (2009), the main reason behind the collapse of structures subjected to earthquake loading is mainly due to the large deformations induced in the structure and not to the seismic lateral forces. Structures often undergo large inelastic displacements in order to dissipate the energy imparted to the structure by the dynamic seismic load. In this respect, most of the current seismic design codes allow for large inelastic deformations in response to seismic loading provided that the integrity of the members and of the whole structure is not compromised. To this end, the combined effect of the seismic lateral displacements and the gravity loading generates an additional bending moment on the vertical elements. This secondary moment is known as the second-order or *P*-Δ effect and is the product of the gravity force *P* and the interstorey drift Δ at any floor level. The second-order effects can have a significant impact on the global stability as the structure is expected to dissipate the seismic energy through large inelastic displacements. Accordingly, most of the seismic design codes require including second-order effects in the analysis whenever the second-order (*P*-Δ) moment exceeds the first-order moment in vertical members at any storey level. This is referenced as well in the provisions of EC8-1 (CEN, 2004a) through the calculation of the interstorey drift seismic coefficient, which is the ratio of the second-order moment to the change in the first-order moment at a given storey. Hence, second-order effects can be ignored as long as this condition is met as illustrated in the following equation:

$$\theta_i = \frac{P_{tot,i}\,\Delta_i}{V_{tot,i}\,h_i} \le 0.1 \quad (3.7)$$

where:

θ_i is the interstorey drift sensitivity coefficient at level *i*,

$P_{tot,i}$ is the total gravity load from the top floor down to the current storey,

Δ_i is the design interstorey drift at level *i* (the difference between the lateral displacement at the top and bottom of the storey),

$V_{tot,i}$ is the total seismic storey shear at level i, and

h_i is the interstorey height.

Eurocode provisions recommend that second order effects should be accounted for when the sensitivity coefficient exceeds the limit value specified by the equation above. In case the condition is not met, the provisions of EC8-1 (CEN, 2004a) recommend multiplying the seismic action effects by a magnification factor in order to account for second-order effects as illustrated in the following:

If $0.1 < \theta \leq 0.2$, the seismic action is multiplied by a factor equal to $1 / (1-\theta)$

Alternatively, second-order effects can be accounted for by performing the P-Δ analysis alongside the nonlinear static or nonlinear dynamic analysis. It is also noted that EC8-1 (CEN, 2004a) requires that the sensitivity coefficient cannot exceed the value of 0.3.

In parallel, the global stability of the structure can be monitored by the interstorey drift profile. The interstorey drift is the relative displacement of adjacent storeys and is reduced to the interstorey drift ratio when normalised with respect to the interstorey height. A uniform distribution of the interstorey drift profile reflects on an appropriate distribution of stiffness across the height of the building. However, a sudden spike in the drift profile at one floor is an indication of the concentration of deformation at that floor and the consequent formation of a soft storey mechanism that can eventually lead to the global collapse of the building. The Eurocode standard that tackles the seismic evaluation and retrofitting of existing buildings, mainly EC8-3 (CEN, 2005a), does not recommend any separate checks in regard to the interstorey drift ratio. Indeed, the provisions of EC8-3 consider that the chord rotation is equal to the element drift ratio, which is the deformation at the end of the shear span with respect to the tangent at the member's end. However, Fardis (2009) stresses that a stiff interstorey drift profile indirectly promotes a building frame system with strong columns and weaker beams, which is the essence of the capacity design method and the appropriate behaviour of frame buildings. Hence, Fardis (2009) promotes the importance of having a performance check of the interstorey drift profile. In this regard, the drift is checked in accordance with the requirements of ATC-40 (ATC, 1996). ATC-40 enlists four performance levels as referred to in Table 3-2. The interstorey drift is checked at the life safety limit state of ATC-40 which simulates a seismic intensity between the SD and NC limit states of EC8-3 (CEN, 2005a). It is worth noting that the deformation limits specified in Table 3-2 are based on the objective of avoiding damage in the structural system and do not address the stability of non-structural components (such as partition walls). Hence, the interstorey drift at each storey level is checked at the limit of 2% as an additional measure of the global stability of the building.

Table 3-2: Maximum allowable limit of interstorey drift ratio as recommended by ATC-40 (ATC, 1996)

Performance Level			
Immediate Occupancy	**Damage Control**	**Life Safety**	**Structural Stability**
0.01	0.01-0.02	0.02	$0.33\ (V_i / P_i)$

3.5 Seismic Assessment of Existing Buildings in the Context of the CSM

This section presents an introduction to the assessment process in the context of the CSM and is followed by a detailed example that presents the application of the CSM to an existing building and the fulfilment of all the required checks.

According to the provisions of EC8-3 (CEN, 2005a), the assessment of an existing building is a quantitative evaluation of the performance that determines whether the building satisfies the minimum requirements that enable it to survive the potential seismic hazards in its region. In this regard, Eurocode specifies that the performance of the building under the seismic loads and other variable loads can be evaluated using one of the following analysis methods:

- Lateral force analysis (Linear)
- Modal response spectrum analysis (Linear)
- Non-linear static pushover analysis
- Non-linear time history dynamic analysis

To begin with, studies by Campbell & Bozorgnia (2004) have proven that most structures including reinforced concrete buildings would likely respond inelastically under a major earthquake and the seismic response is most realistically represented by the nonlinear time history dynamic analysis (NLTHA). However, the method has always been branded as impractical due to its excessive computational requirements. The non-linear static pushover analysis (NSPA) has often been used as an alternative as it presents a reliable yet computationally affordable solution compared to the more sophisticated NLTHA. In this context, the capacity spectrum method (CSM) is one form of NSPA which utilises the dynamic characteristics of a structure to establish whether the seismic capacity of the structure meets the demands of seismic ground motion (ATC, 1996; Freeman, 1998). The CSM is the focal point of this research and is adopted in the seismic assessment of the existing buildings. The method is described in detail in Chapter 2, and it provides a graphical representation of the capacity of a structure versus the demands of earthquake loading, hence allowing for a visual evaluation of the response as the structure is subjected to the specified ground motion (Figure 3.3).

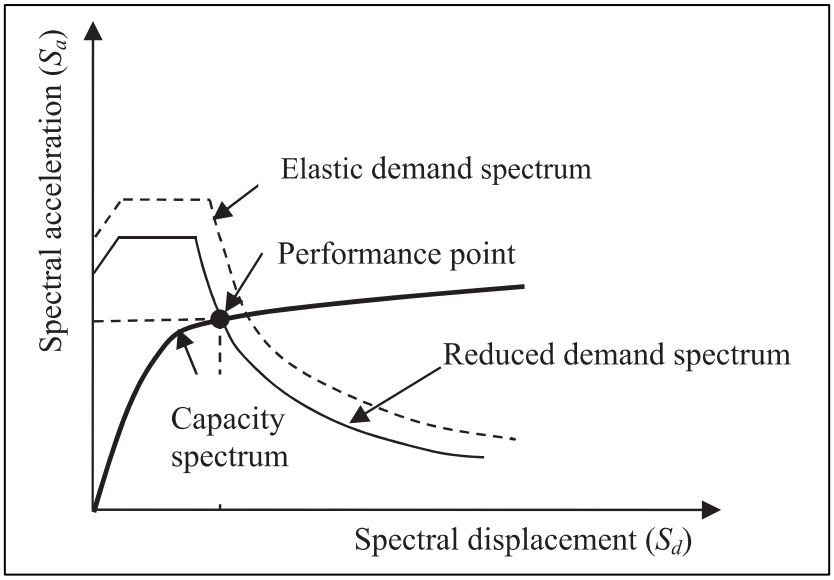


Figure 3.3: Graphical solution of the CSM (Zameeruddin & Sangle, 2016)

The intersection of the capacity and demand curves marks the response of the structure (performance point), at which the maximum lateral roof displacement is evaluated and checked against the limit permitted by the code in the aim to verify the adequacy of the structure against the applied seismic loading.

It is worth recalling that the CSM is based on the simplified assumption that the maximum lateral storey drifts are governed by deformations of the fundamental mode of the originally elastic system (Freeman, 1998). Hence, the applicability of the method is questioned where the maximum storey drifts are not governed by the fundamental mode, such as tall buildings or buildings featuring planar or vertical irregularities (Peter & Badoux, 2000). Emphasis on the applicability of the CSM is previously provided in Chapter 2 and is further discussed at later stages in the thesis. However, the purpose of this chapter is to illustrate the CSM as the analysis tool used in the seismic assessment of buildings. Accordingly, the conditions required for an appropriate application of the CSM are assumed to be satisfied, and the discussion is focused on the seismic assessment procedure.

Supported by the prevalence of the translational component of the fundamental mode in each horizontal direction, the seismic evaluation of RC buildings encompasses two pushover analyses performed separately in each of the two main horizontal directions. The loading vector in each pushover analysis is applied in proportion to the fundamental mode that is predominated by translation in one horizontal direction. The pushover analyses are therefore referred to as Push-X and Push-Y, with the Push-X denoting the pushover analysis that is applied in proportion to the fundamental mode that is governed by translation in direction X, and the Push-Y referring to the one applied in proportion to the mode predominated by translation in Y. As discussed in Chapter 2, ATC-40 (ATC, 1996) and ATC-55 (ATC, 2005) recommend the use of the first mode distribution over other types of invariable single load patterns as the first mode distribution provides good displacement estimates. Hence, the load pattern

applied in each pushover analysis consists of a single vector of loads that is proportional to the first mode components in the direction under consideration.

It is worth noting that gravity loads are fully applied at the start of the pushover analysis before any lateral loading is being applied. The gravity loading initially applied prior to the application of the pushover loads consists of the total dead load (own weight plus the superimposed dead loads) and 25% of the live load which is consistent with the load combinations of Eurocode 2 or EN 1992-1-1 (CEN, 2004b).

Pushover analysis is initially applied in the horizontal X-direction (Push-X) and the performance point in the X-direction is determined using the procedure outlined in Chapter 2. The seismic assessment is carried out at the performance point by applying the aforementioned list of verification checks. This is followed by a separate pushover analysis that is subsequently conducted in the orthogonal Y-direction (Push-Y) along with all the associated verification checks.

The building is deemed adequate to resist the seismic hazard in its vicinity if the results of both pushover analyses prove that all the structural components can sustain potential ductile and brittle failure mechanisms and if the global stability requirements are satisfied as well. If the building is proven to be seismically vulnerable, such an outcome highlights the need to design a simplified retrofitting strategy for strengthening substandard RC buildings located in seismic hazard regions.

3.6 Illustrating Example: Case Study

The main objective of this research is to enhance the seismic performance of multi-storey RC framed buildings that were not historically designed to resist earthquakes. Lebanon is a Mediterranean country located in a seismically active region while its buildings are yet to be designed to resist earthquakes. Seismic regulations in the country were only introduced back in 2005, and its building stock is mostly composed of RC buildings, thus serving a typical fit for the application of the simplified retrofitting strategy that is developed in this research. Accordingly, this section presents an applied example of the seismic assessment procedure of a typical building extracted from the building stock of Beirut, Lebanon.

3.6.1 Structural characteristics of the building

The building investigated consists of a 10-storey RC building which represents the typical building stock of Beirut, Lebanon that belongs to the period of the 1980's. The structural system consists of a moment-resisting frame (MRF) that resists all types of gravity and lateral loading, noting that the latter was then limited to wind load effects only since earthquake provisions were not mandatory until only recently. Plan irregularities are not considered at this stage since the objective of this chapter is to illustrate the seismic assessment in the background of the CSM. The same floor plan is maintained at all floor levels. The columns are dimensioned based on a tributary area analysis in which each column

is proportioned to sustain the floor loading distributed over its tributary area in addition to the incurred load from upper storeys. The steel reinforcement ratio in the columns varies in the range of 0.6 to 0.75% (normalised to the column's cross-section) which was typical during that period before the introduction of the seismic regulations. The columns' cross-section is reduced at upper floors upon the reduction in the gravity loading. The floor system consists of a one-way ribbed slab (Hourdi slab) supported on the primary beams which are oriented along the global X-direction (Figure 3.4). The ribbed Hourdi slab consists of a 7-cm thick topping with ribs (15cm width × 25cm depth) spanning in the global Y-direction at a centre-to-centre spacing of one meter. The ribs are thickened at the location of the columns, forming the so-called double ribs or the interior secondary beams spanning in the Y-direction (Figure 3.4). The height from the ground to the first floor is taken as 4.3 meters, while a typical interstorey height of 3.1 meters is assumed all over from the first floor to the roof. The building properties assumed in this example reflect on the characteristic building stock of Beirut which dates back to the 80's and early 90's. To note also that the structure contains no shear walls since earthquake design was not required then.

The main static gravitational loads used for proportioning the dimensions of beams and columns are summarised in the following:

Dead Load (DL): includes the self-weight of the structural system consisting mainly of the slabs, beams, and columns.

Superimposed Dead Load (SDL): includes the weight of the tiling and floor finishing material as well as the weight of the partition walls (block walls). The self-weight of the partition walls is assumed to be uniformly distributed over the floor area and is estimated around 300 Kg/m^2, while the tiling and floor finish is estimated around 200 Kg/m^2. The same SDL is assumed at all storey levels.

Live Load (LL): includes mainly the weight of the furniture and the residents of the building. It is estimated around 300 Kg/m^2 and is also assumed to be uniform at all floor levels.

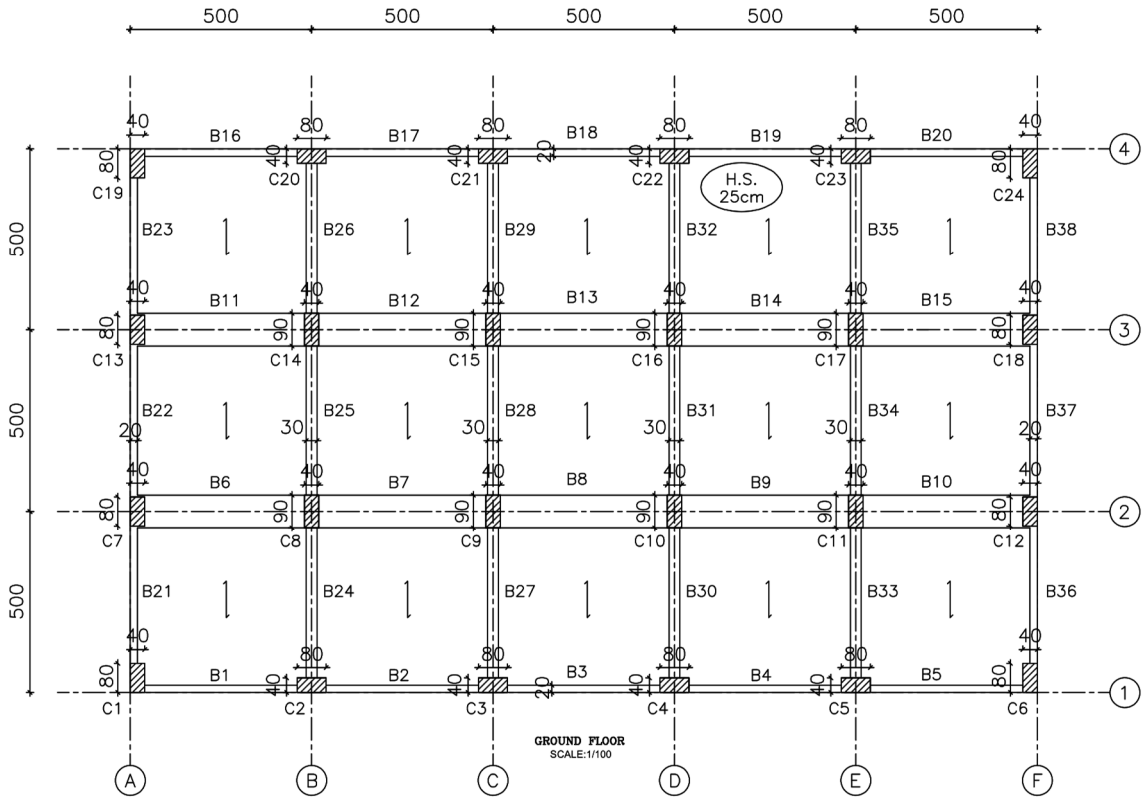


Figure 3.4: Ground floor plan of the typical building (all dimensions in cm)

The material properties considered in the analysis are given by the following:

- Concrete: C25 grade concrete having a compressive strength of 25 MPa on the 28th day after casting
- Steel Reinforcement: Grade 60 steel having a tensile yield strength of 420 MPa

The dimensions and the longitudinal reinforcement in the beams and columns are presented in Tables 3-3 and 3-4. Also, Figures A3.1 and A3.2 in Appendix 3 provide detailed sketches of the columns and the beams cross-sections including the supplied longitudinal and transversal reinforcement.

Table 3-3: Dimensions and reinforcement of beams at all storey levels

	Beam Label	Beam Dimensions Width × Depth (mm)	Beam Longitudinal Reinforcement
Edge Beams	B1, B2, B3, B4, B5, B16, B17, B18, B19, B20, B21, B22, B23, B36, B37, B38	200 × 500	Top: 2 T16 Bottom: 2 T20
Interior Primary Beams	B6, B7, B8, B9, B10, B11, B12, B13, B14, B15	900 × 250	Top: 7 T16 Bottom: 7 T16
Interior Secondary Beams (Double-Rib)	B24, B25, B26, B27, B28, B29, B30, B31, B32 B33, B34, B35	300 × 250	Top: 3 T14 Bottom: 3 T14

Table 3-4: Dimensions and steel reinforcement of columns

	Corner & Edge Columns		Interior Columns	
	C1, C2, C3, C4, C5, C6, C7, C12, C13, C18, C19, C20, C21, C22, C23, C24		C8, C9, C10, C11, C14, C15, C16, C17	
	Col. Dimensions (mm)	**Longitudinal Reinforcement**	**Col. Dimensions (mm)**	**Longitudinal Reinforcement**
Storey 1	400 × 800	12 T16	400 × 900	12 T16
Storey 2	300 × 700	8 T16	300 × 800	10 T16
Storey 3	300 × 700	8 T16	300 × 800	10 T16
Storey 4	200 × 700	8 T14	300 × 700	8 T14
Storey 5	200 × 700	8 T14	300 × 700	8 T14
Storey 6	200 × 600	8 T12	300 × 700	8 T14
Storey 7	200 × 600	8 T12	200 × 600	8 T12
Storey 8	200 × 600	8 T12	200 × 600	8 T12
Storey 9	200 × 500	6 T12	200 × 600	8 T12
Storey 10	200 × 500	6 T12	200 × 600	8 T12

3.6.2 Modelling of the building and pushover analysis performed on ETABS

After determining the material and structural properties, the building is modelled using the finite-element computer software ETABS (2017). Pushover analysis is directly performed on ETABS, and the relevant verification criteria are evaluated in accordance with the provisions of EC8-3 (CEN, 2005a). The building performance is initially checked at the SD limit state noting that the design seismic action (DSA) defined in Eurocode 8 pertains to the SD limit state as discussed in Chapter 2. To this end, exceedance of the chord rotation capacity and/or the shear capacity corresponding to the SD limit state are deemed sufficient to conclude that the structure is inadequate, and a separate performance check at the NC limit state is accordingly deemed unnecessary. The CSM is therefore performed considering the response spectrum attributed to the SD limit state. To summarise, this example aims at illustrating the procedure adopted for the seismic assessment of buildings by checking the performance at the SD limit state, and a subsequent check at the NC limit state is only needed if the building satisfies all the required checks of the SD limit state.

The Lebanese norms relative to the protection from earthquakes NL 135 (LIBNOR, 2012) recommends a seismic coefficient of 0.25g throughout the country. However, recent studies by Huijer et al. (2016) proposed to increase the seismic zone parameter for the coastal cities between Saida and Beirut to 0.3g. Hence, the building in this example is checked at the DSA corresponding to a PGA of 0.3g. The response spectrum of the uniform building code UBC-97 (ICBO, 1997) conforming to seismic zone 3 (PGA of 0.3g) is selected to represent the earthquake loading. The spectrum of UBC-97 (ICBO, 1997) conforming to a PGA of 0.3g is selected as it conforms with the response spectra recommended by

ATC-40 and ATC-55 (ATC, 1996, 2005). The response spectrum used in the CSM is displayed in Figure 3.5.

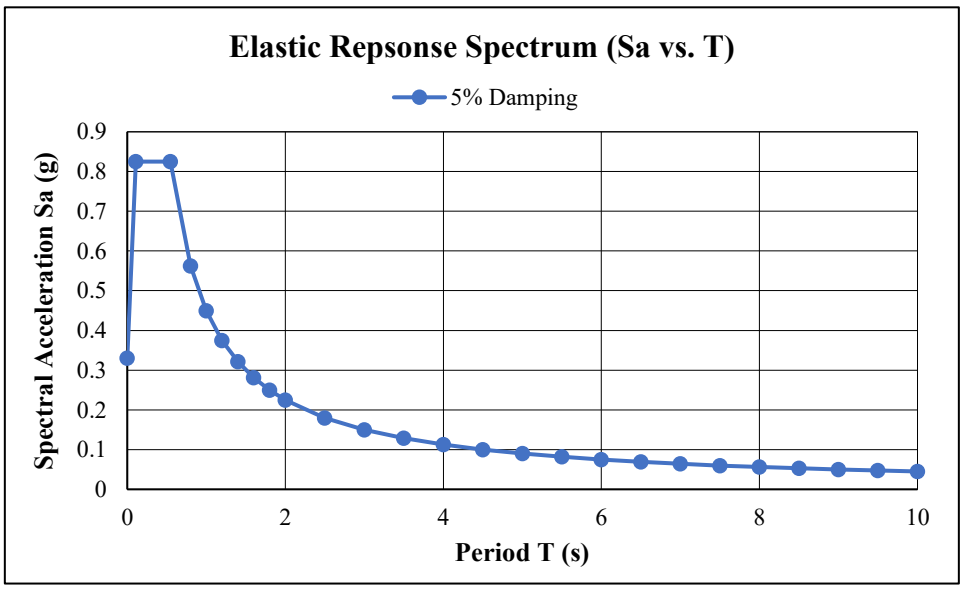


Figure 3.5: Elastic response spectrum conforming to a PGA of 0.3g – UBC-97 (ICBO, 1997)

The beams and columns are modelled as frame elements and the beam-column connection is modelled as a rigid joint. A rigid diaphragm is assigned to the floor slab at each level to reflect on the diaphragm action provided by the 7cm-thick slab topping. The ribbed Hourdi slab is modelled as a membrane that transfers the load to the MRF to avoid having any influence from the slab on the lateral load resisting MRF.

Since the pushover is a nonlinear analysis, the stiffness of the structural members is reduced to account for the loss of stiffness that is caused by the manifestation of cracks during the inelastic response. In this respect, the flexural and shear stiffness of columns and beams is multiplied by a reduction factor of 0.5 as recommended by the provisions of EN 1998-1 (CEN, 2004a).

Once the model is generated and all the static loads are assigned, pushover analysis is performed on ETABS. In each horizontal direction, the pushover loads are applied at the centre of mass which coincides with the geometric centroid of the symmetric floor plan. The characteristics of the fundamental mode of vibration in both horizontal directions are provided in Table 3-5. Accordingly, the load pattern used in the Push-X analysis consists of a vector of loads which is proportional to the fundamental mode of vibration in the X-direction (mode 2). Similarly, Push-Y consists of a load vector proportional to the fundamental mode in direction Y (mode 1).

Table 3-5: Vibration characteristics of the fundamental mode in the main horizontal directions

	Mode 1			Mode 2		
	ω = 1.75 rad/s			ω = 2.35 rad/s		
Storey	**UX** (m)	**UY** (m)	**RZ** (rad)	**UX** (m)	**UY** (m)	**RZ** (rad)
Storey1	0	0.061	0	0.084	0	0
Storey2	0	0.159	0	0.201	0	0
Storey3	0	0.283	0	0.328	0	0
Storey4	0	0.424	0	0.462	0	0
Storey5	0	0.564	0	0.585	0	0
Storey6	0	0.696	0	0.702	0	0
Storey7	0	0.810	0	0.810	0	0
Storey8	0	0.898	0	0.896	0	0
Storey9	0	0.962	0	0.964	0	0
Storey10	0	1.000	0	1	0	0

Plastic hinges based on a lumped plasticity model are assigned at critical locations in order to model the inelastic response of the building. In this respect, plastic hinges are expected to form at both ends of beams and columns as these regions are expected to develop the largest stresses when the building is subjected to seismic loading. Flexural hinges are defined in ETABS and assigned at both ends of beams and columns. These hinges include the combined effect of axial load in columns while the axial force in the beams is negligible. Shear hinges are also defined in ETABS and assigned at both ends in beams and columns. In sum, the hinges assignments at the ends of beams and columns is summarised by the following, noting that all the hinges are uncoupled:

Beams:

- Flexural hinges monitoring the bending moment around the strong axis (M3)
- Shear hinges monitoring the shear force along the strong axis (V2)

Columns:

- Flexural hinges monitoring the bending moment around the strong axis (M3)
- Shear hinges monitoring the shear force along the strong axis (V2)
- Flexural hinges monitoring the bending moment around the weak axis (M2)
- Shear hinges monitoring the shear force along the weak axis (V3)

Figure 3.6 presents the generalised force-deformation relationship adopted by the ASCE/SEI 41-17 standard of the American Society of Civil Engineers (ASCE, 2017), which prescribes values of the modelling parameters a, b, and c for all the structural components in order to establish the associated force-deformation curve. The modelling parameters generally depend on the member's cross-sectional dimensions and steel reinforcement and are evaluated in Tables 10-7 and 10-8 of ASCE 41-17 for RC beams and rectangular columns respectively, which are presented in Figures A3.3 and A3.4 in Appendix 3. The generalised force-deformation curve is defined by 5 major points as illustrated in Figure 3.6:

- Point A is the origin.
- Point B marks the yielding point of the member.
- Point C represents the ultimate capacity (taken as the plastic bending capacity of ductile components).
- Point D represents the residual strength retained after strength degradation. Although the realistic behaviour of RC members is characterised by a gradual degradation of strength when the load reaches the ultimate capacity (sloping line CD), ASCE 41-17 (ASCE, 2017) recommends adopting an immediate drop in strength (vertical line CD) in the absence of additional information regarding strength degradation.
- Point E marks the ultimate deformation the member can sustain before failing, beyond which the load drops to zero.

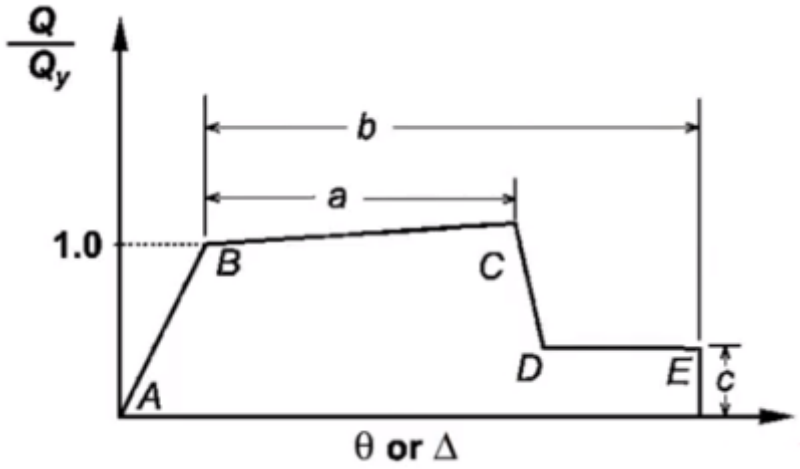


Figure 3.6: Generalised force-deformation relationship of structural members according to ASCE 41-17 (ASCE, 2017)

It is worth noting that the FEMA-356 standard of the Federal Emergency Management Agency (FEMA, 2000) and the ATC-40 standard of the Applied Technology Council (ATC, 1996) also adopt the same force-deformation relationship described in Figure 3.6, and both documents prescribe values for the modelling parameters required to construct the curve. However, the ASCE 41-17 standards were preferred since the Tables of ASCE 41-17 are already implemented in ETABS which permits to directly calculate the modelling parameters of all the structural components.

Following on the current discussion, the modelling of point hinges in ETABS is represented by a rigid-plastic model rather than the elastic-plastic model described in Figure 3.6. This is due to the fact that the point hinge in ETABS is activated at yielding (point B), while the initial elastic behaviour is defined in the general properties of the structural component (cross-section dimensions, modulus of elasticity, section modifiers) and not in the point hinge model which only reflects on the plastic response (Figure 3.7). The hinge modelling in ETABS also permits to define the acceptance criteria or deformation limits pertaining to the three limit states defined in ASCE 41-17 (ASCE, 2017), namely the Immediate

Occupancy, Life Safety, and Collapse Prevention (Figure 3.7). Although these parameters are also provided in the Tables of ASCE 41-17, it should be noted that the behaviour of RC beams and columns is rather checked with respect to the three limit states prescribed by EC8-3 (CEN, 2005a), namely the DL, SD, and the NC limits (Figure 3.7). In conclusion, the plastic rotations (a and b) and the residual strength (c) are directly obtained from ASCE 41-17 (ASCE, 2017) while the maximum allowable rotations are evaluated according to Eurocode 8 and are inserted into the hinge model implemented on ETABS. Exceedance of the maximum rotation corresponding to one of the three limit states is manifested by the formation of a plastic hinge as illustrated in the following:

Green: the formation of a green plastic hinge indicates that the DL limit state has been exceeded. This basically implies that the yield rotation (rotation limit of the DL state) has been exceeded.

Cyan: a cyan hinge indicates that the chord rotation has exceeded the limit of the SD state (the chord rotation has exceeded 75% of the ultimate rotation capacity).

Red: a red hinge is an indication that the ultimate chord rotation capacity of the member is exceeded (the NC limit state is exceeded).

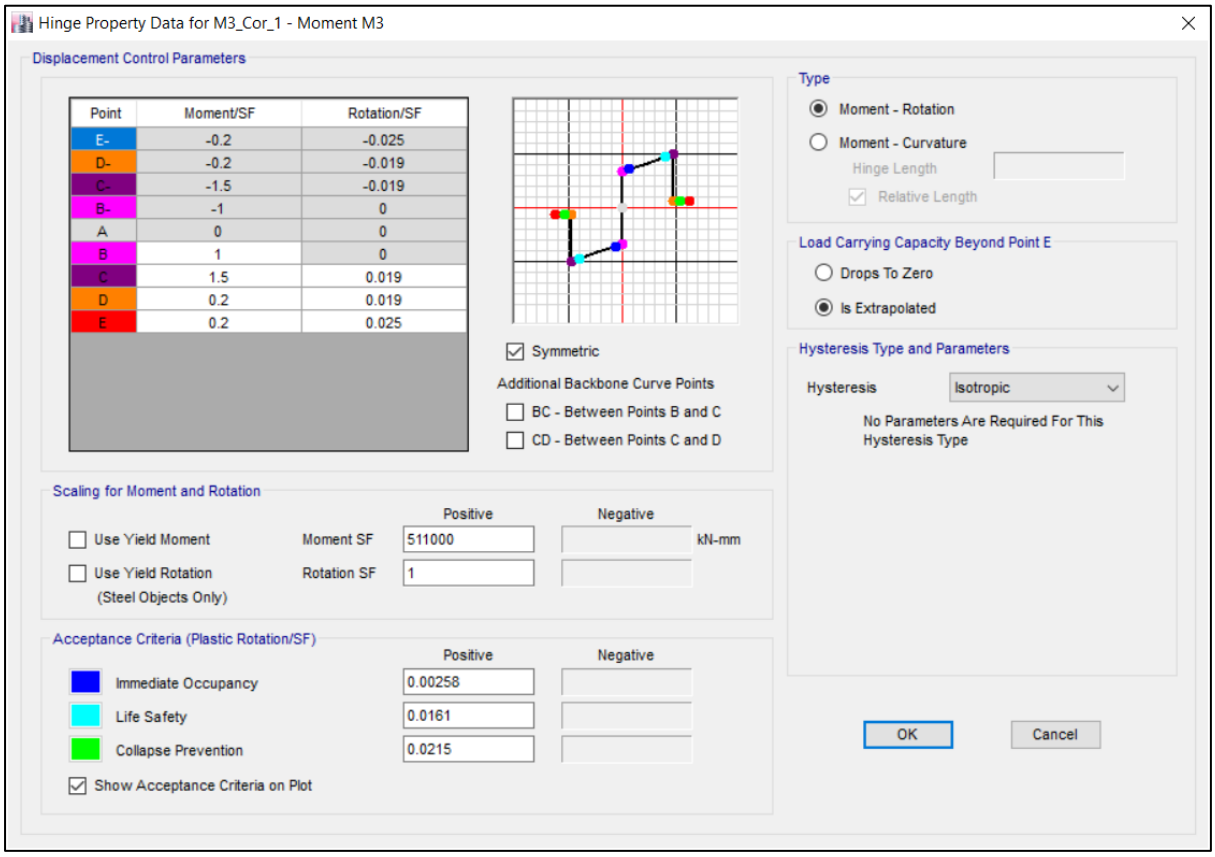


Figure 3.7: Typical modelling of a flexural hinge in ETABS: Immediate Occupancy (DL), Life Safety (SD), Collapse Prevention (NC)

Whereas for shear hinges, exceedance of the shear capacity results in an immediate brittle failure at the end of the member which leads to redistributing the forces among the redundant structural components.

Referring to the generalised force-deformation model in Figure 3.6, strength loss occurs as soon as the shear capacity is reached, and the load drops to zero at point B after reaching the ultimate capacity. Therefore, shear hinges in ETABS are rather modelled as "Force Controlled (Brittle)" hinges which requires defining the allowable force (shear capacity) at each limit state (Figure 3.8). The ultimate shear capacity of beams and columns is calculated according to the provisions of EC8-3 (CEN, 2005a) and is used to define the shear hinge model (Figure 3.8), and the formation of a red hinge indicates brittle failure upon exceedance of the allowable shear capacity.

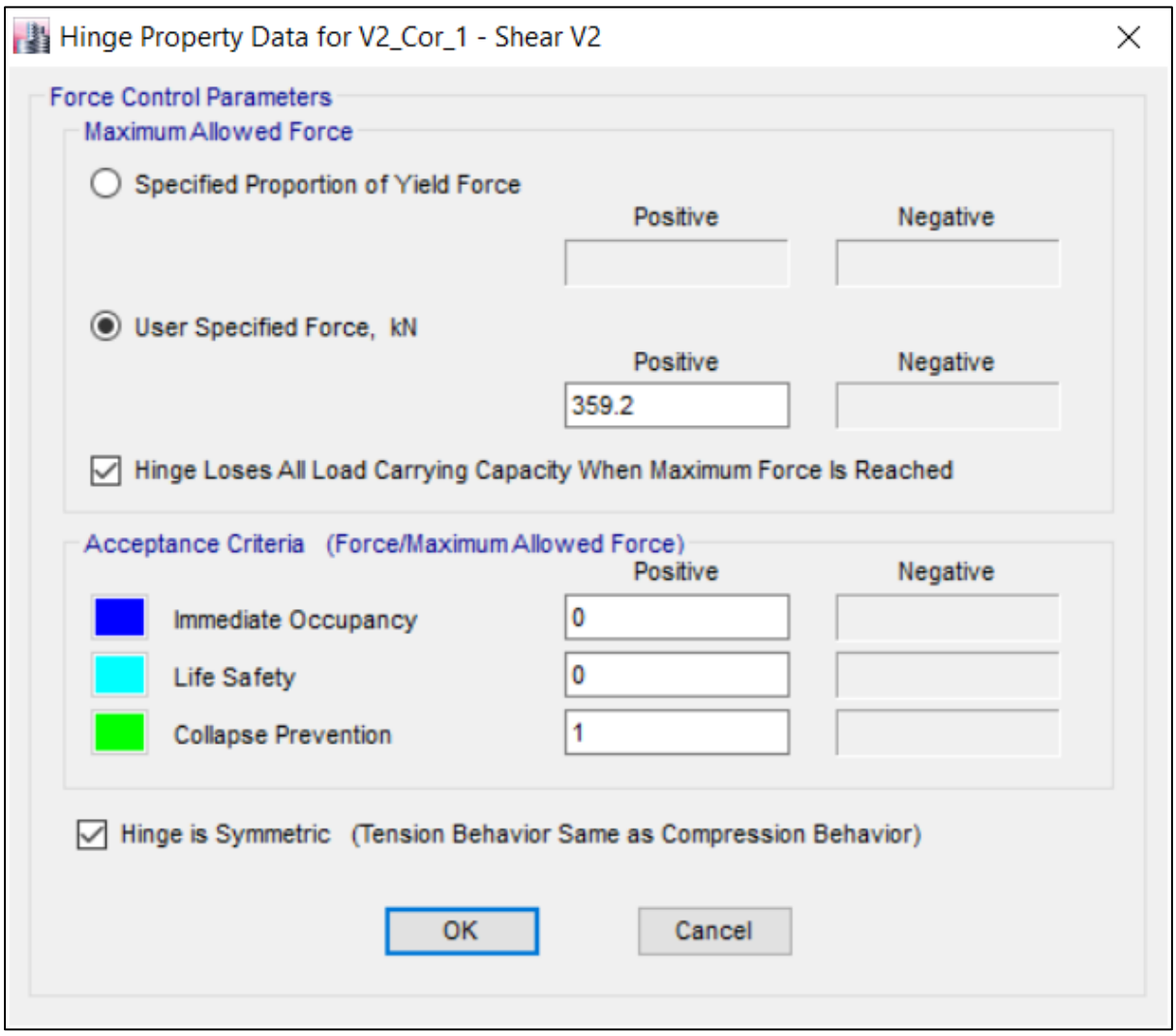


Figure 3.8: Modelling of a typical shear hinge in ETABS

3.6.3 Pushover analysis in the horizontal X-direction

Figure 3.9 displays the capacity curve (base shear vs. roof displacement) obtained from the pushover analysis performed on ETABS in the X-direction (Push-X). The capacity curve is converted into the capacity spectrum, a plot of the spectral acceleration versus the spectral displacement according to the procedure described in Chapter 2 (Figure 3.10).

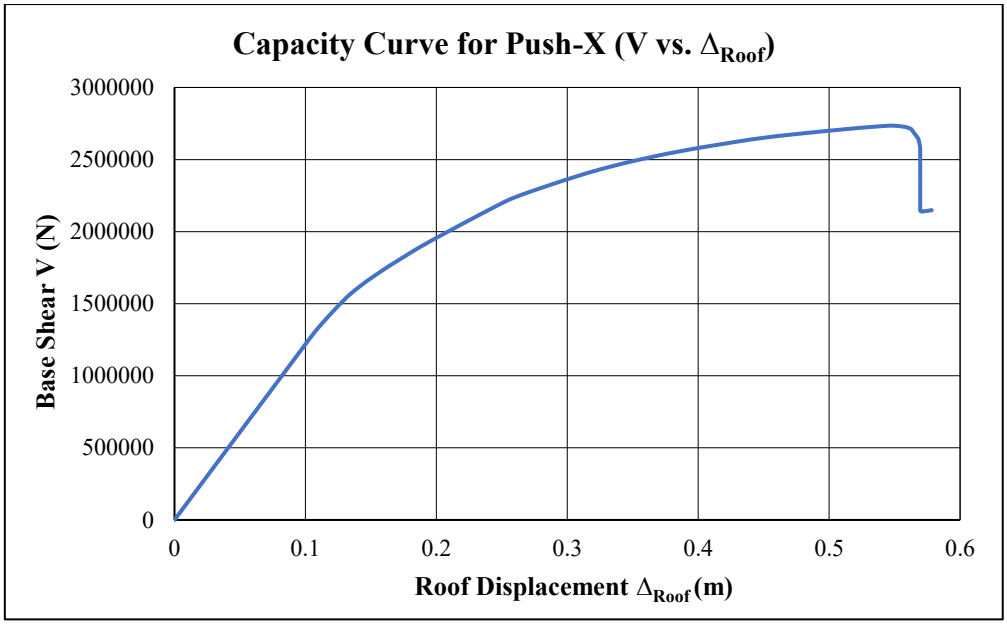


Figure 3.9: Capacity curve of pushover analysis in the X-direction

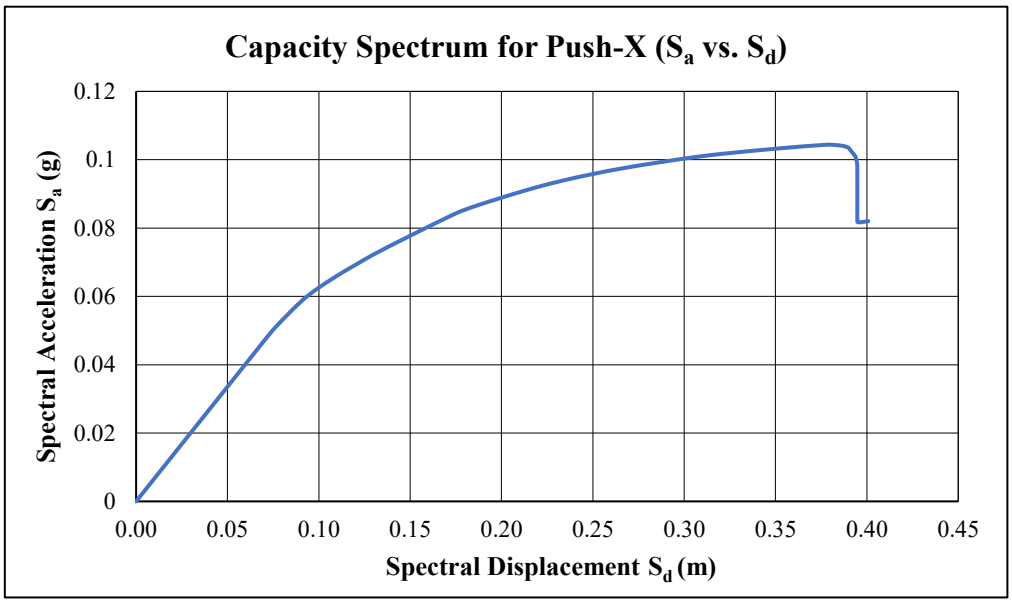


Figure 3.10: Capacity spectrum of pushover analysis in the X-direction

The last step of the CSM involves plotting the capacity spectrum against the earthquake demand response spectrum. Finding the actual performance is an iterative process, and two iterations were required to find the performance point in the Push-X analysis. The initial estimate of performance point is determined based on the equal displacement approximation and the bilinear curve is constructed in accordance with the equal energy approximation, such that the same area (energy) is enclosed by the original curve and the bilinear approximative curve. The spectral reduction factors are accordingly determined, and the new performance point is obtained as the intersection of the capacity spectrum and the reduced response spectrum. The whole procedure is explained in detail in Chapter 2. The yield point (a_{yi}, d_{yi}) and the performance point (a_{pi}, d_{pi}) of the two iterations are presented in Table 3-6, noting that

the iterative process continues until the percentage error between the initial estimate and the final performance point is reduced to less than 5%. The final performance point is assumed to represent the actual response of the building under the applied seismic loading. In this respect, the local as well as the global structural checks are performed at the performance point in order to verify the adequacy of the building to resist the seismic loading. Figure 3.11 presents the final step or final iteration of the CSM in which the capacity and reduced demand curves intersect at the performance point.

Table 3-6: Iterative process of finding the performance point in the Push-X analysis

	a_{yi} (g)	d_{yi} (m)	a_{pi} (g)	d_{pi} (m)	β_{eff}	a_{pf} (g)	d_{pf} (m)	%error in a_p	%error in d_p
Trial 1	0.07	0.103	0.095	0.27	20 %	0.09	0.23	5.3	14.8
Trial 2	0.07	0.095	0.09	0.23	21 %	0.09	0.23	0	0

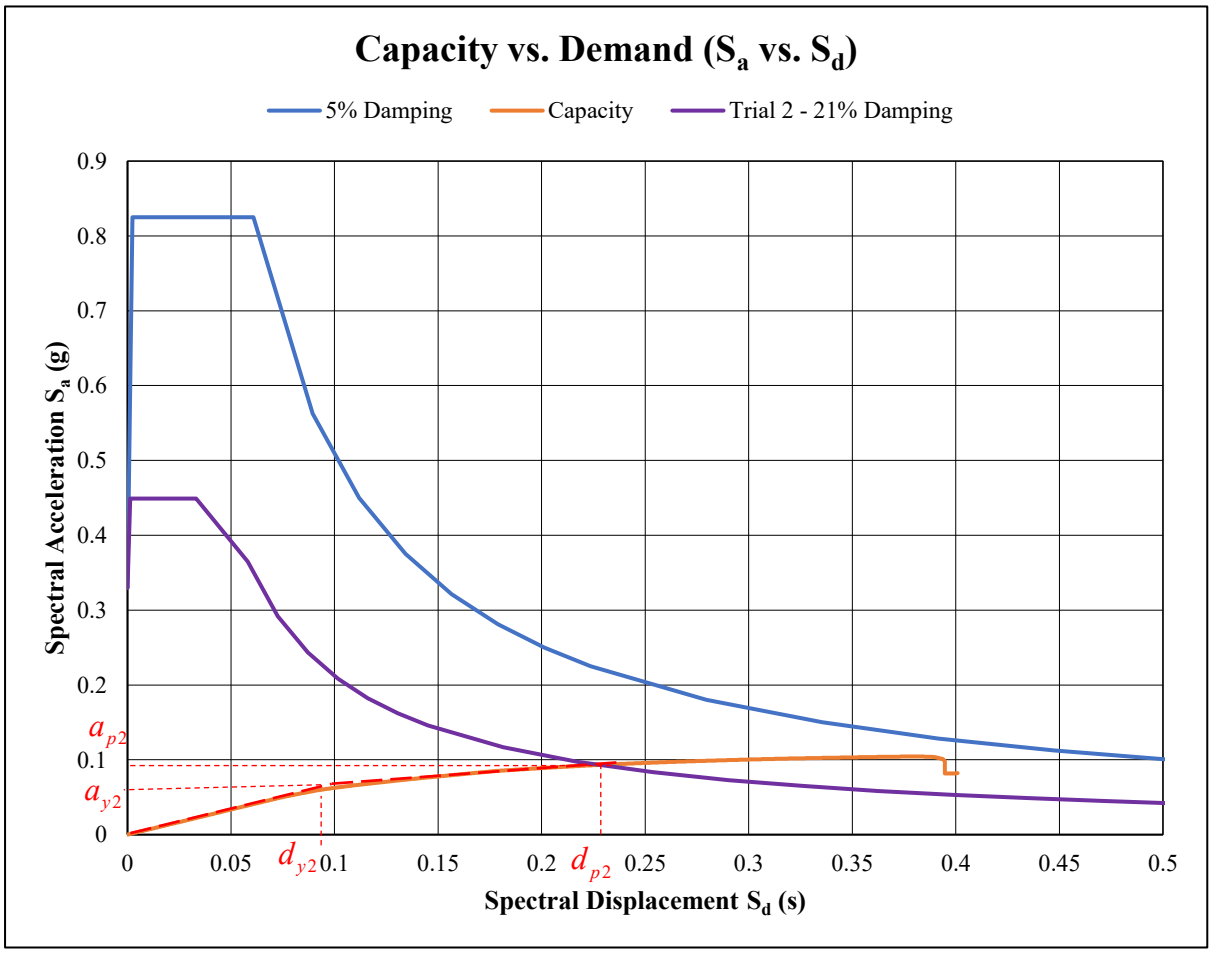


Figure 3.11: Determining the performance point of the CSM in line with the Push-X analysis

Once the performance point is determined in the ADRS plot, its equivalent on the capacity curve is determined by converting the spectral acceleration into the base shear and converting the spectral displacement into the roof displacement. This allows to determine the performance point on the pushover curve (capacity curve) which permits to determine the exact step in the pushover analysis that

corresponds to the performance point. The verification criteria are then evaluated at the performance point and are checked against the allowable values set by the code at the limit state under consideration. Table 3-7 contains the summary of the results obtained from the Push-X analysis.

Table 3-7: Results of the Push-X analysis at the performance point

Participation Factor	Mass Coefficient	Spectral Acc. a_{pf} (g)	Spectral Disp. d_{pf} (m)	Base Shear (N)	Roof Disp. (m)
1.443	0.693	0.09	0.23	2357796	0.332

i. Check against ductile failure (chord rotation)

The flexural plastic hinge properties of each element are manually defined in ETABS taking into account the maximum allowed chord rotation at each limit state as defined in Table 3-1.

The pushover analysis is then executed on ETABS, and flexural hinges start to form at the beam/column's end upon exceeding the predefined chord rotation limits, recalling that the exceedance of the rotation limit of the DL, SD, and NC limit states are manifested by the formation of green, cyan, and red hinges respectively.

Figure 3.12 displays the flexural hinges that have developed in the building at the performance point in the Push-X analysis. While the results prove that the DL limit state is exceeded in most of the beams, the SD limit state was not exceeded in any structural element. Hence, the Push-X results indicate that there is no sign of ductile failure when checking the performance at the SD limit state.

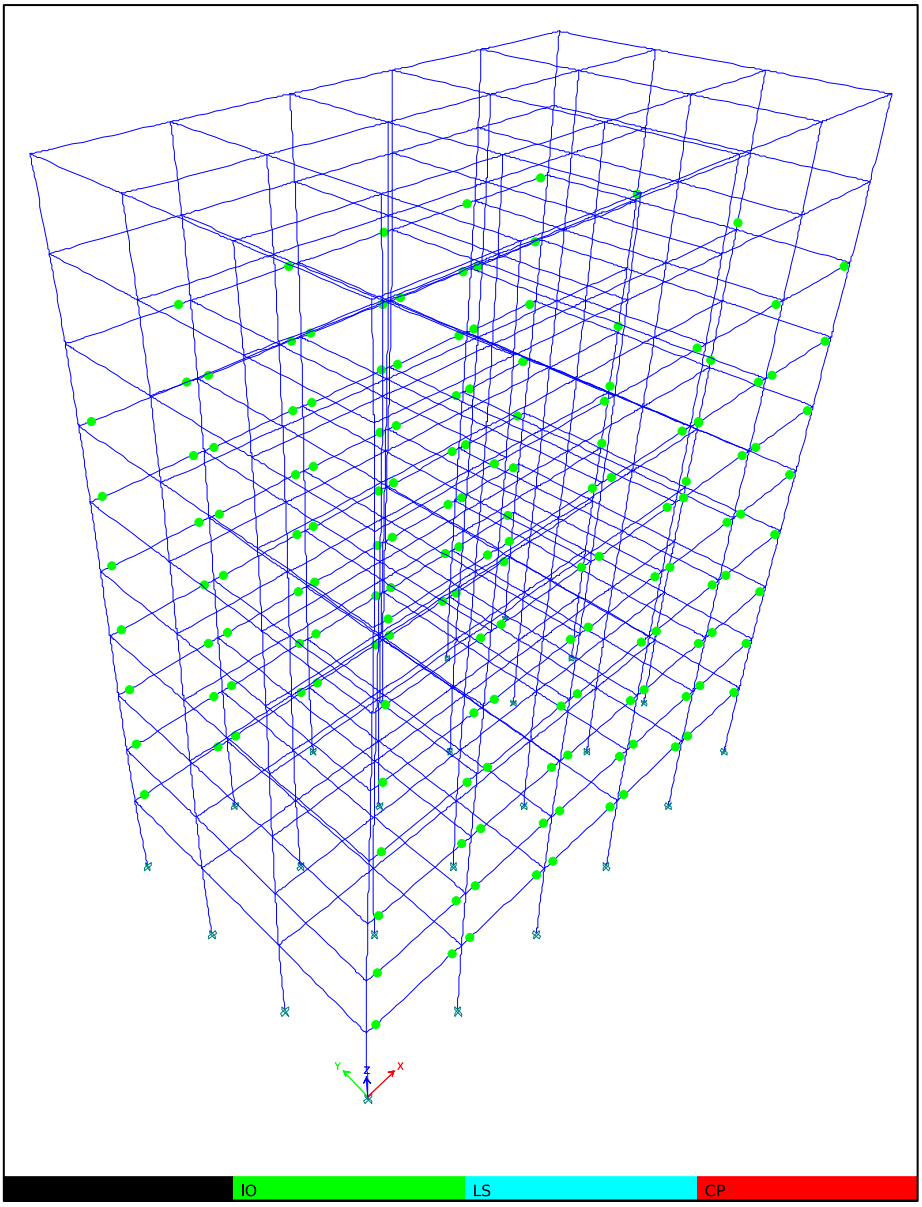


Figure 3.12: Formation of flexural plastic hinges at the performance point in the Push-X analysis

ii. Check against brittle failure (shear)

After successfully passing the ductile mechanism check, the building is checked against potential brittle shear failure. This is performed by assigning shear hinges at both ends of beams and columns in the ETABS model. The shear hinges are solely defined by the ultimate shear capacity of the beam/column which is evaluated according to Eurocode provisions. Therefore, there is only one type of shear hinge (red coloured) that can possibly develop in any single member, and its formation signals that the ultimate shear capacity has been exceeded and the element is suffering a brittle shear failure under the applied earthquake loading. Figure 3.13 depicts the formation of shear hinges at the performance point of the Push-X analysis. The results in the figure clearly point out at the brittle shear failure occurring in most of the beams and expose the weakness of the building against the applied seismic loading.

It is worth noting that the shear check is performed at the level of seismic action corresponding to the SD limit state, recalling that EC8-3 (CEN, 2005a) specifies the same equation for calculating the shear capacity at both the SD and the NC limit states as discussed earlier in this chapter. Therefore, it is implied that the building would suffer further failure (more red hinges) if the shear check is performed at the NC limit state.

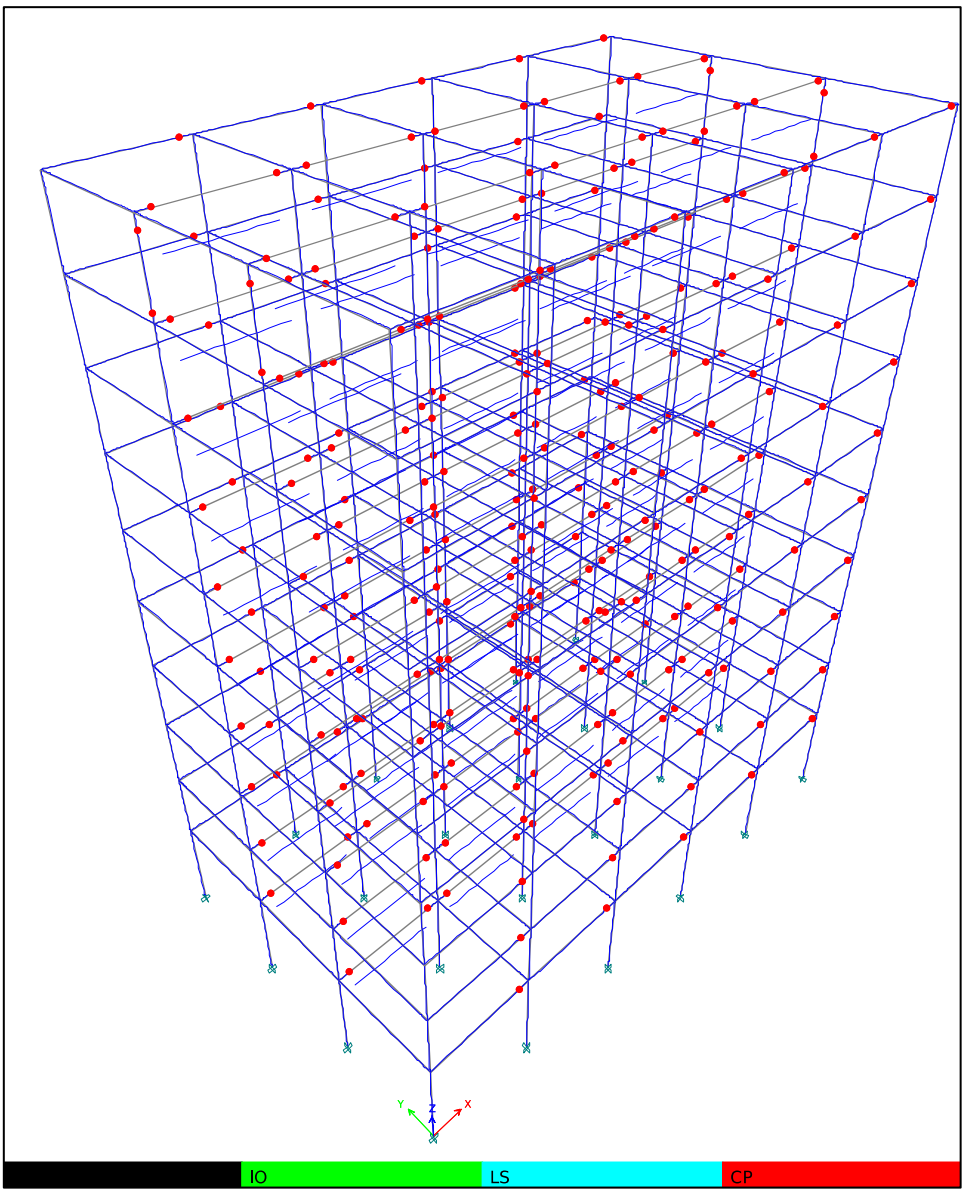


Figure 3.13: Shear hinges obtained in beams and columns at the performance point – Push-X analysis

Alternatively, the shear demand in any beam/column can be obtained from the flexural moments at the member's ends. Noting that the typical seismic response of a beam/column is manifested by the formation of a sagging (positive) moment at one end and a hogging (negative) moment at the other end, the maximum shear demand can be determined from moment equilibrium at the member's end. Unlike columns, beams are also subjected to a uniform load comprising the superimposed dead and the live loads (Figure 3.14).

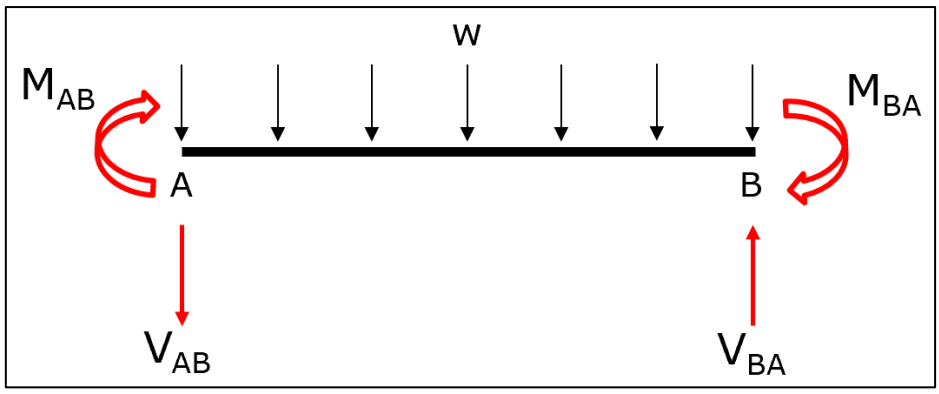


Figure 3.14: Typical sketch of the forces acting on a loaded beam element

Referring to the figure above, the critical section that develops the maximum shear force along beam AB is located at end B. Knowing the flexural moments acting at the ends the beam, the maximum shear is calculated and is checked against the ultimate shear capacity:

$$V_{\max} = V_{BA} = \frac{M_{AB} + M_{BA}}{L_{AB}} + \frac{wL_{AB}}{2} \tag{3.8}$$

$$V_{AB} = -V_{BA} + \frac{wL_{AB}}{2} \tag{3.9}$$

The beams are grouped into three categories in reference to Figure 3.4, with each category containing a set of beams experiencing a similar flexural response:

- Edge: B1, B2, B3, B4, B5, B16, B17, B18, B19, B20
- Interior: B6, B11, B10, B15
- Int-Core: B7, B8, B9, B12, B13, B14

To note that the beams aligned in the orthogonal Y-direction are not checked as they develop negligible flexural moments in the Push-X analysis. The maximum shear demand and accordingly the shear Demand-to-Capacity ratio (D/C) are evaluated in order to determine whether the beams can resist potential brittle shear failure. Results are presented in Table 3-8 and are plotted in Figure 3.15.

Table 3-8: Calculation of the shear D/C ratio in the beams – Push-X

		Max. Shear (KN)	Shear Capacity (KN)	Demand-to-Capacity Ratio (D/C)	Shear Check
Storey 1	**Edge**	107.0	54.5	1.96	Fail
	Interior	163.0	59.6	2.73	Fail
	Int-Core	157.0	59.6	2.63	Fail
Storey 2	**Edge**	108.0	54.5	1.98	Fail
	Int-Left	178.0	59.6	2.99	Fail
	Int-Core	173.0	59.6	2.90	Fail
Storey 3	**Edge**	109.0	54.5	2.00	Fail
	Interior	181.0	59.6	3.04	Fail
	Int-Core	178.0	59.6	2.99	Fail
Storey 4	**Edge**	109.0	54.5	2.00	Fail
	Interior	179.0	59.6	3.00	Fail
	Int-Core	178.0	59.6	2.99	Fail
Storey 5	**Edge**	109.0	54.5	2.00	Fail
	Interior	177.0	59.6	2.97	Fail
	Int-Core	178.0	59.6	2.99	Fail
Storey 6	**Edge**	108.0	54.5	1.98	Fail
	Interior	172.0	59.6	2.89	Fail
	Int-Core	165.0	59.6	2.77	Fail
Storey 7	**Edge**	108.0	54.5	1.98	Fail
	Interior	156.0	59.6	2.62	Fail
	Int-Core	139.0	59.6	1.99	Fail
Storey 8	**Edge**	107.0	54.5	1.96	Fail
	Interior	146.0	59.6	2.45	Fail
	Int-Core	133.0	59.6	2.23	Fail
Storey 9	**Edge**	88.0	54.5	1.61	Fail
	Interior	132.0	59.6	2.21	Fail
	Int-Core	123.0	59.6	2.06	Fail
Storey 10	**Edge**	68.0	54.5	1.25	Fail
	Interior	126.0	59.6	2.11	Fail
	Int-Core	113.0	59.6	1.90	Fail

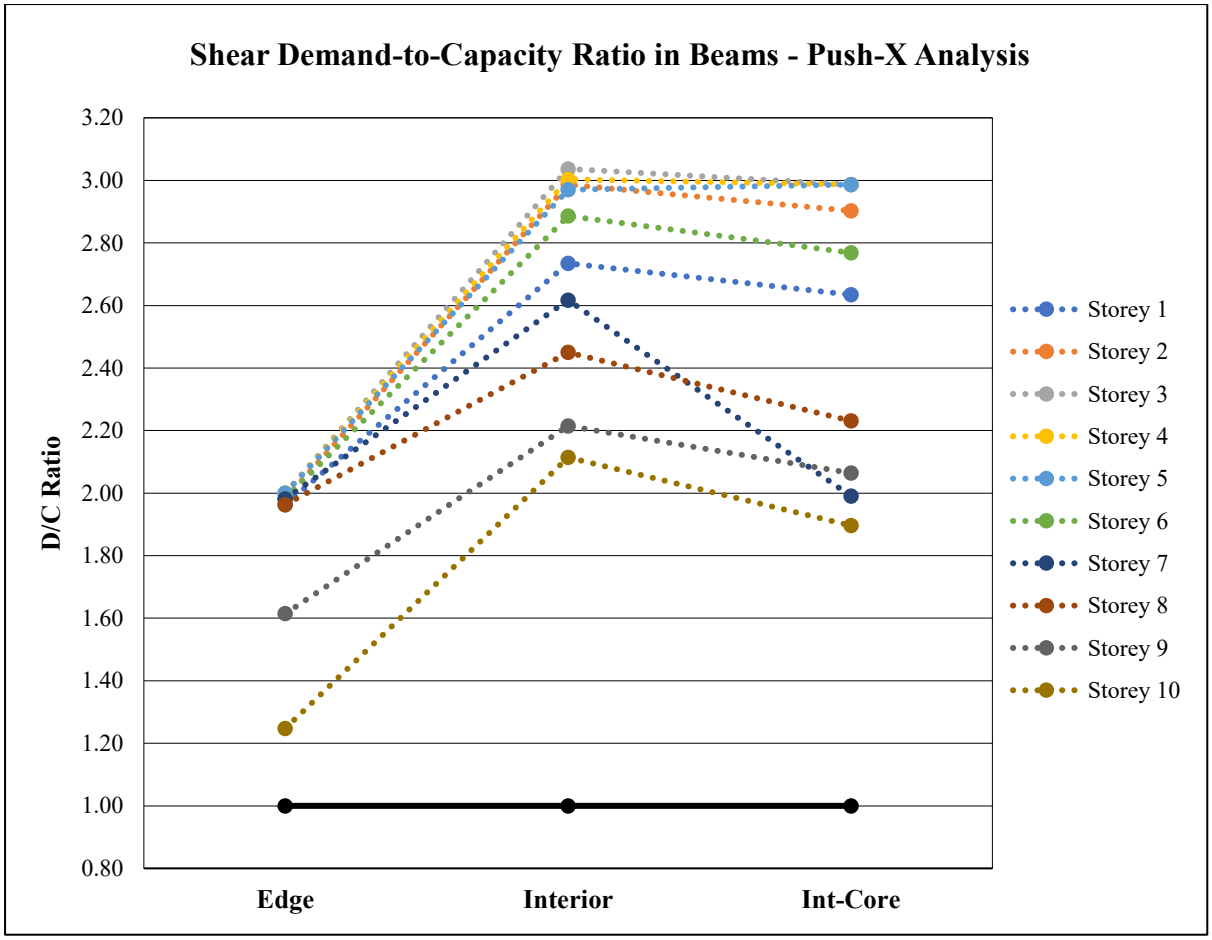


Figure 3.15: Shear Demand-to-Capacity (D/C) ratio in the beams – Push-X

The results above indicate that the shear demand is widely exceeding the capacity (the D/C ratio is excessively greater than 1), and accordingly all the beams would suffer from brittle shear failure at the performance point. These results conform perfectly with those obtained from the results of the shear hinges displayed in Figure 3.13.

The shear resistance of columns is checked in a similar fashion noting that the columns are not subjected to any uniform loading as is the case of beams. Accordingly, the maximum shear in the column develops equally at both ends A and B (Figure 3.16).

$$V_{\max} = V_{AB} = V_{BA} = \frac{M_{AB} + M_{BA}}{L_{AB}} \tag{3.10}$$

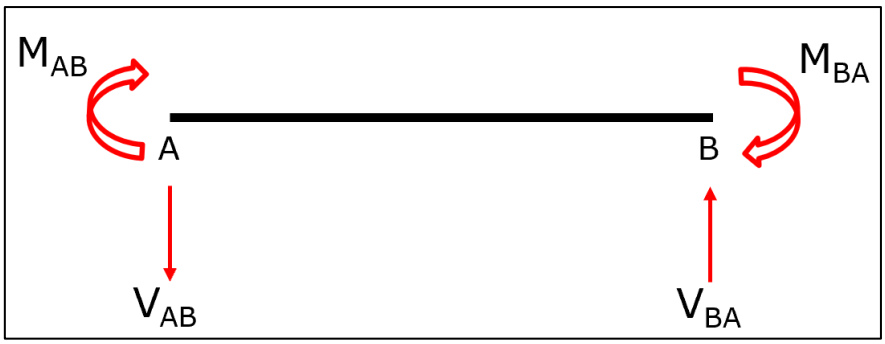


Figure 3.16: Typical sketch of the forces acting on a column

Again, the columns were grouped into the following categories with reference to Figure 3.4:

- Corner columns: C1, C6, C19, C24
- Edge X columns: C2, C3, C4, C5, C20, C21, C22, C23
- Edge Y columns: C7, C12, C13, C18
- Interior columns: C8, C9, C10, C11, C14, C15, C16, C17

Figure 3.17 depicts the calculated shear D/C ratio in all the columns at the performance point. The results show that the columns aligned on Grids 2 and 3 (Interior Columns and Edge Y Columns) are mostly stressed beyond their ultimate shear capacity at upper floors. The strong axis of these columns is aligned in the Y-direction, hence these columns are being exposed under the Push-X analysis as the load is being applied around the column's weak axis. This effect is particularly voiced at upper floors where the columns' width is further reduced (reaching 20 cm at top floors), hence prompting a brittle shear failure along the weak axis of the columns at upper levels.

In conclusion, the local shear checks have proven that most of the columns at upper storeys and all the beams are stressed beyond their capacity and would accordingly suffer from brittle shear failure under the Push-X analysis. It is worth noting that the results obtained at this stage are sufficient to conclude that the building is vulnerable when subjected to earthquake loading. Nevertheless, further performance checks are conducted since the objective of this example is to illustrate the complete seismic assessment procedure.

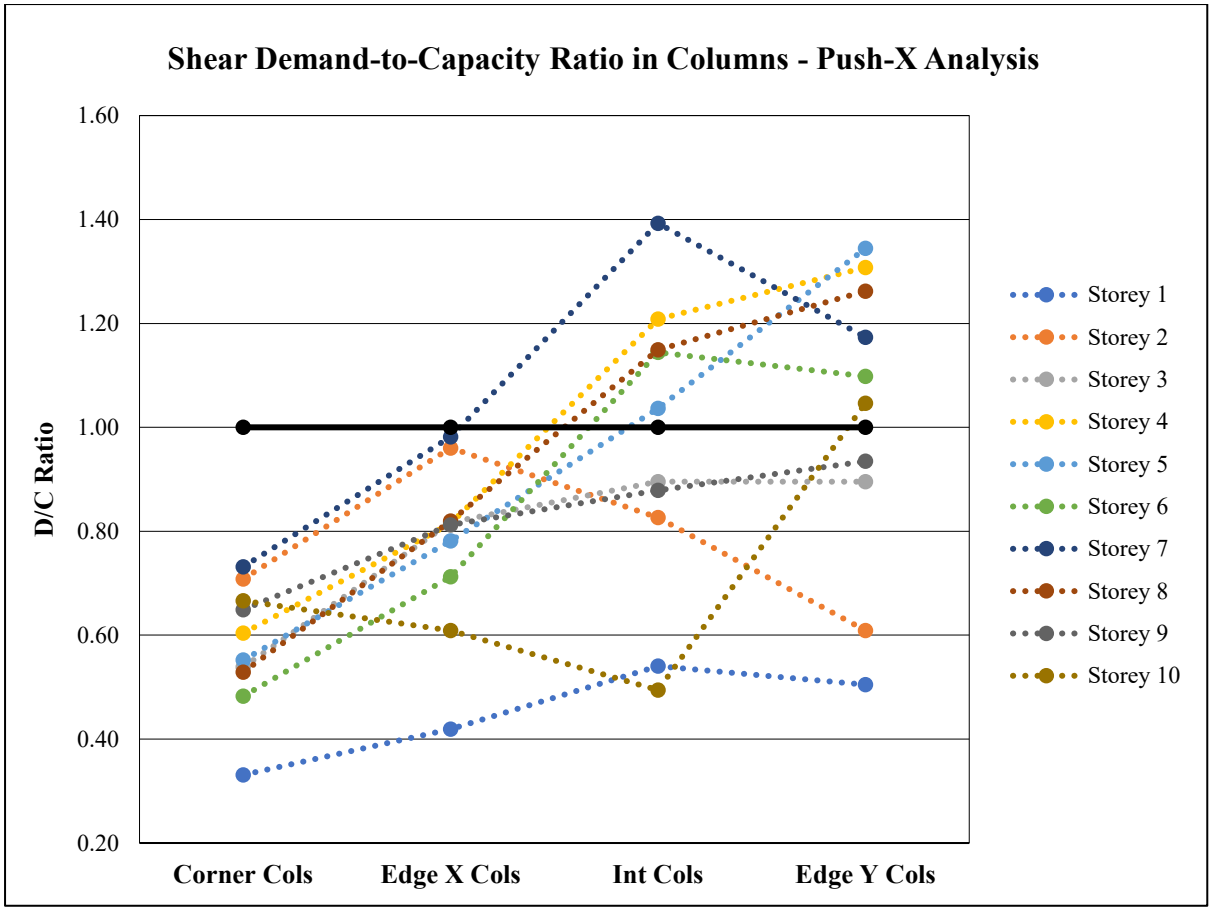


Figure 3.17: Shear Demand-to-Capacity (D/C) ratio in the Columns – Push-X

iii. Check of global stability and interstorey drift

The maximum displacement at each floor level is determined using the participation factor and the spectral displacement obtained at the performance point as discussed in the provisions of ATC-40 (ATC, 1996):

$$\delta_i = PF_{Roof,x}\ \phi_{i,x}\ S_d \tag{3.11}$$

where:

δ_i is the displacement at level *i*,

PF_{Roof} is the participation factor in the X-direction,

$\phi_{i,x}$ is the component of the mode shape vector at level *i*, and

S_d is the spectral displacement obtained at the performance point.

The displacement at all levels is accordingly evaluated, and the interstorey drift ratio is accordingly checked against the 2% limit permitted by the code. The results are presented in Table 3-9 and are

plotted in Figure 3.18. The results reveal that the limit of 2% is not exceeded at any floor level. In conclusion, the interstorey drift check is satisfied at all storeys in the Push-X scenario.

Table 3-9: Interstorey drift results – Push-X

	Lateral Storey Disp. δ_i (m)	Interstorey Drift $\Delta\delta_i$ (m)	Storey Height h_i (m)	Interstorey Drift Ratio $\Delta\delta_i / h_i$	Interstorey Drift Check Limit (1%)
Storey 1	0.0123	0.0123	4.3	0.29%	Pass
Storey 2	0.0369	0.0246	3.1	0.79%	Pass
Storey 3	0.0615	0.0246	3.1	0.79%	Pass
Storey 4	0.0983	0.0369	3.1	1.19%	Pass
Storey 5	0.1352	0.0369	3.1	1.19%	Pass
Storey 6	0.1721	0.0369	3.1	1.19%	Pass
Storey 7	0.2212	0.0492	3.1	1.59%	Pass
Storey 8	0.2581	0.0369	3.1	1.19%	Pass
Storey 9	0.2950	0.0369	3.1	1.19%	Pass
Storey 10	0.3318	0.0369	3.1	1.19%	Pass

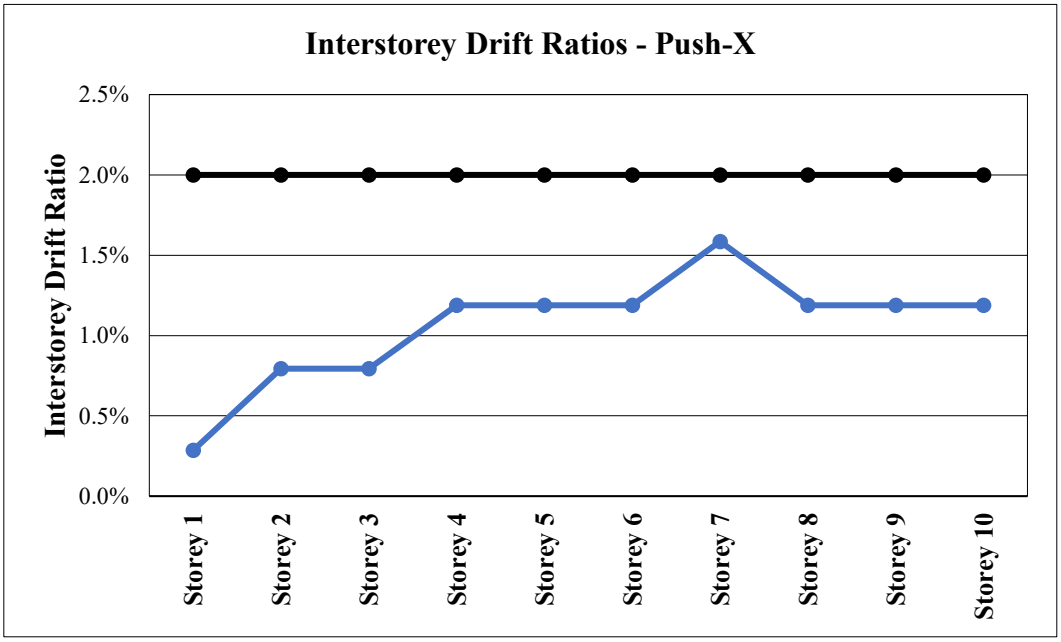


Figure 3.18: Interstorey drift ratios – Push-X

Furthermore, Table 3-10 displays the *P*-Δ check performed in line with the Push-X analysis. The results show that the interstorey drift sensitivity coefficient exceeds the limit of 0.1 at multiple floor levels, and as such the *P*-Δ effect is significant and needs be incorporated into the pushover analysis.

It is worth noting that the Push-X analysis in this example is not repeated by including the second-order effects, since the results obtained when the *P*-Δ effects were excluded are enough to highlight the inadequacy of the building. Hence, including the *P*-Δ effects would only serve to increase the seismic

action applied on the vertical elements and would eventually add to the previous conclusion regarding the inadequacy of the building in resisting the seismic loading. Nevertheless, the *P*-Δ effect is essential and is considered in the analysis of buildings in subsequent stages of this research.

Table 3-10: Checking the second-order effect (*P*-Δ) in the Push-X analysis

	Storey Shear $V_{tot,i}$ (N)	**Total Gravity Load** $P_{tot,i}$ (N)	**Interstorey drift** Δ_i (m)	**Interstorey height** h_i (m)	**ISD sensitivity coefficient** θ_i	**Check**
Storey 1	2357796	38964004	0.0123	4.3	0.047	Not required
Storey 2	2338183	34578264	0.0246	3.1	0.117	*P*-Δ required
Storey 3	2282250	30617413	0.0246	3.1	0.106	*P*-Δ required
Storey 4	2190223	26656563	0.0369	3.1	0.145	*P*-Δ required
Storey 5	2044643	22795055	0.0369	3.1	0.133	*P*-Δ required
Storey 6	1845088	18933547	0.0369	3.1	0.122	*P*-Δ required
Storey 7	1593445	15095413	0.0492	3.1	0.150	*P*-Δ required
Storey 8	1271692	11309873	0.0369	3.1	0.106	*P*-Δ required
Storey 9	896904	7524332	0.0369	3.1	0.100	Not required
Storey 10	468759	3762166	0.0369	3.1	0.095	Not required

3.6.4 Pushover analysis in the horizontal Y-direction

A separate pushover analysis referred to as Push-Y is performed in the global Y direction. In a similar fashion, the load pattern in Push-Y consists of a single vector of forces proportional to the fundamental mode of vibration that is predominated by translation in the horizontal Y-direction. The elastic response spectrum is the same one used in the Push-X analysis. Figures 3.19 and 3.20 sketch the capacity curve and the capacity spectrum respectively.

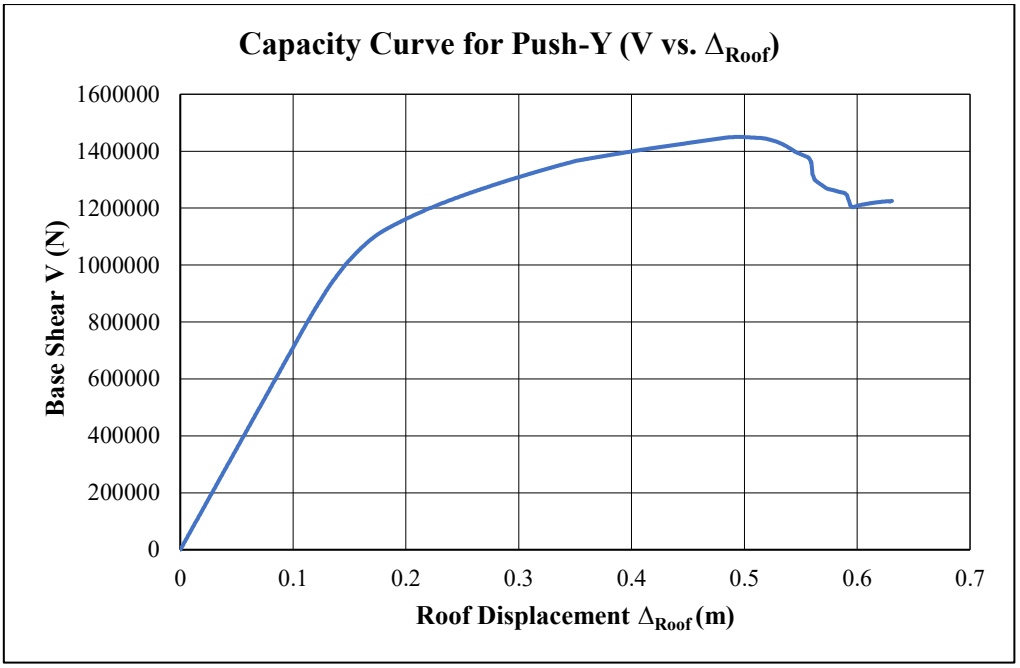


Figure 3.19: Capacity Curve of pushover analysis in the Y-direction

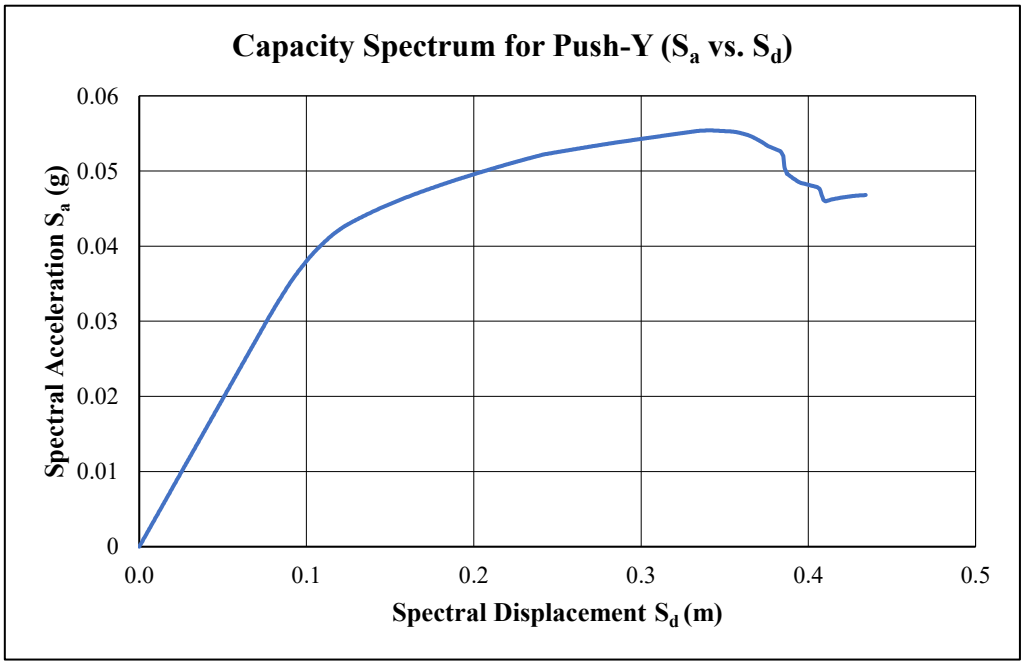


Figure 3.20: Capacity spectrum of pushover analysis in the Y-direction

Two iterations were needed to find the performance point in the Push-Y analysis. The yield point (a_{yi}, d_{yi}) and the performance point (a_{pi}, d_{pi}) of both iterations are summarised in Table 3-11. Once the performance point on the capacity spectrum is determined, its equivalent on the capacity curve is obtained by converting the spectral acceleration into the base shear and converting the spectral displacement into the corresponding roof displacement (Table 3-12). This allows to perform the global and local performance checks at the exact step in the pushover analysis that represents the performance

point. The final iteration of the CSM in which the capacity and demand curves intersect at the actual performance point is presented in Figure 3.21.

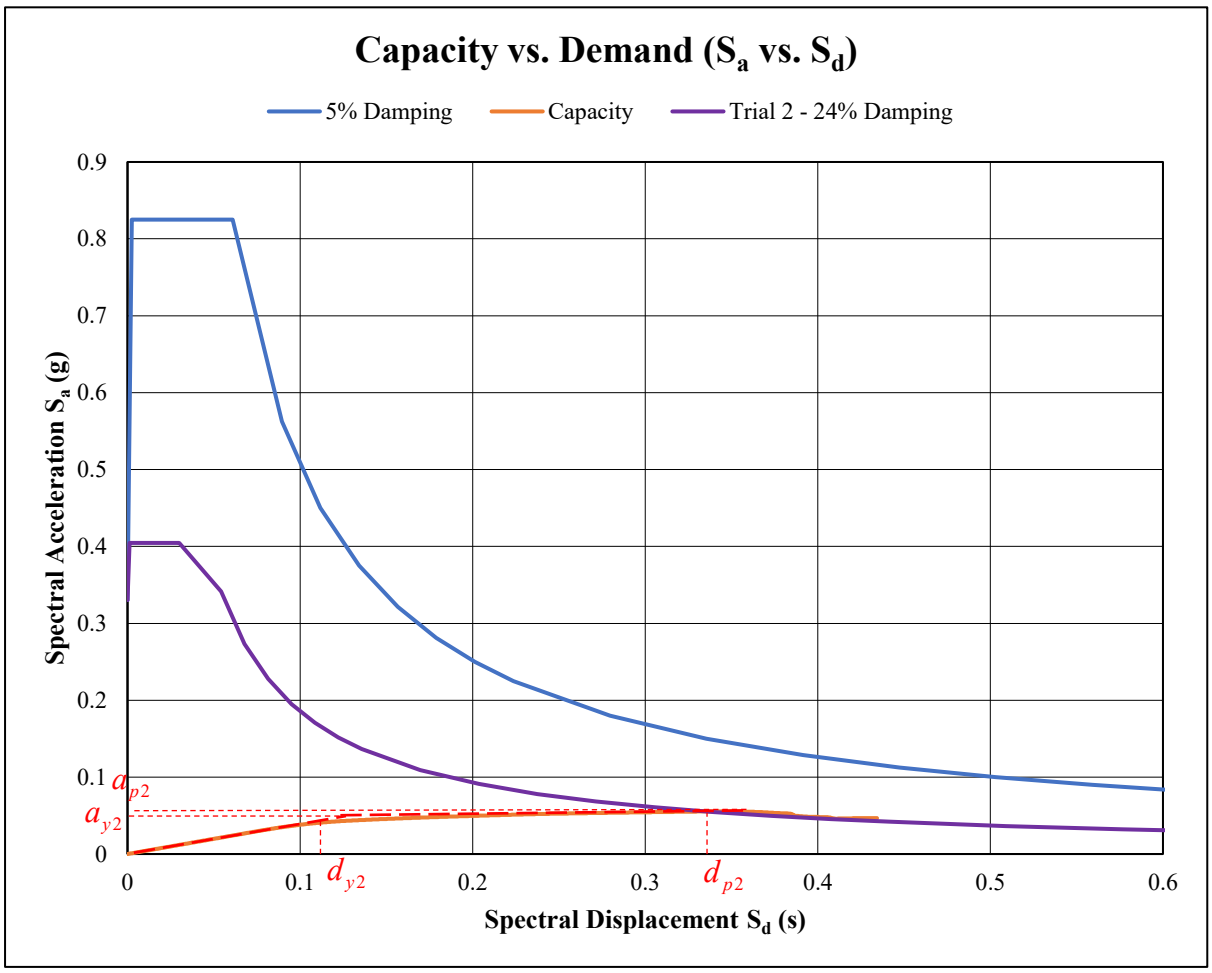


Figure 3.21: Determining the performance point of the CSM in line with the Push-Y analysis

Table 3-11: Iterative process of finding the performance point in the Push-Y analysis

	a_{yi} (g)	d_{yi} (m)	a_{pi} (g)	d_{pi} (m)	β_{eff}	a_{pf} (g)	d_{pf} (m)	%error in a_p	%error in d_p
Trial 1	0.045	0.115	0.055	0.36	25 %	0.054	0.33	1.8	8.3
Trial 2	0.044	0.11	0.054	0.33	24 %	0.055	0.335	1.8	1.5

Table 3-12: Results of the Push-Y analysis at the performance point

Participation Factor	Mass Coefficient	Spectral Acc. a_{pf} (g)	Spectral Disp. d_{pf} (m)	Base Shear (N)	Roof Disp. (m)
1.452	0.692	0.055	0.335	1413348	0.49

i. Checking against ductile failure (chord rotation)

Figure 3.22 displays the flexural hinges that have developed in the building at the performance point in the Push-Y analysis. It is observed that the chord rotation pertaining to the SD limit is exceeded in several beams (cyan hinges), and a few beams have even exceeded the NC limit (red hinges). Hence,

the beams developing cyan-coloured or red-coloured hinges would suffer a ductile failure by developing excessive chord rotation deformations that exceed the permissible limit. It should be noted that even the NC limit is exceeded when the applied seismic loading matches the SD limit state, which further points out at the vulnerability of the building when subjected to earthquake loading. To this end, it is expected that the building would experience further failure (more red hinges are likely to be observed) if the seismic action is further scaled to check the performance at the NC limit state.

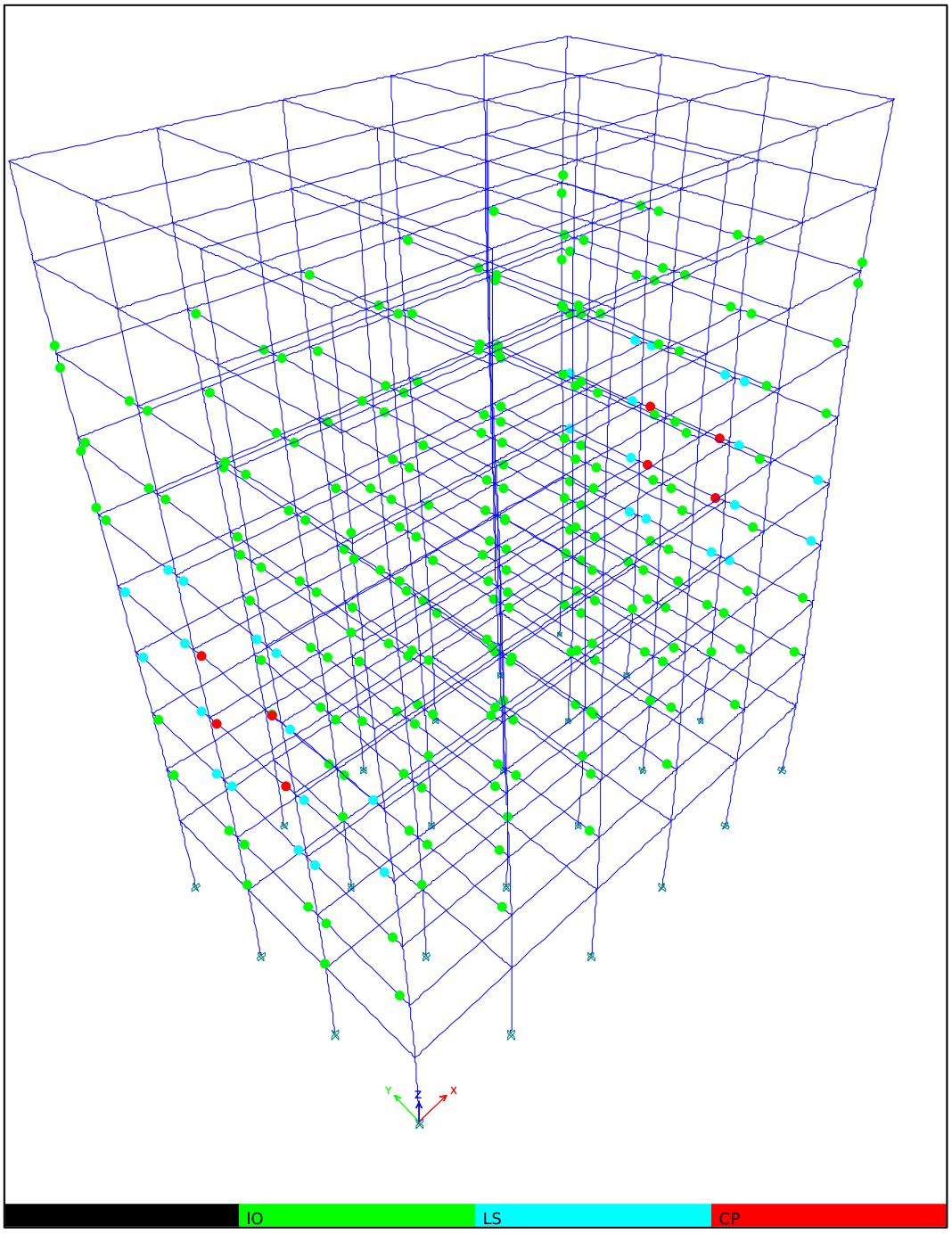


Figure 3.22: Flexural plastic hinges obtained at the performance point – Push-Y analysis

ii. Checking against brittle failure

The brittle shear failure mechanism is first performed by assigning shear hinges at the ends of beams and columns and by monitoring the development of shear hinges at the performance point. Figure 3.23 clearly depicts the exceedance of the ultimate shear capacity in most of the beams and in a few columns as well, which signals the brittle shear failure of these elements in response to the applied loading.

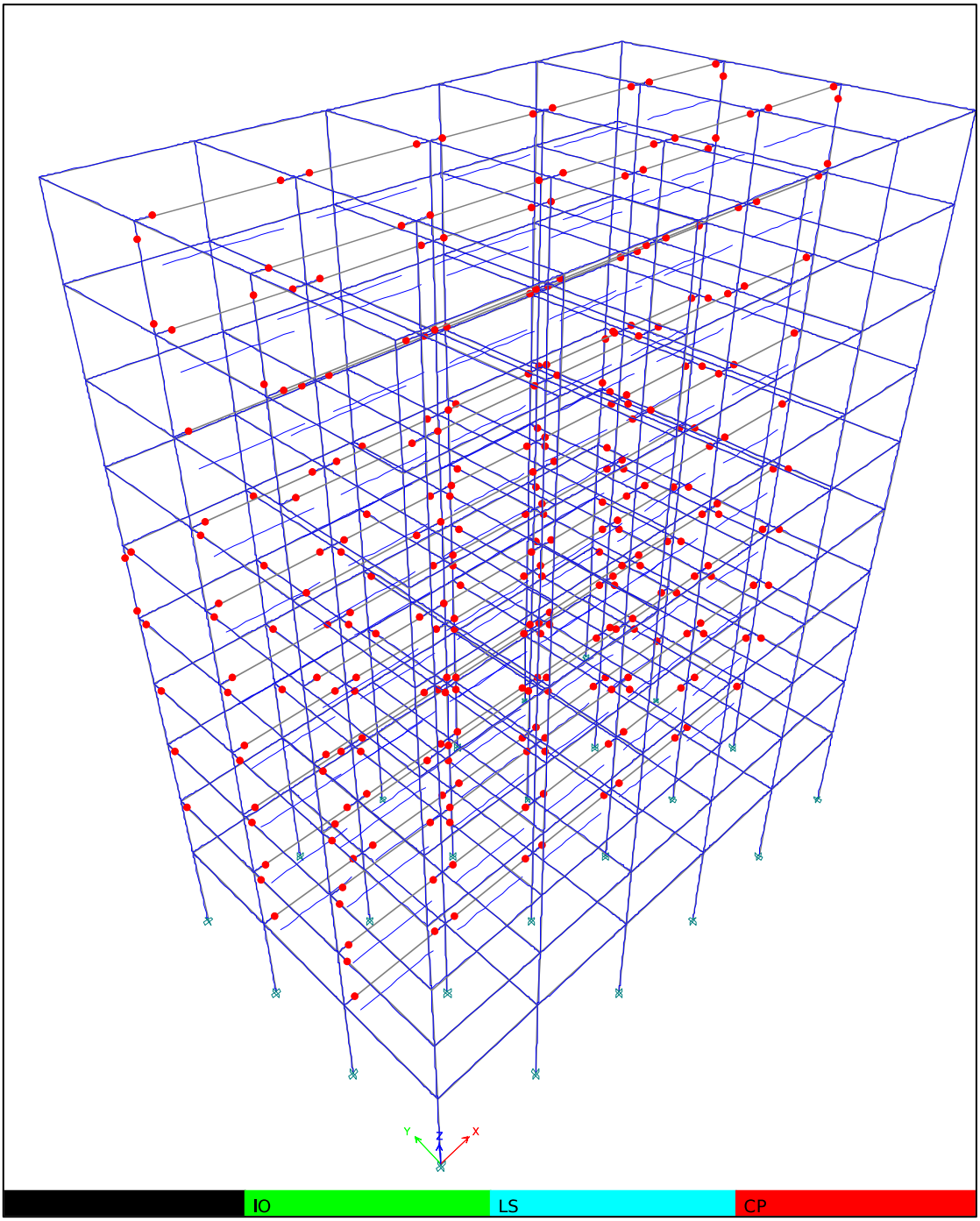


Figure 3.23: Shear hinges obtained at the performance point – Push-Y analysis

Alternatively, the shear demand in beams and columns is derived from the flexural moments in a similar fashion to what is performed in the Push-X analysis. It is worth noting that considerable moments are

developing in all the beams including the ones aligned in the X-direction even though the pushover loads are applied in the Y-direction. This is due to the fact that the beams aligned in the X-direction are supporting the gravity loading which is transferred from the one-way floor slab. The beams are grouped into the following four categories, with each category containing a set of beams showing a similar behaviour.

- B200x500_X: B1, B2, B3, B4, B5, B16, B17, B18, B19, B20
- B200x500_Y: B21, B22, B23, B36, B37, B38
- B900x250: B6, B7, B8, B9, B10, B11, B12, B13, B14, B15
- B300x250: B24, B25, B26, B27, B28, B29, B30, B31, B32, B33, B34, B35

The shear D/C ratio is plotted in Figure 3.24, which indicates that most of the beams are failing in shear, and the rest are overstressed and have a D/C ratio approaching the limit of "1". Again, these results conform very well with the shear hinges results of Figure 3.23.

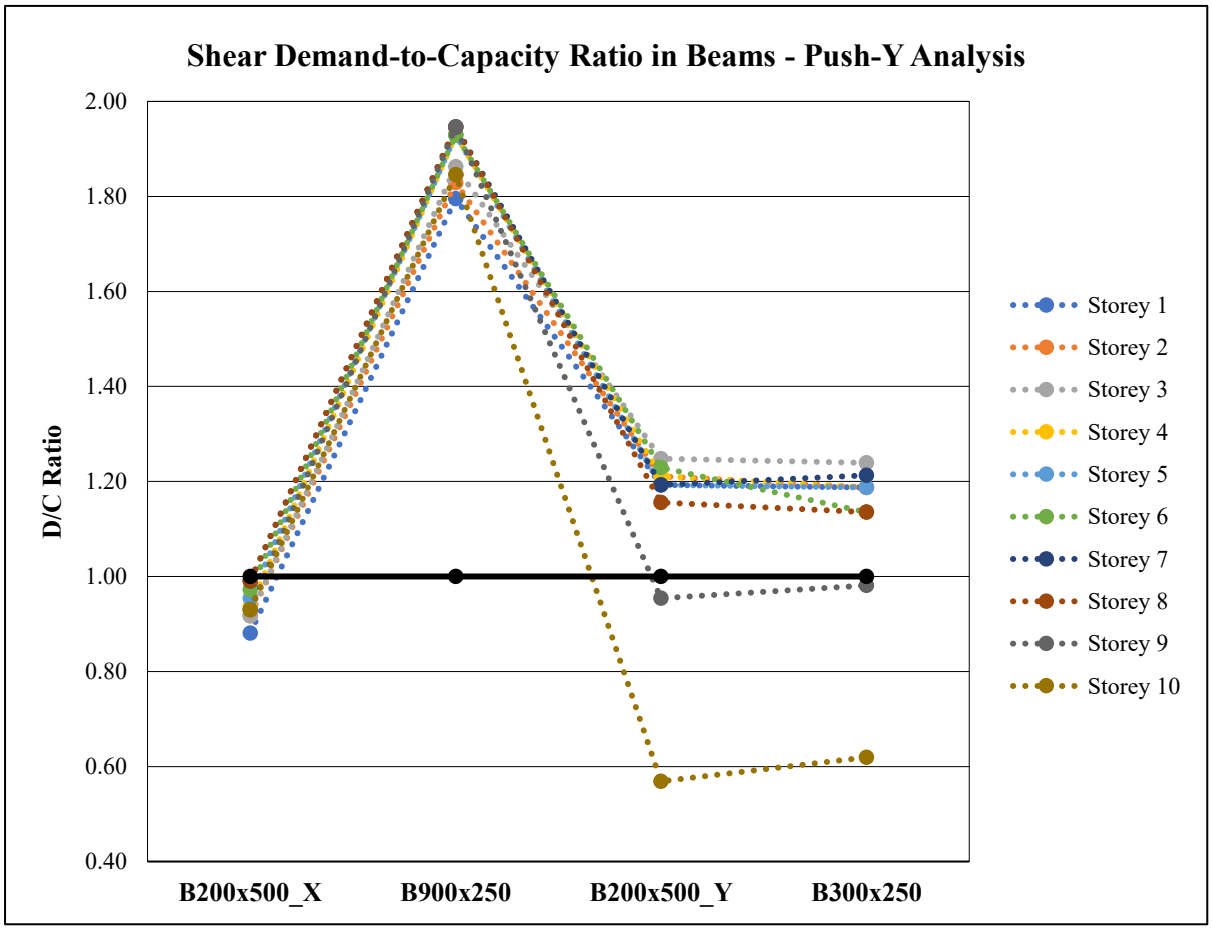


Figure 3.24: Demand-to-Capacity shear ratio in the beams – Push-Y

The columns are grouped into four categories (same ones used for the Push-X analysis) and are checked in a similar fashion. Figure 3.25 displays the shear D/C ratio in the columns at the performance point of the Push-Y analysis. The results point out to a few columns which are failing in shear at the upper

floors as the demand is exceeding the capacity. The shear failure in columns in the Push-Y analysis is lower than that observed in the Push-X analysis. This is attributed to the fact that the ductile failure mechanism has been more expressed in the Push-Y analysis compared to the Push-X (Cyan and Red hinges in Figure 3.22).

In sum, the shear results have shown that most of the beams and a few columns are failing in shear under the Push-Y analysis, which reflects on the brittle shear failure experienced by these structural elements when the building is subjected to the applied seismic loading.

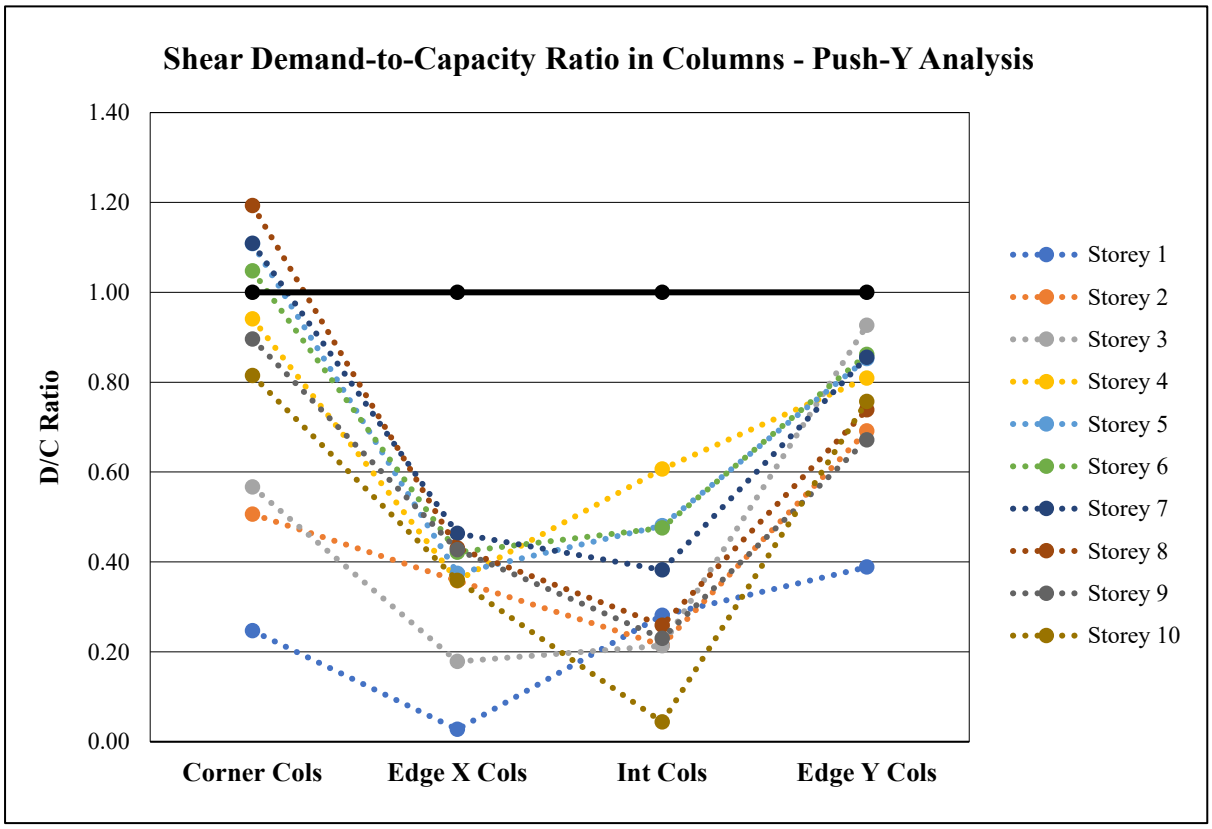


Figure 3.25: Demand to Capacity shear ratio in the Columns – Push-Y

iii. Checking the global stability and the interstorey drift

The displacement at each floor level is determined using the participation factor and the spectral displacement in a similar manner to what is performed in the Push-X analysis. The interstorey drift results are presented in Table 3-13 and are also plotted in Figure 3.26. The results reveal that the limit of 2% is exceeded at the 8th floor. This forms an additional proof of the instability of the building in resisting the earthquake loading in the Y-direction.

Table 3-13: Interstorey drift results – Push-Y

	Lateral Storey Disp. δ_i (m)	Interstorey Drift $\Delta\delta_i$ (m)	Storey Height h_i (m)	Interstorey Drift Ratio $\Delta\delta_i / h_i$	Interstorey Drift Check Limit (1%)
Storey 1	0.0178	0.0178	4.3	0.41%	Pass
Storey 2	0.0533	0.0355	3.1	1.15%	Pass
Storey 3	0.0888	0.0355	3.1	1.15%	Pass
Storey 4	0.1420	0.0533	3.1	1.72%	Pass
Storey 5	0.1953	0.0533	3.1	1.72%	Pass
Storey 6	0.2485	0.0533	3.1	1.72%	Pass
Storey 7	0.3018	0.0533	3.1	1.72%	Pass
Storey 8	0.3728	0.0710	3.1	2.29%	Fail
Storey 9	0.4260	0.0533	3.1	1.72%	Pass
Storey 10	0.4793	0.0533	3.1	1.72%	Pass

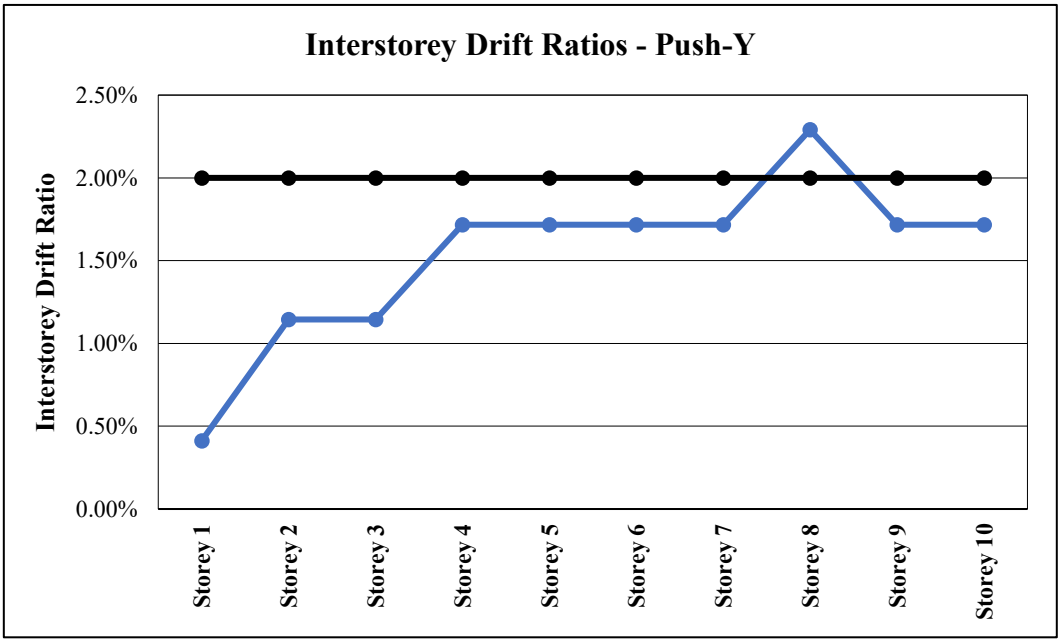


Figure 3.26: Interstorey drift ratios – Push-Y

The *P*-Δ check is performed in the Push-Y- analysis as well (Table 3-14). The results show that the interstorey drift sensitivity coefficient exceeds the limit of 0.1 at all floor levels and highlight the significance of the second-order effects and the need to incorporate it into the pushover analysis.

Using the same analogy applied in the Push-X analysis, the Push-Y analysis is not repeated by including the second-order effects, since the results obtained when the *P*-Δ effects were excluded are enough to highlight the inadequacy of the building. Accordingly, the *P*-Δ effect will be directly included in the analysis at later stages of this research.

Table 3-14: Checking the second-order effects (*P*-Δ) in the Push-Y analysis

	Storey Shear F_i (N)	Total Gravity Load P_{tot} (N)	Interstorey drift d_r (m)	Interstorey height h_i (m)	ISD sensitivity coefficient θ_i	Check
Storey 1	1413348	38964004	0.0178	4.3	0.114	*P*-Δ required
Storey 2	1401502	34578264	0.0355	3.1	0.283	*P*-Δ required
Storey 3	1367717	30617413	0.0355	3.1	0.256	*P*-Δ required
Storey 4	1312132	26656563	0.0533	3.1	0.349	*P*-Δ required
Storey 5	1224199	22795055	0.0533	3.1	0.320	*P*-Δ required
Storey 6	1103665	18933547	0.0533	3.1	0.295	*P*-Δ required
Storey 7	951669	15095413	0.0533	3.1	0.272	*P*-Δ required
Storey 8	768122	11309873	0.0710	3.1	0.337	*P*-Δ required
Storey 9	541744	7524332	0.0533	3.1	0.239	*P*-Δ required
Storey 10	283138	3762166	0.0533	3.1	0.228	*P*-Δ required

iv. Conclusion

The main objective of this exercise is to illustrate the seismic assessment procedure by testing the resistance of an existing 10-storey RC building to potential seismic hazards. The building performance was initially checked at the SD limit state. As inferred from the results, several beams were shown to suffer from ductile failure, and most of the beams and columns were shown to suffer from brittle shear failure, which indicates that the building is incapable of resisting the applied seismic loading.

The standards of EC8-3 (CEN, 2005a) require that every structural member must be declared adequate to resist potential ductile and brittle failure mechanisms in order for the building to be classified as capable of resisting the applied seismic loading. Therefore, it is safe to conclude that the building investigated is unsafe and cannot sustain the applied seismic loading. This consolidates the need for seismic retrofitting to avoid failure and potential loss of lives.

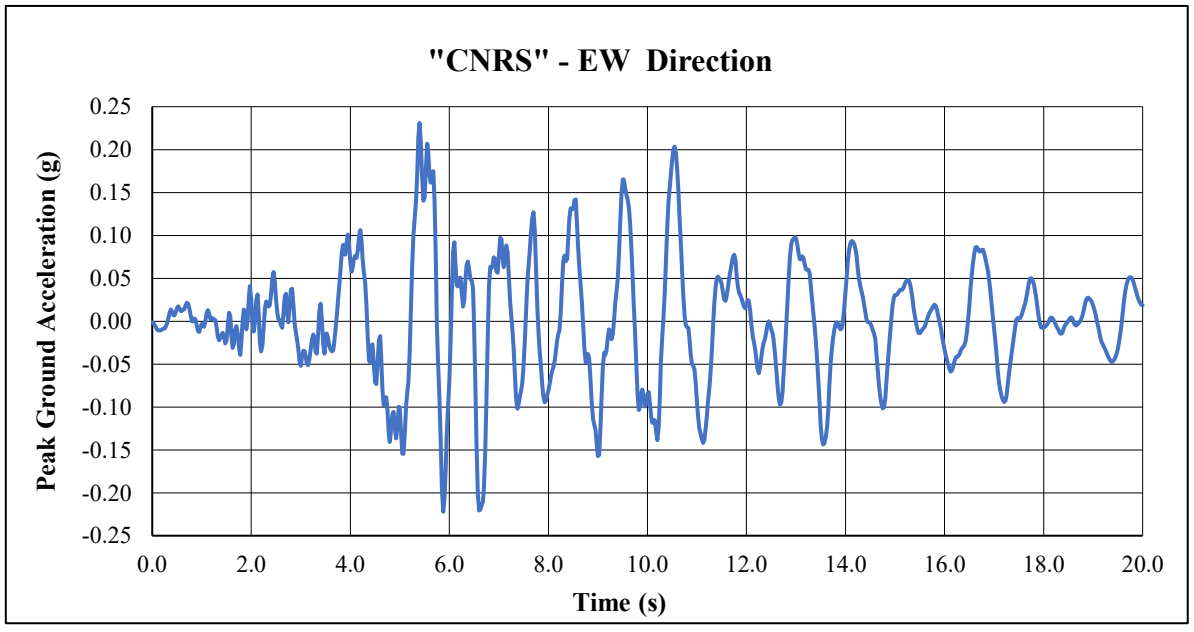
Last, it should be noted that there is no need to check the performance at the higher level of seismic action (the NC limit state), since the results obtained at the SD limit state are sufficient to highlight the vulnerability of the building and the need for retrofitting.

3.6.5 Validation against a complete nonlinear time history analysis

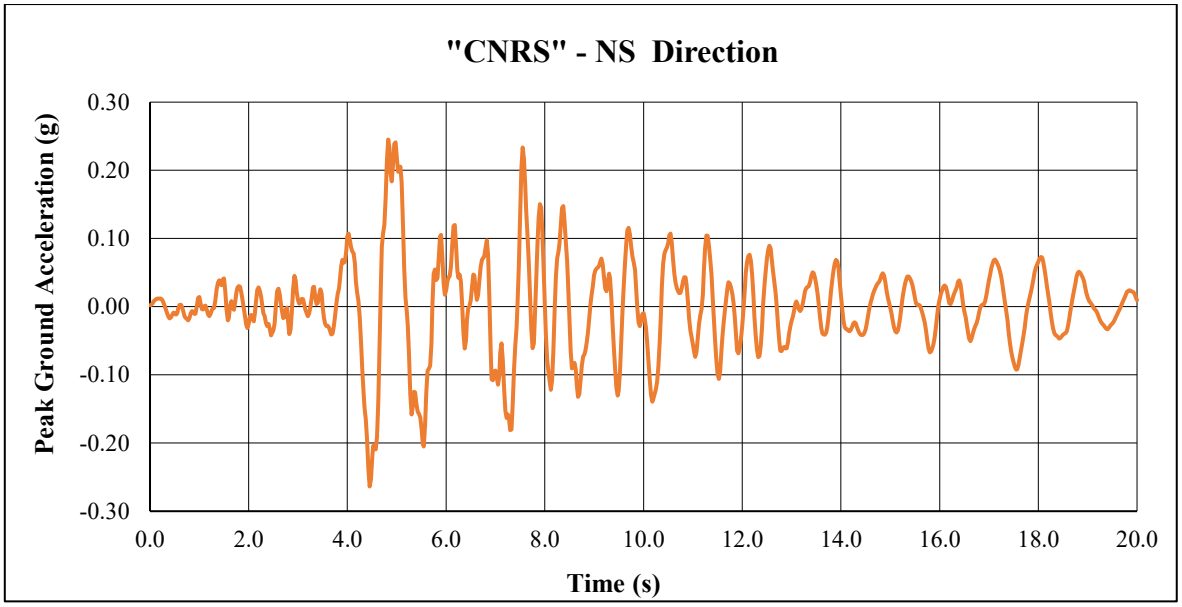
The last step involves testing the assessment results obtained from the nonlinear static pushover analysis (NSPA) against the more integrated nonlinear time history analysis (NLTHA). EC8-1 (CEN, 2004a) requires applying a minimum set of 7 ground motion time histories, and the response of the building is evaluated as the average of the results obtained from the ground motions considered. The Lebanese database of real earthquakes is recently established and is limited to a moderate seismic event of

moment magnitude 5.5 that occurred in February 2008 at the Yammouneh fault (Brax et al., 2014). In this regard, the ground motions considered in this example are obtained from a database of earthquakes that is artificially generated by Brax et al. (2018) and that simulate a seismic event of a moment magnitude of 6.5 occurring at the Yammouneh fault. Furthermore, the results presented in this section correspond to one single ground motion generated artificially by Brax et al. (2018), since this is an illustrative example that serves to validate the assessment results obtained using the CSM method. The ground motions considered are matched to the response spectrum used in the CSM. The matching was performed in the time domain on ETABS. Figure 3.27 below shows the three components of the ground motion labelled as "CNRS", and Figure 3.28 shows the typical spectral matching of one of the ground motion components to the response spectrum used in the CSM. Unlike the pushover analysis which is performed separately in the X and Y directions, the three ground motion components, namely the East-West (EW), the North-South (NS), and the gravitational (Z) components are applied simultaneously in the NLTHA. The load combinations of EC8-1 (CEN, 2004a) are considered in the time history analysis (Table 3-15).

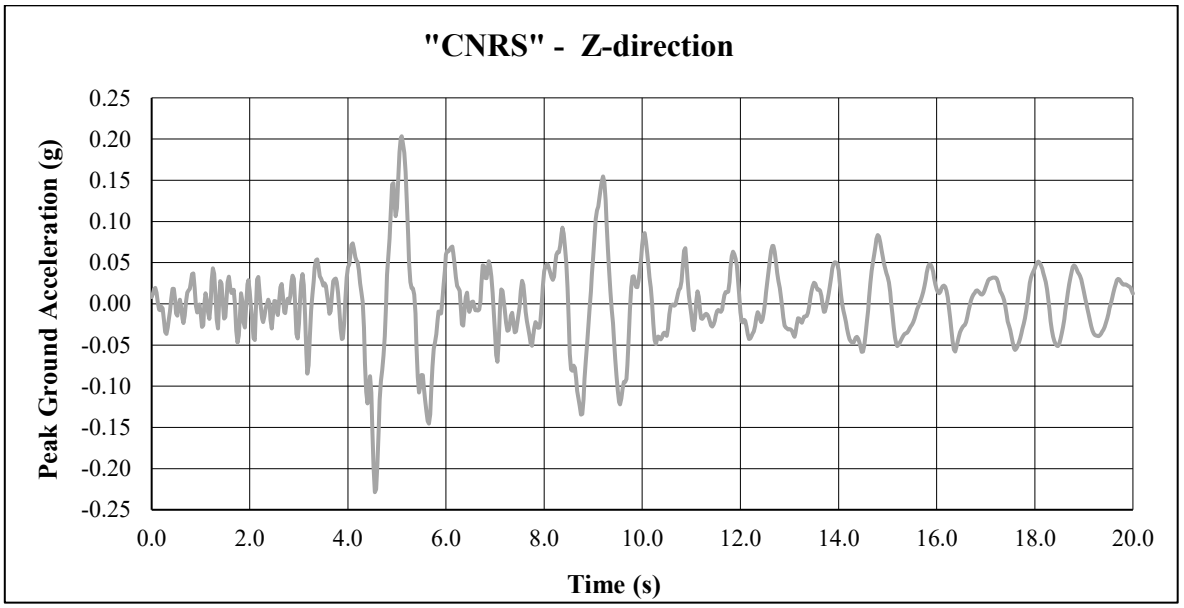
The same performance checks applied in the CSM are considered in the NLTHA, with the latter serving as a reference used to verify the accuracy of the CSM in depicting the seismic response of the building.



(a)



(b)



(c)

Figure 3.27: The three components of the CNRS ground motion time history: (a) EW direction, (b) NS direction, (c) Z-direction

Table 3-15: Load combinations of EN 1992-1-1 (CEN, 2004b): DL (total dead load), LL (live load), EQ (ground motion earthquake load)

Load Combinations
1.35 DL
1.35 DL + 1.5 LL
1.0 DL + 0.3 LL + 1.0 EQ
1.0 DL + 0.3 LL - 1.0 EQ
1.0 DL + 1.0 EQ
1.0 DL - 1.0 EQ

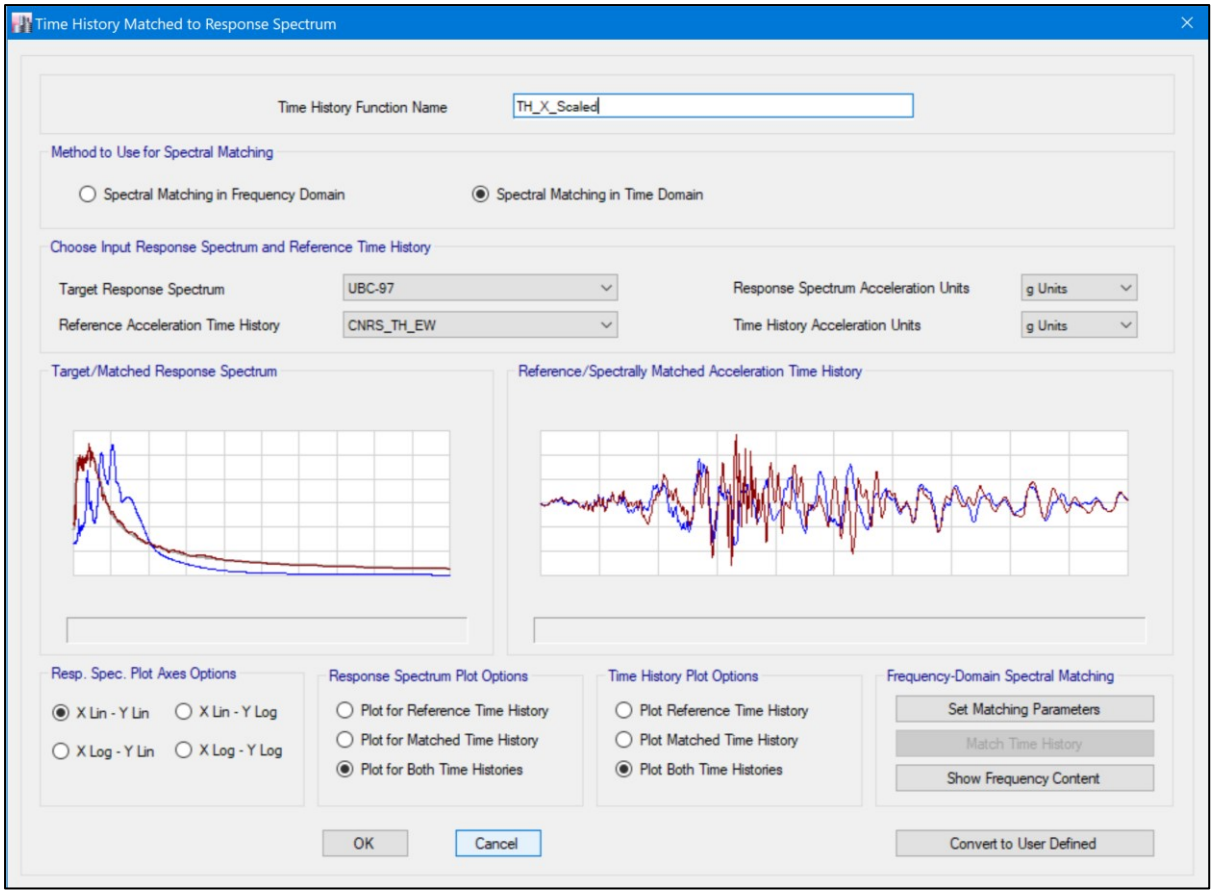


Figure 3.28: Spectral matching of the EW component of the ground motion "CNRS" with the response spectrum corresponding to the SD limit state

i. Checking against ductile failure (chord rotation)

Figure 3.29 presents the chord rotation results of the building obtained at the end of the NLTHA. The results compare well with those obtained from the Push-X and Push-Y analyses. Indeed, the chord rotation in several beams exceeds the SD limit (cyan hinge), and a few beams have exceeded the ultimate chord rotation limit of the NC state (red hinges). Consequently, the beams manifesting cyan and red hinges would suffer from ductile failure, noting that these results comply very well with what was obtained using the CSM.

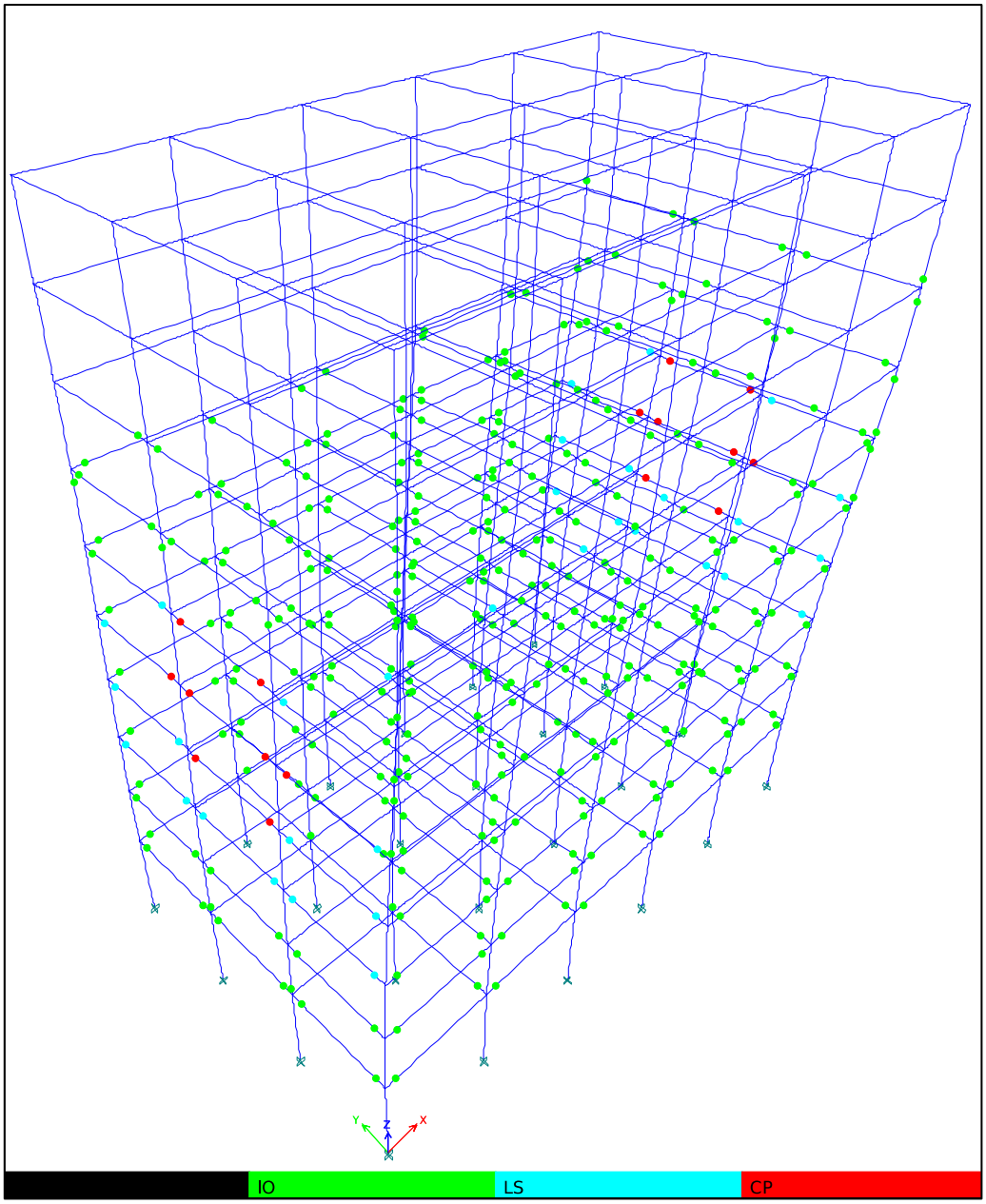


Figure 3.29: Flexural plastic hinges obtained at the end of the NLTHA

ii. Checking against brittle failure (shear)

The maximum shear demand is calculated using the flexural bending moments developing at the ends of beams and columns.

The beams are arranged into the same four categories used in the Push-Y analysis:

- B200x500_X: B1, B2, B3, B4, B5, B16, B17, B18, B19, B20
- B200x500_Y: B21, B22, B23, B36, B37, B38
- B900x250: B6, B7, B8, B9, B10, B11, B12, B13, B14, B15
- B300x250: B24, B25, B26, B27, B28, B29, B30, B31, B32, B33, B34, B35

The shear D/C ratio of all the beams is plotted in Figure 3.30. The results clearly indicate that the majority of the beams are failing in shear with an excessively high D/C ratio, and most importantly the results correlate very well with those obtained from the CSM method. Indeed, the D/C pattern obtained from NLTHA is very similar to what was obtained from the Push-Y analysis (CSM), although the values obtained from NLTHA are higher as expected since the seismic loads are applied in both horizontal directions simultaneously (and in the gravitational direction as well). The main beams aligned in the X-direction (B900x250) have registered the highest (D/C) ratio which is also the case for both the Push-X and Push-Y analyses, noting that the D/C ratio in these beams has approached the value of "3" in both the NSPA (the CSM) and the NLTHA. These results cement the accuracy of the CSM in predicting the shear demand in beams and strengthen the argument that almost all of the beams in the building would suffer a brittle shear failure under the applied seismic loading.

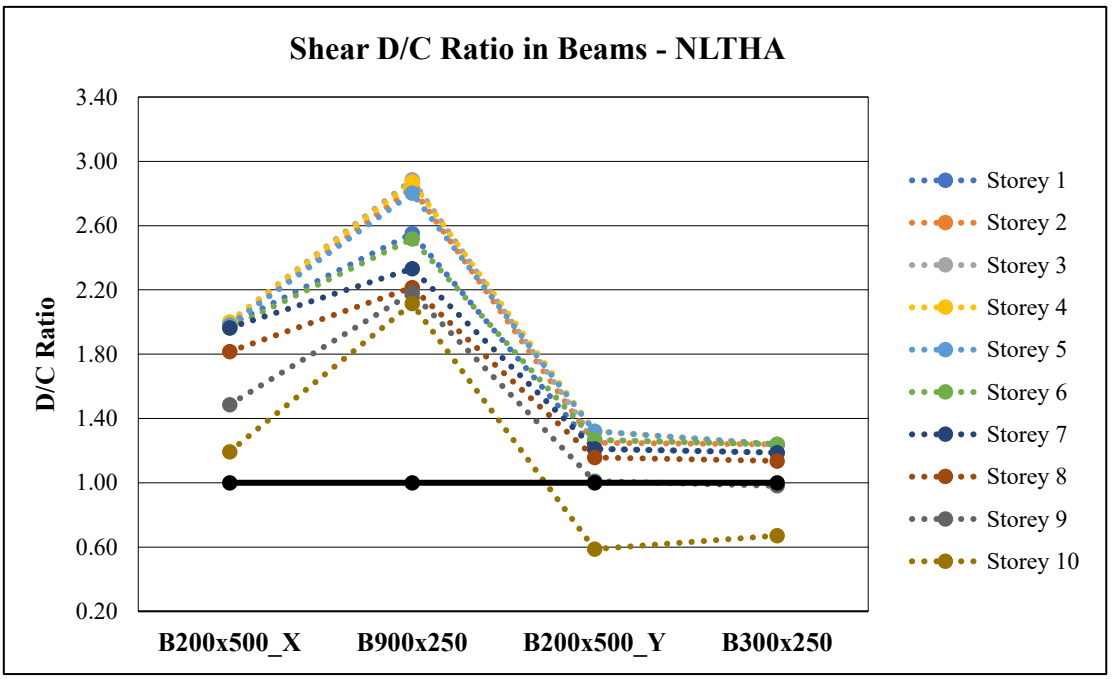


Figure 3.30: Shear D/C ratios in the beams under NLTHA

Since the NLTHA consists of applying the ground motions in both the X and Y directions simultaneously, flexural moments are expected to develop around both the major and minor bending axes of columns. In order to allow for a direct comparison with the CSM results, the shear demand obtained from the NLTHA will be checked in the X and Y directions separately. In this regard, Table 3-16 shows the direction of shear for the same categories of columns that were adopted in the Push-X and Push-Y analyses, with V2 denoting the shear along the major (strong) axis and V3 denoting the shear along the minor (weak) axis. The results of the D/C shear ratio in the columns are plotted in Figures 3.31 and 3.32. Commenting on the results in Figure 3.31, the D/C ratios obtained in the X-direction compare well with those obtained from the Push-X analysis although the CSM is slightly more conservative in this respect, as fewer columns are failing in shear in the NLTHA. Nevertheless, the

results of both analyses compare very well, noting that the pattern of D/C ratio is similar in both graphs, and the columns of category "Edge Y" are failing at upper floors in both the NSPA and the NLTHA as the load is being applied along the column's weak axis. Likewise, the results in Figure 3.32 perfectly correlate with those obtained from the Push-Y analysis, with some of the corner columns failing along their weak axis. Indeed, both the CSM and the NLTHA have displayed the same pattern and almost the same values of shear demand in direction Y.

Drawing on the shear D/C results obtained from the NLTHA, it is safe to conclude that the CSM method has successfully predicted the shear demand in beams and columns, and the method is deemed reliable in testing the building considered in this example against potential brittle shear failure.

Table 3-16: Direction of shear for all categories of columns

	X-direction	Y-direction
Corner	V2	V3
Edge X	V2	V3
Edge Y	V3	V2
Interior	V3	V2

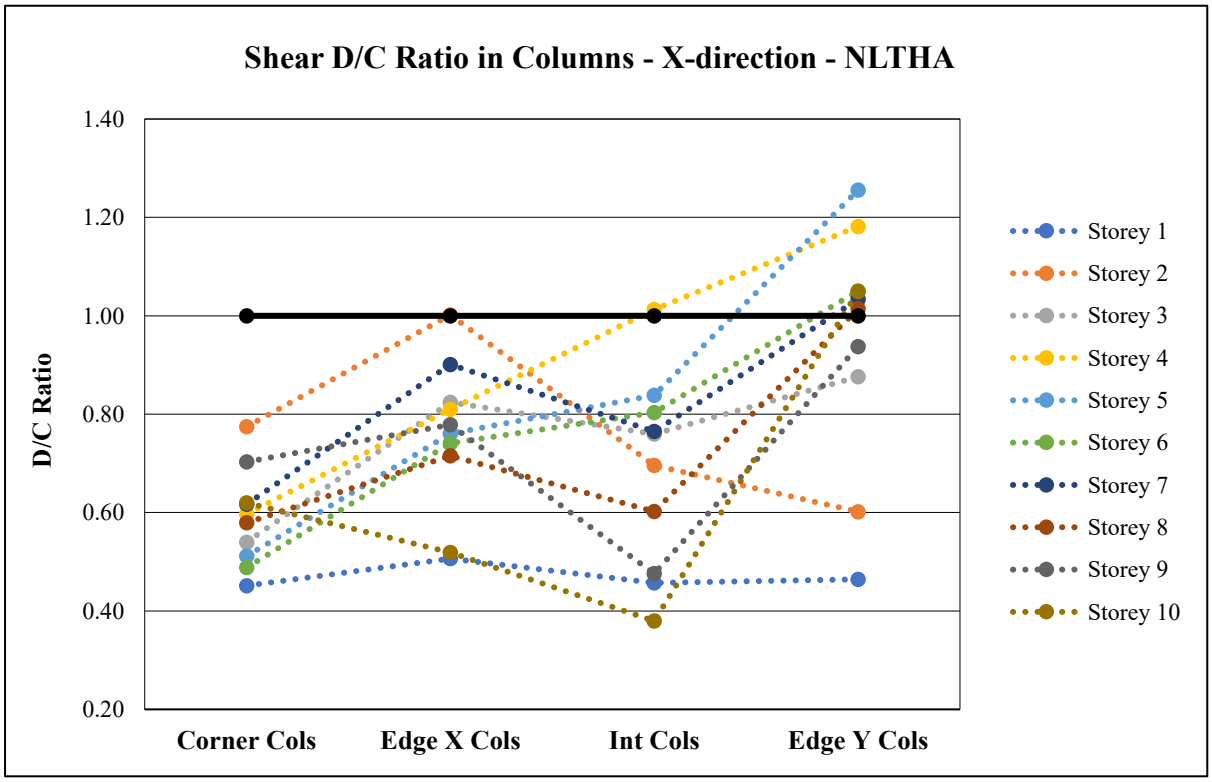


Figure 3.31: Shear D/C ratio in the columns in the X-direction under NLTHA

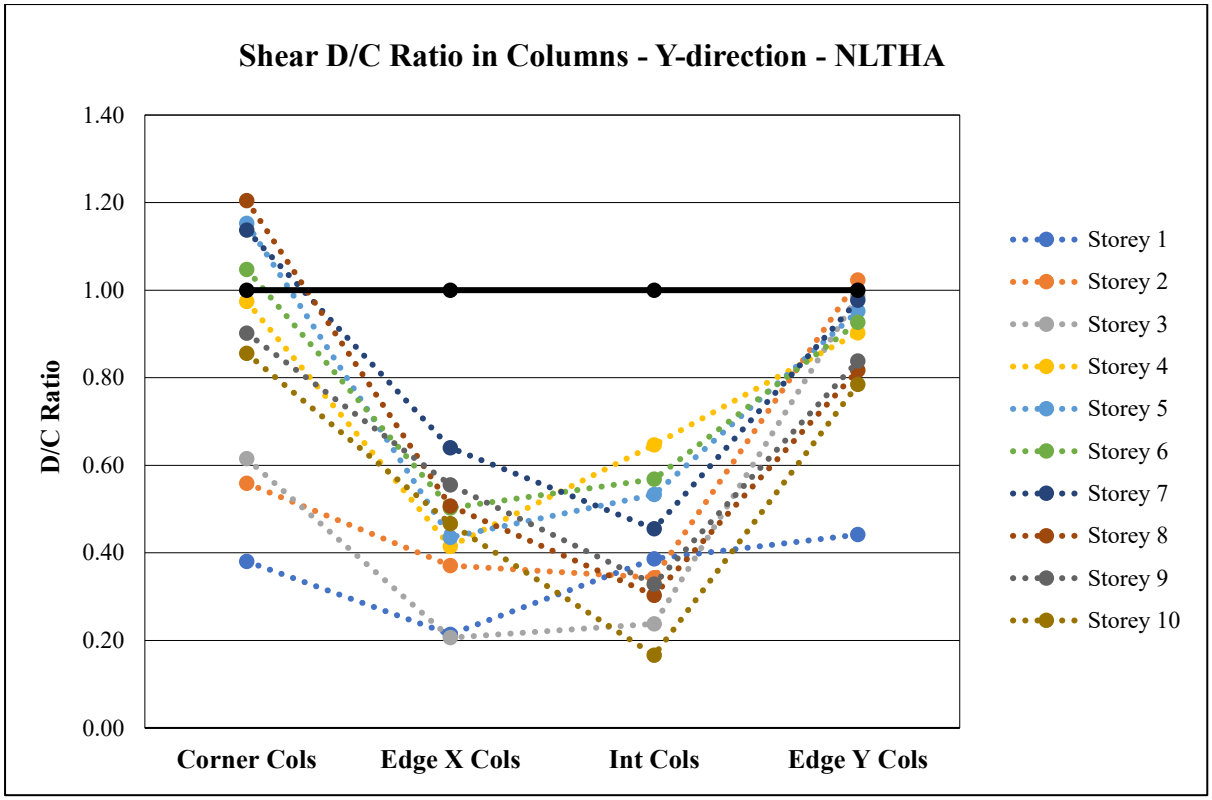


Figure 3.32: Shear D/C ratio in the columns in the Y-direction under NLTHA

iii. Checking the global stability (interstorey drift)

The maximum lateral displacements and interstorey drifts in the X-direction were registered at step 77 (after a time lapse of 7.7 seconds), noting that the ground motion has a duration of 20 seconds and that the output is obtained at time intervals of 0.1 second. The calculation of the maximum interstorey drift ratios is presented in Table 3-17, and the results are plotted in Figure 3.33. Results in Table 3-17 indicate that the CSM is slightly conservative in regard to the maximum displacement in the X-direction compared to the NLTHA, while both methods have almost yielded the same value for the maximum roof displacement in the orthogonal Y-direction. Furthermore, both analyses are generally recording a higher drift ratio in the Y-direction (compared to the ratios in direction X), and the drift ratio is occasionally exceeding the limit and reaching a value as high as 2.5% in both analyses. In sum, the drift results obtained from the NLTHA support the conclusion obtained from the CSM which enhances the reliability of the latter in the seismic assessment of the building. Furthermore, the excessively high drift ratios support the main conclusion that the building investigated is unstable and is experiencing excessive deformations in response to the applied seismic loading.

Table 3-17: Interstorey drift results obtained from the NLTHA

		X-Direction				Y-Direction			
	Storey Height	**Lateral Storey Disp.**	**Inter-storey Drift**	**Inter-storey Drift Ratio**	**Inter-storey Drift Check**	**Lateral Storey Disp.**	**Inter-storey Drift**	**Inter-storey Drift Ratio**	**Inter-storey Drift Check**
	h_i (m)	$\delta_{i,X}$ (m)	$\Delta\delta_{i,X}$ (m)	$\Delta\delta_{i,X}/h_i$	Limit (1%)	$\delta_{i,Y}$ (m)	$\Delta\delta_{i,Y}$ (m)	$\Delta\delta_{i,Y}/h_i$	Limit (1%)
Storey 1	4.3	0.0207	0.0207	0.48%	**Pass**	0.0227	0.0227	0.53%	**Pass**
Storey 2	3.1	0.0499	0.0292	0.94%	**Pass**	0.0679	0.0451	1.46%	**Pass**
Storey 3	3.1	0.0843	0.0344	1.11%	**Pass**	0.1306	0.0628	2.03%	**Fail**
Storey 4	3.1	0.1217	0.0374	1.21%	**Pass**	0.2044	0.0738	2.38%	**Fail**
Storey 5	3.1	0.1562	0.0345	1.11%	**Pass**	0.2851	0.0807	2.60%	**Fail**
Storey 6	3.1	0.1856	0.0294	0.95%	**Pass**	0.3631	0.0781	2.52%	**Fail**
Storey 7	3.1	0.2089	0.0233	0.75%	**Pass**	0.4292	0.0661	2.13%	**Fail**
Storey 8	3.1	0.2249	0.0160	0.51%	**Pass**	0.4671	0.0379	1.22%	**Pass**
Storey 9	3.1	0.2360	0.0111	0.36%	**Pass**	0.4867	0.0197	0.63%	**Pass**
Storey 10	3.1	0.2415	0.0056	0.18%	**Pass**	0.4971	0.0104	0.33%	**Pass**

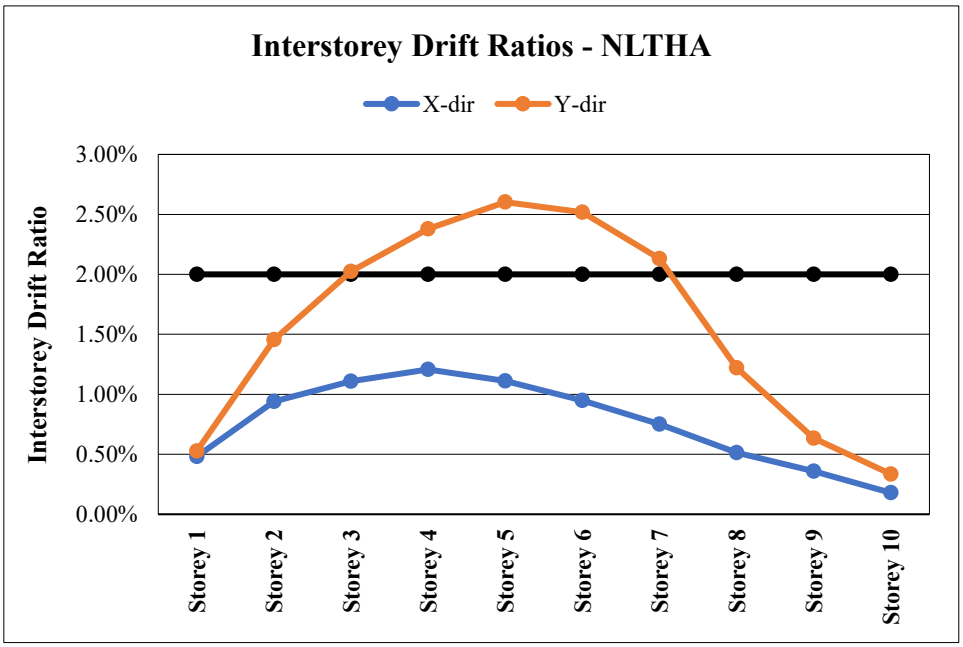


Figure 3.33: Interstorey drift ratios– NLTHA

3.6.6 The N2 Method

Last, the same exercise is performed in the context of the N2 method, which is implemented in Eurocode 8 or EC8-1 (CEN, 2004a) and which is briefly discussed in Chapter 2. The N2 method is believed to provide a better estimate of the seismic response compared to the CSM and other pushover analyses,

since the extended version of the method includes an elastic dynamic analysis which is believed to depict the torsional effects that are overlooked in single-mode pushover analysis. To this end, it is worth noting that the CSM was preferred over the N2 method since the objective of this research is to develop a simplified retrofitting strategy that minimises the torsional effects, which effectively reduces the need for a separate elastic dynamic analysis. Furthermore, the retrofitting strategy developed in this research depends on a simplified application of pushover analysis (the CSM), and accordingly the inclusion of response spectrum analysis is considered to be computationally disadvantageous and would reduce the overall effectiveness of the procedure. Nevertheless, the N2 method is performed and compared to the CSM in order to weigh up on the accuracy of both methods when compared with the NLTHA which serves as the benchmark that depicts the actual seismic response. The pushover response is already obtained from the application of the CSM, yet the difference lies in the bilinearisation of the capacity curve, which is based on engineering judgment in the N2 method. In view of this, Figures 3.34 and 3.35 present the bilinearisation of the capacity curve in both horizontal directions, with the target displacement initially estimated according to the equal displacement approach. To this end, it is worth noting that the procedure converged from the first iteration, such that the ductility factor that is graphically calculated from the trial performance point has produced an inelastic demand curve (reduced by way of the ductility reduction factor) that intersects the bilinear curve at the initial displacement demand. Hence, the final displacement demand is the same as the initial one obtained from the equal displacement approximation (Figures 3.36 and 3.37). This might be attributed to the fact that the building considered is vulnerable and possesses a low elastic stiffness, such that the bilinearisation is smoothly performed with ease, allowing the procedure to converge immediately.

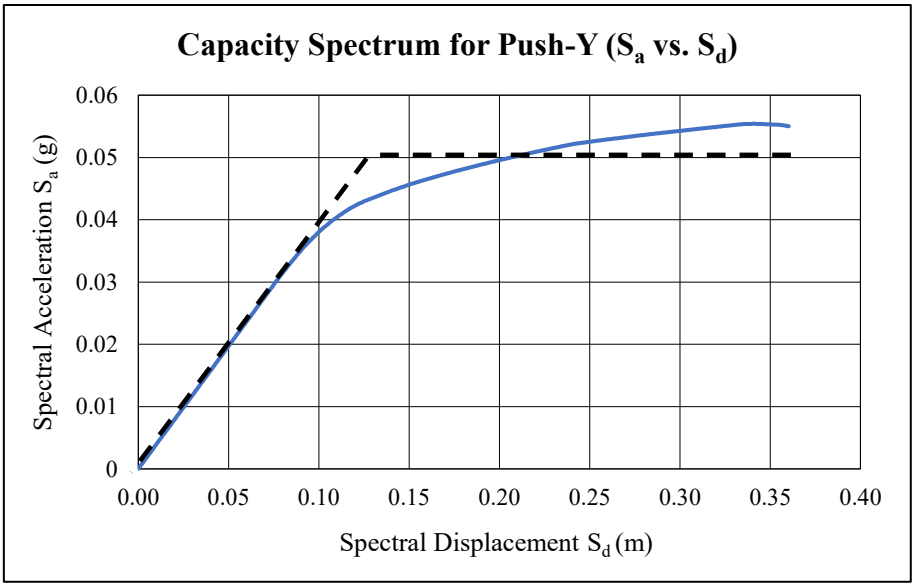


Figure 3.34: Idealisation of the capacity spectrum in the Y-direction (mode 1) into a bilinear curve

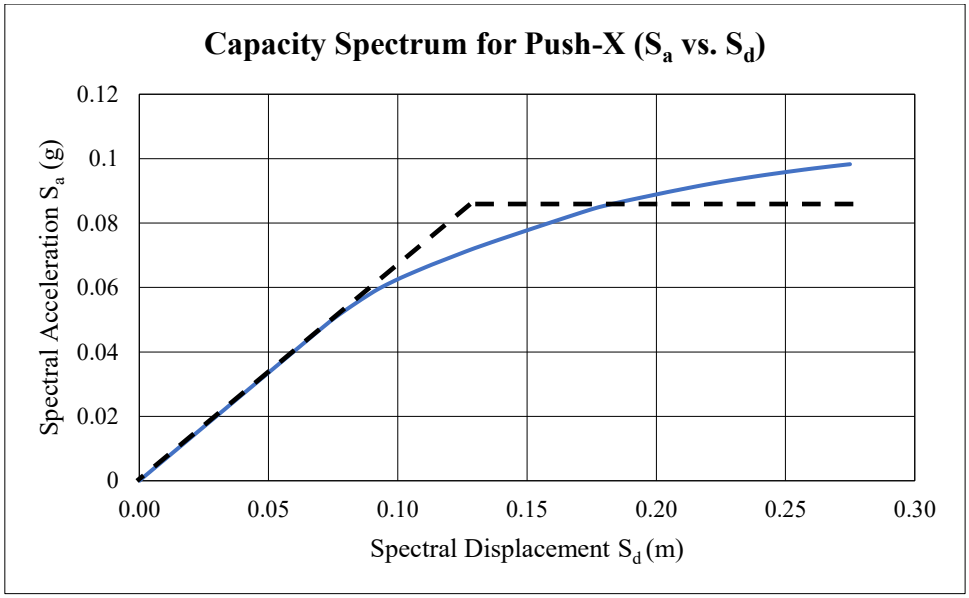


Figure 3.35: Idealisation of the capacity spectrum in the X-direction (mode 2) into a bilinear curve

The calculation of the ductility ratio in both horizontal directions is presented in Table 3-18. As noted, the ductility factor is calculated from the equal displacement approach, and the resultant inelastic spectrum intersects the bilinear capacity curve at the same point, hence achieving convergence at the first iteration (Figures 3.36 and 3.37).

Table 3-18: Calculating the ductility ratio by equivalent linearisation of the capacity curve

	Yield Point		Target Displacement Demand		Ductility
	Spectral Acceleration S_a (g)	**Spectral Displacement S_d (m)**	**Spectral Acceleration S_a (g)**	**Spectral Displacement S_d (m)**	**Ductility Ratio μ**
Mode 1 (Y-direction)	0.05	0.13	0.05	0.36	2.8
Mode 2 (X-direction)	0.085	0.13	0.085	0.275	2.2

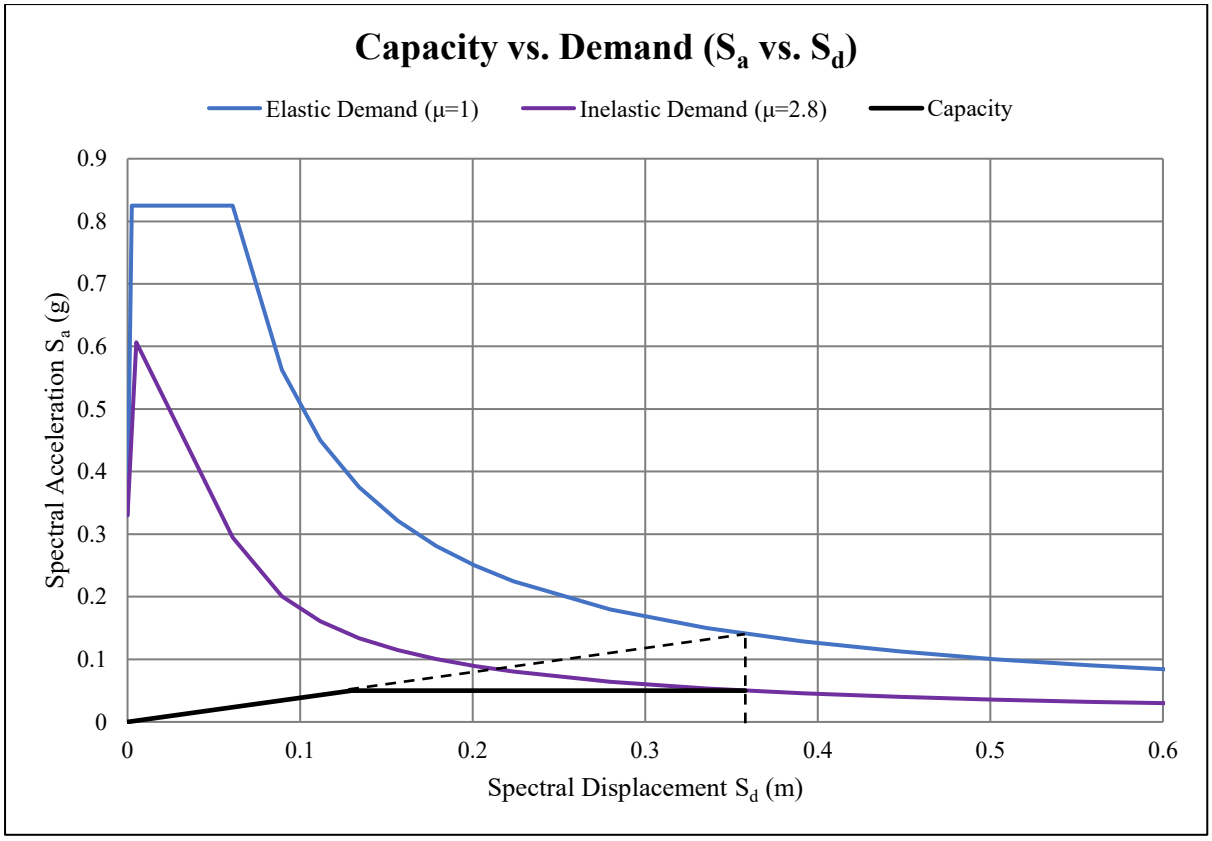


Figure 3.36: Evaluation of the target displacement in the Y-direction (mode 1) according to the N2 method

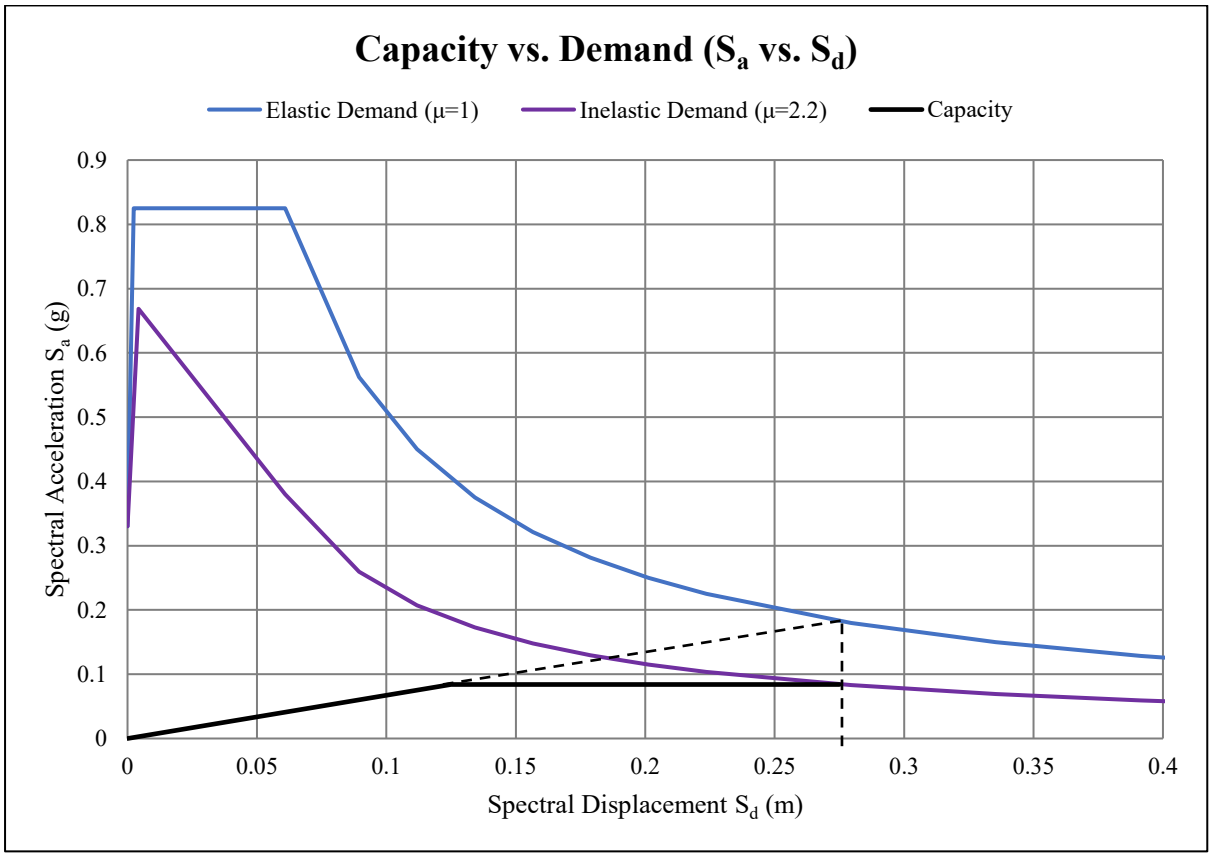


Figure 3.37: Evaluation of the target displacement in the X-direction (mode 2) according to the N2 method

In line with the requirements of the N2 method, a separate elastic response spectrum analysis is performed on ETABS (2017) to estimate the torsional amplification of higher modes. The same response spectrum used in the pushover analysis is used in the elastic dynamic analysis. Spectral load cases were accordingly defined in each horizontal direction according to UBC-97 (ICBO, 1997) and in line with the elastic response spectrum being used. Accordingly, a scale factor equal to (Ig/R) is initially applied to the spectral load case in each horizontal direction, where "I" is the importance factor (equal to 1.0 for residential buildings), g is the gravitational acceleration, and R is the response modification factor which is equal to 3.5 for ordinary frame buildings. Furthermore, in case the base shear calculated by static loading exceeds the one obtained from the dynamic spectral load, this latter is scaled by the ratio between the two values such that the base shear obtained from dynamic analysis cannot be smaller than that obtained from static analysis in line with the code regulations. The final spectral load case includes both horizontal components with their respective scale factor and a vertical component as well, noting that a scale factor equal to (2/3 of the highest scale factor among both horizontal directions) is adopted for the vertical component (Figure 3.38). The displacement results obtained from the response spectrum analysis were shown to be smaller than those obtained from the pushover analysis (Table 3-19). Hence, the finalised seismic displacements calculated by the N2 method are directly obtained from the pushover analysis (correction factors taken as 1.0) since the method does not allow for de-amplification of displacements due to torsion. This is attributed to the fact that the building considered is plan-symmetric, in consequence of which the torsional effects are minimal and the behaviour is mainly regulated by the fundamental mode of vibration.

Table 3-19: Calculating the seismic displacements using the N2 method

	Pushover Analysis		Elastic Dynamic Analysis		N2 Results
	Spectral Displacement S_d (m)	**Roof Displacement Δ_{Roof} (m)**	**Roof Displacement Δ_{Roof} (m)**	**Correction Factors CF**	**Roof Displacement Δ_{Roof} (m)**
Mode 1 (Y-direction)	0.36	0.52	0.45	1.00	0.52
Mode 2 (X-direction)	0.275	0.40	0.255	1.00	0.40

Last, the results of the N2 method are compared to those obtained from the CSM and the NLTHA (Table 3-20), in order to weigh up on the differences between the nonlinear static methods and their accuracy in predicting the seismic displacement demand, noting that the NLTHA serves as the benchmark for the comparison. In view of this, both methods have returned good estimates of the maximum displacement in the slender Y-direction noting that the CSM slightly underestimates the displacement response, despite returning a closer value to the actual displacement. However, both methods have hugely overestimated the maximum displacement in the X-direction, with the N2 method recording a percentage difference as twice that recorded by the CSM.

Table 3-20: Comparing the CSM and the N2 method against the integrated NLTHA

	Maximum Displacement (m)			% Difference	
	CSM	**N2 method**	**NLTHA**	**CSM**	**N2 method**
Mode 1 (Y-direction)	0.49	0.52	**0.50**	2%	4%
Mode 2 (X-direction)	0.33	0.40	**0.24**	37.5%	66.7%

To conclude, both methods have successfully predicted the displacement in the slender Y-direction, while the CSM has returned a better estimate of the displacement in the X-direction which is overestimated by both methods. Although the CSM provided better results than the N2 method for this particular example, it is again worth noting that the main reason behind adopting it in this research is the fluidity and systematic application of the method, with the procedure encompassing a clear and guided approach for determining the bilinear curve and finding the performance point. Furthermore, the retrofitting strategy developed in this research aims at minimising the torsional effects, which relinquishes the need for the linear dynamic analysis that is required by the N2 method to estimate the torsional amplifications.

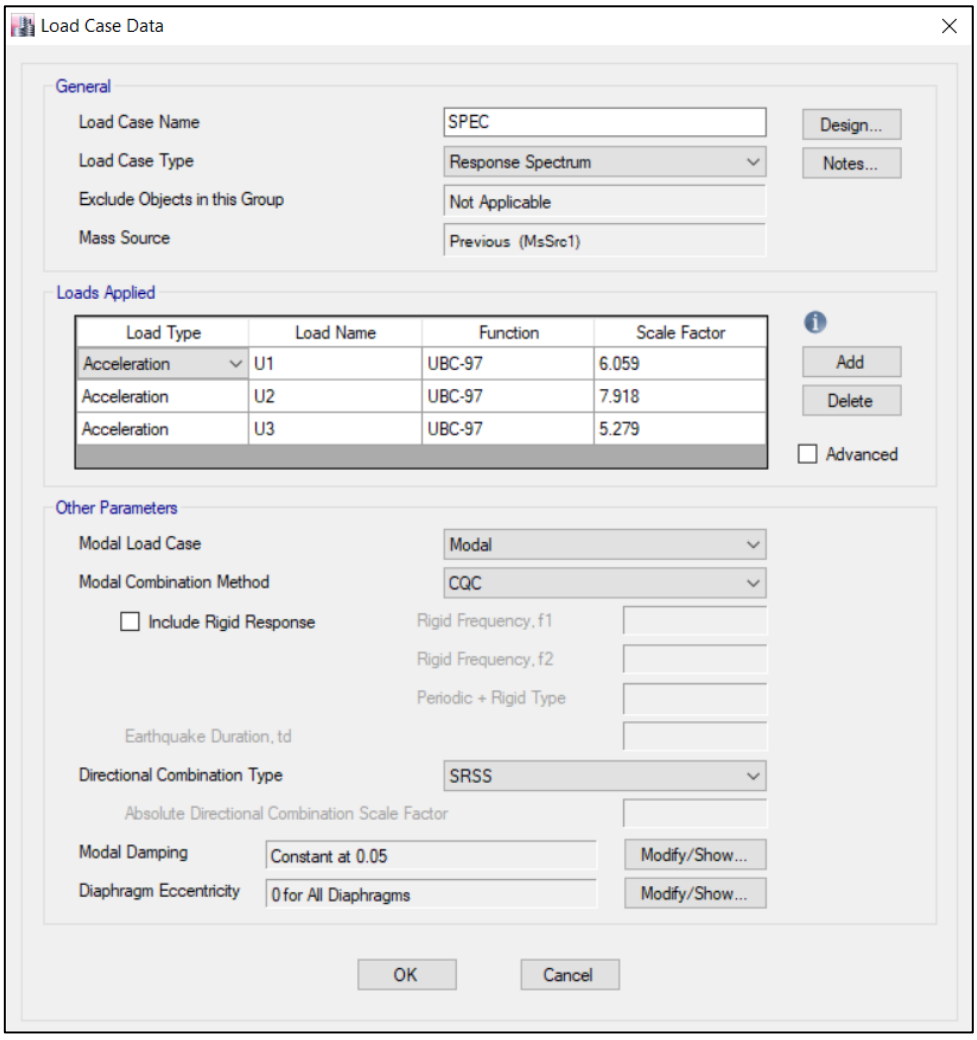


Figure 3.38: Definition of spectral load case in the elastic dynamic analysis performed on ETABS

Chapter 4 Strategy for Minimising Torsional Effects in the Fundamental Mode

4.1 Introduction

The accuracy of nonlinear static pushover analysis (NSPA) in predicting the seismic response has been a subject of interest for researchers over the years. Several researchers have reported that the seismic demand values obtained by NSPA procedures are reliable for symmetric low- and mid-rise structures whose seismic response is governed by deformations of the fundamental mode and which are characterised by a uniform distribution of inelastic action throughout the height (Lawson et al., 1994; Kim & D'Amore, 1999; Zamfirescu & Fajfar, 2001; Albanesi et al., 2002; Bento et al., 2004). The main focus of this research is the capacity spectrum method (CSM), a form of NSPA which is based on the simplified assumption that the maximum lateral storey drifts are governed by deformations of the fundamental mode of the originally elastic system (Freeman, 1998). It is therefore suggested that the method is reliable if the elastic translational first mode governs the dynamic response of the structure. In this regard, Peter & Badoux (2000) consider the CSM to be inappropriate for the analysis of buildings where the maximum storey drifts are not governed by the fundamental mode, such as tall buildings (more than about 15 stories) or buildings under shock-like impacts (near source effects). According to ATC-40 (ATC, 1996), the prevalence of the first mode in the seismic response is a valid assumption if the fundamental period of vibration is below one second. Other studies have also recommended that the CSM is applicable with confidence to buildings having a fundamental period lower than 1 sec (ATC, 1996, 2005; Oguz, 2005; Najam, 2017). The effect of higher modes on the seismic response becomes more pronounced in taller flexible buildings with longer fundamental periods.

In this context, attempts to mitigate the limitations of the method mainly focused on incorporating higher modes into the seismic response (Sasaki et al., 1998; Chopra & Goel, 2002; Gupta & Kunnath, 2000). This is accomplished through the evolution of multi-mode pushover (MMP) procedures in which the seismic response of high-rise buildings can be evaluated from an envelope of three independent pushover analyses involving the first, second, and third modes of vibration. However, recent studies by Najam (2017) showed that the NSPA that include the contribution of higher modes are computationally expensive and offer limited advantage over simplified pushover techniques, and thus may not be considered a suitable alternative to the NLTHA. Therefore, it is essential to come up with an approach that enforces the predominance of the fundamental mode of vibration on the structural response such that the CSM can be applied with ease and confidence.

In light of this discussion, the scope of buildings targeted by this research is in the range of 6 to 12 storeys and as such are expected to be governed by the fundamental translational mode of vibration. However, multi-storey buildings having structural plan or vertical irregularities generally vibrate in a

coupled lateral-torsional motion when subjected to ground seismic motions (Doudoumis & Doudoumis, 2017). The seismic behaviour of these buildings is characterised by a significant combination of swaying and twisting. Hence, the presence of plan or vertical irregularities is expected to reduce the mass participation of the translational component of the fundamental mode. This eventually reduces the reliability of the CSM in predicting the seismic response especially if an elastic first mode force distribution is adopted. Adding this to the limited advantage offered by the MMP procedures which are computationally demanding, a devised approach needs to be implemented to ensure that the CSM can be applied with ease and confidence. This chapter presents a procedure for calculating the centre of mass and the centre of rigidity at each floor level and proposes a strategy that maximises the mass participation of the translational component of the fundamental mode. The strategy is based on the relationship between the floor eccentricity and the modal mass participation ratio. Denoting the floor eccentricity by the distance between the centre of mass and the centre of rigidity, it is shown that the mass participation of the fundamental mode in the translational direction of pushover is maximised when the average floor eccentricity (Euclidean average) of all storey levels is minimised. This condition is an essential component of the retrofitting strategy that is developed in this research, since it enhances the performance of the original frame by reducing the torsional effects as well as it provides a solid foundation for applying the CSM with confidence. Last, it should be noted that the calculation of the modal mass participation factor and the irregularity of buildings are discussed in detail in Appendix 4.

4.2 Individual and Cumulative Centre of Mass

Once a load pattern is adopted, the lateral forces in a pushover analysis are applied at the centre of mass of each floor level. The centre of mass is the point in the floor plan where the resultant gravity force acts. The procedure for finding the centre of mass of each storey level is straightforward, taking into consideration the masses of the structural and non-structural components and their relative distances from a given reference point as per the following:

$$\overline{X}_j = \frac{\sum_{i=1}^{N} m_i x_i}{\sum_{i=1}^{N} m_i} \quad ; \quad \overline{Y}_j = \frac{\sum_{i=1}^{N} m_i y_i}{\sum_{i=1}^{N} m_i} \tag{4.1}$$

where:

$\overline{X}_j$ & $\overline{Y}_j$ are the coordinates of the individual centre of mass at the j^{th} floor,

x_i & y_i are the coordinates of the i^{th} element in the floor plan, and

m_i is the mass of the i^{th} element in the floor plan.

The centre of mass calculated using Equation 4.1 represents the lumped mass of the structural and non-structural components at the current floor. Although lumping the floor mass at one point is a widely used approach in dynamic analysis, it should be noted that the total mass supported at the current storey consists of the mass of the current and the overlying floors as well. In this respect, a more representative centre of mass, referred to as the cumulative centre of mass (CCM) is calculated here. The CCM provides a more realistic representation of the centre of mass at a given storey as it takes into consideration the total mass spanning from the top of the building down to the floor under consideration. The location of the cumulative centre of mass is determined based on the individual centre of mass of different floors. In this respect, the cumulative centre of mass is calculated by taking into consideration the mass and the individual centre of mass of upper floors as per the following:

$$\bar{X}_{CCM,j} = \frac{\sum_{k=j}^{n} M_k \bar{X}_k}{\sum_{k=j}^{n} M_k} \quad ; \quad \bar{Y}_{CCM,j} = \frac{\sum_{k=j}^{n} M_k \bar{Y}_k}{\sum_{k=j}^{n} M_k} \tag{4.2}$$

where:

$\bar{X}_{CCM,j}$ & $\bar{Y}_{CCM,j}$ are the coordinates of the cumulative centre of mass at the j^{th} floor with respect to a pre-determined reference point,

$\bar{X}_k$ & $\bar{Y}_k$ are the coordinates of the individual centre of mass at the k^{th} floor,

M_k is the lumped mass of the k^{th} floor, and

n is the total number of floors in the building.

The cumulative centre of mass is used later in order to calculate the eccentricity at each floor with respect to the centre of rigidity.

4.3 Centre of Rigidity

The concept of the centre of rigidity (CR) is originally attributed to a single-storey building having a rigid floor diaphragm (Lin, 1951). By definition, the centre of rigidity, also referred to as the centre of stiffness, is the location in the floor at which an applied lateral force produces only translational displacement and does not cause any rotation of the diaphragm (Doudounis & Doudounis, 2017). According to the same researchers, there is no conventional definition of the centre of rigidity when the concept is extended to multi-storey asymmetric buildings, as the literature contains several definitions of the centre of rigidity in that regard. Humar (1984) introduced the concept of the single-floor CR as the point in the floor at which an applied lateral load is only associated with a translational displacement and does not cause any rotation of the floor diaphragm. Hence, the CR is defined at the single-storey

level as diaphragm rotations may or may not occur at the other floors. The single-storey definition of the CR is widely adopted in the literature and is implemented in some building analysis software such as ETABS.

This section presents a devised approach to determine the centre of rigidity of each storey. The approach is based on the single-storey concept of the CR and is explained in depth in the following discussion. The process relies on the assumption of having a rigid diaphragm at each floor level. In order to find the CR at one storey, a unit force is applied first in the X-direction at a predefined point in the floor plan (reference point) and the resultant floor rotation at the reference point is calculated (R_{ZX}). Next, a unit force in direction Y is applied at the reference point and the corresponding floor rotation R_{ZY} is calculated. Finally, the floor rotation R_{ZZ} is measured in response to a unit torsional moment applied at the reference point around the Z-axis. The three unit loads are applied separately (one at a time) and the corresponding floor rotation is calculated separately in each case. In this respect, the CR is obtained using Equation 4.3 which determines the distance between the reference point and the CR. Therefore, if the centre of mass is chosen as the reference point (as the point of application of the unit loads), then the location of the CR is determined with respect to the centre of mass. The same process is repeated in order to find the centre of rigidity (CR) of each storey.

$$X_{CR} = \frac{-R_{ZY}}{R_{ZZ}} \quad ; \quad Y_{CR} = \frac{R_{ZX}}{R_{ZZ}} \tag{4.3}$$

where:

X_{CR} & Y_{CR} are the distances between the centre of rigidity and the point at which the unit loads are applied,

R_{ZX} is the floor rotation obtained in response to the unit force applied in the X-direction,

R_{ZY} is the floor rotation obtained in response to the unit force applied in the Y-direction, and

R_{ZZ} is the floor rotation obtained in response to the unit moment applied around the Z-axis.

The previous discussion serves to illustrate the concept required to determine the centre of rigidity. In this regard, calculating the resultant floor rotation at each step requires assembling the stiffness matrix of the whole building and solving for the displacement in response to the applied unit loads.

The following section presents some illustrative examples that approve the accuracy of the method comparing it to the results obtained directly from ETABS.

4.4 Verification of Evaluation of Centre of Rigidity

The developed procedure that attempts at finding the CR has been implemented using the computational software Maple (Maple, 2019) which makes it a practical model for determining the CR. In this section, the accuracy of the procedure is tested by comparing the CR obtained using the proposed approach against results obtained directly from the computerised finite-element-analysis software ETABS (2017).

Figure 4.1 presents the floorplan of a six-storey RC building having a uniform plan at all storeys. The walls have a thickness of 20 cm, and the columns along Grids 1 and 4 have the same dimensions (25cm x 60 cm) while the columns aligned on Grids 2 and 3 have the same dimensions (25cm x 70 cm). The beams on the periphery have a uniform cross-section of (20cm x 50cm) while the inner beams aligned in the X-direction (along Grids 2 and 3) have a uniform cross-section of (80cm x 25cm), and the inner beams aligned in the Y-direction (along Grids B, C, D, and E) have a uniform cross-section of (30cm x 25cm). A slab thickness of 25cm is adopted at all floors. The CR of the building is determined using the aforementioned procedure and the results are compared against those obtained directly from ETABS. In this regard, the results in Table 4-1 indicate that the values obtained using the developed procedure perfectly correlate with those obtained from ETABS. The values in Table 4-1 represent the location of the CR with respect to the origin (lower corner) marked by the intersection of Grids 1 and A.

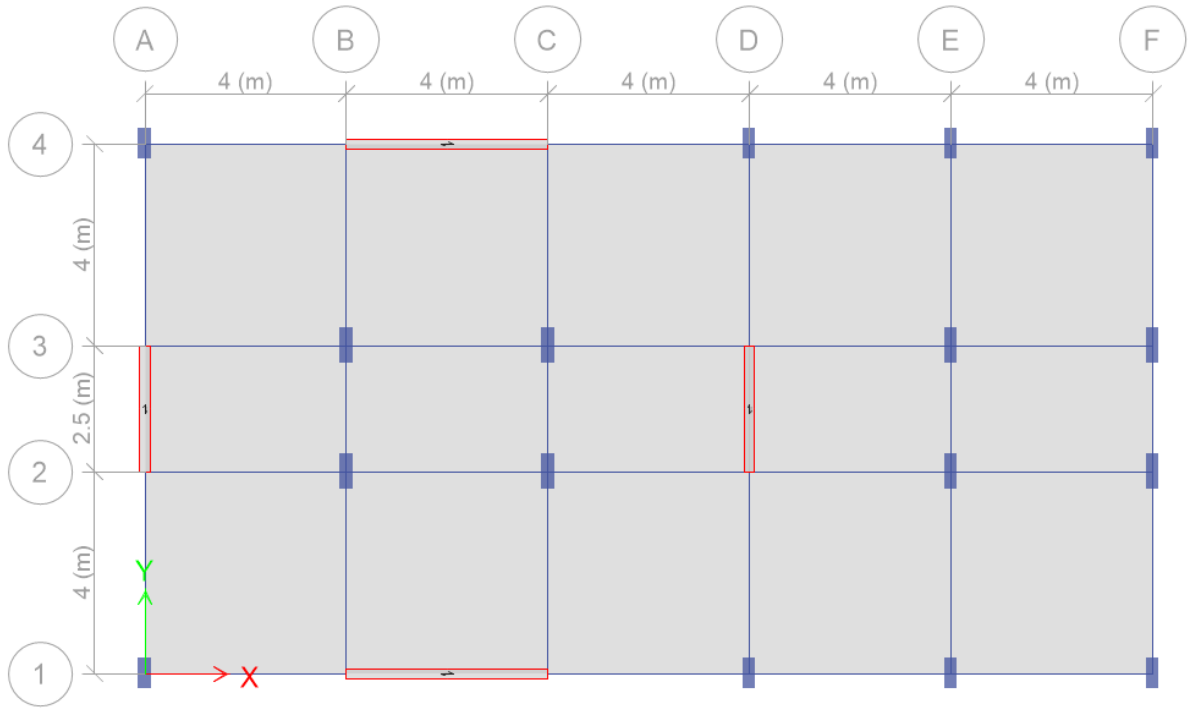


Figure 4.1: First layout of the six-storey building used to verify the calculation of the CR

Table 4-1: Calculation of the centre of rigidity of the first building scenario

	Values Obtained using the Developed Procedure									ETABS	
	Unit Load Applied			Rotations Measured in Response to the Unit Loads			Measured from Centroid of floor		Measured from the Origin		Measured from the Origin	
	P_x (MN)	P_y (MN)	M_z (MN.m)	R_{zz} (Rad)	R_{zx} (Rad)	R_{zy} (Rad)	$X_{C.R.}$ (m)	$Y_{C.R.}$ (m)	$X_{C.R.}$ (m)	$Y_{C.R.}$ (m)	$X_{C.R.}$ (m)	$Y_{C.R.}$ (m)
Storey 1	1				-2E-20							
Storey 1		1				1.9E-05	-2.649	-3E-15	7.351	5.25	7.251	5.25
Storey 1			1	7.1E-06								
Storey 2	1				-3E-19							
Storey 2		1				0.00011	-2.978	-8E-15	7.022	5.25	6.990	5.25
Storey 2			1	3.9E-05								
Storey 3	1				-1E-18							
Storey 3		1				0.00036	-3.041	-1E-14	6.959	5.25	6.941	5.25
Storey 3			1	0.00012								
Storey 4	1				-4E-18							
Storey 4		1				0.00082	-3.063	-1E-14	6.937	5.25	6.923	5.25
Storey 4			1	0.00027								
Storey 5	1				-7E-18							
Storey 5		1				0.00157	-3.073	-1E-14	6.927	5.25	6.915	5.25
Storey 5			1	0.00051								
Storey 6	1				-1E-17							
Storey 6		1				0.00268	-3.079	-1E-14	6.921	5.25	6.911	5.25
Storey 6			1	0.00087								

The procedure is repeated for the same building when the dimensions and location of some of the walls are updated (Figure 4.2). The same framing plan of the building is maintained apart from changing the walls location and dimensions. The results in Table 4-2 prove the accuracy of the developed procedure as it almost produces the same location of the CR compared to ETABS. In conclusion, the developed approach is proven to be accurate and reliable in predicting the location of the CR for both building configurations considered and can therefore be utilised with confidence in the next section involving the maximisation of the mass participation ratio.

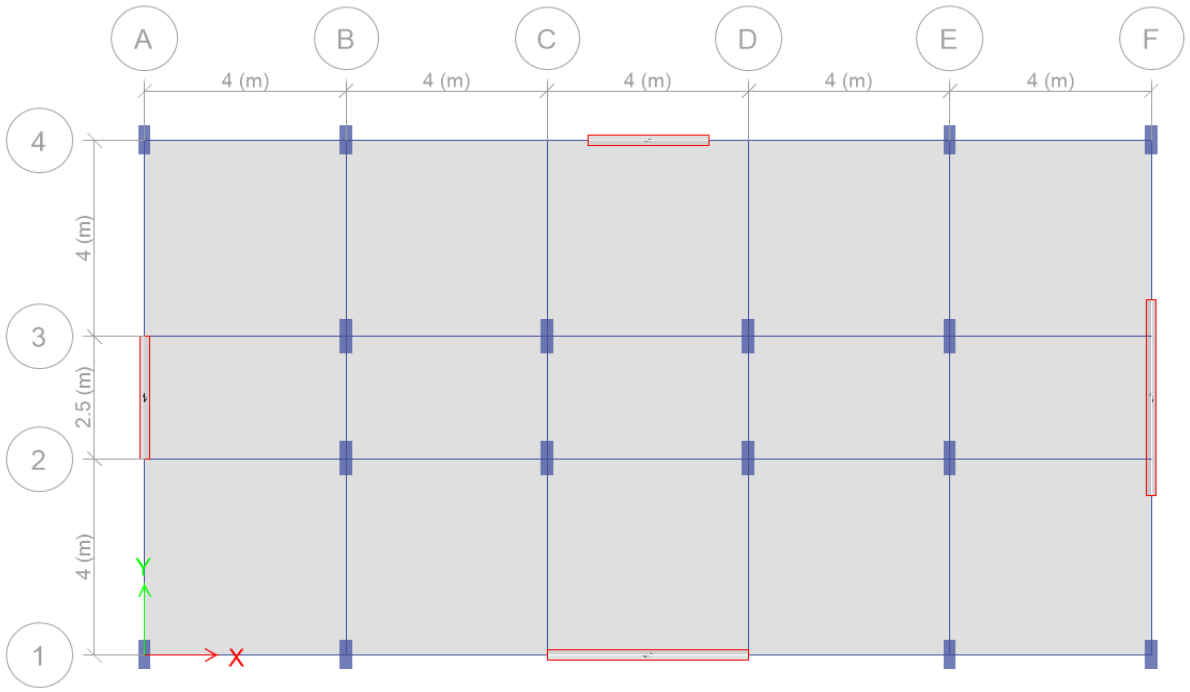


Figure 4.2: Second layout of the 6-storey building used to verify the accuracy of the developed procedure

Table 4-2: Calculation of the centre of rigidity of the second building scenario

	Values Obtained using the Developed Procedure										ETABS	
	Unit Load Applied			Rotations Measured in Response to the Unit Loads			Measured from Centroid of floor		Measured from Lower Corner		Measured from Lower Corner	
	P_x (MN)	P_y (MN)	M_z (MN.m)	R_{zz} (Rad)	R_{zx} (Rad)	R_{zy} (Rad)	$X_{C.R.}$ (m)	$Y_{C.R.}$ (m)	$X_{C.R.}$ (m)	$Y_{C.R.}$ (m)	$X_{C.R.}$ (m)	$Y_{C.R.}$ (m)
Storey 1	1				-1.2E-05							
Storey 1		1				-1.9E-05	4.030	-2.608	14.03	2.64	14.27	2.70
Storey 1			1	4.7E-06								
Storey 2	1				-8.5E-05							
Storey 2		1				-1.4E-04	5.097	-3.112	15.10	2.14	15.20	2.18
Storey 2			1	2.7E-05								
Storey 3	1				-2.8E-04							
Storey 3		1				-4.6E-04	5.398	-3.254	15.40	2.00	15.45	2.04
Storey 3			1	8.6E-05								
Storey 4	1				-6.5E-04							
Storey 4		1				-1.1E-03	5.515	-3.309	15.51	1.94	15.55	1.99
Storey 4			1	2.0E-04								
Storey 5	1				-1.3E-03							
Storey 5		1				-2.1E-03	5.572	-3.336	15.57	1.91	15.60	1.96
Storey 5			1	3.8E-04								
Storey 6	1				-2.2E-03							
Storey 6		1				-3.7E-03	5.603	-3.351	15.60	1.90	15.62	1.94
Storey 6			1	6.5E-04								

4.5 Optimising Mass Participation

In this section, an approach is proposed for maximising the mass participation ratio of the translational component of the fundamental mode in each horizontal direction along with a few supportive examples. It particularly aims at setting a solid foundation for the application of the CSM given the inherent assumption in the method that the seismic response is dominated by the fundamental mode of vibration. The latter assumption holds when the mass participation factor in the translational pushover direction is sufficiently high for the fundamental mode to govern the seismic response of the structure. This section builds upon the findings of the previous sections and devises an approach for maximising the mass participation ratio of the translational component of the fundamental mode of vibration in a given direction. The ultimate objective is to boost the reliability of the CSM and to strengthen the assumption that the seismic response is dictated by deformations of the fundamental mode.

The approach developed is based on minimising the average eccentricity of all floor levels with the expectation, to be demonstrated, that this maximises the mass participation ratio in a specific translational direction. The approach assumes that a high eccentricity between the centre of mass and the centre of rigidity would increase the contribution of the torsional component and consequently reduce the contribution of the translational component of the fundamental mode. Conversely, a minimum average floor eccentricity is assumed to minimise the torsional effect which would eventually lead to the predominance of the translational component in the fundamental mode. Hence, the developed approach requires minimising the average eccentricity at all floors towards an anticipated maximisation of the mass participation ratio. The floor eccentricity is the distance measured between the cumulative centre of mass and the centre of rigidity which are both determined according to the strategies defined in the previous sections, and the average eccentricity represents an average over all the floors. It is worth noting that the average Euclidean norm of the floor eccentricities is also considered in the attempt to maximise the mass participation. In this regard, minimising the average Euclidean eccentricity is expected to be more beneficial since it requires minimising the eccentricity in both horizontal directions simultaneously which is expected to further increase the mass participation ratio. The average Euclidean norm of the floor eccentricities is expressed by the following:

$$\bar{e} = \sqrt{\frac{1}{n}\sum_{i=1}^{n}\left(e_{x,i}^2 + e_{y,i}^2\right)} \tag{4.4}$$

where:

$e_{x,i}$ is the eccentricity in the X-direction at floor *i*,

$e_{y,i}$ is the eccentricity in the Y-direction at floor *i*, and

n is the total number of floors in the building.

The following sections present some illustrative examples to confirm the hypothesis that a maximum mass participation is achieved when the average Euclidean eccentricity of all floors is reduced to the minimum.

4.5.1 Regular building

The first example involves a six-storey RC regular building. The building is regular in plan and in elevation and has the same floor plan all over. The building considered is symmetric along both horizontal directions as shown in Figure 4.3. It is worth noting that the centre of mass is varying from one floor to the other. In this regard, the superimposed dead and the live loads are varied in order to alter the position of the centre of mass at each storey level. The walls aligned in the X-direction are referred to as X-walls (the walls aligned along Grids 1 and 4) while the walls aligned in the Y-direction are referred to as Y-walls (walls aligned on Grids A and F). The columns aligned on Grids 1 and 4 have the same cross-section (20cm x 90cm) at all floors and columns aligned on Grids 2 and 3 have a uniform cross-section of (20cm x 80cm). In this example, the walls dimensions are continuously changed in order to cause a change in the centre of rigidity and in the mass participation factor of the fundamental mode of vibration in each horizontal direction. In practice, changing the dimensions of the X-walls moves the centre of rigidity in the Y-direction, hence causing an eccentricity in the Y-direction and mainly influencing the fundamental mode of vibration in the X-direction. Conversely, updating the dimensions of the Y-walls produces an eccentricity in the X-direction and affects the fundamental mode of vibration in the Y-direction. It is worth noting that the dimensions of the columns are not changed in all of the trials performed. Three separate scenarios of changing the floor eccentricities are considered as explained in the following sections. It is also worth noting that the walls thickness is the dimension that is modified (from a practical perspective) to cause a variation in the centre of rigidity.

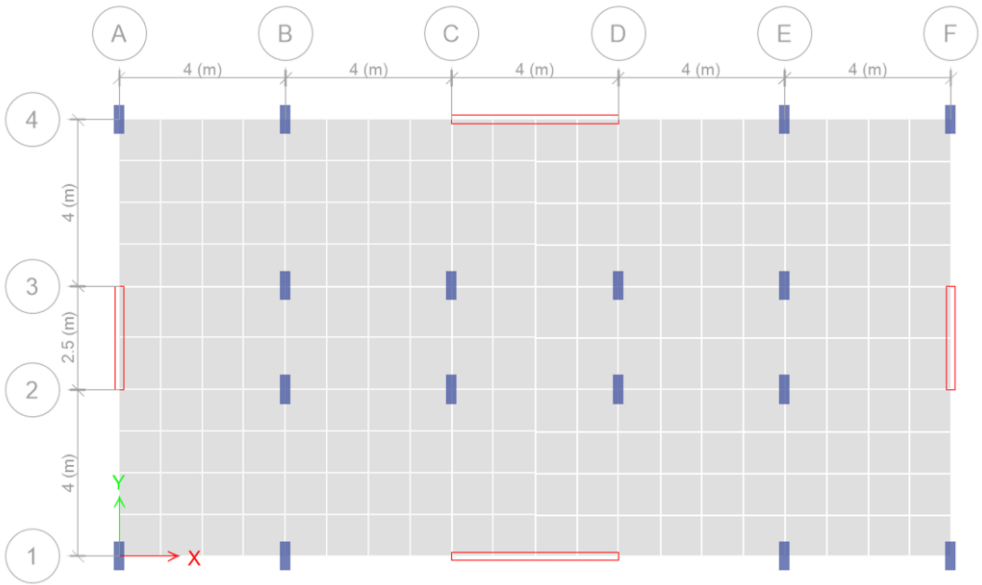


Figure 4.3: Typical floor plan of regular six-storey building

4.5.1.1 Variation of centre of mass in X-direction

The first scenario involves varying the centre of mass in the X-direction only. Figure 4.4 displays the position of the cumulative centre of mass at each floor denoted by CM.1 through CM.6. If the walls aligned in the X-direction have similar dimensions and the walls aligned in the Y-direction also have same dimensions, the centre of rigidity is located at the centroid of the floor plan due to the symmetry of the floor plan along both horizontal directions. In light of this, the current scenario involves modifying the dimensions of the Y-walls without altering the dimensions of the X-walls. This causes the centre of rigidity to vary along the horizontal dotted line in Figure 4.4 in response to the variation of the relative stiffnesses of the Y-walls. To note that the same wall dimensions are maintained across the height as the variation in either of the Y-walls is performed at all floor levels.

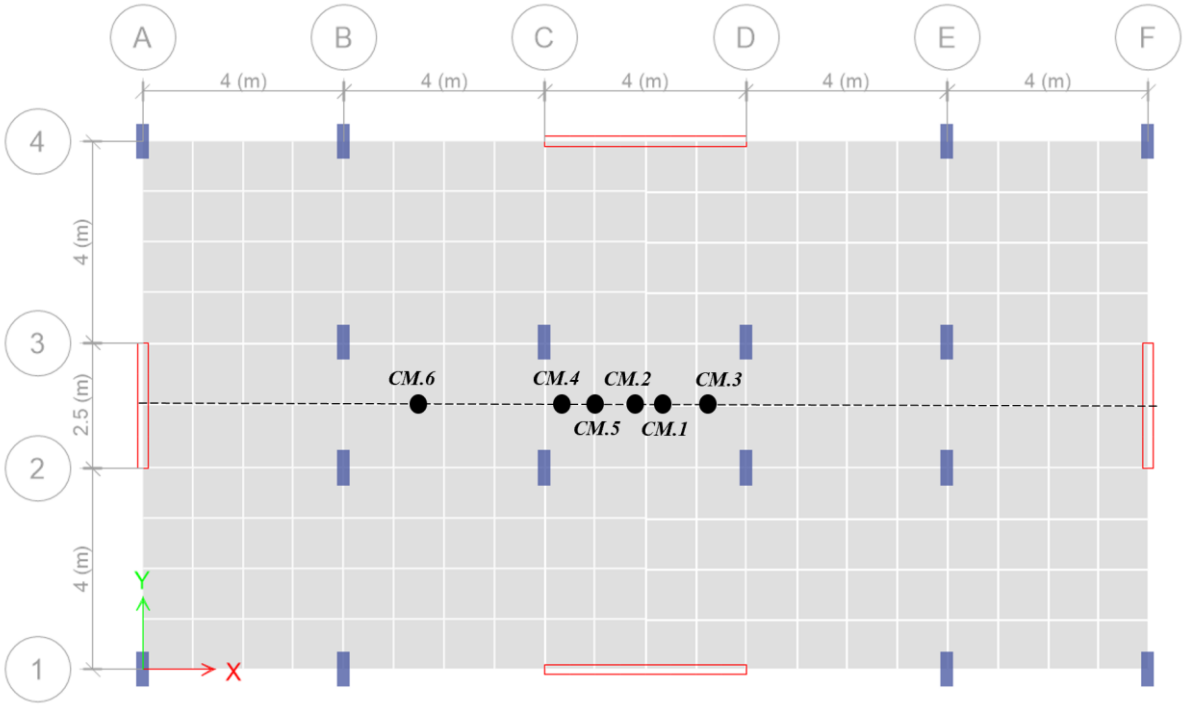


Figure 4.4: Six-storey regular building with the centre of mass varying in the X-direction

Referring to Figure 4.4, the centre of mass and the centre of rigidity are both aligned on the horizontal dotted line such that there is no eccentricity in the Y-direction. The objective here is to monitor the effect of varying the centre of rigidity in the X-direction and the resultant variation of the X-eccentricity on the mass participation of the fundamental mode of vibration in the Y-direction. As the dimensions of the Y-walls are changed, the new position of the centre of rigidity at all storeys is determined by applying the procedure implemented in the previous section. It is expected that higher floor eccentricities in direction X would induce a torsional component besides the translational component in the fundamental translational mode in direction Y. Conversely, a minimum eccentricity would likely increase the mass participation of the translational component. Referring to Figure 4.5, each mass participation value represents the outcome of a single trial and is associated with a series of X-

eccentricities for the six storeys and an average value as well. Focusing on the plot of the average eccentricity, it is clearly observed that the mass participation increases as the absolute value of the average floor eccentricity is reduced. Despite the maximum mass participation ratio occurring when the average floor eccentricity is not equal to zero, the mass participation ratio registered at zero average eccentricity is equal to 67% and is almost equal to the highest value of 68%. Hence, the findings strengthen the claim that the mass participation is optimised as the average floor eccentricity is ultimately reduced.

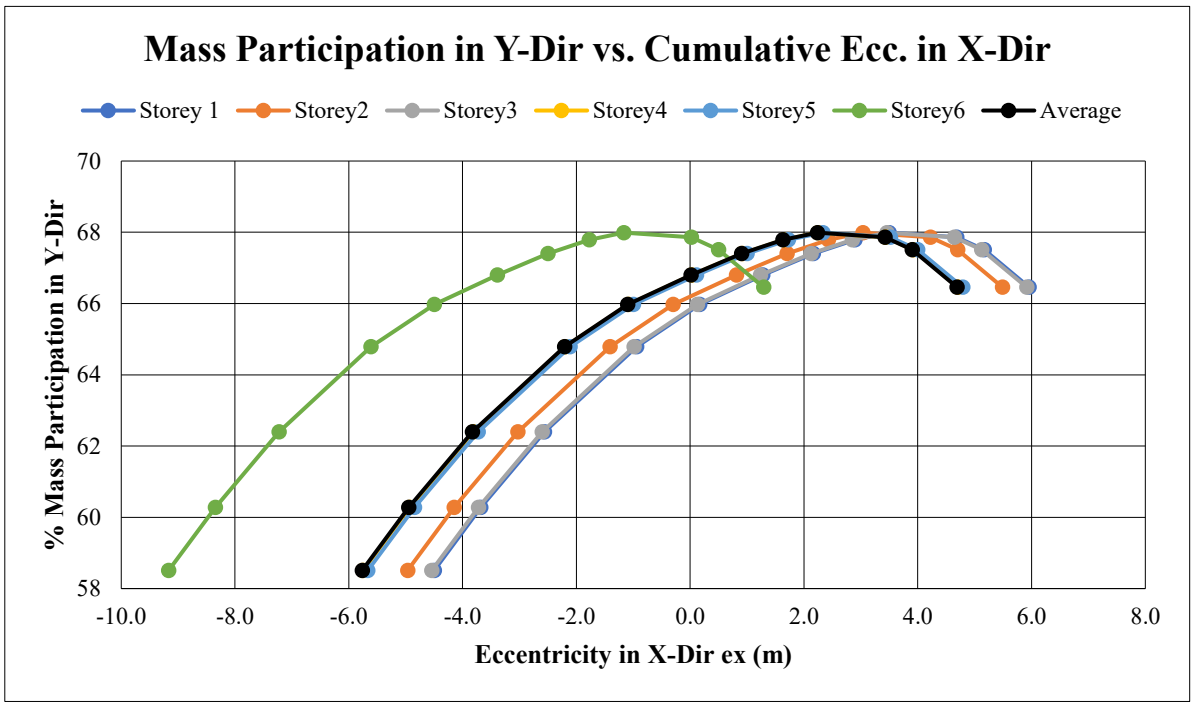


Figure 4.5: Plot of the mass participation in the Y-direction versus the cumulative eccentricity as the centre of mass varies in the X-direction

The next step involves checking if it is possible to achieve a mass participation higher than 68% by further reducing the average Euclidean eccentricity. In this respect, four additional trials are performed in which the average Euclidean eccentricity is being further reduced. The additional trials are represented by the scattered points while the original trials (pertaining to Figure 4.5) are represented by the continuous line in Figure 4.6, which shows that higher mass participation factors up to 72.8% are attained when adopting the average Euclidean eccentricity as the reference parameter to be reduced. It is worth noting also that the maximum mass participation is not exactly obtained at the smallest average Euclidean eccentricity. Nevertheless, there is a clear pattern that the mass participation is maximised as the average Euclidean eccentricity is reduced, and there is an additional advantage of using the Euclidean eccentricity as a control parameter. Furthermore, it is worth mentioning that reducing the average Euclidean eccentricity is practically difficult and mostly involves changing the walls dimensions at each floor to minimise the gap between the centre of rigidity and centre of mass. Nevertheless, the concept is correctly verified from a theoretical perspective.

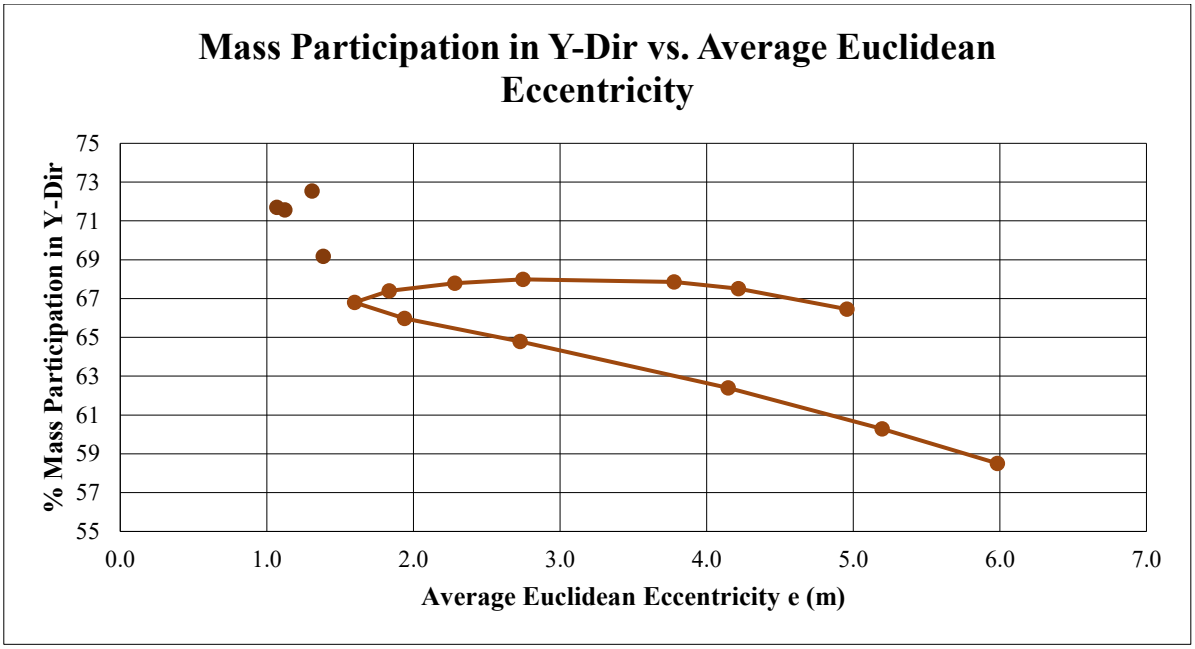


Figure 4.6: Plot of the mass participation in the Y-direction versus the average Euclidean eccentricity as the centre of mass varies in the X-direction

4.5.1.2 Variation of centre of mass in Y-direction

The same exercise is performed when the centre of mass is varying in the Y-direction only. Figure 4.7 displays the positions of the centre of mass at each floor denoted by CM.1 through CM.6. Opposed to the previous scenario, the dimensions of the X-walls are being changed in order to induce a variation in the centre of rigidity in the Y-direction. In this respect, the centre of rigidity is varying along the vertical dotted line in Figure 4.7 in response to the variation of stiffness of the X-walls. The change in the dimensions of the X-walls is performed at all floor levels while the Y-walls are maintaining the same dimensions throughout.

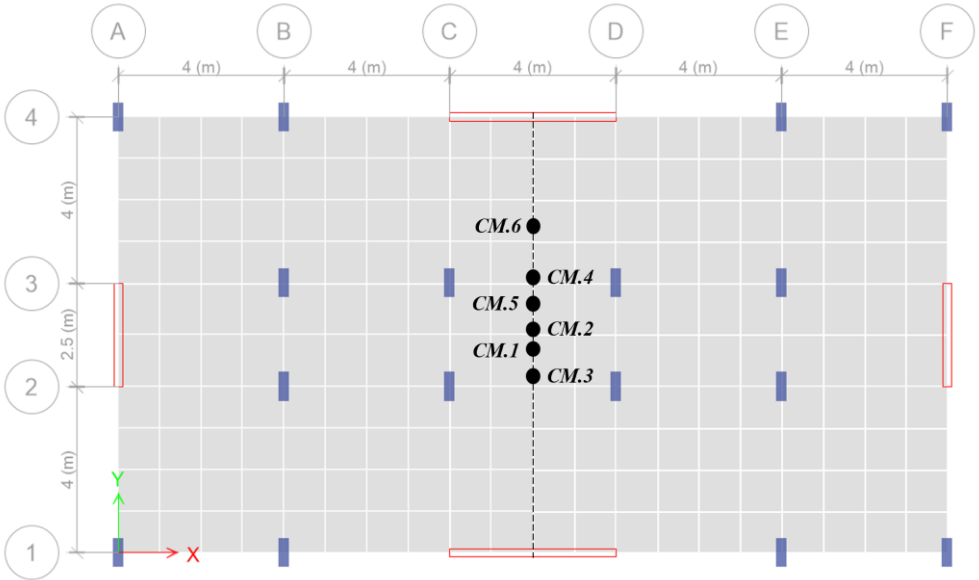


Figure 4.7: Six-storey regular building with the centre of mass varying in the Y-direction

Referring to Figure 4.7, the centre of mass and the centre of rigidity are both aligned on the vertical dotted line such that there is no eccentricity in the X-direction. The objective of this scenario is to monitor the effect of the variation in the centre of rigidity in the Y-direction on the mass participation of the fundamental mode of vibration in the X-direction. The plotted results in Figure 4.8 reveal a significant fluctuation in the mass participation ratio in response to the change in the location of the centre of rigidity. Nevertheless, the results point out at the obvious increase in the mass participation ratio as the average eccentricity is brought closer to zero. Indeed, the maximum mass participation ratio is exactly obtained when the average floor eccentricity is equal to zero. Hence, these results add up to the ones obtained in the first scenario and further strengthen the proposal that the mass participation ratio is maximised as the average eccentricity at all floors is reduced to zero.

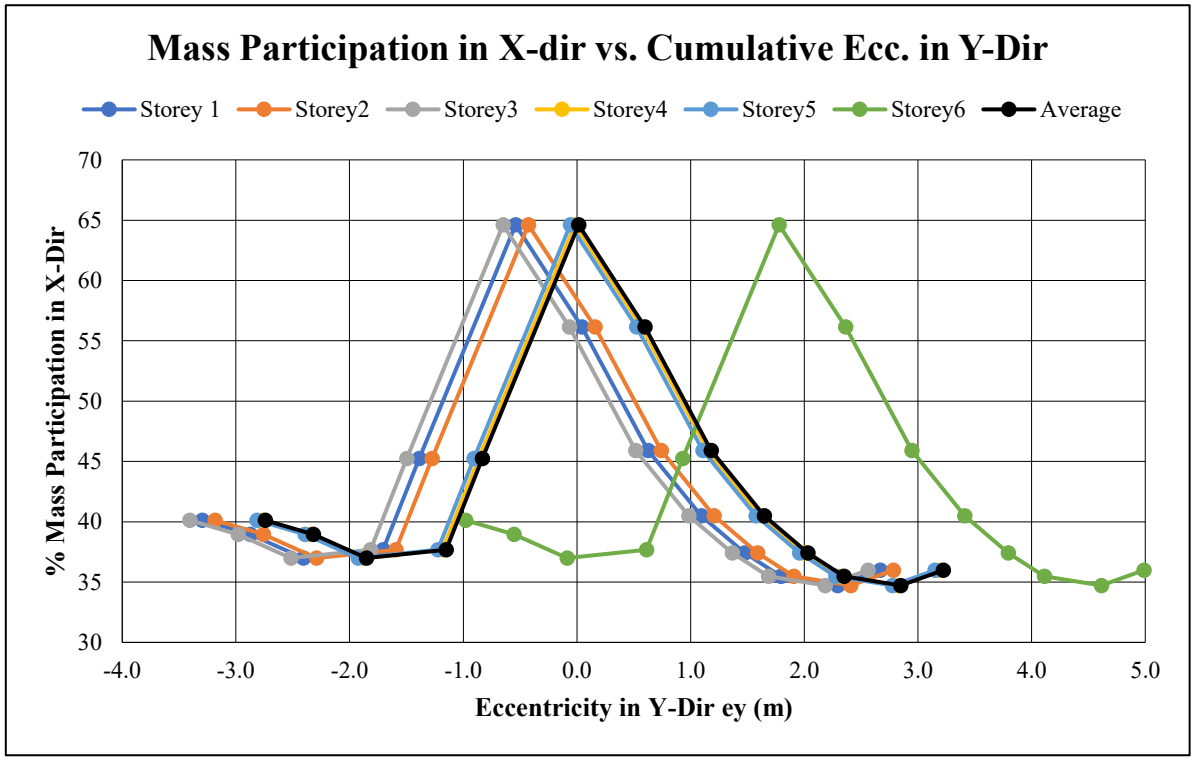


Figure 4.8: Plot of the mass participation in the X-direction versus the cumulative eccentricity as the centre of mass varies in the Y-direction

The average Euclidean eccentricity is investigated in this scenario as well to check if it is possible to further maximise the mass participation by rather reducing the average Euclidean eccentricity. In this respect, nine additional trials are performed in which the average Euclidean eccentricity is being further reduced. The additional trials are represented by the scattered points while the original trials (pertaining to Figure 4.8) are represented by the continuous line in Figure 4.9, which shows that higher mass participation factor up to 70.14% can be obtained compared to the maximum value of 64.61% that was obtained when considering the normal average eccentricity. Despite achieving a higher mass participation, it is worth noting that the maximum mass participation is not exactly obtained at the smallest average Euclidean eccentricity. However, the concept behind reducing the average Euclidean

eccentricity is verified in this case as well, and it is shown again that the Euclidean eccentricity stands out as the more effective parameter for optimising the mass participation.

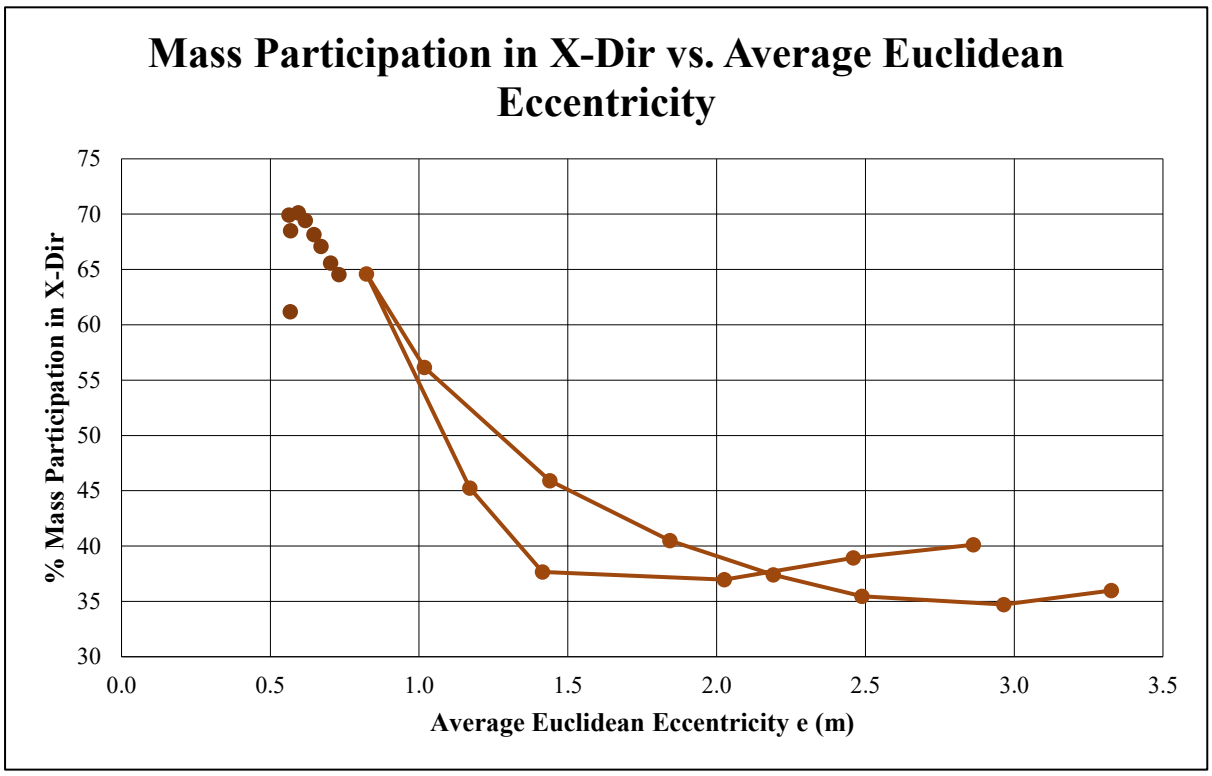


Figure 4.9: Plot of the mass participation in the X-direction versus the average Euclidean eccentricity as the centre of mass varies in the Y-direction

4.5.1.3 Variation of centre of mass in the X- and Y-directions simultaneously

The last scenario involves varying the centre of mass along the X and Y directions simultaneously. Figure 4.10 displays the updated positions of the centre of mass at each floor denoted by CM.1 through CM.6. The dimensions of both the X-walls and Y-walls are concurrently changed, hence producing a shift in the centre of rigidity in both the X and Y directions. The centre of rigidity is varying in plane in response to the variation in the stiffness of the walls, and floor eccentricities are accordingly observed in both horizontal directions.

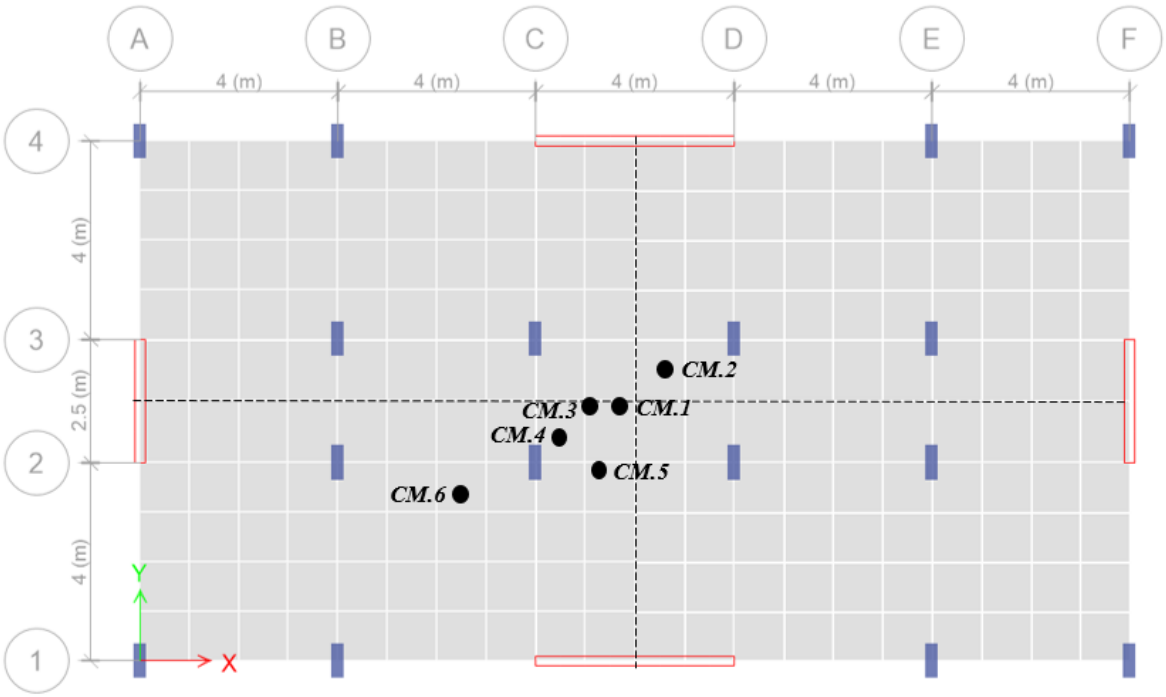


Figure 4.10: Six-storey regular building with the centre of mass varying in the X- and Y-directions

The arbitrary variation in the centre of mass generates a floor eccentricity in both the X and Y directions. This scenario allows to observe the effect of varying the centre of rigidity in the X and Y directions simultaneously on the mass participation in each direction. It is expected that the mass participation in the X-direction is mostly influenced by the eccentricity in the Y-direction while the mass participation in Y is mostly affected by the eccentricity in X. The results in Figure 4.11 reveal a significant fluctuation in the mass participation of the fundamental mode in direction X as the centre of rigidity is changed, with values ranging between 34.4% and 68%. Nevertheless, a mass participation of 66.1% is recorded at zero average eccentricity (in Y-direction) which is very close to the maximum value that is achieved. The close proximity of the mass participation at zero average eccentricity to the maximum value supports the hypothesis especially given the wide range of values recorded. Likewise, the plot in Figure 4.12 further supports the hypothesis since the mass participation ratio of the fundamental mode in direction Y at zero X-eccentricity (66.9%) is almost equal to the maximum recorded value of 67.4%.

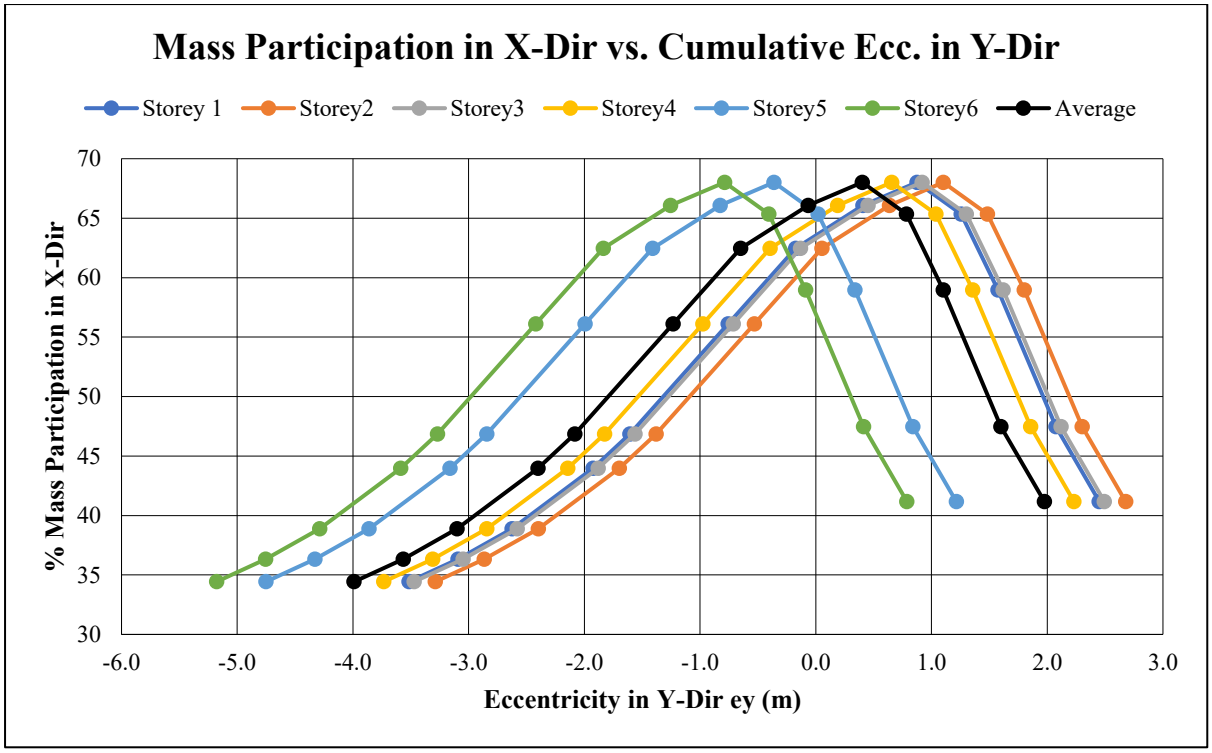


Figure 4.11: Plot of the mass participation in the X-direction versus the cumulative eccentricity as the centre of mass varies in the X and Y directions simultaneously

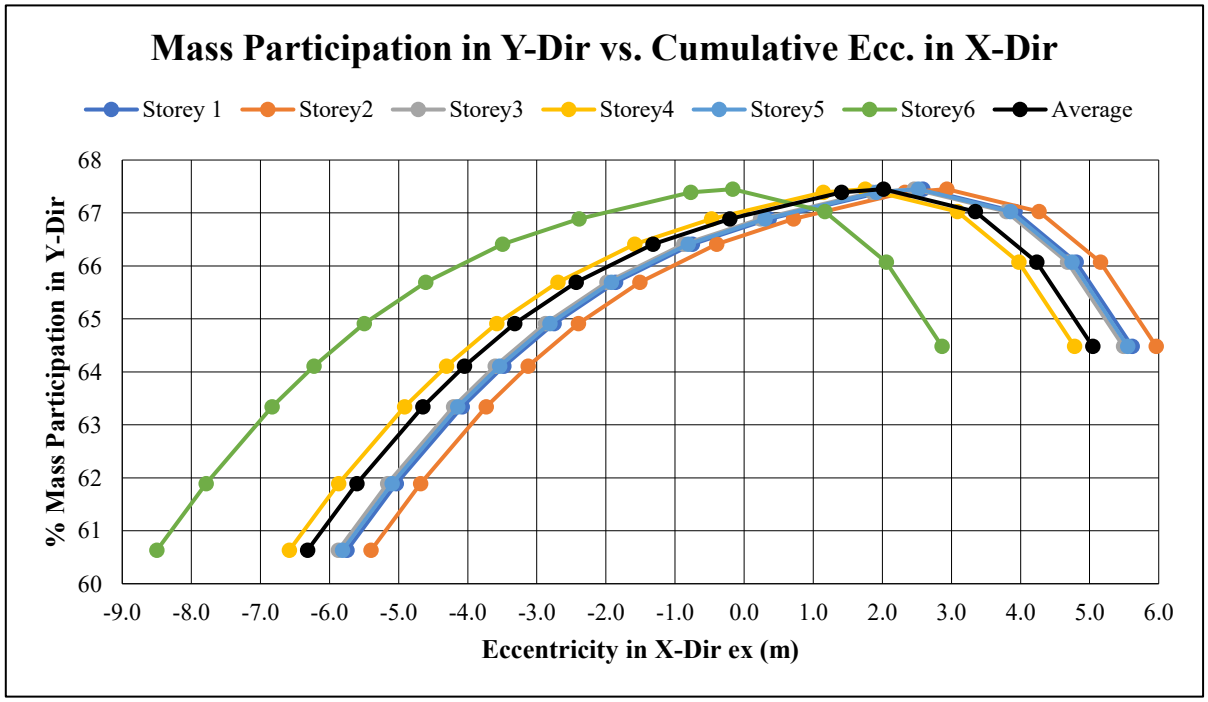


Figure 4.12: Plot of the mass participation in the Y-direction versus the cumulative eccentricity as the centre of mass varies in the X and Y directions simultaneously

As for the previous scenarios, further trials are performed to check if it is possible to further enhance the mass participation by reducing the average Euclidean eccentricity. It is accordingly shown that the mass participation has increased to 71.6% in direction X as the average Euclidean eccentricity is further reduced (Figure 4.13). The additional trials are represented by the scattered green points while the

original trials (pertaining to Figure 4.11) are represented by the continuous line in Figure 4.13. Furthermore, the plot in Figure 4.14 shows that a mass participation up to 70% can be achieved in direction Y as the average Euclidean eccentricity is reduced, compared to a maximum of 67.4% that is previously obtained when considering the normal average eccentricity. Additional trials are also represented by scattered green points while the continuous line in Figure 4.14 represents the original trials previously represented by Figure 4.12. In sum, the hypothesis claiming that reducing the average Euclidean eccentricity is key to maximising the mass participation of the fundamental mode of vibration in each horizontal direction is verified once again.

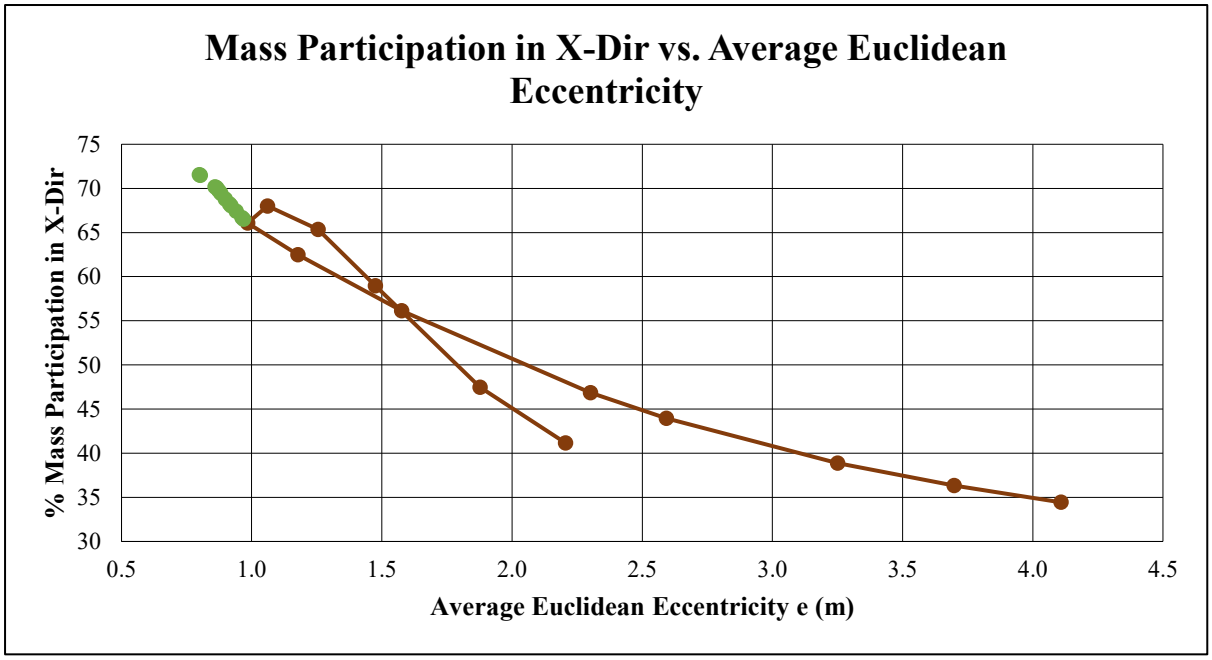


Figure 4.13: Plot of the mass participation in the X-direction versus the average Euclidean eccentricity as the centre of mass varies in the X and Y directions simultaneously

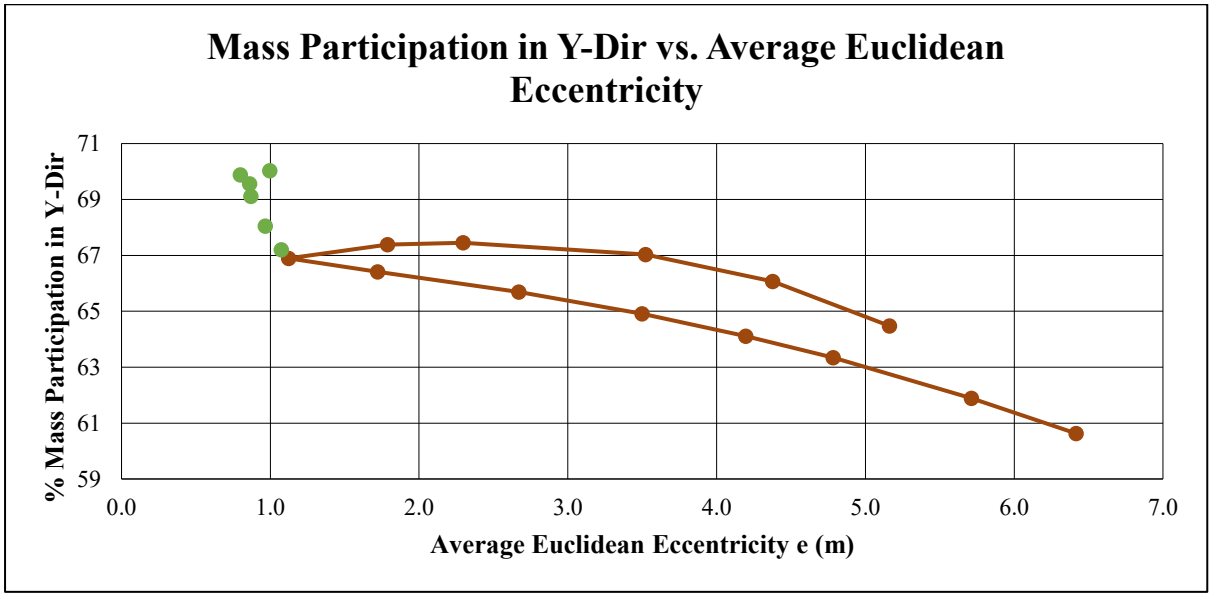
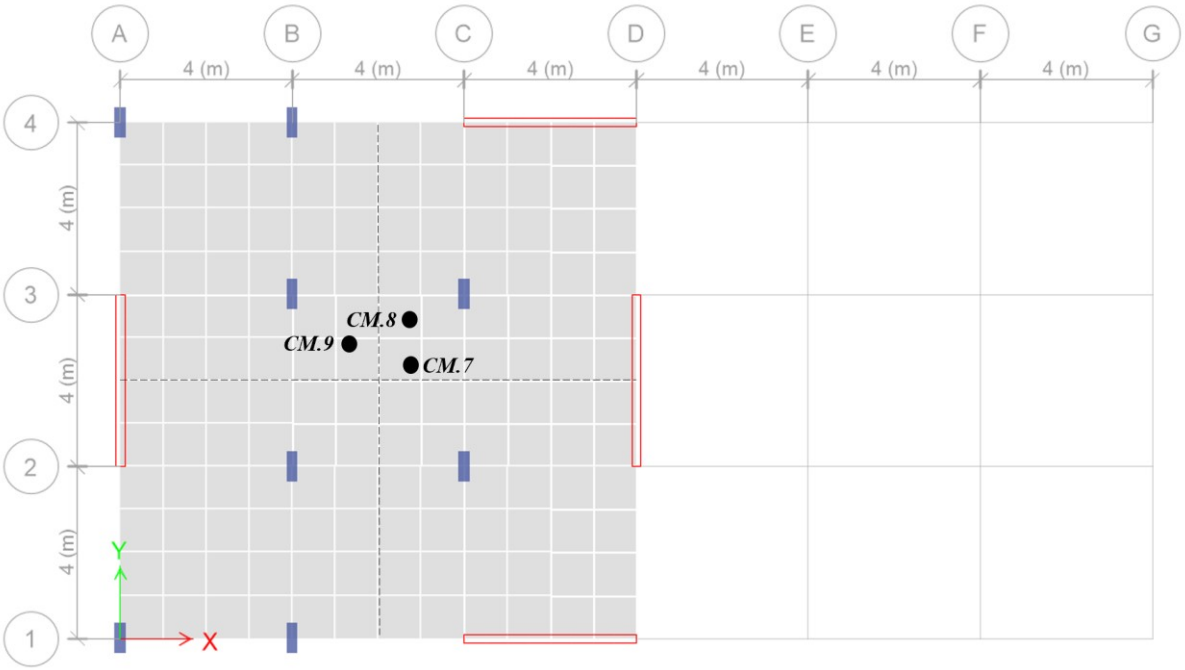


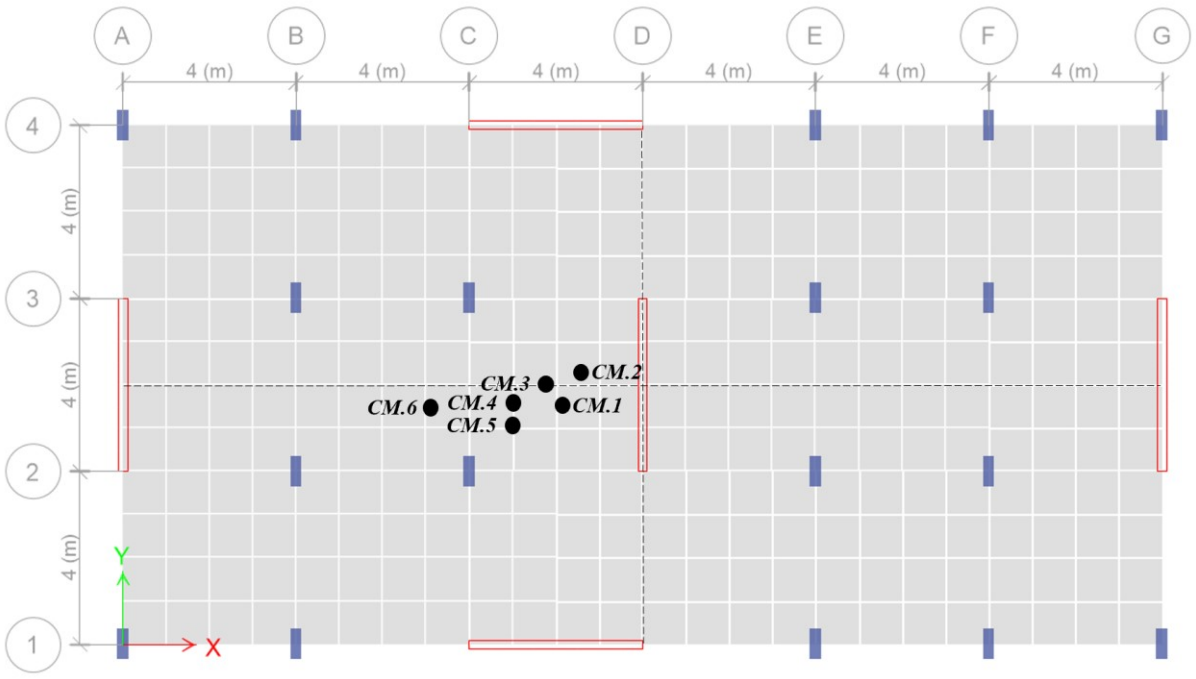
Figure 4.14: Plot of the mass participation in the X-direction versus the average Euclidean eccentricity as the centre of mass varies in the X and Y directions simultaneously

4.5.2 Irregular Building

The same exercise is performed in order to test the accuracy of the hypothesis when applied to the case of an irregular building. Figure 4.15 presents the floor plan of the nine-storey building that is characterised by a vertical irregularity as the floor plan is reduced at the top three floors (irregularity in elevation is discussed in detail in Appendix 4). The centre of mass at different storeys is denoted by CM.1 to CM.9. The suggested theory that a lower average floor eccentricity in a horizontal direction would increase the mass participation of the translational component in the orthogonal direction is tested in both the X and Y directions. The method has already replicated some promising results for a regular six-storey building, and this example attempts at proving its applicability to the case of a nine-storey irregular building. In this regard, the dimensions of both the X-walls and Y-walls are constantly updated, and the centre of rigidity is calculated at all storeys using the procedure implemented earlier. The variation in the dimensions of any wall is performed at all storey levels. The aim is to investigate the effect of varying the centre of rigidity in each horizontal direction on the mass participation of the fundamental mode of vibration in the orthogonal direction.



(a)



(b)

Figure 4.15: Nine-storey irregular building with the centre of mass varying in the X and Y directions: (a) Storeys 7 to 9, (b) Storeys 1 to 6

Figure 4.16 plots the mass participation ratio of the fundamental mode in the Y-direction versus the floor eccentricity in the orthogonal X-direction. The change in the dimensions of the Y-walls is the major influencing factor in this case as it affects the eccentricity in the X-direction. The mass participation obtained at zero average eccentricity is equal to 61.5% and is very close to the maximum of 64.3%, proving so far that the concept is also applicable to the case of the irregular building.

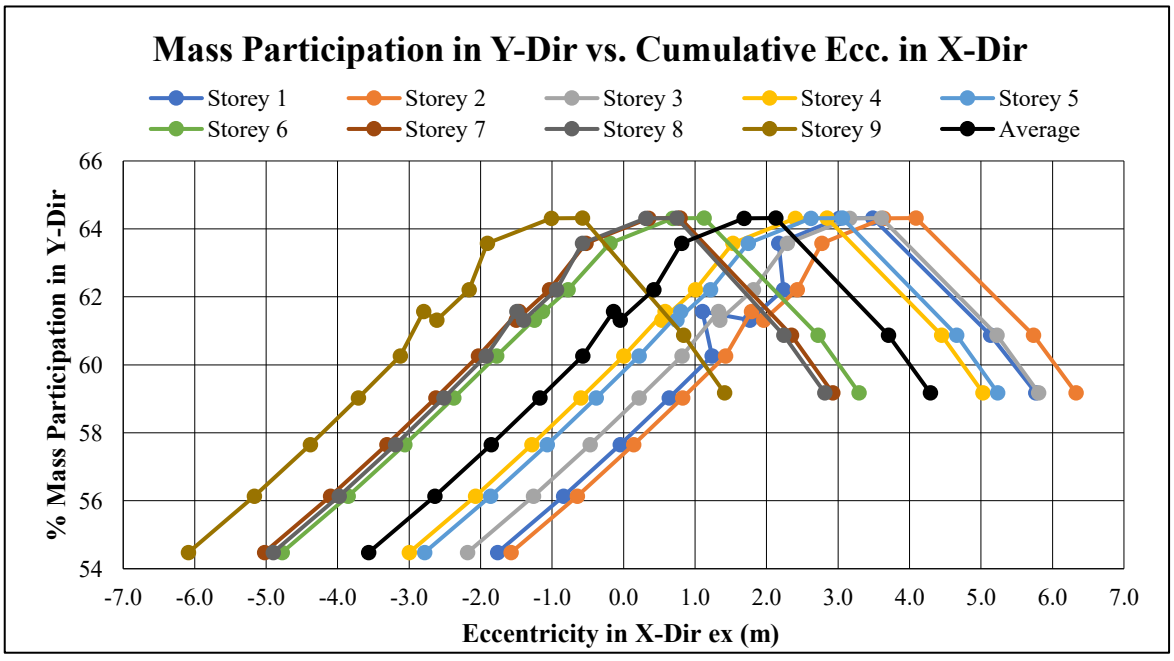


Figure 4.16: Plot of the mass participation in the Y-direction versus the cumulative eccentricity in the X-direction in the irregular building

It remains to be seen whether it is possible to exceed the maximum mass participation of 64.3% if the average Euclidean eccentricity is further decreased. The average Euclidean eccentricity is being further reduced and higher mass participation factors up to 66.8% were accordingly achieved. Like the regular building scenario, the maximum mass participation is not exactly obtained at the smallest average Euclidean eccentricity. However, there is a clear trend that the mass participation is further increased as the average Euclidean eccentricity is being further reduced. The results are plotted in Figure 4.17 with the additional tests represented by scattered green points while the continuous line represents the original results presented in Figure 4.16. It is noted again that reducing the Euclidean eccentricity is practically cumbersome as was the case for the regular building, since it requires altering the wall dimensions at each floor. Nevertheless, the concept is proven once again for the irregular building scenario as the mass participation was further enhanced by rather reducing the average Euclidean eccentricity.

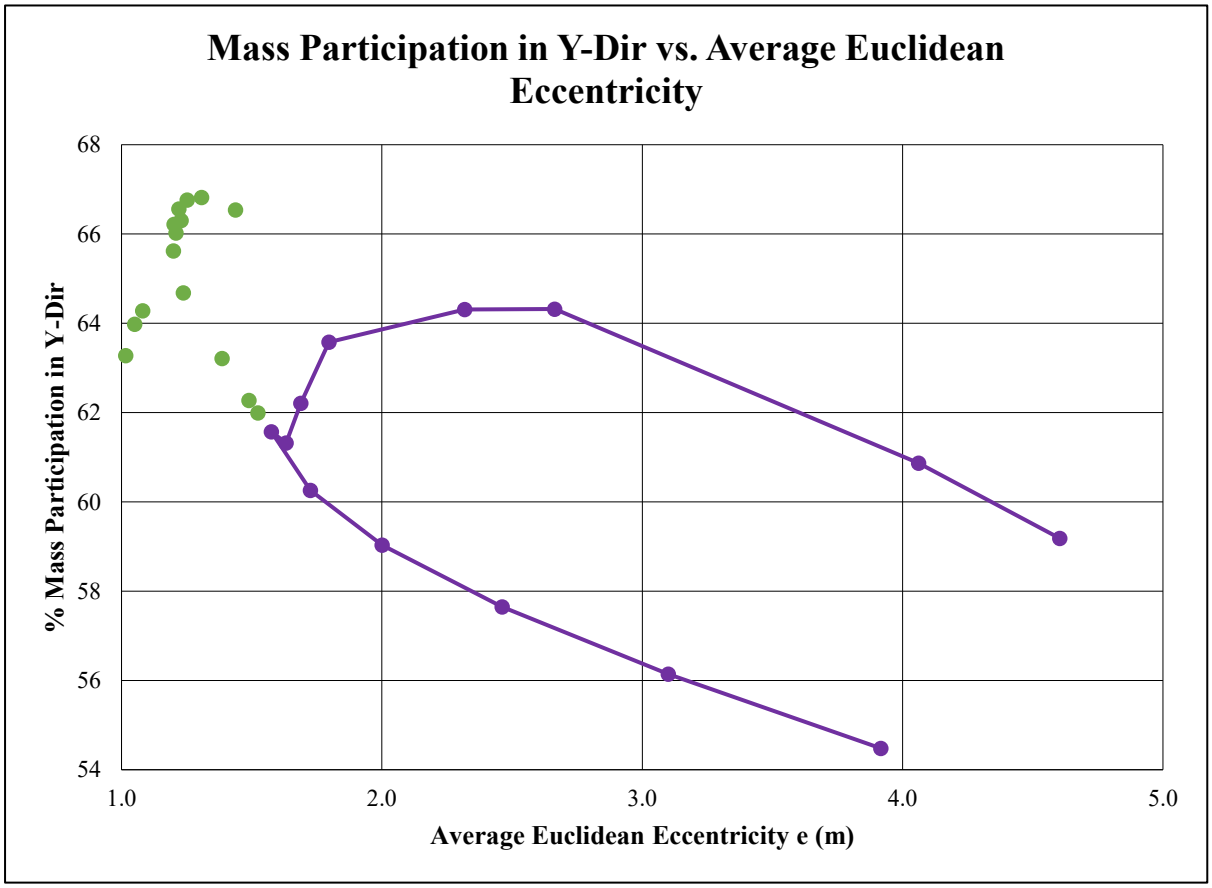


Figure 4.17: Plot of the mass participation in the Y-direction versus the average Euclidean eccentricity in the irregular building

Likewise, the mass participation ratio of the fundamental mode in the X-direction is plotted against the variation of the eccentricity in the Y-direction. The results have shown that the largest mass participation of 63% is observed exactly at zero average eccentricity, thus again proving the accuracy of the concept (Figure 4.18).

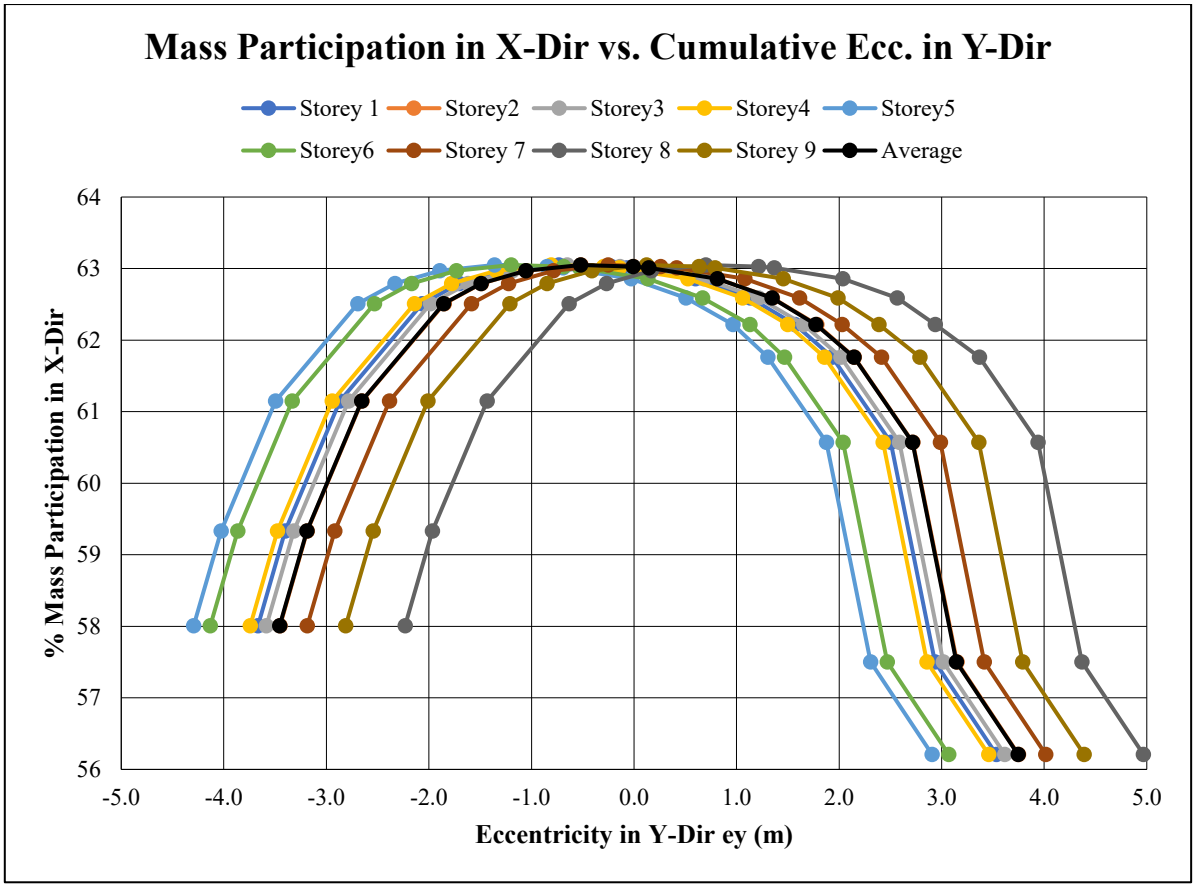


Figure 4.18: Plot of the mass participation in the X-direction versus the cumulative eccentricity in the Y-direction in the irregular building

Additional trials are performed to check if the mass participation is further enhanced by reducing the average Euclidean eccentricity. The additional trials have yielded higher mass participation factors up to 66.9% compared to the value of 63% that is obtained using the normal eccentricity (Figure 4.19). The additional trials are marked by scattered green points while the continuous line in Figure 4.19 represents the original trials previously presented in Figure 4.18.

To summarise, the tests performed on the irregular building confirm the applicability of the concept to this type of building as well. Hence, it is safe to conclude that minimising the average Euclidean eccentricity of all the floors in a building guarantees a sufficiently high mass participation of the translational component of the fundamental mode in each horizontal direction.

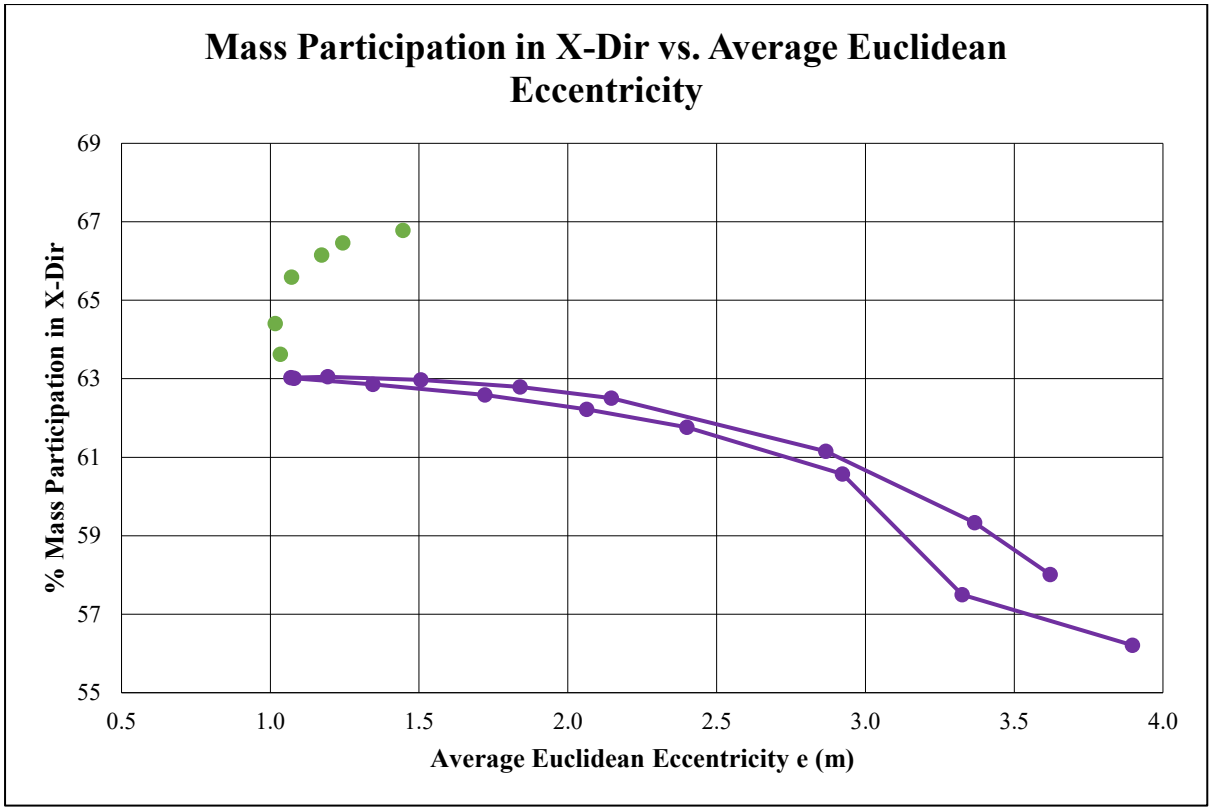


Figure 4.19: Plot of the mass participation in the X-direction versus the average Euclidean eccentricity in the irregular building

4.6 Summary and Conclusions

In this chapter, an approach is developed for maximising the mass participation ratio of the translational fundamental mode of vibration in each horizontal direction. It is suggested that a high mass participation ratio is achieved when the average of the eccentricity of all floor levels is reduced to the minimum. Both the normal average eccentricity and the average Euclidean eccentricity are considered. The concept relies on the argument that a high eccentricity between the centre of mass and the centre of rigidity would induce a significant torsional component and consequently reduce the contribution of the translational component of the fundamental mode of vibration. The main objective is to test the accuracy of the aforementioned hypothesis which relates the mass participation to the eccentricity. The eccentricity at each floor level is defined as the distance between the centre of mass and the centre of rigidity. The cumulative centre of mass is considered as it takes into account the total mass at and above the current storey. This is complemented by a procedure implemented in order to find the centre of rigidity at each floor level.

The last step involves testing the accuracy of the hypothesis regarding the mass participation and the floor eccentricities. A typical six-storey regular building and a nine-storey irregular building are selected for that purpose. In each example, the walls dimensions were continuously changed in order to alter the location of the centre of rigidity. It was accordingly observed for all the cases investigated that the mass participation at zero average eccentricity is in close proximity to the maximum mass

participation that could be achieved. Furthermore, it is shown that the mass participation ratio in each horizontal direction is further increased if the average Euclidean eccentricity is the control parameter to be reduced. Results for all the cases investigated have proven the advantage of reducing the average Euclidean eccentricity over reducing the normal average eccentricity. It is worth noting however that reducing the average Euclidean eccentricity is difficult from a practical perspective, as it involves minimising the eccentricity in both directions and at each floor level. This requires altering the wall dimensions at each storey which is practically unrealistic considering that a massive wall thickness is occasionally required in some trials to increase the stiffness of upper floors without influencing the stiffness of lower ones. Nevertheless, the concept is theoretically proven, and it can be concluded that the key to having a significant mass participation ratio of the fundamental mode in each horizontal direction is to reduce the average Euclidean eccentricity.

The findings of this chapter form a major constituent of the retrofitting procedure to be implemented in this research. Indeed, reducing the average Euclidean eccentricity at all floors is shown to reduce the torsional effects, which consequently enhances the performance of the original frame and particularly assists the framing columns which are located at the farthest distance from the centre of rigidity and which mostly suffer from the torsional stresses. Furthermore, the capacity spectrum method (CSM) is the focus of this research and is based on the assumption that the seismic response of the building is governed by deformations of the fundamental mode of vibration (Peter & Badoux, 2000). Since this latter assumption holds true when the translational mass participation of the fundamental mode is considerably high to ensure its predominance in the seismic response, the concept proposed in this chapter forms the basis for maximising the mass participation factor and for applying the CSM with confidence.

Last, it is worth to note that while a minimum average Euclidean eccentricity seems to be a reasonable indicator of maximum mass participation, it might still be possible to achieve more optimal mass participation. Indeed, the highest mass participation achieved mostly did not coincide with the smallest average Euclidean eccentricity, besides the fact that the Euclidean eccentricity could not be ultimately reduced to zero in order to make a more generalised conclusion. Nevertheless, the findings of this chapter provide a starting point that helps guiding the seismic retrofitting strategy to be developed.

Chapter 5 Static Analysis and Simplified Frequency Analysis

5.1 Introduction

This research is mainly concerned with the assessment and retrofitting of multi-storey RC buildings located in seismic hazard regions. The research makes use of the CSM (Freeman, 1998) in an attempt to develop a simplified strategy that facilitates the design of seismic retrofitting systems for substandard buildings. In concept, the CSM is based on the simplified assumption that the maximum lateral storey drifts are governed by deformations of the fundamental mode of the originally elastic system (Freeman, 1998). Accordingly, the method involves applying a set of pushover loads that is proportional to the fundamental mode of vibration. In that regard, the dynamic characteristics are obtained by performing conventional direct modal analysis which requires assembling the mass and stiffness matrices and solving the eigenvalue problem (Chopra, 2014).

This chapter is composed of three main parts, the first of which illustrates the use of the conventional static approach in an iterative manner in the aim to determine the vibration characteristics of the building. To note that the static approach is based on assembling the global stiffness matrix of the system and setting equilibrium requirements in order to calculate the response against applied loads. Hence, applying the process in an iterative way is computationally exhausting as it involves assembling mass and stiffness matrices and offers little advantage compared to the conventional eigenvalue analysis (modal analysis).

In light of this discussion, the second part of the chapter illustrates a more innovative approach that determines the vibration response in a simplified way that avoids assembling the mass and stiffness matrices. The simplified approach is based on adopting an approximation of the lateral stiffness of walls/columns and includes an integrated iterative procedure to reconstitute the equilibrium and compatibility conditions required to solve the static problem. Furthermore, the approach involves coupling the iterations required to solve the static problem with those required to find the eigenvalue. This enables the procedure to converge in only a few iterations, hence offering a practical advantage over the traditional static procedure. Last, the accuracy of the proposed approach is verified for realistic structures and the results have perfectly correlated with those obtained from direct eigenvalue analysis.

The chapter concludes with a simplified method introduced to add the contribution of the original frame (prior to strengthening) and its impact on the global vibration characteristics of the retrofitted structure. It is noted that the RC frame buildings targeted in this research are assumed to be seismically vulnerable and the response is accordingly expected to be predominated by the seismic retrofitting system. Nevertheless, it is important to assess the contribution of the original frame to the overall vibration response.

The simplified approach developed in this chapter combined with simplified pushover analysis performed in subsequent chapters, allow for a faster and more effective application of the CSM method. This eventually contributes into the ultimate objective of developing a simplified strategy that facilitates the design of seismic retrofitting systems.

5.2 Static Approach

The first approach considered to find the vibration characteristics of the building consists of an iterative application of the conventional static approach. In concept, the process involves assembling the global stiffness matrix of the system such that the response against an applied set of loads can be determined by solving the static equilibrium equations. The static approach is then applied in an iterative manner in order to determine the vibration characteristics of the building.

In the first instance, the response of a typical vertical element (wall or column) can be represented in terms of the relative displacement and rotation at the top (Figure 5.1a). This accordingly permits to establish an initial element stiffness matrix [k] based on Timoshenko's beam approach formulation of the elastic displacement of a beam element subjected to a lateral force and a bending moment (Timoshenko & Gere, 1972). Considering a lateral force F and a bending moment M applied at the top of the element in Figure 5.1a, the displacement and rotation measured at the top are obtained using the following equations:

$$d_F = F\left[\frac{h^3}{3EI} + \frac{h}{\kappa GA}\right] \tag{5.1}$$

$$d_M = M\left[\frac{h^2}{2EI}\right] \tag{5.2}$$

$$\theta_F = F\left[\frac{h^2}{2EI}\right] \tag{5.3}$$

$$\theta_M = M\left[\frac{h}{EI}\right] \tag{5.4}$$

where:

d_F & d_M respectively represent the elastic displacement at the top of the wall segment due to an applied lateral force and the one due to an applied bending moment,

θ_F & θ_M respectively represent the elastic rotation at the top of the wall segment due to an applied lateral force and the one due to an applied bending moment,

E is the modulus of Elasticity of the material,

I is the second moment of area of the cross-section,

G is the shear modulus,

A is the area of the cross-section, and

κ is Timoshenko's shear coefficient (shear correction factor). For rectangular cross-sections, it is given by the following (Hutchinson, 2001) where v is Poisson's ratio of concrete (taken as 0.2 for reinforced concrete):

$$\kappa = \frac{5(1+\nu)}{(6+5\nu)}$$

The previous relationships directly formulate the flexibility matrix and accordingly permit to evaluate the element stiffness matrix [k] as the inverse of the flexibility matrix.

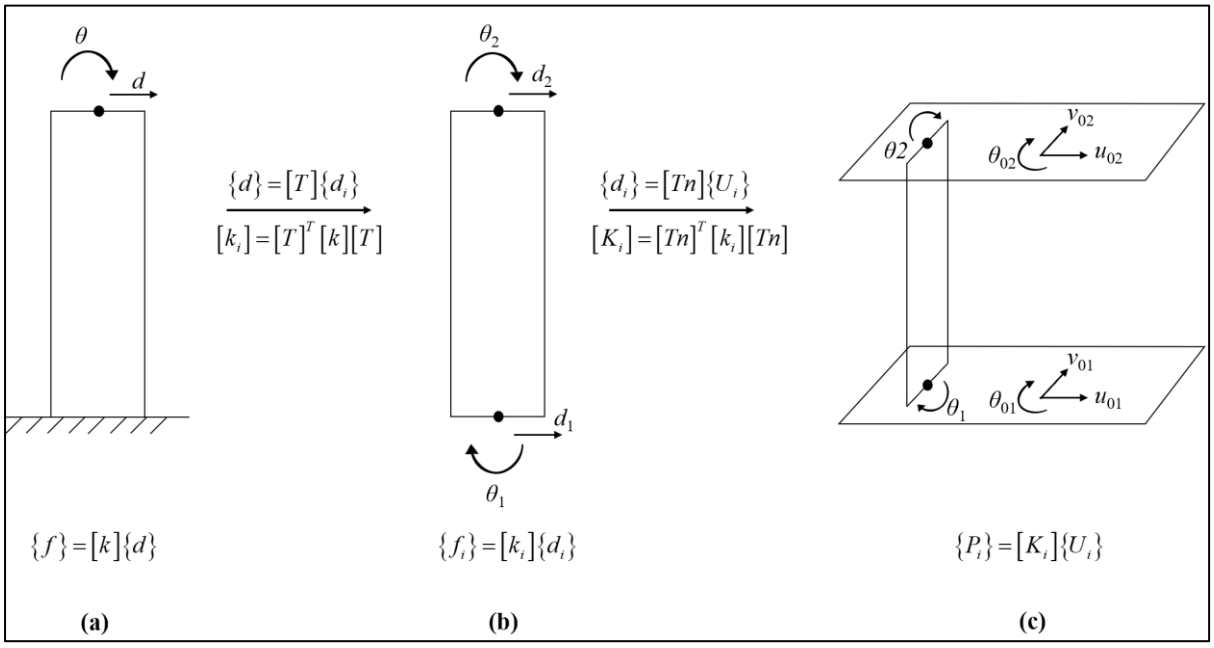


Figure 5.1: Assembly of stiffness matrix of each vertical element in the building

The analysis is then expanded to consider the displacement and rotation at both the top and the base of the element, which simulates the general case of a vertical element at an arbitrary storey level. This basically involves a transformation from the local system having two DOFs (Figure 5.1(a)) to a global system having four DOFs (Figure 5.1(b)). In light of this, a linear transformation [T] is established to connect the DOFs of the element in the local system to the DOFs of the element in the global system. This in turn permits to establish the stiffness matrix of the element in the global domain [k_i] using the stiffness matrix of the element in the local system [k] and the established linear transformation matrix [T] as referred to in Figure 5.1, noting that the transformation matrix [T] is defined by the following while h is the height of the element:

$$\{d\} = [T]\{d_i\} \tag{5.5}$$

$$\{d\} = \{d \;\; \theta\}^T \tag{5.6}$$

$$\{d_i\} = \{d_1 \;\; d_2 \;\; \theta_1 \;\; \theta_2\}^T \tag{5.7}$$

$$[T] = \begin{bmatrix} -1 & 1 & h & 0 \\ 0 & 0 & -1 & 1 \end{bmatrix} \tag{5.8}$$

The last step involves establishing the stiffness matrix of the element considering its interaction with the rigid floor diaphragm. In view of this, the lateral displacement of the column/wall at any storey is linked to the floor resultant displacements through the following linear transformation, which can be rewritten in the form of matrix $[T_w]$ to establish the relationship between the walls displacements and the floor resultant displacements in line with the rigid diaphragm behaviour (Figure 5.2):

$$d = (u_0 \; cos\alpha) \; + \; (v_0 \; sin\alpha) \; + \; (x \; sin\alpha - \; y \; cos\alpha)\,\theta_0 \tag{5.9}$$

$$d = [T_w]\{u_0 \;\; v_0 \;\; \theta_0\}^T \tag{5.10}$$

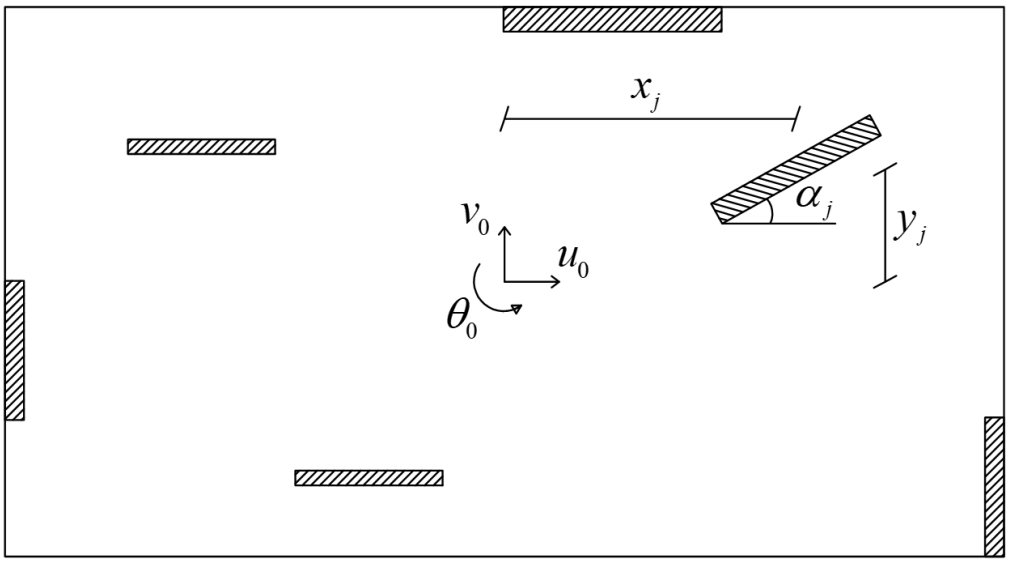


Figure 5.2: Typical representation of the walls displacements and the floor resultant displacements

This subsequently reduces the number of DOFs of the vertical element to two instead of four, with the translational displacement at both ends being directly expressed in terms of the floor resultant displacements. In this regard, the floor displacements are represented by three DOFs at each floor as shown in Figure 5.1(c), and they already contribute to the global stiffness matrix of the building. Therefore, expressing the lateral displacement at both ends of the column/wall in terms of the floor resultants reduces the number of DOFs in the final element matrix. In sum, each vertical element is eventually represented by eight DOFs consisting of the rotation at the top and at the base besides the

floor resultant displacements at both the top and base levels (Figure 5.1(c)). In a similar fashion to what is performed in the first instance, the four DOFs of the element in the new local system (Figure 5.1(b)) are connected to the eight DOFs of the element in the new global system (Figure 5.1(c)) through a linear transformation matrix [*Tn*]:

$$\{d_i\} = [Tn]\,\{U_i\} \tag{5.11}$$

$$\{U_i\} = \{u_{01}\ \ v_{01}\ \ \theta_{01}\ \ u_{02}\ \ v_{02}\ \ \theta_{02}\ \ \theta_1\ \ \theta_2\}^T \tag{5.12}$$

$$[Tn] = \begin{bmatrix} T_w[1,1] & T_w[1,2] & T_w[1,3] & 0 & 0 & 0 & 0 & 0 \\ 0 & 0 & 0 & T_w[1,1] & T_w[1,2] & T_w[1,3] & 0 & 0 \\ 0 & 0 & 0 & 0 & 0 & 0 & 1 & 0 \\ 0 & 0 & 0 & 0 & 0 & 0 & 0 & 1 \end{bmatrix} \tag{5.13}$$

This subsequently permits to establish the global element stiffness matrix [K_i] that represents the eight DOFs referred to earlier by making use of the linear transformation [*Tn*] and the previously established stiffness matrix in the local system [k_i] as referred to in Figure 5.1. Eventually, the global stiffness matrix of the whole building is assembled by adding the contribution of all the vertical elements. To note that the final DOFs of the system comprise the rotational DOFs at both ends of the vertical elements besides the three-component floor resultant displacements at each storey.

Once the global matrix of the whole building is assembled, the displacement of all the DOFs is calculated by applying static equilibrium between the applied loads and the resultant displacements.

The static approach is then applied in an iterative manner in the aim to find the fundamental vibration characteristics of the building. In this respect, the iterative process starts with applying an arbitrary three-component mode shape at a pre-defined location of each storey. Interpreting the applied mode shape as a series of translational and rotational accelerations, the associated inertia forces (applied loads) are calculated by Newton's second law, and the resultant displacements at the DOFs are obtained through the aforementioned static procedure. To recap, each iteration consists of applying an input mode shape to the structure and the output is a displacement vector that balances the applied loads. This basically conforms with the concept of the inverse vector iteration method described in Chapter 2, and accordingly the frequency of vibration (the eigenvalue) is estimated by evaluating Rayleigh's quotient. Next, the output floor displacements are compiled into a vector which is normalised and used as the new input mode vector for the next iteration. The iterative process is repeated until convergence into the mode shape vector and frequency of the fundamental mode of vibration.

The static iterative procedure is implemented using the computational software Maple (Maple, 2019) which makes it a practical tool used to find the vibration characteristics of the building, with a considerably small number of iterations required to achieve convergence.

5.3 Novel Integrated Static/Frequency Analysis Approach

A static analysis capability has a wide range of application, and it can be effectively employed to find the vibration properties of RC buildings as discussed in the previous section. Furthermore, such a capability is already available in most of computerised software to solve static analysis problems. Nevertheless, this section presents a novel and more sophisticated static/frequency analysis approach specifically devised to determine the mode and frequency of vibration of wall structural systems efficiently. The proposed approach avoids the need for assembling the mass and stiffness matrices, hence offering a practical advantage over the conventional static approach. The procedure first addresses the case of a single shear wall, and the analogy is then expanded to find the vibration properties of the fundamental mode of wall systems in a multi-storey building, assuming in the first instance that the overall response is predominated by the walls. The section also outlines a brief procedure to find the mode of vibration in the orthogonal horizontal direction and higher modes if needed. In the last part, the accuracy of the proposed simplified approach is verified for realistic structures via comparisons against direct eigenvalue analysis.

5.3.1 Isolated Shear Wall

The case of an isolated shear wall is first addressed because of the simplicity of this scenario, and the findings are then expanded to cover the anticipated multi-storey building. This section aims at finding the fundamental mode of vibration of an isolated shear wall. The procedure begins with applying an arbitrary mode shape to the wall elevation. A linear inverted triangular mode shape is chosen for simplicity, starting with a zero at the base up to a maximum unitary value at the top. The mode shape values are idealised as lateral accelerations, and the associated inertia forces are calculated by Newton's second law and are directly applied at each floor (Figure 5.3).

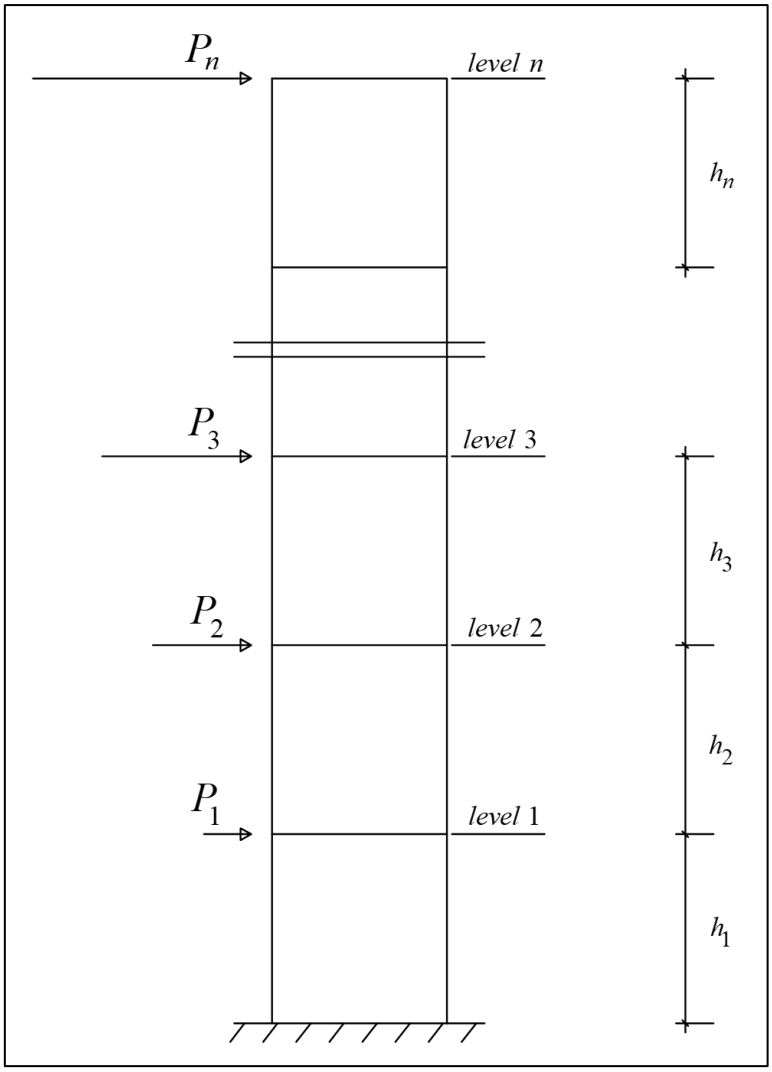


Figure 5.3: Typical wall elevation

The procedure consists of analysing the wall segment successively at each floor, starting from the base and moving up the levels (Figure 5.4). In this regard, the cumulative lateral load and bending moment are calculated at each level by adding the contribution of the loads applied at upper floors. Consequently, the total displacement at the top of the wall segment is calculated as the sum of the total displacement at its base in addition to the displacement incurred by the rotation of the base as well as the elastic displacement due to the force and moment applied at the top. Similarly, the total rotation at the top is equal to the total base rotation besides the elastic rotation caused by the applied force and moment. To note that the elastic displacement and rotation due to the applied loads at the top are evaluated using the Timoshenko beam approach formulations (Timoshenko & Gere, 1972).

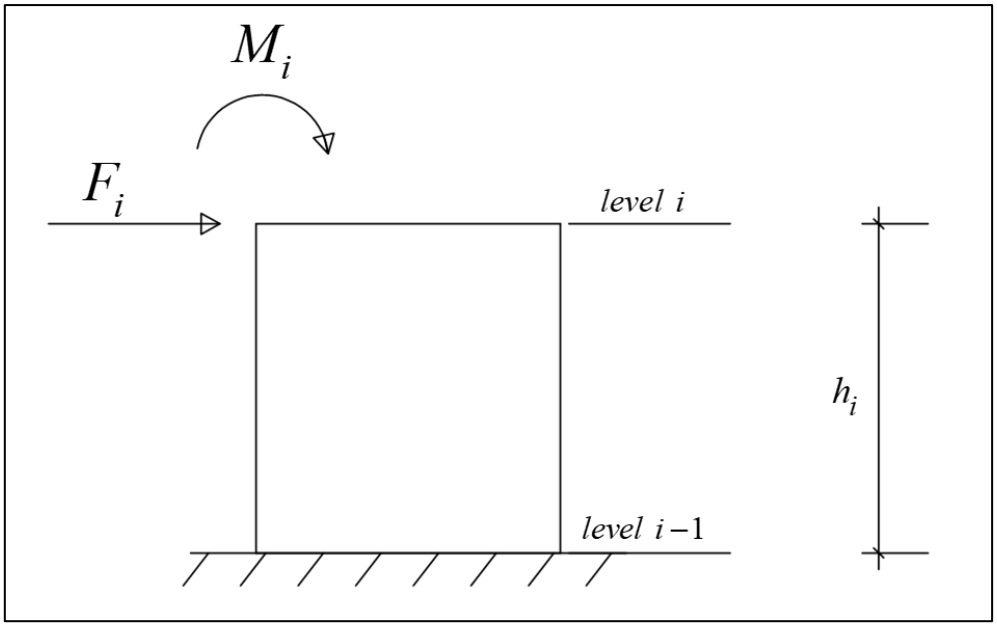


Figure 5.4: Wall segment at typical floor

In sum, the cumulative displacement and rotation at the top of the wall segment are expressed by the following:

$$d_i = d_{i-1} + \bar{u}_i + (\theta_{i-1} \times h_i) \tag{5.14}$$

$$\theta_i = \theta_{i-1} + \bar{\theta}_i \tag{5.15}$$

where:

d_i & θ_i respectively represent the total displacement and total rotation at the top of the wall segment,

d_{i-1} & θ_{i-1} respectively represent the total displacement and total rotation at the base of the wall segment, and

$\bar{u}_i$ & $\bar{\theta}_i$ are the elastic displacement and rotation respectively obtained at the top of the wall in response to an applied lateral load and bending moment (Figure 5.4).

The elastic displacement and rotation are evaluated according to the following expressions (Timoshenko & Gere, 1972):

$$\bar{u}_i = \left\lfloor \frac{F_i h_i^3}{3(EI)_i} + \frac{F_i h_i}{\kappa(GA)_i} \right\rfloor + \left\lfloor \frac{M_i h_i^2}{2(EI)_i} \right\rfloor \tag{5.16}$$

$$\bar{\theta}_i = \left\lfloor \frac{F_i h_i^2}{2(EI)_i} \right\rfloor + \left\lfloor \frac{M_i h_i}{(EI)_i} \right\rfloor \tag{5.17}$$

The procedure starts at the base level which is assumed to be fixed. Hence, the rotation and displacement of the base level are set to zero, and the procedure flows from the bottom to the top, thus calculating the displacement and rotation of the wall at all storeys. The displacements are compiled in a vector which summarises the response of the wall to the applied mode shape vector. To recapitulate, an arbitrary mode shape is applied along the wall height, and the output is a displacement vector that balances the forces associated with the input mode. Therefore, the concept is likened to the inverse vector iteration method even though the output displacement vector is obtained without assembling the stiffness matrix, and an estimate of the eigenvalue is accordingly obtained by evaluating Rayleigh's quotient. The output displacement vector obtained is then normalised and input as the newly applied mode shape vector, and the whole process is repeated until convergence. The final outcome of displacement vector and Rayleigh quotient respectively amount to the fundamental mode and frequency of vibration of the wall.

The approach has been tested for a wide array of walls ranging from four to twelve storeys, and the results obtained perfectly correlated with those obtained from an eigenvalue analysis performed on ETABS.

5.3.2 Integrated Static/Frequency Analysis of a Multi-storey Building

After confirming the effectiveness of the developed approach in predicting the vibration characteristics of a single wall, the concept is expanded in the aim to determine the fundamental vibration characteristics of a multi-storey RC frame building. Unlike the case of a shear wall, the mode shape vector consists of two translational and one planar rotational acceleration components applied at a predefined point across all floors. The corresponding inertia forces are calculated by Newton's second law and are due to be resisted by the lateral-force resisting system mainly composed of shear walls and columns. The general concept follows the same analogy employed in the single wall scenario. Accordingly, the floor resultant displacements are calculated and normalised in order to be input as the updated mode shape vector for the next iteration and so on, until convergence of the procedure into the eigenpair (mode shape and frequency) of the fundamental mode.

In practice, each iteration is reduced to solving a static problem that involves applying a three-component acceleration vector at each storey and calculating the resultant three-component displacements. In this respect, convergence of the solution requires meeting the requirements of the

three main constituents of structural analysis which basically include equilibrium, compatibility, and constitutive requirements. Unlike the single wall case, there are a few challenges encountered in the building scenario since the response is dictated by the complex interaction of the different components of the lateral-force resisting system. Accordingly, a few assumptions have to be made in order to ease the challenges and to set a solid basis for the planned approach.

This section is divided into several sub-sections, the first of which introduces the assumptions taken in regard to simplifying the problem, before addressing the main challenges encountered as the procedure is expanded to cover the building scenario. This is subsequently followed by the steps implemented to solve the static problem, with a detailed illustration of the measures taken to overcome the identified challenges. The section concludes with a brief summary of the whole procedure.

5.3.2.1 Assumptions

The following assumptions are made to help overcoming the challenges encountered and to set a solid foundation for the anticipated approach:

1. The lateral stiffness of the building is solely provided by the shear walls. Hence, the contribution of the columns is neglected, and the applied loads are assumed to be solely resisted by the walls.
2. The out-of-plane resistance of the walls is assumed to be negligible such that the wall can only resist the loads that are parallel to its longitudinal major axis.
3. The floor slab is assumed to have a significant in-plane stiffness and to behave as a rigid diaphragm that transfers the applied loading to the lateral-force resisting system. This assumption literally implies that the internal force is proportional to the relative stiffness of the wall (bearing in mind that the walls cannot resist out-of-plane loading).
4. The torsional stiffness of the walls is ignored. Moreover, a simplified expression of the lateral stiffness is formulated considering a lateral force applied at the top. The resultant elastic displacement is evaluated using Timoshenko's formulation of the bending and shear deformations of a beam element subjected to a lateral force (Timoshenko & Gere, 1972). Considering a rectangular cross-section and rearranging the terms accordingly, a simplified approximation of the stiffness is obtained as per the following:

$$u = \frac{P H^3}{rEI} + \frac{P H}{\kappa GA} = P\left[\frac{H^3}{rEI} + \frac{H}{\kappa GA}\right] \tag{5.18}$$

$$P = K\, u \;\rightarrow\; K = \frac{E t}{\left[\frac{12}{r}\left(\frac{H}{L}\right)^3 + 2.77\left(\frac{H}{L}\right)\right]} \tag{5.19}$$

where:

K is the lateral stiffness of the wall,

E is the modulus of elasticity of concrete,

t, L, H represent the thickness, length, and height of the wall respectively, and

r is equal to 3 for a fixed-pinned support conditions (wall segment at top floor) and is equal to 12 for a fixed-fixed support (at other floors).

5.3.2.2 Main Challenges

The following challenges outline the complexity of the problem when the methodology is expanded to cover the multi-storey building scenario:

1. The main challenge involves violation of compatibility requirements upon imposing static equilibrium between the applied cumulative storey loads and the resisting internal forces in the walls, which is performed at the floor level and which propagates downwards from the top floor to the base (Figure 5.5). In fact, the internal forces depend on the relative stiffness of the walls in line with the rigid diaphragm assumption. With the stiffness being evaluated using a simplified approximation, an approximate distribution of the applied loads and accordingly an approximate evaluation of the internal forces (and displacements) is obtained. This literally implies that the walls are not deforming in a synchronous manner with each other and with the floor rigid diaphragm. As a remedy, corrections to the walls internal forces are applied in order to restore compatibility in conformity with the rigid diaphragm behaviour. This is performed from bottom to top opposed to the process of enforcing equilibrium (Figure 5.5).
2. The formerly discussed enforcement of compatibility is not as straightforward as may be expected, because the existing rotational flexibility at the base of the wall segment affects the response and needs to be taken into consideration. Indeed, correcting the force at the current level produces a bending moment and thus an additional rotation at the base. Consequently, the base rotation incurs an additional displacement and rotation at the top of the wall segment, and these need to be incorporated into the procedure in order for the solution to converge.
3. Adding to the previous discussion on re-establishing compatibility, adjusting the force at the current level produces a bending moment at the base of the wall segment. In fact, this moment carries over to the next lower level and so on, generating a series of bending moments which incur additional displacements and rotations at the lower floors, owing to the translational and rotational flexibility (due to moment) at all floor levels except for the fixed base. Consequently, the procedure should also be amended to include the effect of correcting the forces at the current storey on the storeys beneath it.

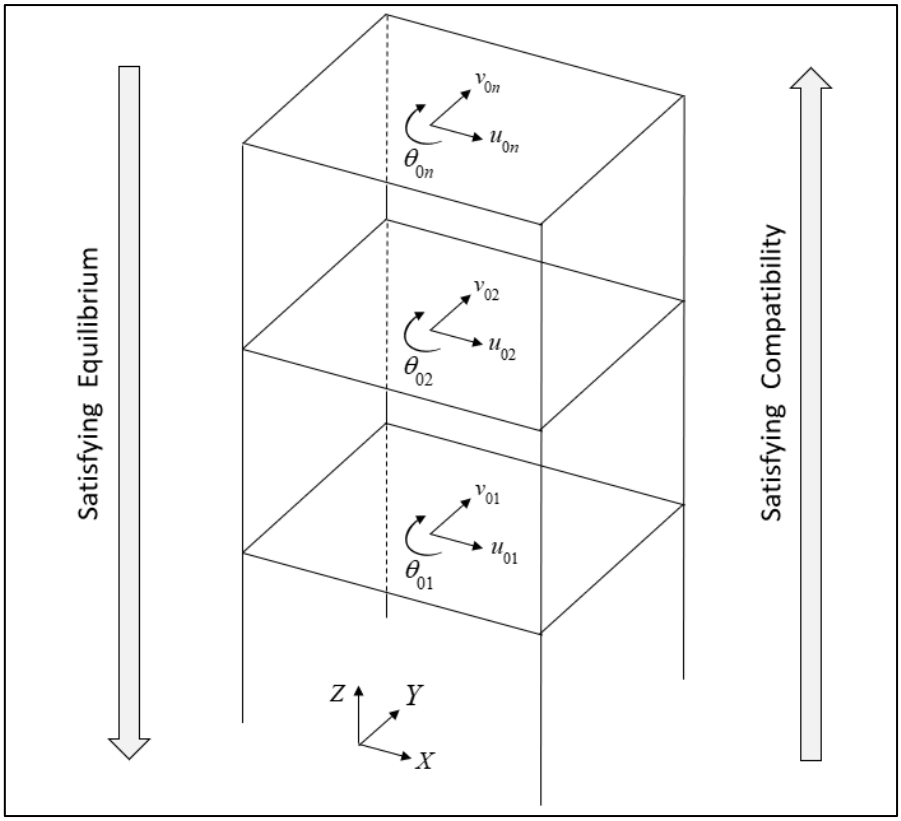


Figure 5.5: Sketching the main DOFs and the flow of events in the static analysis of the building

Briefly reinstating the challenges in succession, the procedure starts by enforcing equilibrium conditions from top to bottom between the internal forces and the applied loads (Figure 5.5). Ensuring equilibrium gives rise to a compatibility issue which mainly stems from the approximative formulation of the wall stiffness. As a remedial measure, the internal forces in the walls are corrected in order to restore compatibility, noting that the enforcement of compatibility proceeds from bottom to top and causes a disruption to the previously established equilibrium (Figure 5.5). Within the process, the secondary effects caused by the force correction at the current floor on the current and lower floors are incorporated into the procedure in order to satisfy all the equilibrium, compatibility, and constitutive requirements and to achieve convergence. To summarise, satisfying equilibrium in the proposed manner leads to violation of compatibility, and subsequent satisfaction of compatibility leads to violation of equilibrium. However, successive applications of equilibrium/compatibility cycles leads to diminishing violations, and the procedure typically converges with a few iterations, importantly without the need for assembling a stiffness matrix.

5.3.2.3 Establishing Equilibrium Conditions

An arbitrary three-component mode shape is applied at a predefined point of each storey (Figure 5.6). For a regular floor plan, the geometric centroid is ideally taken as the reference point for application of the loads. Considering the mode shape as a set of accelerations, inertia forces consisting of two horizontal translational forces and a torsional torque are accordingly calculated. The first step involves

establishing static equilibrium at each storey, starting from the upper floor and moving downwards. Accordingly, the cumulative loads at each storey are balanced by the internal forces in proportion to the relative stiffness of the walls, with the latter being evaluated according to a predefined approximation. The out-of-plane resistance of the walls is assumed to be negligible such that the wall can only resist loads aligned along its main axis, and the columns resistance is assumed to be negligible as well. In view of this, the torsional moment associated with the rotational component causes rotation of the floor plan, hence imparting a lateral shear force to each wall in the plan.

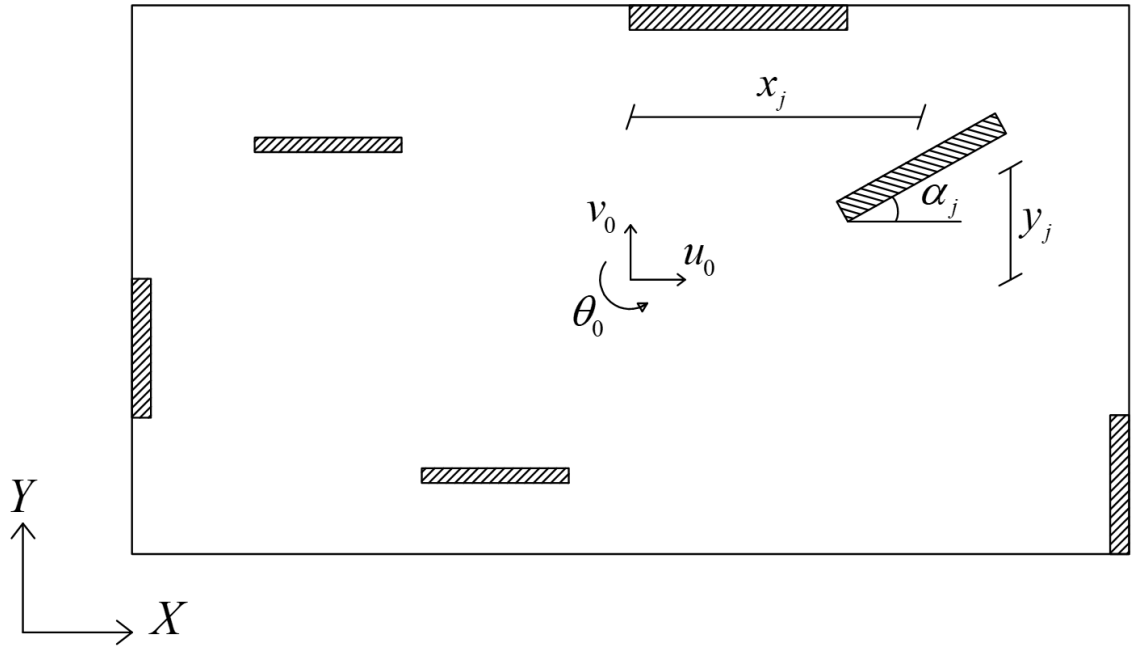


Figure 5.6: Typical floor plan – interaction between the walls and the mode shape

Owing to the rigid diaphragm assumption, the whole floor is expected to deform as a collective unit in response to the applied loading. Hence, the displacement of any wall is linked to the floor resultant displacements through the following linear relationship (Figure 5.6):

$$d = (u_0 \cos\alpha) + (v_0 \sin\alpha) + (x \sin\alpha - y \cos\alpha)\theta_0 \tag{5.20}$$

where:

x & y are the distances from the centroid of the wall to the reference point at which the mode shape is applied, and

α is the angle that defines the orientation of the wall with respect to the global X-axis.

The previous relationship allows to establish a linear transformation matrix [T] that connects the displacements of the walls to the floor resultant displacements. This relationship can be envisaged as a transformation from the local domain (walls displacements) to the global domain (floor resultants). In this respect, the cumulative storey loads are linked to the internal forces in the walls through the

transpose of the linear transformation matrix presently defined. In parallel, the internal forces are related to the displacements via the approximated lateral stiffness. In sum, this allows to establish a direct relationship between the cumulative floor loads and resultant displacements via matrix [Tr], which basically involves a transition from the local domain (wall) to the global domain (floor resultants). Compiling all of these relationships allows to establish equilibrium through a direct relationship that links the forces in the resisting walls to the applied storey loads, as illustrated in the following:

$$\{d\} = [T]\{U\} \tag{5.21}$$

$$\{P\} = [T]^T \{f\} \tag{5.22}$$

$$\{f\} = [k]\{d\} \tag{5.23}$$

$$\{P\} = [T]^T [k]\{d\} = [T]^T [k][T]\{U\} \tag{5.24}$$

$$\rightarrow \{P\} = [Tr]\{U\} \tag{5.25}$$

$$\{U\} = [Tr]^{-1}\{P\} \tag{5.26}$$

$$\{f\} = [k]\{d\} = [k][T]\{U\} \tag{5.27}$$

$$\rightarrow \{f\} = [k][T][Tr]^{-1}\{P\} \text{ (Equilibrium Relationship)} \tag{5.28}$$

where:

$\{d\}$ represent the displacements in the walls,

$\{f\}$ represent the internal shear forces in the walls,

$\{U\}$ represent the floor resultant displacements,

$\{P\}$ are the cumulative storey loads,

$[k]$ represent the stiffness matrix of the walls,

$[T]$ is the linear transformation relating the displacements of the walls to the floor resultant displacements, and

$[Tr]$ is the matrix that links the floor resultant displacements to the cumulative storey loads.

$$[Tr] = [T]^T [k][T]$$

It is worth noting that the equilibrium relationship defined above is applied at the single storey level, such that the cumulative storey forces above the current floor are balanced by the internal forces in the walls at the current storey, noting that the matrix [*Tr*] depends on the approximate wall stiffness defined earlier. Accordingly, equilibrium is established at all storeys starting at the top floor and moving down the levels.

5.3.2.4 Compatibility Requirements

After establishing equilibrium, displacements of the walls at each storey are calculated and checked for compliance with the rigid diaphragm assumption. In this regard, the external loads applied to the wall elevation are obtained by subtracting the internal forces of adjacent floors. The walls displacements are then calculated following the procedure outlined for the single wall scenario in section 5.3.1.

In line with the rigid diaphragm assumption, a compatibility check is performed to ensure that the walls are deforming in a compatible manner that complies with the deformation of the floor rigid diaphragm. In this context, violation of compatibility implies that the internal forces initially obtained at equilibrium are not precise, such that the walls are not deforming along with each other and with the floor rigid diaphragm. Violation of compatibility is the likeliest outcome at equilibrium because a simplified formula has been adopted to represent the stiffness of the walls. In this case, the force distribution in the walls needs to be revisited and corrections are applied in order to restore compatibility.

In order to check for compatibility, any set of three walls, referred to as self-equilibrating walls, is selected granted that the walls are not aligned in the same direction. Assuming the walls are deforming in accordance with the rigid diaphragm, the floor resultant displacements are determined using the linear transformation defined earlier with respect to the displacements of the self-equilibrating walls. This is followed by calculating the displacements of the remaining walls (referred to as redundant walls), presuming the latter are also deforming in conformity with the floor resultant displacements. To this end, the displacement of redundant walls is expressed in terms of the floor resultant displacements, which in turn are expressed in terms of the displacements of the self-equilibrating walls. Hence, the displacements of the redundant walls are connected to those of the self-equilibrating through a linear relationship which is referred to as the compatibility relationship and which forms a basis to check and to restore compatibility if needed, as illustrated per the following:

$$\{d\}_{1..3} = [T]_{1..3} \{U\}_{3x1} \tag{5.29}$$

$$\{U\}_{3x1} = [T]^{-1}_{1..3} \{d\}_{1..3} \tag{5.30}$$

$$\{d\}_{4..n} = [T]_{4..n} \{U\}_{3x1} \tag{5.31}$$

$$\{d\}_{4..n} = [T]_{4..n} [T]^{-1}_{1..3} \{d\}_{1..3} \tag{5.32}$$

$$\rightarrow \{d\}_{4..n} = [Tn] \{d\}_{1..3} \text{ (Compatibility Relationship)} \tag{5.33}$$

where:

$\{d\}_{1..3}$ represent the displacements of the three selected self-equilibrating walls,

$\{d\}_{4..n}$ represent the displacements of the redundant walls,

$\{U\}_{3x1}$ represent the floor resultant displacements (u_0, v_0, θ_0) that are calculated with respect to the displacements of the self-equilibrating walls,

$[T]_{1..3}$ is a (3x3) sub-matrix of the general [T] matrix, and it expresses the relationship between the floor resultant displacements and the displacements of the self-equilibrating walls,

$[T]_{4..n}$ is a sub-matrix of the general [T] matrix, and it expresses the relationship between the floor resultant displacements and the displacements of the redundant walls, and

$[Tn]$ is a matrix that relates the displacements of the redundant walls to those of the three self-equilibrating walls, assuming a rigid floor diaphragm behaviour.

$$[Tn] = [T]_{4..n} [T]^{-1}_{1..3}$$

In consequence, if the last-obtained displacements of the redundant walls are not identical to their equivalents obtained after satisfying equilibrium, it is concluded that compatibility is violated and that the distribution of internal forces in the walls needs to be revised. To this end, violation of compatibility requirements at the current floor can be represented by the following expression:

$$\{d^e\}_{4..n} \neq [Tn] \{d^e\}_{1..3} \tag{5.34}$$

where:

$\{d^e\}_{1..3}$ & $\{d^e\}_{4..n}$ respectively represent the displacements of the self-equilibrating walls and the redundant walls obtained after satisfying equilibrium.

In case compatibility is violated, the walls forces are adjusted such that the modified displacements of the redundant and self-equilibrating walls obey the compatibility relationship described above. In this regard, the correction (change) in displacement is related to the correction in the internal force through the translational flexibility (Timoshenko & Gere, 1972), which is similar to the simplified formula of the stiffness. Furthermore, the force correction in the redundant walls and its equivalent in the self-equilibrating walls are linked through the transpose of the compatibility relationship matrix. Compiling all of these relationships allows to calculate the force correction in the redundant walls and subsequently in the self-equilibrating walls. The newly adjusted internal forces are expected to enforce compatibility at the floor level, such that the updated displacements of the walls in each storey are consistent with each other and with the floor resultant displacements in line with the rigid diaphragm assumption. The whole process is better illustrated in the following discussion.

$$\left\{d^e\right\}_{4..n} \neq \left[Tn\right]\left\{d^e\right\}_{1..3} \tag{5.35}$$

$$\left\{d^e\right\}_{4..n} + \left\{\delta d\right\}_{4..n} = \left[Tn\right]\left(\left\{d^e\right\}_{1..3} + \left\{\delta d\right\}_{1..3}\right) \xleftrightarrow[Equivalent\ to]{} \left\{d\right\}_{4..n} = \left[Tn\right]\left\{d\right\}_{1..3} \tag{5.36}$$

where:

$\left\{\delta d\right\}_{1..3}$ & $\left\{\delta d\right\}_{4..n}$ respectively represent the applied corrections to the displacements of the self-equilibrating walls and to those of the redundant walls, and

$\left\{d\right\}_{1..3}$ & $\left\{d\right\}_{4..n}$ respectively represent the corrected (modified) displacements of the self-equilibrating walls and the redundant walls which are compatible with respect to each other in line with the rigid diaphragm assumption, and which accordingly obey the compatibility relationship defined earlier.

For a single wall, the displacement correction is related to the force correction by way of the Timoshenko formulation of displacement at the tip of a cantilever beam element (Timoshenko & Gere, 1972). Considering all the walls in the floor, the diagonal translational flexibility matrix (due to lateral load) connects the displacement corrections to the force corrections in the walls at the current floor as illustrated in the following:

$$\delta d = \frac{\left(\delta f\right)h^3}{3EI} + \frac{\left(\delta f\right)h}{\kappa GA} \tag{5.37}$$

$$\delta d = \left(\delta f\right) tf^F \ with\ \ tf^F = \frac{h^3}{3EI} + \frac{h}{\kappa GA} \tag{5.38}$$

$$\left\{\delta d\right\} = \left\{\delta f\right\}\left[tf^F\right] \tag{5.39}$$

where:

$\left[tf^F\right]$ is the diagonal translational flexibility matrix (due to lateral load).

Furthermore, the corrections applied to the redundant wall forces are related to the corrections applied to the forces in the self-equilibrating walls through the transpose of matrix [*Tn*]:

$$\{d\}_{4..n} = [Tn]\{d\}_{1..3} \quad \Rightarrow \{\delta f\}_{1..3} = [Tn]^T \{\delta f\}_{4..n} \tag{5.40}$$

This consequently permits to establish the enforcement of compatibility as per the following:

$$\{d^e\}_{4..n} + \{\delta d\}_{4..n} = [Tn]\left(\{d^e\}_{1..3} + \{\delta d\}_{1..3}\right) \tag{5.41}$$

$$\{d^e\}_{4..n} + \left[tf^F\right]_{4..n}\{\delta f\}_{4..n} = [Tn]\left(\{d^e\}_{1..3} + \left[tf^F\right]_{1..3}\{\delta f\}_{1..3}\right) \tag{5.42}$$

$$\{d^e\}_{4..n} + \left[tf^F\right]_{4..n}\{\delta f\}_{4..n} = [Tn]\left(\{d^e\}_{1..3} + \left[tf^F\right]_{1..3}[Tn]^T\{\delta f\}_{4..n}\right) \tag{5.43}$$

The last-derived expression is the compatibility-enforcement relationship. The correction in the internal forces in the redundant walls $\{\delta f\}_{4..n}$ is obtained by solving the equation, which permits to solve for the correction of forces in the self-equilibrating walls $\{\delta f\}_{1..3}$. The process is repeated at all floor levels starting from the bottom and moving up the levels, such that the modified forces in the walls ensure that compatibility of displacements of the walls is restored in line with the rigid diaphragm behaviour.

5.3.2.5 Influence of flexible base on the force correction at the current level

The procedure outlined so far has addressed the process of restoring compatibility at the storey level. However, the procedure is yet to account for the interaction between wall segments across different floors, as to how the force correction at a given storey would alter the behaviour of other storeys. In this respect, this section aims at finding the influence of having a flexible base on the force correction performed at the top of the wall segment, presuming the rotational flexibility (due to a moment) at the base is already established.

To begin with, the elastic displacement and rotation defined earlier (Equations 5.16 and 5.17) permit to establish the translational and rotational flexibility due to a lateral force. However, these flexibility terms are appropriate for an ideal fixed-base scenario and are therefore only applicable at the ground level, since the wall segments at upper floors practically exhibit a rotation at the base as reflected in the realistic scenario (Figure 5.7). It would then be appropriate to inspect the effect of the flexible base on correcting the force at the top.

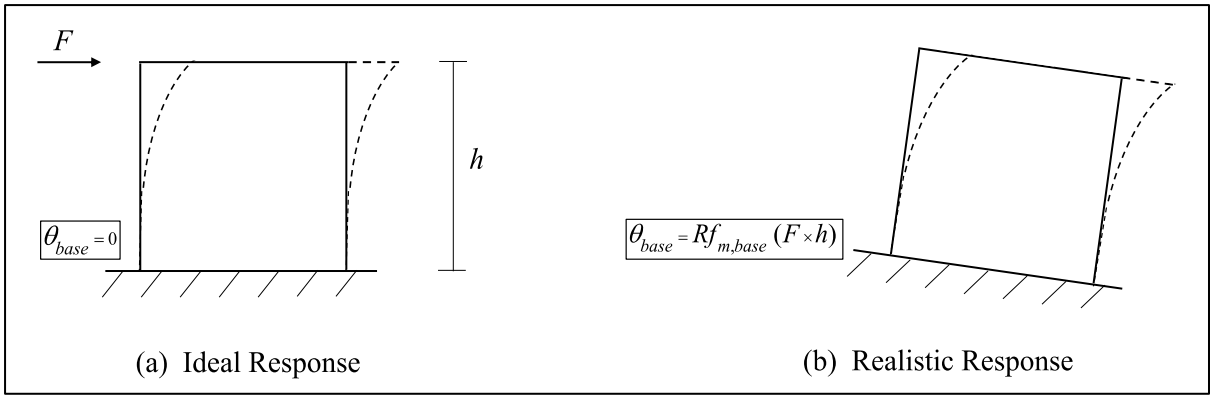


Figure 5.7: Ideal and realistic behaviours in response to a force correction at the top of the wall segment

In this respect, the force applied at the top of the wall segment generates a moment at the base. Assuming that the effective rotational flexibility (due to moment) at the base is already determined, a rotation is induced at the base and is equal to the base moment multiplied by the effective rotational flexibility (Figure 5.7b). In view of this, the base rotation gives rise to an additional rotation and displacement at the top of the wall segment as per the following:

$$\delta\theta_{top} = \theta_{base} \tag{5.44}$$

$$\delta d_{top} = \theta_{base} \times h \tag{5.45}$$

By setting a unit value to the force applied at the top, the increment in rotation/displacement respectively amount to the increment in rotational/translational flexibility due to lateral force, which is added to the initial formulation that conforms to a fixed base.

$$\delta Rf_{F,top} = Rf_{m,base} \times h \tag{5.46}$$

$$\delta Tf_{F,top} = Rf_{m,base} \times h^2 \tag{5.47}$$

where:

$\delta Rf_{F,top}$ is the increment in rotational flexibility due to force at the top of the wall segment,

$\delta Tf_{F,top}$ is the increment in translational flexibility due to force at the top of the wall, and

$Rf_{m,base}$ is the rotational flexibility due to moment at the base (assumed to be known).

To recapitulate, the flexibility of the base increases both the translational and rotational flexibility (due to force) at the top of the wall segment. Consequently, the process undertaken to regenerate compatibility is accordingly amended by adopting the total or effective translational flexibility (due to force) when correcting the forces in the walls.

5.3.2.6 Influence of force correction at current floor on lower floors

In the same context, it is equally important to understand the potential influence of correcting the forces at the current floor on lower levels. This represents the final component that completes the static analysis procedure.

This section aims at finding the effect caused by correcting the force at the current floor on the lower floors. In this regard, a force correction applied at the top of the wall segment produces a moment at the base. This moment carries over to the next lower level and so on, such that a force correction applied at the current level results in a set of moments generated at all the levels beneath it (Figure 5.8). The resulting moments incur an additional rotation at lower floors, considering that the wall displacements below the current floor are locked as part of the upward propagating compatibility procedure.

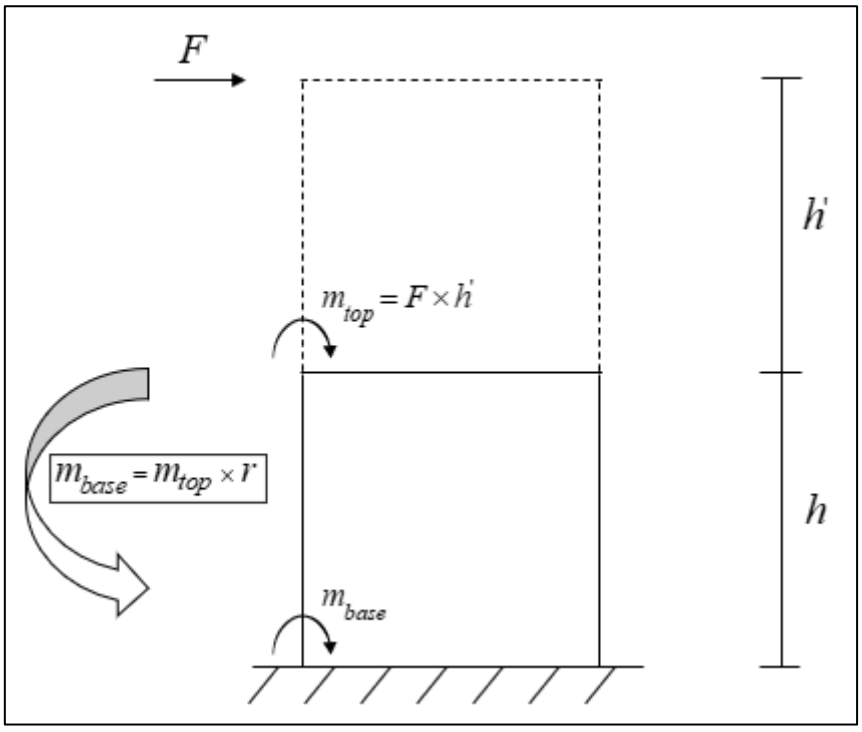


Figure 5.8: Carry-over of moment at top of wall segment to the base

In this respect, the procedure should be updated to include the additional rotations incurred at lower floors as a result of correcting the forces at upper floors. In line with the upward propagating compatibility procedure, the anticipated solution has to cope with one single unknown in the form of the rotation at lower floors as the displacement is assumed to be fixed (Figures 5.8 & 5.9). Accordingly, adjusting the rotations is crucial to restore the rotational equilibrium at the interface of wall segments between the floors such that the wall is envisaged as a continuous beam deforming over pinned supports (the floor slab at each level).

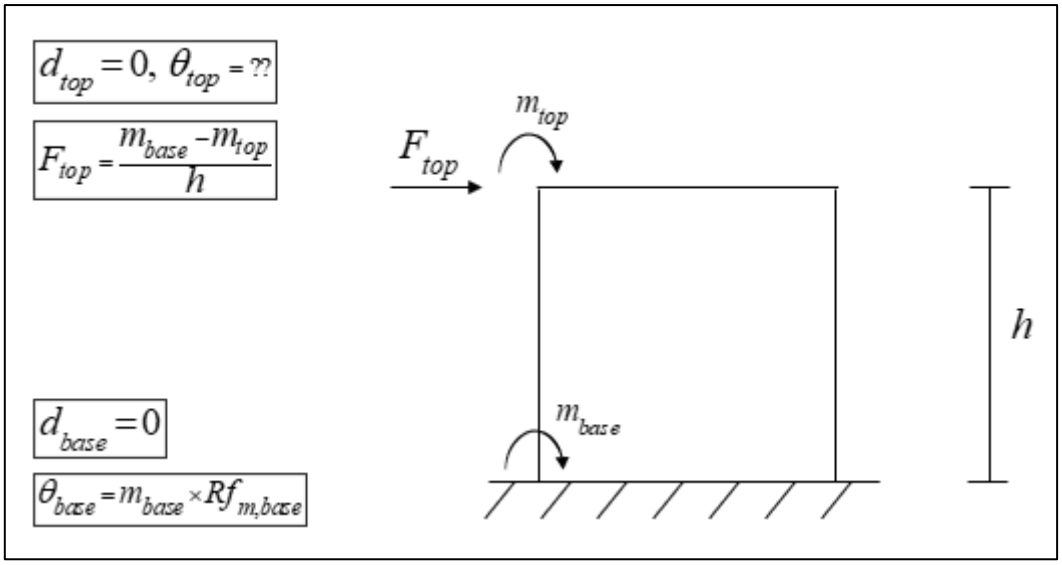


Figure 5.9: Expression of rotation at the top of the wall segment

Accordingly, adjusting the forces at one level gives rise to only a change in the rotation at lower levels. In this case, the problem is reduced to finding out the relationship between the moment at the top and the resultant moment generated at the base, which is obtained by setting the presumptive increment in displacement at the top of the wall to zero in line with the fixed-total-displacement assumption (Figure 5.9):

$$d_{top} = 0 \rightarrow \left(\theta_{base}\ \ h\right) + \left(m_{top}\ Tf_{m,top}\right) + \left(F_{top}\ Tf_{F,top}\right) = 0 \tag{5.48}$$

$$\rightarrow r = \frac{Tf_{F,top} - (Tf_{m,top}\ \ h)}{Tf_{F,top} + (Rf^{e}_{m,base}\ \ h^2)} \tag{5.49}$$

where:

r is the moment carry-over factor from the top to the base of the wall segment, ($r = m_{base}/m_{top}$),

$Tf_{F,top}$ is the translational flexibility due to force at the top of the wall segment,

$Tf_{m,top}$ is the translational flexibility due to moment at the top of the wall segment, and

$Rf^{e}_{m,base}$ is the total or effective rotational flexibility due to moment at the base of the wall segment (assumed to be already known).

Once the carry-over factor is determined, the rotation at the top of the wall segment is calculated as the sum of the base rotation in addition to the rotation caused by the force and moment applied at the top of the wall segment. Furthermore, by setting a unit value for the top moment, the top rotation amounts to the effective rotational flexibility that accounts for the correction of force at the upper floor:

$$\theta_{top} = \theta_{base} + \left(m_{top} \;\; Rf_{m,top}\right) + \left(F_{top} \;\; Rf_{F,top}\right) \tag{5.50}$$

$$\rightarrow \theta_{top} = \left[Rf^{e}_{m,base} \;\; r \;\; m_{top}\right] + \left(m_{top} \;\; Rf_{m,top}\right) + \left[\frac{m_{top}\left(r-1\right)}{h} \;\; Rf_{F,top}\right] \tag{5.51}$$

$$\rightarrow Rf^{e}_{m,top} = \left[Rf^{e}_{m,base} \;\; r\right] + \left(Rf_{m,top}\right) + \left[\frac{\left(r-1\right)}{h} \;\; Rf_{F,top}\right] \tag{5.52}$$

where:

$Rf_{F,top}$ is the rotational flexibility due to force at the top of the wall segment,

$Rf_{m,top}$ is the rotational flexibility due to moment at the top of the wall segment, and

$Rf^{e}_{m,top}$ is the total or effective rotational flexibility due to moment at the top of the wall segment.

To recap, correcting the force at one floor generates a series of moments at the floors below it. Assuming the displacements at the lower levels are fixed, the moment-induced rotation at these floors is accounted for by updating the rotational flexibility as per the outlined procedure. This is crucial to maintain the rotational equilibrium at the interface between the floors as part of the upward propagating compatibility procedure. It is worth noting that the derived effective rotational flexibility at the top of the wall segment is function of its equivalent at the base. Hence, as the forces are corrected at a given storey, the process of updating the rotational flexibility at the lower floors starts at the bottom where the effective rotational flexibility is zero (fixed base) and moves up the height of the building.

Last, it is worth noting that the effective rotational flexibility (due to moment) obtained in this section is adopted to obtain the increment in the translational and the rotational flexibility (due to force) to accommodate the influence of the flexible base. Hence, Equations 5.46 and 5.47 are accordingly updated by rather using the effective rotational flexibility (due to moment) at the base.

5.3.2.7 Integrated frequency analysis approach

As a brief recap, an arbitrary mode shape consisting of two translational and one rotational accelerations is applied at a predefined point at each storey. The corresponding inertia forces are calculated by Newton's second law and the cumulative storey forces are accordingly calculated at each level.

The procedure starts by initiating equilibrium between the applied loads and the internal forces in the walls. The process consists of analysing the wall segment at each floor separately, starting from the top floor and moving down the height of the building.

At the first instance, the initial force distribution in the walls obtained at equilibrium is imprecise by virtue of using a simplified approximation for the wall stiffness, thus prompting corrective measures in order to reinstate compatibility. Within the process, it has been shown that the presence of a flexible base increases the rotational and translational flexibility (due to force) at the top of the wall segment. Hence, this effect is incorporated into the procedure in line with enforcing compatibility. Furthermore, as previously noted, correcting the forces at the current level produces a series of moments that alter the response at the levels beneath it. Again, this effect is integrated into the procedure by updating the rotational flexibility (due to moment) at the lower floors to account for correcting the force at upper levels.

Before proceeding into the next step of the static procedure, it is worth highlighting the sequential order of events up to this stage. The procedure begins by imposing static equilibrium starting from the top floor and moving downwards. Correcting the forces to enforce compatibility at the current level has a significant influence on the lower floors. Therefore, the strategy implemented to restore compatibility should proceed from the bottom floor and propagate upwards, opposed to the satisfaction of equilibrium which propagates downwards. A flowchart summarising the static analysis procedure is presented in Figure 5.10.

The floor resultant displacements are subsequently evaluated at each storey using the linear transformation that connects the displacements of the walls to the floor resultants in line with the rigid diaphragm behaviour. Bearing in mind that the approach is initiated with an input mode shape vector and that the output is a displacement vector, the fundamental frequency of vibration (the eigenvalue) is estimated by evaluating Rayleigh's quotient in the context of the inverse vector iteration method. The floors displacements obtained are then normalised and input as the newly applied mode shape, and the procedure is repeated to deliver an updated estimate of the eigenvalue. Consequently, the iterative process continues until convergence into the fundamental mode shape and frequency of vibration of the building. In view of this, a summary of the frequency analysis procedure is provided in Figure 5.11.

Finally yet importantly, it is worth noting that for an arbitrary input mode shape, a few iterations are required in order to enforce equilibrium and compatibility requirements at all storeys. This process is computationally expensive as a single iteration performed to estimate the eigenvalue encompasses several iterations required to impose equilibrium and compatibility requirements. Towards reducing the computational effort and achieving a faster convergence, the iterations required to find the eigenvalue are coupled with those needed to solve the static problem. Accordingly, once an arbitrary mode shape is applied, at each attempt (a single iteration) made to solve the static problem, the floor resultant displacements are calculated and normalised, even though equilibrium/compatibility requirements are yet to be met. Subsequently, the new mode shape is input at the first step and the procedure is repeated until convergence. This is reflected in Figure 5.12 which presents a flowchart of the integrated approach that combines the static and frequency analyses. This is more advantageous than the ordinary approach

that involves a series of sub-iterations needed to solve the static problem within every iteration required to estimate the eigenvalue. Indeed, coupling the iterations substantially reduces the computational demand, with the approach requiring only a few iterations to converge into the fundamental mode shape and the corresponding fundamental frequency.

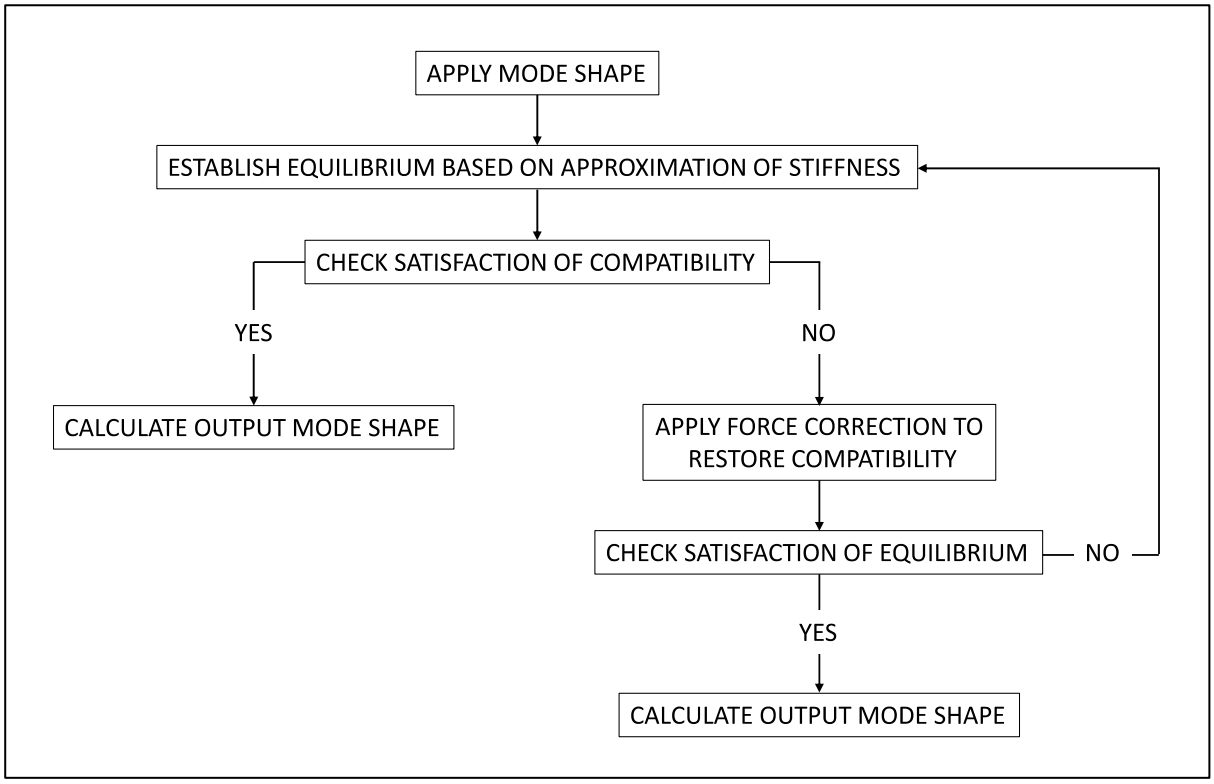


Figure 5.10: Flowchart of the static analysis procedure

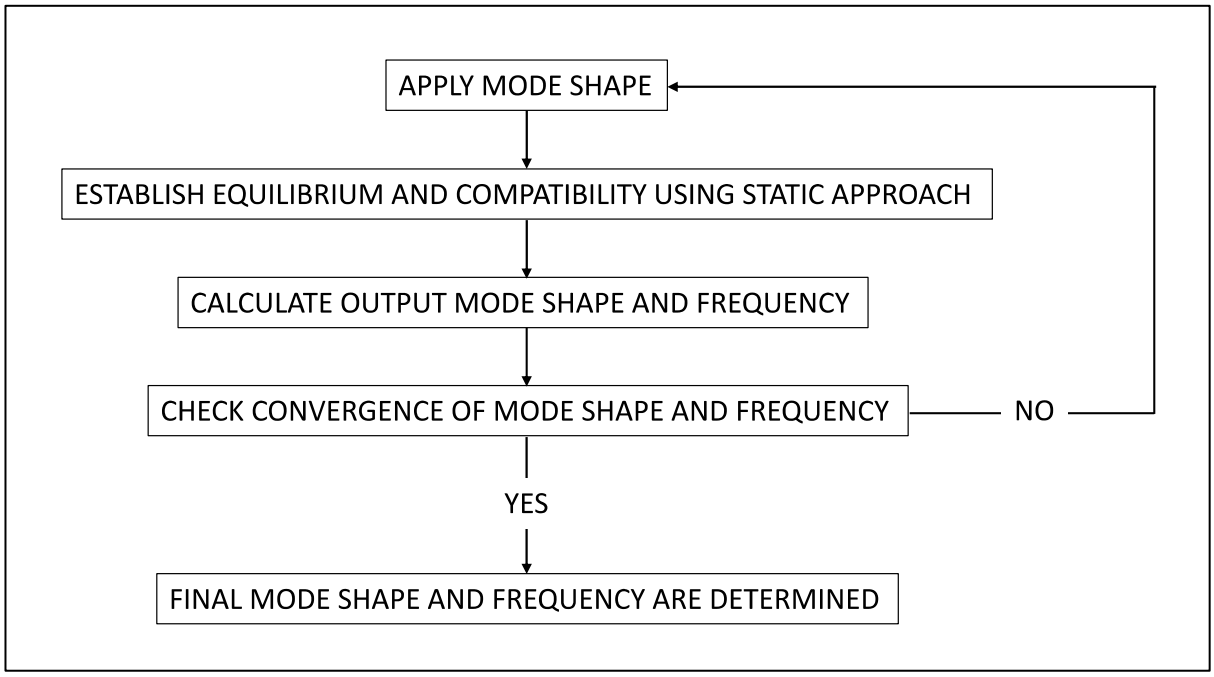


Figure 5.11: Flowchart of the frequency analysis procedure

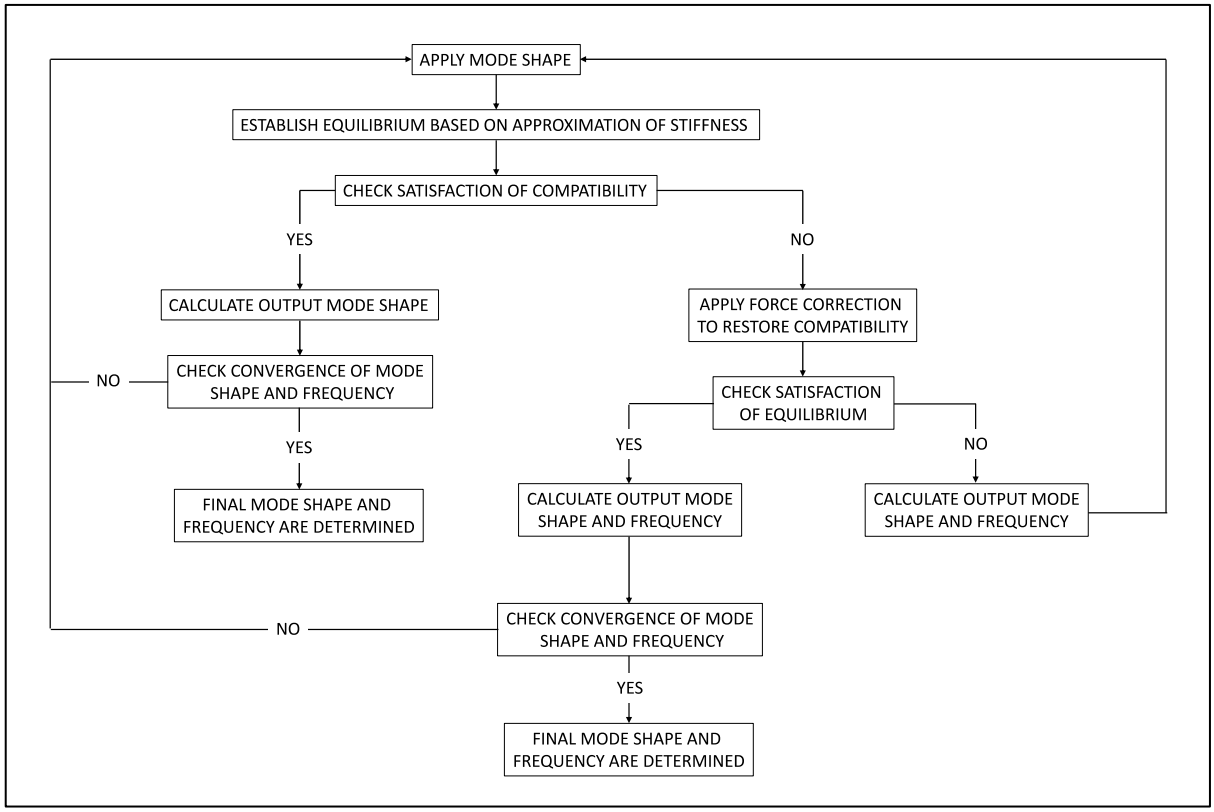


Figure 5.12: Flowchart of the integrated approach combining the iterations of the static and frequency analyses

5.3.2.8 Finding the vibration characteristics of higher modes

The procedure developed in the previous section relies mainly on the concept of the inverse vector iteration method which normally converges to the fundamental mode having the smallest eigenvalue. This is due to the fact that after each iteration, the components of higher modes are further reduced in contrast to the first modal component having the smallest eigenvalue (Chopra, 2014). In this respect, components of the first mode need to be taken out of the starting vector in order to achieve convergence into the next mode in line with the second lowest eigenvalue. It is worth noting that the second mode might not necessarily have the highest mass participation in the orthogonal direction. Higher modes are required in this case, and the procedure requires filtering out all the lower modes components to trigger convergence into the anticipated mode. The process is continued until finding the fundamental mode having the highest mass participation in the orthogonal translational direction.

The following discussion illustrates the reasons behind the convergence of the inverse vector iteration method towards the fundamental mode, such that the procedure can be appropriately modified to exact convergence into higher modes.

To begin with, as the displacement vector is written in the form of a mode shape vector multiplied by a harmonic function, the equation of motion is reformed to the eigenvalue form which is solved to find

out all the eigenpairs (mode shape and frequency) of the natural modes of vibration of the system (Chopra, 2014). The number of solutions (eigenvalues) is equal to the order of the mass and stiffness matrices which basically represents the number of DOFs in the system. For the n^{th} mode of vibration, the eigenvalue equation can be written and rearranged to the following format which is needed later to prove the first-mode convergence theory:

$$[K]\{\phi_n\} = \lambda_n [m]\{\phi_n\} \quad \rightarrow \quad [K]^{-1}[m]\{\phi_n\} = \frac{1}{\lambda_n}\{\phi_n\} \tag{5.53}$$

Applying the previous discussion in the context of the inverse vector iteration method and rewriting the initial trial mode shape vector in terms of the modal coordinates, the displacement vector generated at the end of the first iteration is also expressed in terms of the modal coordinates. Combining the outcome with the rearranged form of the eigenvalue equation provides a systematic expression of the output displacement vector in terms of the modal coordinates and the first-mode eigenvalue:

$$[K]\{\bar{\phi}\}_{t2} = [m]\{\phi\}_{t1} \tag{5.54}$$

$$\{\phi\}_{t1} = \sum_{k=1}^{N} \{\phi_k\} q_k \tag{5.55}$$

$$\rightarrow \{\bar{\phi}\}_{t2} = \sum_{k=1}^{N} \left([k]^{-1}[m]\{\phi_k\} q_k \right) \tag{5.56}$$

$$\rightarrow \{\bar{\phi}\}_{t2} = \frac{1}{\lambda_1} \sum_{k=1}^{N} \left(\frac{\lambda_1}{\lambda_k} \{\phi_k\} q_k \right) \tag{5.57}$$

where:

$\{\phi\}_{t1}$ is the trial vector input at the start of the procedure,

$\{\bar{\phi}\}_{t2}$ is the un-normalised displacement vector output at the end of the first iteration,

$\{\phi_k\}$ is the eigenvector (mode shape vector) of the k^{th} mode of vibration, and

q_k is the modal coordinate (a scalar) which represents the contribution of the k^{th} mode.

Maintaining the same analogy as the inverse vector iteration method is continued, the output displacement vector obtained after n iterations is also expressed in terms of the first-mode eigenvalue and the modal coordinates as follows:

$$\{\bar{\phi}\}_{t,n+1} = \frac{1}{(\lambda_1)^n} \sum_{k=1}^{N} \left(\left(\frac{\lambda_1}{\lambda_k} \right)^n \{\phi_k\} q_k \right) \tag{5.58}$$

Noting that λ_1 is the smallest of all the eigenvalues being that of the fundamental mode, then it is obviously noted that the components of the first or fundamental mode would prevail as the number of iterations increases. Indeed, the ratio $(\lambda_1 / \lambda_k)^n$ becomes negligible as the number of iterations n increases. As a result:

$$\left\{\bar{\phi}\right\}_{t,n+1} \rightarrow \frac{1}{\left(\lambda_1\right)^n} \left\{\phi_1\right\} q_1 \;\; as \; n \rightarrow \infty \tag{5.59}$$

Hence, it is proven that the procedure would always converge to the lowest eigenvalue present in the trial vector (Chopra, 2014). In that regard, if the components of the fundamental mode are eliminated from the trial vector, the procedure would then converge into the mode having the second lowest eigenvalue. In this case, the trial vector becomes orthogonal to the first mode as it only comprises second- and higher-mode components:

$$\left\{\phi\right\}_{t1} = \sum_{k=2}^{N} \left\{\phi_k\right\} q_k = \left\{\phi_2\right\} q_2 + \left\{\phi_3\right\} q_3 + ... + \left\{\phi_N\right\} q_N \tag{5.60}$$

To recap, removing the first-mode components from the trial vector would make it orthogonal to the first mode and would force the procedure to converge into the second mode. Accordingly, the procedure involves starting with an arbitrary trial vector and adjusting it to become orthogonal to the first mode. The adjustment consists of filtering the components of the first mode out of the trial vector as explained in the following:

$$\left\{\phi_1\right\}^T \left[m\right] \left\{\bar{\phi}_2\right\} \neq 0 \tag{5.61}$$

$$\rightarrow \left\{\phi_1\right\}^T \left[m\right] \left(\left\{\bar{\phi}_2\right\} + a_1 \left\{\phi_1\right\}\right) = 0 \tag{5.62}$$

$$\rightarrow \; a_1 = - \frac{\left\{\phi_1\right\}^T \left[m\right] \left\{\bar{\phi}_2\right\}}{\left\{\phi_1\right\}^T \left[m\right] \left\{\phi_1\right\}} \tag{5.63}$$

$$\rightarrow \left\{\phi_2\right\} = \left\{\bar{\phi}_2\right\} + a_1 \left\{\phi_1\right\} \tag{5.64}$$

where:

$\left\{\phi_1\right\}$ is the previously established fundamental mode of vibration,

$\left\{\bar{\phi}_2\right\}$ is the initial trial vector adopted to determine the second mode of vibration,

$\left\{\phi_2\right\}$ is the updated trial vector used to determine the second mode (cleared of first-mode components), and

a_1 is a correction factor applied to filter out the first-mode components.

The updated vector is orthogonal with respect to the fundamental mode vector and exacts convergence into the second mode of vibration. It is worth noting that the first mode components need to be filtered out at every successive iteration. Hence, the output displacement vector produced after each iteration is refined before being input in the next iteration, and the process continues towards convergence into the second mode of vibration.

It is worth noting that the procedure can be further expanded to find the rest of the higher modes as well. For instance, filtering the components of the first and second modes out of the trial vector would force the procedure to converge into the third mode and so on. It is worth noting that the target of this research is to find the mode having the highest mass participation in each of the two main horizontal directions. These can be referred to as the translational fundamental mode of vibration in each of the two main horizontal directions, and occasionally neither of these two modes is the global fundamental mode of vibration that is achieved at the first convergence. In this regard, buildings having torsional or vertical irregularities might exhibit a significant torsional behaviour that could predominate the fundamental mode. In this case, higher modes are sought after since the target is to establish the translational fundamental mode of vibration in each horizontal direction and to perform the pushover analysis accordingly in the context of the CSM.

In general, if the $(n+1)^{th}$ mode needs to be determined, the preliminary trial vector is cleared of the components of the first through to the n^{th} mode.

$$\{\phi_1\}^T [m] \left(\{\bar{\phi}_{n+1}\} + a_1\{\phi_1\} + a_2\{\phi_2\} + ... + a_n\{\phi_n\}\right) = 0$$
$$\{\phi_2\}^T [m] \left(\{\bar{\phi}_{n+1}\} + a_1\{\phi_1\} + a_2\{\phi_2\} + ... + a_n\{\phi_n\}\right) = 0$$
$$\vdots$$
$$\{\phi_n\}^T [m] \left(\{\bar{\phi}_{n+1}\} + a_1\{\phi_1\} + a_2\{\phi_2\} + ... + a_n\{\phi_n\}\right) = 0$$

$$\{\phi_{n+1}\} = \{\bar{\phi}_{n+1}\} + a_1\{\phi_1\} + a_2\{\phi_2\} + ... + a_n\{\phi_n\} \quad (5.65)$$

5.4 Inclusion of Original Frame

The simplified procedure developed in this chapter provides a practical means to determine the vibration properties of multi-storey RC buildings retrofitted with shear walls. In fact, the buildings targeted by this research mostly consist of a frame structure with no shear walls or a proper lateral-force resisting system and are therefore characterised by little to no resistance against earthquake loading. As a result, it is expected that the performance of the retrofitted structure is mainly dictated by the retrofitting system. Accordingly, the fundamental mode (and higher modes if needed) are determined assuming that the shear walls are the principal source of resistance to seismic loading, with the influence of the

frame being secondary. As such, the influence of the frame is reasonably approximated assuming that the mode shape is determined by the wall-system, as obtained using the simplified analysis procedure proposed earlier in this chapter.

As a first step, the response of the retrofitted structure is assumed to be predominated by the strengthening walls due to the vulnerability of the original structure. Hence, the mode shape is determined by considering the reinforcing shear walls to dictate the response of the structure. This permits to approximate the effective stiffness of the structure which in effect is attributed to the walls as per the following:

$$\omega^2 = \frac{\{\phi\}^T [k_w] \{\phi\}}{\{\phi\}^T [m] \{\phi\}} \tag{5.66}$$

where:

ω is the circular frequency of vibration of the structure, which is attributed to the contribution of the walls,

$\{\phi\}$ is the mode shape vector, which is based on the reinforcing walls only,

$[m]$ is the mass matrix, and

$[k_w]$ is the stiffness matrix that is attributed to the walls.

It is worth noting that the main unknown in the equation in the form of the stiffness matrix can only be assembled if all the natural modes and the respective frequencies are obtained. Whilst this may be considered as an extension of the simplified approach, this is a cumbersome process considering the number of DOFs in a multi-storey building. As a result, the effective stiffness of the whole structure is considered instead and is straightforwardly calculated when the previous equation is rewritten as the ratio of the effective stiffness to the effective mass of the system. Accordingly, the effective stiffness (numerator in the main equation) provided by the walls is obtained:

$$\omega^2 = \frac{\{\phi\}^T [k_w] \{\phi\}}{\{\phi\}^T [m] \{\phi\}} = \frac{K_w}{M} \rightarrow K_w = \omega^2 M \tag{5.67}$$

At this stage, it is worth noting that the original frame and the retrofitting system (walls) are envisaged as two structural components acting in parallel. Hence, both contribute to the equivalent stiffness of the system and both resist the applied seismic loads while they experience the same displacement. To recap, the mode shape of the whole system is calculated using the simplified procedure and assuming the mode shape to be dictated by the walls. The frequency of vibration obtained in the process is that attributed to the walls only, which permits to establish the effective stiffness of the walls as explained earlier. The

previously determined mode shape is then applied to the original frame as a series of applied displacements, and the resultant reaction forces are evaluated. The reaction forces obtained are practically the product of the displacement and the stiffness of the frame. This allows to calculate the effective stiffness and the frequency contribution attributed to the original frame (Figure 5.13).

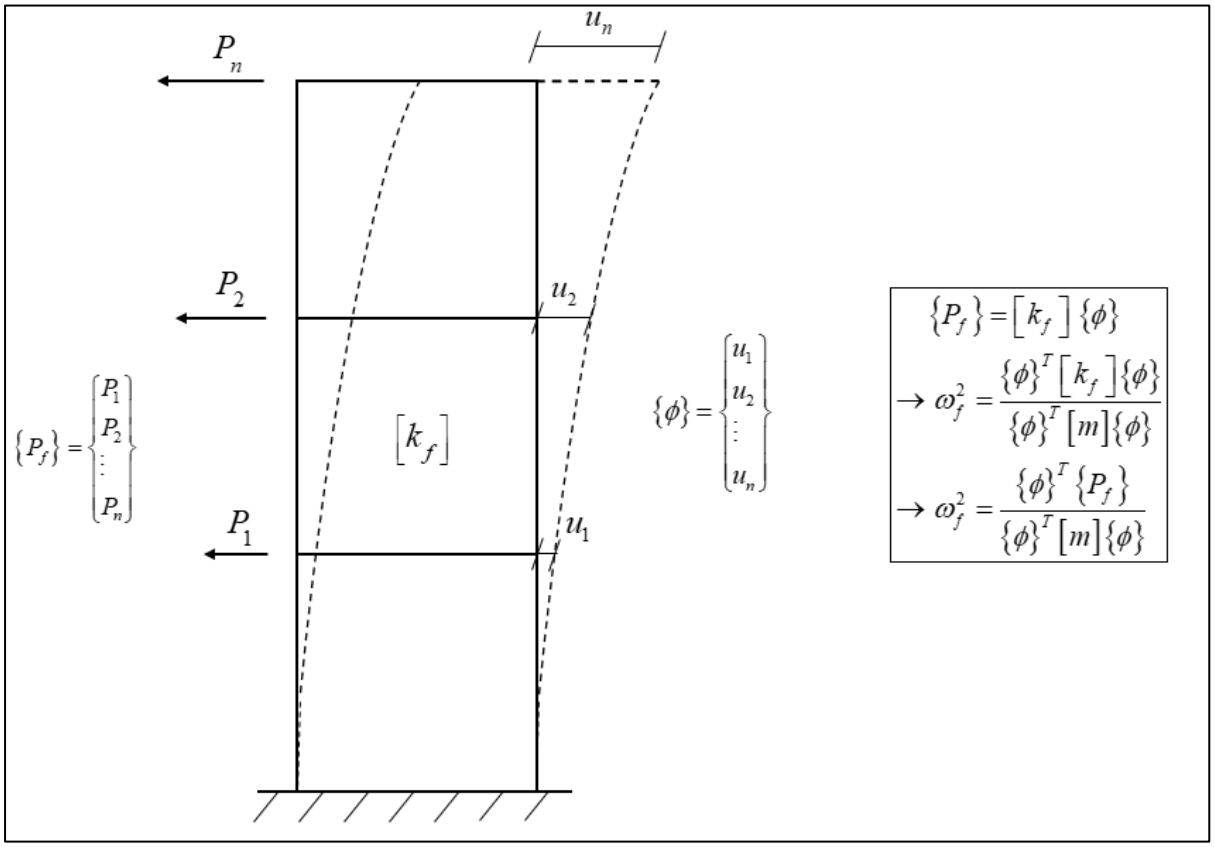


Figure 5.13: Illustrating the process of finding the stiffness contribution of the original frame

Consequently, the overall frequency of vibration of the building is calculated by including the contribution of the frame as per the following:

$$\omega_t^2 = \frac{K_w + K_f}{M} = \frac{\{\phi\}^T [k_w] \{\phi\} \; + \; \{\phi\}^T [k_f] \{\phi\}}{\{\phi\}^T [m] \{\phi\}} \tag{5.68}$$

where:

ω_t is the total circular frequency of vibration of the whole structure,

$[k_f]$ is the stiffness matrix that is attributed to the frame,

K_w is the effective stiffness of the walls,

K_f is the effective stiffness of the original frame, and

M is the effective mass of the system.

The following discussion introduces a brief illustrative example of the outlined strategy. The six-storey frame building considered has a regular and uniform floor plan and is seismically retrofitted by adding shear walls as shown in the plan (Figure 5.14). Columns aligned on the edge have a uniform cross-section of 200x600mm^2 while columns located inside the building have a uniform cross-section of 200x700mm^2 at all floors. The walls added have a thickness of 200mm and the length and location are shown on the plan. It is noted that the floor plan selected is regular, and the walls are randomly added since the objective of this example is limited to presenting the process of integrating the effect of the frame into the analysis. A uniform floor height of 3m is considered at all storeys.

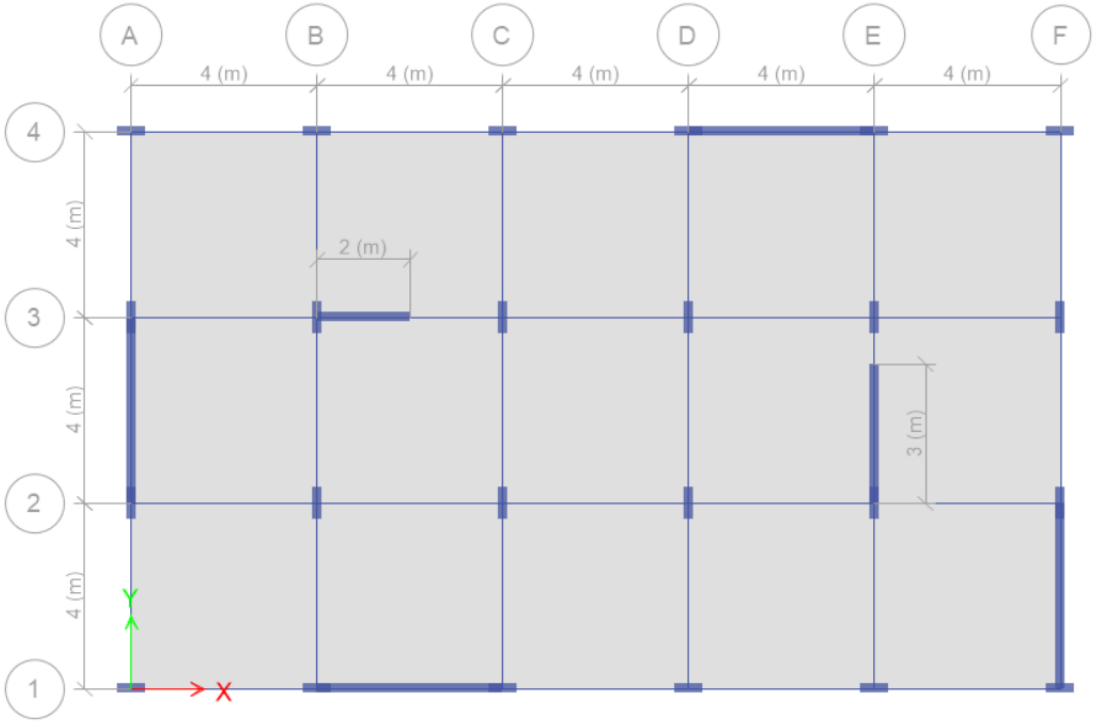


Figure 5.14: Typical floor plan of original frame building along with the reinforcing walls

The fundamental mode shape is calculated assuming the shear walls are the only component contributing to lateral resistance, noting that the results nearly expressed a perfect correlation with those obtained from ETABS (Table 5-1). The corresponding frequency of vibration obtained corresponds to the stiffness pertaining to the walls. In a separate model, the calculated mode shape is applied to the original frame (same plan but without the walls) in the form of a vector of displacements assigned at the DOFs. The resultant reaction forces and effective frame stiffness are calculated accordingly, and consequently the total frequency of vibration is evaluated to include the effect of the frame (Table 5-2).

Table 5-1: Fundamental mode shape and frequency based on the walls

	ETABS: ω = 7.731 rad/s			Integrated Approach: ω = 7.731 rad/s		
Storey	**UX (m)**	**UY (m)**	**RZ (rad)**	**UX (m)**	**UY (m)**	**RZ (rad)**
Storey1	0.0498	-0.0009	0.0002	0.0498	-0.0011	0.0001
Storey2	0.1708	-0.0035	0.0005	0.1708	-0.0039	0.0005
Storey3	0.3434	-0.0071	0.0009	0.3433	-0.0078	0.0009
Storey4	0.5491	-0.0116	0.0014	0.5490	-0.0124	0.0014
Storey5	0.7721	-0.0161	0.0019	0.7720	-0.0175	0.0020
Storey6	1	-0.0210	0.0026	1	-0.0226	0.0026

Table 5-2: Calculating the stiffness of the frame and the effective frequency of vibration of the building

Effective Mass	Circular Frequency (Walls only)	Effective Stiffness of Walls	Effective Stiffness of Frame	Effective Circular Frequency of The Building		Effective Frequency (ETABS)
$\phi^T m \phi$	ω^2	K_w	K_f	ω^2_t	ω_t	ω_t
557836.1	59.77	33340951	10914669	79.33	8.91	8.95

It is observed that the total (effective) circular frequency of the whole building is almost the same as the one obtained from ETABS which illustrates the accuracy of the method. Hence, the procedure applied presents a simple and reliable means to incorporate the contribution of the original frame having obtained the vibration characteristics of the retrofitted building with respect to the shear walls alone. It is also worth noting that the stiffness amounting to the shear walls is larger than that pertaining to the original frame with an approximate ratio of 3:1. These results reinforce the assumption regarding the domination of the shear walls on the response of the retrofitted building.

To summarise, the mode shape is calculated by considering the shear walls contribution, and the stiffness of the frame is subsequently incorporated in order to obtain the frequency of vibration of the retrofitted building in a simplified manner. This strategy further enhances the practicality of the simplified approach and sets the stage for the subsequent work on simplified pushover analysis, and it contributes to the ultimate objective of developing a simplified strategy to retrofit seismically substandard buildings.

Last, the efficiency of the integrated frequency analysis approach is investigated through a detailed illustration of the iterations required for convergence of the procedure into the mode shape and frequency of vibration of the fundamental mode (Table 5-3). To this end, the procedure required around 5-6 iterations to converge, noting that the 7^{th} and 8^{th} iterations are performed since the UY component was still subject to a slight variation from one iteration to another. The results illustrate the efficacy of the developed approach with only a few iterations required to achieve convergence into the eigenpair of the fundamental mode.

Table 5-3: Illustrating the iterative process towards convergence of the integrated frequency analysis approach

	Initial Arbitrary Mode Shape			Iteration 1: ω = 7.168 rad/s			Iteration 2: ω = 7.618 rad/s		
Storey	**UX (m)**	**UY (m)**	**RZ (rad)**	**UX (m)**	**UY (m)**	**RZ (rad)**	**UX (m)**	**UY (m)**	**RZ (rad)**
Storey1	0.1667	0.001	0.091	0.0519	-0.0115	0.0109	0.0501	-0.0087	0.0043
Storey2	0.3333	0.001	0.182	0.1753	-0.0374	0.0368	0.1713	-0.0299	0.0146
Storey3	0.5	0.001	0.273	0.3489	-0.0734	0.0732	0.3439	-0.0602	0.0293
Storey4	0.6667	0.001	0.364	0.5539	-0.1157	0.1162	0.5495	-0.0962	0.0468
Storey5	0.8333	0.001	0.454	0.7748	-0.1610	0.1625	0.7723	-0.1353	0.0658
Storey6	1	0.001	0.545	1	-0.2071	0.2097	1	-0.1753	0.0852

Table 5-3 (Continued)

	Iteration 3: ω = 7.688 rad/s			Iteration 4: ω = 7.713 rad/s			Iteration 5: ω = 7.722 rad/s		
Storey	**UX (m)**	**UY (m)**	**RZ (rad)**	**UX (m)**	**UY (m)**	**RZ (rad)**	**UX (m)**	**UY (m)**	**RZ (rad)**
Storey1	0.0498	-0.0071	0.0002	0.0498	-0.0049	0.0002	0.0498	-0.0018	0.0001
Storey2	0.1708	-0.0245	0.0008	0.1708	-0.0167	0.0007	0.1708	-0.0062	0.0005
Storey3	0.3433	-0.0492	0.0016	0.3433	-0.0335	0.0013	0.3433	-0.0124	0.0010
Storey4	0.5491	-0.0786	0.0025	0.5490	-0.0536	0.0021	0.5490	-0.0199	0.0015
Storey5	0.7720	-0.1106	0.0035	0.7720	-0.0754	0.0029	0.7720	-0.0279	0.0022
Storey6	1	-0.1432	0.0045	1	-0.0976	0.0038	1	-0.0361	0.0028

Table 5-3 (Continued)

	Iteration 6: ω = 7.728 rad/s			Iteration 7: ω = 7.730 rad/s			Iteration 8: ω = 7.731 rad/s		
Storey	**UX (m)**	**UY (m)**	**RZ (rad)**	**UX (m)**	**UY (m)**	**RZ (rad)**	**UX (m)**	**UY (m)**	**RZ (rad)**
Storey1	0.0498	-0.0013	0.0001	0.0498	-0.0012	0.0001	0.0498	-0.0011	0.0001
Storey2	0.1708	-0.0043	0.0005	0.1708	-0.0040	0.0005	0.1708	-0.0039	0.0005
Storey3	0.3433	-0.0086	0.0009	0.3433	-0.0080	0.0009	0.3433	-0.0078	0.0009
Storey4	0.5490	-0.0137	0.0014	0.5490	-0.0128	0.0014	0.5490	-0.0124	0.0014
Storey5	0.7720	-0.0193	0.0020	0.7720	-0.0180	0.0020	0.7720	-0.0175	0.0020
Storey6	1	-0.0250	0.0026	1	-0.0234	0.0026	1	-0.0226	0.0026

Chapter 6 Pushover Response and Contribution of the Original Structure

6.1 Introduction

This research presents a novel simplified approach for the practical assessment and retrofitting of substandard multi-storey reinforced concrete (RC) buildings located in seismic hazard regions. In this context, most structures including reinforced concrete buildings would likely respond inelastically under a major earthquake (Campbell & Bozorgnia, 2004), where the seismic response is most realistically represented by the computationally expensive nonlinear dynamic analysis. Towards reducing such computational demands, a simplified modelling approach is developed based on the capacity spectrum method (CSM) (ATC, 1982, 1996; Freeman, 1998). The CSM utilises nonlinear static pushover analysis in conjunction with the dynamic characteristics of a structure to establish whether the seismic capacity of the structure meets the demands of seismic ground motion. The final output of the CSM is a graphical representation of the capacity of a structure versus the demands of earthquake loading on the structure, hence permitting a visual evaluation of the response of the structure when subjected to the specified ground motion.

This chapter focuses mainly on nonlinear static pushover analysis (NSPA) which is a major constituent of the CSM. NSPA allows to track the progressive and localised damage of the structural components through the manifestation of plastic hinges at localised points (the most stressed elements) in the structure. Despite the simplicity of the method compared to NLTHA which is computationally demanding since it requires applying multiple ground motion records and averaging the response of the structure, NSPA is generally performed using a wide range of computerised software (SAP2000, ETABS, etc.). Flexural and shear hinges are manually assigned at the ends of beams and columns in order to monitor the exceedance of the ultimate deformation capacity of these elements. The analysis progresses and plastic hinges form successively until reaching the target displacement at the monitoring point or attaining the plastic capacity of the structure.

In light of this, this chapter presents a simplified approach based on the application of static analysis to estimate the pushover response of RC frame buildings reinforced with shear walls. A few assumptions are accordingly made in line with simplifying the anticipated procedure. The chapter provides a detailed presentation of the procedure which attempts at finding the pushover response by monitoring the formation of plastic hinges at the base of vertical elements. In the attempt to reduce the computational efforts, the procedure is developed on the basis of determining the pushover response with respect to the walls alone and on incorporating the effect of the original frame in a simplified manner. In view of this, the results obtained using the simplified approach are shown to have a good correlation with the pushover response obtained directly from the computerised software ETABS. Furthermore, the ultimate

collapse load obtained using the procedure correlates well with that obtained from plastic limit analysis. Accordingly, the chapter begins with a brief illustration of the plastic limit analysis which aims at finding the maximum load the structure can sustain before collapsing. The discussion is then concluded by devising a strategy to incorporate the additional effect of the original frame into the pushover response.

The finding of this chapter combined with the previous work on simplified frequency analysis allow for a faster and streamlined application of the CSM and marks a step forward towards achieving the ultimate objective of developing a retrofitting strategy for RC buildings.

6.2 Plastic Limit Analysis

Plastic limit analysis, also referred to as plastic collapse analysis, is generally performed to find the collapse load or the ultimate load the structure can sustain before failing (Horne, 1971). The method serves to find the ultimate state of collapse without determining the sequence of formation of the plastic hinges. In this respect, the structure is characterised by three main conditions that need to be activated or satisfied at plastic collapse:

1. Mechanism condition: the structure must develop a sufficient number of plastic hinges that would render it a "mechanism" or an unstable form that cannot resist any additional applied loading.
2. Equilibrium condition: static equilibrium conditions must be satisfied at collapse, such that the internal forces, including plastic bending moments at the hinges, balance the applied loads.
3. Yield condition: the maximum bending moment that can develop in any structural element cannot exceed the plastic bending moment capacity of the member.

In general, there are two strategies widely adopted to find the collapse load, namely the static and the kinematic approaches. The static approach mainly relies on equilibrium and yield conditions such that the collapse load is solved for by applying static equilibrium requirements, noting that the moment developed in the structural elements cannot exceed the plastic capacity. The kinematic approach relies on conservation of energy which stipulates that the external work done by the loads is balanced by the internal work represented by the plastic dissipation of energy. The kinematic approach is generally implemented through the principle of virtual work and is widely used to find the plastic collapse load. However, it only allows to evaluate the collapse load for a predefined collapse mechanism. Therefore, the process using the kinematic approach mostly requires determining all possible mechanisms in order to determine the true collapse mechanism. In this regard, most structures could manifest more than one potential mechanism with only one of those being the actual collapse mechanism characterised by the lowest collapse load factor.

In the context of finding the collapse mechanism and load factor, Greenberg & Prager (1949) and Horne (1950) have defined three basic theorems:

1. Static theorem: also known as the lower bound theorem and states that if both equilibrium and yield conditions are satisfied under a given load factor, then this load factor is either equal to or smaller than the actual collapse load.
2. Kinematic theorem: also known as the upper bound theorem and states that for a given mechanism, if the external work done by the loads is equal to the internal work associated with the dissipation of energy at the plastic hinges, then this load factor is either equal to or greater than the collapse load.
3. Uniqueness theorem: as the name implies, a given load factor is the real (unique) collapse load factor if it simultaneously satisfies the requirements of mechanism, equilibrium, and yielding conditions.

In this section, the static approach is applied in order to find the collapse load, under the main assumption that plastic flexural hinges can only form at the base of the walls. It is worth noting that this section does not include a separate check to ensure that the walls have sufficient capacity to prevent a plastic mechanism occurring at upper floors, since the current discussion serves to illustrate the plastic limit analysis. However, in subsequent chapters involving seismic retrofitting of existing buildings, the current assumption is checked by verifying that the bending moment at upper floors does not exceed the plastic capacity. Accordingly, equilibrium equations are set along with the yielding requirements which bound the bending moment at the base of the wall by the plastic capacity of the cross-section. Subsequently, the plastic collapse load factor and the associated base moments in the walls are automatically determined using the "Excel Solver", which automatically generates the set of moments that maximise the collapse load factor and satisfy the equilibrium equations and the boundary conditions. Assuming a three-component load is applied at each storey (Figure 6.1) and recalling that plastic hinges can only form at the base, static equilibrium is established between the applied loads and the bending moments at the base of the walls through the following equations:

$$\sum_{i=1}^{N}\left(\lambda P_{xi} z_i\right) = \sum M_x \tag{6.1}$$

$$\sum_{i=1}^{N}\left(\lambda P_{yi} z_i\right) = \sum M_y \tag{6.2}$$

$$\sum_{i=1}^{N}\left(\lambda M_{zi} z_i\right) = \sum\left(-M_x y + M_y x\right) \tag{6.3}$$

where:

P_{xi}, P_{xi}, & M_{zi} are the applied loads at the i^{th} floor,

z_i is the total height of the i^{th} floor measured from the base,

M_x are the bending moments at the base of walls oriented along the global X-axis,

M_y are the bending moments at the base of walls oriented along the global Y-axis, and

x & y are the distances from the centroid of the wall to the origin of application of the storey loads (Figure 6.2).

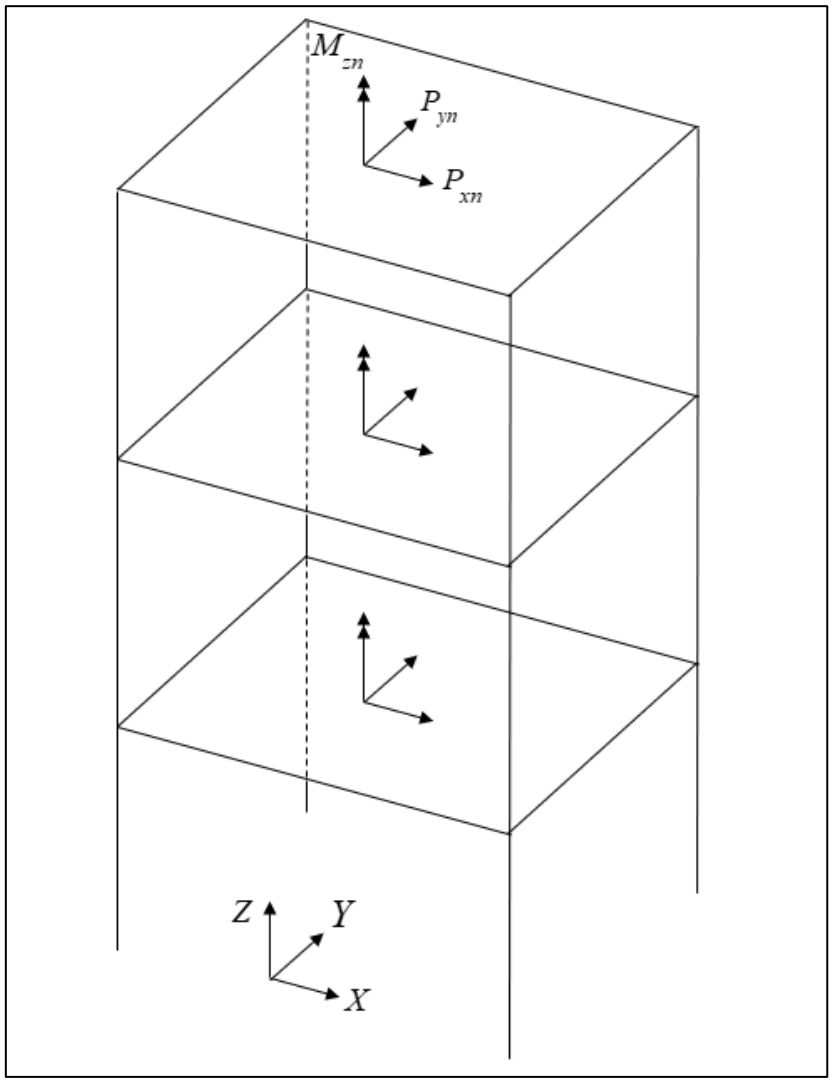


Figure 6.1: Typical 3-D representation of applied loads

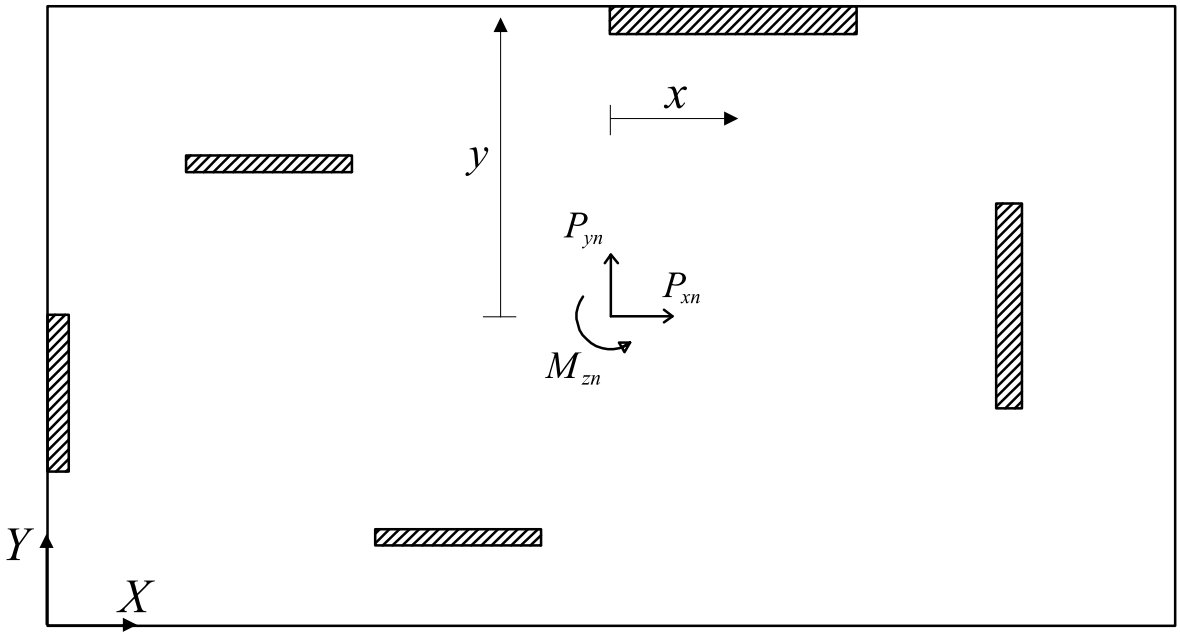


Figure 6.2: Typical floorplan and applied loading

It is worth noting that Equations (6.1) and (6.2) represent lateral equilibrium in the X and the Y directions respectively. Hence, the lateral loads applied in direction X in Equation (6.1) produce a bending moment along the X-axis and are accordingly balanced by the bending moments at the base of walls aligned in the X direction. Same analogy applies in Equation (6.2) which considers lateral equilibrium along the Y direction. Similarly, Equation (6.3) represents twisting equilibrium while considering a unit torsional rotation per meter of height. To this accord, the torsional rotation varies linearly across the height of the building and is equal to the storey height at each floor level. The left side of the equation represents the external work performed by the torsional loads, with z_i being equivalent to the corresponding torsional rotation at each level. This is balanced by the internal work on the right side of the equation, which consists of the product of the bending moment and the rotation at the base of the walls. To note that the base rotation for a wall aligned in direction X/Y is equal to the lateral displacement at the top floor in direction X/Y divided by the total height. For a linearly varying rotation and for a unit rotation per meter of height, the rotation at the top floor is equal to the total height of the building. This permits to establish the lateral displacement of the wall in the X/Y direction, which allows to express the base rotation of the walls aligned in directions X and Y in proportion to y and x respectively, with the latter representing the transverse distance from the point of application of the loads to the centre of the wall (Figure 6.2).

The equilibrium equations are applied along with the following conditions that implement the yielding requirements, such that no wall can develop a moment greater than the plastic capacity:

$$-M_{p1} \leq M_1 \leq M_{p1}$$

$$-M_{p2} \leq M_2 \leq M_{p2}$$

$$\vdots$$

$$-M_{pn} \le M_n \le M_{pn} \tag{6.4}$$

where:

$M_1 \cdots M_n$ represent the bending moment at the base along the longitudinal bending axis of walls, and these are equivalent to M_x and M_y in the equilibrium equations, and

$M_{p1} \cdots M_{pn}$ represent the plastic capacity at the base of the walls.

The collapse load factor is obtained using the "Excel Solver", with the unknown variables being the load factor λ and the moments M_x and M_y in the walls. Hence, the problem is automatically solved using the "Solver" feature which determines the moment values that would maximise the load factor λ while satisfying the conditional statements imposed by the yielding requirements.

6.3 Pushover Response Using Incremental Static Analysis

As reflected in the previous part, plastic limit analysis permits to determine the collapse load factor, yet the method gives no clue about the sequential formation of plastic hinges that amount to the development of the collapse mechanism. Hence, the full response en route to plastic collapse is obtained by performing the integrated nonlinear static pushover analysis (NSPA). NSPA permits to track the progressive and localised damage of the structural components through the manifestation of plastic hinges. As the load is incrementally increased, plastic hinges form in succession until the formation of a mechanism which signals complete collapse, as the redundant vertical members which have not reached their plastic capacity do not form a stable system that can resist the applied loading.

This section presents a simplified approach to estimate the pushover response of RC frame buildings reinforced with shear walls. The procedure relies on a direct application of static analysis to find the pushover response. In this regard, the following assumptions are made to simplify the requirements of the anticipated approach implemented to find the pushover response:

1. Plastic hinges are assumed to form only at the base of walls and columns.
2. The RC frame building is assumed to behave in a strong column-weak beam configuration. Accordingly, the sum of moment capacity of columns is expected to exceed the sum of the moment capacity of beams. As a result, plastic hinges are not expected to form at the end of columns and walls (apart from the base).
3. The pushover response is assumed to be predominated by the flexural deformations. Hence, only flexural hinges are assigned at the base of the walls/columns.

Taking into account the simplifying assumptions, the procedure involves applying a set of arbitrary loading to the structure. The pushover response is obtained by monitoring the sequential formation of

plastic hinges at the base as the load is incrementally increased. In this regard, the ultimate collapse load depends on the configuration of applied loads and most importantly on the configuration of redundant walls that can resist further increments of load. In this regard, this section is composed of two parts, the first of which introduces the possible configurations of redundant walls that are obtained at the end of the analysis. The second part presents a detailed description of the procedure established to determine the pushover response. It is worth noting that the procedure consists of determining the pushover response with respect to the walls alone and adding the effect of the frame in a simplified manner. Hence, the pushover response is first determined considering the walls to be the main source of earthquake resistance, and the overall pushover response is subsequently obtained by including the contribution of the original frame in a similar process to what is performed in the frequency analysis.

6.3.1 Configurations of walls

As discussed earlier, the load is incrementally increased in NSPA until the redundant walls cannot resist the applied loading. In this regard, a minimum set of three walls is required to resist arbitrary loading that might include torsional twisting as well as translation in both horizontal directions. The three walls cannot be aligned in the same direction (Figure 6.3a) and should not be concurrent (Figure 6.3b). The first configuration provides no resistance to loading in the transverse direction while the latter provides no resistance to torsional loads centred around the point of concurrency (intersection of the walls). Furthermore, if two of the three walls are collinear (aligned on the same line), then the configuration provides no torsional resistance (Figure 6.3c). The wall configuration in Figure 6.3d provides an arrangement of walls that can equilibrate any combination of lateral force/torsional moment loading.

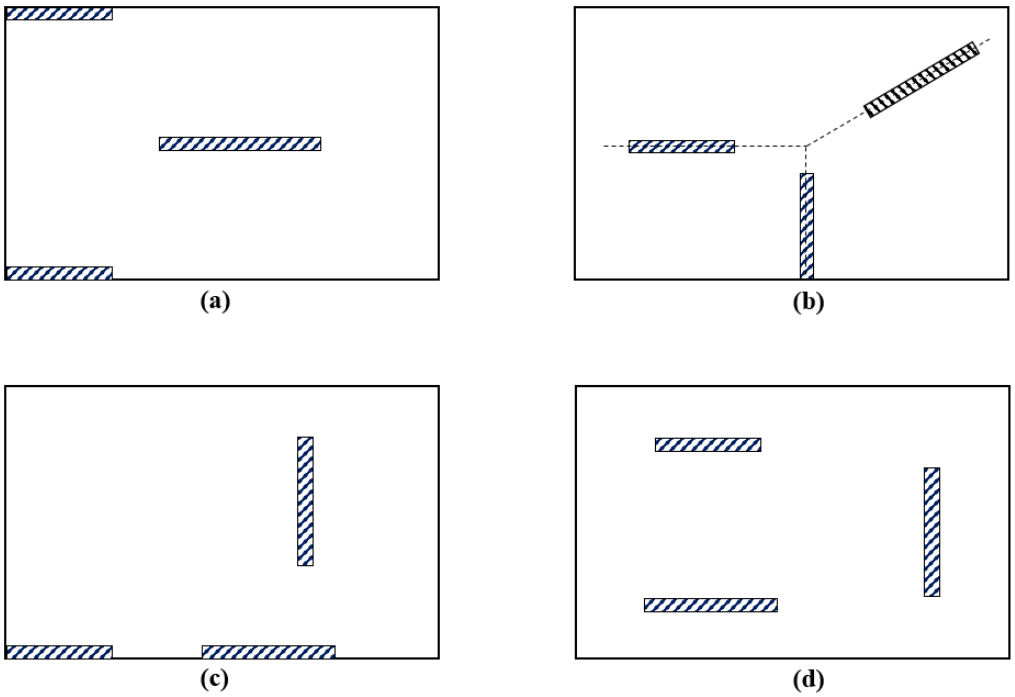


Figure 6.3: Configurations of walls

Accordingly, plastic hinges will form successively as the load is incrementally increased, and the analysis stops when the redundant walls (which have not reached their plastic capacity) provide an unstable configuration that cannot resist the applied loading.

6.3.2 Simplified approach

In line with the basic assumptions, the general procedure involves applying a three-component load at each storey. The response of the floor and the walls is then obtained from static analysis using the approach previously devised in Chapter 5 to determine the vibration characteristics. Once the shear forces and bending moments in the wall segments are obtained after satisfying both equilibrium and compatibility requirements, the moments at the base of the walls are established from:

$$m_{bot} = m_1 + \left(f_1 \times h_1\right) \tag{6.5}$$

where:

m_{bot} is the bending moment determined at the base of the wall,

m_1 is the bending moment at the top of the wall segment at the base (ground) level,

f_1 is the internal shear force in the wall segment at the base level, and

h_1 is the ground floor height.

The base moments are accordingly determined for each stage of load application. To note that the plastic capacity of each wall is already established based on the dimensions and reinforcement of the cross-section. Accordingly, the sequential formation of plastic hinges is traced through the exceedance of the plastic capacity at the base of the walls while the load is being incrementally increased.

As a starting point, a unit load factor is applied, and the response is obtained using the static procedure implemented in the frequency analysis in chapter 5. Calculating the base moments at this initial load permits to establish the yielding point or the initial load factor λ_1 which triggers the formation of the first plastic hinge (Figure 6.4):

$$\lambda_1 = \min\left(\frac{m_{pi}}{\left|m_{bot,i}\right|}\right) \tag{6.6}$$

where:

m_{pi} is the plastic bending moment capacity at the base of wall *i*, and

$m_{bot,i}$ is the bending moment generated at the base of wall *i* in response to an applied unit load factor.

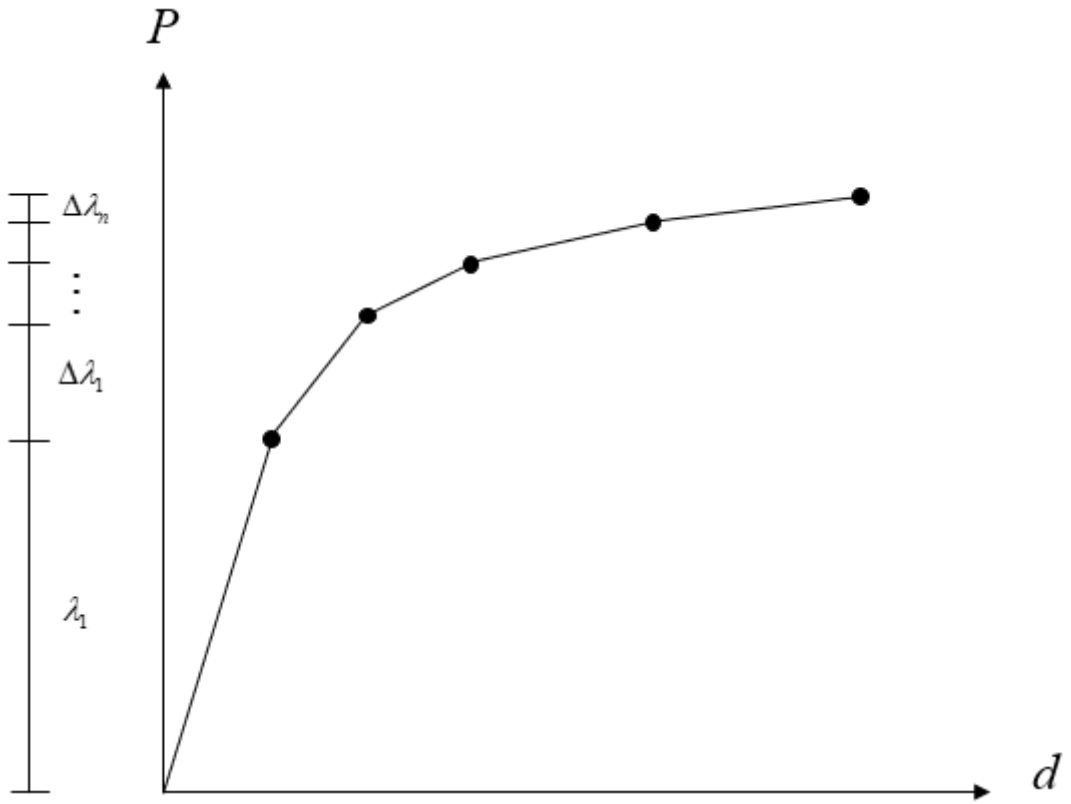


Figure 6.4: Typical pushover response obtained using the simplified approach

As the analysis continues, the wall that has reached its plastic capacity is replaced by a pinned support at the base, and the procedure aims at finding the next wall in line with the formation of a plastic hinge. It is worth noting that the base moments and the initial load factor obtained after the first increment are stored, and from now onwards the procedure deals with the load increments (additional load) which trigger the successive formation of plastic hinges, making use of incremental linear analysis with respectively pinned wall bases. Towards finding the load increment that triggers the formation of the next plastic hinge, a unit load factor is applied, and the incremental moments are calculated from linear analysis with appropriately inserted pins at the base of walls that already reached their plastic capacity. This permits to establish the incremental load factor required to attain the plastic capacity in each of the redundant walls. Consequently, the minimum of these latter is associated with the first redundant wall to attain its plastic capacity upon the additional increase in the load. The procedure is better illustrated in the following:

$$m_{botf,i} + \left(\Delta\lambda_i \, \Delta M_i\right) = \pm m_{pi} \tag{6.7}$$

$$\Delta\lambda = \min\left(\Delta\lambda_i\right) \tag{6.8}$$

where:

$m_{botf,i}$ is the total moment stored at the base of wall *i*,

$\Delta\lambda_i$ is the incremental load factor required to reach the plastic capacity of wall *i*,

ΔM_i is the incremental bending moment in wall *i* due to an applied unit load factor, and

$\Delta\lambda$ is the incremental load factor that induces the formation of the next plastic hinge.

The positive/negative sign of the plastic moment capacity m_{pi} in Equation (6.7) is attributed to the positive/negative sign of the incremental moment ΔM_i, noting that the walls can experience reverse bending (change in the sign of the bending moment at the base) upon inserting pins in the structure. The incremental load factor required to achieve the plastic capacity of each of the redundant walls is calculated by solving Equation (6.7). Consequently, the smallest value returns the finalised increment of load factor $\Delta\lambda$ that induces the formation of the next plastic hinge (Figure 6.4).

The procedure progresses in the same fashion towards finding the collapse load. Within the process, each wall that reaches its plastic capacity is replaced by a pinned support at the base, and the load increment that induces the formation of a new plastic hinge is subsequently determined while the total base moment accumulating from previous steps is stored. The procedure continues until reaching a stage where the redundant walls do not present a stable configuration that can resist the applied loading as explained in the previous section. This point marks the end of the procedure and the failure of the structure to sustain additional loads. Accordingly, the collapse load is evaluated as the sum of loads applied throughout:

$$\lambda_c = \lambda_1 + \Delta\lambda_1 + \cdots + \Delta\lambda_n \tag{6.9}$$

where:

λ_c is the collapse load factor.

The incremental procedure was implemented using Maple (2019) as an extension of the static analysis procedure presented in Chapter 5, and it is practically applied to determine the pushover response of the buildings. The collapse load obtained at the end of the procedure was found to perfectly correlate with the corresponding value determined using plastic limit analysis.

6.4 Influence of the Original Frame on the Pushover Response

The simplified approach allows to determine the pushover response of the structure by monitoring the formation of plastic hinges at the base of vertical elements. The procedure is further simplified by determining the pushover response with respect to the walls alone and by adding the effect of the frame in a simplified manner. Accordingly, the pushover response is first determined considering the successive formation of plastic hinges at the base of the walls. The overall pushover response is subsequently determined by including the contribution of the original frame in a similar process to what is performed in the frequency analysis.

It is worth recalling that the original frame and the retrofitting walls experience the same displacement in response to the applied loads as they are analogous to two springs connected in parallel. In order to incorporate the frame effect into the pushover response, the displacement is fixed in line with the aforementioned analogy. However, the total capacity (base shear) is modified to accommodate the additional stiffness (increase in slope) provided by the frame. Noting that the effective stiffness attributed to the walls is already represented by the pushover response based on the walls, the additional stiffness provided by the frame serves to increase the total capacity (base shear) at each segment of the pushover curve (Figure 6.5). In this respect, the relative contribution of the frame and the walls into the overall pushover response is measured by the relative energy or the work performed by each component over the displacements of the whole system. Considering the initial pushover response that is based solely on the walls, the energy attributed to the walls in each segment of the curve is represented by the external work performed by the applied loads over the resultant displacements. To this accord, the frame contribution is included through the equivalent work performed by the frame over the resultant displacements. For this purpose, the resultant displacements obtained at each step of the initial pushover curve (based on the walls) are applied to the original frame, and the resultant reaction forces are calculated which permits to evaluate the external work performed by the frame.

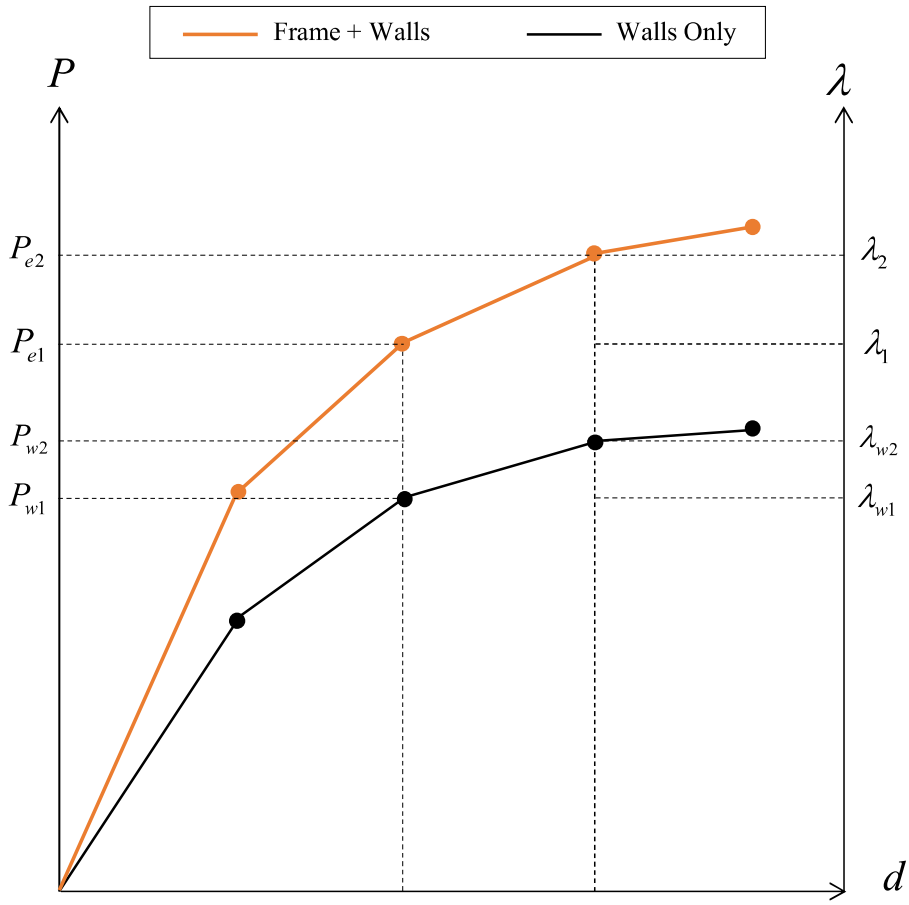


Figure 6.5: Equivalent pushover response including the frame effect: left vertical axis (Base Shear *P*), right vertical axis (Collapse Load Factor *λ*), horizontal axis (Displacement *d*)

The process of including the frame effect in the pushover response is based on the conservation of energy. Therefore, each segment of the original pushover response based on the walls is updated on the basis that the incremental work performed by the whole system is equal to the sum of the incremental work performed by the frame and that performed by the walls. This is better illustrated in the following discussion with reference to Figure 6.5:

$$\Delta W_{eq} = \Delta W_w + \Delta W_f \tag{6.10}$$

$$\rightarrow \left(\frac{\{P_{e1}\} + \{P_{e2}\}}{2} \right) \{\Delta U\} = \left(\frac{\{P_{w1}\} + \{P_{w2}\}}{2} \right) \{\Delta U\} + \left(\frac{\{R_{f1}\} + \{R_{f2}\}}{2} \right) \{\Delta U\} \tag{6.11}$$

$$\rightarrow \left(\frac{\lambda_1 + \lambda_2}{2} \right) \{P_i\} \{\Delta U\} = \left(\frac{\lambda_{w1} + \lambda_{w2}}{2} \right) \{P_i\} \{\Delta U\} + \left(\frac{\{R_{f1}\} + \{R_{f2}\}}{2} \right) \{\Delta U\} \tag{6.12}$$

where:

ΔW_{eq} is the incremental work of the equivalent system over a segment of the pushover curve,

ΔW_w is the incremental work attributed to the walls over a segment of the pushover response,

ΔW_f is the incremental work attributed to the frame over a segment of the pushover response,

$\{P_{e1}\} \& \{P_{e2}\}$ are the vector of equivalent forces at the start and end of the pushover segment respectively,

$\{P_{w1}\} \& \{P_{w2}\}$ are the vector of loads applied to the walls at the start and end of the pushover segment respectively,

$\{R_{f1}\} \& \{R_{f2}\}$ are the vector of reaction forces in the frame obtained in response to the applied displacements $\{U_1\}$ and $\{U_2\}$ which correspond to the total displacements respectively obtained at the start and end of the pushover segment,

$\{\Delta U\}$ is the vector of incremental displacements measured over the pushover segment,

$\{P_i\}$ is the vector of initial loads applied to the walls (in proportion to the first mode),

$\lambda_1 \& \lambda_2$ are the load factors of the equivalent pushover response measured at the start and end of the pushover segment respectively, and

λ_{w1} & λ_{w2} are the load factors of the initial pushover response (based on the walls) measured at the start and end of the pushover segment respectively.

Dividing both sides of Equation (6.10) by the incremental work performed by the walls ΔW_w yields a more simplified version of the equation that can be directly linked to updating the original base shear and obtaining the equivalent one:

$$\frac{(\lambda_1 + \lambda_2)/2}{(\lambda_{w1} + \lambda_{w2})/2} = \frac{\Delta W_w + \Delta W_f}{\Delta W_w} \tag{6.13}$$

$$\rightarrow \frac{(P_{e1} + P_{e2})/2}{(P_{w1} + P_{w2})/2} = \frac{\Delta W_w + \Delta W_f}{\Delta W_w} \tag{6.14}$$

where:

P_{w1} & P_{w2} represent the base shear based on the response of the walls only at both ends of the pushover segment, and

P_{e1} & P_{e2} represent the equivalent base shear of the whole system (including the frame effect) at both ends of the pushover segment.

Equations (6.12) and (6.14) are equivalent to one another and both yield the total pushover response including the frame contribution, noting that the initial collapse load and base shear (λ_1 and P_{e1} respectively) are set to zero at the start of the procedure (for the first segment of the pushover curve). The same procedure progresses afterwards and calculates the equivalent (total) collapse load or base shear at each segment by ensuring the conservation of incremental work (Figure 6.5).

The following example serves to illustrate the full procedure which involves determining the pushover response on the basis of the walls only and including the frame contribution using the simplified strategy described above. The same frame building considered to illustrate the frequency analysis in Chapter 5 is adopted for this purpose. The location and dimensions of the walls are shown on the plan (Figure 6.6) along with the plastic bending capacity of each wall (in N.m). It is worth noting that the dimensions and locations of the reinforcing walls are randomly selected since the purpose of this example is limited to illustrating the outlined procedure of finding the overall pushover response.

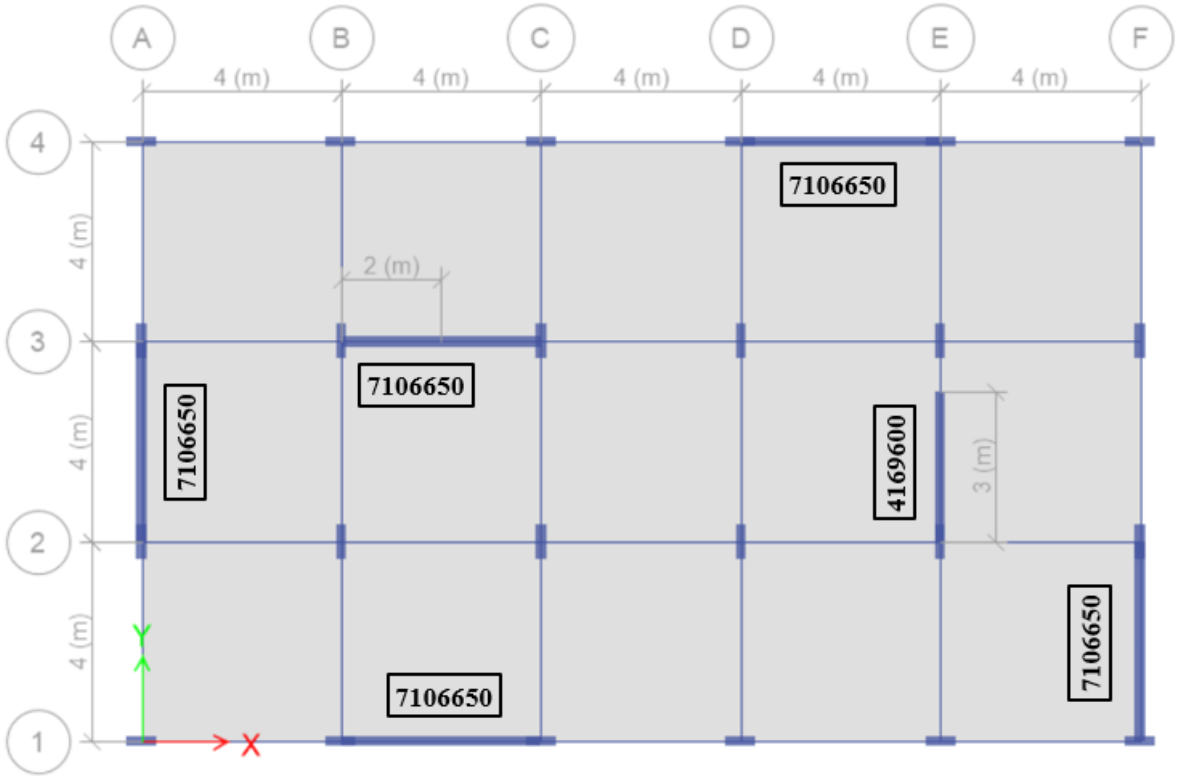


Figure 6.6: Typical floor plan of original frame building along with the reinforcing walls

Pushover loads are applied at the centroid of the floor plan in proportion to the fundamental mode of vibration which is determined while assuming the walls govern the displacement response of the building. The first stage involves finding the pushover response with respect to the walls. Accordingly, the initial pushover loads summarised in Table 6-1 are applied and incrementally increased, and plastic hinges were shown to form successively in the walls oriented in the Y-direction as the load factor is being increased (Figure 6.7). A collapse load factor of 9.36 is eventually obtained, at which a mechanism occurs by virtue of reaching the plastic capacity of all the walls aligned in direction Y, such that the redundant walls left are oriented in the X-direction and therefore do not provide a stable configuration that can resist increased loading. The pushover response based on the walls is plotted in Figure 6.8.

Table 6-1: Initial pushover loads proportional to the fundamental mode

	Storey 1	Storey 2	Storey 3	Storey 4	Storey 5	Storey 6
P_x (N)	148	503	1009	1610	2262	2629
P_y (N)	-2527	-8666	-17422	-27866	-39185	-45872
M_z (N.m)	2360	7912	15783	25141	35256	40536

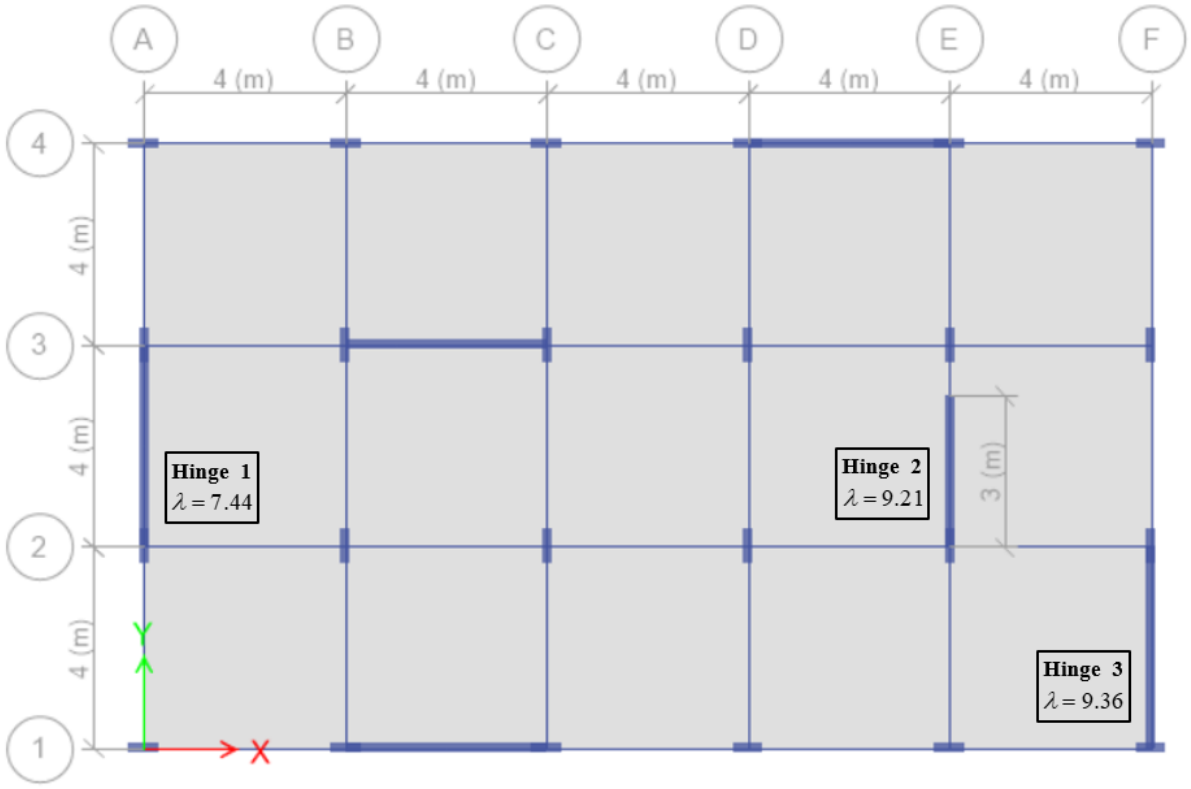


Figure 6.7: Location of the plastic hinges in the walls

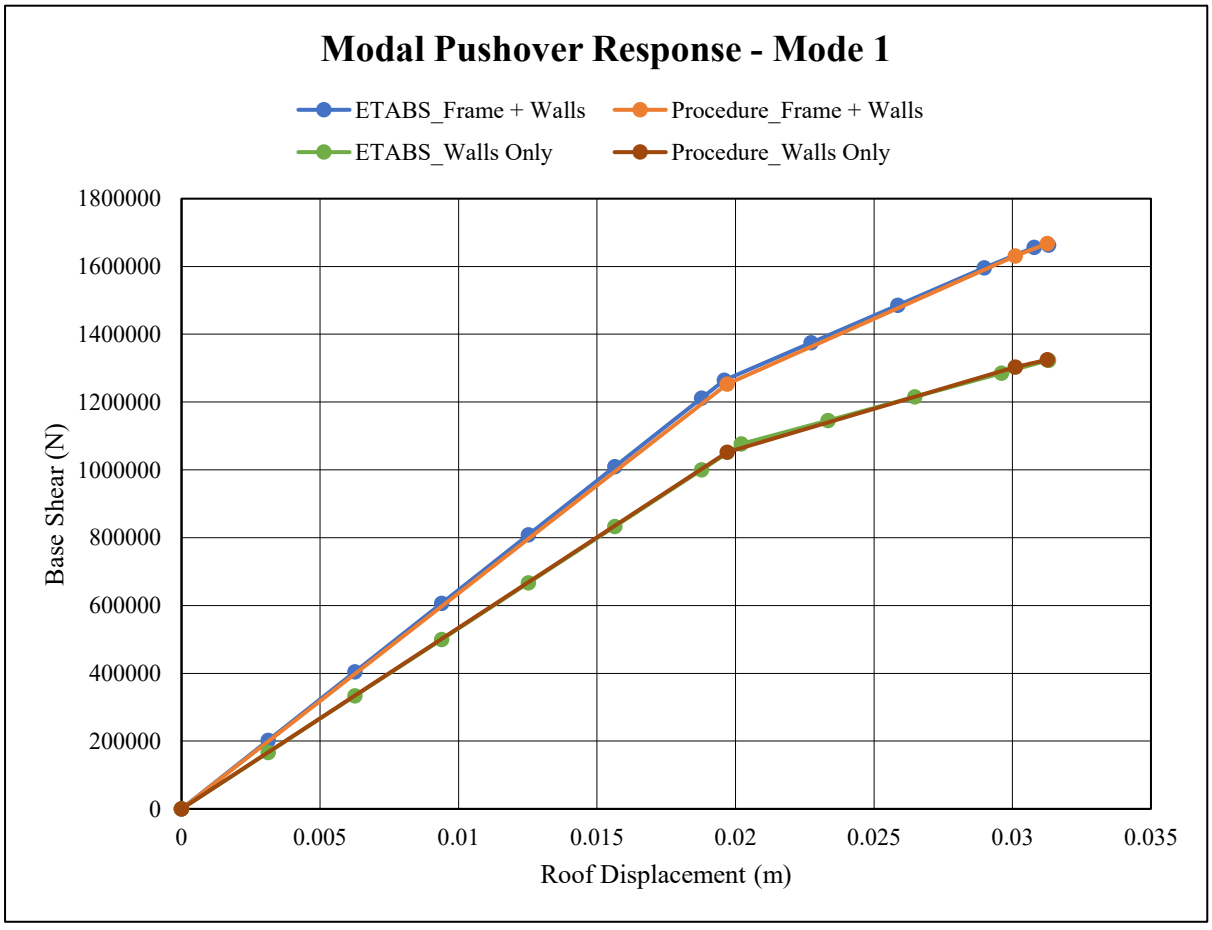


Figure 6.8: Pushover response in proportion to the fundamental mode

The collapse load factor is also calculated using the plastic limit analysis which only determines the ultimate collapse load without reflecting on the sequential formation of plastic hinges or the gradual increase in the load factor en route to plastic collapse. The problem is set up using the Solver function in Excel and the results are presented in Tables 6-2 and 6-3. The coordinates of the walls in Table 6-3 (x and y) are measured with reference to the geometric centroid of the floorplan. It can be noted that Wall3, Wall4, and Wall6 which are aligned in the Y direction have reached their plastic capacity, which is compatible with the results obtained using the simplified procedure (Figure 6.7). Furthermore, the collapse load factor obtained from plastic limit analysis is equal to 9.3588 which is the same value obtained using the procedure. It is worth noting that all the requirements of Equations 6.1 to 6.3 are satisfied, and the bending moment developed in each wall lies within the bounds of the plastic capacity.

Table 6-2: Setting up the solution for plastic limit analysis

Storey	Height (m)	Z (m)	P_{0x} (N)	P_{0y} (N)	P_{0z} (N)	$\sum(P_{0x}*z)$ (N.m)	$\sum(P_{0y}*z)$ (N.m)	$\sum(P_{0z}*z)$ (N.m)
Storey 1	3	3	148	-2527	2360	445	-7582	7081
Storey 2	3	6	503	-8666	7912	3020	-51994	47471
Storey 3	3	9	1009	-17422	15783	9077	-156802	142048
Storey 4	3	12	1610	-27866	25141	19323	-334389	301690
Storey 5	3	15	2262	-39185	35256	33923	-587769	528846
Storey 6	3	18	2629	-45872	40536	47317	-825693	729645

Table 6-3: Bending moments in the walls obtained from plastic limit analysis

Walls	x (m)	y (m)	M_{px} (N.m)	M_{py} (N.m)	M_x (N.m)	M_y (N.m)
Wall1	-4	-6	7106650		4117532	
Wall2	-4	2	7106650		- 400098	
Wall3	-10	0		7106650		-7106650
Wall4	6	-0.5		4169600		-4169600
Wall5	4	6	7106650		-2658913	
Wall6	10	-4		7106650		-7106650

Last, it is worth noting that the pushover response based on the walls compared very well against the one obtained directly from ETABS (Figure 6.8), which points out at the accuracy of the simplified procedure.

The next stage involves finding the equivalent pushover response by incorporating the contribution of the frame as per the outlined procedure. The overall pushover response is also plotted and compared against the one obtained directly from ETABS (Figure 6.8). To this end, it is worth noting the close similarity of the response obtained using the simplified procedure and the one obtained from ETABS, which highlights the accuracy of the proposed approach to incorporate the frame into the pushover

response that is based on the walls. The slight difference between the two curves might be attributed to the main assumption that the deformation mode is governed by the shear walls. Nevertheless, the results obtained still present a high level of correlation with what is directly obtained from ETABS. Furthermore, it is worth pointing out at the additional strength provided by the frame as the ultimate capacity increased from 1350 kN to more than 1650 kN.

So far, the discussion has covered the pushover response up to the collapse load based on the walls alone, which is characterised by the presence of an unstable configuration of walls that cannot resist further loading. Hence, the rest of the problem consists of anticipating the subsequent response beyond the formation of a wall system mechanism. For the response involving the walls only, this is basically represented by a perfectly plastic pushover response extending beyond the formation of the wall system mechanism (Figure 6.9).

Accordingly, the final task requires finding the overall pushover response obtained after achieving a wall system mechanism which is briefly referred to as the post-mechanism response. It is assumed that the additional displacements of the system in the post-mechanism region depend on the collapse mode of the wall system mechanism. Therefore, the total displacements in the post-mechanism region are equal to the total displacements obtained at formation of the wall system mechanism in addition to the post-mechanism displacements, with the latter being a fraction of the collapse mode that is characterised by the formation of a wall system mechanism. The collapse mode can be determined by plastic limit analysis or by visual observation of the wall system mechanism. In this respect, the current example features a wall sway mechanism in the Y direction, since all the walls aligned in the Y direction have attained their plastic limit. Therefore, the post-mechanism mode is solely composed of a linear variation of displacements in the Y direction across the height, and it features no torsional rotation or displacements in the X direction.

Consequently, the total displacements of the whole system in the post-collapse region are calculated and applied to the original frame in order to find the overall pushover response on the basis of conservation of energy as outlined in the procedure. The overall pushover response is plotted in Figure 6.9 which also displays the normalised base shear (the ratio of the base shear V to the seismic weight W of the building).

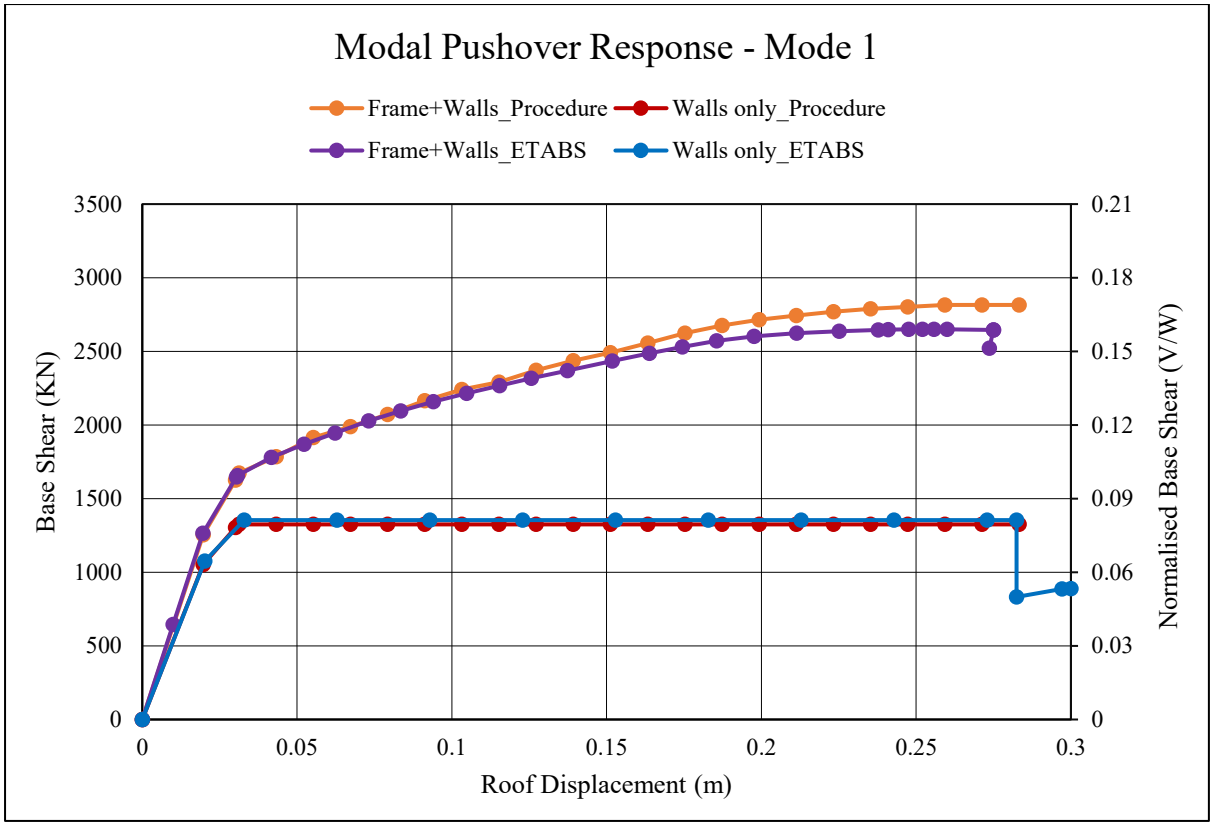


Figure 6.9: Complete pushover response in proportion to the fundamental mode

It is noted that the equivalent response shows a slight variation compared to what is directly obtained from ETABS (Figure 6.9). In particular, the first few segments of the post-mechanism response showed a similar response while the latter segments showed a small variation compared to what is obtained from ETABS. There is a 6% increase in the maximum capacity obtained from the procedure compared to what is obtained from ETABS. This is mainly attributed to the main assumption regarding the predominance of the shear walls on the displacement of the retrofitted structure. However, the results still show a considerably high level of correlation given all the assumptions made to simplify the approach.

Chapter 7 Application and Case Studies

7.1 Introduction:

In this chapter, the major findings of the previous parts are compiled in the context of the CSM and integrated to form a structured approach that facilitates the strengthening of existing buildings which is currently based on engineering judgment and performed on a trial and error basis. Hence, the major contributions of the research, including the simplified approaches developed in regard to the frequency and the pushover analyses, as well as the findings regarding the optimisation of the modal mass participation are assembled in a coordinated way to build a solid retrofitting strategy for strengthening existing substandard RC frame buildings by using shear walls.

In light of this, the aim is to develop a standardised approach that could be applicable in the strengthening of various configurations of substandard buildings. Accordingly, the chapter begins with an in-depth illustration of the retrofitting procedure, and the case studies that emulate existing real-life scenarios follow in the subsequent sections. Three building configurations are discussed in that regard, the first of which involves regular buildings which are commonly encountered and which are represented by a simple rectangular configuration. Furthermore, L-shaped buildings characterised by an irregularity in their plan constitute another building prototype that is widely encountered in real life and that needs to be investigated. The last type involves buildings that feature a setback (reduction in the floorplan) at one or a few storey levels, upon which the building is classified as irregular in elevation. It is recalled that the provisions of EC8-1 (CEN, 2004a) that define irregularity in plan and in elevation are addressed in detail in Appendix 4. To this end, the intended procedure mainly relies on reducing the average Euclidean eccentricity at all the floors, which results in reducing the torsional effects that is manifested by the associated increase of the mass participation of the fundamental mode in the translational direction. This consequently enforces the applicability of the pushover analysis (the CSM) in proportion to the fundamental mode of vibration in each horizontal direction. Unlike the rectangular scenario, the L-shaped and the vertically irregular buildings pose a challenge in regard to reducing the average Euclidean eccentricity, as the fundamental modes of the retrofitted building might include a significant torsional component which hinders the application of the CSM to model the response. Therefore, it is worth checking the applicability of the method to these two types of buildings, such that the procedure can be standardised and recommended as a simplistic yet reliable method for retrofitting substandard RC buildings subjected to seismic loading.

Furthermore, the chapter encompasses a section that discusses the significant contribution of the original frame into the overall pushover response, as reflected in the results drawn on the simplified pushover analysis. This actually prompts a separate discussion in that regard to investigate the extent

of contribution of the frame when the plastic capacity and the resultant contribution of the walls is maximised.

7.2 Illustrating the Procedure

A generalised strategy is devised to retrofit the various configurations of buildings which are assumed to represent the old building stock of Beirut. The procedure is illustrated in full details in this section such that the subsequent sections directly present the outcomes of the case studies. In this respect, the opening stage includes performing a seismic assessment of the existing building as discussed in Chapter 3, during which the individual structural components are checked against potential ductile and brittle failures. It is worth noting that the scope of this research encompasses buildings which were not historically designed to resist earthquakes, and accordingly retrofitting is likely to be required and shear walls are needed to enhance the lateral resistance of the buildings. To this end, the main objective is to develop a simplified guiding approach for the design and detailing of the retrofitting walls, and to verify its effectiveness by checking the resistance of the original structural frame components after the addition of shear walls.

In light of this discussion, the performance of the building needs to be verified at both the Significant Damage (SD) and Near Collapse (NC) limit states. Hence, the response spectrum is accordingly scaled to represent the limit state under consideration, such that the CSM can be performed in both horizontal directions to estimate the performance of the building when subjected to the applied seismic loading. Accidental torsion effects are also taken into consideration which requires shifting the centre of mass from the nominal position by an accidental eccentricity measured in both the positive and negative directions. A brief illustration of the Eurocode requirements for accidental torsion is presented in Appendix 7. It is worth noting that the frame buildings considered in the case studies have similar properties and layout compared to the building considered in the illustration of the seismic assessment procedure in Chapter 3. Hence, the buildings are deemed inadequate to resist the seismic loading by virtue of the conclusion drawn in Chapter 3, which proclaims that most of the structural elements would suffer from brittle shear failure when the seismic level is matching the SD limit state. To conclude, the seismic assessment is skipped as the buildings are already deemed to be seismically vulnerable, and the focus is directly aimed at developing the retrofitting strategy to help the buildings resist potential seismic loading.

The retrofitting strategy is described in the following steps which are further illustrated in the subsequent sections:

1. Defining the location and the number of walls required.
2. Preliminary design of shear walls.
3. Finding the fundamental mode of vibration in the global X and Y directions.

4. Performing modal pushover analysis (CSM) in the X and Y directions and checking the drift demand.
5. Checking the shear and flexural requirements of shear walls.
6. Checking the local ductility requirements in the shear walls.
7. Checking the adequacy of the original frame members against potential ductile and brittle failures.
8. Validating the retrofitting strategy by testing the results against the fully integrated NLTHA.

Step 1: Location and dimensions of shear walls

The location of walls in the floor plan is determined in line with the previous findings regarding the optimisation of the mass participation in the direction of pushover. Accordingly, the initial target is to minimise the average Euclidean eccentricity measured at the floor levels between the centre of mass and the centre of rigidity, in the aim to reduce the torsional effects and to subsequently increase the mass participation of the fundamental translational mode as discussed in Chapter 4. Indeed, reducing the torsional effects would eliminate the torsion-induced stresses experienced by the framing elements, and it particularly assists the columns that are situated at the farthest distance from the centre of rigidity as these latter are mostly affected by the potential torsional rotation of the floorplan. In view of this, walls are straightforwardly added in the regular building scenario to reduce the average Euclidean eccentricity to zero by virtue of the symmetry of the floorplan. However, for cases involving irregularity in plan or in elevation, achieving a zero average eccentricity is practically difficult, and the target is therefore set to minimising the average Euclidean eccentricity which is expected to boost the mass participation of the fundamental mode in each translational direction.

It is also worth noting that the selected location of walls must conform with the architectural constraints in the building. From a practical perspective, structural shear walls are added at locations already occupied by architectural partition walls, hence posing minimum disturbance to the architectural layout of the building. Accordingly, the maximum length of the wall is bound by the clear span between the columns while the thickness is determined in line with the code requirements.

Step 2: Preliminary design and detailing of walls

Having defined the layout of walls, a preliminary design is performed to determine the initial dimensions and detailing which are verified at a later stage after determining the actual forces applied to the walls. The preliminary design of the walls is summarised in the following steps.

Preliminary dimensioning of shear walls

The first step involves estimating the cross-section dimensions required to resist the gravity load resisted by the wall. Walls are not expected to interfere with resisting the superimposed dead load and the self-

weight of the original frame, as these loads are already supported by the frame columns. Accordingly, the wall is expected to sustain its own weight as well as the live load supported along its tributary area.

The minimum thickness of the walls is firstly calculated in line with the requirements of EC8-1 (CEN, 2004a) as discussed in Chapter 2, with h_s being the storey height:

$$b_{w0} \geq \max\left[0.15,\ h_s / 20\right] = 0.215m \tag{7.1}$$

Furthermore, the ultimate axial compressive capacity can be approximated using the following simplified equation recommended by the design manual of the Institution of Structural Engineers (IStructE, 2006), which permits to determine the preliminary dimensions of the wall required to resist the gravitational load:

$$F_c \leq 0.43 f_{ck} A_c + 0.77 f_{yd} A_s \tag{7.2}$$

where:

F_c is the ultimate axial compressive load applied on the wall; EN 1992-1-1 (CEN, 2004b) recommends the gravity load combination of (1.35 DL + 1.5 LL) in that regard, where DL is the total dead load and LL is the live load,

A_c is the area of concrete per unit length of wall, and

A_s is the area of vertical reinforcement per unit length of wall.

Since the maximum permissible length of wall is bound by the clear span between the framing columns, the thickness is practically increased whenever required to satisfy the axial load requirements.

Calculating the loads applied on the walls

The standards of EC8-1 (CEN, 2004a) require designing shear walls such that plastic hinging forms only at the base. In this regard, Fardis (2009) stated that walls must act as vertical cantilevers that can only develop plastic hinges at their fixed base in order to enforce the beam sway mechanism in the frame. Accordingly, the wall is pictured as a cantilever with lateral forces applied at the storey levels by virtue of having a sufficiently elongated cross-section that exacts the formation of plastic hinge at the base only. In this respect, the wall is expected to develop large bending moment and consequently long shear span (moment to shear ratio, $L_s = M/V$) at the base. Under these conditions, the shear span is approximated as a fixed fraction of the total height of the wall and is estimated around one-half of the total height for commonly used beam sizes (Fardis, 2009).

To this end, the buildings addressed in this research are seismically vulnerable and as such the lateral resistance is mainly provided by the reinforcing shear walls. Hence, the moment at the base is assumed to attain the plastic limit at the performance point, and the wall detailing at the base level (including the

confined regions) is accordingly performed to resist a bending moment equal to the plastic capacity of the cross-section. Whereas for the base shear, it is estimated by approximating the shear span at the base as one-half of the total height of the wall as explained in the aforementioned discussion. This permits to obtain a preliminary evaluation of the moment and shear diagrams in line with the Eurocode requirements. In this respect, the bending moment diagram is modified through the tension shift applied at the base while the shear diagram is modified by a magnification factor (equal to 1.5 for DCM walls) applied at the base as discussed in Chapter 2.

To note that the detailing of the vertical and shear reinforcement of the wall at upper floors (apart from the base level) is verified against the moment and shear values obtained at the performance point of the CSM. In this regard, if the moment/shear value obtained from the analysis exceeds the one adopted in the preliminary design, the wall reinforcement is accordingly increased to resist the actual moment and shear forces. In this regard, updating the wall reinforcement at upper floors ensures that the plastic capacity is not exceeded at these locations without altering the pushover response which is solely based on the formation of plastic hinges at the base.

Preliminary dimensioning and reinforcement of the confined zones (boundary elements)

As previously discussed, the gravity load resisted by the wall consists of its own weight as well as the live load supported along its tributary area, and it is equally resisted by the boundary columns at the ends of the wall. In light of this, the boundary elements are fundamentally provided to resist the axial stresses associated with the seismic bending moment, which induces compression on one end and tension at the opposite end of the wall (Figure 7.1). Accordingly, the total axial load resisted by each boundary column is represented by the following:

$$P_t = \frac{P_{O.W.} + P_{LL}}{A_w} \cdot A_{bc} \pm \frac{M_{EQ}}{l_0} \tag{7.3}$$

where:

P_t is the total axial load resisted by the boundary column,

$P_{O.W.}$ is the self-weight of the wall,

P_{LL} is the live load supported by the tributary area of the wall,

A_w is the total area of the wall's cross-section,

A_{bc} is the area of one boundary column,

l_0 is the bending moment lever arm (Figure 7.1), and

M_{EQ} is the bending moment due to the earthquake loading applied along the length of wall.

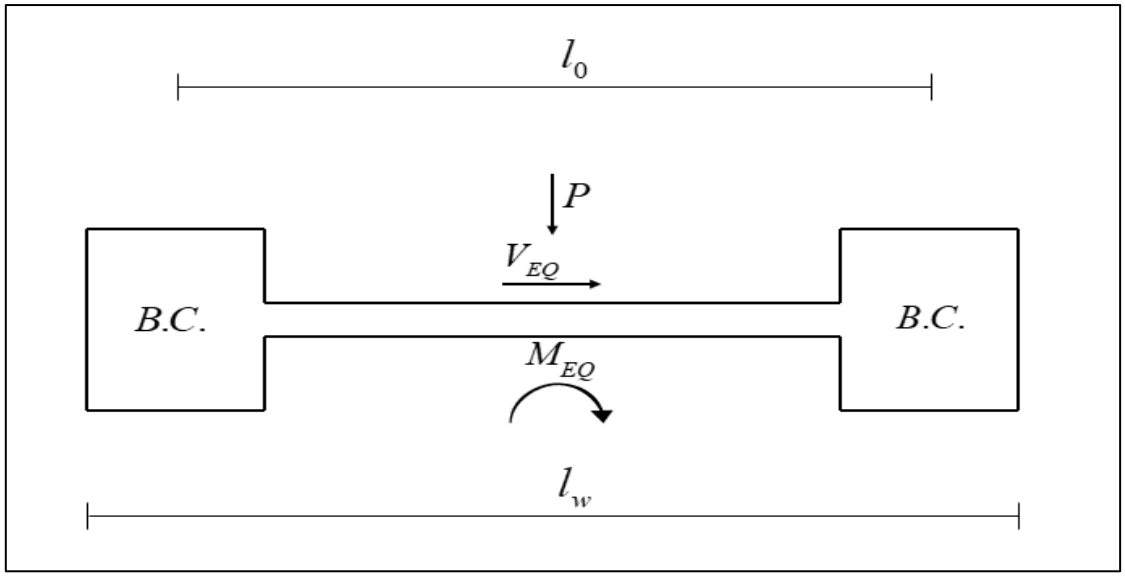


Figure 7.1: Total loads applied on the wall

Once the axial load is determined, the required dimensions and the steel reinforcement in the boundary columns can be evaluated using the simplified formulation suggested for the dimensioning of columns in the design manual of the Institution of Structural Engineers (IStructE, 2006), noting that the axial stress is equal to the axial load divided by the cross-sectional area of the boundary column:

$$axial\ \ stress = 0.44 f_{ck} + \frac{\rho}{100}\left(0.67 f_{yk} - 0.44 f_{ck}\right) \tag{7.4}$$

where:

ρ is the percentage ratio of steel reinforcement in the cross-section (f_{ck} & f_{yk} are in MPa).

Detailing of the confined regions follows the requirements of EC8-1 (CEN, 2004a) as discussed in depth in Chapter 2. The boundary columns extend across the critical region defined by the code which approximately spans from the base through to the first storey (in a 10-storey building). The axial load requirements and the effectiveness of confinement in the boundary columns are also verified as per the following formulas which are reinstated from Chapter 2:

$$\nu_d = \frac{N_{Ed}}{h_c\, b_c\, f_{cd}} \le 0.4 \tag{7.5}$$

$$\alpha\,\omega_{wd} \ge 30\,\mu_\varphi\,(\nu_d + \omega_v)\,\varepsilon_{sy,d}\,\frac{b_c}{b_0} - 0.035 \tag{7.6}$$

In regard to satisfying the axial load requirements, the dimensions of the confined regions need to be controlled to avoid buckling of the boundary columns under the subjected gravity loading. The force N_{Ed} is evaluated using the combination (1.35 DL + 1.5 LL) where DL and LL represent the dead load and the live load resisted by the boundary column, and the associated checks are performed to decide

whether the previously adopted dimensions of the boundary column are satisfactory or need to be increased to satisfy the axial load requirement of Equation 7.5. Furthermore, the confining reinforcement (stirrups) needed in the boundary columns is provided to ensure that the effectiveness of confinement is satisfied as per the requirement of Equation 7.6.

Vertical and transverse reinforcement in the shear panel

The vertical reinforcement in the shear panel is defined with respect to the minimum ratio set by the code since the axial load is mainly resisted by the confined boundary elements. On the other hand, horizontal reinforcement in the web is mainly provided to resist the applied shear force. Accordingly, the shear capacity is set to balance the seismic shear demand which permits to determine the shear reinforcement as per the following:

$$V_u = V_{Rd,s} \quad with \quad V_{Rd,s} = \frac{A_{sw}}{s} z f_{ywd} \cot\theta \tag{7.7}$$

$$\rightarrow \frac{A_{sw}}{s} = \frac{V_u}{z f_{ywd} \cot\theta} \tag{7.8}$$

where:

A_{sw} & s are respectively the area and spacing of required transverse reinforcement in the wall,

V_u is the ultimate seismic shear demand, and

$V_{Rd,s}$ is the ultimate shear capacity of a member with shear reinforcement which is already defined in chapter 2.

To note also that the shear reinforcement required is checked against the minimum code requirements (minimum ratio of transverse reinforcement is 0.002), and that the shear capacity is also checked against the maximum value allowed by the code as discussed in Chapter 2.

Step 3: Finding the vibration characteristics of the building in the two main horizontal directions

The next step involves calculating the vibration characteristics of the fundamental mode in each horizontal direction in order to apply the CSM. The mode shape and frequency of vibration are calculated using the simplified approach developed in this research, which is based on the assumption that the displacement response (mode shape) is governed by the shear walls. The frame contribution is subsequently added in a simplistic manner as explained in the previous chapters in order to obtain the overall fundamental frequency of vibration of the structure. The mass participation is also calculated according to the procedure underlined in Chapter 2, in order to ensure that the response is governed by the fundamental mode and to support the argument that the CSM provides a reasonable approximation of the actual response of the building.

Step 4: Modal pushover analysis in the global X and Y directions

Having determined the fundamental mode shape vector in each translational direction, the CSM is performed in accordance with the simplified approach developed in this research. The pushover curve is first obtained by considering the walls to be the lone component of earthquake resistance, and the frame contribution is added in a simplistic manner as discussed in the procedure. The performance point is subsequently determined which permits to evaluate the maximum roof displacement in response to the applied seismic loading.

As discussed earlier, Fardis (2009) underlines the interconnection between a stiff interstorey drift profile and an appropriate frame behaviour (beam sway mechanism). To this end, the retrofitting process is controlled by a maximum allowable drift ratio of 2% at the NC limit state which is believed to ensure that the lateral resistance provided by the walls is significant and would reduce the stresses originally experienced by the substandard frame components. To note that the proposed 2% limit is actually defined by ATC-40 (ATC, 1996, 2005) at the Life Safety limit state which represents a seismic level of lower intensity than the NC limit state defined in EC8-3 (CEN, 2005a). Hence, in case the drift ratio measured at the performance point exceeds the 2% limit, retrofitting is revisited by increasing the walls dimensions or by adding more walls.

Step 5: Verifying the flexural and shear capacities of the retrofitting walls against the seismic demand

After determining the performance point, the actual shear forces and bending moments applied are determined and are checked against the capacity of the walls at all floors. If the moment/shear demand measured at the performance point is smaller than the moment/shear capacity, it is concluded that the current wall dimensions and detailing are deemed satisfactory to resist the applied seismic loading. Otherwise, the walls reinforcement and detailing are updated to ensure that the flexural and shear requirements are satisfied.

It is worth noting that adjusting the flexural reinforcement of the walls at upper floors ensures that the plastic capacity is not exceeded at these levels, yet it does not affect the pushover response that is already derived upon the formation of plastic hinges at the base only. Whereas the moment at the base of the wall is expected to reach the plastic capacity and as such detailing of the vertical reinforcement at the base is not subjected to any modification.

Step 6: Checking the local ductility requirements in the shear walls

Local ductility checks are performed to ensure an appropriate ductile behaviour of the newly designed walls. Although the retrofitting process involves checking the effectiveness of confinement in the boundary elements in line with the Eurocode 8 requirements, an approximation of the curvature ductility factor that depends on the behaviour factor of the whole building is adopted in the equation to check the effectiveness of confinement (Appendix 2). However, the retrofitting procedure is centred around a

nonlinear static analysis that is based on the formation of plastic hinges at the base of the walls. Therefore, it is necessary to check that the ductility supply that depends on the detailing of confining reinforcement in the added shear walls is sufficient to meet the ductility demand imposed by the earthquake loading.

To this end, the ductility demand is measured in terms of the plastic rotation at the performance point and is directly obtained from ETABS. Concerning the capacity, there are several models available in the literature to determine the ultimate rotational capacity of flexural members including shear walls.

To begin with, the most straightforward approach that calculates the ultimate rotational capacity of members subjected to flexural action is based on a direct application of plane section analysis and first principles of mechanics. Considering the deformation of a cantilever member subjected to flexural action, the curvature varies in an idealised triangular form as it increases from zero at the end of the shear span to the yielding point. The variation from the yield point to the ultimate curvature measured at the section of highest moment (face of support) is characterised by a nearly triangular variation having a steeper slope compared to the variation preceding the yielding point (Figure 7.2). Denoting the plasticity length l_{pl} by the distance from the yielding point to the ultimate curvature at the face of the support, it is assumed that the curvature is constant and is equal to the ultimate value over a region called the plastic hinge length L_{pl} which is approximated to one-half of the plasticity length defined earlier (Fardis, 2009). Applying first principles of mechanics, the plastic rotation at ultimate conditions within the zone of the plastic hinge length is constant and is equal to the product of the constant curvature and the plastic hinge length L_{pl}:

$$\theta_{pl,u} = \left(\varphi_u - \varphi_y\right) L_{pl} \tag{7.9}$$

Assuming that this rotation is acting at the centre of the plastic hinge length, it generates a plastic deformation at the end of the shear span:

$$\delta_{pl,B} = \theta_{pl,u}\left(L_s - \frac{L_{pl}}{2}\right) \tag{7.10}$$

Assuming the total deformation at the end of the shear span (point B) is attributed to flexure, its elastic component is obtained with respect to the yield curvature. This consequently permits to establish the total ultimate chord rotation at the section of maximum moment (point A) which consists of the elastic and the plastic components, and which is obtained as the ratio of the ultimate displacement at the end to the length of the shear span (Fardis, 2009):

$$\delta_{el,B} = \varphi_y \frac{L_s^{\,2}}{3} \tag{7.11}$$

$$\theta_{u,A} = \frac{\delta_B}{L_s} \tag{7.12}$$

$$\theta_{u,A} = \varphi_y \frac{L_s}{3} + \left(\varphi_u - \varphi_y\right) L_{pl} \left(1 - \frac{L_{pl}}{2L_s}\right) \tag{7.13}$$

where:

$\delta_{el,B}$ is the elastic deformation at the end of the shear span,

δ_B is the total deformation (elastic and plastic) at the end of the shear span, and

$\theta_{u,A}$ is the ultimate chord rotation at the section of maximum moment.

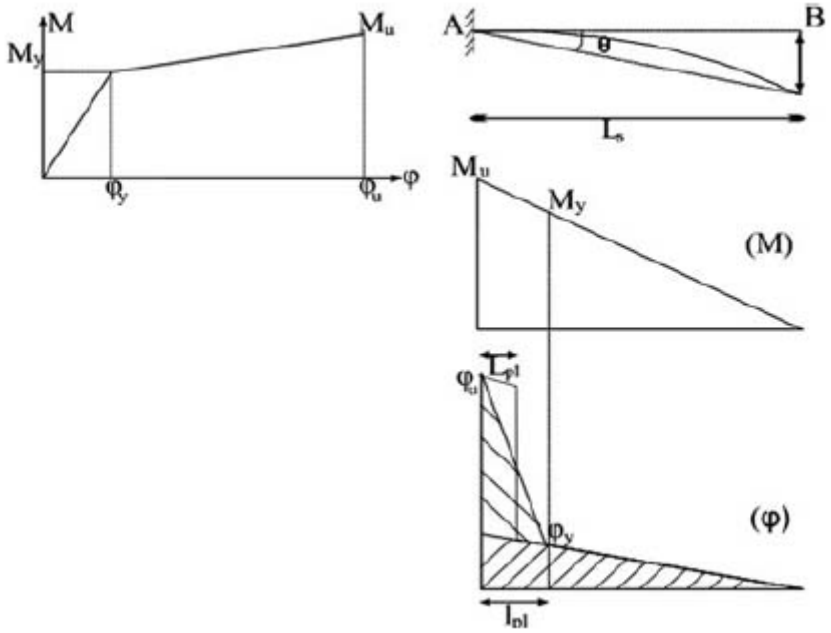


Figure 7.2: Variation of moment and curvature in the shear span of a typical cantilever (Fardis, 2009)

To this end, the yield and ultimate curvature values can be evaluated from plane section analysis. Furthermore, it is worth noting that it is possible to refine the previous equation by adding a component that accounts for the effect of slippage of reinforcement bars from the anchorage zone beyond the section of maximum moment. However, influencing factors such as the bond slippage and type of loading are mostly accounted for through the plastic hinge length L_{pl}.

To this end, studies by Biskinis (2007) considering 1350 tests involving multiple types of beams, columns, and walls sections including rectangular as well as T-, H-, U- and hollow rectangular sections,

and considering both monotonic loading (300 tests) as well as cyclic loading (1050 tests) allowed to derive empirical equations for determining the plastic hinge length depending on the type of loading and on the model used to obtain the ultimate concrete strain:

For monotonic loading: $\varepsilon_{cu} = 0.0035 + \left(\frac{10}{h_c}\right)^2 + 0.57\frac{p}{f_c^*}$ (7.14)

$$L_{pl,mon} = h\left(1.1 + 0.04\min\left(9; \frac{L_s}{h}\right)\right) \quad (7.15)$$

For cyclic loading: $\varepsilon_{cu} = 0.0035 + \left(\frac{10}{h_c}\right)^2 + 0.4\frac{p}{f_c^*}$ (7.16)

$$L_{pl,cy} = 0.2h\left(1 + \frac{1}{3}\min\left(9; \frac{L_s}{h}\right)\right) \quad (7.17)$$

For monotonic or cyclic loading: $\varepsilon_{cu} = 0.0035 + \left(\frac{1}{x_c}\right)^{3/2} + \frac{1}{3}\frac{p}{f_c^*}$ (7.18)

$$L_{pl,mon} = h\left(1.2 + 0.04\min\left(9; \frac{L_s}{h}\right)\right) \quad (7.19)$$

$$L_{pl,cy} = 0.2h\left(1 + \frac{3}{8}\min\left(9; \frac{L_s}{h}\right)\right) \quad (7.20)$$

where:

$L_{pl,mon}$ & $L_{pl,cy}$ are the length of the plastic hinge for monotonic and cyclic loading respectively,

h_c is the depth of the confined concrete core in the plane of bending (mm),

h is the depth of the section in the plane of bending,

x_c is the depth of the compression zone (depth of neutral axis) in the confined core (mm),

L_s is the shear span length,

p is the confining pressure and is given by the following:

$p = 0.5\,\rho_w\, f_{yw}$

f_{yw} is the yield reinforcement of the ties,

ρ_w is the ratio of the volume of stirrups to that of the confined concrete core, measured to the centreline of the perimeter stirrup, and

f_c^* is the confined concrete compressive strength.

To this end, the provisions of Eurocode 8 contain new formulations of the plastic hinge length that are based on fitting the previous equations derived by Biskinis (2007) such that each expression for calculating the plastic hinge length is directly applied with the corresponding model used to calculate the ultimate curvature. Accordingly, EC8-3 (CEN, 2005a) contains two formulations for calculating the plastic hinge length depending on each concrete confinement model adopted in Eurocode:

For the first concrete confinement model defined in EC8-3 (CEN, 2005a):

$$\varepsilon_{cu} = 0.004 + 0.5\frac{p}{f_c^*} \tag{7.21}$$

$$L_{pl} = \frac{L_s}{30} + 0.2h + a_{sl}\frac{0.11 d_{bL} f_{yL}}{\sqrt{f_c}} \quad \left(f_{yL} \text{ and } f_c \text{ in MPa}\right) \tag{7.22}$$

For the second concrete confinement model which is basically defined in Eurocode 2 (CEN, 2004b):

$$\varepsilon_{cu} = 0.0035 + 0.2\frac{p}{f_c} \tag{7.23}$$

$$L_{pl} = 0.1L_s + 0.17h + a_{sl}\frac{0.24 d_{bL} f_{yL}}{\sqrt{f_c}} \quad \left(f_{yL} \text{ and } f_c \text{ in MPa}\right) \tag{7.24}$$

where:

f_c is the cylindrical concrete strength,

f_{yL} is the yield stress of longitudinal steel,

d_{bL} is the bar diameter of longitudinal steel reinforcement, and

a_{sl} is the bond slippage coefficient.

Another expression that is widely adopted to calculate the plastic hinge length is the following one proposed by Paulay and Priestley (1992). This equation is based on the two concrete confinement models defined by Mander et al. (1988) and by Priestley (1997), and on the ultimate steel strain that is calculated according to EC8-3 (CEN, 2005a):

$$L_{pl} = 0.08L_s \; + \; a_{sl}\left(0.22 d_{bL} f_{yL}\right) \quad \left(f_{yL} \; and \; f_c \; in \; MPa\right) \tag{7.25}$$

The previous discussion covered a range of formulations available in the literature to calculate the ultimate rotation at failure of flexural members by using the curvature and plastic hinge length along with a direct application of first principles of mechanics. Accordingly, the accuracy of these equations can vary depending on the concrete confinement model and on the steel strain as well as the model used to calculate the length of the plastic hinge. In view of this, studies by Panagiotakos and Fardis (2001) have formulated empirical formulations for calculating the ultimate flexural chord rotation under both monotonic and cyclic loading. Further studies by Biskinis (2007) and by Biskinis and Fardis (2004, 2007) attempted at improving the former expressions and have accordingly formulated three empirical expressions to evaluate the ultimate chord rotation at flexure-controlled failure. The first equation calculates the total ultimate rotation directly, while the other equations calculate the elastic and plastic components separately. Hence, these latter equations permit to obtain the required plastic component of the ultimate flexural rotational capacity and allow for a direct comparison against the rotation demand obtained at the performance point of the CSM. It is also worth noting that the three empirical equations were calibrated based on the results of 300 monotonic and 1050 cyclic tests, and the results obtained using the equations provided better estimates of the ultimate plastic rotational capacity compared to all the models that are based on calculating the curvatures and the plastic hinge length. The three empirical equations are given by the following:

$$\theta_u \; = \; a_{st}\left(1-0.43a_{cy}\right)\left(1+\frac{a_{sl}}{2}\right)\left(1-0.42a_{w,r}\right)\left(1-\frac{2}{7}a_{w,nr}\right)\left(0.3^{\nu}\right)\left[\frac{\max\left(0.01;\omega_2\right)}{\max\left(0.01;\omega_1\right)} f_c\right]^{0.225} \left[\min\left(9;\frac{L_s}{h}\right)\right]^{0.35} 25^{\left(a\rho_s f_{yw}/f_c\right)} \; 1.25^{100\rho_d} \tag{7.26}$$

$$\theta_u = \theta_y \; + \; \theta_u^{pl} \tag{7.27}$$

$$\theta_u^{pl} \; = \; a_{st}^{pl}\left(1-0.52a_{cy}\right)\left(1+\frac{a_{sl}}{1.6}\right)\left(1-0.44a_{w,r}\right)\left(1-\frac{1}{4}a_{w,nr}\right)\left(0.25^{\nu}\right)\left[\frac{\max\left(0.01;\omega_2\right)}{\max\left(0.01;\omega_1\right)}\right]^{0.3} f_c^{\,0.2} \left[\min\left(9;\frac{L_s}{h}\right)\right]^{0.35} 25^{\left(a\rho_s f_{yw}/f_c\right)} \; 1.275^{100\rho_d} \tag{7.28}$$

$$\theta_u^{pl} \; = \; a_{st}^{hbw}\left(1-0.525a_{cy}\right)\left(1+0.6a_{sl}\right)\left|1-0.052\max\left(1.5;\min\left(10,\frac{h}{b_w}\right)\right)\right| \left(0.2^{\nu}\right) \left[\frac{\max\left(0.01;\omega_2\right)}{\max\left(0.01;\omega_1\right)}\min\left(9;\frac{L_s}{h}\right)\right]^{1/3} f_c^{\,0.2} \; 25^{\left(a\rho_s f_{yw}/f_c\right)} \; 1.225^{100\rho_d} \tag{7.29}$$

where:

$a_{st}, a_{st}^{pl}, a_{st}^{hbw}$ are coefficients that depend on the steel type,

For ductile hot-rolled or heat-treated steel: $a_{st} = a_{st}^{pl} = 0.0185$

$$a_{st}^{hbw} = 0.022$$

For cold-worked steel: $a_{st} = 0.0115$

$$a_{st}^{pl} = 0.009$$

$$a_{st}^{hbw} = 0.0095$$

a_{cy} is a coefficient that depends on the type of loading, it is equal to 0 for monotonic loading and to 1.0 for cyclic loading,

a_{sl} is the bar slippage coefficient, it is equal to 0 if there is no slippage and to 1.0 if there is a slippage of the longitudinal bars from their anchorage beyond the section of maximum moment,

$a_{w,r}$ is a coefficient that is equal to 1.0 for rectangular walls and to 0 otherwise,

$a_{w,nr}$ is a coefficient that is equal to 1.0 for walls with T-, H-, U- or hollow rectangular section and that is equal to 0 for other sections,

ν is the normalised axial load:

$\nu = N / bhf_c$

b is the width of compression zone,

N is the axial force (positive for compression),

ω_1 is the mechanical reinforcement ratio of tension and web longitudinal reinforcement,

$\omega_1 = (\rho_1 + \rho_v) f_{yL} / f_c$

ω_2 is the mechanical reinforcement ratio of compression longitudinal reinforcement,

$\omega_2 = \rho_2 f_{yL} / f_c$

f_c is the cylindrical concrete strength (MPa),

L_s / h is the shear span ratio at the section of maximum moment,

$L_s / h = M / Vh$

ρ_s is the ratio of transverse steel parallel to the loading direction,

$\rho_s = A_{sh} / b_w s_h$

f_{yw} is the yield stress of transverse steel,

a is the confinement effectiveness factor (Figure 7.3),

$$a = \left(1 - \frac{s}{2b_{x0}}\right)\left(1 - \frac{s}{2b_{y0}}\right)\left(1 - \frac{\sum b_i^2}{6b_{x0}b_{y0}}\right)$$

ρ_d is the ratio of diagonal steel reinforcement in each diagonal direction, and

b_w is the width of one web, even in cross-sections with one or more parallel webs.

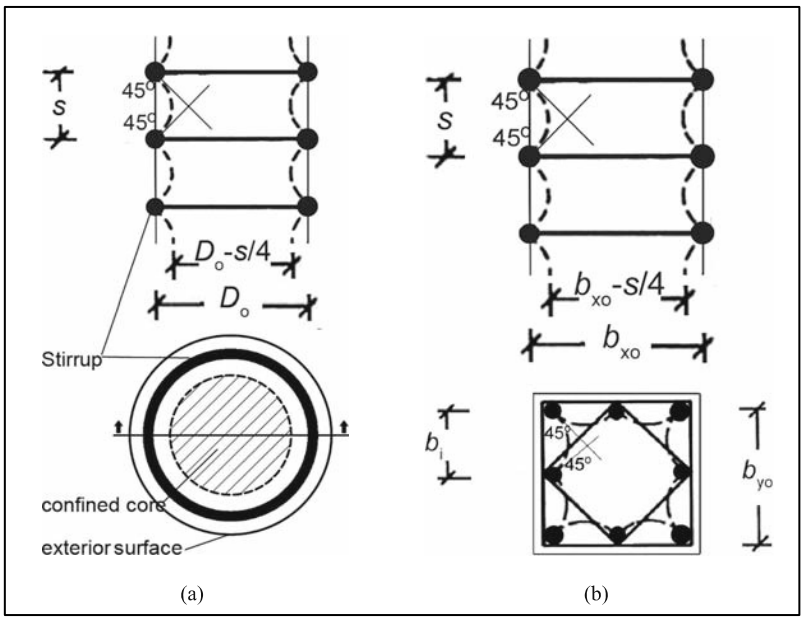


Figure 7.3: Confined and unconfined parts of a member's: (a) circular cross-section with circular hoops; or (b) square section and multiple ties (Fardis, 2009)

Furthermore, noting that the plastic rotational capacity is determined according to both the second and third equations, the second equation was shown to provide a better estimate of the rotational capacity in rectangular walls and returned a slightly smaller test-to-prediction ratio than the other two equations.

In view of this, it is worth noting that the equations pertaining to the ultimate chord rotation in EC8-3 (CEN, 2005a), which were discussed in Chapter 3, are actually extended from the first and second empirical equations discussed above while considering cyclic loading (a_{cy} = 1) and slippage of reinforcement bars (a_{sl} = 1), but with a slight modification for walls which involves multiplying the coefficient $a_{w,r}$ by 0.4 instead of 0.42 or 0.44 as per the empirical equations.

To conclude, the previous discussion serves to shed some light on the vast range of formulation available in the literature to calculate the ultimate flexural rotation of rectangular walls. The discussion concludes that the empirical equations defined by Biskinis (2007) and by Biskinis and Fardis (2004, 2007) were proven to provide more accurate estimate of the ultimate flexural rotations compared to all the models that are based on plane section analysis and on calculating the curvature and the plastic

length. Consequently, the plastic component of the ultimate flexural rotation is calculated according to the last-presented empirical equations, and the local ductility requirements are verified by checking that supply is larger than the plastic rotation demand determined at the performance point of the CSM. Furthermore, the last-discussed Eurocode 8 equation that is already presented in Chapter 3 is also adopted as an additional check when verifying the local ductility supply in the walls.

Step 7: Checking the performance of the original frame against potential brittle and shear failures

The last step involves verifying the objective of retrofitting by checking the original frame against potential brittle and ductile failure mechanisms. Recalling that the structural members have shown excessive vulnerability to brittle shear failure in particular, the inclusion of shear walls is expected to hugely assist the original frame in resisting the applied loading. It is reminded that the standards of EC8-3 (CEN, 2005a) require that every structural component (beam/column) must be able to resist potential ductile and brittle failures in order for the building to be deemed adequate to resist the earthquake loading. Accordingly, the retrofitting is deemed successful if all the original frame elements behave adequately after retrofitting. Hence, manifestation of flexural and/or shear hinges in the model point out at the exceedance of the member's capacity and implies that retrofitting should be revisited. In view of this, if the exceedance of the flexural/shear capacity is limited to only one or a few members, jacketing of these elements would be more feasible (from a practical and economic perspective) rather than updating the design of shear walls and repeating the whole procedure.

The check against the ductile mechanism of failure is performed on ETABS, and exceedance of the NC limit state is monitored by the manifestation of red-coloured hinges while cyan-coloured hinges point out at the exceedance of the SD limit state. Whereas for the shear check, it is worth recalling that the provisions of EC8-3 (CEN, 2005a) do not require verification at the SD limit state as long as the structure is verified at the NC limit state, since the code recommends the same formulation for evaluating the shear capacity at both limit states. Therefore, verification of the shear requirements of the frame members is only performed at the NC limit state. The shear checks are represented by the demand-to-capacity ratio (D/C), which is measured along both the major and minor axes of the columns cross-section and along the major bending axis in the beams. Hence, the shear demand in the frame elements is measured as the envelope of all the nonlinear pushover analyses performed in both horizontal directions and accounting for accidental eccentricity on either side of the nominal centre of mass.

Step 8: Validating the outcome of retrofitting using nonlinear time history analysis (NLTHA)

The final step involves validating the promising results of the retrofitting strategy against the comprehensive NLTHA. The provisions of EN 1998-1 (CEN, 2004a) require considering a minimum set of 7 ground motion records for the analysis, with the response of the building being measured as the average of the individual responses obtained from each ground motion. The Lebanese database of

seismic ground motions has only been established two decades ago, and the most intense ground motion time history recorded since then belongs to a moderate seismic event of moment magnitude 5.5 that occurred in February 2008 at the Yammouneh fault (Brax et al., 2014). To this end, a set of ground motions that were artificially generated by Brax et al. (2018) and which simulate an earthquake with a moment magnitude of 6.5 at the Yammouneh fault were employed to represent the time history ground motions. The artificial records were generated at different locations in Beirut, with the name of each one representing the site at which the recording station was installed. The ground motions selected are scaled to match the response spectrum of the NC limit state and are presented in Figures A7.23-A7.29 in Appendix 7. Each record consists of three components that represent the three main directions of ground motion, described by the East-West (EW), the North-South (NS), and the gravitational (Z) components which are simultaneously applied to the structure. The load combinations of EN 1990 (CEN, 2002) are adopted in the analysis (Table 7-1). Checks against both ductile and brittle mechanisms of failure are performed to validate the developed retrofitting procedure and to approve the accuracy of the CSM in approximating the nonlinear seismic response of the retrofitted building.

Checking against potential ductile failure is performed by monitoring the formation of cyan and red hinges in beams and columns in parallel to what is performed in the NSPA. Conversely, the shear checks in the NLTHA are represented by the shear D/C ratio which allows for a direct comparison and reflects on the accuracy of the approximative NSPA and the improvised retrofitting strategy. To this end, the ultimate shear demand is accordingly taken as the envelope of all the NLTHA performed to account for the accidental eccentricity in both horizontal directions and on either side of the centre of mass. To note also that the shear demand amounting to a single NLTHA is measured as the average response of the 7 time histories considered in line with the code requirements.

Table 7-1: Load combinations of EN 1990 (CEN, 2002): DL (dead load), LL (live load), EQ (earthquake load)

Load Combinations
1.35 DL
1.35 DL + 1.5 LL
1.0 DL + 0.3 LL ± 1.0 EQ
1.0 DL ± 1.0 EQ

7.3 Regular Building Scenario

By virtue of their simplicity compared to other layouts, typical buildings having a regular configuration are addressed first, and the findings are expanded to cover more complex irregular buildings. A rectangular shape is adopted to portray typical regular buildings, despite the presence of minor setbacks that do not alter the regularity of real-life buildings. The 10-storey frame building considered in this section is the same as the one adopted in the illustration of the seismic assessment procedure in Chapter

3 (Figure 7.4). Accordingly, the building is already deemed as inappropriate to resist the seismic loading, and the discussion directly addresses the process of retrofitting in line with the strategy underlined in the previous section. The material properties and characteristics of the structural system are reinstated from Chapter 3, and more information about the building can be found in Figure A7.1 and Tables A7.1 & A7.2 in Appendix 7, and in Figures A3.1 & A3.2 in Appendix 3 (for the cross-sectional detailing of beams and columns).

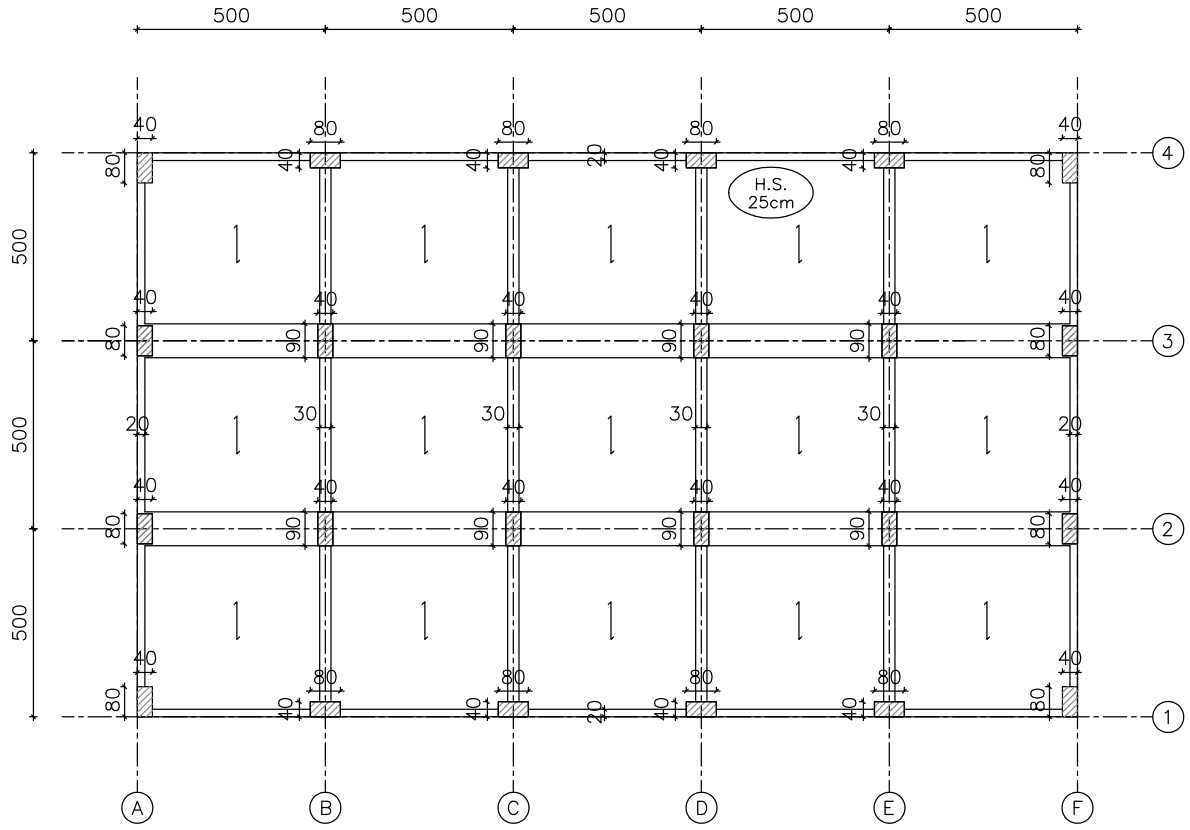


Figure 7.4: Ground floor plan and typical layout of the regular-shaped building (dimensions in cm)

Step 1: Location and dimensions of shear walls

By virtue of the symmetric floor plan, walls are straightforwardly added in both directions such that the nominal centre of mass coincides with the centre of rigidity at each floor (Figure 7.5). Accordingly, the mass participation of the fundamental mode in both horizontal directions is boosted as the Euclidean eccentricity is minimised. It is expected that more walls are required to stiffen the building in the elongated X direction as reflected in the figure.

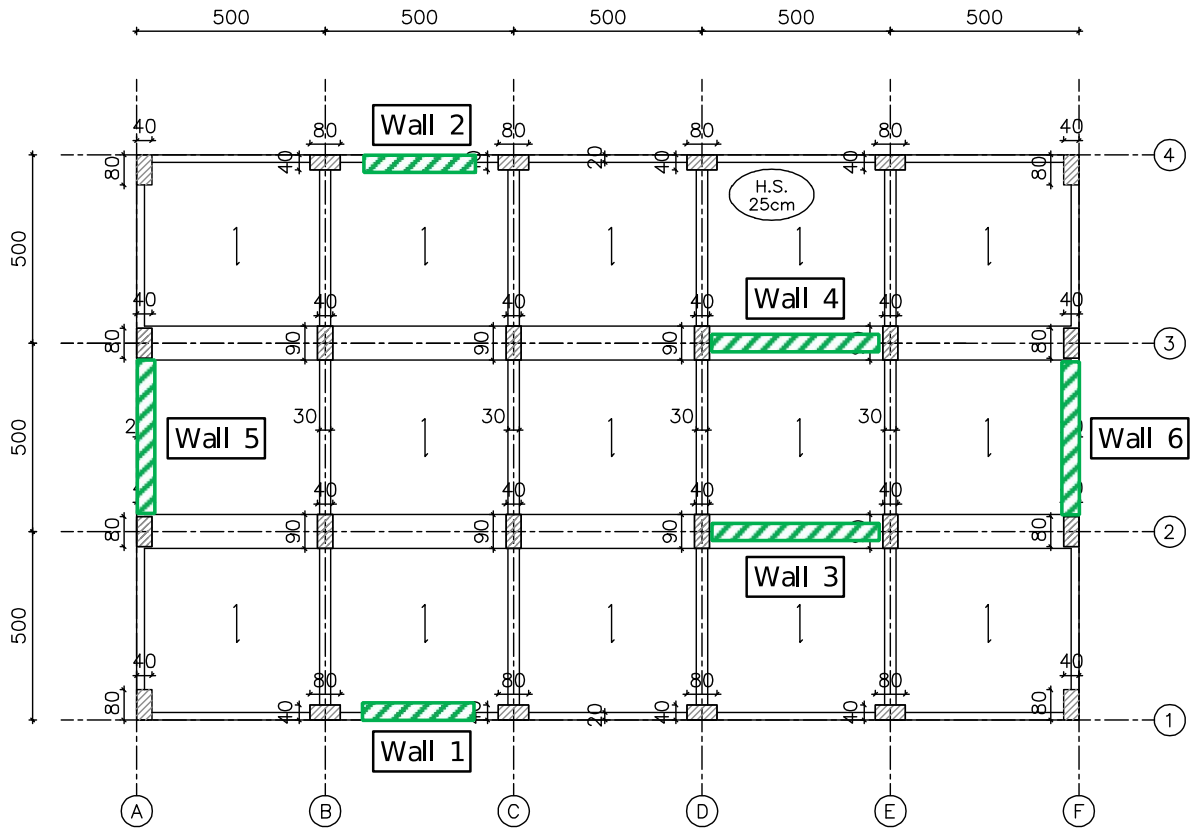


Figure 7.5: Location of reinforcing walls in the rectangular building (dimensions in cm)

Step 2: Preliminary design and detailing of walls

The walls added in direction Y have a thickness of 300 mm and a length of 4200 mm which is bound by the span between the columns. Whereas for the X direction, walls on the periphery have a length of 3000 mm and a thickness of 300 mm, while walls aligned on Grids 2 and 3 have a length of 4500 mm and a thickness of 300 mm. The characteristic compressive strength of concrete of reinforcing shear walls is taken as 35 MPa.

Preliminary dimensioning of shear walls

The thickness of the walls is checked against the minimum code requirement as per the following equation, and the axial load-resisting capacity is verified as well (Table 7-2).

$$b_{w0} \geq \max\left[0.15,\ h_s / 20\right] = 0.215m$$

Table 7-2: Verification of the axial load-resisting capacity per unit length of wall in the rectangular building

	Length (mm)	**Width** (mm)	**Axial Load** (KN)	**Axial Capacity** (KN)
Walls 1 & 2	3000	300	340	4830
Walls 3 & 4	4500	300	375	4830
Walls 5 & 6	4200	300	340	4830

Calculating the loads applied on the walls

Table 7-3 presents the initial estimate of shear force and overturning moment applied at the base, recalling that the bending moment is equal to the plastic capacity of the wall and the shear is accordingly calculated by assuming the shear span at the base to be equal to one half of the wall height as described in the general procedure. These values are used to generate the preliminary bending moment and shear diagrams at all floors in line with the underlined procedure and are checked at later stages against the ones obtained from the CSM at the performance point.

Table 7-3: Preliminary estimate of the base moment and shear demand in the rectangular building

	$V_{base}\,(KN)$	$M_{base}\,(KN.m)$
Walls 1 & 2	615	9900
Walls 3 & 4	1230	19850
Walls 5 & 6	1040	16700

Preliminary dimensioning and reinforcement of the confined zones (boundary columns)

The confinement at the end of the walls (boundary columns) is provided in the critical region which approximately spans across the first floor of the buildings under consideration. Detailing of the walls cross-sections is summarised in Figures 7.6 and 7.7. It is noted that the normalised axial load satisfies the code-permissible limit, as shown in Table 7-4 which also includes other necessary checks performed in that regard.

Table 7-4: Dimensioning of boundary elements and the major checks performed in the rectangular building

	Detailing of Boundary Column			Checking The Effectiveness of Confinement		
	Length (mm)	Width (mm)	Vertical Reinf. Ratio	Normalised Axial Load ($\nu_d \le 0.4$)	$\alpha\,\omega_{wd}$	$30\,\mu_\varphi\,(\nu_d+\omega_v)\,\varepsilon_{sy,d}\,\frac{b_c}{b_0}-0.035$
Walls 1 & 2	600	300	1.34 %	0.035	0.066	0.061
Walls 3 & 4	900	300	1.49 %	0.053	0.094	0.071
Walls 5 & 6	840	300	1.43 %	0.049	0.098	0.076

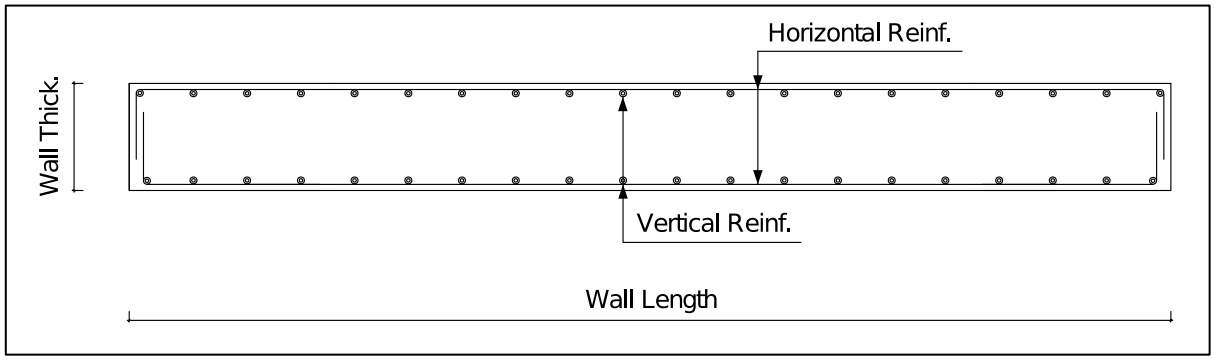


Figure 7.6: Typical detailing of walls above the critical region

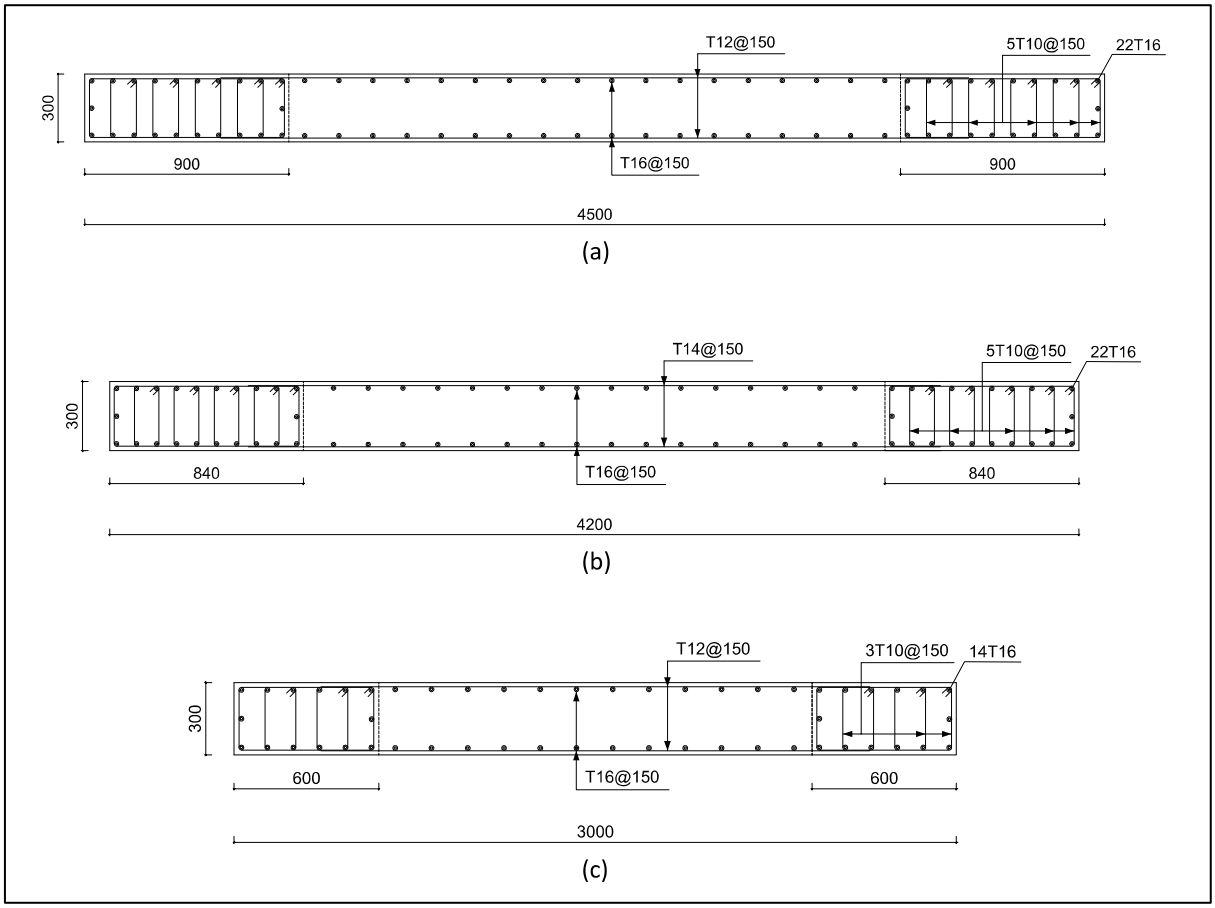


Figure 7.7: Detailing of Walls in the critical region (dimensions in mm)

Step 3: Finding the vibration characteristics of the building in the two main horizontal directions

The vibrational characteristics of the fundamental mode in each horizontal direction are summarised in Table 7-5. Mode 1 has a mass participation of 66% in the global Y direction and Mode 2 has a 66% participation in direction X, both of which are sufficiently high and refer to the predominance of the fundamental translational components of the modes, which supports the application of the CSM to evaluate the building response.

Table 7-5: Fundamental vibration characteristics of the rectangular building

	Mode 1			**Mode 2**		
	ω = 2.92 rad/s			**ω = 3.68 rad/s**		
Storey	**UX** (m)	**UY** (m)	**RZ** (rad)	**UX** (m)	**UY** (m)	**RZ** (rad)
Storey1	0.00001	0.029	0.00001	0.030	-0.00001	0.00013
Storey2	0.00002	0.080	0.00002	0.081	-0.00002	0.00035
Storey3	0.00003	0.154	0.00003	0.155	-0.00004	0.00070
Storey4	0.00005	0.246	0.00005	0.248	-0.00006	0.00104
Storey5	0.00007	0.354	0.00008	0.356	-0.00009	0.00174
Storey6	0.00009	0.473	0.00010	0.474	-0.00012	0.00209
Storey7	0.00012	0.600	0.00013	0.601	-0.00016	0.00279
Storey8	0.00014	0.731	0.00016	0.732	-0.00035	0.00348
Storey9	0.00017	0.865	0.00035	0.866	-0.00035	0.00383
Storey10	0.00035	1.000	0.00035	1.000	-0.00035	0.00453

Step 4: Modal pushover analysis in the global X and Y directions

Modal pushover analysis in the context of the CSM is performed in both horizontal directions at each of the NC and SD limit states. Accidental eccentricity is considered during the application of the pushover loads, and the symmetry of the floor plan makes the consideration of the accidental eccentricity on either side of the nominal centre mass equivalent to one another. The output of the CSM is summarised in Table 7-6, and the results prove that the drift level is well maintained below the 2% limit which is suggested to control the response at the NC limit state. In view of this, Figures A7.2 & A7.4 in Appendix 7 present the calculation of the performance point of the Push-Y analysis (in proportion to Mode 1) at the NC and SD limit states respectively. Similarly, Figures A7.3 & A7.5 in Appendix 7 represent the performance point of the Push-X analysis (Mode 2) at the NC and SD limit states respectively. To illustrate the procedure outlined in detail in Chapter 2, Figures 7.8-7.10 present the steps required to determine the performance point in the X-direction (Push-X analysis) at the NC limit state.

Table 7-6: Summary of all the CSM analyses performed in the rectangular building

	Performance Point		Participation Factor	Mass Coefficient	Performance Point		
	Spectral Acc. a_{pf} (g)	**Spectral Disp. d_{pf} (m)**	**PF_{Roof}**	**α**	**Base Shear (KN)**	**Roof Disp. (m)**	**Drift Ratio**
Push-X (NC)	0.18	0.22	1.49	0.657	4750	0.32	1.00%
Push-Y (NC)	0.12	0.26	1.49	0.656	3160	0.39	1.20%
Push-X (SD)	0.16	0.15	1.49	0.657	4200	0.23	0.68%
Push-Y (SD)	0.11	0.17	1.49	0.656	3000	0.25	0.87%

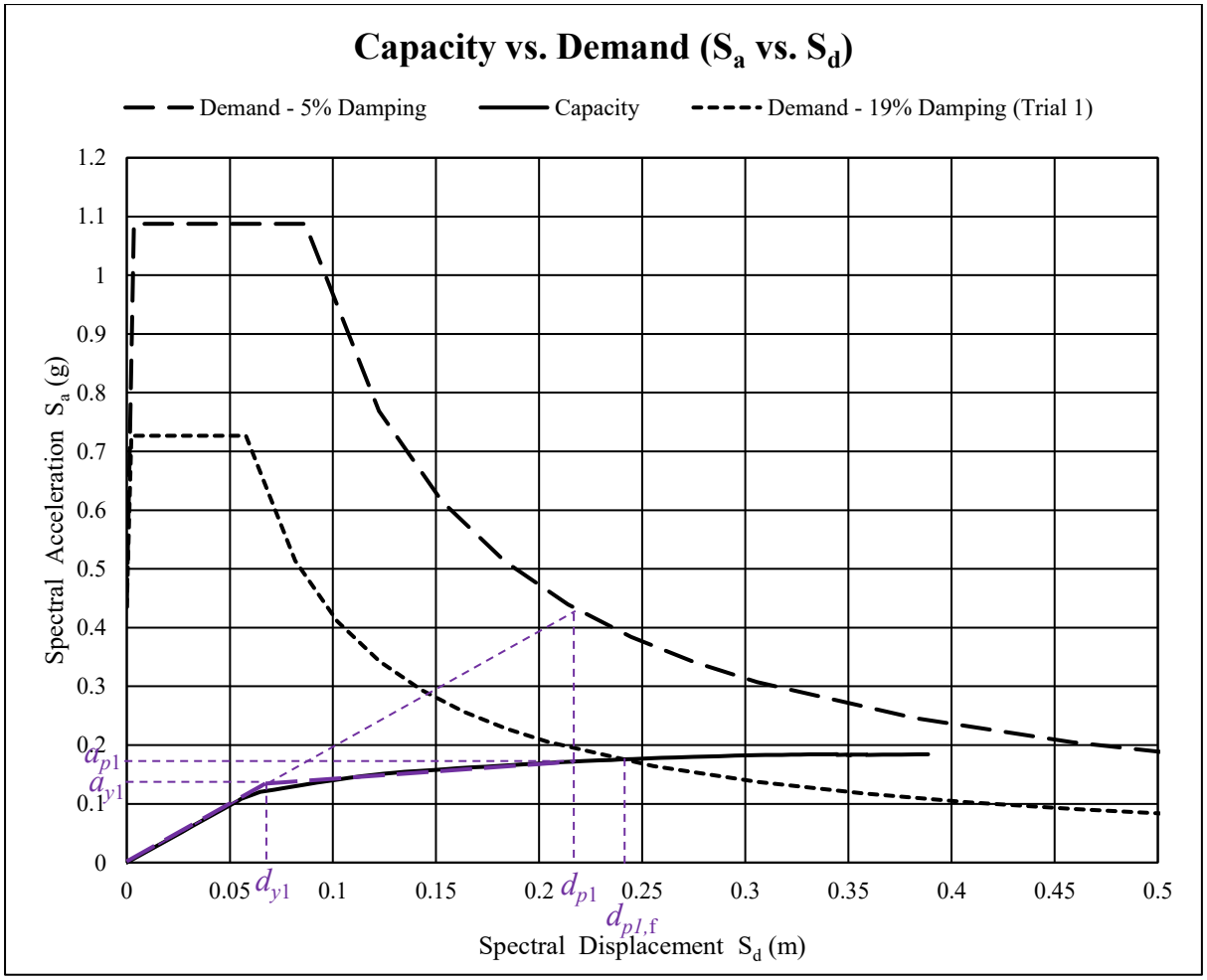


Figure 7.8: Procedure of finding the performance point of the Push-X analysis (Mode 2) at the NC limit state in the rectangular building (Step 1)

Trial 1:

$a_{y1} = 0.13 \qquad d_{y1} = 0.07$

$a_{p1} = 0.18 \qquad d_{p1} = 0.22$

$$\mu = \frac{d_{p1}}{d_{y1}} = 3.14$$

Equivalent Damping: $\beta_{eff} = 19\%$ (Equations 2.16 – 2.18)

Spectral Reduction Factor: $B = 1.50$ (Equation 2.22)

$a_{p1,f} = 0.185 \qquad d_{p1,f} = 0.242$

$$\%\text{Difference} = \frac{\left|d_{p1,f} - d_{p1}\right|}{d_{p1}} = 10\% > 5\%$$

$\rightarrow$ Iterate

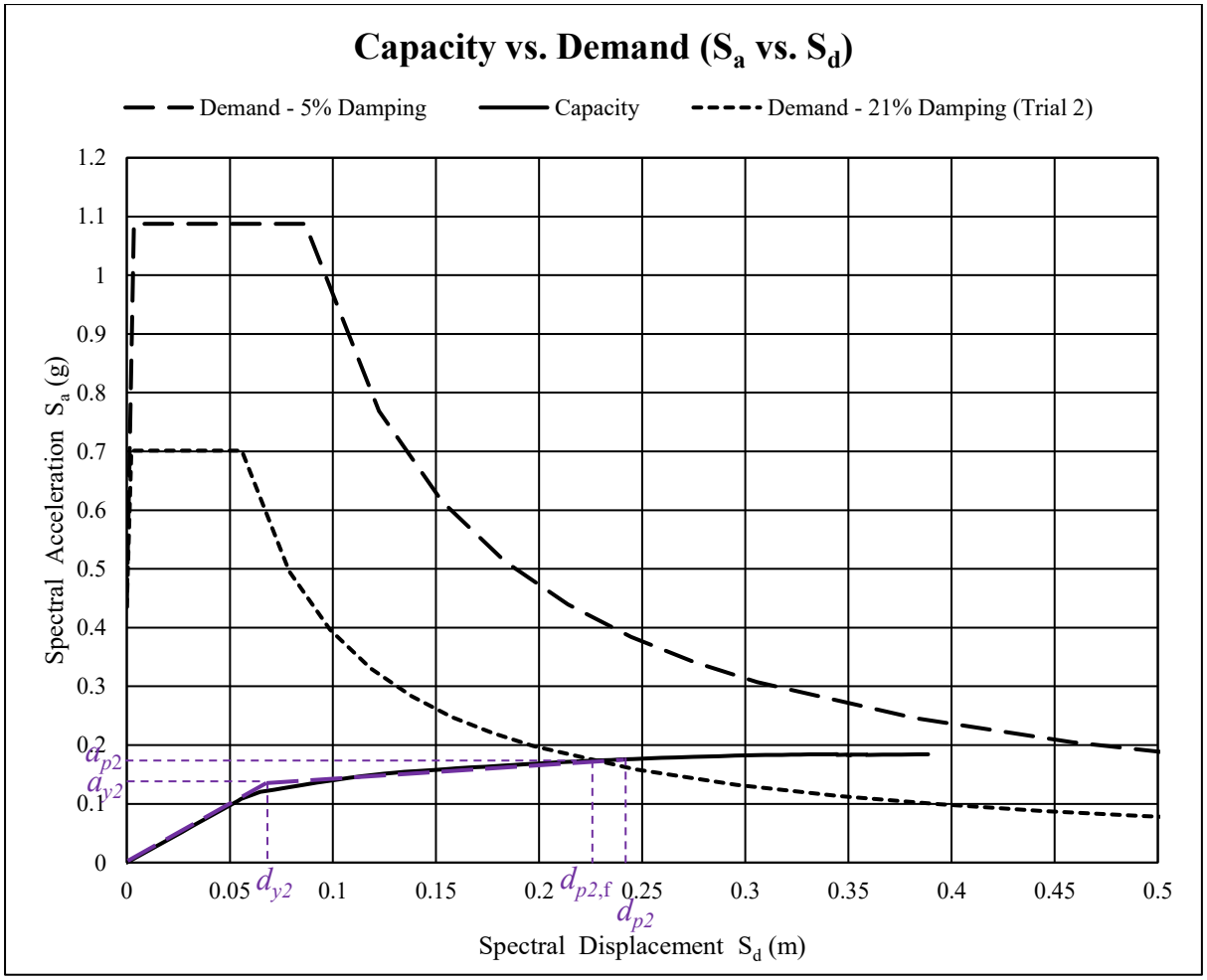


Figure 7.9: Procedure of finding the performance point of the Push-X analysis (Mode 2) at the NC limit state in the rectangular building (Step 2)

Trial 2:

$a_{y2} = 0.133 \qquad d_{y2} = 0.07$

$a_{p2} = 0.185 \qquad d_{p2} = 0.242$

$$\mu = \frac{d_{p2}}{d_{y2}} = 3.46$$

Equivalent Damping: $\beta_{eff} = 21\%$ (Equations 2.16 – 2.18)

Spectral Reduction Factor: $B = 1.57$ (Equation 2.22)

$a_{p2,f} = 0.18 \qquad d_{p2,f} = 0.225$

$$\%\text{Difference} = \frac{\left|d_{p2,f} - d_{p2}\right|}{d_{p2}} = 7\% > 5\%$$

$\rightarrow$ Iterate

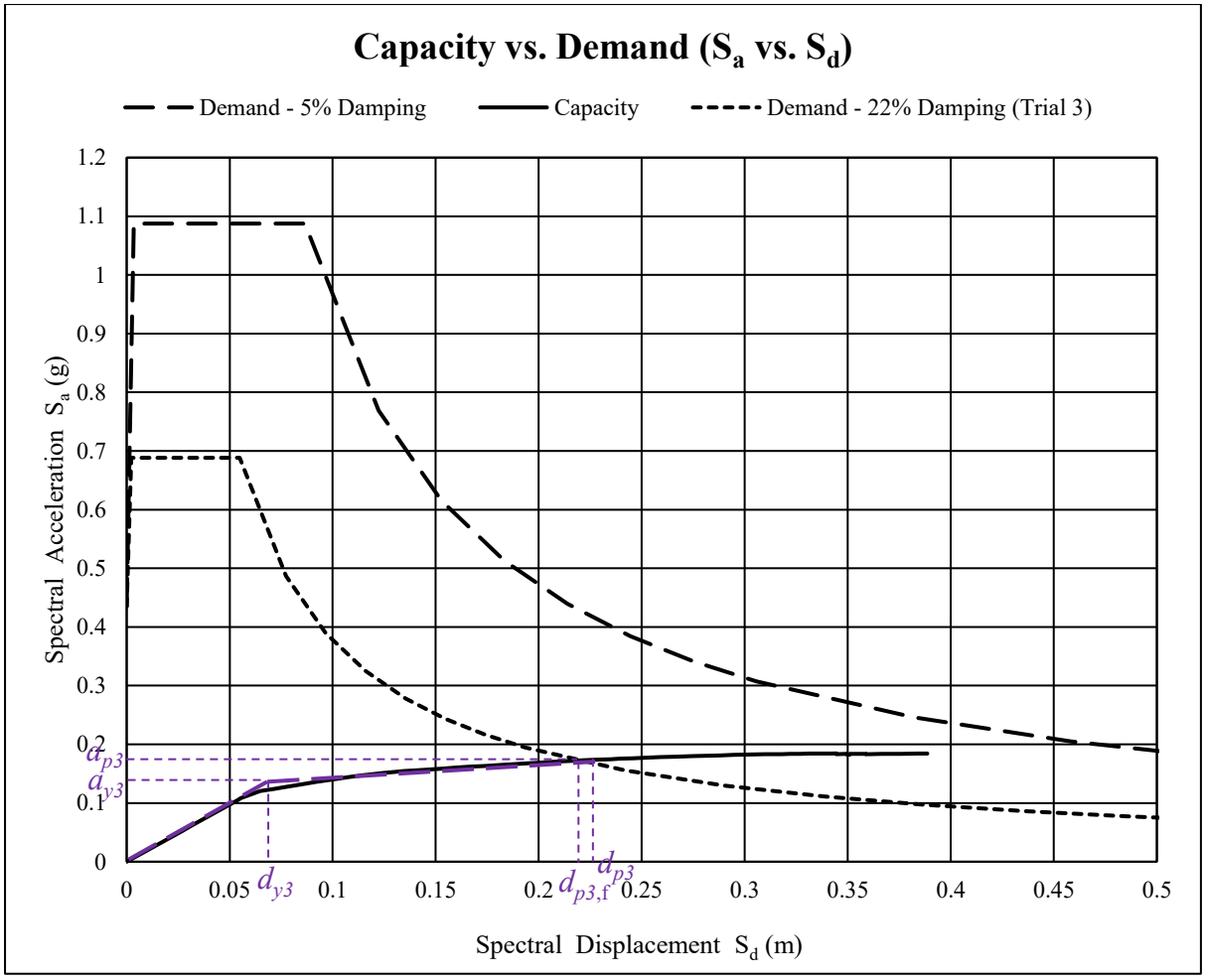


Figure 7.10: Procedure of finding the performance point of the Push-X analysis (Mode 2) at the NC limit state in the rectangular building (Step 3)

Trial 3:

$a_{y3} = 0.13 \qquad d_{y3} = 0.067$

$a_{p3} = 0.18 \qquad d_{p3} = 0.225$

$$\mu = \frac{d_{p3}}{d_{y3}} = 3.36$$

Equivalent Damping: $\beta_{eff} = 22\%$ (Equations $2.16 - 2.18$)

Spectral Reduction Factor: $B = 1.60$ (Equation 2.22)

$a_{p3,f} = 0.18 \qquad d_{p3,f} = 0.22$

$$\%\text{Difference} = \frac{\left|d_{p3,f} - d_{p3}\right|}{d_{p3}} = 2.2\% < 5\%$$

$\rightarrow$ Performance point is determined:

$a_{p,final} = 0.18g \qquad d_{p,final} = 0.22m$

Step 5: Verifying the flexural and shear capacities of the retrofitting walls against the seismic demand

Once the performance point is determined, the actual shear force and bending moment in the walls are evaluated from the envelope of the pushover analyses performed. Accordingly, the shear reinforcement is provided such that the shear capacity is not exceeded at all floors (Table 7-7). Whereas for the flexural reinforcement, detailing of the first storey (base level) has been already set up and encompasses the confined regions at the ends of the walls (Figure 7.7), while the reinforcement at upper floors is provided to ensure that the plastic capacity is not exceeded and no plastic hinges form at these levels (Table 7-7). In view of this, Tables 7-8 and 7-9 respectively present the flexural and shear checks which are also plotted in graphical form in Figures 7.11 and 7.12.

Table 7-7: Provisioned flexural and shear reinforcement of walls in the rectangular building

	Wall 4200 x 300		Wall 4500 x 300		Wall 3000 x 300	
Storey	**Vertical Reinf.**	**Shear Reinf.**	**Vertical Reinf.**	**Shear Reinf.**	**Vertical Reinf.**	**Shear Reinf.**
Storey10	T12@150	T10@200	T12@150	T10@200	T12@150	T10@200
Storey9	T12@150	T10@200	T12@150	T10@200	T12@150	T10@200
Storey8	T12@150	T10@150	T12@150	T10@200	T12@150	T10@200
Storey7	T12@150	T10@150	T12@150	T10@200	T12@150	T10@200
Storey6	T16@150	T12@150	T14@150	T10@150	T16@150	T10@150
Storey5	T16@150	T12@150	T16@150	T10@150	T16@150	T10@150
Storey4	T20@150	T12@150	T16@150	T10@150	T16@150	T10@150
Storey3	T20@150	T14@150	T20@150	T10@150	T20@150	T10@150
Storey2	T25@150	T14@150	T25@150	T12@150	T25@150	T12@150
Storey1	B.C.	T14@150	B.C.	T12@150	B.C.	T12@150

Table 7-8: Checking the flexural requirements of walls in the rectangular building

	Wall 4200 x 300			Wall 4500 x 300			Wall 3000 x 300		
Storey	**Demand** KN-m	**Capacity** KN-m	**D/C**	**Demand** KN-m	**Capacity** KN-m	**D/C**	**Demand** KN-m	**Capacity** KN-m	**D/C**
Storey1	16000	16050	1.00	19750	19850	0.99	8300	8300	1.00
Storey2	22900	24000	0.95	21050	28250	0.74	8450	9600	0.88
Storey3	17650	20200	0.87	17550	23650	0.74	7500	10250	0.73
Storey4	14400	19950	0.72	15350	16800	0.91	6600	7200	0.91
Storey5	10650	13950	0.77	13150	16400	0.80	5650	7050	0.80
Storey6	8900	13650	0.65	10950	13200	0.83	4700	6950	0.68
Storey7	7100	8450	0.84	8750	10000	0.88	3750	4250	0.88
Storey8	5350	8100	0.66	6600	9500	0.69	2800	4100	0.69
Storey9	3550	7750	0.46	4400	9050	0.48	1900	3950	0.47
Storey10	1800	7450	0.24	2200	8600	0.26	950	3800	0.25

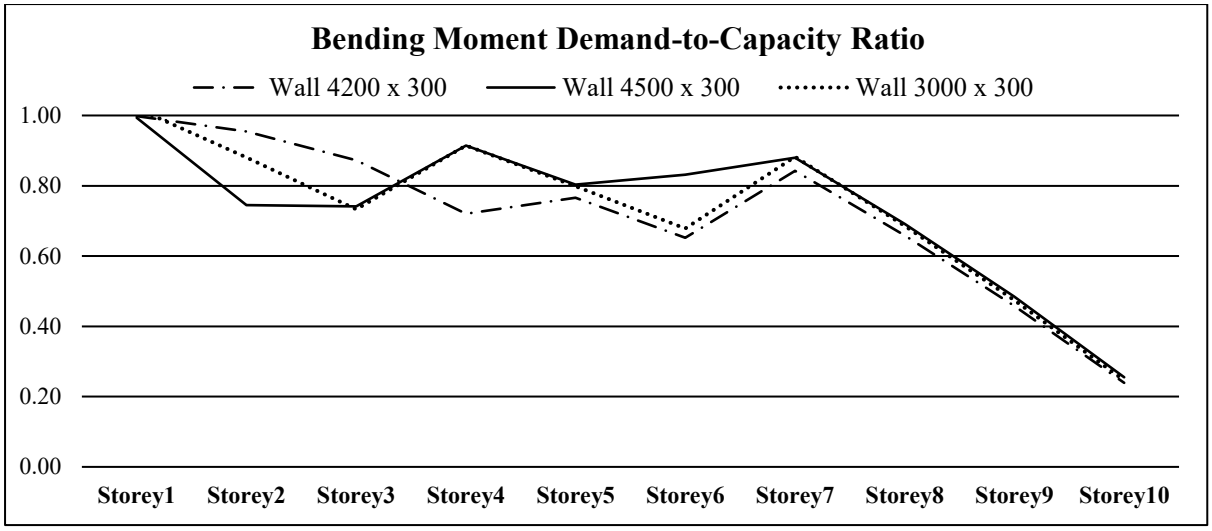


Figure 7.11: Checking the flexural requirements of walls in the rectangular building

Table 7-9: Checking the shear requirements of walls in the rectangular building

	Wall 4200 x 300			Wall 4500 x 300			Wall 3000 x 300		
Storey	**Demand** (KN)	**Capacity** (KN)	**D/C**	**Demand** (KN)	**Capacity** (KN)	**D/C**	**Demand** (KN)	**Capacity** (KN)	**D/C**
Storey1	2500	2550	0.97	1550	2000	0.78	700	1300	0.54
Storey2	2150	2550	0.84	1450	2000	0.72	600	1300	0.47
Storey3	1900	2550	0.75	1050	1400	0.77	550	900	0.60
Storey4	1700	1850	0.91	1100	1400	0.79	500	900	0.52
Storey5	1450	1850	0.78	900	1400	0.67	400	900	0.45
Storey6	1200	1850	0.65	800	1400	0.58	350	900	0.37
Storey7	950	1300	0.74	750	1050	0.71	250	700	0.40
Storey8	700	1300	0.56	450	1050	0.45	200	700	0.30
Storey9	500	950	0.50	300	1050	0.31	150	700	0.20
Storey10	250	950	0.25	50	1050	0.04	50	700	0.10

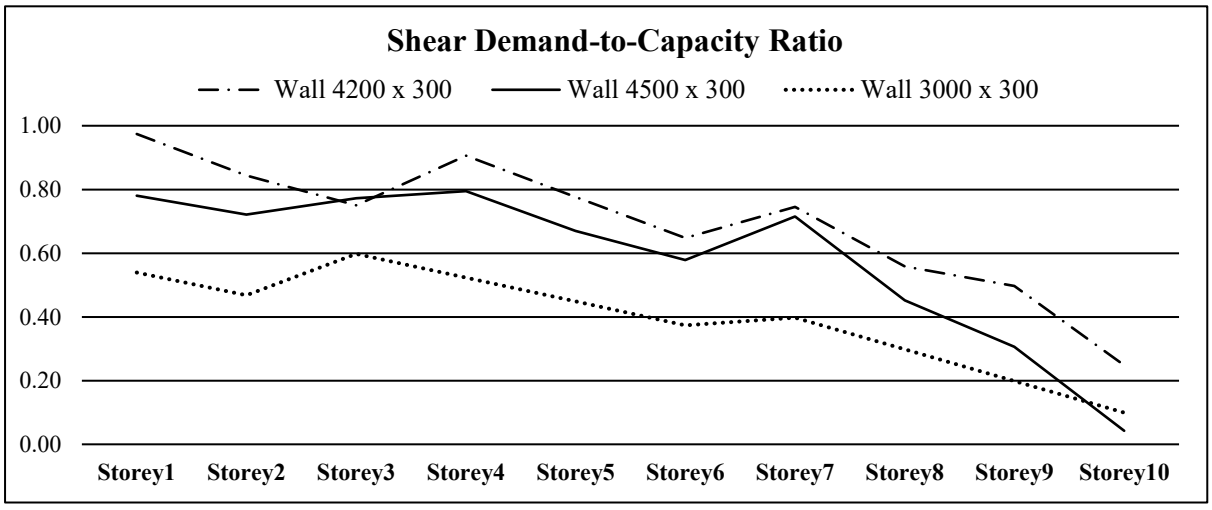


Figure 7.12: Checking the shear requirements of walls in the rectangular building

Step 6: Checking the local ductility requirements in the shear walls

As explained earlier, the ductility supply in the shear walls is checked to ensure that the ductility supply is sufficient to meet the seismic demand. As discussed, the ductility demand is measured in the form of the plastic rotation that is directly obtained from ETABS at the performance point, while the ultimate plastic rotational capacity is calculated according to the equations formulated by Biskinis (2007) and by Biskinis and Fardis (2004, 2007) and that of EC8-3 (CEN, 2005a). The results for all the walls are presented in Table 7-10 and prove that the plastic rotational capacity exceeds by far the maximum plastic rotation in each wall, hence proving the effectiveness of confinement in the boundary elements in satisfying the local ductility requirements.

Table 7-10: Verification of the local ductility requirements in the shear walls of the rectangular building

	Demand	Capacity		
	Max. Rotation (rad)	**EC8-3 (rad)**	**Empirical Equation 2 (rad)**	**Empirical Equation 3 (rad)**
Walls 1 & 2	0.0068	0.040	0.056	0.050
Walls 3 & 4	0.0070	0.085	0.118	0.108
Walls 5 & 6	0.0091	0.096	0.133	0.124

Step 7: Checking the performance of the original frame against potential brittle and shear failures

Ductile mechanism check (chord rotation):

Figures 7.13 and 7.14 present the chord rotation checks performed at the NC and SD limit states respectively. The absence of red hinges at the NC limit state indicates that the ultimate chord rotation limit is never exceeded (Figure 7.13). Likewise, the absence of cyan-coloured hinges proves that the chord rotation limit pertaining to the SD limit state is never exceeded (Figure 7.14). In this regard, cyan hinges were even absent when the seismic demand was scaled to match the NC limit state (Figure 7.13), meaning that the chord rotation limit corresponding to the SD limit state was not even attained at the NC limit state. To this end, this is sufficient to conclude that the chord rotation requirements at the SD limit state are satisfied and are not required to be proven in a separate check. Nevertheless, checks at the SD limit state were performed and support the previously drawn conclusion (Figure 7.14). Consequently, it is concluded that the chord rotation requirements of the retrofitted building are satisfied.

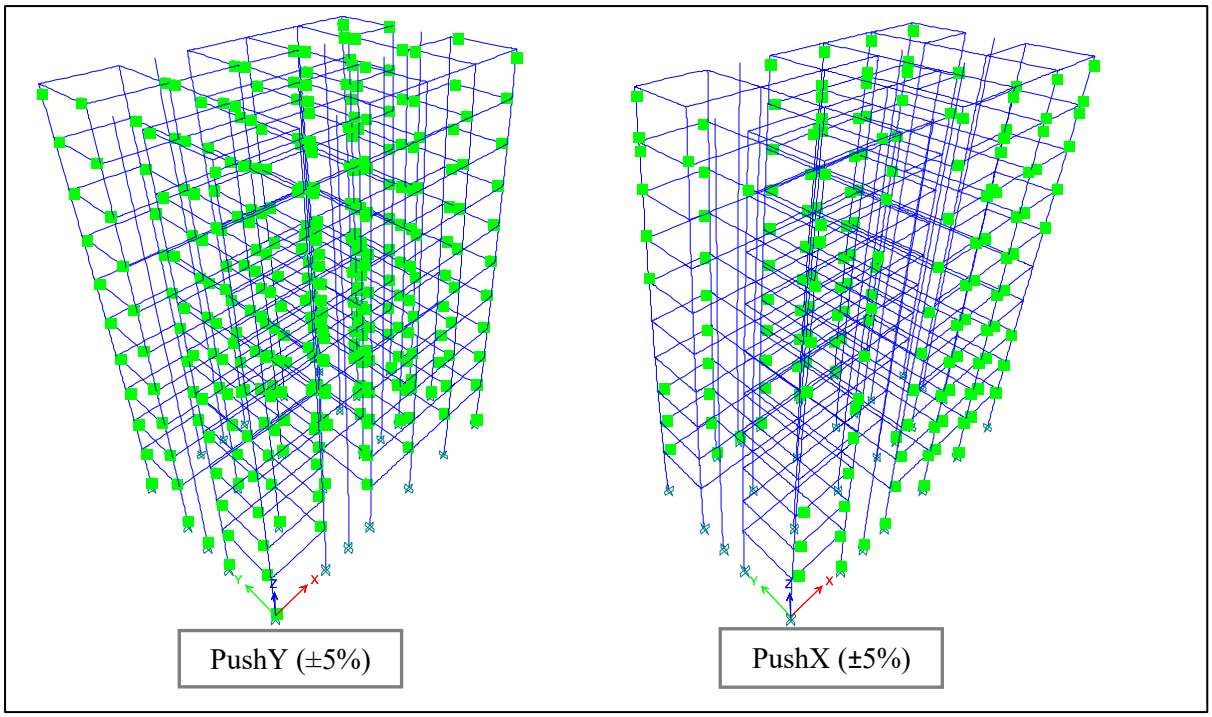


Figure 7.13: Flexural hinges at the NC limit state in the rectangular building

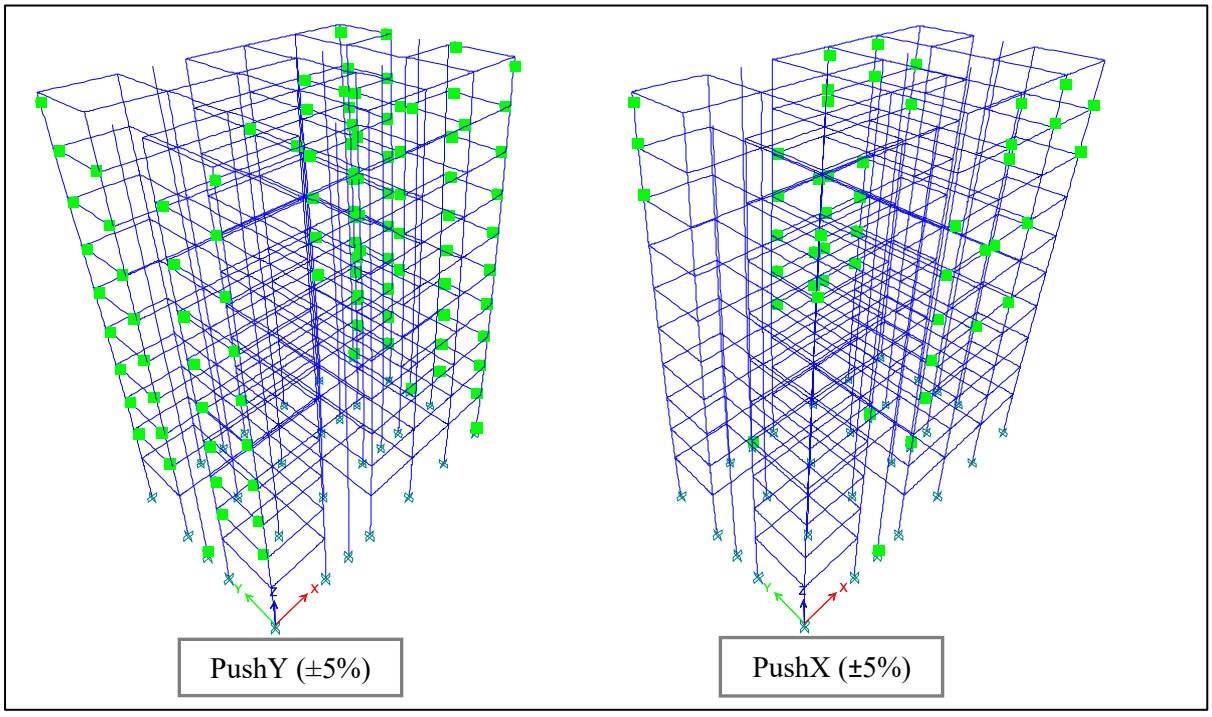


Figure 7.14: Flexural hinges at the SD limit state in the rectangular building

Brittle mechanism check (Shear Failure):

By virtue of the symmetric floorplan along both horizontal directions, columns are categorised into four groups defined in Table 7-11. Likewise, symmetric beams are grouped together and share the same beam label (Figure 7.15).

Figures 7.16 and 7.17 present the shear checks along the major and minor axes of the columns cross-sections respectively, while Figure 7.18 presents the shear checks in the beams. As noted, the shear capacity exceeds the demand in all the structural members which validates the effectiveness of the improvised retrofitting solution. Apart from the first floor which shows a significant shear demand in view of the fixity at the base of the building, it is noted that that the D/C ratio in the columns generally increases by moving up the height by virtue of the reduced cross-section at upper floors, with the highest D/C ratio mostly registered at the tenth floor where the columns cross-section is significantly reduced. Whereas the maximum shear in beams is mostly recorded at the first floor, and the D/C ratio decreases by moving up the levels which sounds reasonable since the beams possess the same cross-section and reinforcement detailing at all storeys, while the seismic shear is expected to decrease moving up the height.

Table 7-11: Groups of columns considered in the rectangular building

	Columns
Corner	C1, C6, C19, C24
Edge X	C2, C3, C4, C5, C20, C21, C22, C23
Edge Y	C7, C12, C13, C18
Interior	C8, C9, C10, C11, C14, C15, C16, C17

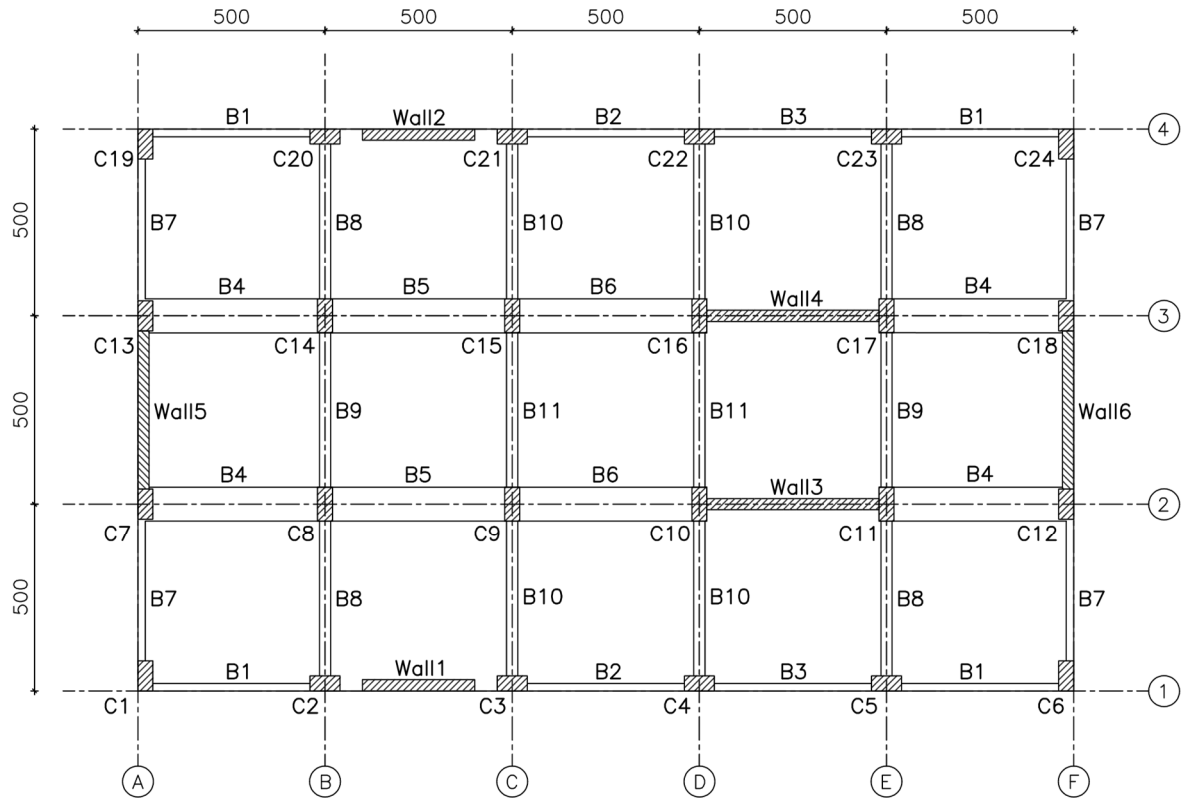


Figure 7.15: Labels of beams and columns in the rectangular building

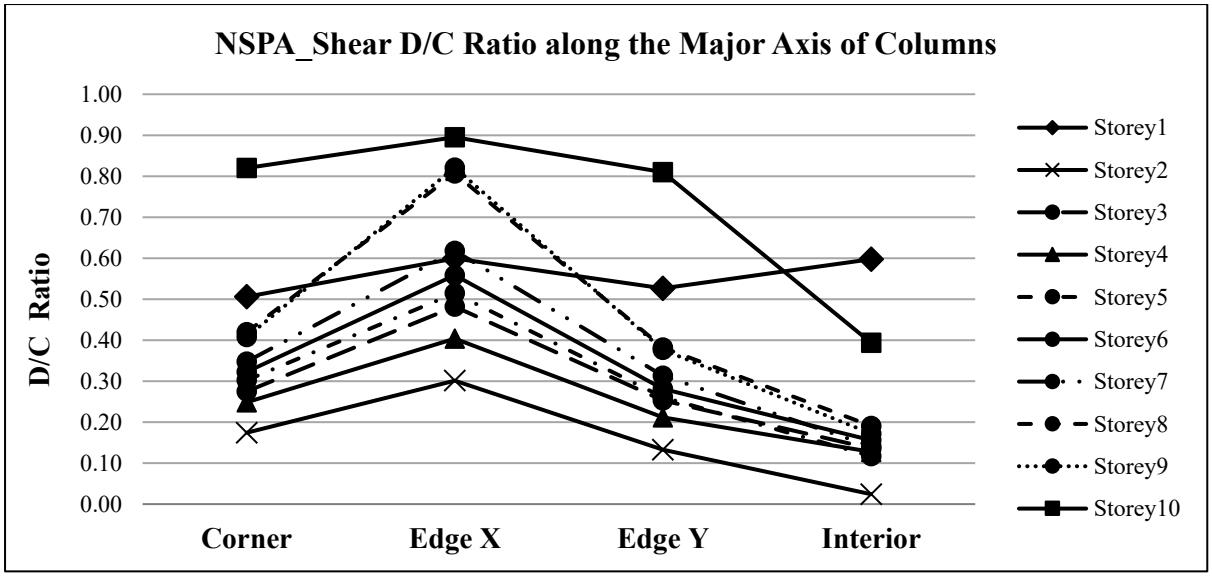


Figure 7.16: NSPA results of the shear D/C ratio measured along the major bending axis of columns in the rectangular building

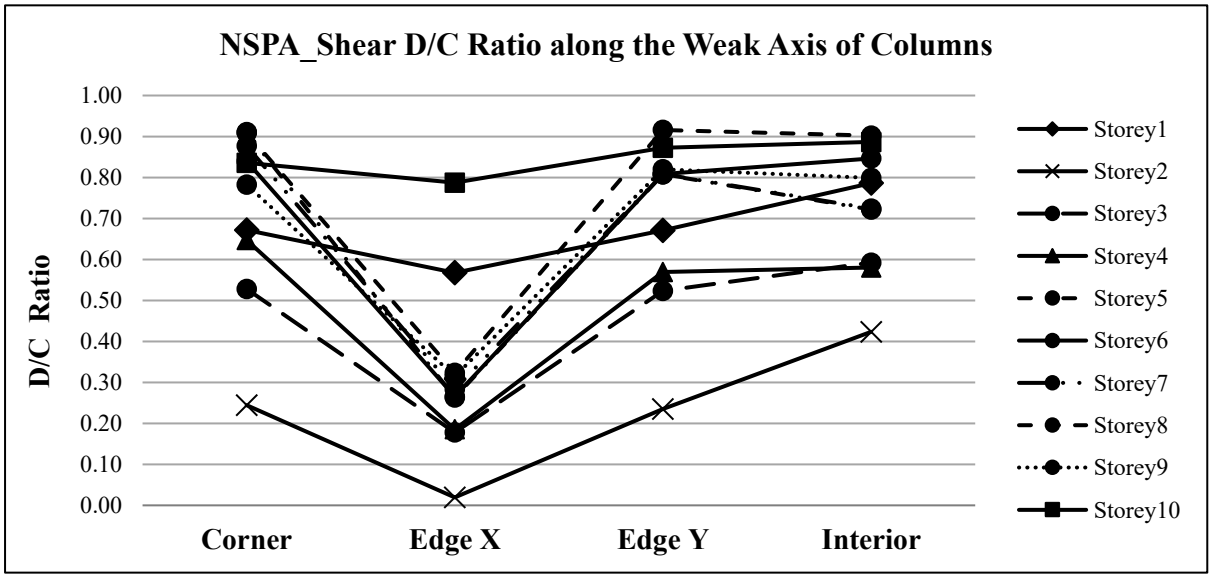


Figure 7.17: NSPA results of the shear D/C ratio measured along the weak axis of columns in the rectangular building

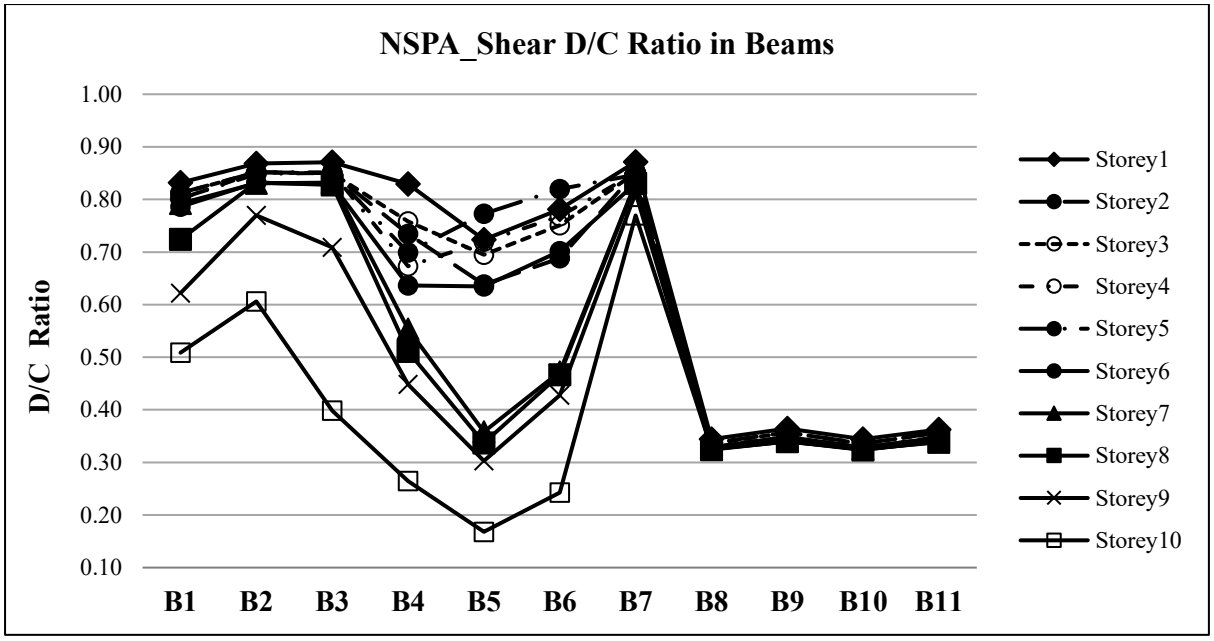


Figure 7.18: NSPA results of the shear D/C ratio measured along the strong bending axis of beams in the rectangular building

Step 8: Validation against complete nonlinear time history analysis (NLTHA)

The chord rotation results of the NLTHA are presented in Figures 7.19 & 7.20, accounting for the accidental eccentricity in each horizontal direction in parallel to what is considered in the NSPA. The results compare well with those obtained using the CSM (or NSPA), as the absence of red hinges under all the ground motions considered indicates that the ultimate chord rotation limit of the NC limit state is never attained or exceeded. In sum, the results point out at the effectiveness of the developed retrofitting strategy in overcoming potential ductile failure in the building scenario under consideration.

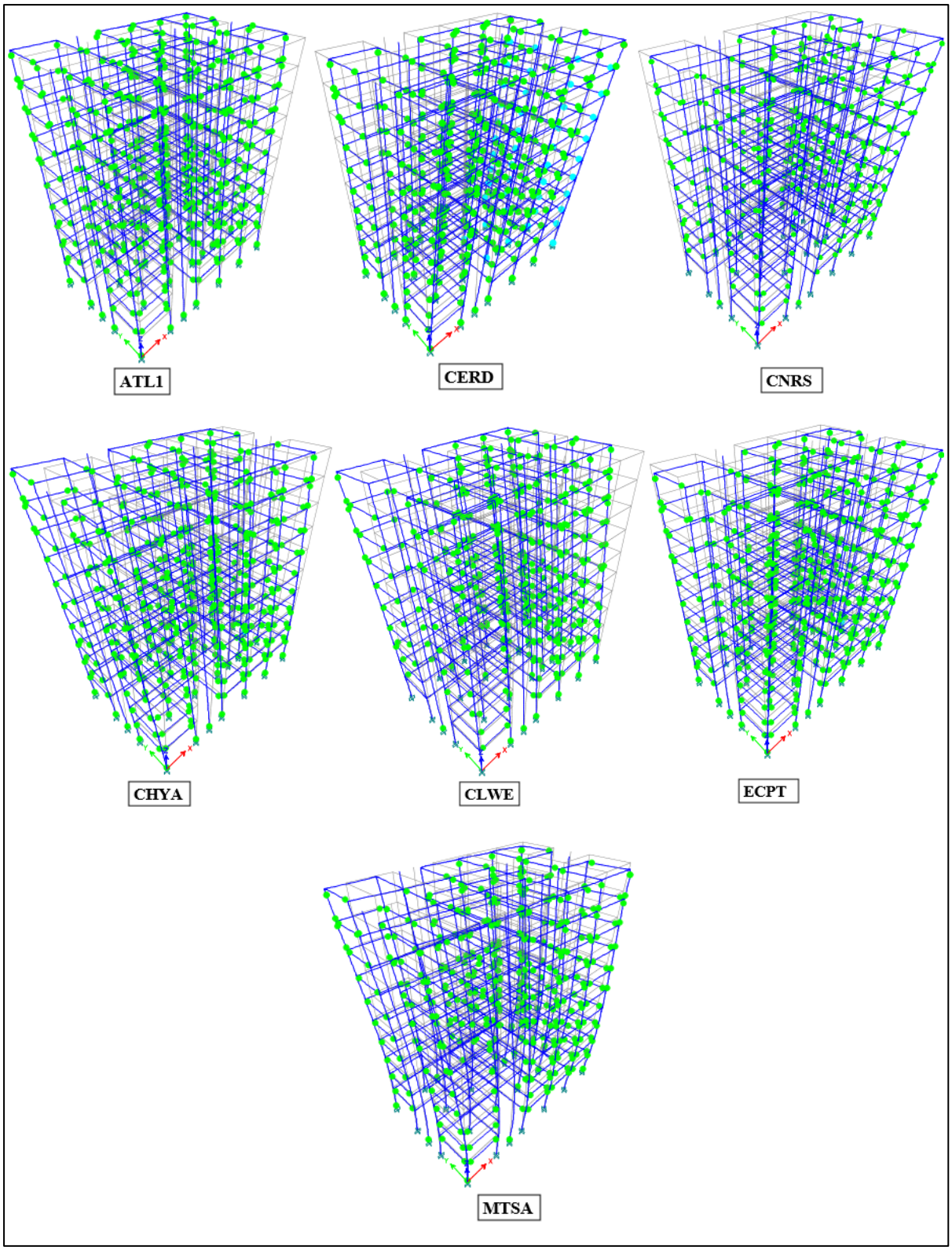


Figure 7.19: Flexural hinges obtained at the end of the NLTHA performed in the rectangular building (ecc. ±5% in X)

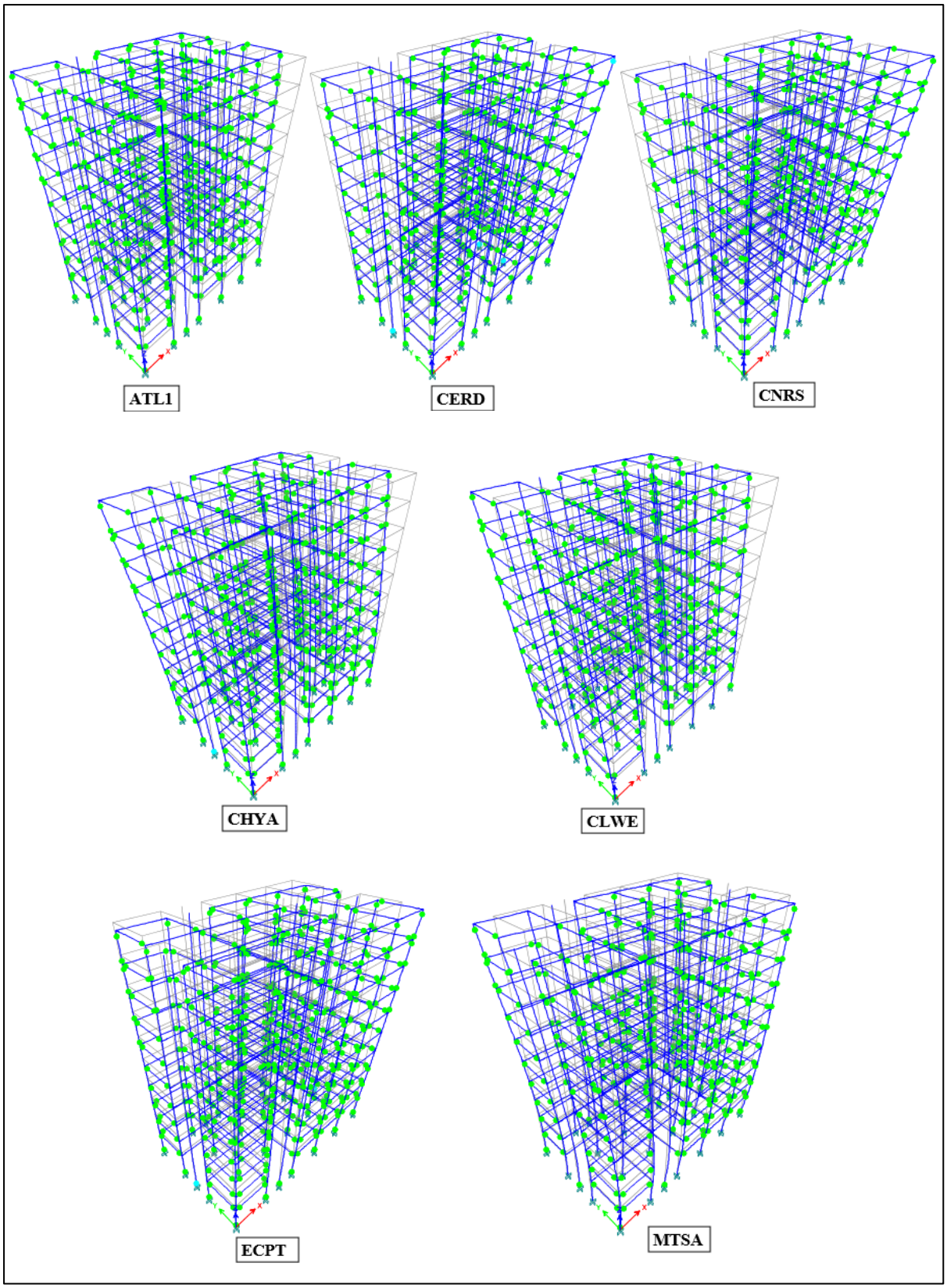


Figure 7.20: Flexural hinges obtained at the end of the NLTHA performed in the rectangular building (ecc. ±5% in Y)

In contrast to the results obtained using the CSM, the shear results of the NLTHA are presented in the form of D/C plots and are presented in Figures 7.21-7.23. First, it is noted that the shear capacity exceeds

the demand in all the structural members and most importantly, the results are showing a high level of correlation with those obtained using the NSPA. Indeed, the pattern of variation of the shear D/C ratio in both the beams and columns is very similar to what is obtained from NSPA, and the D/C values in all the plots are very comparable to what is observed from the NSPA.

These results highlight the accuracy of the approximative NSPA in predicting the shear demand in the frame components and highlight the effectiveness of the developed retrofitting strategy in strengthening the original frame building against seismic loading.

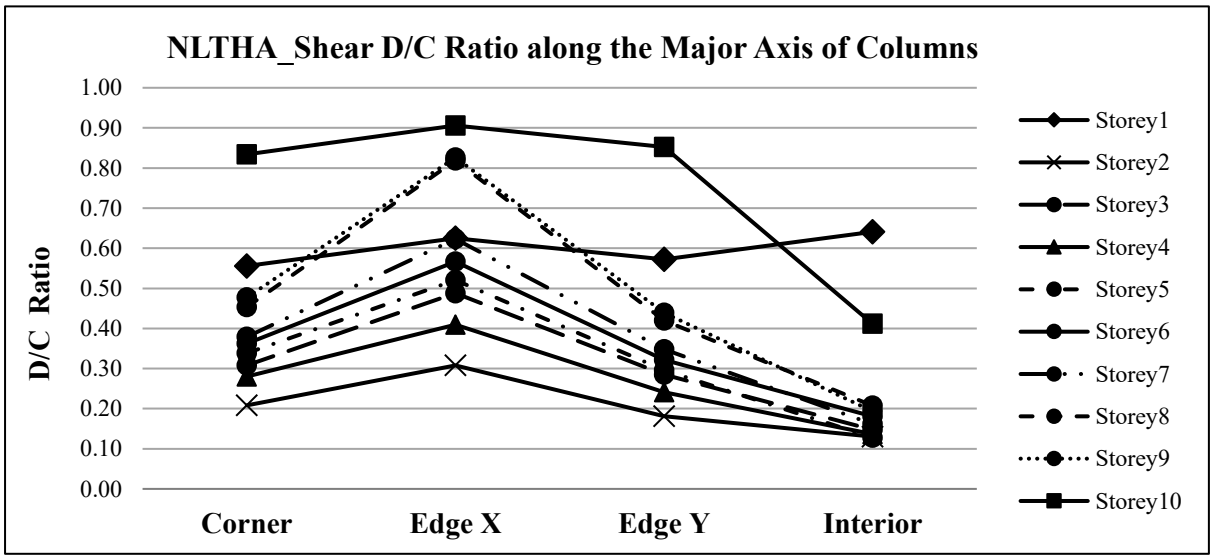


Figure 7.21: NLTHA results of the shear D/C ratio measured along the major bending axis of columns in the rectangular building

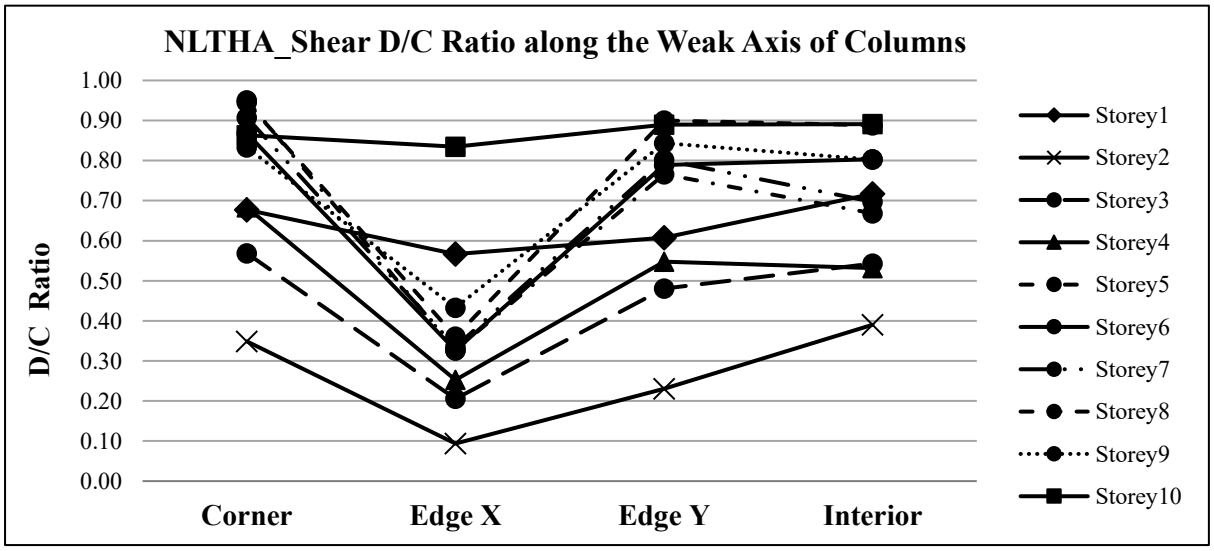


Figure 7.22: NLTHA results of the shear D/C ratio measured along the weak axis of columns in the rectangular building

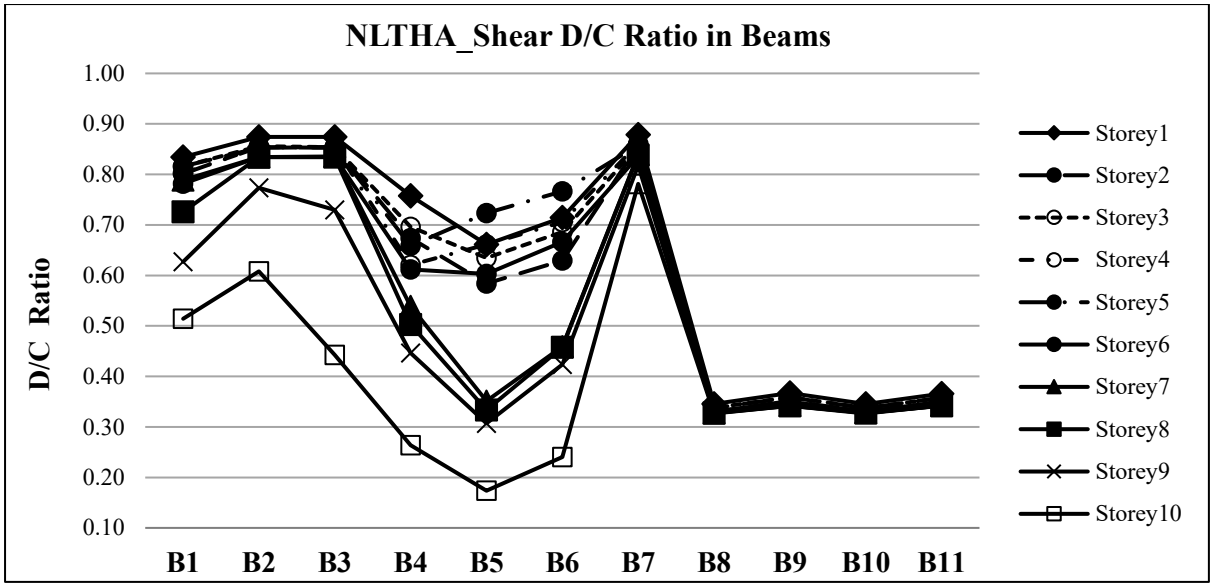


Figure 7.23: NLTHA results of the shear D/C ratio measured along the strong bending axis of beams in the rectangular building

7.4 L-shaped Scenario

Step 1: Location and dimensions of shear walls

L-shaped buildings are commonly present in all countries, and they typically consist of an existing rectangular building which was subjected to an expansion that resulted in disrupting the regularity of the floorplan. The L-shaped building considered in this example is composed of ten storeys and is characterised by the same span lengths between the columns observed in the rectangular scenario. Accordingly, the dimensions of the structural beams and columns are comparable to those observed in the rectangular scenario, as well as the material properties and detailing of the structural framing members. Further details regarding the original building can be found in Figure A7.6 and Tables A7.3 & A7.4 in Appendix 7, and in Figures A3.1 & A3.2 in Appendix 3 (for the cross-sectional detailing of beams and columns). In view of this, seismic retrofitting is mandatory as the unreinforced building is deemed inappropriate to resist potential seismic loading.

In regard to retrofitting, the location of walls is selected on a trial basis to reduce the average Euclidean eccentricity and to maximise the mass participation of the fundamental mode in each translational direction, as illustrated in Figure 7.24. In this regard, two retrofitting scenarios are proposed for the L-shaped building, with the first one serving as a practical solution and is accordingly recommended (Figure 7.25), while the second one is only being presented to highlight that the mass participation can theoretically be further increased upon further reduction of the average Euclidean eccentricity (Figure 7.26). The first scenario is more appealing from a practical perspective and involves a smaller number of walls which is more beneficial during construction. To note that the two retrofitting scenarios illustrated correspond to the two leftmost points having the two smallest Euclidean eccentricities in Figure 7.24.

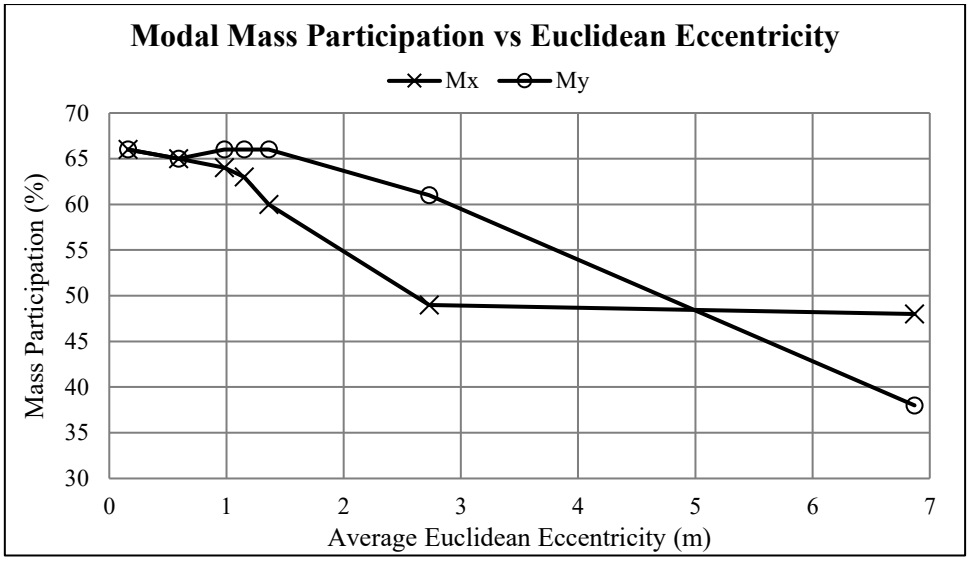


Figure 7.24: Optimising the mass participation ratio of the fundamental modes in the L-shaped building

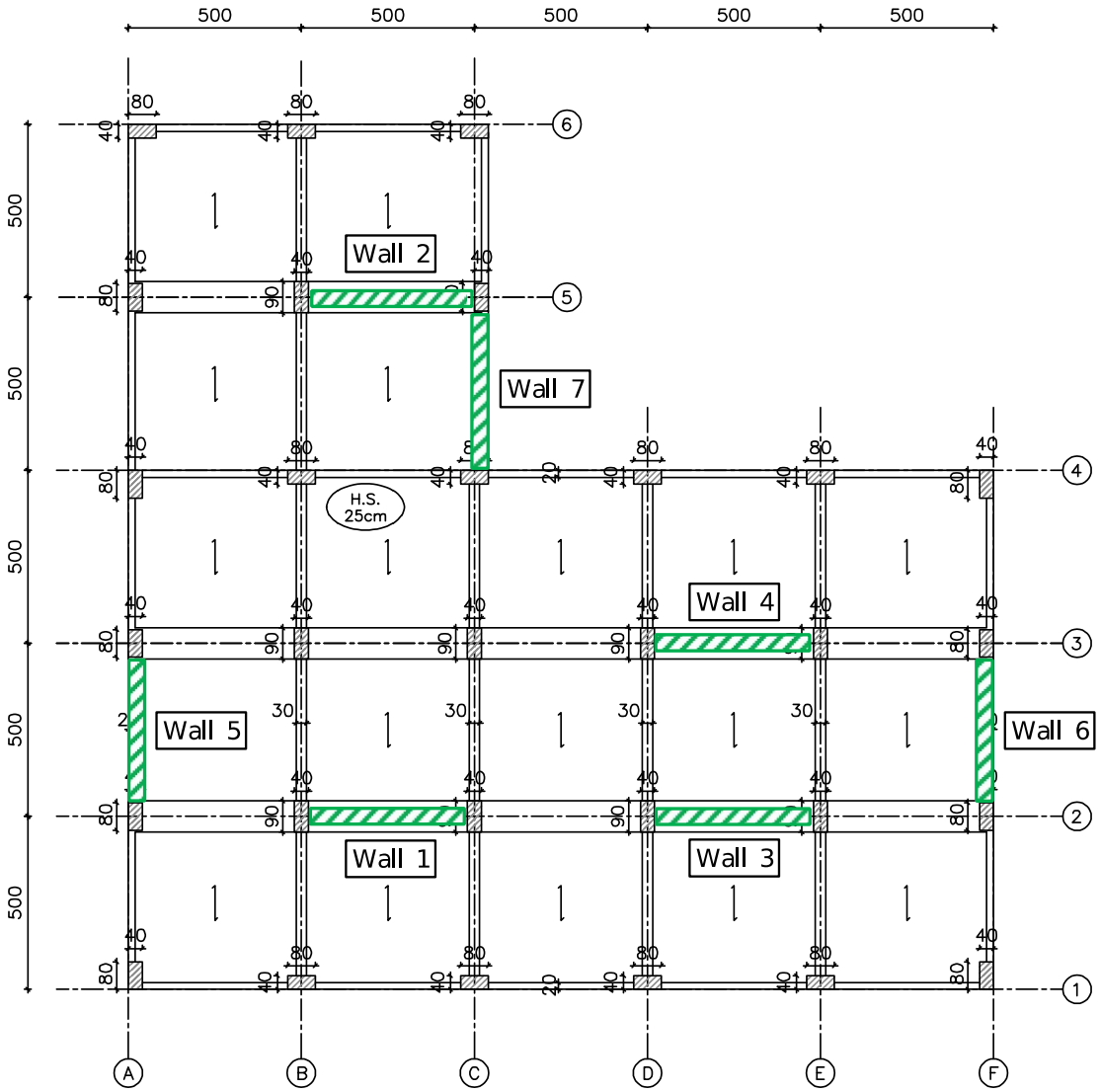


Figure 7.25: Ground floor plan and reinforcing walls in the L-shaped building (dimensions in cm)

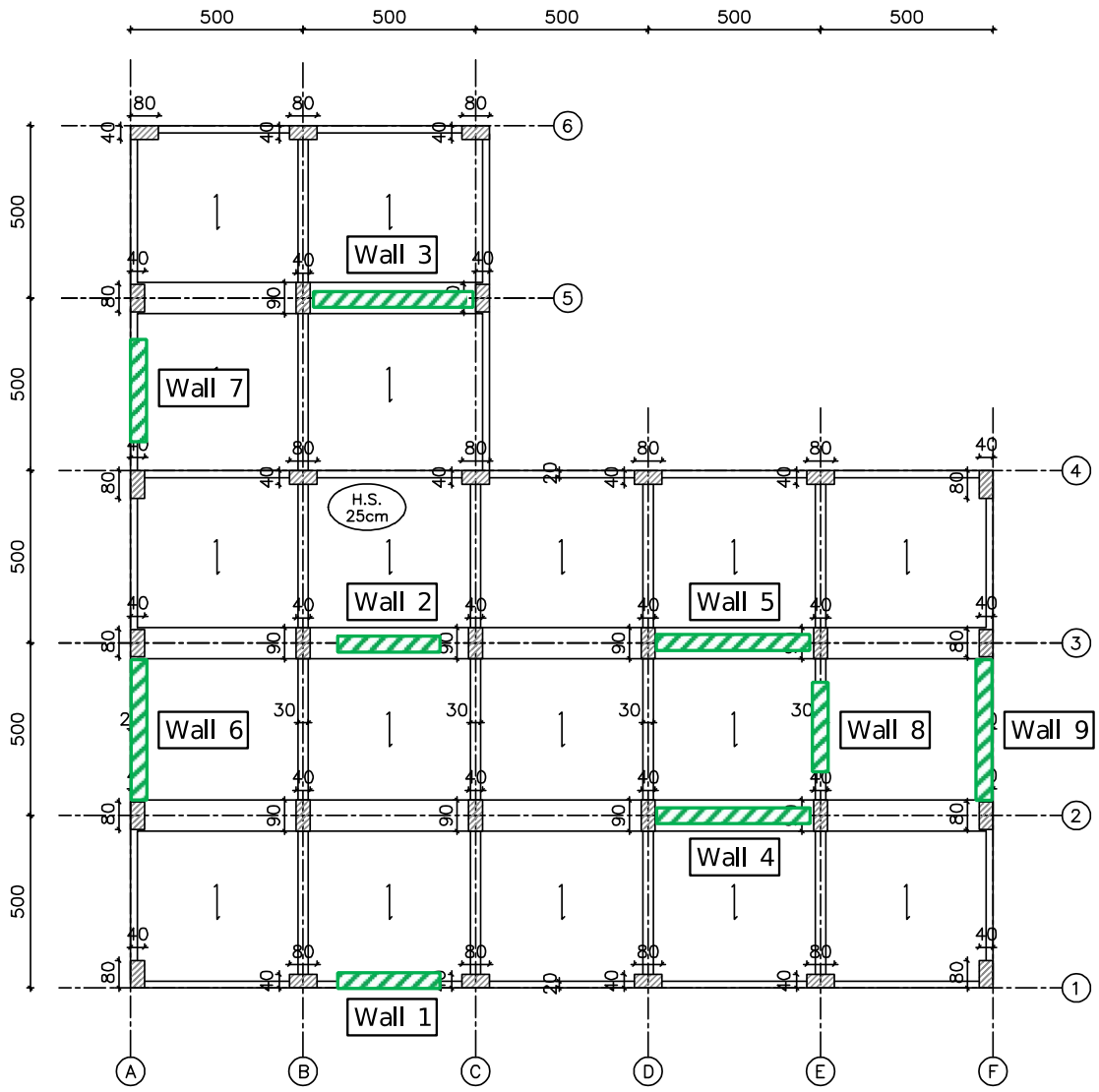


Figure 7.26: Alternative retrofitting scenario of the L-shaped building (dimensions in cm)

The walls dimensions are displayed in Table 7-12, noting that the initial characteristic compressive strength of concrete of the walls is equal to 35 MPa. Despite the slight increase in the mass participation offered by Scenario 2 (Table 7-13), the mass participation of the fundamental modes in Scenario 1 are sufficiently high and reliable for applying the CSM with confidence. As a result, the first scenario is adopted for retrofitting and is accordingly represented in the subsequent steps of the procedure.

Table 7-12: Preliminary dimensions of walls in the L-shaped building

	Scenario 1		Scenario 2 (Alternative)	
	Length (mm)	**Thickness (mm)**	**Length (mm)**	**Thickness (mm)**
Wall 1	4200	300	3000	300
Wall 2	4500	300	3000	300
Wall 3	4500	300	4300	300
Wall 4	4500	300	4500	300
Wall 5	4200	300	4500	300
Wall 6	4200	300	4200	300
Wall 7	4200	300	3000	300
Wall 8	–	–	2300	300
Wall 9	–	–	4200	300

Table 7-13: Modal mass participation of the retrofitting scenarios considered in the L-shaped building

	Average Euc. Ecc. (m)	**Mass Participation in X (Mode 2)**	**Mass Participation in Y (Mode 1)**
Scenario 1	0.60	65 %	65 %
Scenario 2	0.16	66 %	66 %

Step 2: Preliminary design and detailing of walls

Preliminary dimensioning of shear walls

The thickness of the walls is checked against the minimum code requirement as per the following equation, and the axial load-resisting capacity of the walls is verified as well (Table 7-14).

$$b_{w0} \geq \max\left[0.15,\ h_s / 20\right] = 0.215m$$

Table 7-14: Verification of the axial load-resisting capacity per unit length of wall in the L-shaped building

	Length (mm)	**Width** (mm)	**Axial Load** (KN)	**Axial Capacity** (KN)
Wall 1	4200	300	375	4830
Walls 2, 3, 4	4500	300	375	4830
Walls 5, 6, 7	4200	300	340	4830

Calculating the loads applied on the walls

Table 7-15 presents the original estimate of shear force and overturning moment applied at the base. These values are used to generate the preliminary bending moment and shear diagrams at all floors in line with the procedure and are checked at later stages against the ones obtained at the performance point of the CSM. Referring to the table, although wall 1 is resisting a larger amount of live load along its tributary area, the contribution of the live load into the axial load and into the plastic capacity is negligible, and consequently all the walls having the same dimensions are assumed to have the same plastic capacity.

Table 7-15: Preliminary estimate of the base moment and shear demand in the L-shaped building

	$V_{base}\ (KN)$	$M_{base}\ (KN.m)$
Walls 1, 5, 6, 7	1040	16700
Walls 2, 3, 4	1230	19850

Preliminary dimensioning and reinforcement of the confined zones (boundary elements)

The walls dimensions adopted in the L-shaped scenario have been already used in the previous case involving the rectangular building. Accordingly, the walls detailing already addressed in the rectangular scenario (Figures 7.6 and 7.7) are considered along with the verification checks performed in Table 7-4.

Step 3: Finding the vibration characteristics of the building in the two main horizontal directions

Table 7-16 presents the vibrational characteristics of the fundamental mode in the horizontal directions. As indicated in Table 7-13, the mass participation of both modes equals 65%, which underlines the predominance of the fundamental translational mode on the response and supports the application of the CSM to approximate the building response.

Table 7-16: Fundamental vibration characteristics of the L-shaped building

	Mode 1			**Mode 2**		
	ω = 3.80 rad/s			**ω = 4.60 rad/s**		
Storey	**UX** (m)	**UY** (m)	**RZ** (rad)	**UX** (m)	**UY** (m)	**RZ** (rad)
Storey1	-0.0001	0.031	-0.0003	0.030	0.0007	0.0006
Storey2	-0.0004	0.085	-0.0009	0.081	0.0020	0.0016
Storey3	-0.0008	0.160	-0.0018	0.154	0.0038	0.0030
Storey4	-0.0012	0.254	-0.0028	0.247	0.0061	0.0049
Storey5	-0.0017	0.362	-0.0040	0.354	0.0088	0.0070
Storey6	-0.0023	0.480	-0.0053	0.473	0.0117	0.0093
Storey7	-0.0028	0.605	-0.0066	0.600	0.0148	0.0118
Storey8	-0.0035	0.735	-0.0081	0.731	0.0181	0.0144
Storey9	-0.0041	0.867	-0.0095	0.865	0.0214	0.0170
Storey10	-0.0047	1.000	-0.0110	1.000	0.0230	0.0197

Step 4: Modal pushover analysis in the global X and Y directions

Unlike the rectangular scenario, the asymmetry of the L-shaped building implies that this step should be performed twice in each horizontal direction to account for the accidental eccentricity in both the positive and negative directions. Adding this to the fact that the building performance is checked at both the SD and NC limit states, a total number of 8 analyses are required to cover the L-shaped building as referred to in Table 7-17. The drift level is well maintained below the 2% limit which is suggested to control the response at the NC limit state. In view of this, Figures A7.7-A7.10 in Appendix 7 present the calculation of the performance point of the Push-Y analysis (in proportion to Mode 1) at the NC and SD limit states, with the accidental eccentricity being considered on either side of the centre of mass.

Similarly, Figures A7.11-A7.14 represent the performance point of the Push-X analysis (Mode 2) at the NC and SD limit states. It is worth noting that the direction of the accidental eccentricity has only a minor effect on the pushover response as the spectral displacement and acceleration results obtained for positive and negative eccentricity are nearly identical.

Table 7-17: Summary of all the CSM analyses performed in the L-shaped building

	Performance Point		Participation Factor	Mass Coefficient	Performance Point		
	Spectral Acc. a_{pf} (g)	**Spectral Disp. d_{pf} (m)**	**PF_{Roof}**	**α**	**Base Shear (KN)**	**Roof Disp. (m)**	**Drift Ratio**
PushX_+5% (NC)	0.18	0.20	1.49	0.656	6060	0.30	0.93%
PushX_-5% (NC)	0.18	0.21	1.49	0.656	6060	0.31	0.96%
PushY _+5% (NC)	0.13	0.26	1.49	0.662	4420	0.38	1.18%
PushY _-5% (NC)	0.13	0.27	1.49	0.662	4420	0.40	1.25%
PushX_+5% (SD)	0.16	0.14	1.49	0.656	5390	0.20	0.62%
PushX_-5% (SD)	0.16	0.14	1.49	0.656	5560	0.20	0.62%
PushY _+5% (SD)	0.12	0.17	1.49	0.662	4250	0.27	0.84%
PushY _-5% (SD)	0.12	0.17	1.49	0.662	4250	0.27	0.84%

Step 5: Verifying the flexural and shear capacities of the retrofitting walls against the seismic demand

Once the performance point is determined, the actual shear force and bending moment in the walls are evaluated from the envelope of the pushover analyses performed. Accordingly, the shear reinforcement is provided such that the shear capacity is not exceeded at all floors (Table 7-19). Whereas for the flexural reinforcement, detailing at the first storey (base level) has been already set up and encompasses the confined regions at the ends of the walls (Figure 7.7), while the reinforcement at upper floors is provided to ensure that the plastic capacity is not exceeded and no plastic hinges form at these levels (Table 7-18). In light of this, Tables 7-20 and 7-21 respectively present the flexural and shear checks which are also plotted in graphical form in Figures 7.27 and 7.28.

Table 7-18: Provisioned flexural reinforcement of walls in the L-shaped building

Storey	**Wall 1 4200x300**	**Wall 2 4500x300**	**Wall 3 4500x300**	**Wall 4 4500x300**	**Wall 5 4200x300**	**Wall 6 4200x300**	**Wall 7 4200x300**
Storey10	T12@150	T12@150	T12@150	T12@150	T12@150	T12@150	T12@150
Storey9	T12@150	T12@150	T12@150	T12@150	T12@150	T12@150	T12@150
Storey8	T12@150	T12@150	T12@150	T12@150	T12@150	T12@150	T12@150
Storey7	T12@150	T12@150	T12@150	T12@150	T12@150	T12@150	T12@150
Storey6	T16@150	T14@150	T14@150	T14@150	T16@150	T16@150	T16@150
Storey5	T16@150	T16@150	T16@150	T16@150	T16@150	T16@150	T16@150
Storey4	T20@150	T16@150	T16@150	T16@150	T20@150	T20@150	T20@150
Storey3	T20@150	T20@150	T20@150	T20@150	T20@150	T20@150	T20@150
Storey2	T25@150	T20@150	T25@150	T20@150	T25@150	T25@150	T25@150
Storey1	B.C.	B.C.	B.C.	B.C.	B.C.	B.C.	B.C.

Table 7-19: Provisioned shear reinforcement of walls in the L-shaped building

Storey	Wall 1 4200x300	Wall 2 4500x300	Wall 3 4500x300	Wall 4 4500x300	Wall 5 4200x300	Wall 6 4200x300	Wall 7 4200x300
Storey10	T10@200	T10@200	T10@200	T10@200	T10@200	T10@200	T10@200
Storey9	T10@200	T10@200	T10@200	T10@200	T10@200	T10@200	T10@200
Storey8	T10@200	T10@200	T10@200	T10@200	T10@200	T10@200	T10@200
Storey7	T10@200	T10@150	T10@200	T10@200	T10@150	T10@150	T10@150
Storey6	T10@150	T10@150	T10@150	T10@150	T10@150	T10@150	T10@150
Storey5	T10@150	T12@150	T10@150	T10@150	T12@150	T12@150	T12@150
Storey4	T10@150	T12@150	T12@150	T12@150	T12@150	T12@150	T12@150
Storey3	T12@150	T14@150	T12@150	T12@150	T14@150	T14@150	T14@150
Storey2	T12@150	T14@150	T12@150	T12@150	T14@150	T14@150	T14@150
Storey1	T12@150	T14@150	T14@150	T14@150	T14@150	T14@150	T14@150

Table 7-20: Checking the flexural requirements of walls in the L-shaped building

	W1_4200 x 300			W2_4500 x 300			W3_4500 x 300			W4_4500 x 300		
Storey	**Dem.** KN-m	**Cap.** KN-m	**D/C**	**Dem.** KN-m	**Cap.** KN-m	**D/C**	**Dem.** KN-m	**Cap.** KN-m	**D/C**	**Dem.** KN-m	**Cap.** KN-m	**D/C**
Storey1	16000	16050	1.00	19750	19850	0.99	19750	19850	0.99	19750	19850	0.99
Storey2	18450	24000	0.77	19750	23050	0.86	22500	28250	0.80	19750	23050	0.86
Storey3	14800	20200	0.73	17550	23650	0.74	18200	23650	0.77	17550	23650	0.74
Storey4	12450	19950	0.62	15350	16800	0.91	15350	16800	0.91	15350	16800	0.91
Storey5	10650	13950	0.77	13150	16400	0.80	13150	16400	0.80	13150	16400	0.80
Storey6	8900	13650	0.65	10950	13200	0.83	10950	13200	0.83	10950	13200	0.83
Storey7	7100	8450	0.84	8750	10000	0.88	8750	10000	0.88	8750	10000	0.88
Storey8	5350	8100	0.66	6600	9500	0.69	6600	9500	0.69	6600	9500	0.69
Storey9	3550	7750	0.46	4400	9050	0.48	4400	9050	0.48	4400	9050	0.48
Storey10	1800	7450	0.24	2200	8600	0.26	2200	8600	0.26	2200	8600	0.26

Table 7-20 (Continued)

	W5_4200 x 300			W6_4200 x 300			W7_4200 x 300		
Storey	**Dem.** KN-m	**Cap.** KN-m	**D/C**	**Dem.** KN-m	**Cap.** KN-m	**D/C**	**Dem.** KN-m	**Cap.** KN-m	**D/C**
Storey1	16000	16050	1.00	16000	16050	1.00	16000	16050	1.00
Storey2	22800	24000	0.95	19800	24000	0.83	20300	24000	0.85
Storey3	17900	20200	0.89	15200	20200	0.75	15550	20200	0.77
Storey4	14550	19950	0.73	12450	19950	0.62	12600	19950	0.63
Storey5	10650	13950	0.77	10650	13950	0.77	10650	13950	0.77
Storey6	8900	13650	0.65	8900	13650	0.65	8900	13650	0.65
Storey7	7100	8450	0.84	7100	8450	0.84	7100	8450	0.84
Storey8	5350	8100	0.66	5350	8100	0.66	5350	8100	0.66
Storey9	3550	7750	0.46	3550	7750	0.46	3550	7750	0.46
Storey10	1800	7450	0.24	1800	7450	0.24	1800	7450	0.24

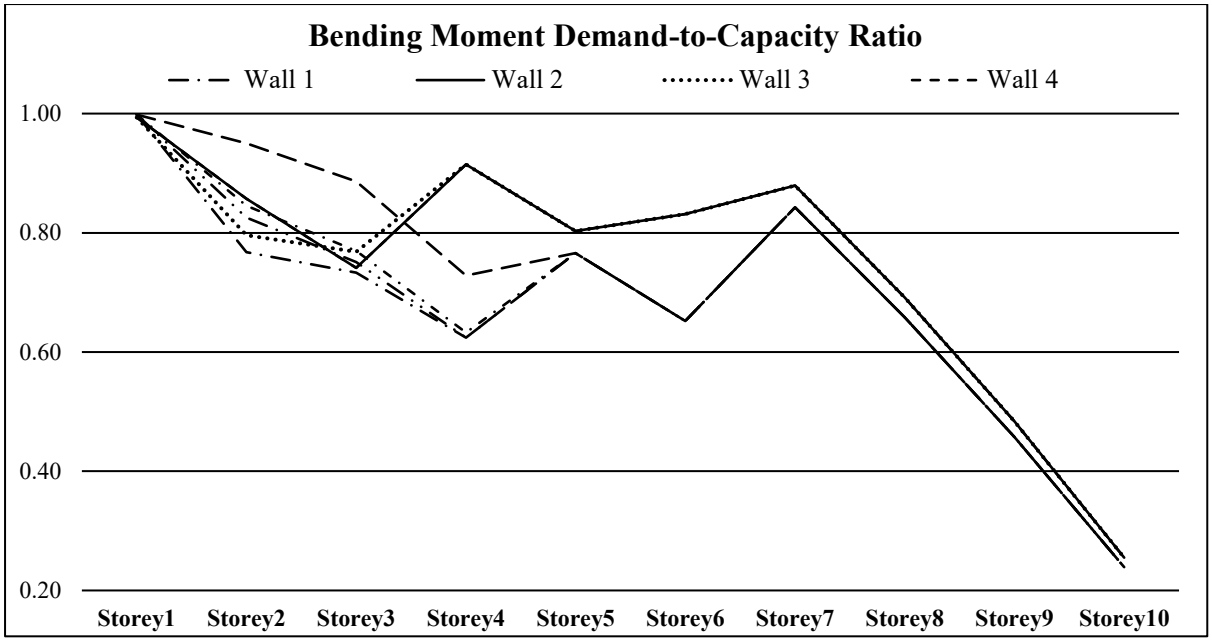


Figure 7.27: Checking the flexural requirements of walls in the L-shaped building

Table 7-21: Checking the shear requirements of walls in the L-shaped building

	W1_4200 x 300			W2_4500 x 300			W3_4500 x 300			W4_4500 x 300		
Storey	**Dem.** KN	**Cap.** KN	**D/C**	**Dem.** KN	**Cap.** KN	**D/C**	**Dem.** KN	**Cap.** KN	**D/C**	**Dem.** KN	**Cap.** KN	**D/C**
Storey1	1750	1850	0.95	2700	2800	0.97	2000	2800	0.73	1950	2800	0.70
Storey2	1550	1850	0.83	2300	2800	0.84	1750	2000	0.88	1700	2000	0.85
Storey3	1350	1850	0.73	2050	2800	0.74	1550	2000	0.78	1500	2000	0.75
Storey4	1200	1300	0.92	1800	2000	0.91	1350	2000	0.69	1300	2000	0.66
Storey5	1000	1300	0.79	1550	2000	0.78	1150	1400	0.85	1100	1400	0.81
Storey6	850	1300	0.66	1300	1400	0.94	950	1400	0.71	950	1400	0.68
Storey7	700	950	0.70	1050	1400	0.75	800	1050	0.79	750	1050	0.72
Storey8	500	950	0.53	750	1050	0.75	600	1050	0.56	550	1050	0.54
Storey9	350	950	0.35	500	1050	0.50	400	1050	0.38	350	1050	0.36
Storey10	150	950	0.18	250	1050	0.25	200	1050	0.19	200	1050	0.18

Table 7-21 (Continued)

	W5_4200 x 300			W6_4200 x 300			W7_4200 x 300		
Storey	**Dem.** KN	**Cap.** KN	**D/C**	**Dem.** KN	**Cap.** KN	**D/C**	**Dem.** KN	**Cap.** KN	**D/C**
Storey1	2450	2550	0.95	2300	2550	0.89	2350	2550	0.91
Storey2	2100	2550	0.83	2000	2550	0.77	2000	2550	0.79
Storey3	1900	2550	0.73	1750	2550	0.69	1800	2550	0.70
Storey4	1650	1850	0.89	1550	1850	0.83	1550	1850	0.85
Storey5	1400	1850	0.76	1300	1850	0.71	1350	1850	0.73
Storey6	1150	1300	0.91	1100	1300	0.85	1100	1300	0.87
Storey7	950	1300	0.73	900	1300	0.68	900	1300	0.70
Storey8	700	950	0.73	650	950	0.68	650	950	0.70
Storey9	450	950	0.49	450	950	0.46	450	950	0.46
Storey10	250	950	0.24	200	950	0.23	200	950	0.23

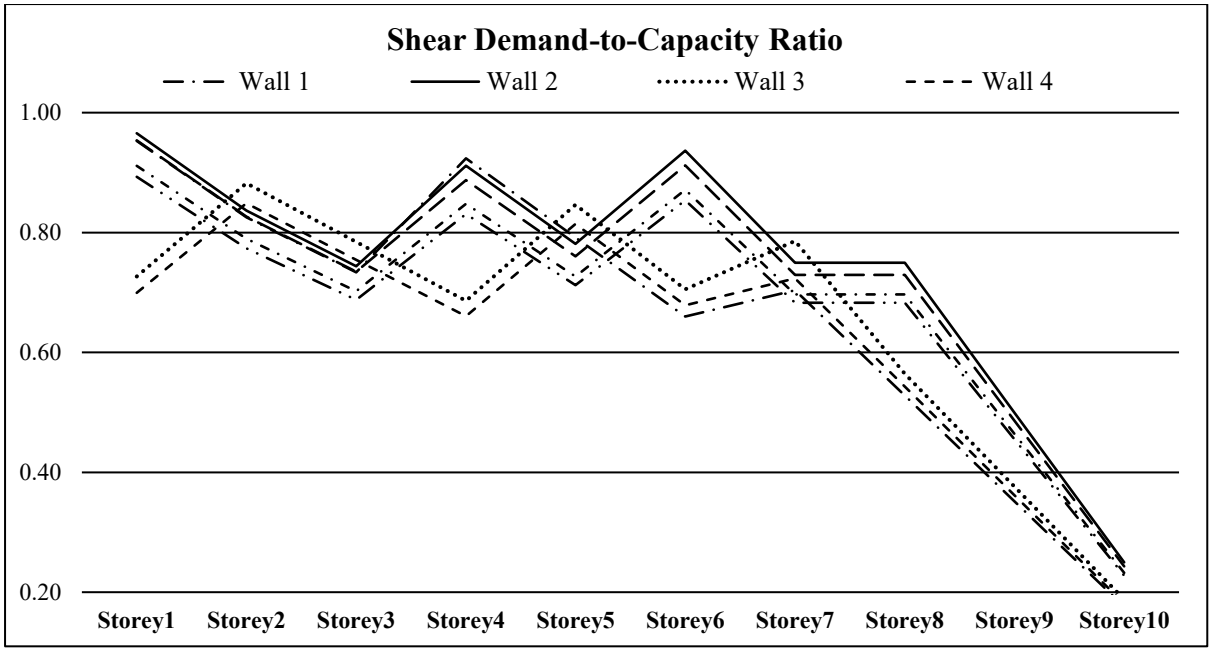


Figure 7.28: Checking the shear requirements of walls in the L-shaped building

Step 6: Checking the local ductility requirements in the shear walls

The local ductility checks for all the walls are presented in Table 7-22, and the results prove that the plastic rotational capacity exceeds by far the maximum plastic rotation in each wall, hence proving the effectiveness of confinement in the boundary elements in satisfying the local ductility requirements.

Table 7-22: Verification of the local ductility requirements in the shear walls of the L-shaped building

	Demand	Capacity		
	Max. Rotation (rad)	**EC8-3 (rad)**	**Empirical Equation 2 (rad)**	**Empirical Equation 3 (rad)**
Wall 1	0.0068	0.095	0.132	0.122
Walls 2, 3, 4	0.0069	0.082	0.114	0.105
Walls 5, 6, 7	0.0096	0.096	0.133	0.124

Step 7: Checking the performance of the original frame against potential brittle and shear failures

Ductile mechanism check (chord rotation):

Figures 7.29 & 7.30 present the chord rotation checks performed at the NC and SD limit states respectively. The absence of red hinges at the NC limit state indicates that the ultimate chord rotation limit is never exceeded. Likewise, the absence of cyan-coloured hinges proves that the chord rotation limit pertaining to the SD limit state is never exceeded. Consequently, it is concluded that the chord rotation requirements of the retrofitted building are satisfied.

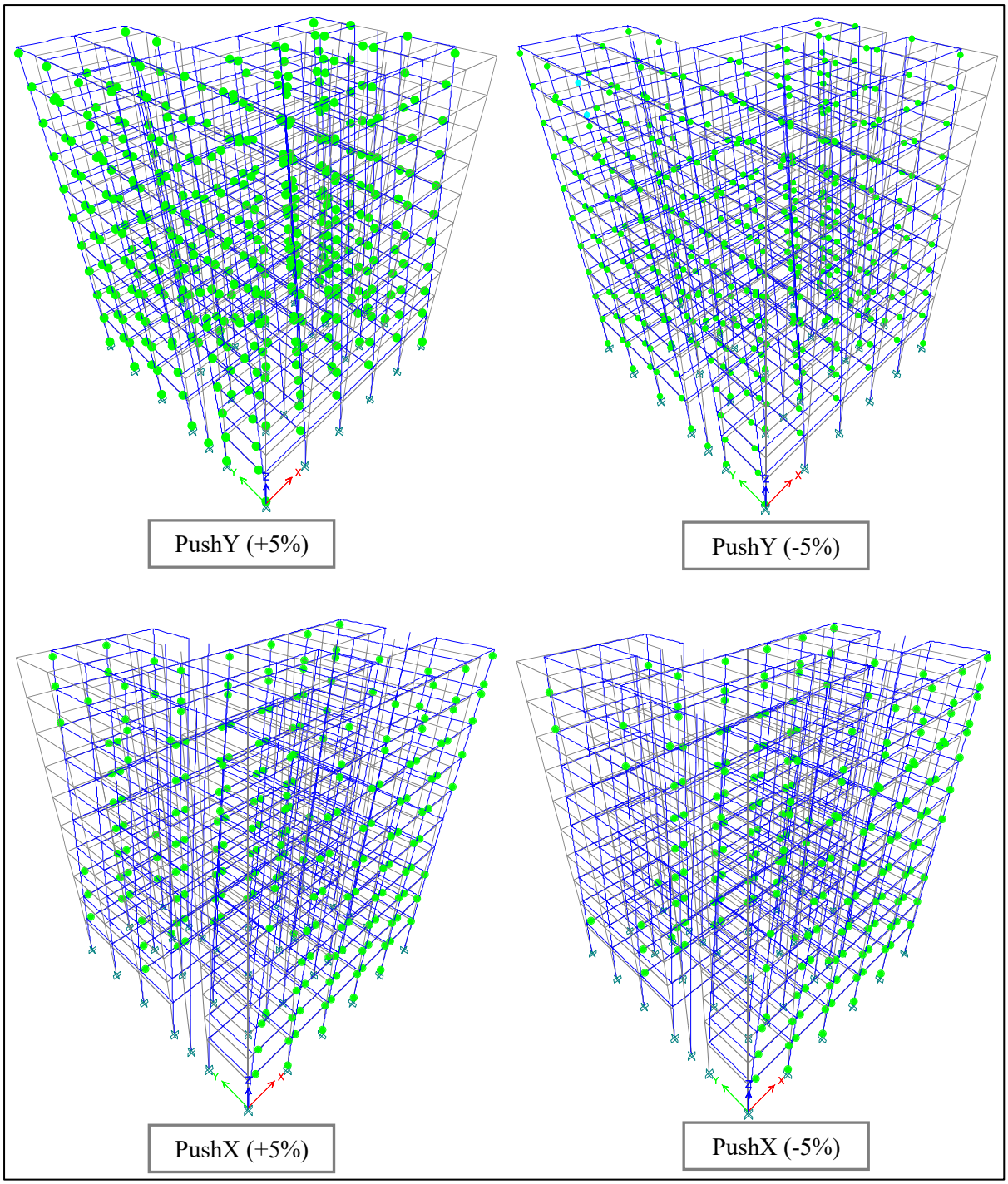


Figure 7.29: Flexural hinges at the NC limit state in the L-shaped building

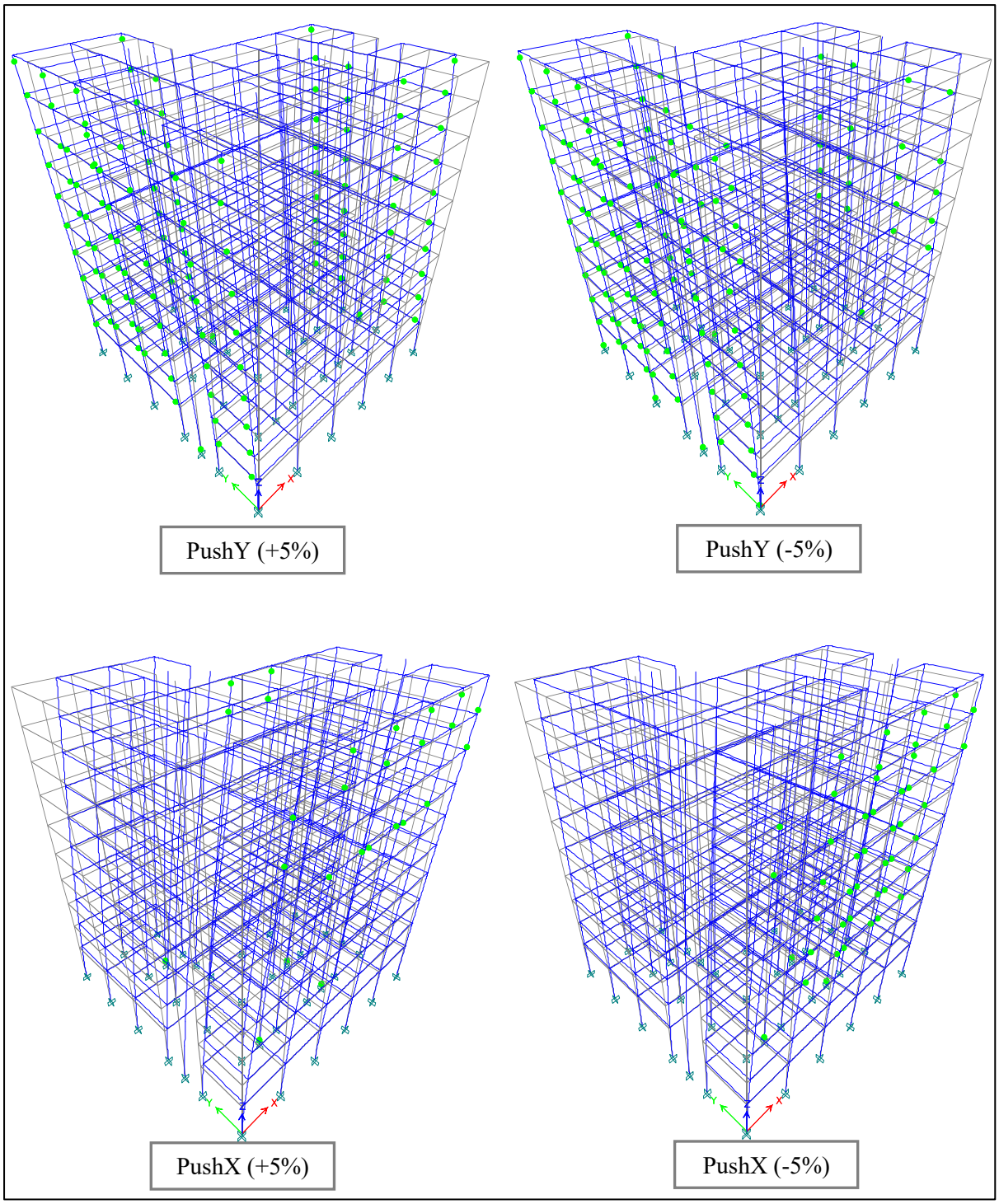


Figure 7.30: Flexural hinges at the SD limit state in the L-shaped building

Brittle mechanism check (Shear Failure):

Beams and columns are simply characterised by their respective labels because of the asymmetric floor plan in the L-shaped building (Figure 7.31).

Figures 7.32-7.34 present the shear results in the columns and beams. It is shown that the shear capacity exceeds the demand in all the structural members which validates the effectiveness of the proposed retrofitting solution. Concerning the columns, the first floor shows a significant shear demand in view

of the fixed base, with a constant D/C ratio registered among all columns. Otherwise, the shear D/C ratio increases at upper floors in line with the reduced cross-section. Whereas for beams, the shear capacity is unaltered while the shear demand is reduced going up the storey levels, and this is reflected in the results as the D/C ratio decreases by moving up the height of the building.

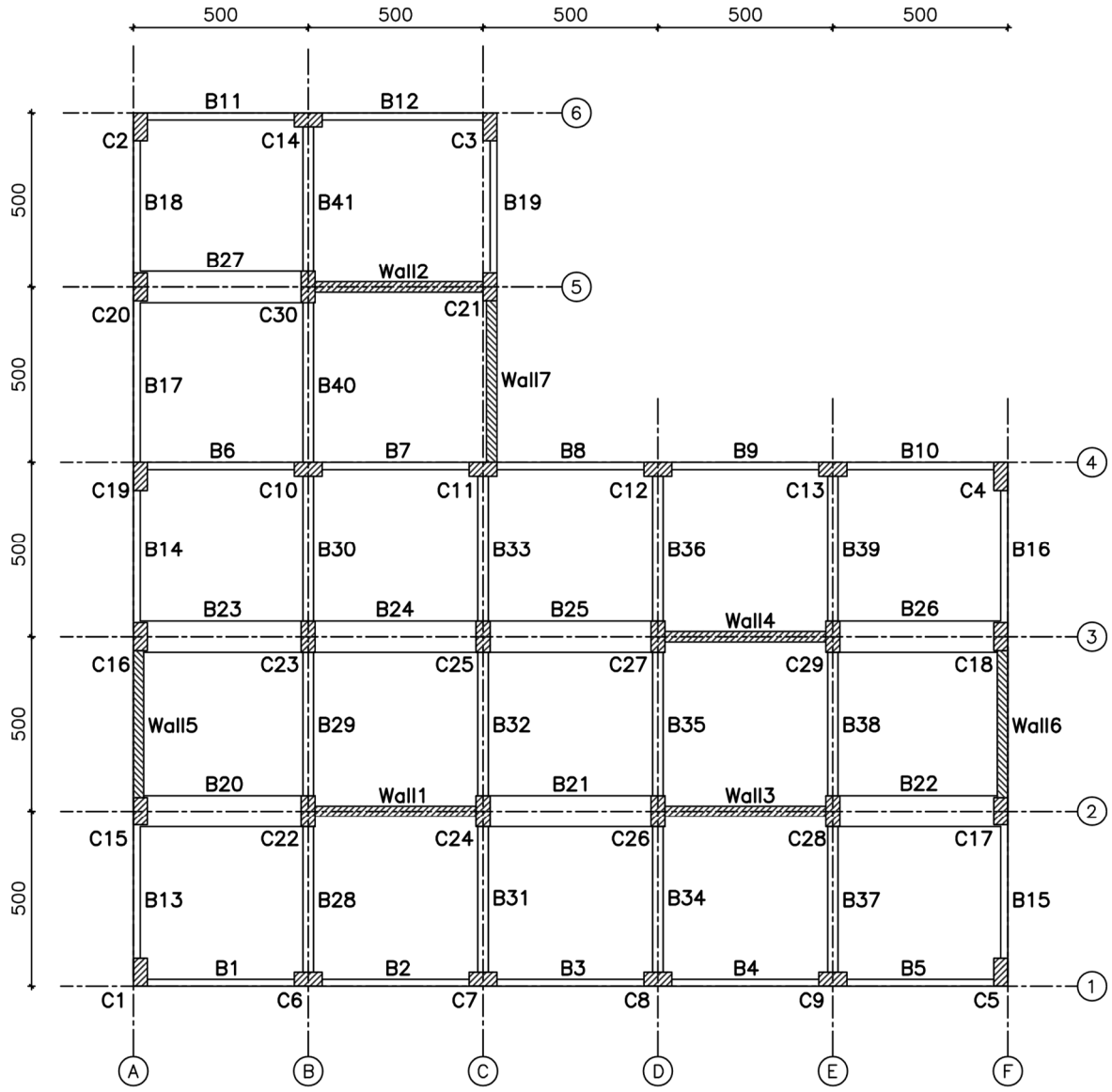


Figure 7.31: Labels of beams and columns in the L-shaped building

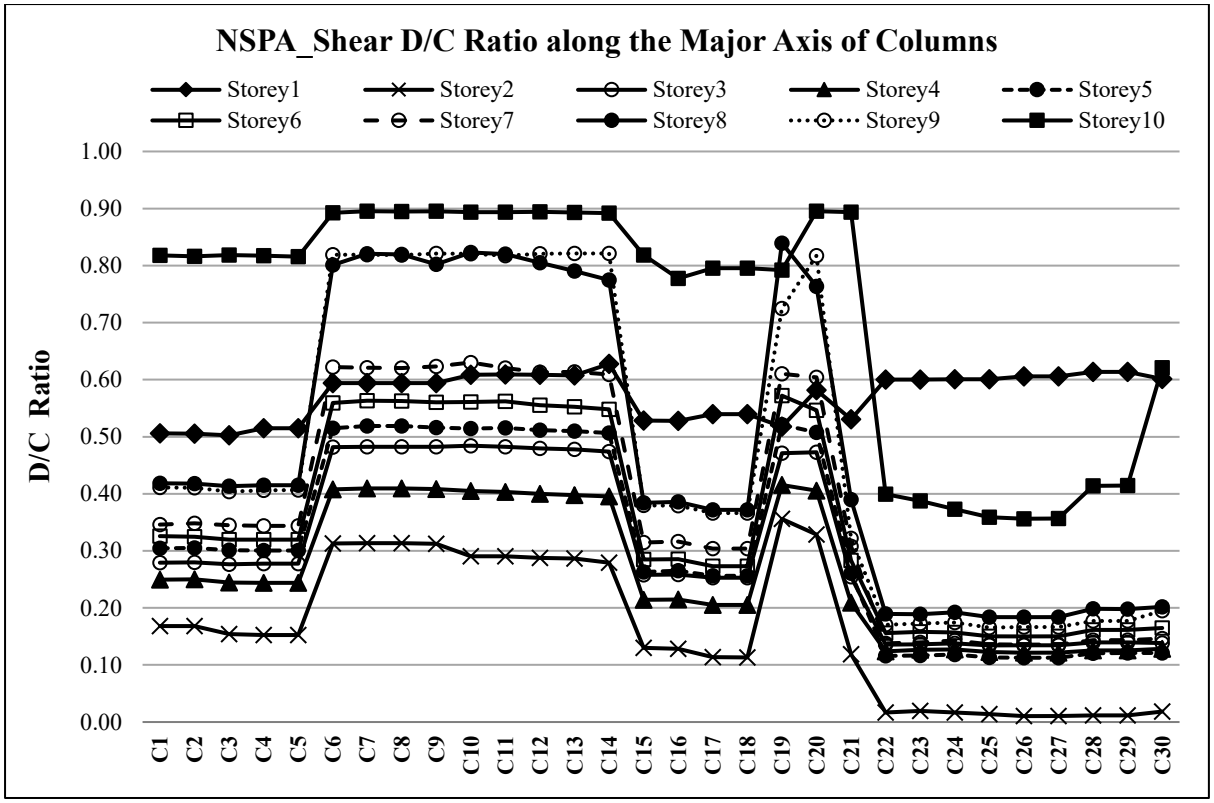


Figure 7.32: NSPA results of the shear D/C ratio measured along the major bending axis of columns in the L-shaped building

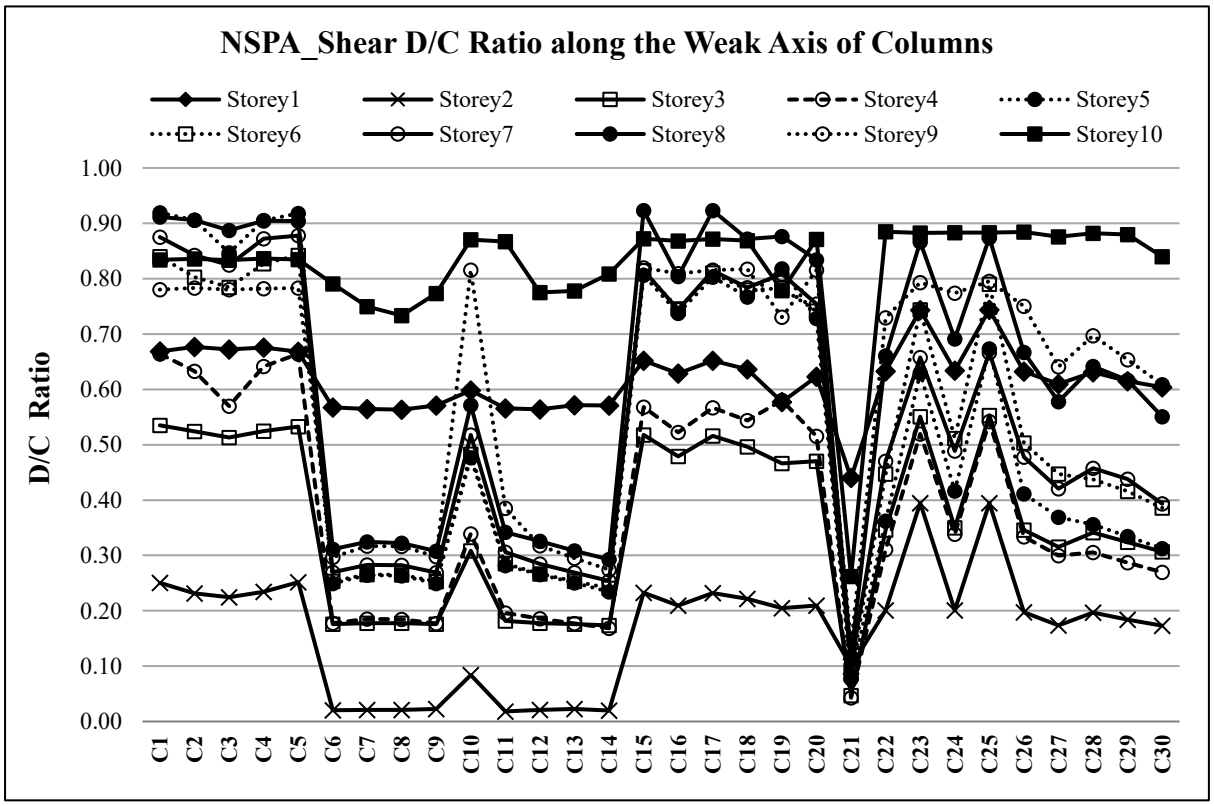


Figure 7.33: NSPA results of the shear D/C ratio measured along the weak axis of columns in the L-shaped building

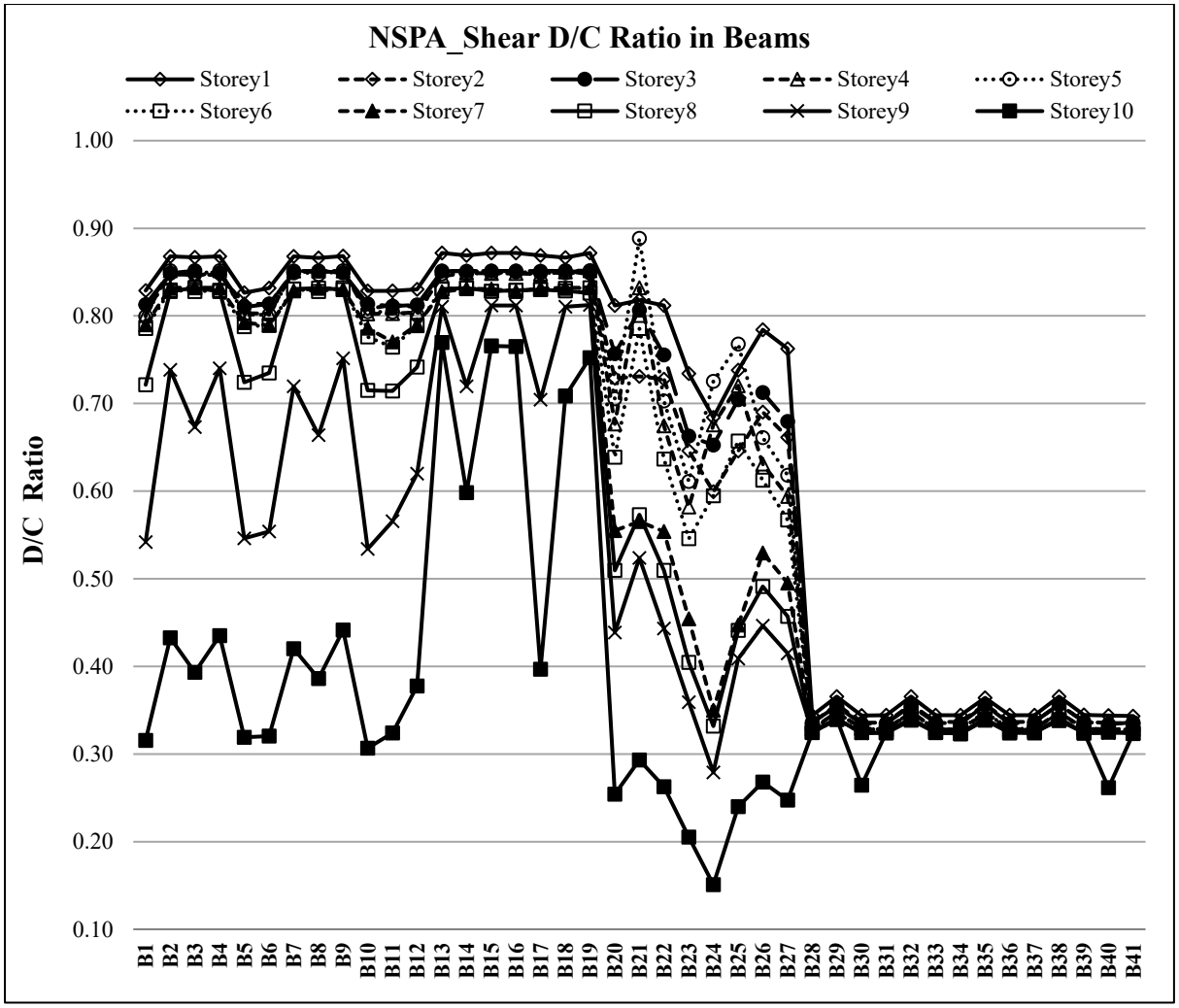


Figure 7.34: NSPA results of the shear D/C ratio measured along the strong bending axis of beams in the L-shaped building

Step 8: Validation against complete nonlinear time history analysis (NLTHA)

The chord rotation results of the NLTHA are presented in Figures 7.35-7.38, noting that four separate models were generated to account for the accidental eccentricity in each horizontal direction and on either side of the nominal centre of mass. The results compare well with those obtained using the CSM (or NSPA), as the absence of red hinges under all the ground motions considered indicates that the ultimate chord rotation limit of the NC limit state is never attained or exceeded. Consequently, the results prove the success of retrofitting in enabling the L-shaped building to resist potential ductile failure when subjected to earthquake loading.

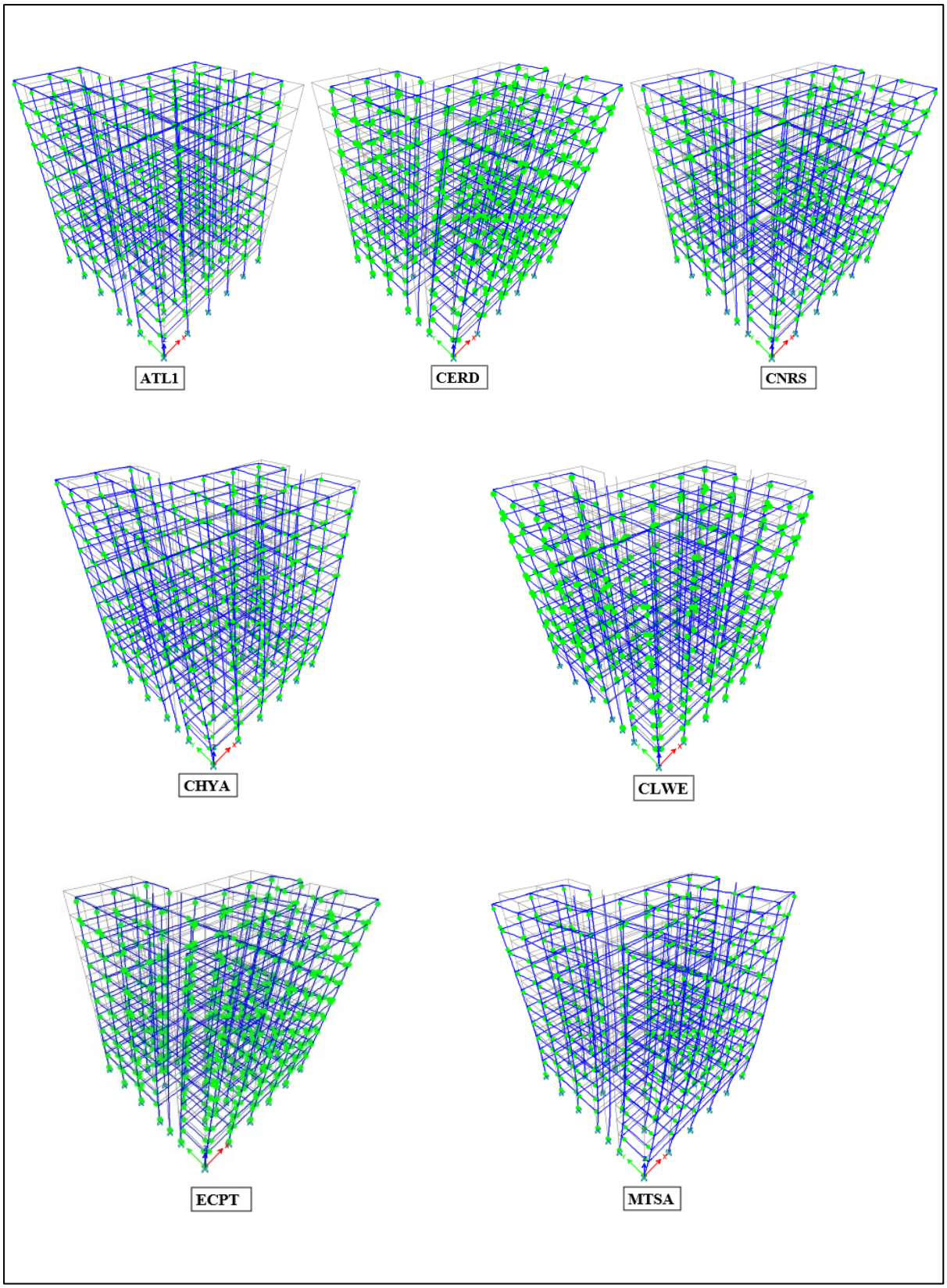


Figure 7.35: Flexural hinges obtained at the end of the NLTHA performed in the L-shaped building (ecc. +5% in X)

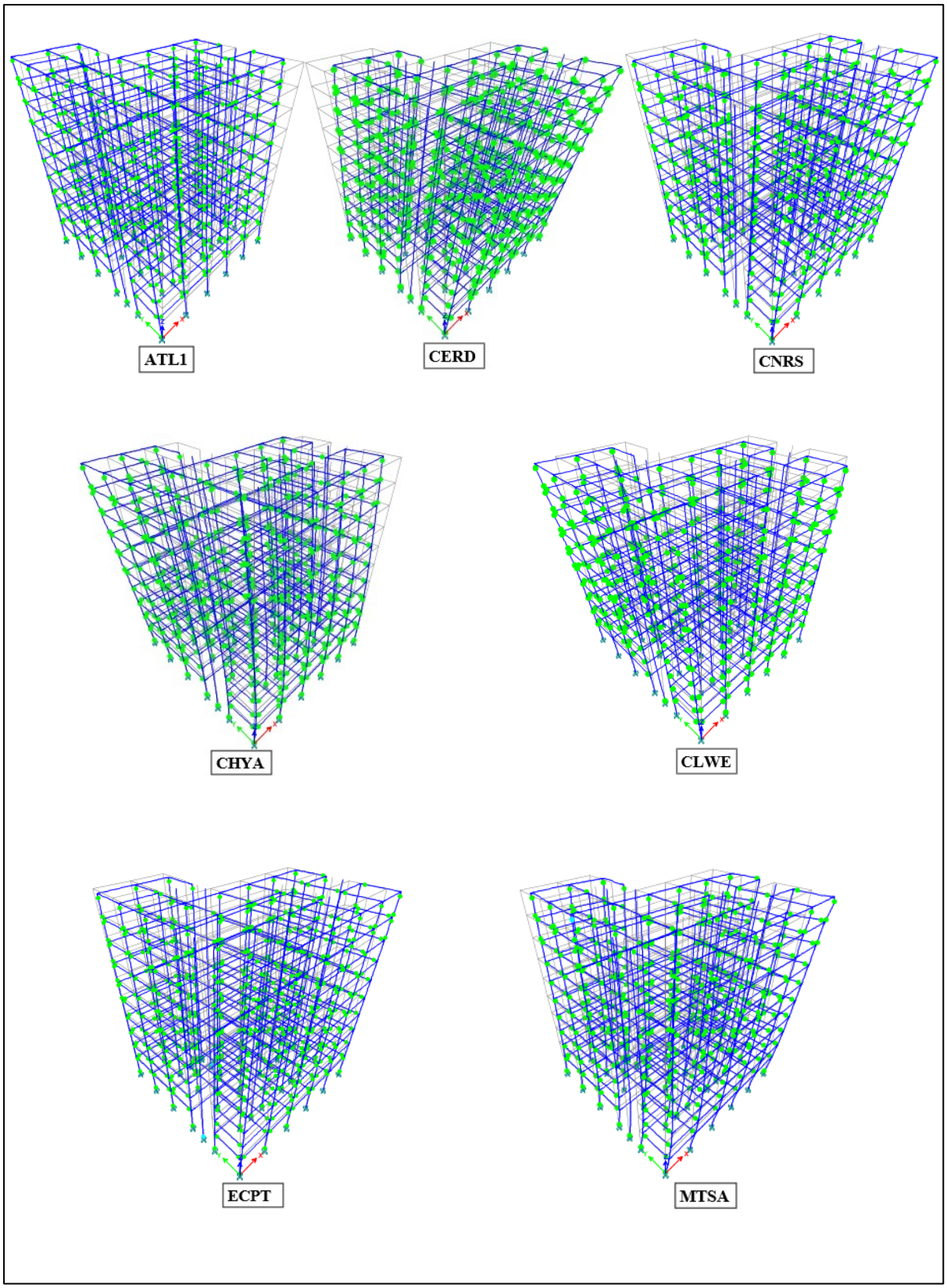


Figure 7.36: Flexural hinges obtained at the end of the NLTHA performed in the L-shaped building (ecc. -5% in X)

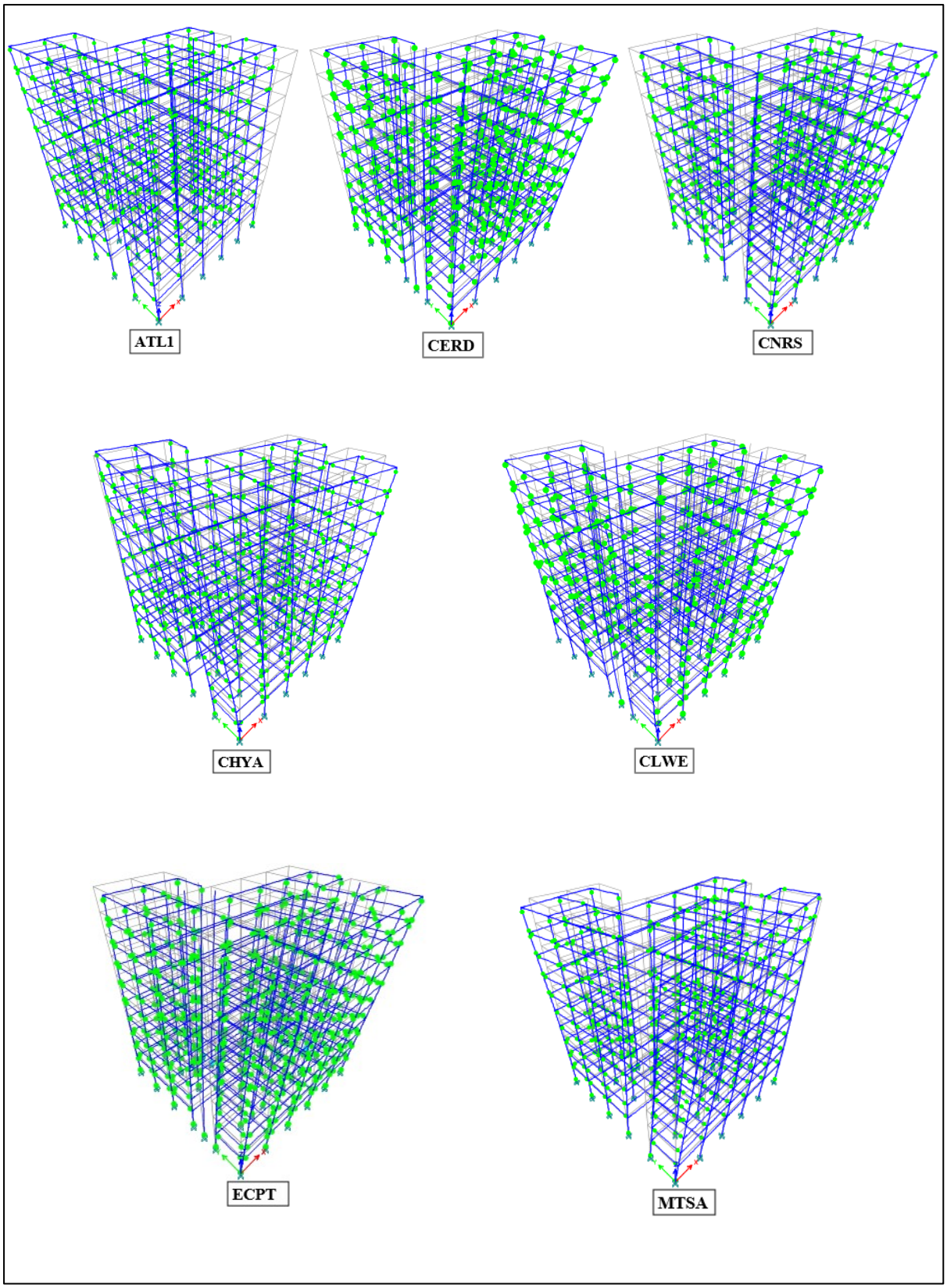


Figure 7.37: Flexural hinges obtained at the end of the NLTHA performed in the L-shaped building (ecc. +5% in Y)

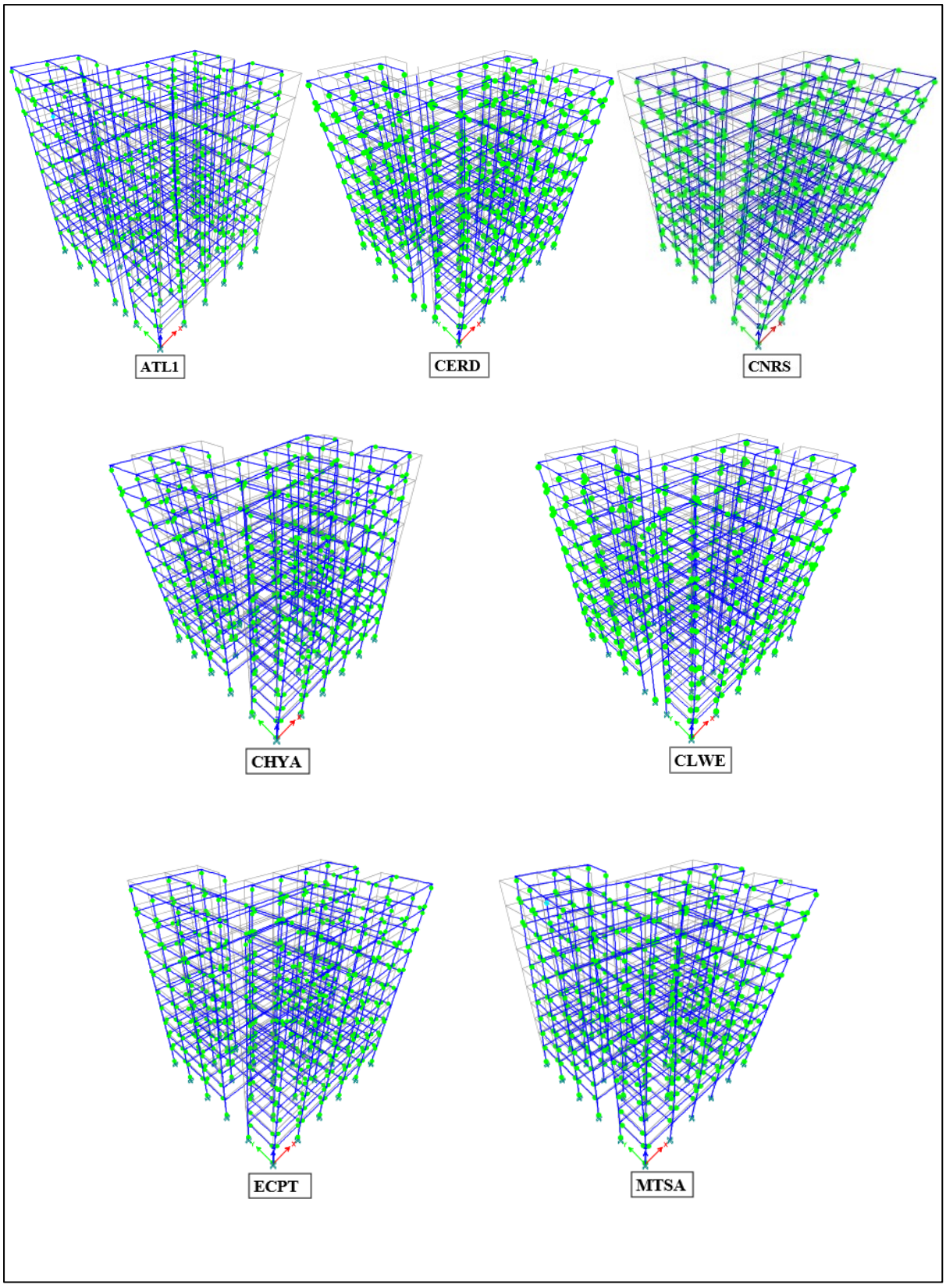


Figure 7.38: Flexural hinges obtained at the end of the NLTHA performed in the L-shaped building (ecc. -5% in Y)

Whereas for shear, results of the NLTHA are presented in the form of D/C plots and are presented in Figures 7.39-7.41. It is noted that the shear capacity of all the structural member exceeds the associated

demand and most importantly, the shear D/C plots are showing a high level of correlation with those obtained using the CSM, although the CSM is shown to slightly underestimate the shear demand compared to the NLTHA. Nevertheless, the pattern of variation of the shear D/C ratio in both the beams and columns is very similar to what is obtained in the CSM, and the D/C values from both analyses are almost identical as reflected in all the plots.

Adding to the conclusion previously drawn on the rectangular building, the current results highlight the effectiveness of the developed retrofitting strategy in strengthening substandard L-shaped frame buildings characterised by planar irregularities against potential seismic loading.

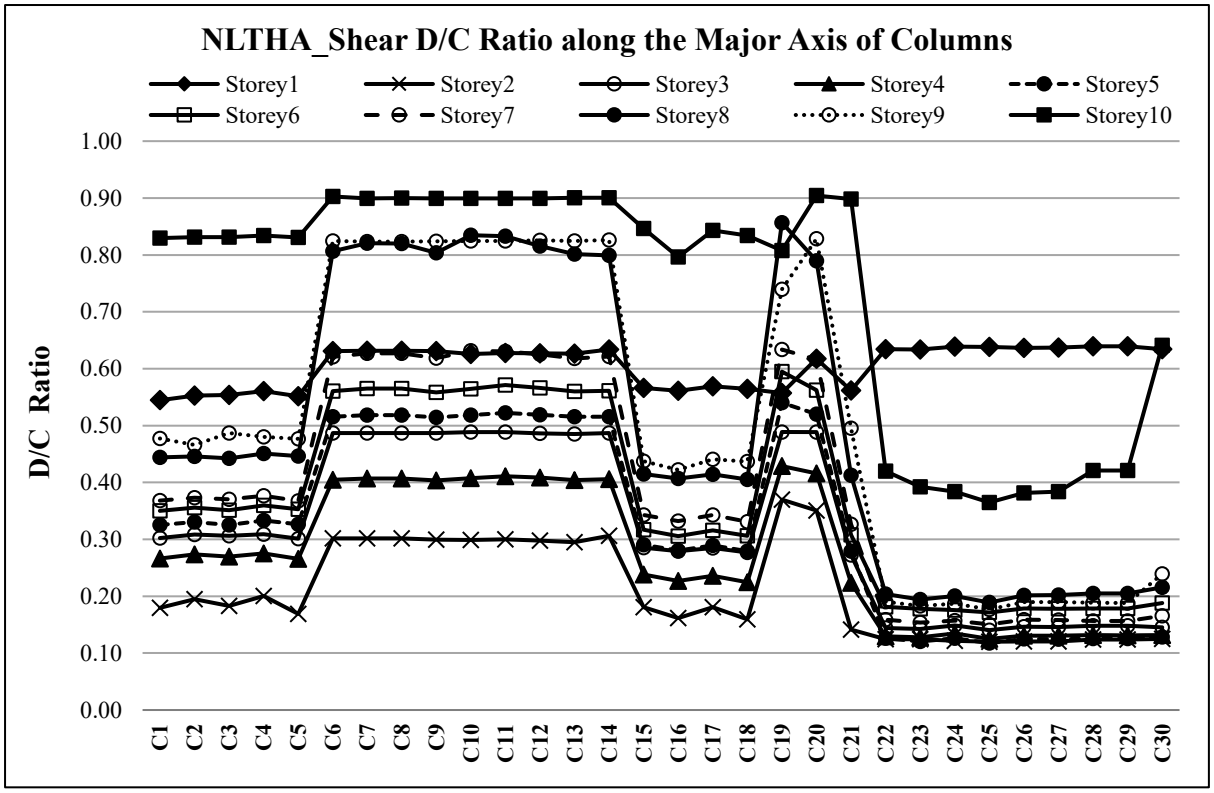


Figure 7.39: NLTHA results of the shear D/C ratio measured along the major bending axis of columns in the L-shaped building

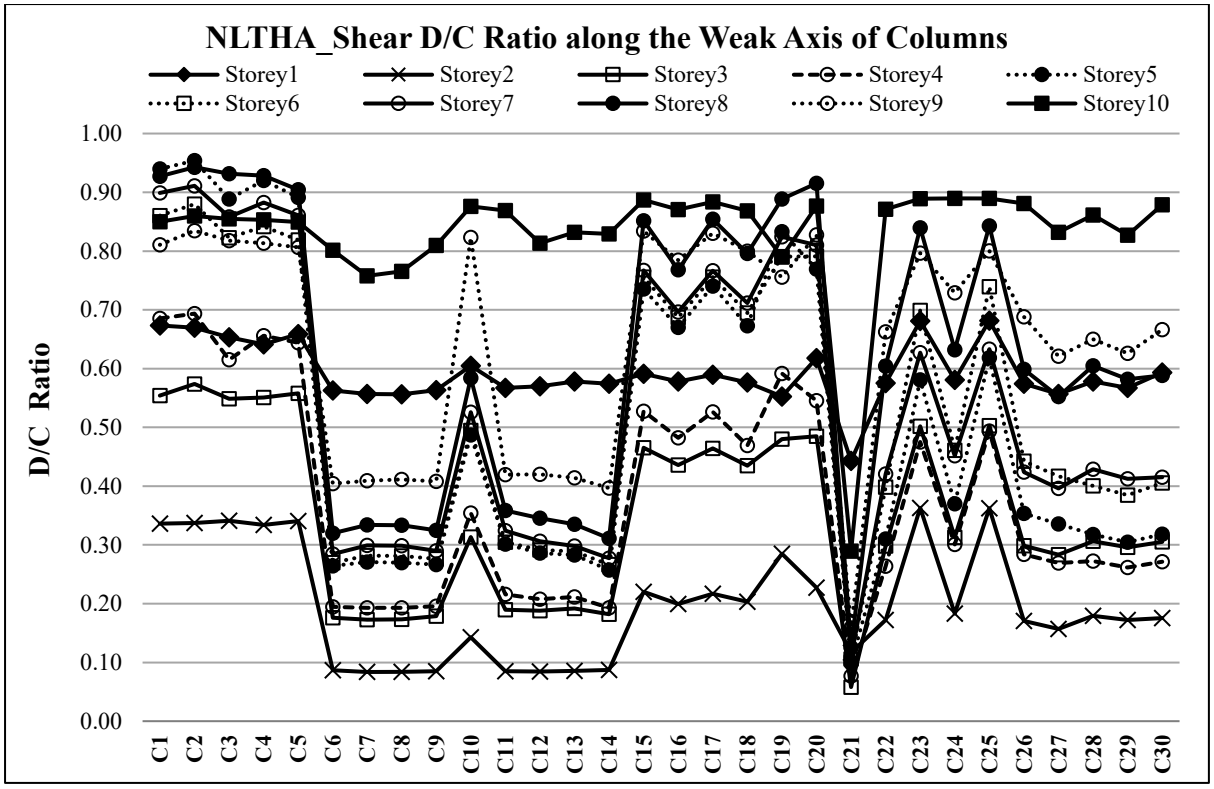


Figure 7.40: NLTHA results of the shear D/C ratio measured along the weak axis of columns in the L-shaped building

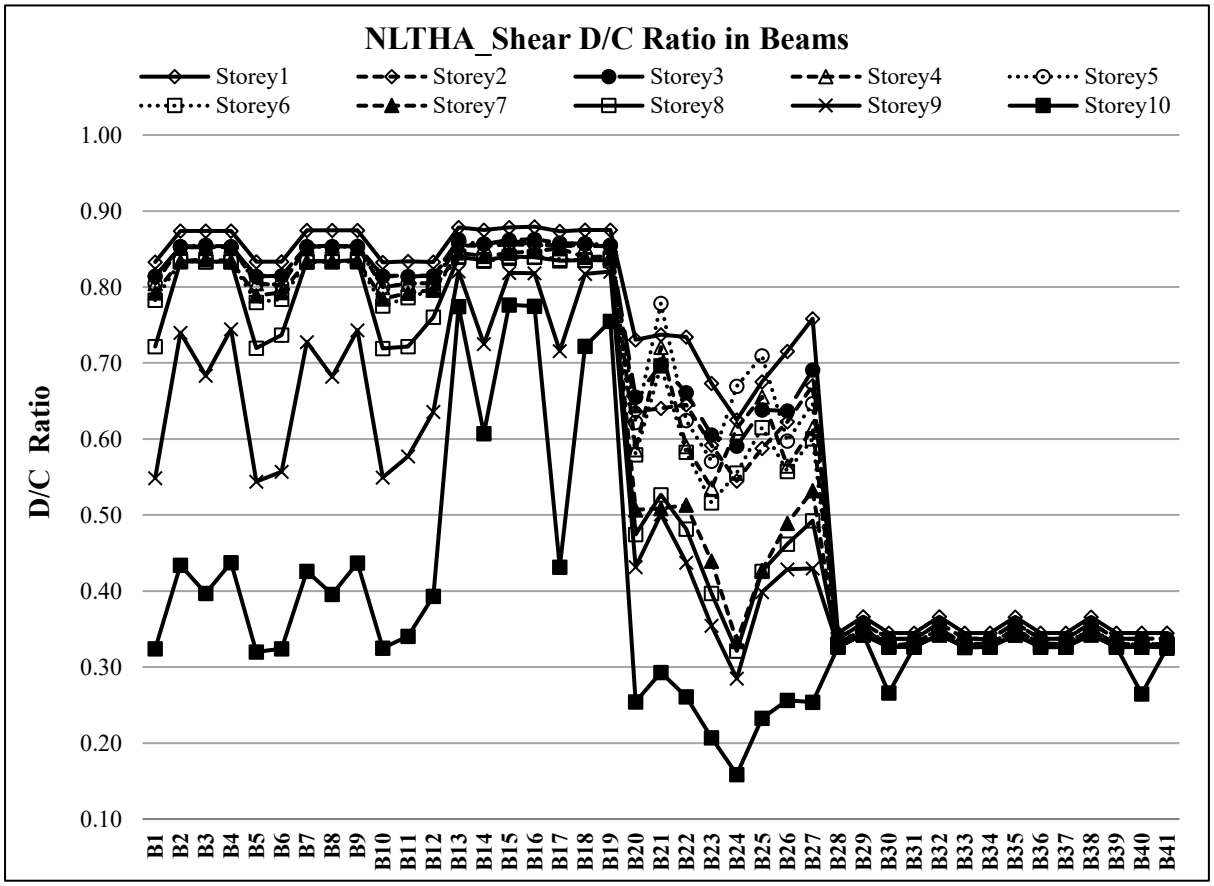


Figure 7.41: NLTHA results of the shear D/C ratio measured along the strong bending axis of beams in the L-shaped building

7.5 Building Having Irregularity in Elevation

Step 1: Location and dimensions of shear walls

The last scenario involves another prototype commonly found in the old building stock of Beirut, and it involves multistorey buildings that have a reduced floorplan at upper storeys. The provisions of EC8-1 (CEN, 2004a) illustrate the criteria upon which buildings having setbacks (reduction in floor plan) at certain levels are classified as irregular in elevation as discussed in detail in Appendix 4. To this end, the building addressed involves a typical scenario where the setback is greater than 10% of the previous floor and is disrupting the symmetry of the floorplan. Also, the sum of the setbacks exceeds 30% of the plan dimension of the ground floor. According to the code provisions, each of these two aberrant features are sufficient to classify the building as irregular in elevation.

The building considered is composed of ten storeys and is similar in plan to the rectangular case, yet the general layout is reduced at the top 3 floors as referred to in Figures 7.43 and 7.44. The beams dimensions and properties are similar to those in the rectangular building. Whereas columns that span up to the 10^{th} floor have the same dimensions as their equivalent in the rectangular building, while columns stopping at the 7^{th} floor are similar to their equivalent which spans from the 4^{th} to the 10^{th} floor in the rectangular building. Further details regarding the original building can be found in Figures A7.15 & A7.16 and in Tables A7.5 & A7.6 in Appendix 7, and in Figures A3.1 & A3.2 in Appendix 3 (for the cross-sectional detailing of beams and columns).

In light of retrofitting, the walls location is adjusted on a trial basis to reduce the average Euclidean eccentricity (Figure 7.42). The leftmost point in the graph corresponds to the retrofitting scenario illustrated in Figures 7.43 and 7.44, and it amounts to a maximised mass participation of 64% in each horizontal direction which strengthens the case for adopting the CSM to model the response of the building. Walls 1 & 2 have a length of 4500 mm, walls 3, 4, & 7 have a length of 3000mm, walls 5 & 6 have a length of 4200mm and 3500 mm respectively, and all the walls have a uniform thickness of 300 mm which is preserved along with the length at all storeys. The characteristic compressive strength of concrete of the shear walls is taken as 35 MPa.

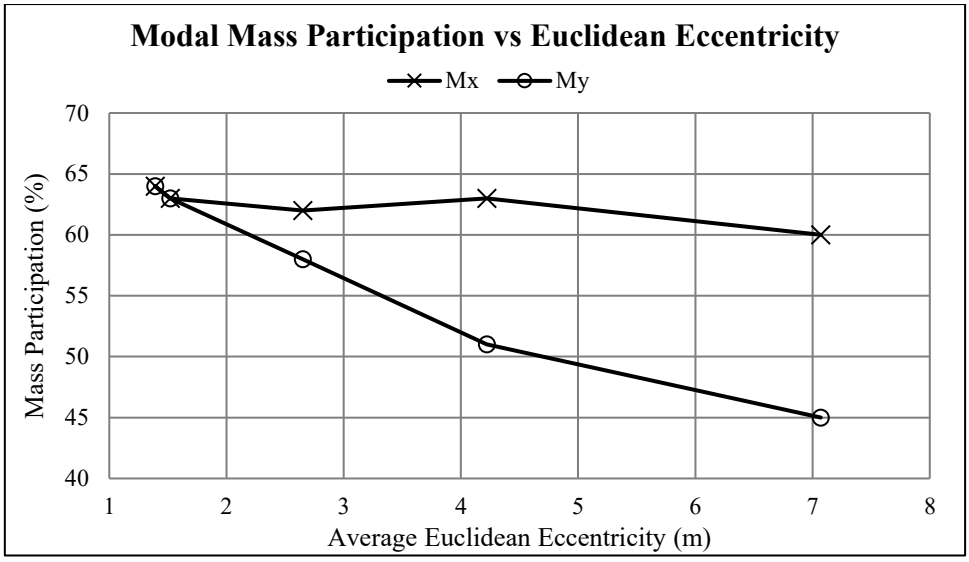


Figure 7.42: Optimising the mass participation of the fundamental modes in the vertically irregular building

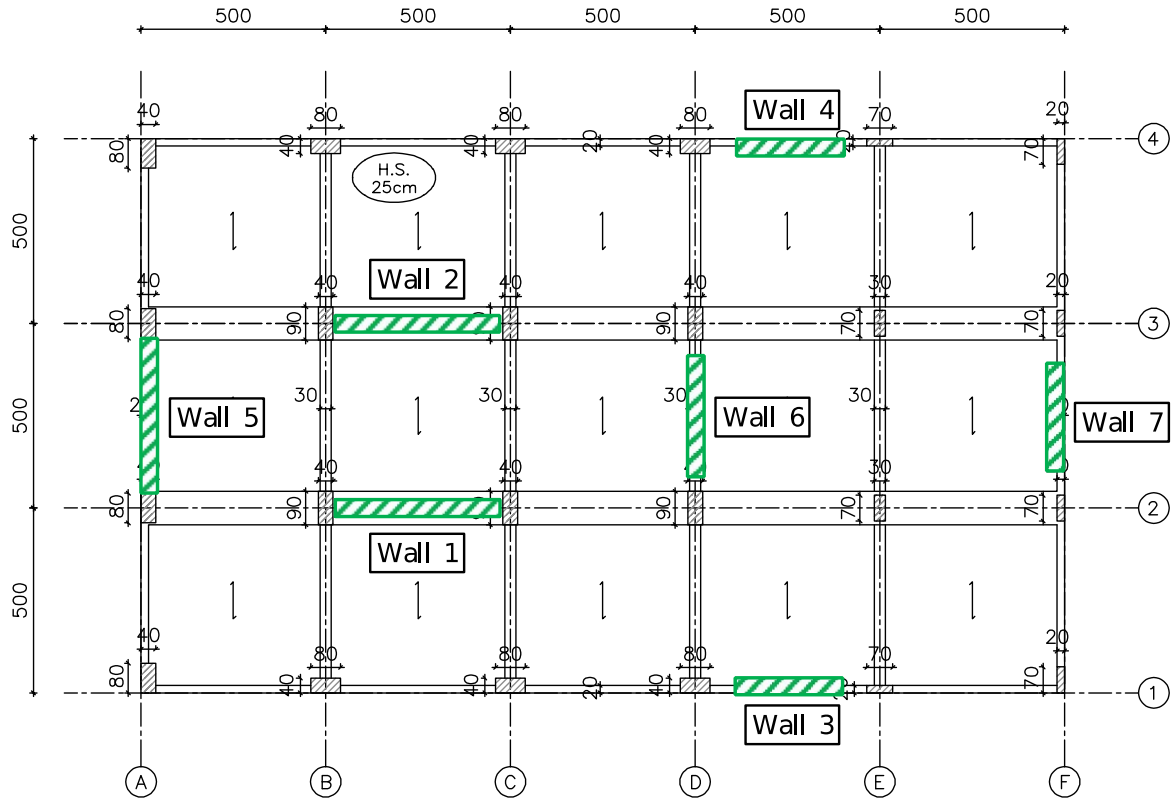


Figure 7.43: Ground floor plan of the vertically irregular building and characteristic layout up to the 7th floor (dimensions in cm)

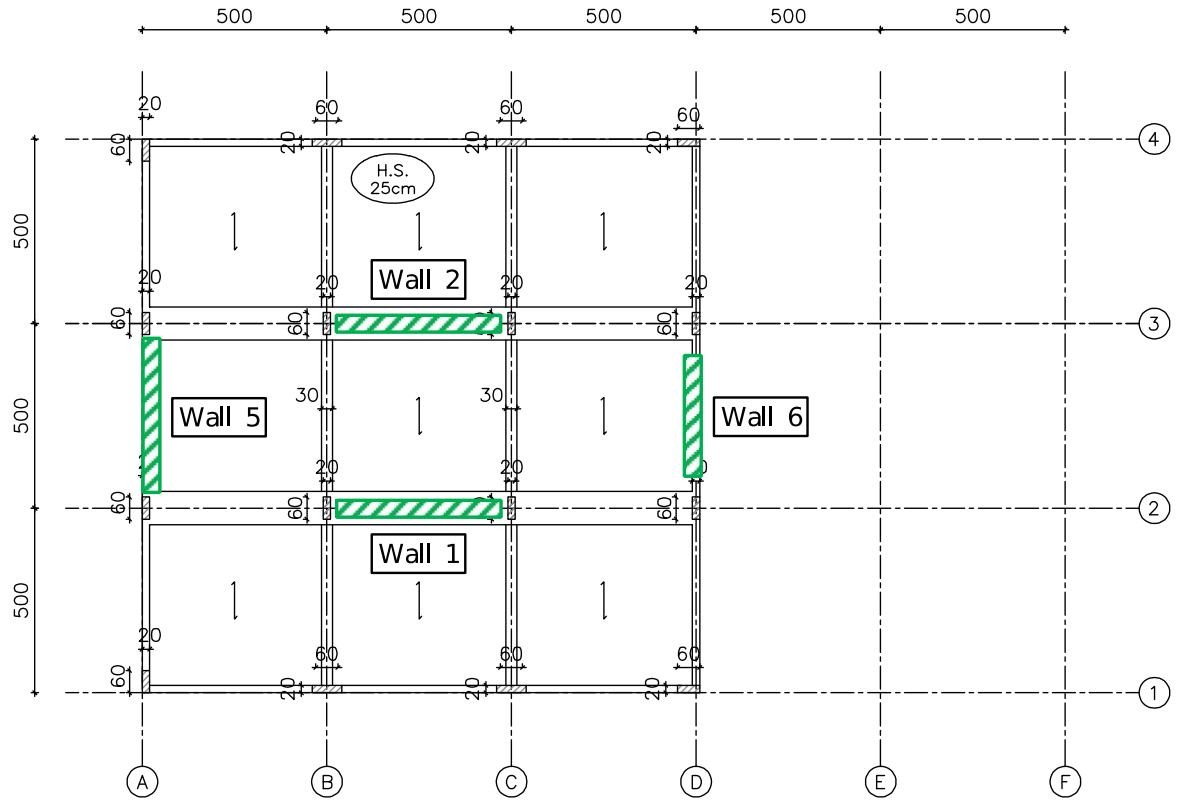


Figure 7.44: Eighth floor plan and characteristic layout of the 8th, 9th, and 10th floors of the vertically irregular building (dimensions in cm)

Step 2: Preliminary design and detailing of walls

Preliminary dimensioning of shear walls

The thickness of the walls is checked against the minimum code requirement as per the following equation, and the axial load-resisting capacity of the walls is verified as well (Table 7-23).

$$b_{w0} \geq \max\left[0.15,\ h_s / 20\right] = 0.215m$$

Table 7-23: Verification of the axial load-resisting capacity in the vertically irregular building

	Length (mm)	**Width** (mm)	**Axial Load** (KN)	**Axial Capacity (KN)**
Walls 1 & 2	4500	300	375	4830
Walls 3, 4, 7	3000	300	340	4830
Wall 5	4200	300	340	4830
Wall 6	3500	300	375	4830

Calculating the loads applied on the walls

Table 7-24 presents the original estimate of shear force and overturning moment applied at the base. These values are used to generate the preliminary bending moment and shear diagrams at all floors in line with the procedure and are checked at later stages against the ones obtained from the CSM at the performance point.

Table 7-24: Preliminary estimate of the base moment and shear demand in the vertically irregular building

	$V_{base}\,(KN)$	$M_{base}\,(KN.m)$
Walls 1 & 2	1230	19850
Walls 3, 4, 7	615	9900
Wall 5	1040	16700
Wall 6	725	11640

Preliminary dimensioning and reinforcement of the confined zones (boundary elements)

Figure 7.45 presents the typical detailing of walls having a length of 3500 mm, while the detailing of walls having a length of 4500, 4200, and 3000 mm are already presented in previous sections (Figure 7.7). It is noted that the special detailing in the confined zones extends across the critical height required by the code. In conformity with the other buildings, the normalised axial load was shown to satisfy the code-permissible limit, as noted in Table 7-25 along with other necessary checks.

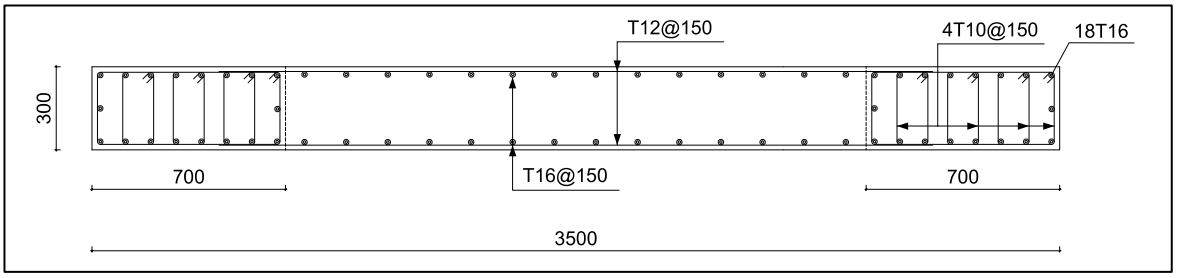


Figure 7.45: Detailing of Wall 6 in the critical region in the vertically irregular building (dimensions in mm)

Table 7-25: Boundary elements and the associated checks performed in the vertically irregular building

	Boundary Column			Checking The Effectiveness of Confinement		
	Length (mm)	Width (mm)	Vertical Reinf. Ratio	Normalised Axial Load ($\nu_d \le 0.4$)	$\alpha\,\omega_{wd}$	$30\,\mu_\varphi\,(\nu_d+\omega_v)\,\varepsilon_{sy,d}\,\frac{b_c}{b_0}-0.035$
Walls 1 & 2	900	300	1.49 %	0.053	0.094	0.071
Walls 3, 4, 7	600	300	1.34 %	0.035	0.066	0.061
Wall 5	840	300	1.43 %	0.049	0.098	0.076
Wall 6	700	300	1.72 %	0.053	0.087	0.076

Step 3: Finding the vibration characteristics of the building in the two main horizontal directions

The vibrational characteristics of the fundamental mode in each horizontal direction are presented in Table 7-26. The mass participation of both modes equals 64%, which underlines the predominance of the fundamental translational mode on the response and supports the application of the CSM to approximate the building response.

Table 7-26: Fundamental vibration characteristics of the vertically irregular building

	Mode 1			Mode 2		
	ω = 3.95 rad/s			ω = 4.93 rad/s		
Storey	**UX** (m)	**UY** (m)	**RZ** (rad)	**UX** (m)	**UY** (m)	**RZ** (rad)
Storey1	0.000	0.032	0.0011	0.032	0.000	0.000
Storey2	0.000	0.087	0.0031	0.087	0.000	0.000
Storey3	0.000	0.165	0.0059	0.164	0.000	0.000
Storey4	0.000	0.260	0.0093	0.258	0.000	0.000
Storey5	0.000	0.369	0.0132	0.366	0.000	0.000
Storey6	0.000	0.487	0.0174	0.483	0.000	0.000
Storey7	0.000	0.611	0.0218	0.607	0.000	0.000
Storey8	0.000	0.735	0.0270	0.736	0.000	0.000
Storey9	0.000	0.867	0.0324	0.868	0.000	0.000
Storey10	0.000	1.000	0.0380	1.000	0.000	0.000

Step 4: Modal pushover analysis in the global X and Y directions

After the inclusion of shear walls, the vertically irregular building considered is characterised by a monosymmetric plan along the X-axis only. In view of this, the asymmetry of the plan about the Y-axis entitles that modal pushover analysis needs to be performed twice when considering the accidental eccentricity in the X-direction. Hence, the CSM (NSPA) is performed 3 times as the building performance is checked at each of the SD and NC limit states (Table 7-27). The drift level is well maintained below the 2% limit which is suggested to control the response at the NC limit state. In this regard, Figures A7.17-A7.20 in the Appendix present the calculation of the performance point of the Push-Y analysis (in proportion to Mode 1) at the NC and SD limit states. Similarly, Figures A7.21 & A7.22 represent the performance point of the Push-X analysis (Mode 2) at both limit states. It is worth noting that the direction of the accidental eccentricity had only a minor effect on the pushover response, as the spectral displacement and acceleration measured at positive and negative eccentricity are almost matching.

Table 7-27: Summary of all the CSM analyses performed in the rectangular building

	Performance Point		Participation Factor	Mass Coefficient	Performance Point		
	Spectral Acc. a_{pf} (g)	**Spectral Disp. d_{pf} (m)**	**PF_{Roof}**	**α**	**Base Shear (KN)**	**Roof Disp. (m)**	**Drift Ratio**
PushX_±5% (NC)	0.19	0.19	1.62	0.642	4520	0.30	0.93%
PushY _+5% (NC)	0.14	0.24	1.62	0.643	3220	0.39	1.21%
PushY _-5% (NC)	0.14	0.25	1.62	0.643	3340	0.40	1.25%
PushX_±5% (SD)	0.18	0.13	1.49	0.656	4280	0.21	0.65%
PushY _+5% (SD)	0.14	0.16	1.49	0.662	3220	0.25	0.78%
PushY _-5% (SD)	0.14	0.16	1.49	0.662	3220	0.25	0.78%

Step 5: Verifying the flexural and shear capacities of the retrofitting walls

Once the performance point is determined, the actual shear force and bending moment in the walls are evaluated from the envelope of the pushover analyses performed. Accordingly, the shear reinforcement is provided such that the shear capacity is not exceeded at all floors (Table 7-29). Whereas for the flexural reinforcement, detailing at the first storey (base level) has been already set up and encompasses the confined regions at the ends of the walls (Figures 7.7 & 7.45), while the reinforcement is provided to ensure that the plastic capacity is not exceeded and no plastic hinges form at upper floors (Table 7-28). To this end, Tables 7-30 and 7-31 respectively present the flexural and shear checks which are plotted in graphical form in Figures 7.46 and 7.47.

Table 7-28: Provisioned flexural reinforcement of walls in the vertically irregular building

Storey	Walls 1&2 4500x300	Walls 3&4 3000x300	Wall 5 4200x300	Wall 6 3500x300	Wall 7 3000x300
Storey10	T12@150	-	T12@150	T12@150	-
Storey9	T12@150	-	T12@150	T12@150	-
Storey8	T12@150	-	T12@150	T12@150	-
Storey7	T12@150	T12@150	T12@150	T16@150	T12@150
Storey6	T14@150	T12@150	T16@150	T16@150	T12@150
Storey5	T16@150	T16@150	T16@150	T16@150	T16@150
Storey4	T16@150	T16@150	T20@150	T20@150	T16@150
Storey3	T20@150	T20@150	T20@150	T20@150	T20@150
Storey2	T20@150	T20@150	T25@150	T25@150	T25@150
Storey1	B.C.	B.C.	B.C.	B.C.	B.C.

Table 7-29: Provisioned shear reinforcement of walls in the vertically irregular building

Storey	Walls 1&2 4500x300	Walls 3&4 3000x300	Wall 5 4200x300	Wall 6 3500x300	Wall 7 3000x300
Storey10	T10@200	-	T10@200	T10@200	-
Storey9	T10@200	-	T10@200	T10@200	-
Storey8	T10@200	-	T10@200	T10@200	-
Storey7	T10@200	T10@200	T10@150	T10@200	T10@200
Storey6	T10@150	T10@200	T10@150	T10@150	T10@200
Storey5	T10@150	T10@200	T12@150	T10@150	T10@200
Storey4	T12@150	T10@200	T12@150	T12@150	T10@150
Storey3	T12@150	T10@150	T14@150	T12@150	T10@150
Storey2	T12@150	T10@150	T14@150	T12@150	T12@150
Storey1	T14@150	T12@150	T14@150	T14@150	T12@150

Table 7-30: Checking the flexural requirements of walls in the vertically irregular building

	Walls 1&2_4500 x 300			Walls 3&4_3000 x 300			Wall 5_4200 x 300		
Storey	**Dem.** KN-m	**Cap.** KN-m	**D/C**	**Dem.** KN-m	**Cap.** KN-m	**D/C**	**Dem.** KN-m	**Cap.** KN-m	**D/C**
Storey1	19850	19850	1.00	8300	8250	1.00	16000	16050	1.00
Storey2	20400	23050	0.89	8300	10000	0.83	21100	24000	0.88
Storey3	17650	22950	0.77	6900	9900	0.70	16350	20200	0.81
Storey4	15450	16800	0.92	5550	6750	0.82	13250	19950	0.66
Storey5	13250	16400	0.81	4150	6650	0.62	10650	13950	0.77
Storey6	11050	13200	0.84	2750	3950	0.70	8900	13650	0.65
Storey7	8800	10000	0.88	1400	3800	0.36	7100	8450	0.84
Storey8	6600	9500	0.69	-	-	-	5350	8100	0.66
Storey9	4400	9050	0.49	-	-	-	3550	7750	0.46
Storey10	2200	8600	0.26	-	-	-	1800	7450	0.24

Table 7-30 (Continued)

	Wall 6_3500 x 300			Wall 7_3000 x 300		
Storey	**Dem.** KN-m	**Cap.** KN-m	**D/C**	**Dem.** KN-m	**Cap.** KN-m	**D/C**
Storey1	12150	12150	1.00	8250	8250	1.00
Storey2	13700	17000	0.81	9900	14250	0.69
Storey3	10800	13500	0.80	7300	9900	0.74
Storey4	9450	13400	0.71	5700	6750	0.84
Storey5	8100	9300	0.87	4100	6650	0.62
Storey6	6750	9150	0.74	2750	3950	0.69
Storey7	5400	9000	0.60	1400	3800	0.36
Storey8	4050	5400	0.75	-	-	-
Storey9	2700	5250	0.52	-	-	-
Storey10	1350	5050	0.27	-	-	-

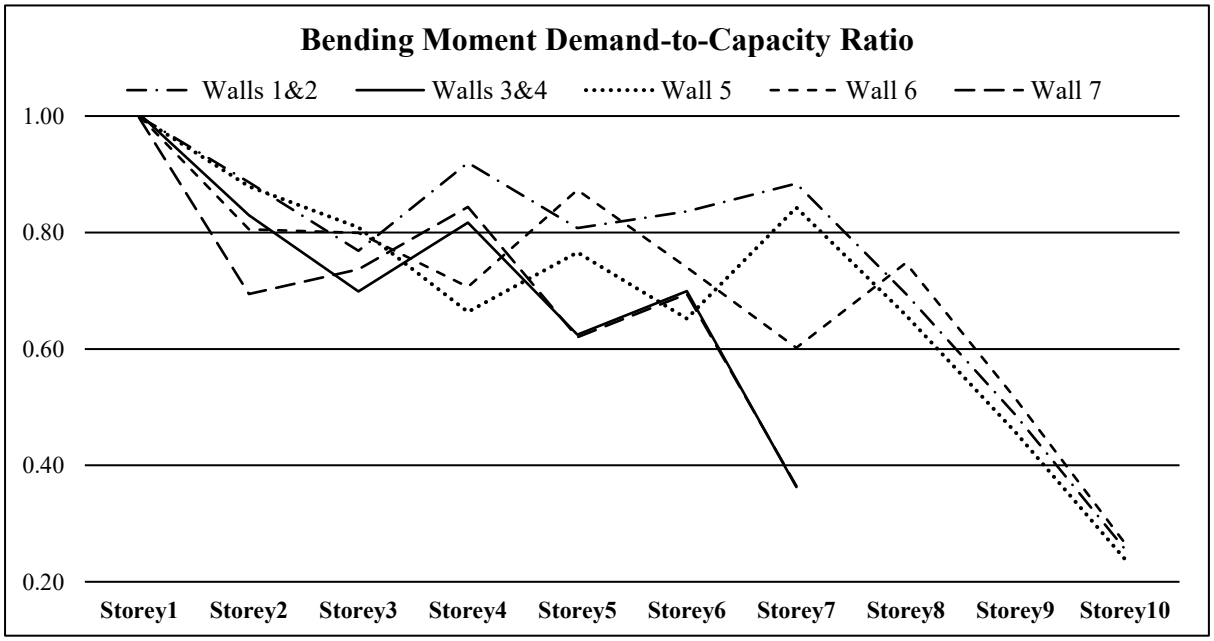


Figure 7.46: Checking the flexural requirements of walls in the vertically irregular building

Table 7-31: Checking the shear requirements of walls in the vertically irregular building

	Walls 1&2_4500 x 300			Walls 3&4_3000 x 300			Wall 5_4200 x 300		
Storey	**Dem.** KN	**Cap.** KN	**D/C**	**Dem.** KN	**Cap.** KN	**D/C**	**Dem.** KN	**Cap.** KN	**D/C**
Storey1	2000	2800	0.73	950	1300	0.74	2350	2550	0.92
Storey2	1750	2000	0.88	800	900	0.86	2050	2550	0.80
Storey3	1550	2000	0.78	650	900	0.72	1800	2550	0.71
Storey4	1350	2000	0.69	550	700	0.76	1600	1850	0.86
Storey5	1150	1400	0.85	400	700	0.57	1350	1850	0.74
Storey6	950	1400	0.71	300	700	0.40	1150	1300	0.88
Storey7	800	1050	0.75	400	700	0.55	900	1300	0.71
Storey8	600	1050	0.56	-	-	-	700	950	0.71
Storey9	400	1050	0.38	-	-	-	450	950	0.47
Storey10	200	1050	0.19	-	-	-	250	950	0.24

Table 7-31 (Continued)

	Wall 6_3500 x 300			Wall 7_3000 x 300		
Storey	**Dem.** KN	**Cap.** KN	**D/C**	**Dem.** KN	**Cap.** KN	**D/C**
Storey1	1650	2150	0.79	1300	1300	0.97
Storey2	1450	1550	0.94	1050	1300	0.79
Storey3	1300	1550	0.84	850	900	0.94
Storey4	1150	1550	0.73	700	900	0.75
Storey5	950	1050	0.90	500	700	0.75
Storey6	800	1050	0.75	400	700	0.60
Storey7	650	800	0.80	450	700	0.65
Storey8	600	800	0.72	-	-	-
Storey9	400	800	0.48	-	-	-
Storey10	150	800	0.20	-	-	-

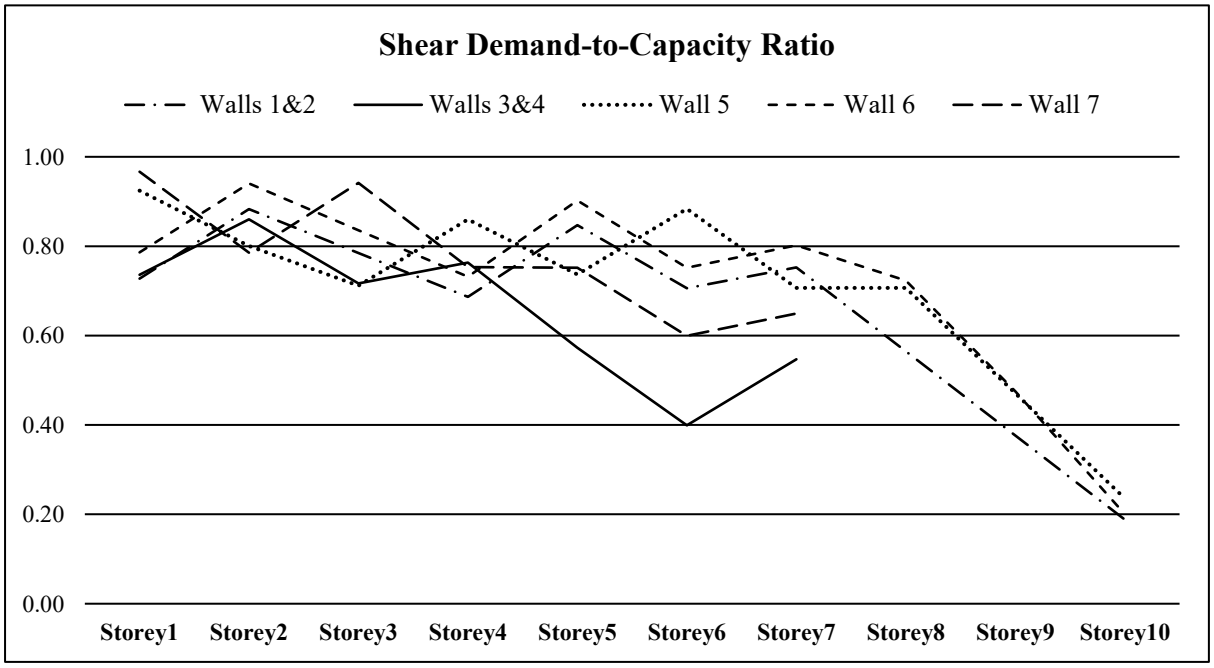


Figure 7.47: Checking the shear requirements of walls in the vertically irregular building

Step 6: Checking the local ductility requirements in the shear walls

The local ductility checks for all the walls are presented in Table 7-32, and the results prove that the plastic rotational capacity exceeds by far the maximum plastic rotation in each wall, hence proving the effectiveness of confinement in the boundary elements in satisfying the local ductility requirements.

Table 7-32: Verification of the local ductility requirements in the walls of the vertically irregular building

	Demand	Capacity		
	Max. Rotation (rad)	**EC8-3 (rad)**	**Empirical Equation 2 (rad)**	**Empirical Equation 3 (rad)**
Walls 1 & 2	0.0065	0.082	0.114	0.105
Walls 3, 4	0.0063	0.040	0.055	0.050
Wall 5	0.0093	0.085	0.119	0.109
Wall 6	0.0087	0.062	0.087	0.080
Wall 7	0.0082	0.040	0.055	0.050

Step 7: Checking the performance of the original frame against potential brittle and shear failures

Ductile mechanism check (chord rotation):

Figures 7.48 and 7.49 present the chord rotation checks performed at the NC and SD limit states respectively. The absence of red hinges at the NC limit state indicates that the ultimate chord rotation limit is never exceeded. Likewise, the absence of cyan-coloured hinges proves that the chord rotation limit pertaining to the SD limit state is never exceeded. Consequently, it is concluded that the chord rotation requirements of the retrofitted building are satisfied.

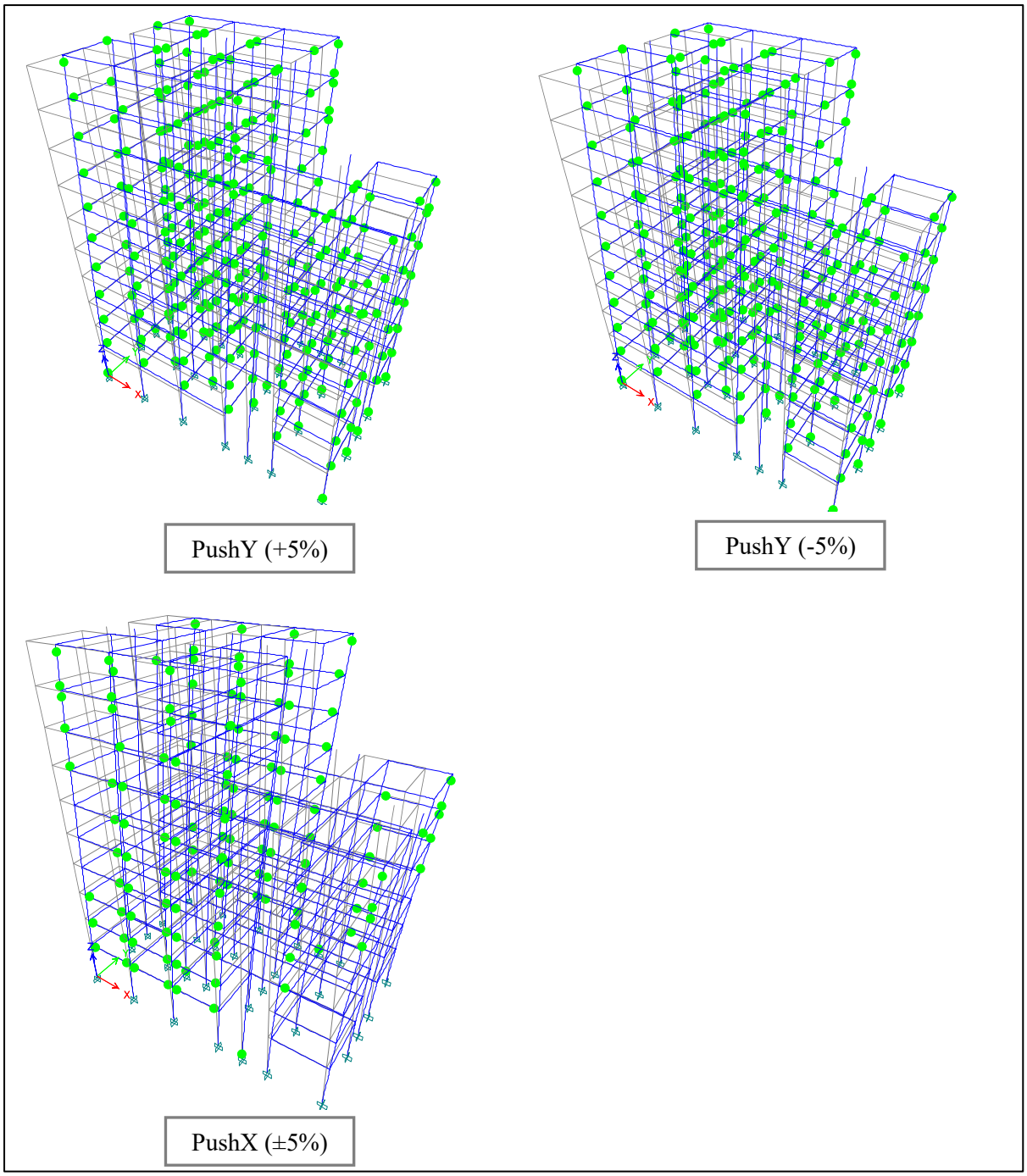


Figure 7.48: Flexural hinges at the NC limit state in the vertically irregular building

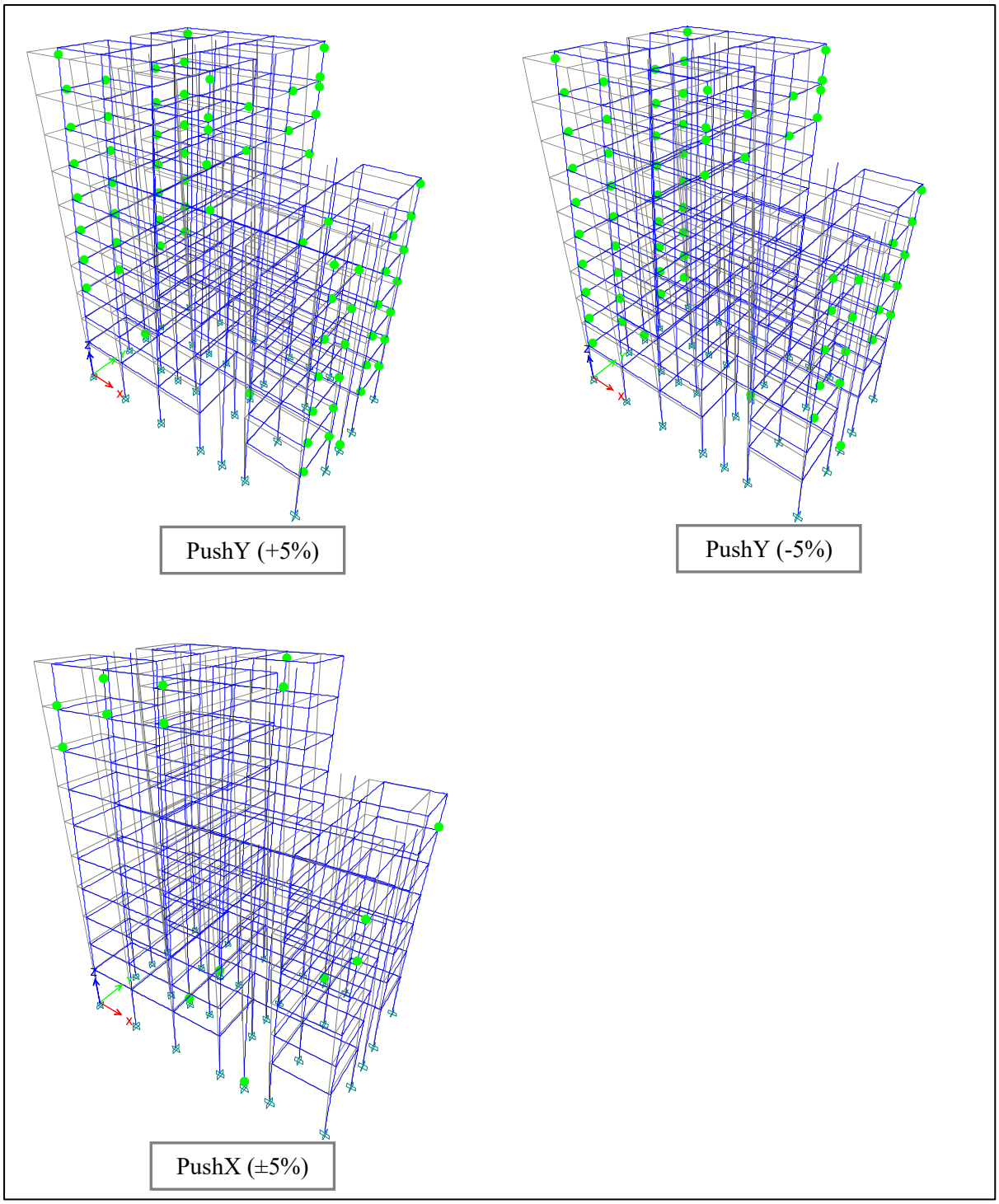


Figure 7.49: Flexural hinges at the SD limit state in the vertically irregular building

Brittle mechanism check (Shear Failure):

Noting that the retrofitted building is symmetric about the X-axis, symmetric beams/columns having the same dimensions are characterised by the same label (Figure 7.50).

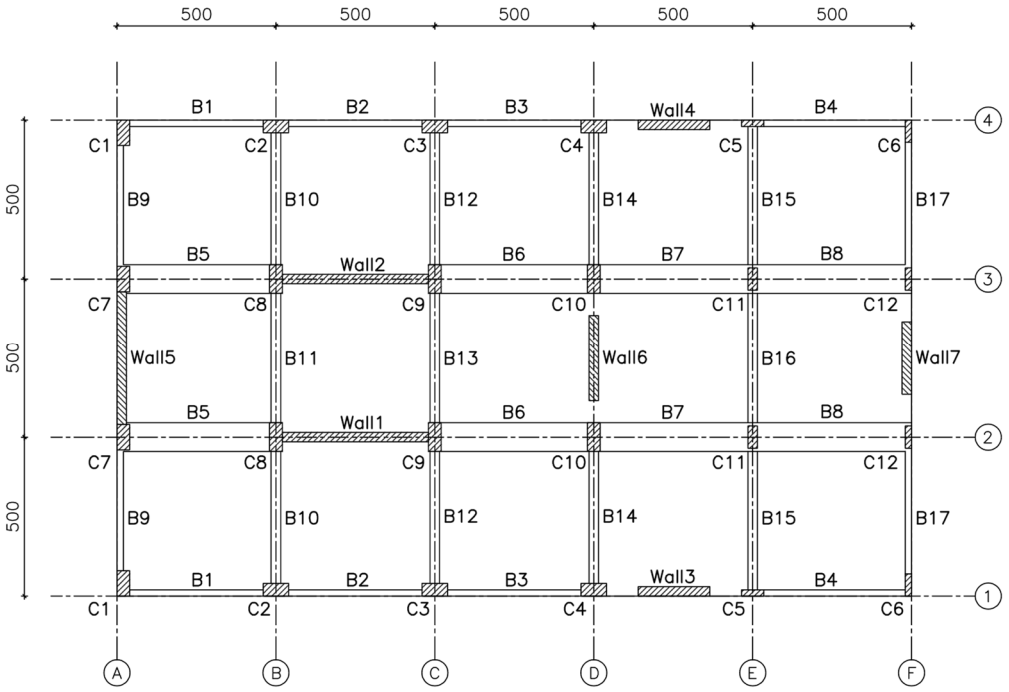


Figure 7.50: Labels of beams and columns in the in the vertically irregular building

Figures 7.51-7.53 present the shear results in the columns and beams. Adding to the results of the rectangular and the L-shaped scenarios, the shear capacity is shown to exceed the demand in all the structural members which validates the effectiveness of the proposed retrofitting solution. Again, the same trend is observed in the columns, with the shear demand increasing at upper floors in line with the reduced cross-section, and a significant shear demand is observed at the first floor in relation to the fixed base. Whereas for beams, the shear capacity is unaltered while the shear demand is reduced going up the levels, which is observed as the D/C ratio decreases by moving up the height of the building.

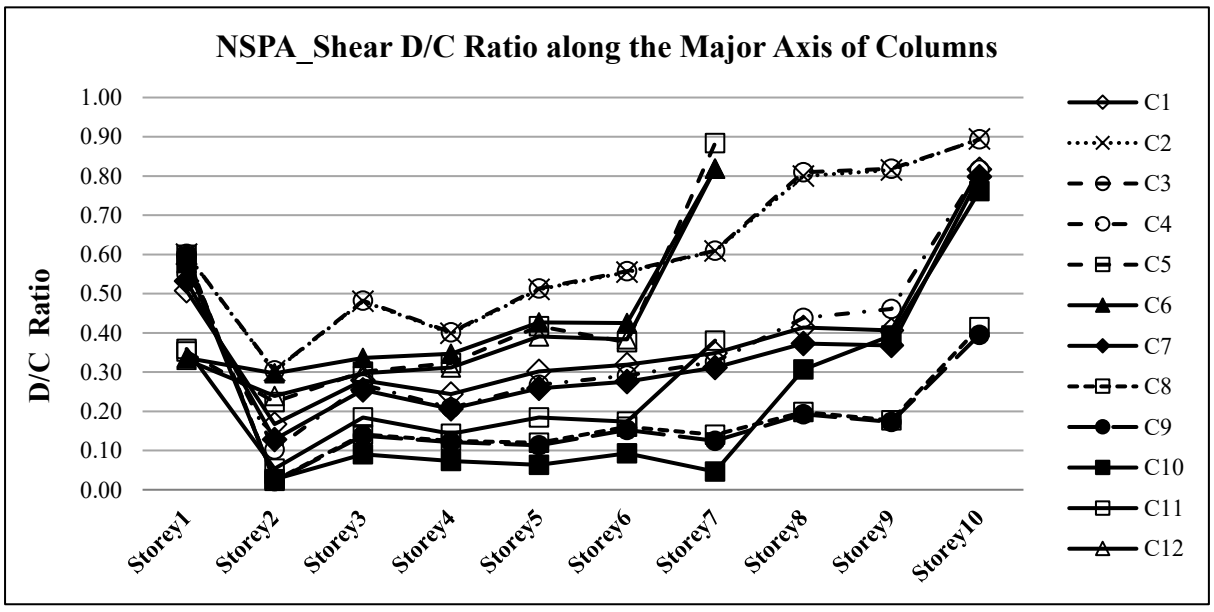


Figure 7.51: NSPA results of the shear D/C ratio measured along the major bending axis of columns in the vertically irregular building

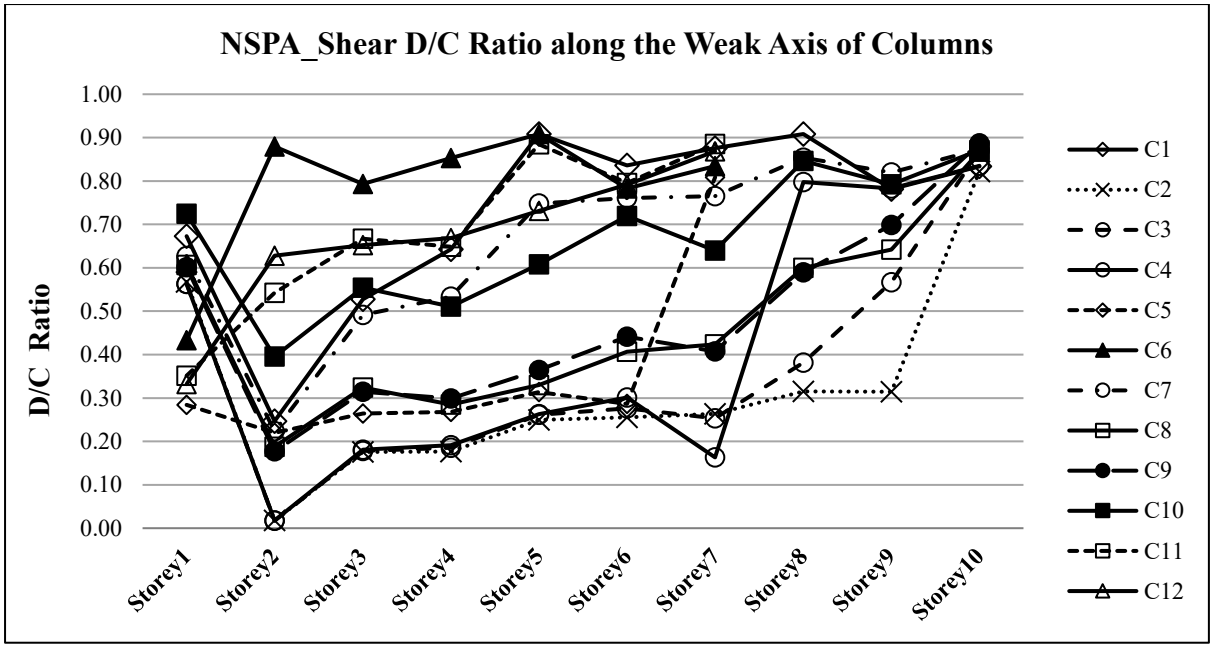


Figure 7.52: NSPA results of the shear D/C ratio measured along the weak axis of columns in the vertically irregular building

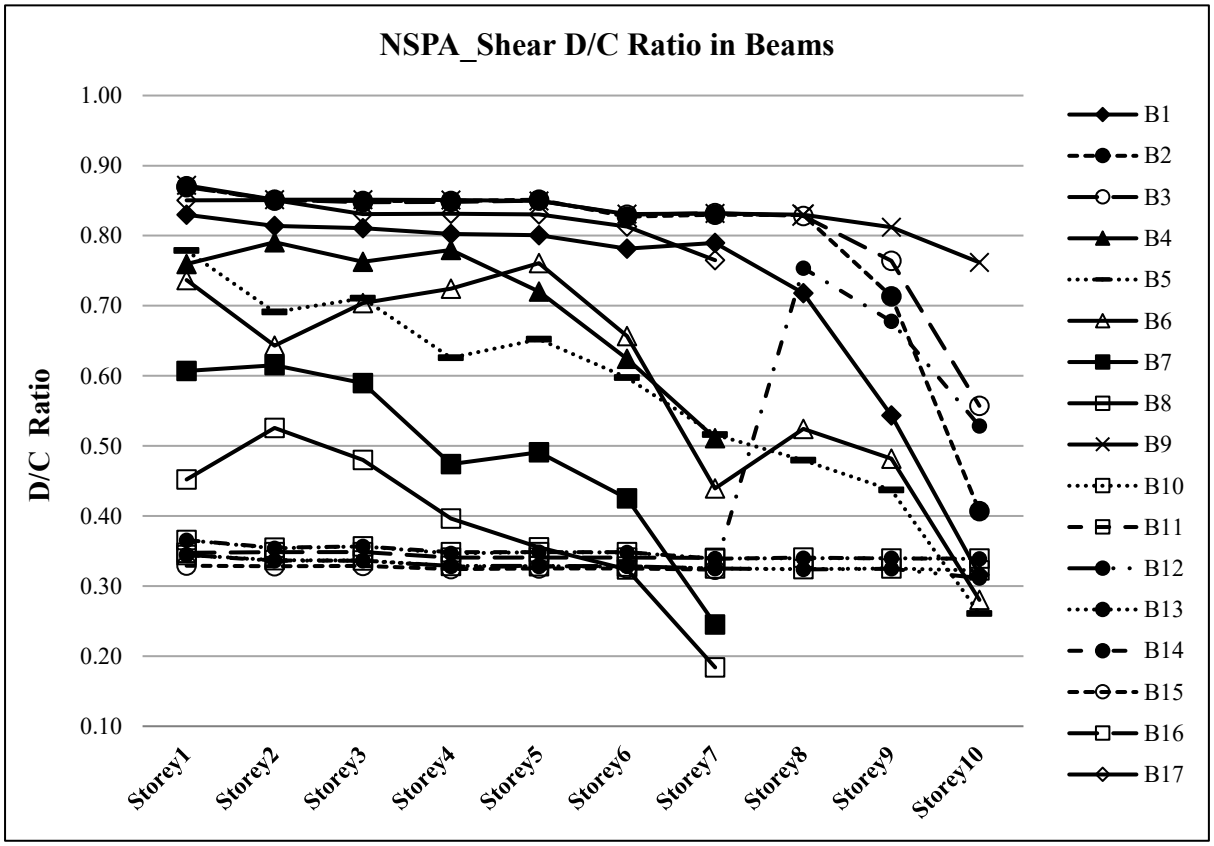


Figure 7.53: NSPA results of the shear D/C ratio measured along the strong bending axis of beams in the vertically irregular building

Step 8: Validation against complete nonlinear time history analysis (NLTHA)

The chord rotation results of the NLTHA are presented in Figures 7.54-7.56, accounting for the accidental eccentricity in each horizontal direction and on either side of the nominal centre of mass.

The results in the figures support those obtained using the CSM (NSPA), as the absence of red hinges under all the ground motions considered indicates that the ultimate chord rotation limit of the NC limit state is never attained or exceeded. In sum, the results point out at the effectiveness of the developed retrofitting strategy in overcoming potential ductile failure in the building scenario under consideration.

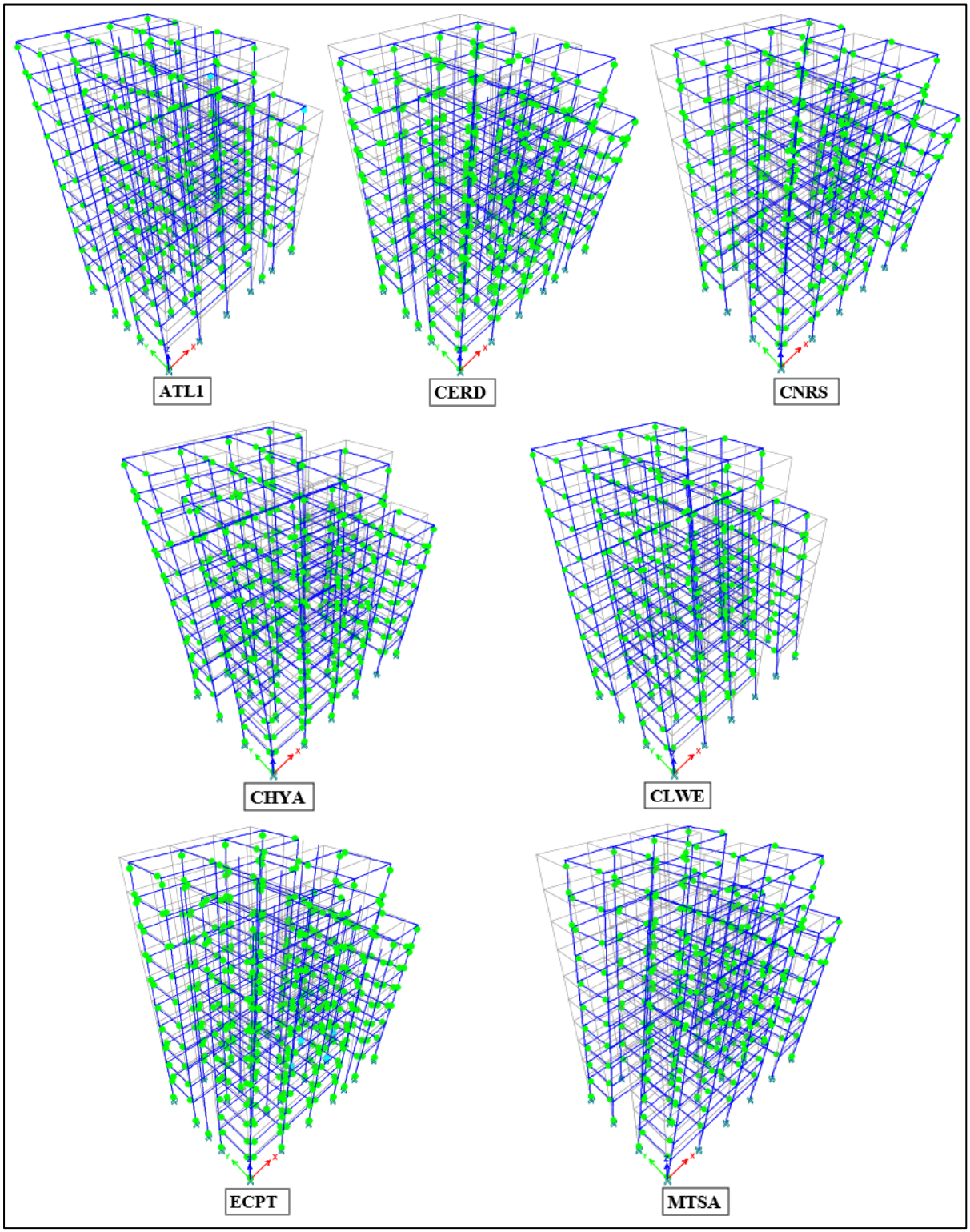


Figure 7.54: Flexural hinges obtained at the end of the NLTHA performed in the vertically irregular building (ecc. +5% in X)

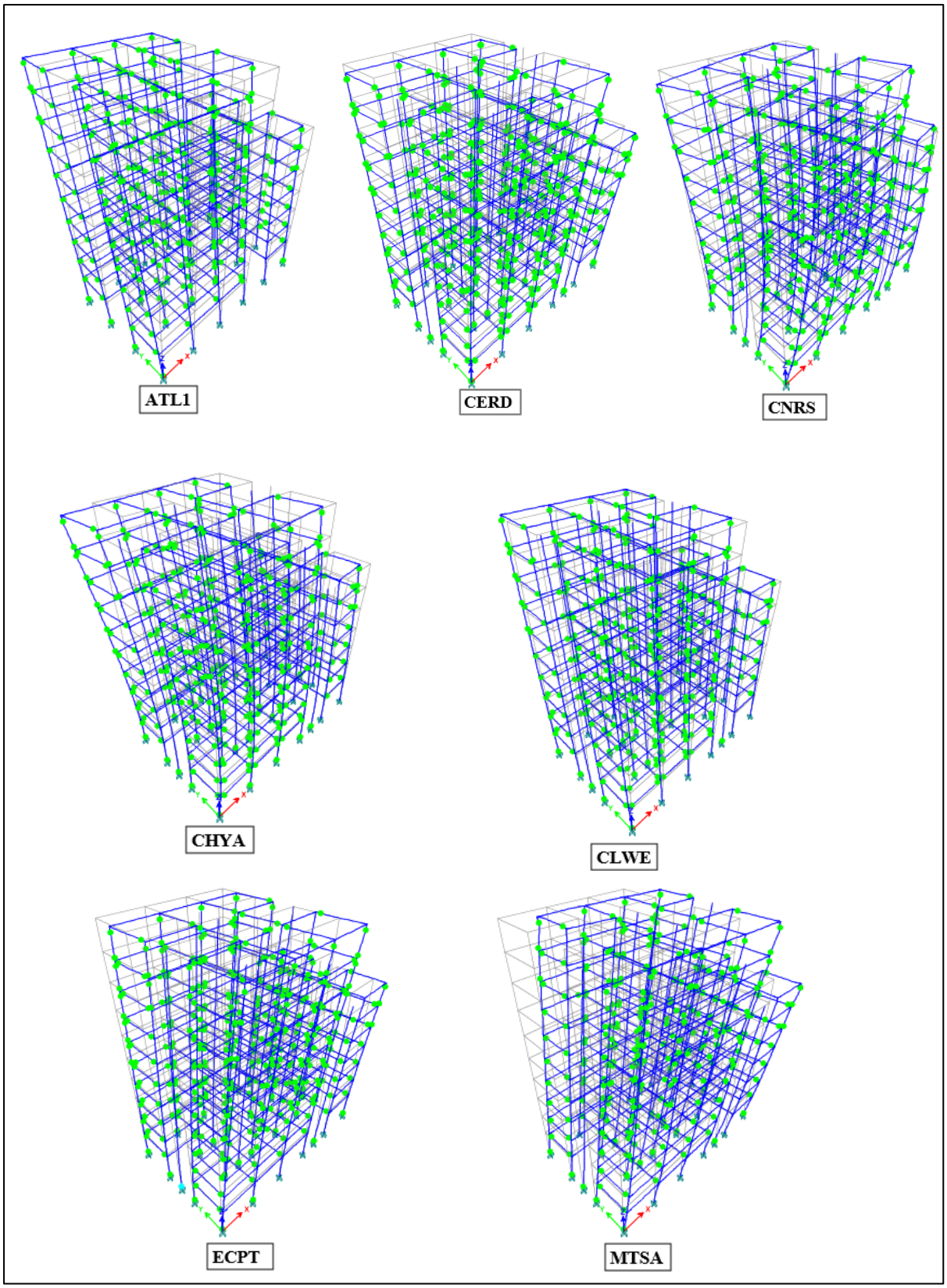


Figure 7.55: Flexural hinges obtained at the end of the NLTHA performed in the vertically irregular building (ecc. -5% in X)

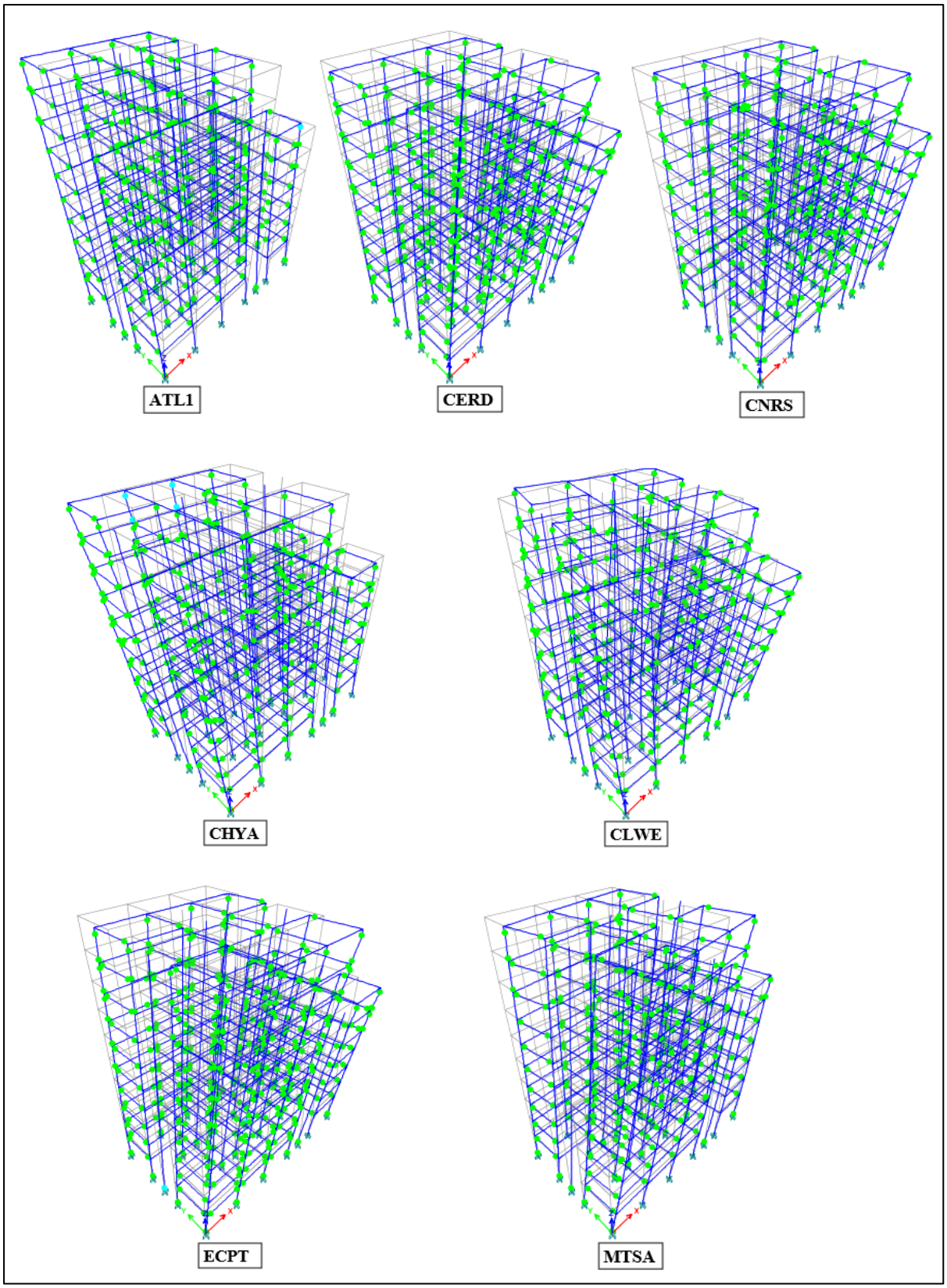


Figure 7.56: Flexural hinges obtained at the end of the NLTHA performed in the vertically irregular building (ecc. ±5% in Y)

Conversely, the shear results of the NLTHA are presented in the form of D/C plots and are presented in Figures 7.57-7.59. In conformity with what is observed in the rectangular and L-shaped buildings,

the shear capacity exceeds the demand in all the elements, and the shear D/C plots show a high level of correlation with those obtained from the CSM. Indeed, the pattern of variation of the shear D/C ratio as well as the D/C values in both the beams and columns are very similar to what is obtained using the CSM.

To conclude, these results cement the previously drawn conclusion and also approve the applicability of the developed retrofitting strategy in strengthening substandard frame buildings characterised by an irregularity along their height.

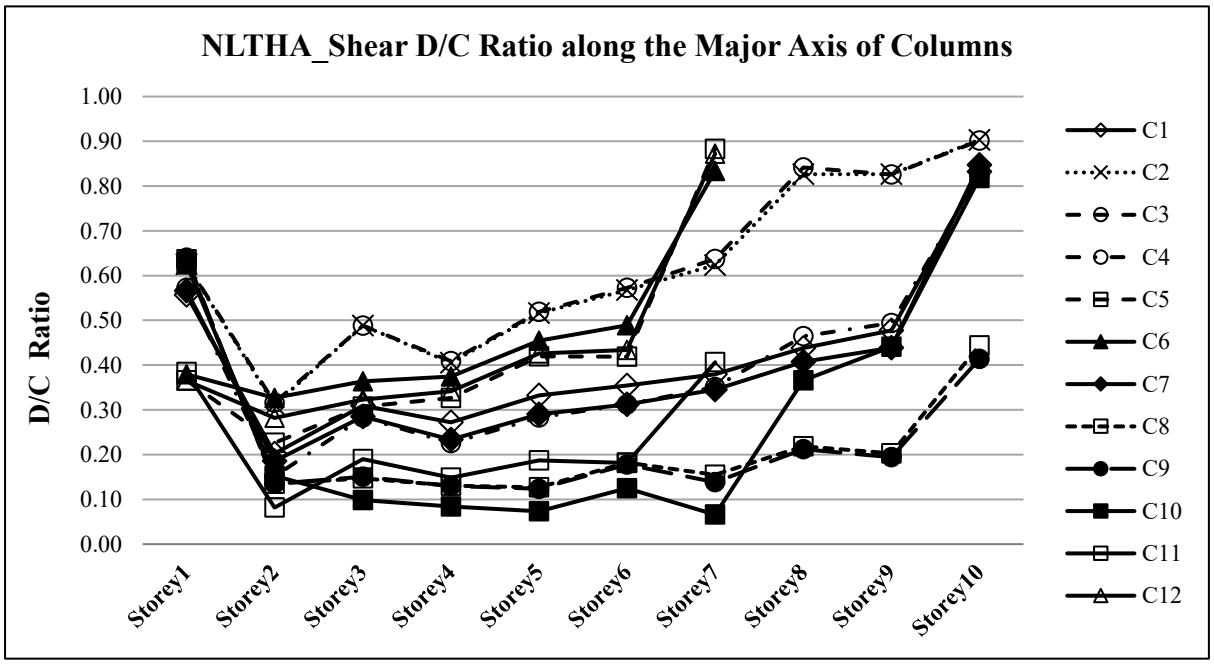


Figure 7.57: NLTHA results of the shear D/C ratio measured along the major bending axis of columns in the vertically irregular building

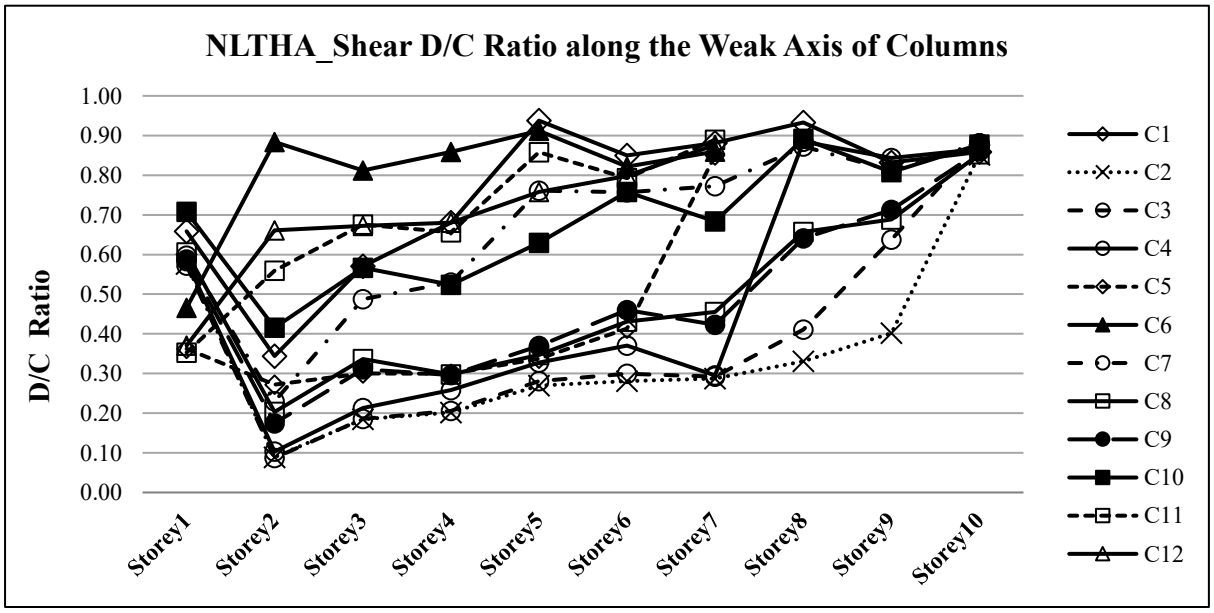


Figure 7.58: NLTHA results of the shear D/C ratio measured along the weak axis of columns in the vertically irregular building

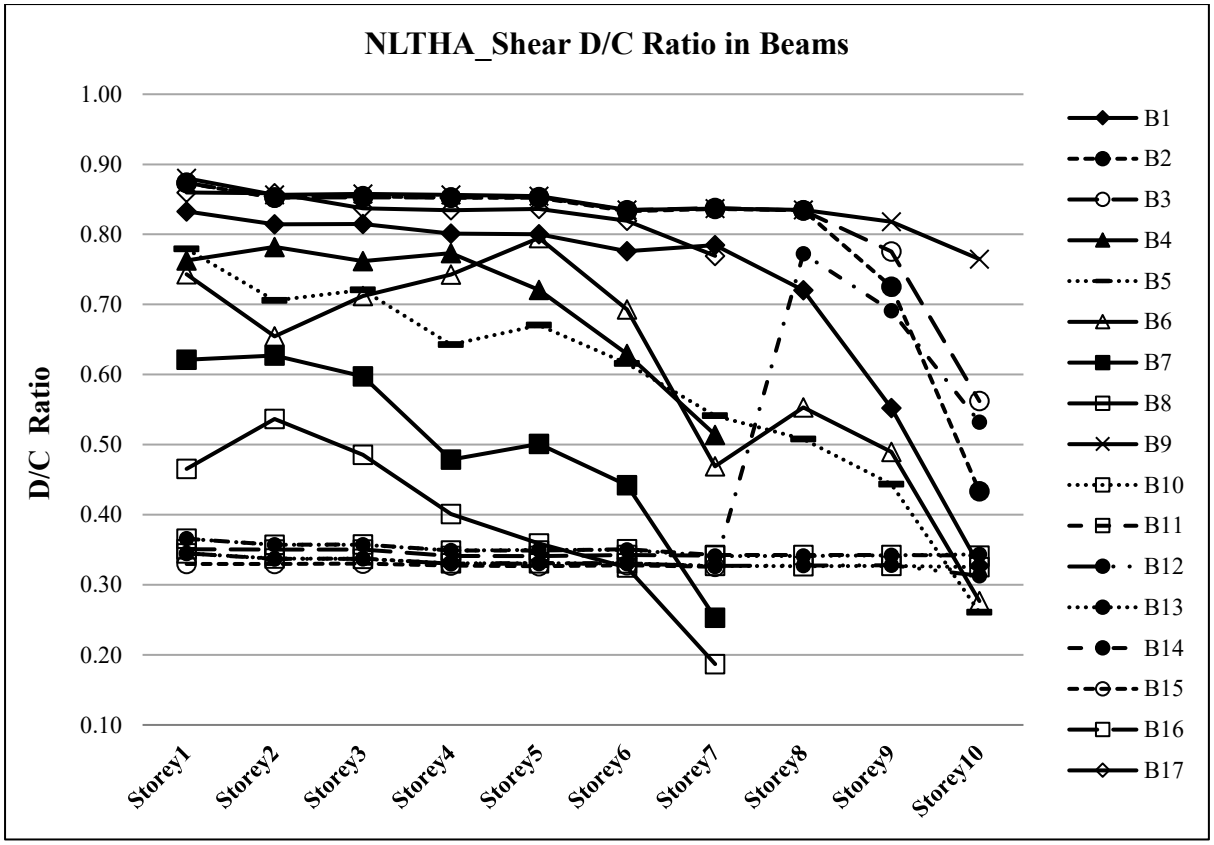


Figure 7.59: NLTHA results of the shear D/C ratio measured along the strong bending axis of beams in the vertically irregular building

7.6 Effect of the Original Frame and of the Wall Reinforcement

This research features two major contributions that enable engineers and researchers to find the vibration characteristics and the pushover response of retrofitted buildings in a simplistic manner, hence saving the computational time and effort required by conventional methods. Both approaches follow the same strategy as the response is initially evaluated with respect to the walls, and the frame response is subsequently incorporated in a simplistic manner. To this end, results of the frequency analysis have strongly supported the main assumption regarding the predominance of the walls, since the displacement response (mode shape) was accurately shown to be predominated by the walls, with a slight reduction in the period of vibration (reflecting on the increase in the elastic stiffness) observed upon the inclusion of the frame. On the other hand, the pushover results have drawn attention to the significant influence of the original frame, particularly when the plastic capacity of the walls is reduced upon a reduction in the walls reinforcement.

This section illustrates the effect of the original frame on the pushover response, noting that the increase in the flexural reinforcement increases the plastic capacity of the walls and consequently enhance their contribution into the overall pushover response. In view of this, the example considered involves the regular building considered in the case studies (Figure 7.60). The locations and dimensions of the walls are already presented in previous sections, with the discussion herein being focused on the frame effect

in line with increasing the plastic capacity of the walls. Three scenarios are investigated in that regard and are referred to as Low, Medium, and High M_p with reference to the plastic capacity of the walls. Noting that the provisions of EC8-1 (CEN, 2004a) define a ratio between 0.5% and 4% for the flexural reinforcement in the confined regions at the ends of the wall, the low and the high plastic capacity approximately characterise the minimum and maximum wall reinforcement respectively permitted by the code. Whereas the medium case represents a reinforcement ratio that is commonly adopted in RC buildings, since a higher reinforcement ratio requires extensive detailing as explained in the previous sections. The dimensions and reinforcement in the boundary columns are summarised in Table 7-33.

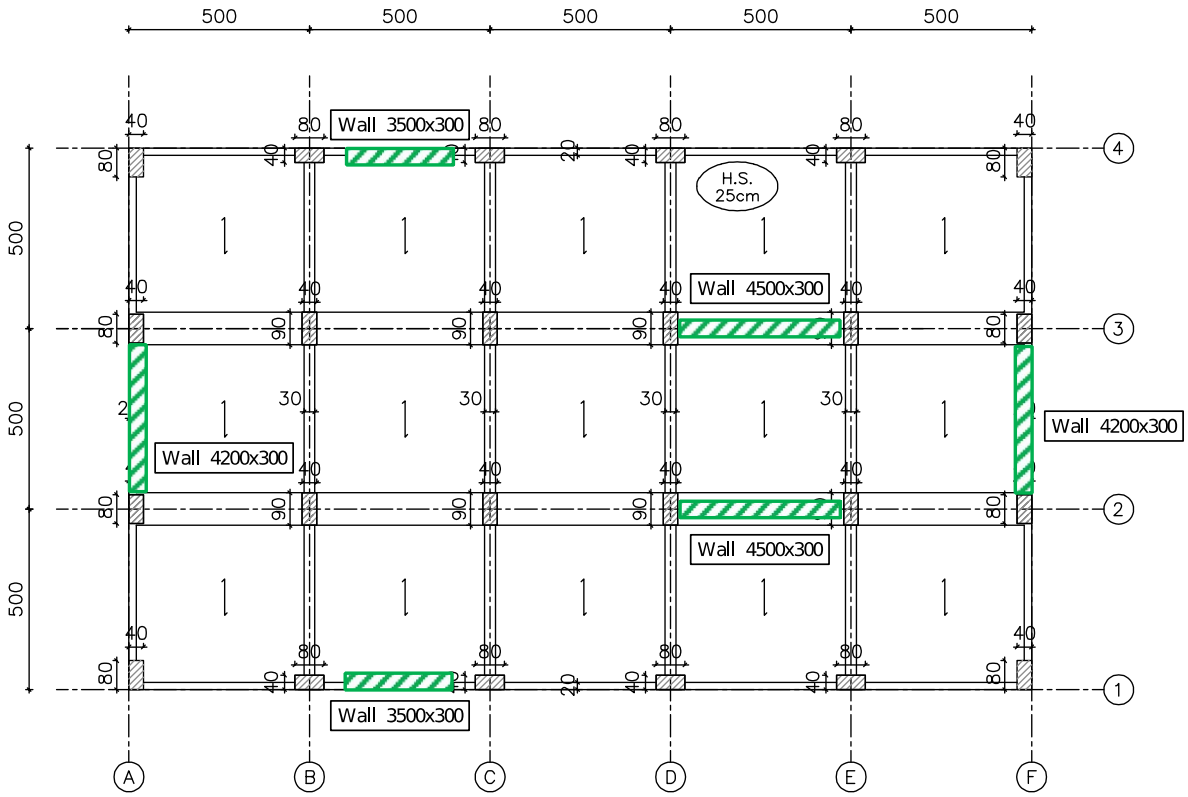


Figure 7.60: General layout of building and location of shear walls

Table 7-33: Characteristic properties of the three wall scenarios considered

	Boundary Col.		Case 1 - Low M_p			Case 2 - Medium M_p			Case 3 - High M_p		
Wall Dimensions	**Length mm**	**Width mm**	**Vertical Reinf.**	**Reinf. Ratio**	**M_p KN-m**	**Vertical Reinf.**	**Reinf. Ratio**	**M_p KN-m**	**Vertical Reinf.**	**Reinf. Ratio**	**M_p KN-m**
4500 x 300	900	300	14 T12	0.58%	12400	22 T16	1.64%	19800	22 T25	3.99%	36000
4200 x 300	840	300	14 T12	0.63%	10500	20 T16	1.60%	16700	20 T25	3.89%	30800
3000 x 300	600	300	10 T12	0.63%	5300	14 T16	1.56%	8300	14 T25	3.81%	15500

In light of this discussion, the frame impact is the same for the three scenarios considered while the walls contribution increases by increasing the ratio of flexural reinforcement. Modal pushover analysis follows in the context of the CSM, and the pushover response as well as the performance point are calculated for all three scenarios. In view of this, the plots in Figures 7.61 and 7.62 highlight the

significant contribution of the frame into the overall pushover response. As observed in the figures, although the increased plastic capacity of the walls reduces the gap between the overall pushover response and the one based only on the walls, the frame contribution is always significant and cannot be overlooked on that account. In this regard, the ratio of the ultimate load resistance provided by the walls to that of the original frame is in the ratio of 1:2 for the Low plastic capacity case, and this ratio correspondingly increases to 1:1 for the Medium case and to 2:1 for the High case. Accordingly, the frame is still contributing to one third of the total capacity of the retrofitted building in the case where the reinforcement in the boundary column is maximised. Hence, these results highlight the effective contribution of the original frame to the overall pushover response and its impact on the building displacement that is calculated at the performance point.

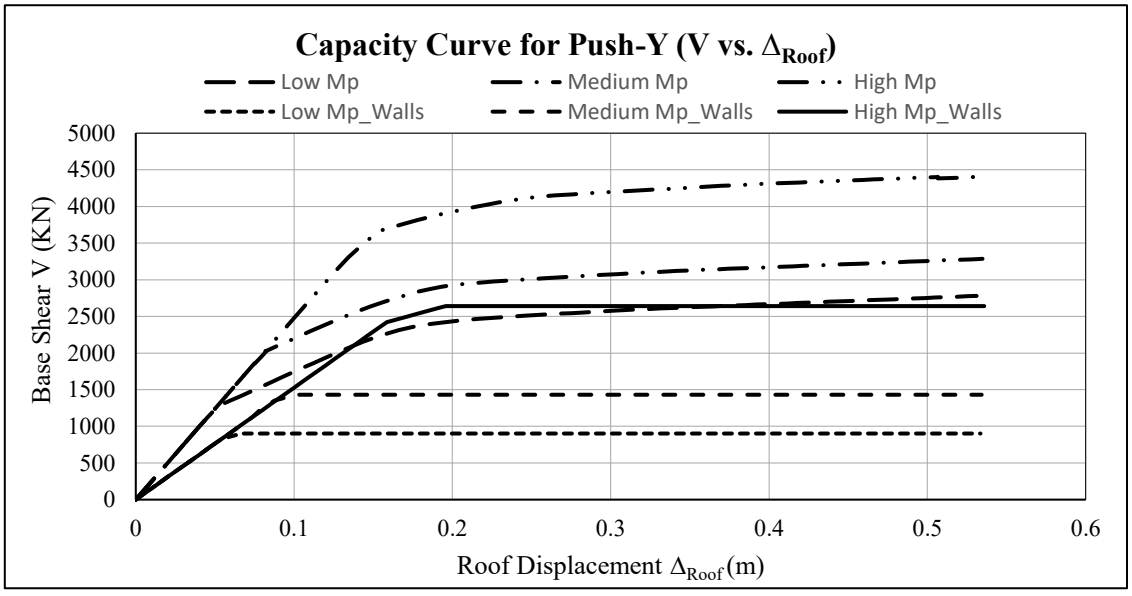


Figure 7.61: Variation of the pushover response in the Y-direction against the plastic capacity of the walls

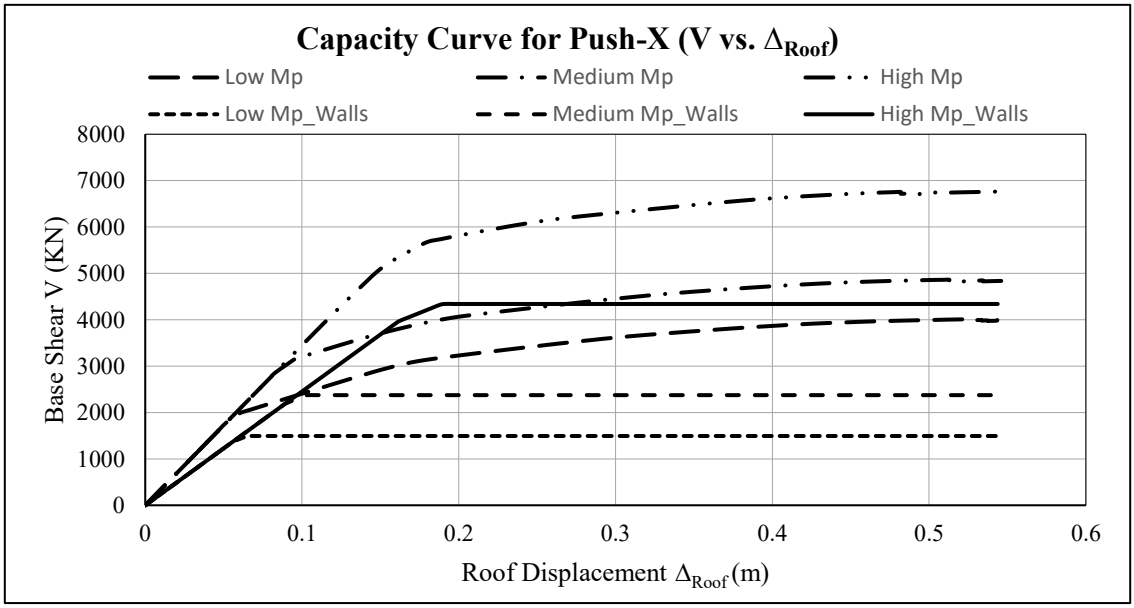


Figure 7.62: Variation of the pushover response in the X-direction against the plastic capacity of the walls

On the same hand, the displacement values measured at the performance point highlight the crucial effect of the frame (Figure 7.63), especially on the case involving a low plastic bending capacity of the walls. The plotted displacements point out at the substantial gap between the roof displacement based on the pushover response involving the walls only and the actual displacement calculated using the pushover response of the retrofitted building. To this end, even for the case involving the largest plastic capacity in which the walls are relatively expected to dominate the pushover response, the approximate displacement (in the Y-direction) based on the walls response is 35% higher than the actual displacement based on the retrofitted building response, which further highlights the significant contribution of the frame. In conclusion, including the original frame is crucial for obtaining a realistic representation of the pushover response and for obtaining a reasonable estimate of the lateral displacement in response to the applied seismic loading.

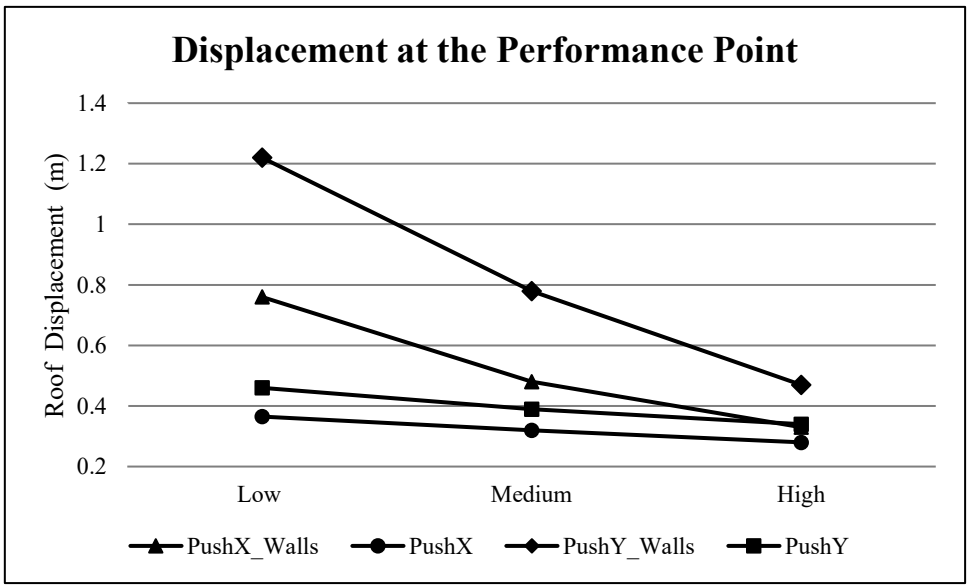


Figure 7.63: Roof displacement measured at the performance point at the NC limit state

In light of this discussion, the simplified approach implemented in this research outlines the methodology required to determine the pushover response of the retrofitted building, but it is worth mentioning that the frame-inclusion process was executed with the help of computerised software (such as ETABS). Recalling that the simplified procedure is mainly based on monitoring the exceedance of the plastic capacity at the base of the walls, specific amendments are required to accommodate the possible formation of plastic hinges at the ends of beams and columns. This would permit to determine the overall pushover response in a simplistic way without the use of computationally expensive software that require modelling of the original frame. To this end, the frame contribution could not be implemented in a simplistic manner on Maple because of the limited time scope of the research and since the major focus is to develop a retrofitting strategy to strengthen substandard buildings subjected to seismic action. Therefore, the limited time scope prevented the possibility to elaborate on specific details within each task, and the focus was rather shifted towards the generalised retrofitting strategy.

Nevertheless, the results obtained are promising and underline the essential contribution of the frame, which opens the door for future work that could be performed in that regard.

Chapter 8 Conclusion and Recommendations

8.1 Summary and Conclusion

This research presented a novel simplified approach that serves to ease and optimise the design of retrofitting systems for substandard multi-storey RC buildings located in seismic hazard regions using shear walls. This chapter presents a summary of the major accomplishments and the main drawn-out conclusions, and it also highlights the shortcomings of the method and pinpoints at further investigation that could be performed to that end.

8.1.1 Assessment of Substandard Buildings Located in Seismic Hazard Regions

The procedure employed for the assessment of buildings follows the guidelines of EC8-3 (CEN, 2005a) which stands amongst the most internationally approved standards that tackle the seismic assessment of existing buildings. The assessment is carried out at both the SD and NC limit sates and is performed before and after the inclusion of walls in order to judge on the effectiveness of retrofitting.

The standards of EC8-3 (CEN, 2005a) require that every single beam/column must be able to resist potential ductile and brittle failures in order for the building to be deemed adequate to resist earthquake loading. Accordingly, the retrofitting performed is deemed satisfactory if all the frame elements behave adequately after the addition of shear walls. Hence, manifestation of flexural and/or shear hinges in the model point out at the exceedance of the member's capacity and implies that retrofitting should be revisited.

In view of this, the assessment results have exposed the vulnerability of the typical buildings investigated and confirmed the necessity for retrofitting, since it is revealed that most of the structural elements and in particular the beams suffer from brittle shear failure upon exposure to earthquakes. To this end, the conclusion is not surprising given that the buildings were not originally designed to resist earthquakes despite being located in seismically active regions.

8.1.2 Basis for Ensuring the Applicability of the CSM

The capacity spectrum method (CSM) is the focus of this research and is based on the assumption that the seismic response of the building is governed by deformations of the fundamental mode of vibration (Freeman, 1998). Hence, the method is only reliable when this latter assumption is satisfied, which basically occurs when the mass participation of the translational component of the fundamental mode is considerably high to ensure its predominance in the seismic response (Peter & Badoux, 2000).

Therefore, a certain level of confidence needs to be established before the application of the CSM, which constitutes the cornerstone of the retrofitting strategy developed in this research. A novel approach is proposed for enhancing the applicability of the CSM, even to irregular buildings, and this

is based on the finding that reducing the eccentricity between the centre of mass and the centre of rigidity reduces the mass participation of the torsional component and increases the translational counterpart in the fundamental modes of vibration. The hypothesis is tested for a 6-storey regular building and for a 9-storey building featuring an irregularity in elevation. The cumulative centre of mass is considered as it provides a more realistic representation by accounting for the total mass of the current and overlying storeys. The location of the centre of rigidity (CR) is determined according to the single-storey concept which defines the CR as the point in the floor at which an applied lateral load is only associated with a translational displacement and does not cause any rotation of the floor diaphragm (Humar, 1984). The average Euclidean norm of the floor eccentricities is also considered in the aim to maximise the mass participation.

In both examples, the walls dimensions were continuously changed in order to alter the location of the centre of rigidity. It was accordingly observed that the mass participation of the translational component at zero average eccentricity is always in close proximity to the maximum that could be achieved. Furthermore, reducing the average Euclidean eccentricity was shown to be more advantageous than reducing the normal average, as the mass participation was further increased to that end.

It is worth noting, however, that reducing the average Euclidean eccentricity is difficult from a practical perspective, as it literally requires minimising the eccentricity at each floor level and in both horizontal directions. This indeed requires altering the wall dimensions at each storey which is not practically appealing. Nevertheless, it is demonstrated that the key to increase the mass participation ratio of the fundamental mode in each horizontal direction is to minimise the average Euclidean eccentricity.

Lastly, it is noted that while a minimum Euclidean eccentricity seems to be a reasonable indicator of high and reliable mass participation, it might still be possible to achieve higher mass participation. Indeed, the smallest Euclidean eccentricity was always associated with a mass participation ratio close to but not equal to the maximum that could be achieved. Furthermore, the Euclidean eccentricity could not be practically reduced to zero in order to make a more generalised conclusion, particularly in the presence of plan or vertical irregularities. Nevertheless, the current findings established a solid argument and cemented the case for applying the CSM in the assessment and retrofitting of buildings, paving the way for future work that could be performed on this front.

8.1.3 Static Analysis and Simplified Frequency Analysis

Having established a solid base for the application of the CSM, a novel simplified approach is proposed for determining the vibration characteristics of the building. Frequency analysis is usually performed using the conventional eigenvalue analysis which requires assembling the mass and stiffness matrices in order to solve the eigenvalue problem (Chopra, 2014). Although this can be readily completed through the static approach which also requires assembling the global stiffness matrix and which offers little advantage compared to the eigenvalue analysis, a more innovative approach is developed to

determine the vibration response in a simplified way that avoids the complexity of assembling the stiffness matrix.

Briefly summarising the procedure, a mode shape vector consisting of two translational and one planar rotational acceleration components are applied at a predefined point at all floors. The associated inertia forces are calculated by Newton's second law, and the floor resultant displacements are calculated and normalised in order to be input as the updated mode shape vector for the next iteration and so on, until achieving convergence into the mode shape and frequency of vibration of the fundamental mode. Furthermore, the iterations required to solve the static problem are coupled with those required to find the eigenvalue, which further reduces the computational time required for convergence. The procedure also permits to find the properties of higher modes of vibration if needed. This is achieved by filtering out all the lower mode components in order to trigger convergence into the anticipated mode.

A few assumptions were made to eliminate the uncertainties and to overcome the challenges encountered in the anticipated approach:

1. The contribution of columns is ignored, and shear walls are assumed to be the lone component resisting the applied seismic loading.
2. The out-of-plane resistance of the walls is assumed to be negligible, and accordingly the wall can only resist loads that are parallel to its longitudinal major axis.
3. The floor slab is assumed to deform in a rigid diaphragm; hence the seismic load is resisted by the walls in proportion to the relative stiffness of the latter.
4. The torsional stiffness of the walls is ignored, and the lateral stiffness is approximated by assuming that only a lateral force is applied at the top and by rearranging the elastic displacement evaluated using Timoshenko's beam approach formulation (Timoshenko & Gere, 1972).

The approach is summarised in the following steps which basically outline the answers to the main challenges encountered in the process:

1. The procedure starts by initiating equilibrium between the applied storey loads and the internal forces in the walls, on the basis of the relative stiffness of the latter in line with the rigid diaphragm assumption. This step propagates downwards starting at the top floor and moving down the levels. With the stiffness being evaluated using a simplified approximation, an imprecise evaluation of the internal forces is obtained, which causes violation of the compatibility requirements. As a remedy, the procedure involves applying corrections to the internal forces in order to restore compatibility of displacements, noting that this process propagates upwards from the base to the top floor and causes disruption of the previously established equilibrium. In sum, satisfying equilibrium causes violation of compatibility requirements, and the subsequent enforcement of compatibility leads to violation of

equilibrium. However, successive applications of equilibrium/compatibility cycles leads to reducing the violations and achieving convergence within a few iterations.

2. Upon restoring compatibility, the influence of a flexible base on the force correction at the current floor as well as the influence of correcting the force at the current level on lower levels are incorporated into the procedure in order to achieve convergence.

3. Most importantly, the iterations required to solve the static problem are coupled to those required to find the eigenvalue, which substantially reduces the computational demands and allows for the procedure to converge into the eigenpair of the fundamental mode in a few iterations, remarkably without the need for assembling the stiffness matrix.

Furthermore, the procedure is further simplified by assuming the mode shape to be governed by the reinforcing walls by virtue of the vulnerability of the existing RC frame building to earthquakes. Consequently, the mode shape and frequency of vibration are determined on the basis that the walls are the principal source of resistance to seismic loading, and the overall frequency of the whole system is subsequently determined by incorporating the effect of the original frame in a simplified way by envisaging the walls and the original frame as two springs connected in parallel which experience the same displacement and share the resistance of the applied seismic loading.

The proposed approach is verified for realistic structures, and the total (effective) circular frequency of the whole building has perfectly correlated with the one obtained from the conventional eigenvalue analysis performed on ETABS (2017). Although the results highlight the predominance of the walls, it should be noted that the effective stiffness of the frame was always significant and could not be overlooked, which hints at further work that could be done in the future to emphasize on the main assumption that the displacement is mainly dictated by the shear walls.

8.1.4 Simplified Pushover Response

Another contribution of this research that allows for a simplified application of the CSM is a novel simplified approach that estimates the pushover response of RC frame buildings reinforced with shear walls. The procedure relies on a simplified application of static analysis to find the pushover response by monitoring the formation of plastic hinges at the base of vertical elements. In parallel to what is performed in the simplified frequency analysis, the response is first generated with respect to the walls alone, and the frame effect is subsequently incorporated in order to obtain the overall pushover response of the building.

A few assumptions are made in order to reduce the challenges facing the anticipated procedure:

1. Plastic hinges are assumed to form only at the base of walls and columns.

2. The original RC frame building is assumed to be governed by a beam sway mechanism (strong column versus weak beam behaviour). Accordingly, the formation of plastic hinges in columns and walls cannot occur at upper floors and is only restricted to the fixed base.
3. The pushover response is assumed to be predominated by the flexural deformations. Hence, only flexural hinges are assigned at the base of the walls/columns.

Taking into account the aforementioned assumptions, the procedure involves applying a set of arbitrary loads to the structure and monitoring the sequential formation of plastic hinges at the base as the load is incrementally increased. During the process, each wall that reaches its plastic capacity is replaced by a pinned support at the base, and the procedure progresses by applying successive increments of load, making use of incremental linear analysis with respectively pinned wall bases. The total base moments are stored, and plastic hinges continue to form in succession until obtaining an unstable configuration of redundant walls that cannot resist additional loading. The cumulative load obtained at the end of the analysis represents the collapse load that is characterised by the inability of the structure to sustain additional loads.

The pushover response is initially determined with respect to the walls, and the procedure is complemented by adding the effect of the frame in a simplified manner. Recalling that the frame and the walls are analogous to two springs connected in parallel, the pre-determined displacement is fixed while the base shear is modified to accommodate the additional stiffness provided by the frame. Towards finding the equivalent pushover response, the relative contribution of the frame and the walls is measured by the work performed by each component over the displacements of the whole system. The total energy attributed to the walls at each stage of the pushover curve is represented by the external work performed by the applied loads over the resultant displacements. In parallel to what is performed in the frequency analysis in Chapter 5, the total displacements obtained at each step of the pushover curve are applied to the original frame and the corresponding reaction forces are calculated, which permits to evaluate the work performed by the frame and to consequently determine the overall pushover response.

For all the examples considered, the pushover curve obtained using the simplified approach was shown to have a good correlation with the pushover response directly obtained from detailed pushover analysis performed on ETABS (2017). Furthermore, the ultimate collapse load obtained using the procedure perfectly correlates with the one evaluated from plastic limit analysis.

8.1.5 Simplified Strategy for Retrofitting Substandard RC Frame Buildings

The final contribution of this research consists of developing a strategy to guide the retrofitting of substandard RC buildings subjected to seismic loading with shear walls, a process that normally depends on engineering judgment and on the computationally demanding NLTHA. The procedure relies on assembling the major findings of this research, including the approach implemented to optimise the

mass participation as well as the frequency analysis and the simplified pushover analysis in order to form a solid and simplified retrofitting strategy which is briefly summarised in the following steps:

1. Defining the location and the number of walls required.
2. Preliminary design of shear walls.
3. Finding the fundamental mode of vibration in the global X and Y directions.
4. Performing modal pushover analysis (CSM) in the X and Y directions and checking the drift demand.
5. Checking the shear and flexural requirements of shear walls.
6. Checking the local ductility requirements in the shear walls.
7. Verifying the adequacy of the original frame members against potential ductile and brittle failures.
8. Validating the approach against the fully integrated NLTHA.

In the first step, walls are added with the aim of reducing the average Euclidean eccentricity and maximising the mass participation of the translational component of the fundamental mode, in order to ensure the applicability of the CSM. A maximum drift ratio of 2% at the NC limit state is assumed to control the initial extent of retrofitting, noting that a stiff interstorey drift profile favours the beam sway mechanism (Fardis, 2009). Accordingly, the lateral resistance provided by the walls is assumed to be sufficient to reduce the stresses experienced by the substandard frame components when the interstorey drift ratio is maintained below the limit of 2%.

The retrofitting procedure is verified against the fully integrated NLTHA for regular buildings as well as for buildings featuring an irregularity in plan or in elevation. For all the building scenarios considered, the results obtained using the NLTHA followed the same trend and compared well with those obtained from the retrofitting strategy. Opposed to what is observed prior to retrofitting, the absence of red flexural hinges in both methods proves that the chord rotation capacity is never attained or exceeded, hence supporting the effectiveness of retrofitting in endorsing existing beams and columns to resist potential ductile failure. Likewise, the shear results are plotted in the form of Demand-to-Capacity ratio (D/C) and have indicated that the shear capacity is always exceeding the demand, hence certifying the effectiveness of retrofitting in protecting the original frame members from potential brittle shear failure.

In addition to helping the original frame to sustain the applied seismic loads, the similarity of the results obtained from the retrofitting strategy and the NLTHA speak volumes. Indeed, the pattern of variation of the shear D/C ratio in both the beams and columns is very similar in both the retrofitting strategy and the NLTHA, and the D/C values are very comparable in both methods, although those obtained from NLTHA were shown to be slightly more conservative. To note that although the chord rotation results are visually presented in the form of flexural hinges, the NLTHA was shown to be slightly more

conservative as well. This is actually observed in the results which reveal that more hinges have reached the DL limit state (green hinges) in the NLTHA than in the CSM or the retrofitting approach. The extent of variation between the two methods could have been better assessed if the chord rotations were numerically evaluated. Nevertheless, both methods have vindicated the success of retrofitting since the chord rotation capacity pertaining to the NC limit state was never exceeded.

In conclusion, the results highlight the accuracy of the developed retrofitting strategy as a simplified yet reliable alternative to the more sophisticated NLTHA, and most importantly they support the effectiveness of the standardised procedure in strengthening existing substandard RC frame buildings located in seismic hazard regions.

8.2 Recommendations for Future Work

8.2.1 Applicability of the CSM

Concerning the optimisation of the modal mass participation, the proposed approach guarantees a high mass participation of the translational component which enforces the applicability of the CSM. Reducing the average Euclidean eccentricity was shown to be key in achieving a sufficiently high mass participation in close proximity to the maximum. However, the process of determining the configuration of walls associated with a reduced Euclidean eccentricity is currently performed on a trial basis based on engineering judgment. The procedure starts with an initial layout of walls for which the average Euclidean eccentricity is calculated, and the walls configuration is continually adjusted based on engineering judgment with the aim of reducing the average Euclidean eccentricity and achieving a satisfactory mass participation. The procedure assumes that a sufficiently high mass participation is guaranteed at the end in view of the reduced eccentricity. Hence, the mass participation is only calculated for the final configuration of walls because the objective is to develop a simplified approach, and accordingly it would not be computationally advantageous to calculate the mass participation at each iteration. In light of this discussion, the procedure could become more efficient if the location and dimensions of walls could be automatically determined such that the average Euclidean eccentricity is minimised. This task could potentially be achieved with the help of optimisation techniques such as Genetic Algorithms, and it is worth being investigated in the future as it would further solidify the current approach and eliminate the iterative process required to find the optimum configuration of walls.

Furthermore, it is noted that the minimum Euclidean eccentricity yields a mass participation in close proximity but not necessarily equal to the maximum that could be achieved. To this end, further work could also be performed towards finding the absolute factor that results in maximising the mass participation factor.

8.2.2 Contribution of the Original Frame into the Overall Response

The frequency analysis and the simplified pushover analysis constitute two of the major contributions of this research. Both approaches follow the same strategy, as the response is initially evaluated with respect to the walls, and the frame contribution is subsequently incorporated in a simplified manner. In both methods, the frame contribution is obtained by applying a vector of displacements to the initial frame and by extracting the resultant reaction forces, in order to find the effective stiffness in the frequency analysis approach or to calculate the work performed by the frame in the simplified pushover approach. To this end, extracting the frame effect in a simplified way requires expanding the current procedure to include the properties of the beams and columns as well as the joints connecting the elements, such that the equivalent response of the retrofitted building could be evaluated. Because of the limited time scope of the research, the frame-inclusion process in both approaches is currently executed with the help of computerised software ETABS (2017). In view of this, the results of both the frequency analysis and the simplified pushover analysis compared very well with those obtained directly from ETABS. This underlines the accuracy of the concept and opens the door for future work that could be performed to further simplify the procedure and to encompass the frame effect in a simplified form that does not require standard structural analysis software.

Furthermore, the results performed to investigate the frame effect on the overall pushover response have highlighted the significant contribution of the frame, even for the case where the plastic capacity of the walls is maximised. Based on these results, the frame effect could not be overlooked, even for substandard RC buildings, which prompts to further investigate the main assumption that the displacement of the building is dictated by walls, although the results obtained using the complete approach compared very well against those obtained from computerised software ETABS (2017).

8.2.3 Simplified Retrofitting Strategy

In the retrofitting strategy, the validation of the proposed retrofitting is initially based on maintaining the drift ratio at the NC limit state below the limit of 2%. This limit is proposed upon reviewing the literature, with studies by Fardis (2009) pointing out that a stiff interstorey drift profile promotes a beam sway mechanism. Furthermore, the provisions of ATC-40 (ATC, 1996, 2005) specify a drift limit of 2% for the Life Safety limit state, which simulates a state of damage that lies between the SD and the NC limit states defined by EC8-3 (CEN, 2005a). Accordingly, the 2% drift limit at the NC limit state is based on engineering judgment and is assumed to be a safe bet to ensure that the lateral resistance provided by the walls is significant and would reduce the stresses originally experienced by the substandard frame components. In view of this, this topic is worth further investigation in the future, although the proposed 2% limit is shown to successfully control the retrofitting provided for all the buildings considered. Indeed, it would be interesting to investigate if the 2% limit state could be further

optimised or if there is a factor other than the drift ratio that could be better adopted to decide on the initial outcome of the retrofitting solution provided.

8.2.4 General

The strategy developed in this research imposed some guidance on the ongoing retrofitting of substandard RC frame buildings with the addition of shear walls. The discussion was mainly focused on shear walls because this technique is one of the most widespread retrofitting practices, especially in developing countries in view of the ease of adding walls which requires no special expertise among local contractors. To this end, core walls are widely considered whenever shear walls are adopted for retrofitting of existing buildings and for the design of new ones as well. Core walls are generally added around lifts and stairs and are widely favoured as a more economical solution, as they generally provide more stability to the structure compared to isolated walls, because of the bracing action at the corners which makes the whole core function as one single unit that resists the lateral loads. To this end, core walls could potentially be considered in the current retrofitting procedure; this would basically require an approximative formula to estimate the lateral stiffness of core walls in parallel to what is considered for isolated walls, and the other steps would follow sequentially as per the current procedure. It is worth noting that core walls were not considered in this research by virtue of the weakness of existing columns, which would practically represent the boundary elements at the corners of the core walls. Hence, the reinforcement of existing columns is not sufficient to provide the confinement required to resist the seismic loading, and accordingly existing columns need to be jacketed and reinforced first in order to function as the boundary elements at the corners of the core walls. Nevertheless, core walls remain a viable option when it comes to retrofitting existing buildings using RC walls, and it would be interesting to investigate this option in the future in the context of the retrofitting strategy proposed in this research.

Furthermore, it should be noted that the addition of RC shear walls is also believed to have some setbacks, especially during installation which includes the excavation and execution of the foundation of the walls. This might cause some serious disruption to the operating services, especially if the building is required to remain in operation during retrofitting and if walls are to be added in the interior. Hence, it is worth investigating other retrofitting techniques that could be accommodated within the method. In view of this, the procedure mainly depends on reducing the Euclidean eccentricity to maximise the mass participation and enforce the applicability of the CSM. This is not restricted to the use of shear walls and could be achieved with other techniques such as the addition of steel bracing or including the effect of existing masonry infill walls, which are also known to enhance the lateral stiffness and to reduce the lateral displacement in existing buildings. It is noted that the frequency analysis and the simplified pushover analysis should be adjusted in that regard, as the current procedure depends mainly on extracting the response with respect to shear walls and on adding the frame

contribution separately. Therefore, the success of using shear walls leaves the door open for future research investigating the applicability of other retrofitting technique. This would further generalise the proposed strategy and would expand the range of applicability to other scenarios in which alterative retrofitting techniques might be more appealing from a practical perspective.

Bibliography

ALBANESI, T., BIONDI, S. & PETRANGELI, M. 2002. Pushover analysis: An energy based approach. Proc. of the Twelfth European Conference on Earthquake Engineering, London, United Kingdom, Paper No. 605.

ANGEL, R., ABRAMS, D. P., SHAPIRO, D., UZARSKI, J. & WEBSTER, M. 1994. Behavior of reinforced concrete frames with masonry infills. University of Illinois Engineering Experiment Station. College of Engineering. University of Illinois at Urbana-Champaign.

ASCE, 2016. Minimum design loads and associated criteria for buildings and other structures. American Society of Civil Engineers, Reston, VA, USA.

ASCE, 2017. Seismic evaluation and retrofit of existing buildings. American Society of Civil Engineers. ASCE/SEI 41-17, Reston, VA, USA.

AŞıKOĞLU, A., VASCONCELOS, G. & LOURENÇO, P. B. 2021. Overview on the nonlinear static procedures and performance-based approach on modern unreinforced masonry buildings with structural irregularity. *Buildings,* 11**,** 147.

ATC, 1982. *An Investigation of the Correlation Between Earthquake Ground Motion and Building Performance*. Applied Technology Council, Redwood City, California, USA.

ATC, 1996. *Seismic Evaluation and Retrofit of Concrete Buildings.* Report ATC-40, Applied Technology Council, Redwood City, California, USA.

ATC, 2005. *Improvement of Nonlinear Static Seismic Analysis Procedures.* Report FEMA-440 (ATC-55 Project), Applied Technology Council, Redwood City, California, USA.

AVRAMIDIS, I., ATHANATOPOULOU, A., MORFIDIS, K., SEXTOS, A. & GIARALIS, A. 2016. *Eurocode-compliant seismic analysis and design of R/C buildings : concepts, commentary and worked examples with flowcharts,* Cham, Springer.

BAI, J. 2003. Seismic retrofit for reinforced concrete building structures. Mid-America Earthquake Center, CM-4, Texas A&M University.

BENTO, R., FALCAO, S. & RODRIGUES, F. 2004. Nonlinear static procedures in performance based seismic design. Proceedings of the 13th world conference on earthquake engineering, Vancouver, Canada.

BERTERO, V. V. & BOZORGNIA, Y. 2004. The early years of earthquake engineering and its modern goal. Ch.1 in: *Earthquake Engineering: From Engineering Seismology to Performance-Based Engineering.* CRC Press, Boca Raton, FL, USA, pp. 1-1 – 1-17.

BERTERO, V.V. & BROKKEN, S. 1983. Infills in seismic resistant building. *Journal of Structural Engineering,* 109**,** 1337-1361.

BERTERO, V. V., POPOV, E. P., WANG, T. Y. & VALLENAS, J. 1977. Seismic design implications of hysteretic behavior of reinforced concrete structural walls. Proceedings, 6 th World Conference on Earthquake Engineering, 1898-1904.

BHANDARI, M., BHARTI, S., SHRIMALI, M. & DATTA, T. 2018. Assessment of proposed lateral load patterns in pushover analysis for base-isolated frames. *Engineering Structures,* 175**,** 531-548.

BIOT, M. A. 1941. A mechanical analyzer for the prediction of earthquake stresses. *Bulletin of the Seismological Society of America,* 31**,** 151-171.

BISKINIS, D. E. 2007. *Resistance and Deformation Capacity of Concrete Members with or without Retrofitting*. Doctoral Thesis, Civil Engineering Department, University of Patras, Patras, Greece.

BISKINIS, D. E. & FARDIS, M.N. 2004. *Cyclic Strength and Deformation Capacity of RC Members, Including Members Retrofitted for Earthquake Resistance.* 5th International Ph.D Symposium in Civil Engineering, Balkema, Rotterdam, pp. 1125-1133.

BISKINIS, D. E. & FARDIS, M.N. 2007. Effect of lap splices on flexural resistance and cyclic deformation capacity of RC members. *Beton- und Stahlbetonbau*, *102*(S1), pp. 51-59.

BOLT, B. A. 1999. *Earthquakes,* New York, NY : W.H. Freeman & Co.

BOLT, B. A. 2004. *Earthquakes,* New York, NY : W. H. Freeman & Co.

BOND, A.J., BROOKER, O., HARRIS, A.J., HARRISON, T., MOSS, R.M., NARAYANAN, R.S. and WEBSTER, R., 2006. *How to design concrete structures using Eurocode 2*. Concrete Centre.

BOOTH, E. 2018. *Beam Column Joints & Shear Walls.* [Lecture notes] Imperial College London, 5th March.

BRACCI, J. M., KUNNATH, S. K. & REINHORN, A. M. 1997. Seismic performance and retrofit evaluation of reinforced concrete structures. *Journal of structural engineering,* 123**,** 3-10.

BRAX, M., CORNOU, C., VOISIN, C. & BARD, P.-Y. 2014. Mapping the fundamental frequencies in the city of Beirut using ambient noise measurements. Second European Conference on Earthquake Engineering and Seismology (2ECEES).

BRAX, M., CAUSSE, M. & BARD, P.-Y. 2016. Ground motion prediction in Beirut: a multi-step procedure coupling empirical Green's functions, ground motion prediction equations and instrumental transfer functions. *Bulletin of Earthquake Engineering,* 14**,** 3317-3341.

BRAX, M., BARD, P.-Y., DUVAL, A.-M., BERTRAND, E., RAHHAL, M.-E., JOMAA, R., CORNOU, C., VOISIN, C. & SURSOCK, A. 2018. Towards a microzonation of the Greater Beirut area: an instrumental approach combining earthquake and ambient vibration recordings. *Bulletin of Earthquake Engineering,* 16**,** 5735-5767.

BRIAIS, A., SINGH, S., TAPPONNIER, P., ELIAS, A., SURSOCK, A., JOMAA, R., CARTON, H., DAËRON, M., KING, G. & JACQUES, E. 2004. Neogene and active shortening offshore the reactivated Levant margin in Lebanon: results of the SHALIMAR cruise. AGU Fall Meeting Abstracts.

BRODERICK, B., ELNASHAI, A., AMBRASEYS, N., BARR, J., GOODFELLOW, R. & HIGAZY, E. J. R. R. E.-. 1994. The Northridge (California) earthquake of 17 January 1994: observations, strong motion and correlative response analyses. Research Report, Imperial College London.

CAMPBELL, K. W. & BOZORGNIA, Y. 2004. Engineering Characterization of Ground Motion. Ch.5 in: *Earthquake Engineering: From Engineering Seismology to Performance-Based Engineering.* Ed. by Bertero, V.V. and Bozorgnia, Y. CRC Press, Boca Raton, FL, USA, pp. 5-1 – 5-74.

CARTON, H., SINGH, S., TAPPONNIER, P., ELIAS, A., BRIAIS, A., SURSOCK, A., JOMAA, R., KING, G., DAËRON, M. & JACQUES, E. 2009. Seismic evidence for Neogene and active shortening offshore of Lebanon (Shalimar cruise). *Journal of Geophysical Research: Solid Earth,* 114.

CBSC, 1995. California Building Standards Code. California Building Standards Commission and International Conference of Building Officials.

CEN, 2002. Eurocode: Basis of Structural Design. European Committee for Standardisation, Brussels, Belgium.

CEN, 2004a. Eurocode 8: Design of Structures for Earthquake Resistance—Part 1: General Rules, Seismic Actions and Rules for Buildings. European Committee for Standardisation, Brussels, Belgium.

CEN, 2004b. Eurocode 2: Design of Concrete Structures-Part 1–1: General Rules and Rules for Buildings. European Committee for Standardisation, Brussels, Belgium.

CEN, 2005a. Eurocode 8: Design of Structures for Earthquake Resistance—Part 3: Assessment and Retrofitting of Buildings. European Committee for Standardisation, Brussels, Belgium.

NAJA, A. K. 1995. *Dynamics of structures : theory and applications to earthquake engineering,* New Jersey, Prentice-Hall.

CHOPRA, A. K. 2005. *Earthquake dynamics of structures: A primer*, 2nd Ed. Earthquake Engineering Research Institute, Oakland, CA, USA, 129 p.

CHOPRA, A. K. 2014. *Dynamics of structures : theory and applications to earthquake engineering,* Boston, Pearson Education.

CHOPRA, A.K. and GOEL, R.K., 1999a. Capacity-demand-diagram methods based on inelastic design spectrum. *Earthquake spectra*, *15*(4), pp. 637-656.

CHOPRA, A.K. and GOEL, R.K., 1999b. Capacity-demand-diagram methods for estimating seismic deformation of inelastic structures: SDF systems. *Report No. PEER1999/02*.

CHOPRA, A. K. & GOEL, R. K. 2000. Evaluation of NSP to estimate seismic deformation: SDF systems. *Journal of Structural Engineering,* 126**,** 482-490.

CHOPRA, A. K. & GOEL, R. K. 2002. A modal pushover analysis procedure for estimating seismic demands for buildings. *Earthquake engineering & structural dynamics,* 31**,** 561-582.

COBURN, A. & SPENCE, R. 2002. *Earthquake Protection,* United Kingdom, John Wiley & Sons Ltd.

CORNELL, C. A. 1968. Engineering seismic risk analysis. *Bulletin of the seismological society of America,* 58**,** 1583-1606.

DAËRON, M., KLINGER, Y., TAPPONNIER, P., ELIAS, A., JACQUES, E. & SURSOCK, A. 2005. Sources of the large AD 1202 and 1759 Near East earthquakes. *Geology,* 33**,** 529-532.

DAËRON, M., KLINGER, Y., TAPPONNIER, P., ELIAS, A., JACQUES, E. & SURSOCK, A. 2007. 12,000-year-long record of 10 to 13 paleoearthquakes on the Yammouneh fault, Levant fault system, Lebanon. *Bulletin of the seismological society of America,* 97**,** 749-771.

DEIERLEIN, G. G., REINHORN, A. M. & WILLFORD, M. R. 2010. Nonlinear structural analysis for seismic design. *NEHRP seismic design technical brief,* 4**,** 1-36.

DI SARNO, L. 2013. Effects of multiple earthquakes on inelastic structural response. *Engineering Structures,* 56**,** 673-681.

DI SARNO, L. & ELNASHAI, A. S. 2002. Seismic retrofitting of steel and composite building structures. *Mid-America Earthquake Center* Civil and Environmental Engineering Department at University of Illinois at Urbana-Champain.

DOUDOUMIS, I. & DOUDOUMIS, N. 2017. Centres of rigidity in multi-storey asymmetric diaphragm systems for general lateral static loading. *Engineering Structures,* 150**,** 39-51.

DOWRICK, D. J. 1988. Earthquake resistant design.

EL-AMOURY, T. & GHOBARAH, A. 2005. Retrofit of RC Frames Using FRP Jacketing or Steel Bracing. *Journal of Seismology and Earthquake Engineering,* 7**,** 83-94.

ELIAS, A., TAPPONNIER, P., SINGH, S. C., KING, G. C., BRIAIS, A., DAËRON, M., CARTON, H., SURSOCK, A., JACQUES, E. & JOMAA, R. 2007. Active thrusting offshore Mount Lebanon: Source of the tsunamigenic AD 551 Beirut-Tripoli earthquake. *Geology,* 35**,** 755-758.

ELNASHAI, A. S. 1998. Earthquake Resistance of High Strength Reinforced Concrete Buildings. *Seismic Design Practice into the Next Century***,** 3-14.

ELNASHAI, A. S. 1999. The Kocaeli (Turkey) earthquake of 17 August 1999: Assessment of spectra and structural response analysis. Report, Imperial College London.

ELNASHAI, A. S. 2001. Advanced inelastic static (pushover) analysis for earthquake applications. *Structural engineering and mechanics,* 12**,** 51-70.

ELNASHAI, A. S. & DI SARNO, L. 2015. *Fundamentals of earthquake engineering: from source to fragility*, John Wiley & Sons.

ETABS, 2017. Version 17.0.1. Computers and Structures, Inc. https://www.csiamerica.com

EUROPEAN-MEDITERRANEAN SEISMOLOGICAL CENTRE, 2010. http://www.emsc-csem.org

FAJFAR, P. 2021. *The Story of the N2 Method*, International association for earthquake engineering.

FAJFAR, P. & FISCHINGER, M. 1988. N2-A method for non-linear seismic analysis of regular buildings. Proceedings of the ninth world conference in earthquake engineering, 111-116.

FAJFAR, P., KILAR, V., MARUSIC, D., PERUS, I. & MAGLIULO, G. 2005. The extension of the N2 method to asymmetric buildings. Proceedings of the 4th European workshop on the seismic behaviour of irregular and complex structures.

FARDIS, M. N. 2009. *Seismic design, assessment and retrofitting of concrete buildings: based on EN-Eurocode 8*, Springer.

FEMA, 1997. *NEHRP Guidelines for the Seismic Rehabilitation of Buildings*. Report No. 273, Federal Emergency Management Agency, Washington DC

FEMA, 2000. *Prestandard and Commentary for Seismic Rehabilitation of Buildings*. Report No. 356, Federal Emergency Management Agency, Washington DC

FREEMAN, S. 1975. The Capacity Spectrum Method as a tool for seismic design, Wiss, Janney, Elstner Associates. Inc.

FREEMAN, S.A. 1998. The Capacity Spectrum Method as a Tool for Seismic Design. *Proceedings of the 11th European Conference on Earthquake Engineering*, Paris, France.

FREEMAN, S.A., NICOLETTI, J.P. & TYRELL, J.V. 1975. Evaluations of Existing Buildings for Seismic Risk - A Case Study of Puget Sound Naval Shipyard, Bremerton, Washington. *Proceedings of U.S. National Conference on Earthquake Engineering*, Berkeley, U.S.A., pp. 113-122.

GOEL, R. K. & CHOPRA, A. K. 2001. Improved direct displacement-based design procedure for performance-based seismic design of structures. *Structures 2001: A Structural Engineering Odyssey.*

GOLTZ, J. D. 1994. The Northridge, California earthquake of January 17, 1994: General reconnaissance report. *Technical Report NCEER.* US National Center for Earthquake Engineering Research.

GOMEZ, F., MEGHRAOUI, M., DARKAL, A. N., HIJAZI, F., MOUTY, M., SULEIMAN, Y., SBEINATI, R., DARAWCHEH, R., AL-GHAZZI, R. & BARAZANGI, M. 2003. Holocene faulting and earthquake recurrence along the Serghaya branch of the Dead Sea fault system in Syria and Lebanon. *Geophysical Journal International,* 153**,** 658-674.

GRANT, D. 2018. *Principles of the design and detailing of RC moment frame structures.* [Lecture Notes] Imperial College London, 26th February.

GREENBERG, H.J. & PRAGER, W. 1949. On Limit Design of Beams and Frames. *Division of Applied Mathematics*, Technical Report, Brown University, Rhode Island, 18 p.

GUPTA, B. & KUNNATH, S. K. 2000. Adaptive spectra-based pushover procedure for seismic evaluation of structures. *Earthquake spectra,* 16**,** 367-391.

HARAJLI, M., TABET, C., SADEK, S., MABSOUT, M., MOUKADDAM, S. & ABO, M. 1994. Seismic Hazard Assessment of Lebanon, Zoning Maps, and Structural Seismic Design Regulations. *Submitted to the Directorate of Urbanism, Ministry of Public Works, Beirut, Lebanon,* 195.

HARRIES, K., RICLES, J., SAUSE, R., PESSIKI, S. & WALKUP, L. 1998. Seismic retrofit of non-ductile reinforced concrete building columns using FRPC jackets. Proc., 6th US national conference on earthquake engineering.

HORNE, M. R. 1950. FUNDAMENTAL PROPOSITIONS IN THE PLASTIC THEORY OF STRUCTURES. *Journal of the Institution of Civil Engineers,* 34**,** 174-177.

HORNE, M.R., 1971. *Plastic theory of structures*. Nelson, London, UK.

HOUSNER, G. W. 1959. Behavior of structures during earthquakes. *Journal of Engineering Mechanics,* 85**,** 109-130.

HUIJER, C., HARAJLI, M. & SADEK, S. 2016. Re-evaluation and updating of the seismic hazard of Lebanon. *Journal of Seismology,* 20**,** 233-250.

HUMAR, J. 1984. Design for seismic torsional forces. *Canadian Journal of Civil Engineering,* 11**,** 150-163.

HUTCHINSON, J. 2001. Shear coefficients for Timoshenko beam theory. *J. Appl. Mech.,* 68**,** 87-92.

ICBO, 1997. Uniform Building Code. International Conference of Building Officials, Whittier, CA, USA.

ICC, 2015. International Building Code. International Code Council, Falls Church, VA, USA.

ISTRUCTE, 2006. *Manual for the Design of Concrete Building Structures to Eurocode 2*, Institution of Structural Engineers, London, UK.

JAN, T. S., LIU, M. W. & KAO, Y. C. 2004. An upper-bound pushover analysis procedure for estimating the seismic demands of high-rise buildings. *Engineering structures,* 26**,** 117-128.

JEONG, G. D. & IWAN, W. D. 1988. The effect of earthquake duration on the damage of structures. *Earthquake Engineering and Structural Dynamics,* 16**,** 1201-1211.

KANAI, K. 1983. *Engineering seismology*, University of Tokyo Press, Tokyo, 251 p.

KHAIR, K., KARAKAISIS, G. F. & PAPADIMITRIOU, E. E. 2000. Seismic zonation of the Dead Sea transform fault area. *Ann. Geofis.,* 43**,** 61-79.

KIM, S. & D'AMORE, E. 1999. Push-over analysis procedure in earthquake engineering. *Earthquake Spectra,* 15**,** 417-434.

KLINGNER, R. & BERTERO, V. V. 1976. Infilled frames in earthquake-resistant construction. Earthquake Engineering Research Center, University of California, Berkeley, CA.

KOBATAKE, Y. 1998. A seismic retrofitting method for existing reinforced concrete structures using CFRP. *Advanced Composite Materials,* 7**,** 1-22.

KRAMER, S. L. 1996. *Geotechnical Earthquake Engineering,* New Jersey, Prentice-Hall.

KRAWINKLER, H. & NASSAR, A. A. 1992. Seismic design based on ductility and cumulative damage demand and capacities. *Nonlinear Seismic Analysis and Design of Reinforced Concrete Buildings*, 23-39.

KUSUMA, A. & ANWAR, N. 2010. Comparative Assessment of Enhanced Multi-mode Pushover Analysis Methods for Performance Based Design. IABSE Symposium: Large Structures and Infrastructures for Environmentally Constrained and Urbanised Areas, Venice, Italy.

LAWSON, R. S., VANCE, V. & KRAWINKLER, H. 1994. Nonlinear static pushover analysis — why, when and how?. Proceedings of the Fifth US National Conference on Earthquake Engineering, 283-292.

LESLIE, R. 2013. The pushover analysis, explained in its simplicity. National Conference (Recent Advances in Civil Engineering) RACE" 13 at SAINTGITS College of Engineering, Kottayam.

LEKKAS, E., ANDREADAKIS, E., ALEXOUDI, V., KAPOURANI, E. & KOSTAKI, I. 2011. The Mw= 9.0 Tohoku Japan earthquake (March 11, 2011) tsunami impact on structures and infrastructure. Environmental Geosciences and Engineering Survey for Territory Protection and Population Safety (EngeoPro) International conference, Moscow, 97-103.

LIBNOR, 2012. *Protection from earthquakes: general rules*. Report No. NL135, Lebanese Standards Institution, LIBNOR, Lebanon.

LIN, T. Y. 1951. Lateral force distribution in a concrete building story. *ACI Journal Proceedings*, Vol. 48, No. 12, 281-296.

LOUCA, L.A. 2020. *Ground Motions.* [Lecture Notes] Imperial College London, 16th March.

MANDER, J. B., PRIESTLEY, M. J. & PARK, R. 1988. Theoretical stress-strain model for confined concrete. *Journal of structural engineering,* 114, 1804-1826.

MANDER, J. B., NAIR, B., WOJTKOWSKI, K. & MA, J. 1993. An experimental study on the seismic performance of brick-infilled steel frames with and without retrofit. *Technical Report.* National Center for Earthquake Engineering Research (NCEER).

MAPLE, 2019. Maplesoft, a division of Waterloo Maple Inc., Waterloo, Ontario.

MILNE, W. 1969. Distribution of earthquake risk in Canada. *Bulletin of the Seismological Society of America,* 59, 729-754.

MIRANDA, E. & BERTERO, V. V. 1994. Evaluation of strength reduction factors for earthquake-resistant design. *Earthquake Spectra,* 10, 357-379.

MIRANDA, E. & AKKAR, S. 2002. Evaluation of approximate methods to estimate target displacements in nonlinear static procedures. Rep. PEER-2002/21; Proc., 4th US-Japan Workshop on Performance-Based Earthquake Engineering Methodology for Reinforced Concrete Building Structures, 75-86.

MOEHLE, J. P., HOOPER, J. D. & LUBKE, C. D. 2008. Seismic Design of Reinforced Concrete Special Moment Frames. *NEHRP Seismic Design Technical Brief.*

MURAD, Y. Z. 2015. *Analytical and numerical assessment of seismically vulnerable corner connections under bidirectional loading in RC framed structures.* Research Report, Imperial College London.

NAJAM, F. A. 2017. Nonlinear Static Analysis Procedures for Seismic Performance Evaluation of Existing Buildings–Evolution and Issues. International Congress and Exhibition" Sustainable Civil Infrastructures: Innovative Infrastructure Geotechnology". Springer, 180-198.

NEWMARK, N. M. & ROSENBLUETH, E. 1971. *Fundamentals of earthquake engineering,* Englewood Cliffs ; [Hemel Hempstead], Englewood Cliffs ; Hemel Hempstead : Prentice-Hall.

NEWMARK, N. M. & HALL, W. J. 1982. *Earthquake spectra and design,* Berkeley, Earthquake Engineering Research Institute.

OĞUZ, S. 2005. *Evaluation of pushover analysis procedures for frame structure.* Master Thesis, Middle East Technical University, Ankara, Turkey.

PANAGIOTAKOS, T. B. & FARDIS, M. N. 2001. Deformations of reinforced concrete members at yielding and ultimate. *Structural Journal,* 98**,** 135-148.

PAULAY, T. & PRIESTLEY, M.N., 1992. Seismic design of reinforced concrete and masonry buildings. J. Wiley, New York.

PENELIS, G. G. & PENELIS, G. G. 2014. *Concrete buildings in seismic regions*, CRC Press Boca Raton, FL, USA.

PETER, K. & BADOUX, M. 2000. Application of the capacity spectrum method to RC buildings with bearing walls. Proceedings of the 12th World Conference on Earthquake Engineering, Auckland, New Zealand.

PLASSARD, J. & KOGOJ, B. 1981. Seismicité du Liban. *Beirut, Conseil National de la Recherche Scientifique***,** 47.

POURSHA, M., KHOSHNOUDIAN, F. & MOGHADAM, A. 2009. A consecutive modal pushover procedure for estimating the seismic demands of tall buildings. *Engineering structures,* 31**,** 591-599.

PRIESTLEY, M. 1997. Displacement-based seismic assessment of reinforced concrete buildings. *Journal of earthquake engineering,* 1**,** 157-192.

REID, H. F. 1910. The mechanics of the earthquake. *The California Earthquake of April 18, 1906, Report of the State Earthquake Investigation Commission*.

REITER, L. 1990. *Earthquake hazard analysis : issues and insights,* New York, New York : Columbia University Press.

REQUENA, M. & AYALA, G. 2000. Evaluation of a simplified method for the determination of the nonlinear seismic response of RC frames. Proceedings of the twelfth world conference on earthquake engineering, Citeseer.

RODRIGUEZ, M. & PARK, R. 1991. Repair and strengthening of reinforced concrete buildings for seismic resistance. *Earthquake Spectra,* 7**,** 439-459.

SAKINO, K. & SUN, Y. 2000. Steel jacketing for improvement of column strength and ductility. *Proceedings of the 12th World Conference on Earthquake Engineering*, Auckland, New Zealand.

SALAMEH, C., GUILLIER, B., HARB, J., CORNOU, C., BARD, P.-Y., VOISIN, C. & MARISCAL, A. 2016. Seismic response of Beirut (Lebanon) buildings: instrumental results from ambient vibrations. *Bulletin of Earthquake Engineering,* 14**,** 2705-2730.

SASAKI, K.K., FREEMAN, S.A. & PARET, T.F. 1998. Multi-Mode Pushover Procedure (MMP) — A Method to Identify the Effects of Higher Modes in a Pushover Analysis. *Proceedings of 6th US National Conference on Earthquake Engineering*, Seattle, Washington, U.S.A., Paper No. 271.

SCHOLZ, C. H. 1990. *The mechanics of earthquakes and faulting,* Cambridge University Press, 439 p.

SCHOLZ, C. H. 2002. *The mechanics of earthquakes and faulting*, 2nd Ed., Cambridge University Press, 496 p.

SOLOMOS, G. 1979. *Considerations in the Statistical Description of Seismicity for Structural Design*. Master of Engineering Science Thesis, The University of Western Ontario, London, Canada.

SOLOMOS, G., PINTO, A. & DIMOVA, S. 2008. A review of the seismic hazard zonation in national building codes in the context of Eurocode 8. *JRC Scientific and Technical reports*.

SUN, Z. L., SEIBLE, F. & PRIESTLEY, M. J. N. 1993. Flexural Retrofit of Rectangular Reinforced Concrete Bridge Columns by Steel Jacketing. *Structural System Research Project Report.* Department of Applied Mechanics and Engineering Science, U.C. San Diego.

TIMOSHENKO, S. & GERE, J. 1972. Mechanics of materials. Van Nordstrand Reinhold Company, New York, USA.

TSAI, K. C. & LIN, M. L. 2001. Steel Jacket Retrofitting of Rectangular RC Bridge Columns to Prevent Lap-spliced and Shear Failure. Technical Report, National Center for Research on Earthquake Engineering.

TSAI, K. C. & LIN, M. L. 2002. Seismic jacketing of RC columns for enhanced axial load carrying performance. *Journal of the Chinese Institute of Engineers,* 25**,** 389-402.

VELETSOS, A. & NEWMARK, N. M. 1960. Effect of inelastic behavior on the response of simple systems to earthquake motions. *Proceedings of the 2nd World Conference on Earthquake Engineering*, Tokyo, Japan, pp. 895-912.

VIDIC, T., FAJFAR, P. & FISCHINGER, M. 1994. Consistent inelastic design spectra: strength and displacement. *Earthquake Engineering and Structural Dynamics,* 23**,** 507-521.

VIJAYAKUMAR, A. & BABU, V. D. 2011. A survey of methods and techniques used for Seismic retrofitting of RC buildings. *International Journal of Civil and Structural Engineering,* Vol. 2**,** No. 1, 56 p.

ZAMEERUDDIN, M. & SANGLE, K. K. 2016. Review on Recent developments in the performance-based seismic design of reinforced concrete structures. *Structures,* 6**,** 119-133.

ZAMFIRESCU, D. & FAJFAR, P. 2001. Comparison of simplified procedures for nonlinear seismic analysis of structures. Proceedings of the 3rd US Japan Workshop on Performance-Based Earthquake Engineering Methodology for Reinforced Concrete Buildings.

Appendices

Appendix 2

Curvature Ductility Factor

According to EC8-1 (CEN, 2004a), primary seismic elements are designed to develop a sufficient curvature ductility that ensure the formation of plastic hinges at critical locations in order to achieve the required overall ductility of the structure. This condition is deemed to be satisfied if the curvature ductility factor, which is the ratio of the post-ultimate curvature (at 85% of the moment resistance) to the yield curvature, is equal to the following value:

$$\mu_\varphi = 2q_0 - 1 \qquad if\ T_1 \geq T_C \tag{A2.1}$$

$$\mu_\varphi = 1 + 2(q_0 - 1)T_C / T_1 \qquad if\ T_1 < T_C \tag{A2.2}$$

where:

q_0 is the basic value of the behaviour factor which is determined on the basis of the structural type of building. The frame buildings targeted by this research rely on shear walls for resisting the seismic load and are accordingly considered as uncoupled wall system. In view of this, the recommended value of q_0 is 3.0 for DCM walls (CEN, 2004a),

T_1 is the fundamental period of the building in the direction of bending, and

T_C is the upper limit of the period of the constant acceleration region of the spectrum. EC8-1 (CEN, 2004a) recommends specific values for different types of response spectra and for different soil profile types. For a Type 2 spectrum ($M_S > 5.5$) and for a Type C soil profile, a value of 0.25 sec is recommended for T_C as per Table 3.3 in EC8-1 (CEN, 2004a).

Appendix 3

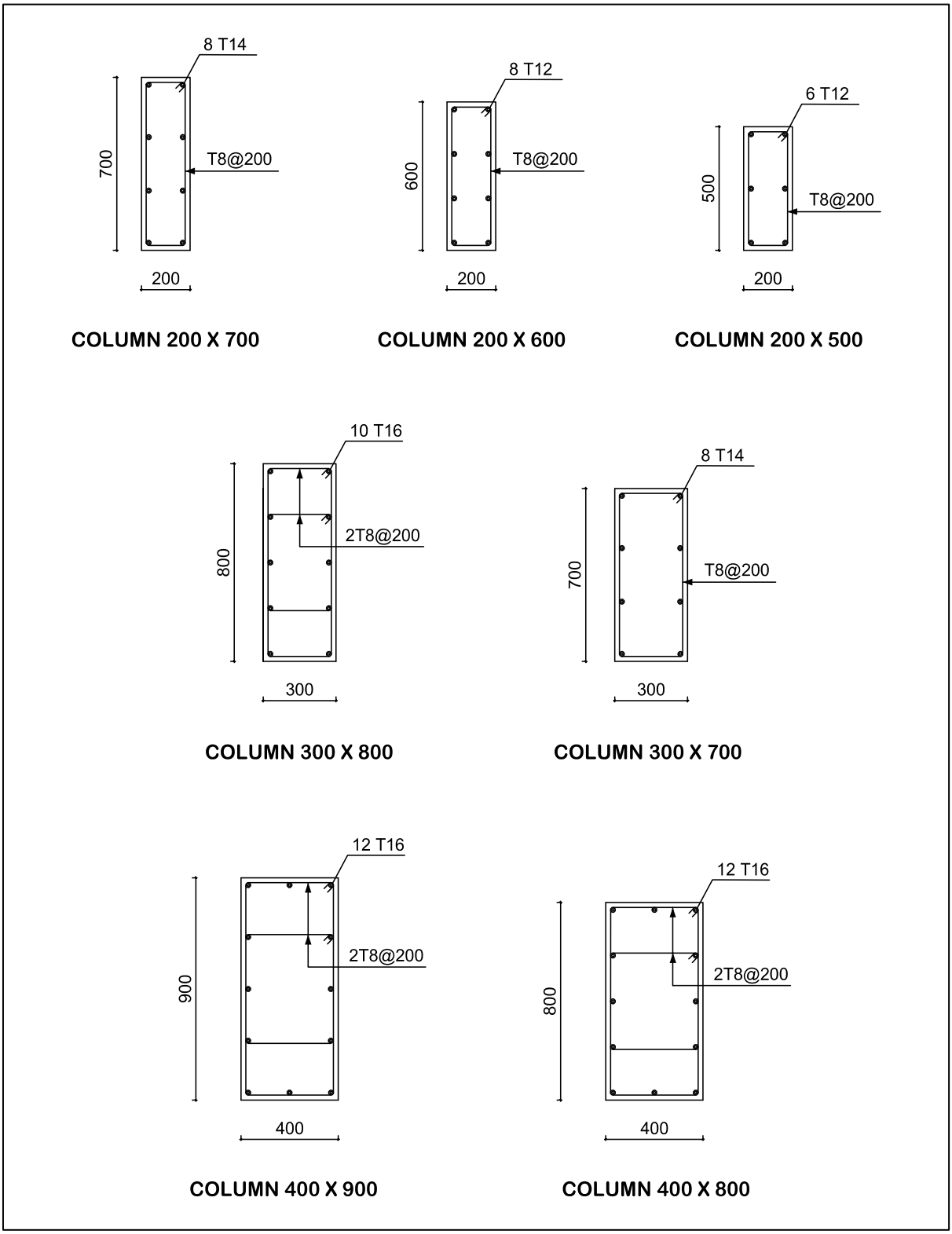


Figure A3. 1: Detailing of longitudinal and transversal reinforcement in the columns cross-sections

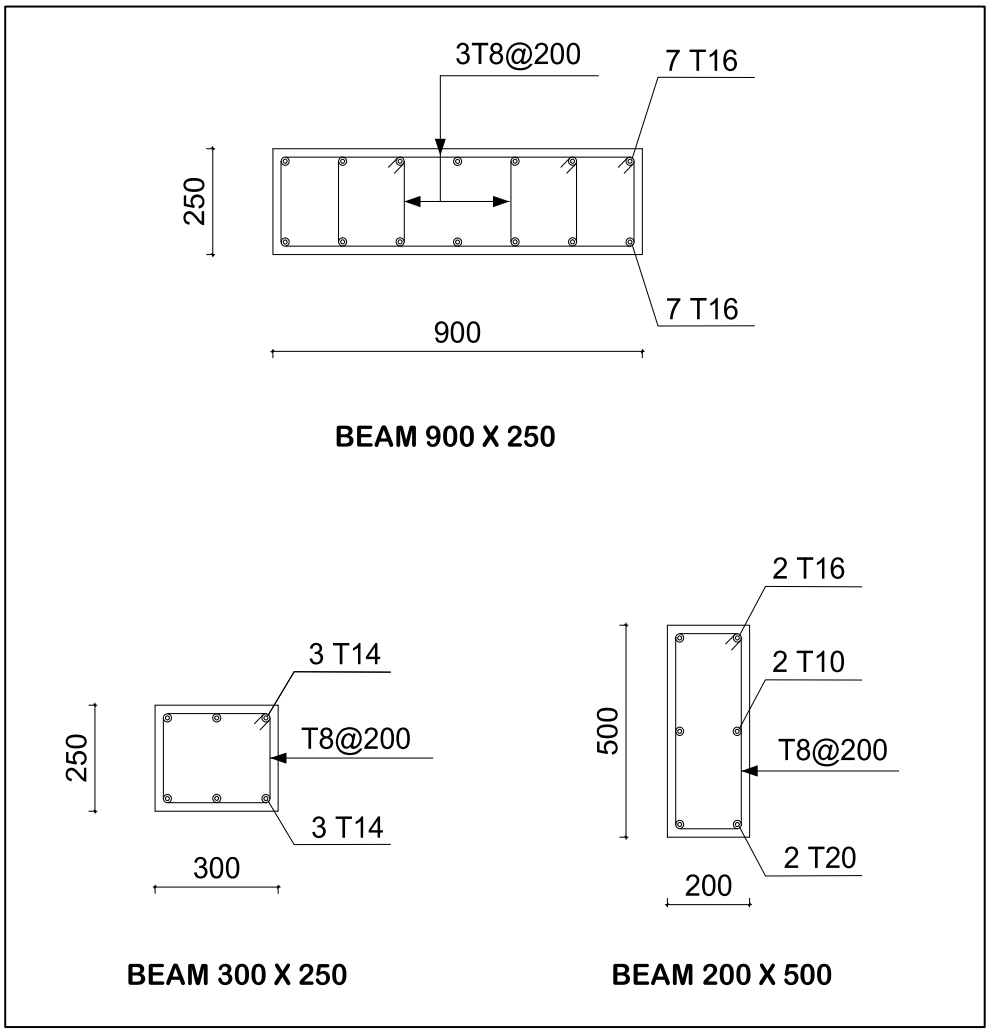


Figure A3. 2: Detailing of longitudinal and transversal reinforcement in the beams cross-sections

Conditions			Modeling Parameters[a]			Acceptance Criteria[a]		
			Plastic Rotation Angle (radians)		Residual Strength Ratio	Plastic Rotation Angle (radians)		
						Performance Level		
			a	*b*	*c*	IO	LS	CP
Condition i. Beams controlled by flexure[b]								
$\frac{\rho-\rho'}{\rho_{bal}}$	Transverse reinforcement[c]	$\frac{V^d}{b_w d\sqrt{f'_{cE}}}$						
≤0.0	C	≤3 (0.25)	0.025	0.05	0.2	0.010	0.025	0.05
≤0.0	C	≥6 (0.5)	0.02	0.04	0.2	0.005	0.02	0.04
≥0.5	C	≤3 (0.25)	0.02	0.03	0.2	0.005	0.02	0.03
≥0.5	C	≥6 (0.5)	0.015	0.02	0.2	0.005	0.015	0.02
≤0.0	NC	≤3 (0.25)	0.02	0.03	0.2	0.005	0.02	0.03
≤0.0	NC	≥6 (0.5)	0.01	0.015	0.2	0.0015	0.01	0.015
≥0.5	NC	≤3 (0.25)	0.01	0.015	0.2	0.005	0.01	0.015
≥0.5	NC	≥6 (0.5)	0.005	0.01	0.2	0.0015	0.005	0.01
Condition ii. Beams controlled by shear[b]								
Stirrup spacing ≤ *d*/2			0.0030	0.02	0.2	0.0015	0.01	0.02
Stirrup spacing > *d*/2			0.0030	0.01	0.2	0.0015	0.005	0.01
Condition iii. Beams controlled by inadequate development or splicing along the span[b]								
Stirrup spacing ≤ *d*/2			0.0030	0.02	0.0	0.0015	0.01	0.02
Stirrup spacing > *d*/2			0.0030	0.01	0.0	0.0015	0.005	0.01
Condition iv. Beams controlled by inadequate embedment into beam–column joint[b]			0.015	0.03	0.2	0.01	0.02	0.03

Note: f'_{cE} in lb/in.^{2} (MPa) units.
[a] Values between those listed in the table should be determined by linear interpolation.
[b] Where more than one of conditions i, ii, iii, and iv occur for a given component, use the minimum appropriate numerical value from the table.
[c] "C" and "NC" are abbreviations for conforming and nonconforming transverse reinforcement, respectively. Transverse reinforcement is conforming if, within the flexural plastic hinge region, hoops are spaced at ≤ *d*/3, and if, for components of moderate and high ductility demand, the strength provided by the hoops (V_s) is at least 3/4 of the design shear. Otherwise, the transverse reinforcement is considered nonconforming.
[d] *V* is the design shear force from NSP or NDP.

Figure A3. 3: Modelling parameters and acceptance criteria for RC beams (ASCE, 2017)

Modeling Parameters	Acceptance Criteria		
	Plastic Rotation Angle (radians)		
	Performance Level		
Plastic Rotation Angles, *a* and *b* (radians) Residual Strength Ratio, *c*	IO	LS	CP
Columns not controlled by inadequate development or splicing along the clear height[a]			
$a = \left(0.042 - 0.043\frac{N_{UD}}{A_g f'_{cE}} + 0.63\rho_t - 0.023\frac{V_{yE}}{V_{ColOE}}\right) \geq 0.0$	0.15 *a* ≤ 0.005	0.5 *b*[b]	0.7 *b*[b]
For $\frac{N_{UD}}{A_g f'_{cE}} \leq 0.5$ $\left\{ b = \frac{0.5}{5 + \frac{N_{UD}}{0.8 A_g f'_{cE}} \frac{1}{\rho_t} \frac{f'_{cE}}{f_{ytE}}} - 0.01 \geq a \right.$[a]			
$c = 0.24 - 0.4\frac{N_{UD}}{A_g f'_{cE}} \geq 0.0$			
Columns controlled by inadequate development or splicing along the clear height[c]			
$a = \left(\frac{1}{8}\frac{\rho_t f_{ytE}}{\rho_l f_{ylE}}\right) \begin{matrix} \geq 0.0 \\ \leq 0.025^d \end{matrix}$	0.0	0.5 *b*	0.7 *b*
$b = \left(0.012 - 0.085\frac{N_{UD}}{A_g f'_{cE}} + 12\rho_t{}^e\right) \begin{matrix} \geq 0.0 \\ \geq a \\ \leq 0.06 \end{matrix}$			
$c = 0.15 + 36\rho_t \leq 0.4$			

Notes: ρ_t shall not be taken as greater than 0.0175 in any case nor greater than 0.0075 when ties are not adequately anchored in the core. Equations in the table are not valid for columns with ρ_t smaller than 0.0005.

V_{yE}/V_{ColOE} shall not be taken as less than 0.2.

N_{UD} shall be the maximum compressive axial load accounting for the effects of lateral forces as described in Eq. (7-34). Alternatively, it shall be permitted to evaluate N_{UD} based on a limit-state analysis.

[a] *b* shall be reduced linearly for $N_{UD}/(A_g f'_{cE}) > 0.5$ from its value at $N_{UD}/(A_g f'_{cE}) = 0.5$ to zero at $N_{UD}/(A_g f'_{cE}) = 0.7$ but shall not be smaller than *a*.

[b] $N_{UD}/(A_g f'_{cE})$ shall not be taken as smaller than 0.1.

[c] Columns are considered to be controlled by inadequate development or splices where the calculated steel stress at the splice exceeds the steel stress specified by Eq. (10-1a) or (10-1b). Modeling parameter for columns controlled by inadequate development or splicing shall never exceed those of columns not controlled by inadequate development or splicing.

[d] *a* for columns controlled by inadequate development or splicing shall be taken as zero if the splice region is not crossed by at least two tie groups over its length.

[e] ρ_t shall not be taken as greater than 0.0075.

Figure A3. 4: Modelling parameters and acceptance criteria for RC rectangular columns (ASCE, 2017)

Appendix 4

Modal Mass Participation Factor

Noting that the application of the CSM in this research requires a significant mass participation of the fundamental mode in the translational direction, it is necessary to illustrate the procedure implemented to calculate the mass participation factor of the modes of vibration of a given MDOF system.

Denoting the ground displacement in a given direction by u_g, the total displacement of the jth degree of freedom (DOF) at a given floor is given by the sum of the relative displacement with respect to the ground in addition to the ground displacement:

$$u_j^t = u_j + u_g \tag{A4.1}$$

where:

u_j is the relative displacement of the mass at the jth degree of freedom with respect to the ground,

u_j^t is the total displacement of the mass at the jth degree of freedom, and

u_g is the applied ground displacement.

Considering the displacements of all the DOFs in a MDOF system, the previous expression can be written in vector form:

$$\{u^t\} = \{u\} + \{u_g\} \tag{A4.2}$$

$$\{u^t\} = \{u\} + \{i\}u_g \tag{A4.3}$$

where:

$\{i\}$ is an influence vector that represents the displacements of the masses at all the DOFs when the building is subjected to a ground displacement (u_g = 1) in the direction being considered.

By rearranging the equation of motion of a MDOF system having N degrees of freedom and subjected to a ground motion u_g, the ground motion is interpreted as a series of equivalent dynamic forces applied at the DOFs when the base is fixed as per the following (Chopra, 2014):

$$[m]\{\ddot{u}^t\} + [c]\{\dot{u}\} + [k]\{u\} = \{0\} \tag{A4.4}$$

$$[m]\left(\{\ddot{u}\} + \{i\}\ddot{u}_g\right) + [c]\{\dot{u}\} + [k]\{u\} = \{0\} \tag{A4.5}$$

$$[m]\{\ddot{u}\} + [c]\{\dot{u}\} + [k]\{u\} = -[m]\{i\}\ddot{u}_g \tag{A4.6}$$

$$[m]\{\ddot{u}\} + [c]\{\dot{u}\} + [k]\{u\} = -\{s\}\ddot{u}_g \tag{A4.7}$$

where:

$\{s\}$ is referred to as the spatial distribution of the effective earthquake mass, $\{s\}=[m]\{i\}$.

Writing the previous equation in terms of the modal coordinates and multiplying by the transpose of the modal matrix leads to the following:

$$\{u\} = [\phi]\{q\} \tag{A4.8}$$

$$[\phi]^T [m][\phi]\{\ddot{q}\} + [\phi]^T [c] [\phi]\{\dot{q}\} + [\phi]^T [k][\phi]\{q\} = -[\phi]^T [m]\{i\}\ddot{u}_g \tag{A4.9}$$

$$[M]\{\ddot{q}\} + [C]\{\dot{q}\} + [K]\{q\} = -[\phi]^T [m]\{i\}\ddot{u}_g \tag{A4.10}$$

where:

$\{q\}$ is the vector of the modal coordinates,

$[\phi]$ is the modal matrix which assembles all the modal vectors,

$$[\phi] = [\{\varphi_1\}\ \{\varphi_2\}.....\{\varphi_N\}]$$

$[M],[C],[K]$ are the modal mass, damping, and stiffness matrices respectively.

The modal mass and stiffness matrices are diagonal matrices owing to the orthogonality of the natural modes of vibration, and for simplicity the modal damping matrix [C] is also assumed to be diagonal along with [M] and [K]. Consequently, the equation of motion (in modal form) of the system can be decomposed into *N* independent equations, each one corresponding to an independent SDOF system. The equation of motion of the nth mode of vibration can be expressed as:

$$M_n\ddot{q}_n + C_n\dot{q}_n + K_n q_n = -\{\varphi_n\}^T [m]\{i\}\ddot{u}_g \tag{A4.11}$$

$$\ddot{q}_n + 2\xi_n\omega_n\dot{q}_n + \omega_n^2 q_n = \frac{-\{\varphi_n\}^T [m]\{i\}\ddot{u}_g}{M_n} \tag{A4.12}$$

$$\ddot{q}_n + 2\xi_n\omega_n\dot{q}_n + \omega_n^2 q_n = -\Gamma_n\ddot{u}_g \tag{A4.13}$$

$$M_n = \{\varphi_n\}^T [m]\{\varphi_n\} \tag{A4.14}$$

$$\Gamma_n = \frac{L_n}{M_n} \tag{A4.15}$$

$$\alpha_n = \Gamma_n \ddot{u}_g \tag{A4.16}$$

where:

M_n, C_n, K_n are the modal mass, damping, and stiffness of the nth mode respectively,

Γ_n is referred to as the modal participation factor or the mass participation factor (Chopra, 2014),

α_n is the modal acceleration associated with the nth mode,

ξ_n is the damping ratio associated with the nth mode,

$$C_n = 2\xi_n M_n \omega_n$$

ω_n is the natural circular frequency of vibration of the nth mode.

$$\omega_n^2 = \frac{K_n}{M_n}$$

The mass participation factor Γ_n represents the ratio of the mass participating in the forcing function to the mass participating in the inertia effects. However, it cannot be used to compare the contribution of different modes to the overall response because it depends on the process by which the modes are normalised. In this regard, the numerator L_n contains $\{\varphi_n\}^T$ while the denominator M_n contains $\{\varphi_n\}^T$ and $\{\varphi_n\}$. Hence, normalising the eigenvector by multiplying by a factor k will result in a net multiplication of the mass participation factor by the factor $(1/k)$. Therefore, the current expression of the mass participation factor needs to be modified to make it impervious to the normalisation of individual modes, such that it becomes reliable for comparing the contribution of the modes. The process is addressed in the following discussion.

Noting that the modal matrix is non-singular, the influence vector can be written as an expansion of the linear independent eigenvectors (Louca, 2020):

$$\{i\} = a_1\{\varphi_1\} + a_2\{\varphi_2\} + \ldots\ldots + a_N\{\varphi_N\} = \sum_{r=1}^{N} a_r\{\varphi_r\} \tag{A4.17}$$

$$L_n = \Gamma_n M_n \tag{A4.18}$$

$$\{\varphi_n\}^T [m]\{i\} = \Gamma_n \{\varphi_n\}^T [m]\{\varphi_n\} \tag{A4.19}$$

$$\{\varphi_n\}^T [m]\{i\} - \Gamma_n \{\varphi_n\}^T [m]\{\varphi_n\} = 0 \tag{A4.20}$$

$$\sum_{r=1}^{N}\left(a_r \{\varphi_n\}^T [m]\{\varphi_r\}\right) - \Gamma_n \{\varphi_n\}^T [m]\{\varphi_n\} = 0 \tag{A4.21}$$

By virtue of orthogonality of the modes:

$$\{\varphi_n\}^T [m]\{\varphi_r\} = 0 \ for \ r \neq n \xrightarrow{Then} \tag{A4.22}$$

$$a_n \{\varphi_n\}^T [m]\{\varphi_n\} - \Gamma_n \{\varphi_n\}^T [m]\{\varphi_n\} = 0 \tag{A4.23}$$

$$(a_n - \Gamma_n)\{\varphi_n\}^T [m]\{\varphi_n\} = 0 \tag{A4.24}$$

$$M_n = \{\varphi_n\}^T [m]\{\varphi_n\} \neq 0 \ for \ \{\varphi_n\} \neq \{0\} \xrightarrow{Then} \tag{A4.25}$$

$$a_n - \Gamma_n = 0 \ or \ a_n = \Gamma_n \tag{A4.26}$$

Hence, the influence vector reduces to the following simplified expression:

$$\{i\} = \sum_{n=1}^{N} \Gamma_n \{\varphi_n\} \tag{A4.27}$$

$$\{s\} = [m]\{i\} = \sum_{n=1}^{N} \Gamma_n [m]\{\varphi_n\} = \Gamma_1 [m]\{\varphi_1\} + \Gamma_2 [m]\{\varphi_2\} + ... + \Gamma_N [m]\{\varphi_N\} \tag{A4.28}$$

$$\{s_n\} = \Gamma_n [m]\{\varphi_n\} \tag{A4.29}$$

$$\{s_n\} = \frac{\{\varphi_n\}^T [m]\{i\}}{\{\varphi_n\}^T [m]\{\varphi_n\}} [m]\{\varphi_n\} \tag{A4.30}$$

To conclude, the latest expression of the spatial distribution of mass is unaffected by the normalisation of the mode and is accordingly reliable to assess the contribution of each mode into the overall structural response. Hence, the contribution of the nth mode into the overall response is given by the spatial distribution of the effective earthquake mass of the nth mode, which explicitly shows that both $\{\varphi_n\}^T$ and $\{\varphi_n\}$ appear in the numerator and in the denominator, which makes $\{s_n\}$ independent of the normalisation of the eigenvectors.

It is important to underline the concept of the influence vector in the context of a multi-storey building which is analysed using three DOFs (two translational and one rotational) at each storey level. In this regard, the influence vector $\{i\}$ references the acceleration that is applied in each direction. In order to get the mass participating in the X-direction, an acceleration in the X-direction is applied and is manifested by an influence vector $\{ix\}$ having a unit value at all the DOFs in the X-direction and zero at the DOFs aligned in the Y- and RZ-directions. Similarly, an influence vector having a unit value at the DOFs aligned in the Y-direction and zeros elsewhere is used to calculate the mass participating in the Y-direction. The same analogy is followed by using an influence vector $\{irz\}$ with unit values at the rotational DOFs (RZ-direction) and zeros elsewhere is used to determine the mass participating in the rotational direction RZ.

Last, the mass participation of the n[th] mode in a predefined direction (determined by predefining the influence vector as described in the preceding paragraph) is calculated as the sum of the components of $\{s_n\}$ divided by the sum of the masses at all floors:

$$MP_n = \left(\frac{\sum s_{jn}}{\sum m_j} \right) 100 \tag{A4.31}$$

where:

MP_n is the percentage mass participation of the n[th] mode in the direction under consideration,

s_{jn} is the participating mass of the j[th] floor in the n[th] mode (in the direction under consideration), and it is obtained from the vector $\{s_n\}$,

m_j is the total floor mass at level *j*.

Regularity of Buildings

According to EC8-1 (CEN, 2004a), all of the following conditions must be met in order for the building to be deemed regular in plan:

(i) In terms of lateral stiffness and mass distribution, the building must be approximately plan-symmetric in two orthogonal directions.

(ii) In case planar setbacks exist, the building would still be classified as regular if the area between the outline of the floorplan and a convex polygonal line that envelops the floorplan does not exceed 5% of the floor area.

(iii) The in-plan stiffness must be significantly large to ensure that the floor is deforming as a rigid diaphragm that does not interfere with the transfer of loads to the lateral-load resisting system.

(iv) The slenderness ratio, defined as the length of the longer plan dimension to the shorter one, must not exceed the limit of 4.0, noting that the aforementioned dimensions must be orthogonal to each other.

(v) The floor eccentricity and torsional radius must satisfy the following conditions at all storey levels and in both horizontal directions:

$$e_o \leq 0.30\, r_o$$

$$r_o \geq l_s$$

where:

e_o is the eccentricity between the centre of mass and the centre of stiffness and is perpendicular to the direction under consideration,

r_o is the torsional radius which is equal to the square root of the torsional stiffness to the lateral stiffness in the direction considered, and

l_s is the radius of gyration of the floor mass which is equal to the square root of the polar moment of inertia (with respect to the centre of mass) divided by the floor mass.

(vi) Components of the lateral load resisting system, including core walls, shear walls, and spatial frames extend all the way from the foundation to the top of the building.

(vii) Individual systems must have a similar deflected shape in response to the applied lateral load.

Concerning regularity in elevation, the building is classified as regular if all of the following conditions are satisfied (CEN, 2004a):

(i) Components of the lateral load resisting system, including core walls, shear walls, and spatial frames must extend all the way from the foundation to the top of the building or to the top floor under consideration if setbacks exist at upper storeys.

(ii) Only gradual and mild decline in the lateral stiffness or mass is allowed between consecutive storeys.

(iii) The ratio of the actual resistance to that required by analysis must not vary significantly between adjacent storeys.

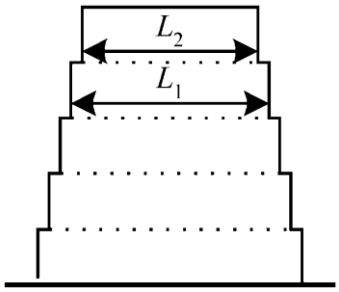
(iv) The following conditions must be met in the presence of setbacks:

(a) If axial symmetry is preserved, gradual setback between adjacent floors must not exceed 20% of the lower floor dimension measured in the direction of the setback (Figures A4.1a and A4.1b).

(b) For a single setback occurring in the lower 15% of the height of the building, the length of setback must not exceed 50% of the previous plan dimension (Figure A4.1c).

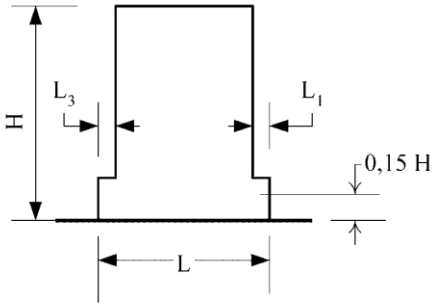
(c) In case setbacks are not symmetric, regularity is preserved if the setback between adjacent floors is less than 10% of the lower floor dimension, and if the setback at all storeys is not greater than 30% of the ground floor dimension in the direction of the setback (Figure A4.1d).

(a)



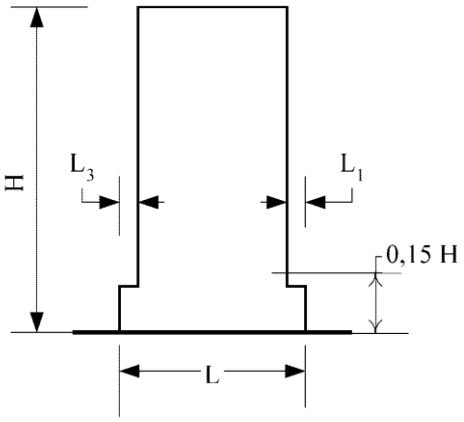
Criterion for (a): $\frac{L_1 - L_2}{L_1} \leq 0{,}20$

(b) (setback occurs above 0,15H)



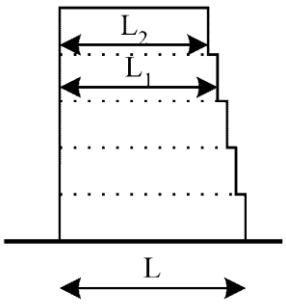
Criterion for (b): $\frac{L_3 + L_1}{L} \leq 0{,}20$

(c) (setback occurs below 0,15H)



Criterion for (c): $\frac{L_3 + L_1}{L} \leq 0{,}50$

d)



Criteria for (d): $\frac{L - L_2}{L} \leq 0{,}30$

$\frac{L_1 - L_2}{L_1} \leq 0{,}10$

Figure A4. 1: Criteria for regularity of buildings in elevation in the presence of setbacks (CEN, 2004a)

Appendix 7

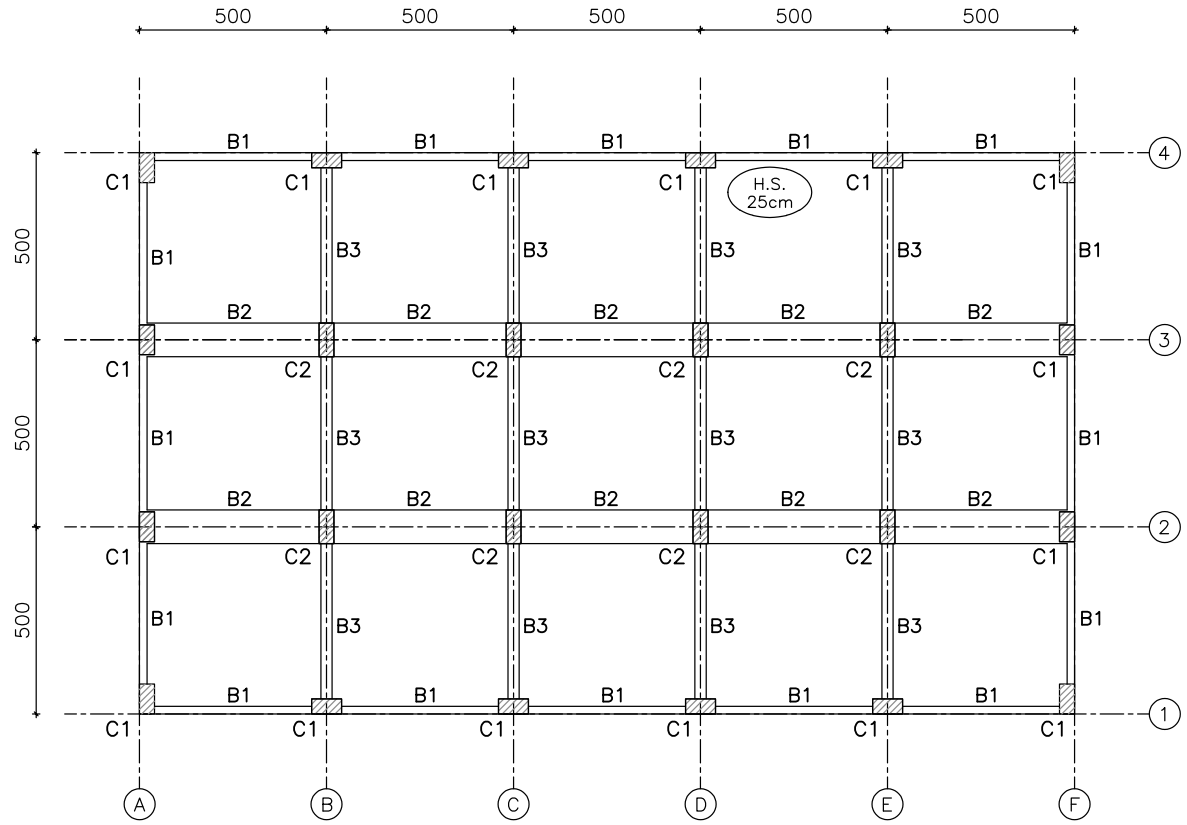


Figure A7. 1: General layout of rectangular building (Dimensions in cm)

Table A7. 1: Typical dimensions of beams in the rectangular building (dimensions in mm)

	Storey 1	Storey 2	Storey 3	Storey 4	Storey 5	Storey 6	Storey 7	Storey 8	Storey 9	Storey 10
B1	200x500	200x500	200x500	200x500	200x500	200x500	200x500	200x500	200x500	200x500
B2	900x250	900x250	900x250	900x250	900x250	900x250	900x250	900x250	900x250	900x250
B3	300x250	300x250	300x250	300x250	300x250	300x250	300x250	300x250	300x250	300x250

Table A7. 2: Typical dimensions of columns in the rectangular building (dimensions in mm)

	Storey 1	Storey 2	Storey 3	Storey 4	Storey 5	Storey 6	Storey 7	Storey 8	Storey 9	Storey 10
C1	400x800	300x700	300x700	200x700	200x700	200x600	200x600	200x600	200x500	200x500
C2	400x900	300x800	300x800	300x700	300x700	300x700	200x600	200x600	200x600	200x600

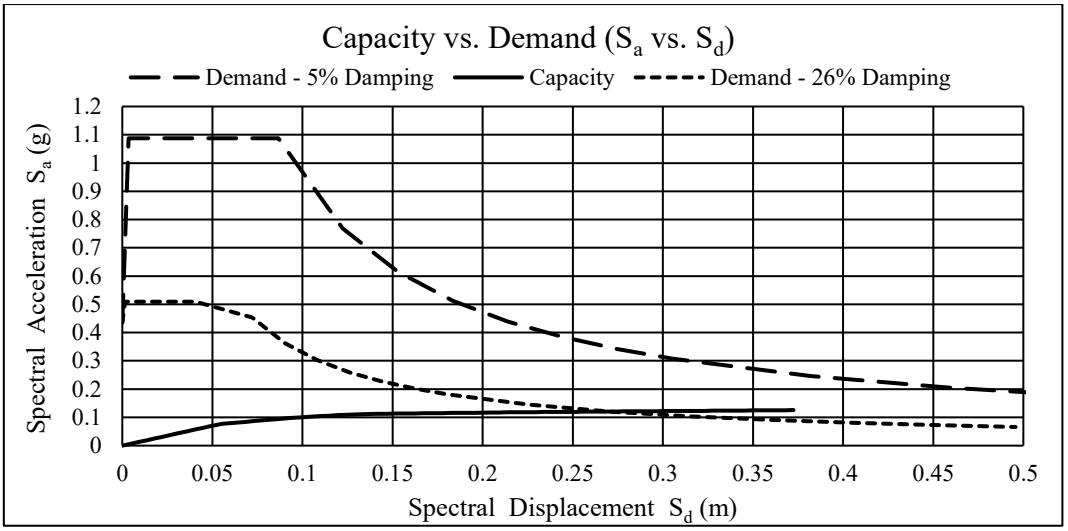


Figure A7. 2: Performance point of the Push-Y analysis (Mode 1) at the NC limit state in the rectangular building scenario

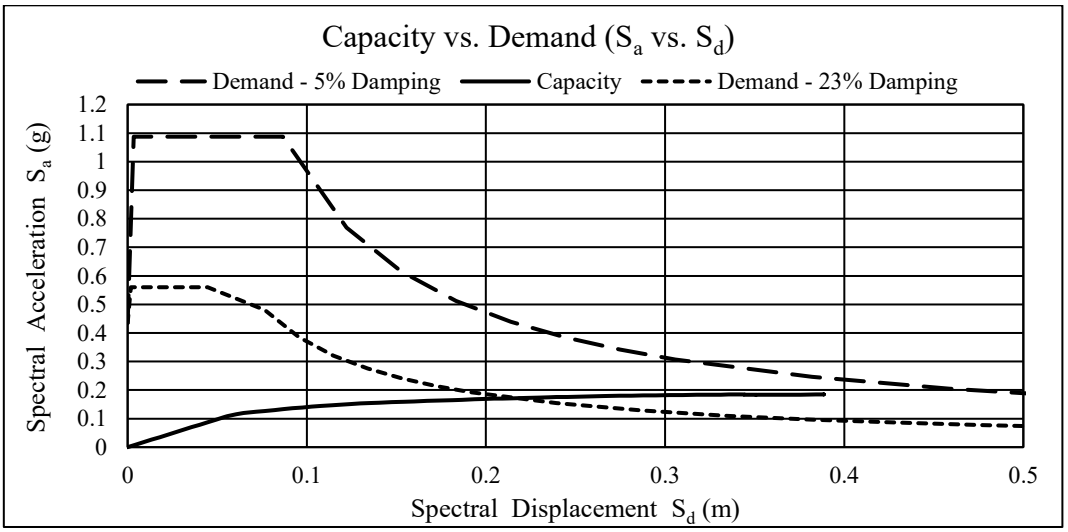


Figure A7. 3: Performance point of the Push-X analysis (Mode 2) at the NC limit state in the rectangular building scenario

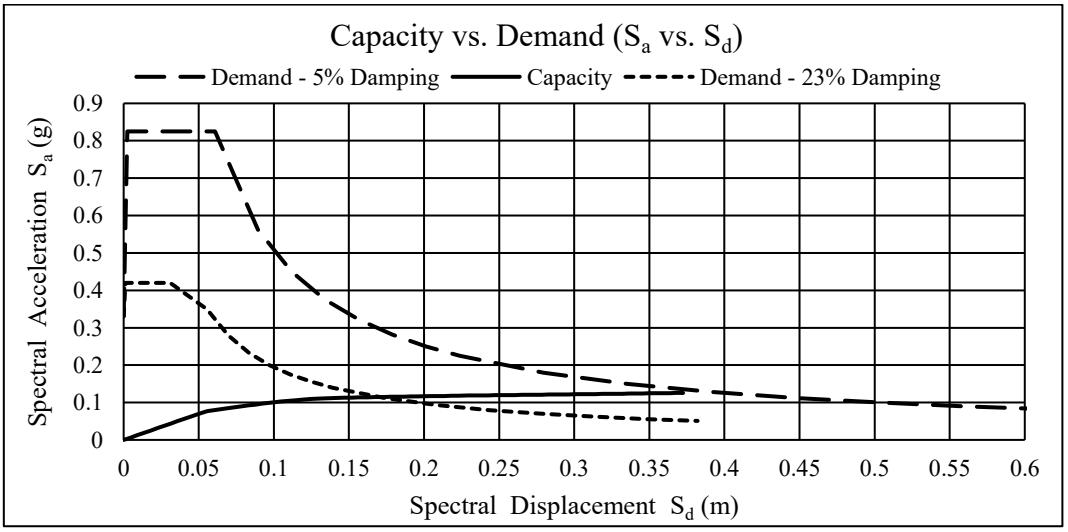


Figure A7. 4: Performance point of the Push-Y analysis (Mode 1) at the SD limit state in the rectangular building scenario

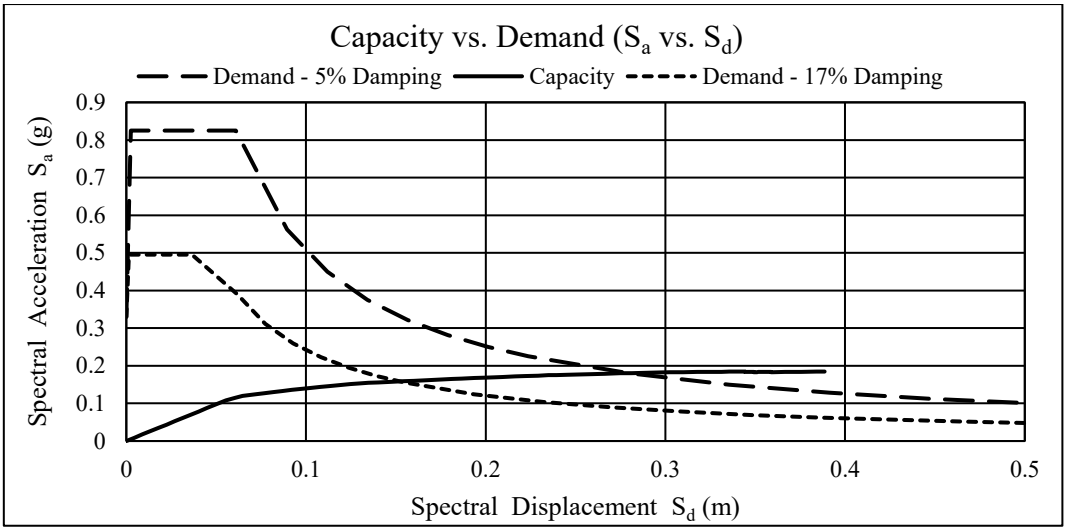


Figure A7. 5: Performance point of the Push-X analysis (Mode 2) at the SD limit state in the rectangular building scenario

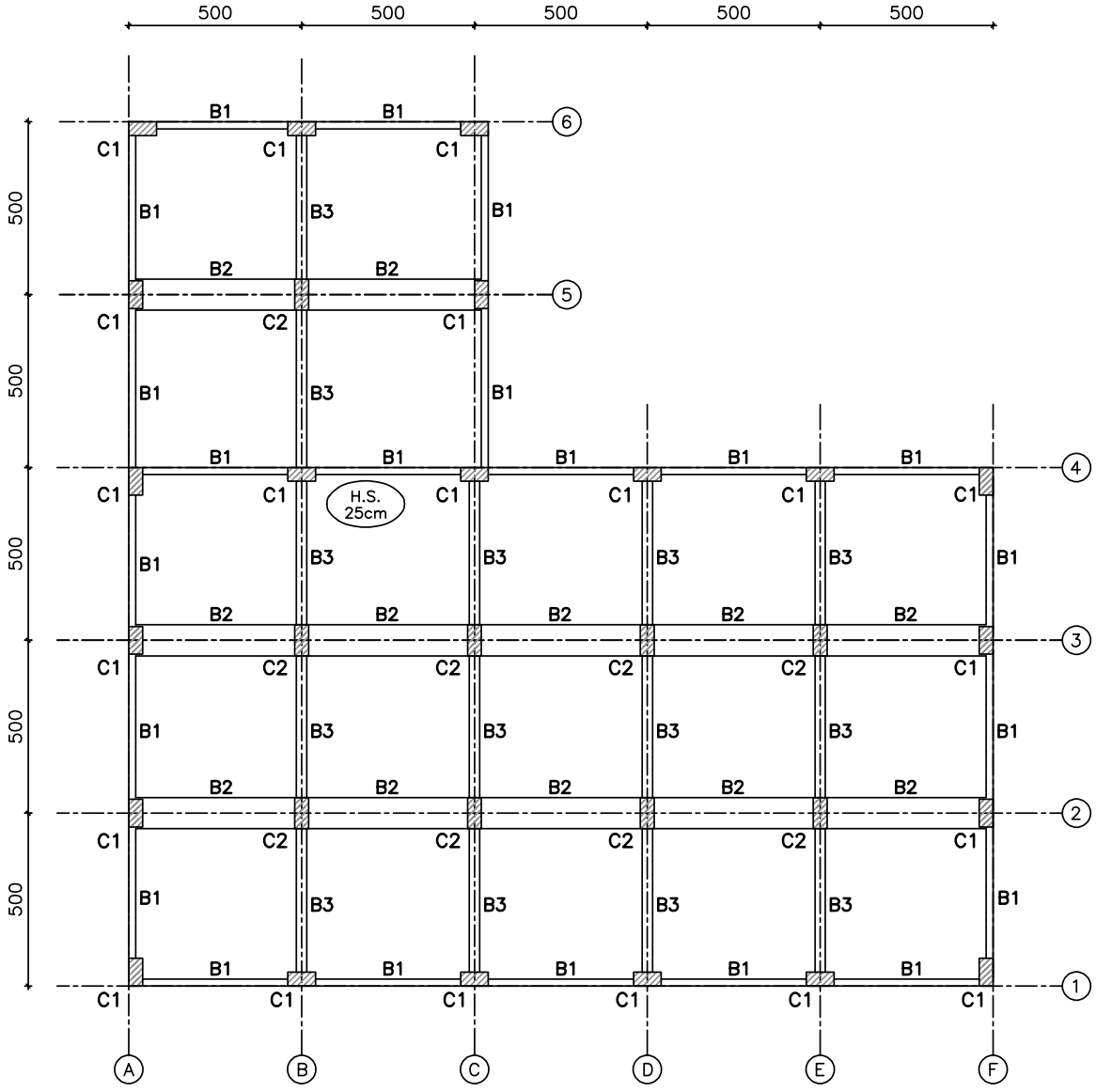


Figure A7. 6: General layout of L-shaped building (Dimensions in cm)

Table A7. 3: Typical dimensions of beams in the L-shaped building (dimensions in mm)

	Storey 1	Storey 2	Storey 3	Storey 4	Storey 5	Storey 6	Storey 7	Storey 8	Storey 9	Storey 10
B1	200x500	200x500	200x500	200x500	200x500	200x500	200x500	200x500	200x500	200x500
B2	900x250	900x250	900x250	900x250	900x250	900x250	900x250	900x250	900x250	900x250
B3	300x250	300x250	300x250	300x250	300x250	300x250	300x250	300x250	300x250	300x250

Table A7. 4: Typical dimensions of columns in the L-shaped building (dimensions in mm)

	Storey 1	Storey 2	Storey 3	Storey 4	Storey 5	Storey 6	Storey 7	Storey 8	Storey 9	Storey 10
C1	400x800	300x700	300x700	200x700	200x700	200x600	200x600	200x600	200x500	200x500
C2	400x900	300x800	300x800	300x700	300x700	300x700	200x600	200x600	200x600	200x600

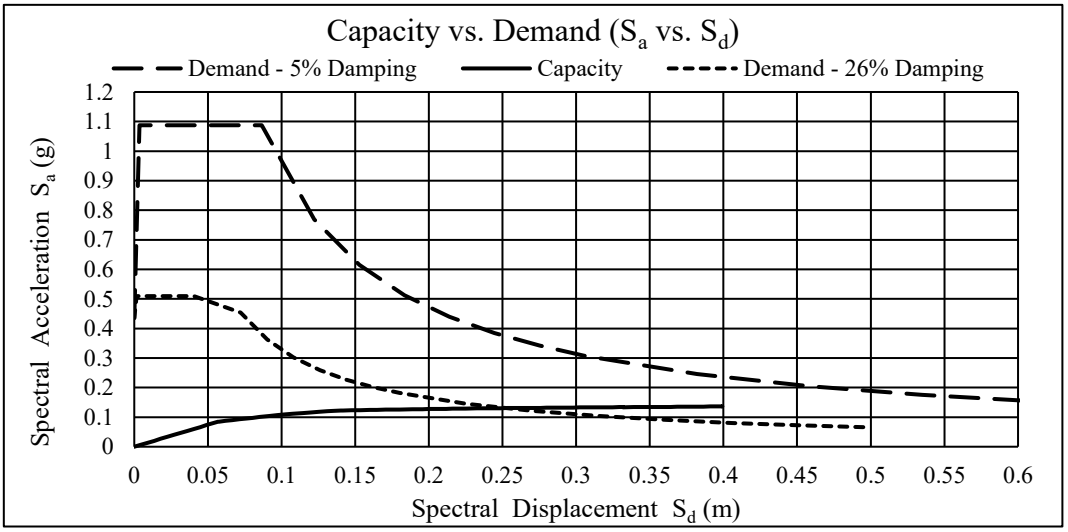


Figure A7. 7: Performance point of the Push-Y analysis (Mode 1) at the NC limit state in the L-shaped building (+5% eccentricity in X)

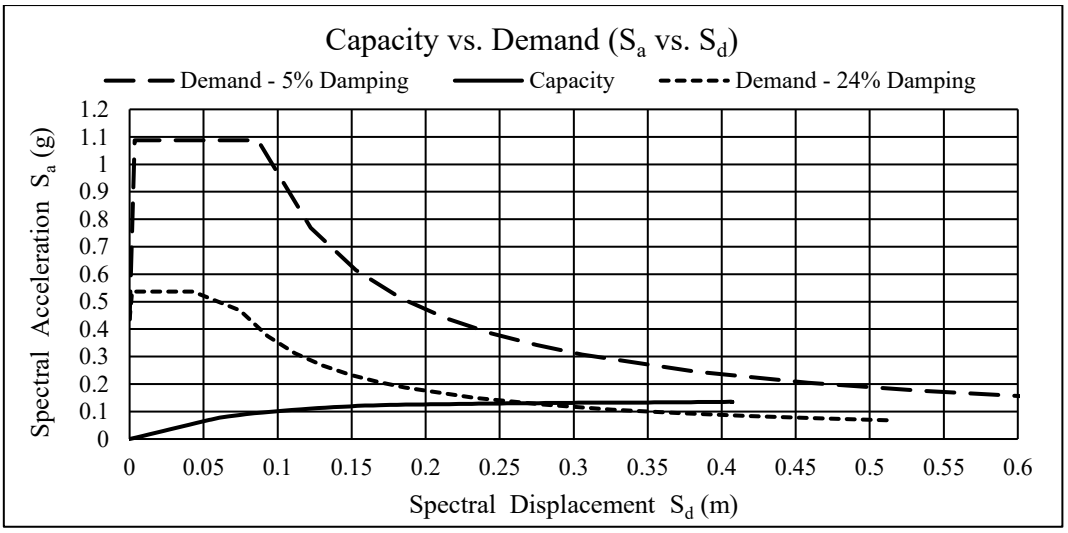


Figure A7. 8: Performance point of the Push-Y analysis (Mode 1) at the NC limit state in the L-shaped building (-5% eccentricity in X)

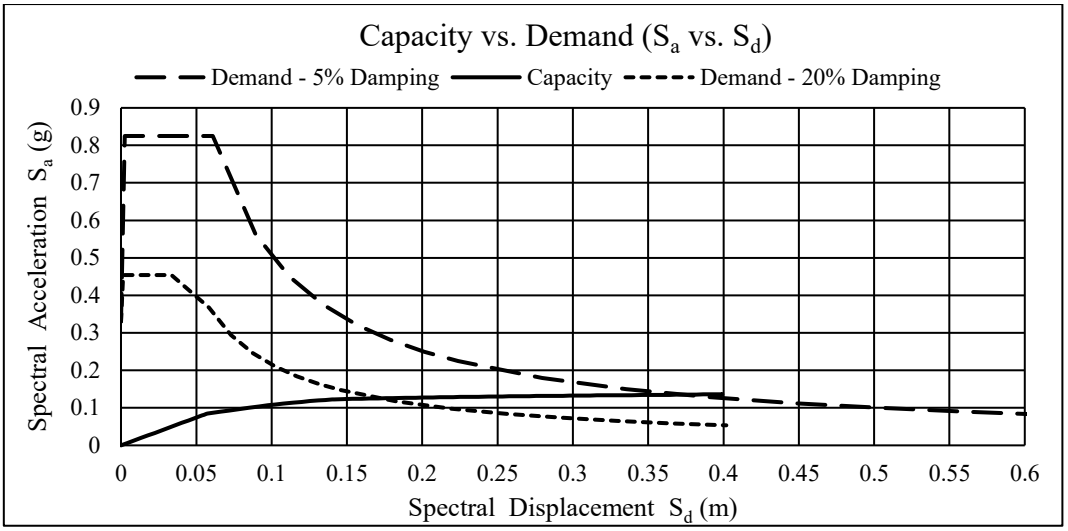


Figure A7. 9: Performance point of the Push-Y analysis (Mode 1) at the SD limit state in the L-shaped building (+5% eccentricity in X)

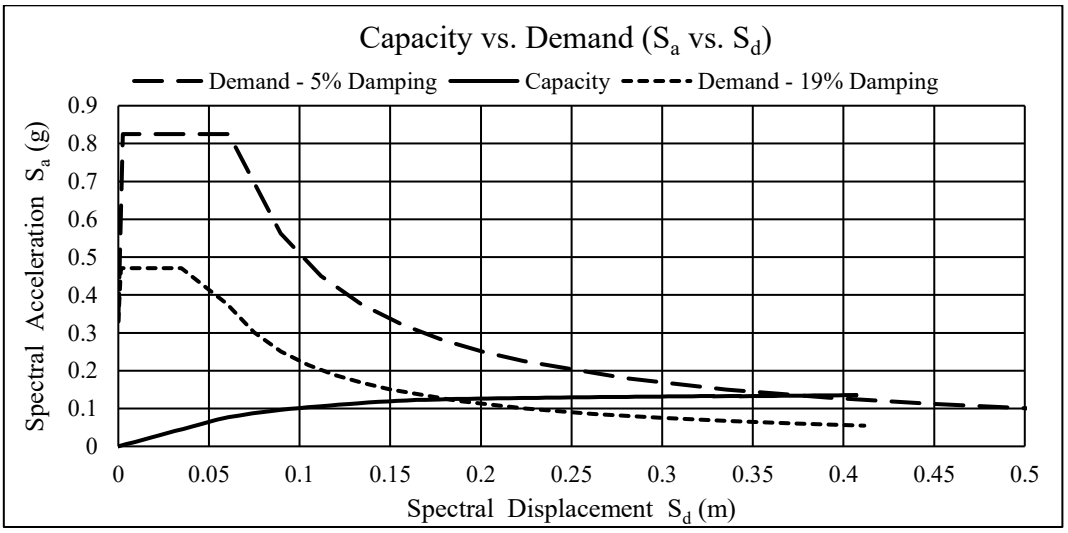


Figure A7. 10: Performance point of the Push-Y analysis (Mode 1) at the SD limit state in the L-shaped building (-5% eccentricity in X)

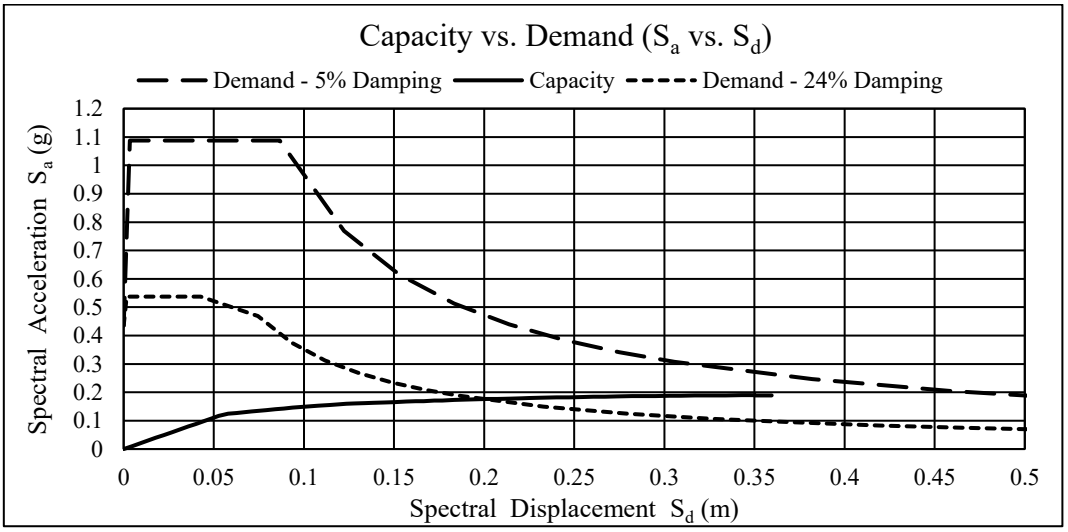


Figure A7. 11: Performance point of the Push-X analysis (Mode 2) at the NC limit state in the L-shaped building (+5% eccentricity in Y)

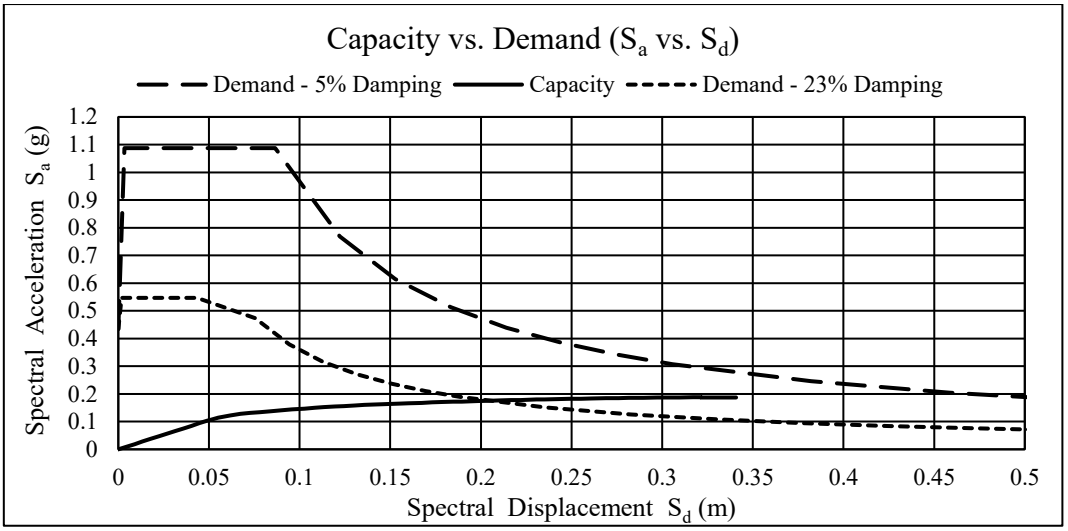


Figure A7. 12: Performance point of the Push-X analysis (Mode 2) at the NC limit state in the L-shaped building (-5% eccentricity in Y)

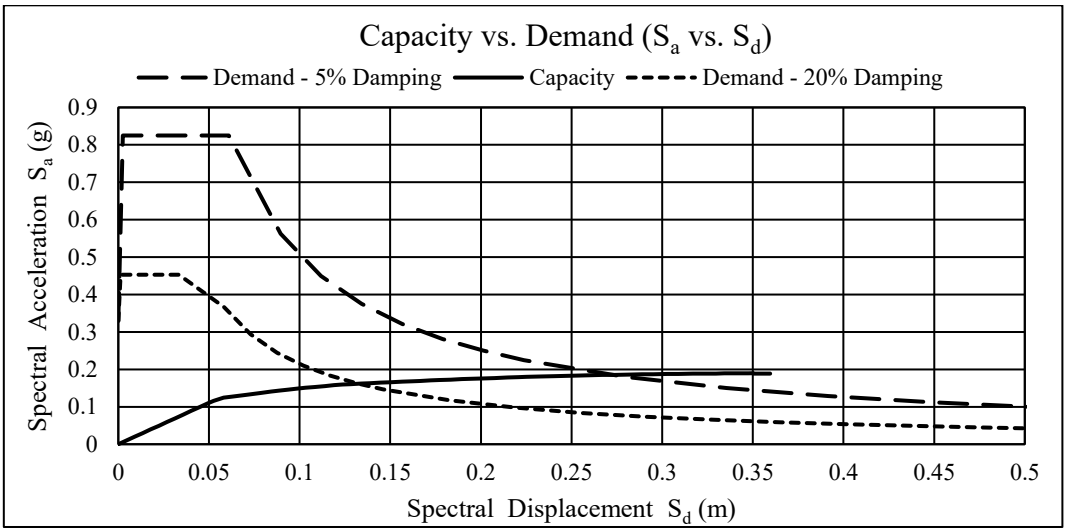


Figure A7. 13: Performance point of the Push-X analysis (Mode 2) at the SD limit state in the L-shaped building (+5% eccentricity in Y)

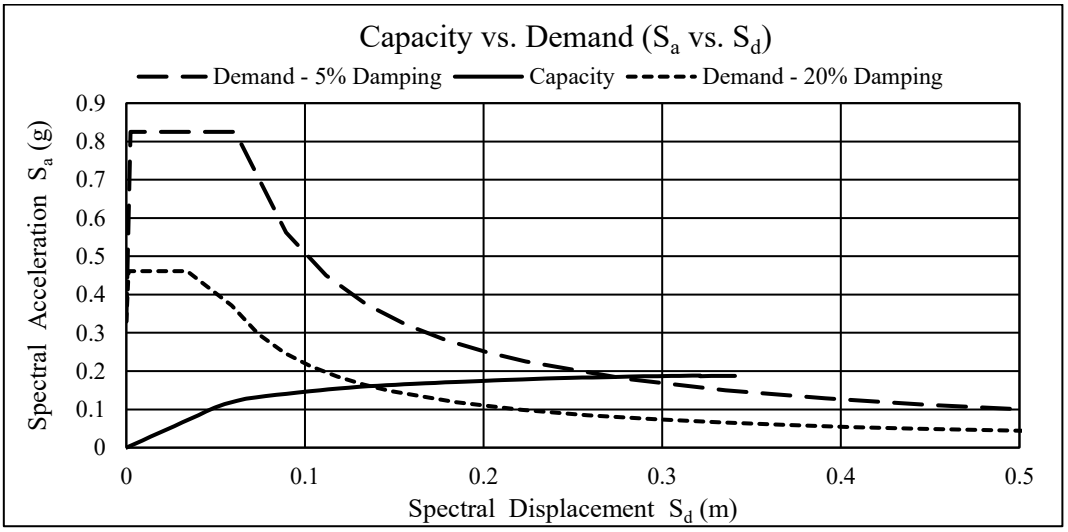


Figure A7. 14: Performance point of the Push-X analysis (Mode 2) at the SD limit state in the L-shaped building (-5% eccentricity in Y)

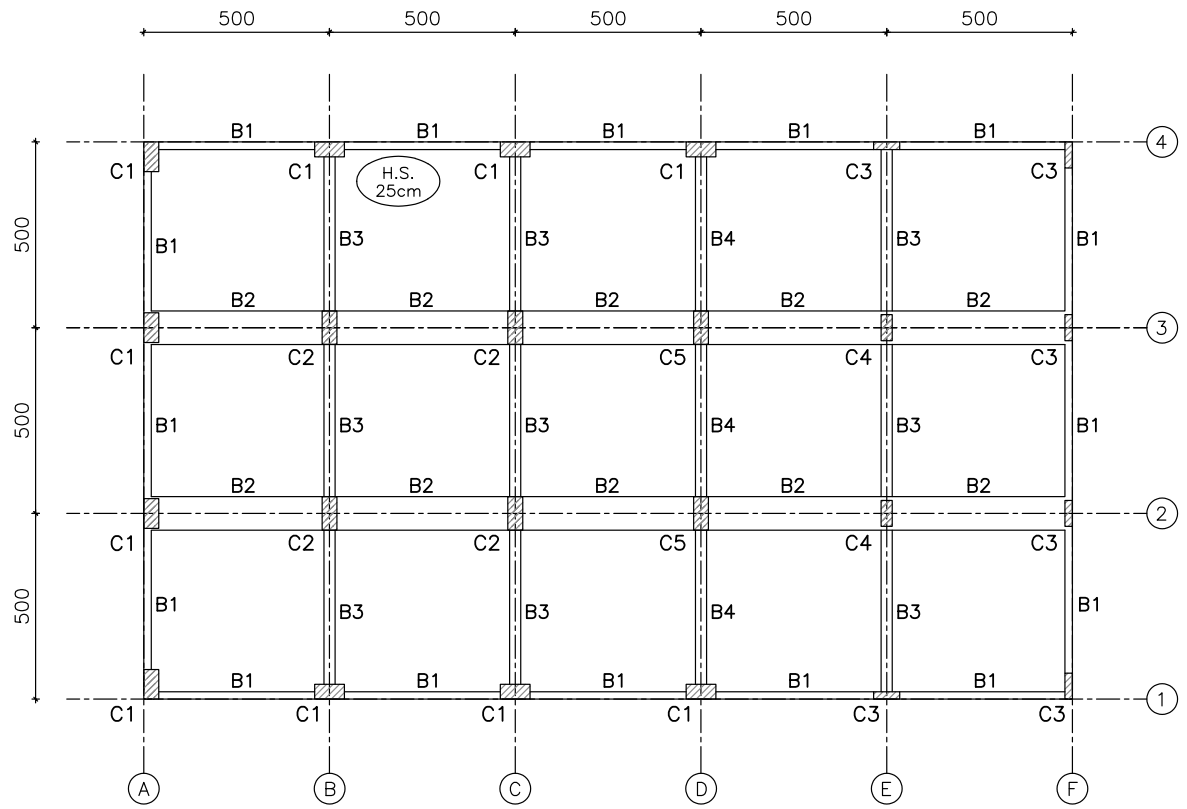


Figure A7. 15: General layout of vertically irregular building from the Ground till the 7th floor (dimensions in cm)

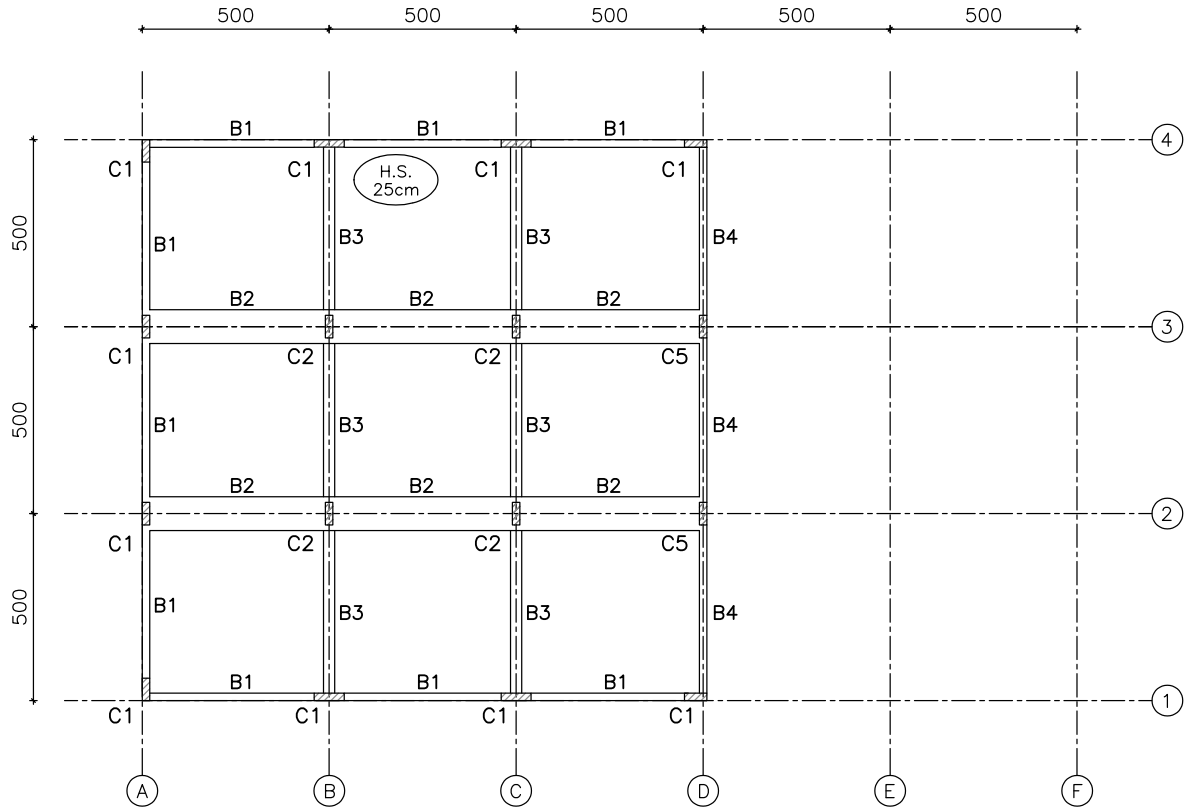


Figure A7. 16: General layout of vertically irregular building from the 8th till the 10th floor (dimensions in cm)

Table A7. 5: Typical dimensions of beams in the vertically irregular building (dimensions in mm)

	Storey 1	Storey 2	Storey 3	Storey 4	Storey 5	Storey 6	Storey 7	Storey 8	Storey 9	Storey 10
B1	200x500	200x500	200x500	200x500	200x500	200x500	200x500	200x500	200x500	200x500
B2	900x250	900x250	900x250	900x250	900x250	900x250	900x250	900x250	900x250	900x250
B3	300x250	300x250	300x250	300x250	300x250	300x250	300x250	300x250	300x250	300x250
B4	300x250	300x250	300x250	300x250	300x250	300x250	300x250	200x500	200x500	200x500

Table A7. 6: Typical dimensions of columns in the vertically irregular building (dimensions in mm)

	Storey 1	Storey 2	Storey 3	Storey 4	Storey 5	Storey 6	Storey 7	Storey 8	Storey 9	Storey 10
C1	400x800	300x700	300x700	200x700	200x700	200x600	200x600	200x600	200x500	200x500
C2	400x900	300x800	300x800	300x700	300x700	300x700	200x600	200x600	200x600	200x600
C3	200x700	200x700	200x600	200x600	200x600	200x500	200x500	-	-	-
C4	300x700	300x700	300x700	200x600	200x600	200x600	200x600	-	-	-
C5	400x900	300x800	300x800	300x700	300x700	300x700	200x600	200x600	200x500	200x500

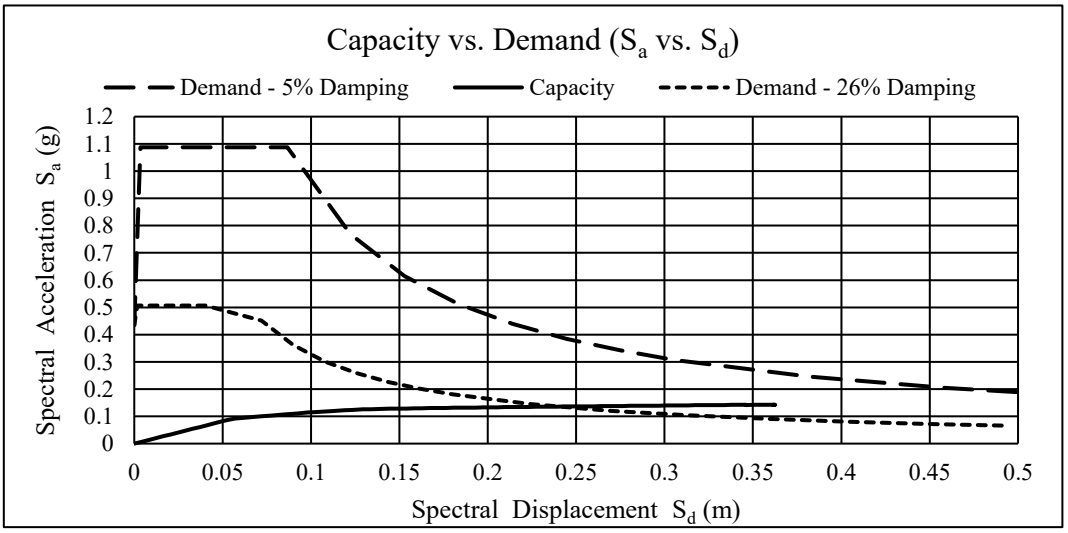


Figure A7. 17: Performance point of the Push-Y analysis (Mode 1) at the NC limit state in the vertically irregular building (+5% eccentricity in X)

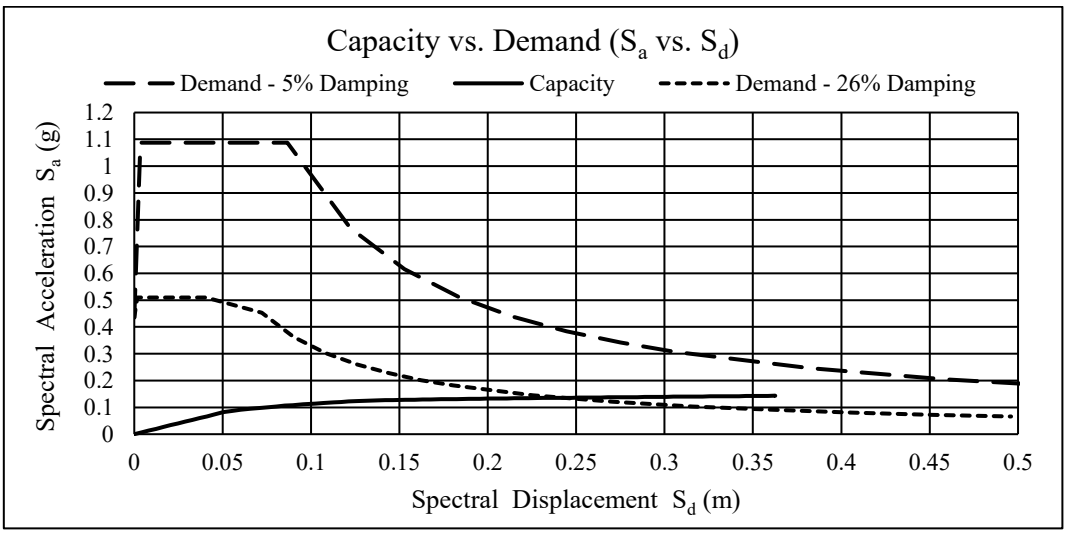


Figure A7. 18: Performance point of the Push-Y analysis (Mode 1) at the NC limit state in the vertically irregular building (-5% eccentricity in X)

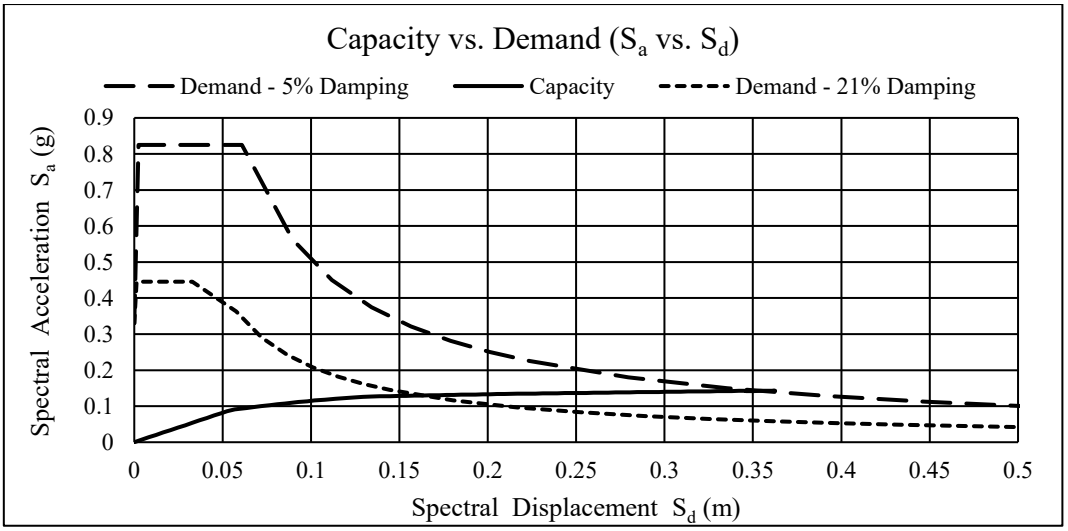


Figure A7. 19: Performance point of the Push-Y analysis (Mode 1) at the SD limit state in the vertically irregular building (+5% eccentricity in X)

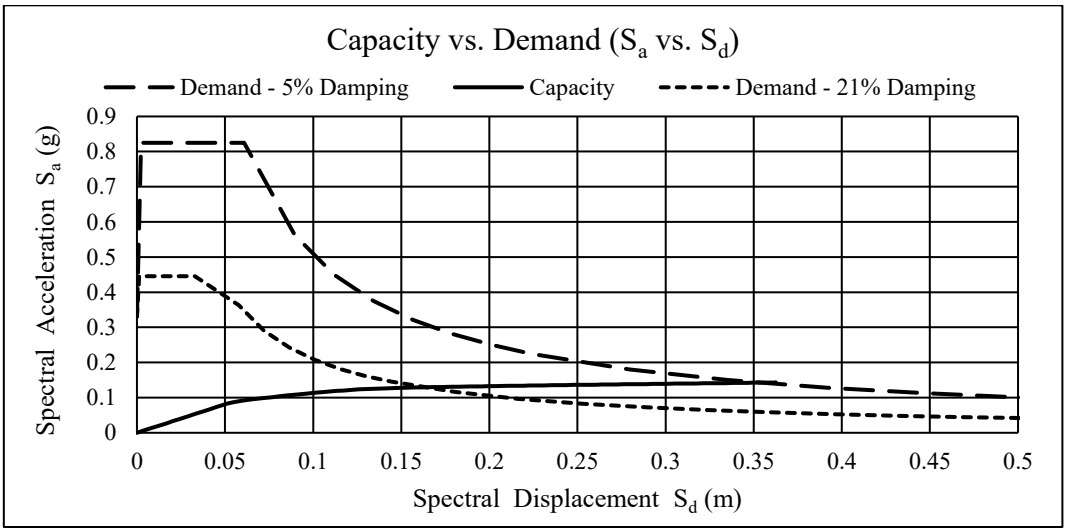


Figure A7. 20: Performance point of the Push-Y analysis (Mode 1) at the SD limit state in the vertically irregular building (-5% eccentricity in X)

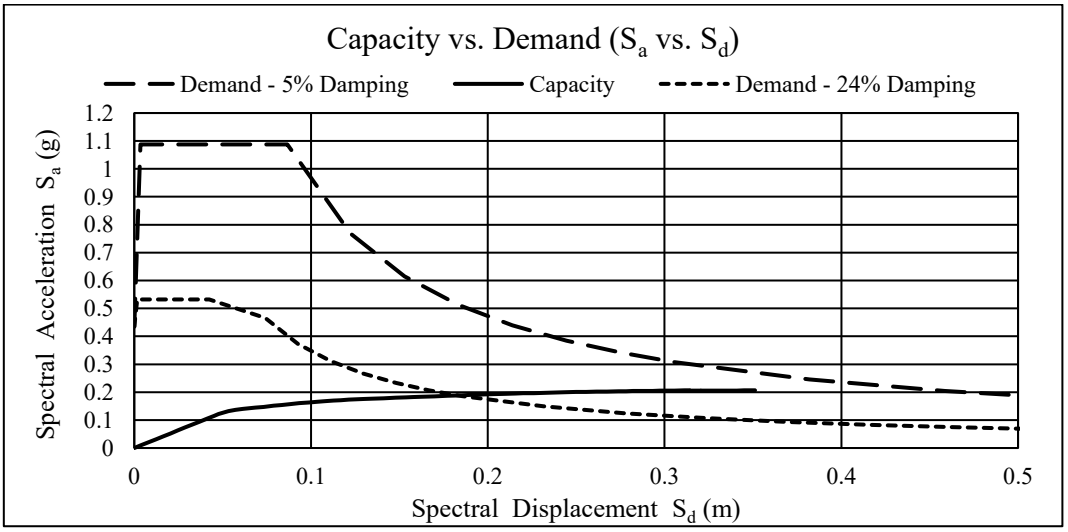


Figure A7. 21: Performance point of the Push-X analysis (Mode 2) at the NC limit state in the vertically irregular building (±5% eccentricity in Y)

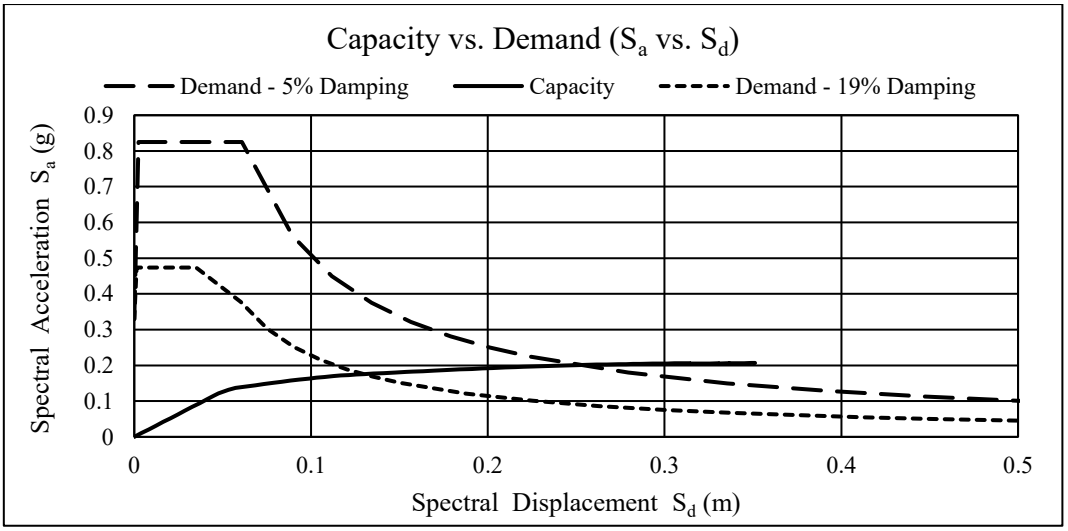


Figure A7. 22: Performance point of the Push-X analysis (Mode 2) at the SD limit state in the vertically irregular building (±5% eccentricity in Y)

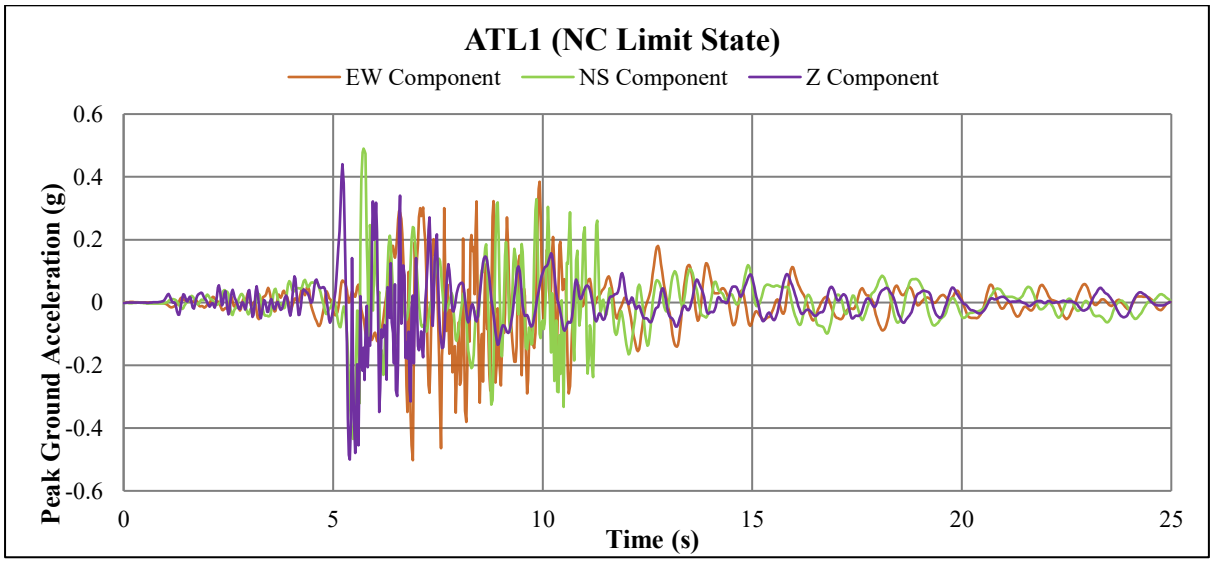


Figure A7. 23: The three components of the artificially generated ground motion "ATL1"

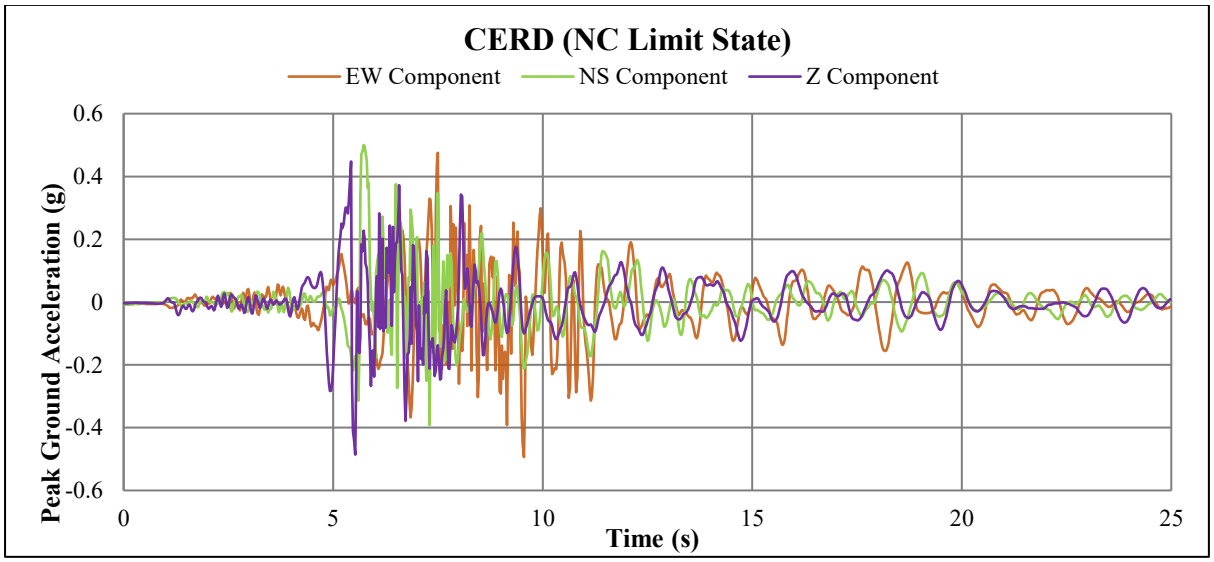


Figure A7. 24: The three components of the artificially generated ground motion "CERD"

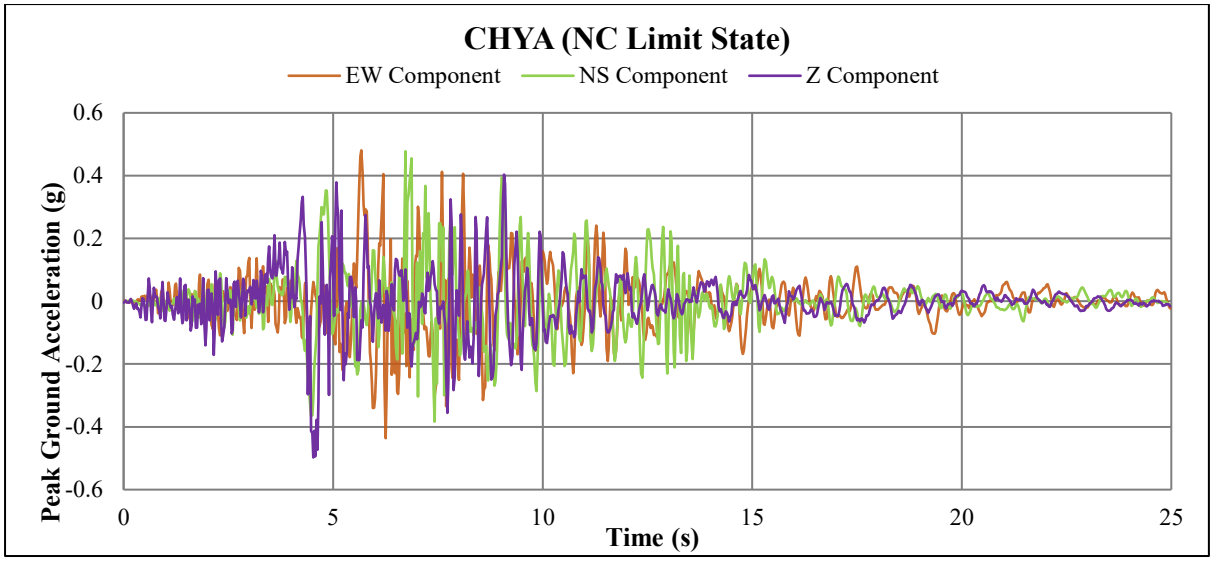


Figure A7. 25: The three components of the artificially generated ground motion "CHYA"

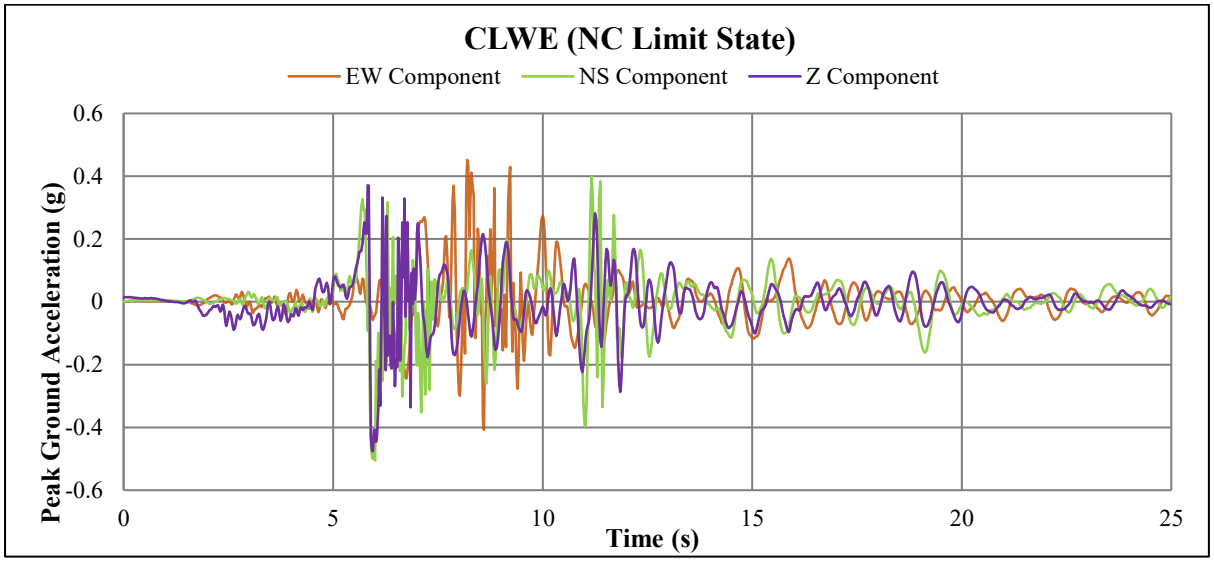


Figure A7. 26: The three components of the artificially generated ground motion "CLWE"

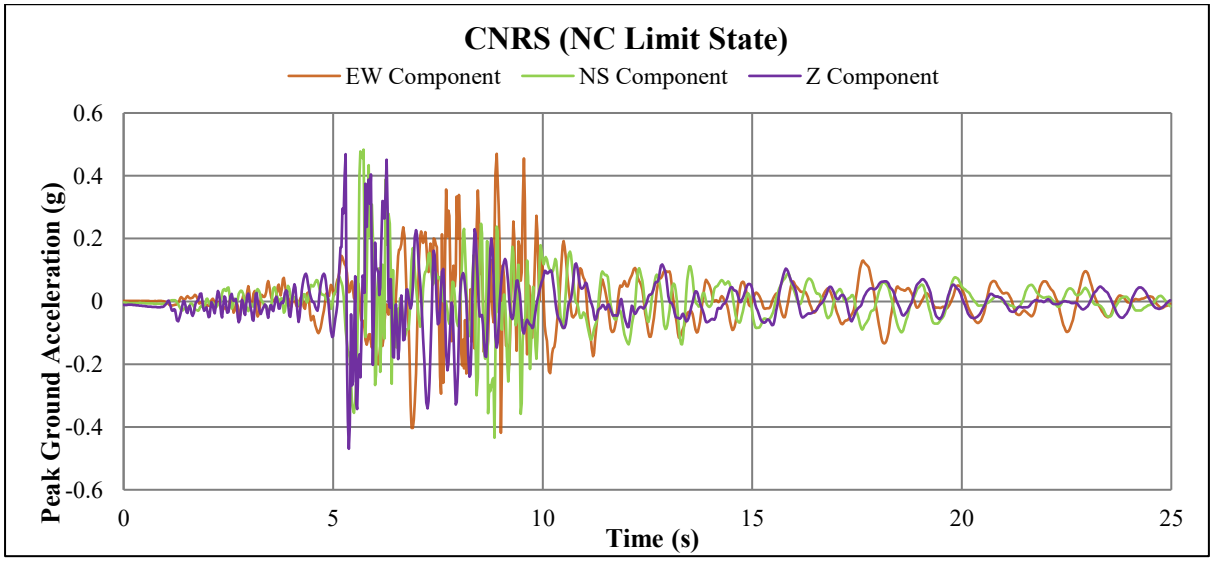


Figure A7. 27: The three components of the artificially generated ground motion "CNRS"

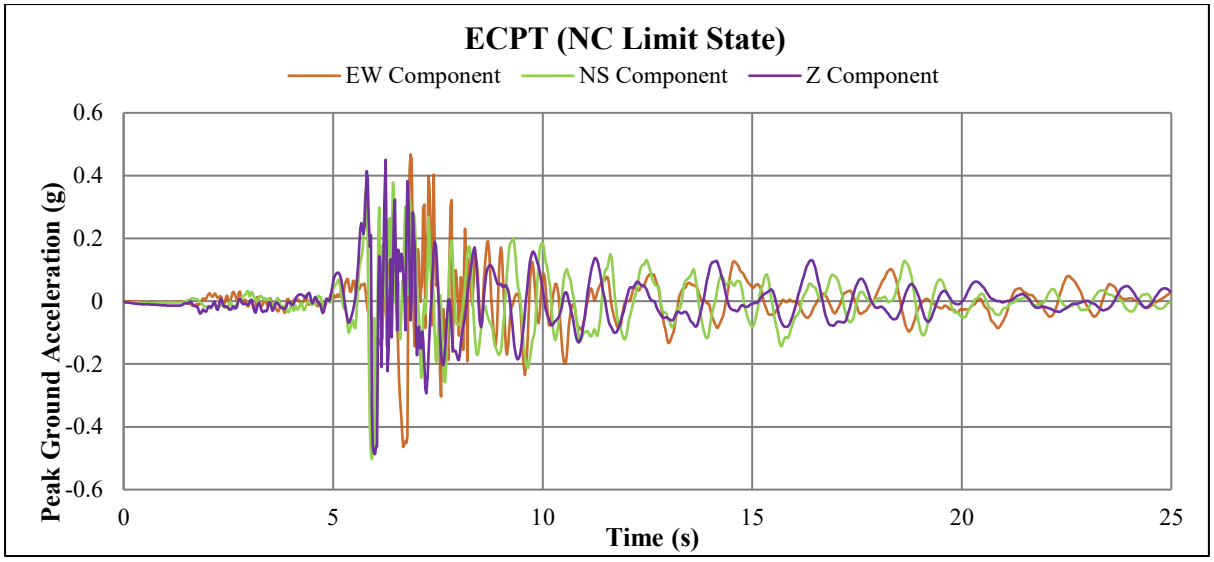


Figure A7. 28: The three components of the artificially generated ground motion "ECPT"

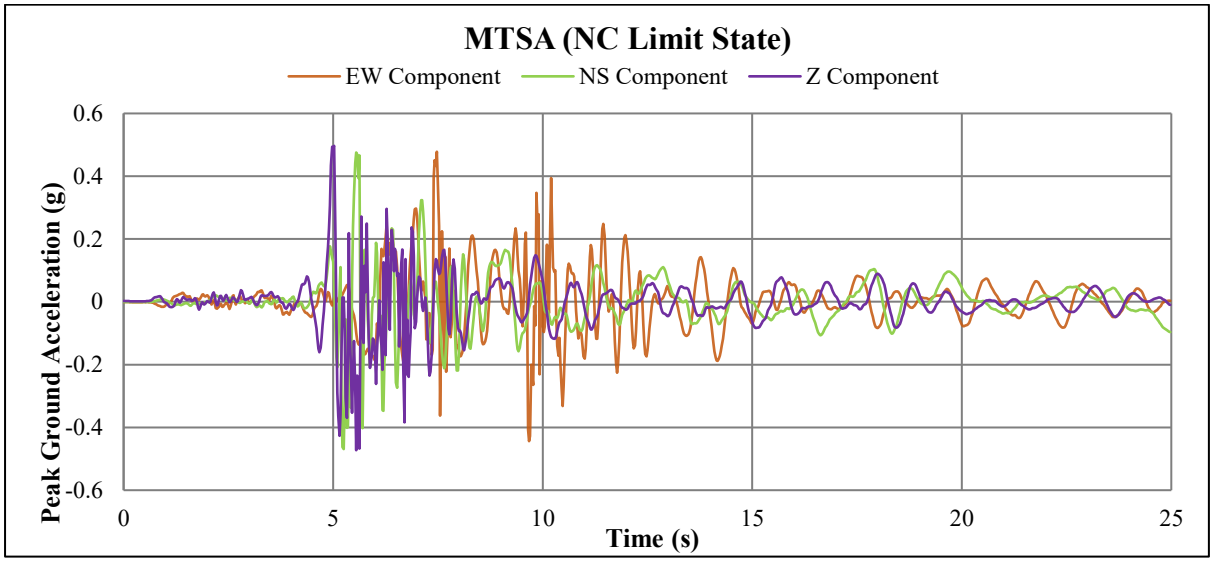


Figure A7. 29: The three components of the artificially generated ground motion "MTSA"

Accidental Torsion

The location of the centre of mass is surrounded with a degree of imprecision because of the spatial variation of the seismic motion and the possible variation of the mass distribution from the nominal one. To this end, most design codes including EC8-1 (CEN, 2004a) entail checking for accidental torsion effects by shifting the centre of mass from its actual position by an accidental eccentricity applied in the same direction at all floors. This procedure is recommended by EC8-1 (CEN, 2004a) if nonlinear static or dynamic analysis is adopted for the design or checking of buildings. Accordingly, four different spatial models are required to cover accidental torsion effects including all possible scenarios of accidental eccentricity (Figure A7.30). In each case, the total storey mass is lumped at a point located away from the nominal centre of mass by a distance equal to the accidental eccentricity which is measured in the same direction at all storeys (Figure A7.30). The accidental eccentricity is determined according to the following expression:

$$e_i = \pm 0.05 L_i \quad \text{(A7.1)}$$

where:

L_i is the floor dimension perpendicular to the direction of the seismic action.

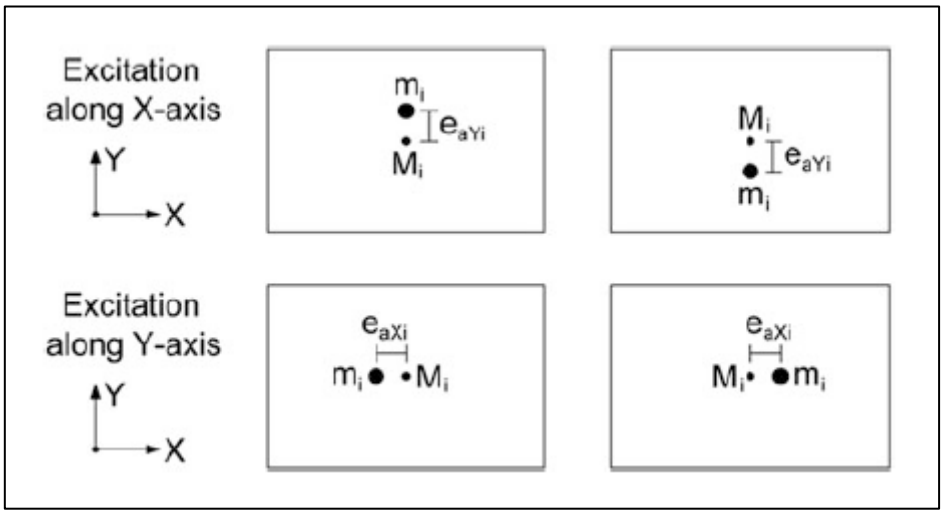


Figure A7. 30: Analysis cases considering all possible scenarios of accidental eccentricity (Avramidis et al., 2016)